Climate impacts of oxygen in the atmosphere *pp. 1210 & 1238*

How our brains remember to keep us breathing *p. 1255*

Sex conversion makes a harmless mosquito *p. 1268*

Science

$10
12 JUNE 2015
sciencemag.org

AAAS

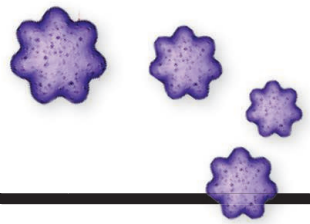


Entrepreneurial dreams

From campus to commercialization

pp. 1179, 1190, & 1200

CONTENTS



1207 & 1251
Bacterial metabolite drives immunity

12 JUNE 2015 • VOLUME 348 • ISSUE 6240



NEWS

IN BRIEF

1180 Roundup of the week's news

IN DEPTH

1183 AMID PANIC, A CHANCE TO LEARN ABOUT MERS
South Korea's explosive outbreak gives scientists fresh opportunities to study the virus *By K. Kupferschmidt*

1184 SIGNS OF ANCIENT PROTEINS SEEN INSIDE DINOSAUR BONES
Can soft tissue survive 75 million years? *By R. F. Service*

1185 DINOSAUR CLIMATE PROBED
Ancient lake sediments in China record epic temperature swings, biotic turnover before the mass extinction *By J. Qiu*

1186 BRAIN IMPLANT TRIALS RAISE ETHICAL CONCERNS
NIH workshop delves into challenges of testing invasive neuromodulation technology *By E. Underwood*

1187 THE SCIENTIST BEHIND THE 'PERSONHOOD' CHIMPS
Susan Larson defends her work with two research chimpanzees at the heart of a legal battle *By D. Grimm*

1188 HIV FAMILY TREES REVEAL VIRAL SPREAD
New studies could aid public health efforts *By J. Cohen*

FEATURES

1190 BUSINESS DECISIONS
What does it take for an academic scientist to become an entrepreneur? Here are some of their stories *By J. Mervis*
▸ EDITORIAL P. 1179; PERSPECTIVES P. 1200; QUIZ

1194 GIVE US YOUR BEST PITCH
Two venture capitalists explain the investor's mindset *By J. Cohen*
▸ EDITORIAL P. 1179; PERSPECTIVES P. 1200

1196 GOT A STARTUP? RENT A BENCH
Biotech incubators such as LabCentral are lowering barriers to entrepreneurship *By T. Gura*
▸ EDITORIAL P. 1179; PERSPECTIVES P. 1200

INSIGHTS

PERSPECTIVES

ENTREPRENEURSHIP

1200 Financing experiments
By R. Nanda and M. Rhodes-Kropf

1200 Founders and joiners
By M. Roach and H. Sauermann

1201 Cash from the crowd
By M. G. Colombo et al.

1202 Intangible but bankable
By Y. V. Hochberg et al.

1202 Accelerators and ecosystems
By Y. V. Hochberg and D. C. Fehder

1203 Linking and leveraging
By F. Murray and S. Stern
▸ EDITORIAL P. 1179; NEWS STORIES PP. 1190, 1194, & 1196



1204 EARTHQUAKES INDUCED BY FLUID INJECTIONS
Controlling fluid injection may mitigate the extent of induced earthquakes *By F. H. Cornet*
▸ REPORT P. 1224

1205 MAKING HEADS OR TAILS OF SHATTERED CHROMOSOMES
Isolation of lagging chromosomes in micronuclei causes catastrophic genome rearrangements *By W. P. Kloosterman*

1207 MICROBIAL METABOLITE TRIGGERS ANTIMICROBIAL DEFENSE
Bacteria can activate innate immune responses by releasing a metabolite that enters host cells *By S. W. Brubaker and D. M. Monack*
▸ REPORT P. 1251

1208 BRINGING PGE_2 IN FROM THE COLD
A small molecule that prevents the breakdown of a prostaglandin promotes tissue regeneration *By G. A. FitzGerald*
▸ RESEARCH ARTICLE P. 1223

1210 CAN CLIMATE FEEL THE PRESSURE?
Changes in atmospheric pressure may be an important long-term climate forcing mechanism *By D. J. Peppe and D. L. Royer*
▸ REPORT P. 1238

1211 ECONOMICAL ROUTES TO COLLOIDAL NANOCRYSTALS
A new precursor library yields high-quality quantum dots for device applications *By Z. Hens*
▸ REPORT P. 1226

1212 VISUAL TRACKING IN THE DEAD OF NIGHT
Even in dim light, hawkmoths can track the motions of wind-tossed flowers *By E. Warrant*
▸ REPORT P. 1245

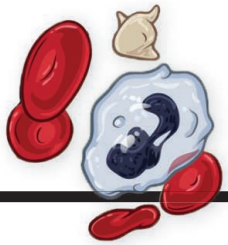
BOOKS *ET AL.*

1214 THE OUTSOURCER
By D. C. Sharma, reviewed by S. Banerjee

1215 THE END OF PLENTY
By J. K. Bourne Jr., reviewed by J. L. Steiner

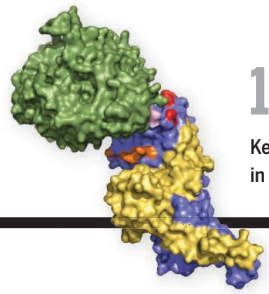
Science Staff 1178
New Products 1274
Science Careers 1275

Published by AAAS



1208 & 1223

Accelerating tissue regeneration



1260 & 1264

Keeping the cell cycle in check

LETTERS

1216 DEFINING THE HAPPINESS GAP
By A. Van Hiel et al.

1216 RESPONSE
By S. P. Wojcik et al.

1216 PROTECT RESEARCHERS FROM HARASSMENT
By S. E. Hyman and M. E. Goldberg

1217 TECHNICAL COMMENT ABSTRACTS

RESEARCH

IN BRIEF

1218 From *Science* and other journals

REVIEWS

ECOLOGY

1221 Aquatic animal telemetry: A panoramic window into the underwater world *N. E. Hussey* et al.
REVIEW SUMMARY; FOR FULL TEXT: dx.doi.org/10.1126/science.1255642
▸ PODCAST

1222 Terrestrial animal tracking as an eye on life and planet *R. Kays* et al.
REVIEW SUMMARY; FOR FULL TEXT: dx.doi.org/10.1126/science.aaa2478

RESEARCH ARTICLE

1223 TISSUE REGENERATION
Inhibition of the prostaglandin-degrading enzyme 15-PGDH potentiates tissue regeneration *Y. Zhang* et al.
RESEARCH ARTICLE SUMMARY; FOR FULL TEXT: dx.doi.org/10.1126/science.aaa2340
▸ PERSPECTIVE P. 1208

REPORTS

1224 INDUCED SEISMICITY
Seismicity triggered by fluid injection–induced aseismic slip *Y. Guglielmi* et al.
▸ PERSPECTIVE P. 1204



1212 & 1245

1226 NANOMATERIALS
A tunable library of substituted thiourea precursors to metal sulfide nanocrystals *M. P. Hendricks* et al.
▸ PERSPECTIVE P. 1211

1230 ELECTROCHEMISTRY
High-performance transition metal–doped Pt_3Ni octahedra for oxygen reduction reaction *X. Huang* et al.

1234 SOLAR CELLS
High-performance photovoltaic perovskite layers fabricated through intramolecular exchange *W. S. Yang* et al.

1238 CLIMATE CHANGE
Long-term climate forcing by atmospheric oxygen concentrations *C. J. Poulsen* et al.
▸ PERSPECTIVE P. 1210

1241 BRAIN NETWORKS
Correlated gene expression supports synchronous activity in brain networks *J. Richiardi* et al.

1245 INSECT FLIGHT
Luminance-dependent visual processing enables moth flight in low light *S. Sponberg* et al.
▸ PERSPECTIVE P. 1212

1248 BIOGEOGRAPHY
The dispersal of alien species redefines biogeography in the Anthropocene *C. Capinha* et al.

1251 INNATE IMMUNITY
Cytosolic detection of the bacterial metabolite HBP activates TIFA-dependent innate immunity *R. G. Gaudet* et al.
▸ PERSPECTIVE P. 1207

1255 PHYSIOLOGY
Regulation of breathing by CO_2 requires the proton-activated receptor GPR4 in retrotrapezoid nucleus neurons *N. N. Kumar* et al.

CELL DIVISION CYCLE

1260 Kinetochore attachment sensed by competitive Mps1 and microtubule binding to Ndc80C *Z. Ji* et al.

1264 Competition between MPS1 and microtubules at kinetochores regulates spindle checkpoint signaling *Y. Hiruma* et al.

1268 SEX DETERMINATION
A male-determining factor in the mosquito *Aedes aegypti A. B. Hall* et al.

DEPARTMENTS

1179 EDITORIAL
The entrepreneurial gardeners
By Iqbal Quadir
▸ NEWS STORIES PP. 1190, 1194, & 1196; PERSPECTIVES P. 1200

1282 WORKING LIFE
You'll be OK
By Michelle E. Portman

ON THE COVER



With governments pushing for innovations to bolster economies and universities eager to make money off of technology transfer, academic scientists are increasingly considering how to commercialize their research discoveries—and others are studying what makes such entrepreneurship flourish. See pages 1179, 1190, 1194, 1196, and 1200. *Illustration: Davide Bonazzi*

SCIENCE (ISSN 0036-8075) is published weekly on Friday, except the last week in December, by the American Association for the Advancement of Science, 1200 New York Avenue, NW, Washington, DC 20005. Periodicals mail postage (publication No. 484460) paid at Washington, DC, and additional mailing offices.

Copyright © 2015 by the American Association for the Advancement of Science. The title SCIENCE is a registered trademark of the AAAS.

Domestic individual membership and subscription (51 issues): $153 ($74 allocated to subscription). Domestic institutional subscription (51 issues): $1282; Foreign postage extra: Mexico, Caribbean (surface mail) $55; other countries (air assist delivery) $85. First class, airmail, student, and emeritus rates on request. Canadian rates with GST available upon request, GST #1254 88122. Publications Mail Agreement Number 1069624. **Printed in the U.S.A.**
Change of address: Allow 4 weeks, giving old and new addresses and 8-digit account number. **Postmaster:** Send change of address to AAAS, P.O. Box 96178, Washington, DC 20090–6178. **Single-copy sales:** $10.00 current issue, $15.00 back issue prepaid includes surface postage; bulk rates on request.

Authorization to photocopy material for internal or personal use under circumstances not falling within the fair use provisions of the Copyright Act is granted by AAAS to libraries and other users registered with the Copyright Clearance Center (CCC) Transactional Reporting Service, provided that $30.00 per article is paid directly to CCC, 222 Rosewood Drive, Danvers, MA 01923. The identification code for *Science* is 0036-8075. *Science* is indexed in the *Reader's Guide to Periodical Literature* and in several specialized indexes.

Published by AAAS

Science
AAAS
1200 New York Avenue, NW, Washington, DC 20005
Bateman House, 82-88 Hills Road, Cambridge, UK CB2 1LQ

Editor-in-Chief Marcia McNutt
Executive Editor Monica M. Bradford **News Editor** Tim Appenzeller
Managing Editor, Research Journals Katrina L. Kelner
Deputy Editors Barbara R. Jasny, Andrew M. Sugden(UK), Valda J. Vinson, Jake S. Yeston

Research and Insights

SR. EDITORS Caroline Ash(UK), Gilbert J. Chin, Lisa D. Chong, Julia Fahrenkamp-Uppenbrink(UK), Pamela J. Hines, Stella M. Hurtley(UK), Paula A. Kiberstis, Marc S. Lavine(Canada), Kristen L. Mueller, Ian S. Osborne(UK), Beverly A. Purnell, L. Bryan Ray, Guy Riddihough, H. Jesse Smith, Jelena Stajic, Peter Stern(UK), Phillip D. Szuromi, Brad Wible, Nicholas S. Wigginton, Laura M. Zahn **ASSOCIATE EDITORS** Brent Grocholski, Sacha Vignieri **ASSOCIATE BOOK REVIEW EDITOR** Valerie B. Thompson **ASSOCIATE LETTERS EDITOR** Jennifer Sills **CHIEF CONTENT PRODUCTION EDITOR** Cara Tate **SR. CONTENT PRODUCTION EDITORS** Harry Jach **CONTENT PRODUCTION EDITORS** Jeffrey E. Cook, Chris Filiatreau, Cynthia Howe, Lauren Kmec, Barbara P. Ordway **SR. EDITORIAL COORDINATORS** Carolyn Kyle, Beverly Shields **EDITORIAL COORDINATORS** Ramatoulaye Diop, Joi S. Granger, Lisa Johnson, Anita Wynn **PUBLICATIONS ASSISTANTS** Aneera Dobbins, Jeffrey Hearn, Dona Mathieu, Le-Toya Mayne Flood, Shannon McMahon, Scott Miller, Jerry Richardson, Rachel Roberts(UK), Alice Whaley(UK), Brian White **EXECUTIVE ASSISTANT** Anna Bashkirova **ADMINISTRATIVE SUPPORT** Janet Clements(UK), Monika Magon(UK, Intern), Lizanne Newton(UK), Maryrose Madrid, John Wood(UK)

News

NEWS MANAGING EDITOR John Travis **INTERNATIONAL EDITOR** Richard Stone **DEPUTY NEWS EDITORS** Daniel Clery(UK), Robert Coontz, Elizabeth Culotta, David Grimm, David Malakoff, Leslie Roberts **CONTRIBUING EDITOR** Martin Enserink(Europe) **SR. CORRESPONDENTS** Jeffrey Mervis, Elizabeth Pennisi **NEWS WRITERS** Adrian Cho, Jon Cohen, Jennifer Couzin-Frankel, Carolyn Gramling, Eric Hand, Jocelyn Kaiser, Catherine Matacic, Kelly Servick, Robert F. Service, Erik Stokstad(Cambridge, UK), Emily Underwood **INTERNS** Emily Conover, Emily DeMarco **CONTRIBUTING CORRESPONDENTS** Michael Balter(Paris), John Bohannon, Ann Gibbons, Mara Hvistendahl, Sam Kean, Richard A. Kerr, Eli Kintisch, Kai Kupferschmidt(Berlin), Andrew Lawler, Christina Larson(Beijing), Mitch Leslie, Charles C. Mann, Eliot Marshall, Virginia Morell, Dennis Normile(Tokyo), Heather Pringle, Tania Rabesandratana(London), Gretchen Vogel(Berlin), Lizzie Wade(Mexico City) **CAREERS** Jim Austin(Editor), Donisha Adams, Rachel Bernstein **COPY EDITORS** Kara Estelle (Chief), Julia Cole, Jennifer Levin **ADMINISTRATIVE SUPPORT** Jessica Williams

Executive Publisher Rush D. Holt
Publisher Kent R. Anderson **Chief Digital Media Officer** Rob Covey

BUSINESS OPERATIONS AND ADMINISTRATION DIRECTOR Sarah Whalen **BUSINESS SYSTEMS AND FINANCIAL ANALYSIS DIRECTOR** Randy Yi **MANAGER OF FULFILLMENT SYSTEMS** Neal Hawkins **SYSTEMS ANALYST** Nicole Mehmedovich **ASSISTANT DIRECTOR, BUSINESS OPERATIONS** Eric Knott **MANAGER, BUSINESS OPERATIONS** Jessica Tierney **BUSINESS ANALYSTS** Cory Lipman, Cooper Tilton, Celeste Troxler **FINANCIAL ANALYST** Robert Clark **RIGHTS AND PERMISSIONS ASSISTANT DIRECTOR** Emilie David **PERMISSIONS ASSOCIATE** Elizabeth Sandler **RIGHTS, CONTRACTS, AND LICENSING ASSOCIATE** Lili Kiser

MARKETING DIRECTOR Ian King **MARKETING MANAGER** Julianne Wielga **MARKETING ASSOCIATE** Elizabeth Sattler **SR. MARKETING EXECUTIVE** Jennifer Reeves **SR. ART ASSOCIATE, PROJECT MANAGER** Tzeitel Sorrosa **ART ASSOCIATE** Seil Lee **JR. ART ASSOCIATE** Kim Huynh **ASSISTANT COMMERCIAL EDITOR** Selby Frame **MARKETING PROJECT MANAGER** Angelissa McArthur **PROGRAM DIRECTOR, AAAS MEMBER CENTRAL** Peggy Mihelich **FULFILLMENT SYSTEMS AND OPERATIONS** membership@aaas.org **MANAGER, MEMBER SERVICES** Pat Butler **SPECIALISTS** LaToya Casteel, Terrance Morrison, Latasha Russell **MANAGER, DATA ENTRY** Mickie Napoleoni **DATA ENTRY SPECIALISTS** JJ Regan, Brenden Aquilino, Fiona Giblin

DIRECTOR, SITE LICENSING Tom Ryan **DIRECTOR, CORPORATE RELATIONS** Eileen Bernadette Moran **SR. PUBLISHER RELATIONS SPECIALIST** Kiki Forsythe **PUBLISHER RELATIONS MANAGER** Catherine Holland **PUBLISHER RELATIONS, EASTERN REGION** Keith Layson **PUBLISHER RELATIONS, WESTERN REGION** Ryan Rexroth **SALES RESEARCH COORDINATOR** Aiesha Marshall **MANAGER, SITE LICENSE OPERATIONS** Iquo Edim **SENIOR PRODUCTION SPECIALIST** Robert Koepke **SENIOR OPERATIONS ANALYST** Lana Guz **FULFILLMENT ANALYST** Judy Lillibridge **ASSOCIATE DIRECTOR, MARKETING** Christina Schlecht **MARKETING ASSOCIATES** Thomas Landreth, Isa Sesay-Bah

DIRECTOR OF WEB TECHNOLOGIES Ahmed Khadr **SR. DEVELOPER** Chris Coleman **DEVELOPERS** Dan Berger, Jimmy Marks **SR. PROJECT MANAGER** Trista Smith **SYSTEMS ENGINEER** Luke Johnson

CREATIVE DIRECTOR, MULTIMEDIA Martyn Green **DIRECTOR OF ANALYTICS** Enrique Gonzales **SR. WEB PRODUCER** Sarah Crespi **WEB PRODUCER** Alison Crawford **VIDEO PRODUCER** Nguyen Nguyen **SOCIAL MEDIA PRODUCER** Meghna Sachdev

DIRECTOR OF OPERATIONS PRINT AND ONLINE Lizabeth Harman **DIGITAL/PRINT STRATEGY MANAGER** Jason Hillman **QUALITY TECHNICAL MANAGER** Marcus Spiegler **DIGITAL PRODUCTION MANAGER** Lisa Stanford **ASSISTANT MANAGER DIGITAL/PRINT** Rebecca Doshi **DIGITAL MEDIA SPECIALIST** Tara Kelly **SENIOR CONTENT SPECIALISTS** Steve Forrester, Antoinette Hodal, Lori Murphy, Anthony Rosen **CONTENT SPECIALISTS** Jacob Hedrick, Kimberley Oster

DESIGN DIRECTOR Beth Rakouskas **DESIGN EDITOR** Marcy Atarod **SENIOR SCIENTIFIC ILLUSTRATORS** Chris Bickel, Katharine Sutliff **SCIENTIFIC ILLUSTRATOR** Valerie Altounian **SENIOR ART ASSOCIATES** Holly Bishop, Preston Huey **SENIOR DESIGNER** Garvin Grullón **DESIGNER** Chrystal Smith **SENIOR PHOTO EDITOR** William Douthitt **PHOTO EDITORS** Leslie Blizard, Christy Steele

DIRECTOR, GLOBAL COLLABORATION, CUSTOM PUBLICATIONS, ADVERTISING Bill Moran **EDITOR, CUSTOM PUBLISHING** Sean Sanders: 202-326-6430 **ASSISTANT EDITOR, CUSTOM PUBLISHING** Tianna Hicklin: 202-326-6463 **ADVERTISING MARKETING MANAGER** Justin Sawyers: 202-326-7061 science_advertising@aaas.org **ADVERTISING MARKETING ASSOCIATE** Javia Flemmings **ADVERTISING SUPPORT MANAGER** Karen Foote: 202-326-6740 **ADVERTISING PRODUCTION OPERATIONS MANAGER** Deborah Tompkins **SR. PRODUCTION SPECIALIST/GRAPHIC DESIGNER** Amy Hardcastle **PRODUCTION SPECIALIST** Yuse Lajiminmuhip **SR. TRAFFIC ASSOCIATE** Christine Hall **SALES COORDINATOR** Shirley Young **ASSOCIATE DIRECTOR, COLLABORATION, CUSTOM PUBLICATIONS/CHINA/TAIWAN/KOREA/SINGAPORE** Ruolei Wu: +86-186 0822 9345, rwu@aaas.org **COLLABORATION/CUSTOM PUBLICATIONS/JAPAN** Adarsh Sandhu + 81532-81-5142 asandhu@aaas.org **EAST COAST/E. CANADA** Laurie Faraday: 508-747-9395, FAX 617-507-8189 **WEST COAST/W. CANADA** Lynne Stickrod: 415-931-9782, FAX 415-520-6940 **MIDWEST** Jeffrey Dembksi: 847-498-4520 x3005, Steven Loerch: 847-498-4520 x3006 **UK EUROPE/ASIA** Roger Goncalves: TEL/FAX +41 43 243 1358 **JAPAN** Katsuyoshi Fukamizu(Tokyo): +81-3-3219-5777 kfukamizu@aaas.org **CHINA/TAIWAN** Ruolei Wu: +186-0082-9345

WORLDWIDE ASSOCIATE DIRECTOR OF SCIENCE CAREERS Tracy Holmes: +44 (0) 1223 326525, FAX +44 (0) 1223 326532 tholmes@science-int.co.uk **CLASSIFIED** advertise@sciencecareers.org **U.S. SALES** Tina Burks: 202-326-6577, Nancy Toema: 202-326-6578 **SALES ADMINISTRATOR** Marci Gallun **EUROPE/ROW SALES** Axel Gesatzki, Sarah Lelarge **SALES ASSISTANT** Kelly Grace **JAPAN** Hiroyuki Mashiki(Kyoto): +81-75-823-1109 hmashiki@aaas.org **CHINA/TAIWAN** Ruolei Wu: +86-186 0082 9345 rwu@aaas.org **MARKETING MANAGER** Allison Pritchard **MARKETING ASSOCIATE** Aimee Aponte

AAAS BOARD OF DIRECTORS RETIRING PRESIDENT, CHAIR Gerald R. Fink **PRESIDENT** Geraldine (Geri) Richmond **PRESIDENT-ELECT** Barbara A. Schaal **TREASURER** David Evans Shaw **CHIEF EXECUTIVE OFFICER** Rush D. Holt **BOARD** Bonnie L. Bassler, May R. Berenbaum, Carlos J. Bustamante, Stephen P.A. Fodor, Claire M. Fraser, Michael S. Gazzaniga, Laura H. Greene, Elizabeth Loftus, Mercedes Pascual

SUBSCRIPTION SERVICES For change of address, missing issues, new orders and renewals, and payment questions: 866-434-AAAS (2227) or 202-326-6417, FAX 202-842-1065. Mailing addresses: AAAS, P.O. Box 96178, Washington, DC 20090-6178 or AAAS Member Services, 1200 New York Avenue, NW, Washington, DC 20005

INSTITUTIONAL SITE LICENSES 202-326-6755 **REPRINTS:** Author Inquiries 800-635-7181 **COMMERCIAL INQUIRIES** 803-359-4578 **PERMISSIONS** 202-326-6765, permissions@aaas.org **AAAS Member Services** 202-326-6417 or http://membercentral.aaas.org/discounts

Science serves as a forum for discussion of important issues related to the advancement of science by publishing material on which a consensus has been reached as well as including the presentation of minority of conflicting points of view. Accordingly, all articles published in *Science*—including editorials, news and comment, and books reviews—are signed and reflect the individual views of the authors and not official points of view adopted by AAAS or the institutions with which the authors are affiliated.

INFORMATION FOR AUTHORS See pages 678 and 679 of the 6 February 2015 issue or access www.sciencemag.org/about/authors

SENIOR EDITORIAL BOARD

Gary King, *Harvard University*
Susan M. Rosenberg, *Baylor College of Medicine,* **Ali Shilatifard,** *Northwestern University Feinberg School of Medicine,* **Michael S. Turner**, *U. of Chicago*

BOARD OF REVIEWING EDITORS (Statistics board members indicated with **(S)**)

Adriano Aguzzi, *U. Hospital Zürich*
Takuzo Aida, *U. of Tokyo*
Leslie Aiello, *Wenner-Gren Foundation*
Judith Allen, *U. of Edinburgh*
Sonia Altizer, *U. of Georgia*
Sebastian Amigorena, *Institut Curie*
Kathryn Anderson, *Memorial Sloan-Kettering Cancer Center*
Meinrat O. Andreae, *Max-Planck Inst. Mainz*
Paola Arlotta, *Harvard U.*
Johan Auwerx, *EPFL*
David Awschalom, *U. of Chicago*
Jordi Bascompte, *Estación Biológica de Doñana CSIC*
Facundo Batista, *London Research Inst.*
Ray H. Baughman, *U. of Texas, Dallas*
David Baum, *U. of Wisconsin*
Carlo Beenakker, *Leiden U.*
Kamran Behnia, *ESPCI-ParisTech*
Yasmine Belkaid, *NIAID, NIH*
Philip Benfey, *Duke U.*
Stephen J. Benkovic, *Penn State U.*
May Berenbaum, *U. of Illinois*
Gabriele Bergers, *U. of California, San Francisco*
Bradley Bernstein, *Massachusettes General Hospital*
Peer Bork, *EMBL*
Bernard Bourdon, *Ecole Normale Supérieure de Lyon*
Chris Bowler, *École Normale Supérieure*
Ian Boyd, *U. of St. Andrews*
Emily Brodsky, *U. of California, Santa Cruz*
Ron Brookmeyer, *U. of California Los Angeles* **(S)**
Christian Büchel, *U. Hamburg-Eppendorf*
Joseph A. Burns, *Cornell U.*
Gyorgy Buzsaki, *New York U. School of Medicine*
Blanche Capel, *Duke U.*
Mats Carlsson, *U. of Oslo*
David Clapham, *Children's Hospital Boston*
David Clary, *U. of Oxford*
Joel Cohen, *Rockefeller U., Columbia U.*
James Collins, *Boston U.*
Robert Cook-Deegan, *Duke U.*
Alan Cowman, *Walter & Eliza Hall Inst.*
Robert H. Crabtree, *Yale U.*
Roberta Croce, *Vrije Universiteit*
Janet Currie, *Princeton U.*
Jeff L. Dangl, *U. of North Carolina*
Tom Daniel, *U. of Washington*
Frans de Waal, *Emory U.*
Stanislas Dehaene, *Collège de France*
Robert Desimone, *MIT*
Claude Desplan, *New York U.*
Ap Dijksterhuis, *Radboud U. of Nijmegen*
Dennis Discher, *U. of Pennsylvania*
Gerald W. Dorn II, *Washington U. School of Medicine*
Jennifer A. Doudna, *U. of California, Berkeley*
Bruce Dunn, *U. of California, Los Angeles*
Christopher Dye, *WHO*
Todd Ehlers, *U. of Tuebingen*
David Ehrhardt, *Carnegie Inst. of Washington*
Tim Elston, *U. of North Carolina at Chapel Hill*
Gerhard Ertl, *Fritz-Haber-Institut, Berlin*
Barry Everitt, *U. of Cambridge*
Ernst Fehr, *U. of Zurich*
Anne C. Ferguson-Smith, *U. of Cambridge*
Michael Feuer, *The George Washington U.*
Toren Finkel, *NHLBI, NIH*
Kate Fitzgerald, *U. of Massachusetts*
Peter Fratzl, *Max-Planck Inst.*
Elaine Fuchs, *Rockefeller U.*
Daniel Geschwind, *UCLA*
Andrew Gewirth, *U. of Illinois*
Karl-Heinz Glassmeier, *TU Braunschweig*
Ramon Gonzalez, *Rice U.*
Julia R. Greer, *Caltech*
Elizabeth Grove, *U. of Chicago*
Nicolas Gruber, *ETH Zurich*
Kip Guy, *St. Jude's Children's Research Hospital*
Taekjip Ha, *U. of Illinois at Urbana-Champaign*
Christian Haass, *Ludwig Maximilians U.*
Steven Hahn, *Fred Hutchinson Cancer Research Center*
Michael Hasselmo, *Boston U.*
Martin Heimann, *Max-Planck Inst. Jena*
Yka Helariutta, *U. of Cambridge*
James A. Hendler, *Rensselaer Polytechnic Inst.*
Janet G. Hering, *Swiss Fed. Inst. of Aquatic Science & Technology*
Kai-Uwe Hinrichs, *U. of Bremen*
Kei Hirose, *Tokyo Inst. of Technology*
David Hodell, *U. of Cambridge*
David Holden, *Imperial College*
Lora Hooper, *UT Southwestern Medical Ctr. at Dallas*
Raymond Huey, *U. of Washington*
Steven Jacobsen, *U. of California, Los Angeles*
Kai Johnsson, *EPFL Lausanne*
Peter Jonas, *Inst. of Science & Technology (IST) Austria*
Matt Kaeberlein, *U. of Washington*
William Kaelin Jr., *Dana-Farber Cancer Inst.*
Daniel Kahne, *Harvard U.*
Daniel Kammen, *U. of California, Berkeley*
Masashi Kawasaki, *U. of Tokyo*
V. Narry Kim, *Seoul National U.*
Joel Kingsolver, *U. of North Carolina at Chapel Hill*
Robert Kingston, *Harvard Medical School*
Etienne Koechlin, *Ecole Normale Supérieure*
Alexander Kolodkin, *Johns Hopkins U.*
Alberto R. Kornblihtt, *U. of Buenos Aires*
Leonid Kruglyak, *UCLA*
Thomas Langer, *U. of Cologne*
Mitchell A. Lazar, *U. of Pennsylvania*
David Lazer, *Harvard U.*
Thomas Lecuit, *IBDM*
Virginia Lee, *U. of Pennsylvania*
Stanley Lemon, *U. of North Carolina at Chapel Hill*
Ottoline Leyser, *Cambridge U.*
Marcia C. Linn, *U. of California, Berkeley*
Jianguo Liu, *Michigan State U.*
Luis Liz-Marzan, *CIC biomaGUNE*
Jonathan Losos, *Harvard U.*
Ke Lu, *Chinese Acad. of Sciences*
Christian Lüscher, *U. of Geneva*
Laura Machesky, *CRUK Beatson Inst. for Cancer Research*
Anne Magurran, *U. of St. Andrews*
Oscar Marin, *CSIC & U. Miguel Hernández*
Charles Marshall, *U. of California, Berkeley*
C. Robertson McClung, *Dartmouth College*
Graham Medley, *U. of Warwick*
Tom Misteli, *NCI*
Yasushi Miyashita, *U. of Tokyo*
Mary Ann Moran, *U. of Georgia*
Richard Morris, *U. of Edinburgh*
Alison Motsinger-Reif, *NC State U.* **(S)**
Sean Munro, *MRC Lab. of Molecular Biology*
Thomas Murray, *The Hastings Center*
James Nelson, *Stanford U. School of Med.*
Daniel Neumark, *U. of California, Berkeley*
Kitty Nijmeijer, *U. of Twente*
Pär Nordlund, *Karolinska Inst.*
Helga Nowotny, *European Research Advisory Board*
Ben Olken, *MIT*
Joe Orenstein, *U. of California Berkeley & Lawrence Berkeley National Lab*
Harry Orr, *U. of Minnesota*
Andrew Oswald, *U. of Warwick*
Steve Palumbi, *Stanford U.*
Jane Parker, *Max-Planck Inst. of Plant Breeding Research*
Giovanni Parmigiani, *Dana-Farber Cancer Inst.* **(S)**
Donald R. Paul, *U. of Texas, Austin*
John H. J. Petrini, *Memorial Sloan-Kettering Cancer Center*
Joshua Plotkin, *U. of Pennsylvania*
Albert Polman, *FOM Institute AMOLF*
Philippe Poulin, *CNRS*
Jonathan Pritchard, *Stanford U.*
David Randall, *Colorado State U.*
Colin Renfrew, *U. of Cambridge*
Felix Rey, *Institut Pasteur*
Trevor Robbins, *U. of Cambridge*
Jim Roberts, *Fred Hutchinson Cancer Research Ctr.*
Barbara A. Romanowicz, *U. of California,Berkeley*
Jens Rostrup-Nielsen, *Haldor Topsoe*
Mike Ryan, *U. of Texas, Austin*
Mitinori Saitou, *Kyoto U.*
Shimon Sakaguchi, *Kyoto U.*
Miquel Salmeron, *Lawrence Berkeley National Lab*
Jürgen Sandkühler, *Medical U. of Vienna*
Alexander Schier, *Harvard U.*
Randy Seeley, *U. of Cincinnati*
Vladimir Shalaev, *Purdue U.*
Robert Siliciano, *Johns Hopkins School of Medicine*
Denis Simon, *Arizona State U.*
Alison Smith, *John Innes Centre*
Richard Smith, *U. of North Carolina* **(S)**
John Speakman, *U. of Aberdeen*
Allan C. Spradling, *Carnegie Institution of Washington*
Jonathan Sprent, *Garvan Inst. of Medical Research*
Eric Steig, *U. of Washington*
Paula Stephan, *Georgia State U. and National Bureau of Economic Research*
Molly Stevens, *Imperial College London*
V. S. Subrahmanian, *U. of Maryland*
Ira Tabas, *Columbia U.*
Sarah Teichmann, *Cambridge U.*
John Thomas, *North Carolina State U.*
Shubha Tole, *Tata Institute of Fundamental Research*
Christopher Tyler-Smith, *The Wellcome Trust Sanger Inst.*
Herbert Virgin, *Washington U.*
Bert Vogelstein, *Johns Hopkins U.*
Cynthia Volkert, *U. of Göttingen*
Douglas Wallace, *Dalhousie U.*
David Wallach, *Weizmann Inst. of Science*
Ian Walmsley, *U. of Oxford*
Jane-Ling Wang, *U. of California, Davis*
David A. Wardle, *Swedish U. of Agric. Sciences*
David Waxman, *Fudan U.*
Jonathan Weissman, *U. of California, San Francisco*
Chris Wikle, *U. of Missouri* **(S)**
Ian A. Wilson, *The Scripps Res. Inst.* **(S)**
Timothy D. Wilson, *U. of Virginia*
Rosemary Wyse, *Johns Hopkins U.*
Jan Zaanen, *Leiden U.*
Kenneth Zaret, *U. of Pennsylvania School of Medicine*
Jonathan Zehr, *U. of California, Santa Cruz*
Len Zon, *Children's Hospital Boston*
Maria Zuber, *MIT*

BOOK REVIEW BOARD

David Bloom, *Harvard U.,* **Samuel Bowring,** *MIT,* **Angela Creager,** *Princeton U.,* **Richard Shweder,** *U. of Chicago,* **Ed Wasserman,** *DuPont*

Published by AAAS

EDITORIAL

The entrepreneurial gardeners

In 2008, a Ghanaian entrepreneur established a drug company in her country. This motivated a young Ghanaian woman to study biotechnology, and a Ghanaian man, employed at a U.S. pharmaceutical company, to return to Ghana. In the past decade, enterprising young Nigerians with few resources went to China and found ways to bring cheap computers and other equipment home, allowing Nigerian students to access the Internet and learn. Profit-driven entrepreneurs like these, big and small, are promoting learning in low-income countries in different fields, including science and engineering. How can this process be furthered and accelerated in such countries?

Entrepreneurs are gardeners who plant innovations in the economy. The growth and flowering of these innovations attract bees—scientists and engineers—and advance their skills, pushing them toward new techniques, discoveries, and careers. Subsequent entrepreneurs work on a richer landscape, and a virtuous cycle sets in. Through either innovations or competition, entrepreneurs empower the average person economically, leading to tax revenues for governments. Over time, an interlocking economic arrangement among entrepreneurs, citizens, and governments emerges that hosts scientists and engineers.

Every population has entrepreneurs who push forward to the extent possible. The tragedy of the past 70 years has been state bureaucracies impeding this natural push. This push can also be misdirected. In the 1960s, South Asian and African governments invested in universities to train students in science and engineering. These efforts did not lead to economic vibrancy, but instead came with state-dominated economies that suppressed commerce and entrepreneurship and kept citizens economically weak. Science and engineering bees flew to blooming Western commercial flowers. Today, about 70% of African-born immigrants to North America have a university education.



"Entrepreneurs are gardeners who plant innovations in the economy."

Fortunately, entrepreneurs don't just plant; they also transplant. A prominent example is mobile technology, which serves average citizens and has spurred thousands to study associated science and engineering. This market directly paved the way for another layer of ventures for the efficient movement of money, people, goods, and market information. These ventures are now giving rise to new industrial organizations, potentially affecting science and engineering and political economies positively.

How can entrepreneurship be promoted in low-income countries? To start, it must be seen as a natural force that enriches many—citizens, authorities, scientists, engineers, and other entrepreneurs. Because they generally recognize people as their source of sustenance, entrepreneurs direct scientists and engineers toward human needs and aspirations. Scientists and engineers then confront physical realities in new ways and advance their disciplines. A virtuous cycle ensues, multiplying knowledge and choices in terms of products, jobs, and careers. The best place to start is by introducing entrepreneurship training that includes courses in basic business education, the history of Western economic progress, recent entrepreneurial achievements in China and East Asia, discussions with successful entrepreneurs from high- and low-income countries, analysis of successful entrepreneurial trajectories, and competition among students on their ideas. Governments can improve regulations, establish equity and credit funds, and provide national recognition to successful entrepreneurs. Universities can galvanize and bridge these efforts.

Scientists and engineers solve important problems. However, entrepreneurs identify what is important, in terms of relevance to people and economic sustainability. In countries where economic resources are limited, it is the gardeners—focused on what will take root—who can entice, nurture, and direct the bees.

– **Iqbal Quadir**



Iqbal Quadir is Founder and Director Emeritus of the Legatum Center for Development and Entrepreneurship at the Massachusetts Institute of Technology, Cambridge, MA. E-mail: iqbalquadir@mit.edu

10.1126/science.aac7414

PHOTOS: (TOP RIGHT) LEGATUM CENTER, MASSACHUSETTS INSTITUTE OF TECHNOLOGY; (INSET) © KTSIMAGE/ISTOCKPHOTO.COM

Downloaded from www.sciencemag.org on June 14, 2015

Published by AAAS

NEWS

> “Let’s be bold—let’s join the rest of the world and go metric.”
>
> **Former Rhode Island governor and senator Lincoln Chafee** last week on CNN, announcing his presidential candidacy—and one part of his platform.

IN BRIEF



An oil sands refinery in Fort McMurray, Canada.

Researchers call for Canada mining ban

More than 100 researchers are calling on Canadian officials to stop new mining of the nation’s oil sands. New projects shouldn’t start “unless consistent with an implemented plan to rapidly reduce carbon pollution, safeguard biodiversity, protect human health, and respect treaty rights,” the researchers wrote in a 10 June statement posted on www.OilSandsMoratorium.org. The signers, who include a Nobel laureate, 12 fellows of the Royal Society of Canada, and 22 members of the U.S. National Academy of Sciences, offer 10 arguments for a moratorium, “each grounded in science.” For example, they write, a 2014 report by the government of Alberta—where large oil sands deposits are located—suggests that less than 0.2% of the area affected by oil sands mining has been reclaimed, despite the industry’s assurances. They also note that studies suggest Canada can’t meet its existing commitments to curb carbon emissions if mining expands. New development would show that “Canada has gone rogue,” said one signer, policy specialist Thomas Homer-Dixon of the University of Waterloo.

AROUND THE WORLD

LHC is back in business

GENEVA, SWITZERLAND | The long wait for the new, improved Large Hadron Collider (LHC) is over. On Wednesday, 3 June, physicists at the European particle physics lab CERN got their first taste of data from new experiments that smash protons together at record energies of 13 tera-electronvolts (TeV)—nearly twice as high as the accelerator’s first run. The LHC was shuttered for 2 years to allow for maintenance, repairs, and upgrades. In recent months, the physicists at CERN have slowly brought the machine back online. The LHC achieved its first 13-TeV collisions on 20 May, and Wednesday marked the first collisions at that energy with beams stable enough to produce data for the four large experiments located around the LHC’s 27-kilometer ring. The LHC’s energy boost will aid scientists in the search for exotic physics, including the elusive dark matter and supersymmetry.

PHOTO: © DANIEL BARNES/ISTOCKPHOTO

Downloaded from www.sciencemag.org on June 14, 2015

Published by AAAS

BY THE NUMBERS

3%

Fraction of humans—including some who are seemingly healthy—who have a genetic condition, according to a recent study in the *American Journal of Human Genetics*.

54

Number of laboratories—all but three of them in the United States—to which the Defense Department mistakenly sent live samples of anthrax, it announced last week.

0%

Snowpack in Oregon's Klamath Basin, as a proportion of the 8 June average, according to the state's Natural Resources Conservation Service. The region is preparing for a 4th year of severe drought.



Ancient bones from black-tailed jackrabbits helped reveal El Niño's effects.

When it was wet, Baja's bunnies went wild

In 2010, undergraduate student Isaac Hart of the University of Utah took on a monumental and menial task, sorting thousands of hare and rabbit bones collected in 2008 from an outcrop in Baja California into species. Five years later, Hart (now a graduate student at the university) and his colleagues say the bones are helping highlight the impact of climate change on vertebrate populations over the past 10,000 years. The 3463 bones, ranging from a few millimeters to about 10 centimeters long, belong to two cottontail species—which thrive in dense, moist habitats—and one hare, a jackrabbit that does well in dry, open spaces. By comparing the relative abundances in the layers of bones, they found that warm, wet El Niño years led to bunny booms even when rabbits farther inland were on the decline, the researchers report in the July issue of *Quaternary Research*. The work drives home the impact of precipitation on small mammals' survival, as well as differences in how climate change will affect coastal and inland populations, the researchers say.

ESA picks mission finalists

PARIS | The European Space Agency has narrowed a field of 27 proposals down to three in a search for its next medium-sized mission. The finalists include projects to study the chemistry and physical conditions of atmospheres of planets around nearby stars, the polarization of x-rays from distant high-energy objects, and how the sun heats the solar wind and planetary atmospheres. The three teams will receive funding to develop their concepts for several years before a final decision is made. The winning mission will get a budget up to €450 million and will launch in 2025. http://scim.ag/ESAfinalists



A black hole at a galaxy's center drives jets of material.

IMAGES: (LEFT TO RIGHT) ESA/AOES MEDIALAB; © B CHRISTOPHER/ALAMY

Green light to build the GMT

LAS CAMPANAS, CHILE | The Giant Magellan Telescope (GMT), one of a trio of mega-telescopes that will peer skyward next decade, on 3 June received $500 million to begin construction. The GMT, which will ultimately cost about $1 billion, will have a mirror 25 meters across, giving it vision 10 times sharper than the Hubble Space Telescope. The telescope, set to be fully operational by 2024, is backed by 11 institutions in Australia, Brazil, Chile, Korea, and the United States. Today's top optical and infrared telescopes have mirrors about 10 meters across, but advances in optics mean the next generation, including the GMT, the European Extremely Large Telescope, and the Thirty Meter Telescope, will be much bigger. This new generation of telescopes will allow huge advances in studies of the early universe, Earth-like planets around other stars, and the mysterious dark matter and dark energy that influence the structure and expansion of the universe. http://scim.ag/GMTconst

NIH contamination scare

BETHESDA, MARYLAND | Some people enrolled in clinical trials with the U.S. National Institutes of Health (NIH) will continue the use of certain experimental

Published by AAAS

drugs—although the compounds may have fungal contaminations. After an inspection by the Food and Drug Administration in May revealed multiple problems that could expose sterile drugs to contamination, NIH suspended operations last week at a facility that makes experimental drugs for the agency's Clinical Center. NIH is searching for alternate sources of products for 46 potentially affected studies. However, a few trial subjects, after being informed of the risks, have requested to continue with their experimental treatments made by the now-closed facility. NIH Director Francis Collins has granted exceptions to those whose conditions could be severely compromised if they failed to receive their next scheduled dose. They will be monitored for signs of infection. **http://scim.ag/NIHdrugcont**

Anti-animal research plan rejected

BRUSSELS | The European Commission last week rejected a plea to abolish animal experiments across the European Union, saying that doing so would harm biomedical research. On 3 March, a European Citizens' Initiative called Stop Vivisection, signed by 1.17 million signatories, formally urged the commission to scrap a 2010 directive regulating the use of animals in scientific research and to propose new rules phasing out animal research in favor of "more accurate, reliable, human-relevant methods." Many science organizations and a group of Nobel laureates spoke out in defense of animal research. In its official decision, the commission told the petitioners that it shares the "belief that animal testing should be phased out." However, budget commissioner Kristalina Georgieva told reporters, an abrupt stop to animal testing would be premature "because too many scientific advances are dependent on this form of testing." The commission said it will seek to speed up the development and uptake of alternative methods. **http://scim.ag/EUanires**

Protests against research reforms

MOSCOW | About 3000 Russian scientists rallied on 6 June to protest government reforms of the research system. A reform has been ongoing since 2013, but a few weeks ago, the Ministry of Education and Science and the Federal Agency for Scientific Organizations issued a reform road map that researchers feared would deeply damage science in Russia, largely because it would increase the proportion of the science budget devoted to competitive funding. The plans suggest that "two-thirds of the basic budget funding will be withdrawn to run competitions between researchers and laboratories," says Evgeny Onishchenko of the Russian Academy of Sciences' (RAS's) Lebedev Physical Institute in Moscow. Whereas grant-winners and successful laboratories would receive salaries up to four times the average salary in their regions, critics say other labs would suffer. For example, three-quarters of RAS's institutes could end up without salaries or funding for equipment and will end up being closed. **http://scim.ag/Russprot**



Many European fish on brink of extinction

More than 90 species of marine fish in Europe's waters are threatened with extinction, finds a report published 3 June by the International Union for Conservation of Nature and funded by the European Commission. Sharks (such as the blue shark, pictured), rays, and other cartilaginous fish are at greatest risk, with about 40% facing extinction. Unregulated overfishing is a primary culprit, but fisheries are also being harmed by pollution, coastal development, offshore oil and gas development, and mining. "There's been no effective movement on fisheries management in the Mediterranean in the last decade," says Nicholas Dulvy, a marine ecologist at Simon Fraser University, Burnaby, in Canada, and one of the report's authors. The report is the first complete assessment of extinction risk for the more than 1200 species of marine fish native to the Mediterranean, Black, Baltic, and North seas, as well as the European part of the Atlantic Ocean. **http://scim.ag/Eurfish**

FINDINGS

Pregnancy screening flags cancer

As prenatal screening for genetic disorders gets more sophisticated, surprises are cropping up. This week, researchers in Belgium describe discovering three cases of cancer in pregnant women thanks to blood tests designed to detect chromosomal abnormalities in their fetuses. The tests, which aim to capture free-floating DNA fragments from the placenta circulating in mom's bloodstream, inevitably catch some of the mother's DNA, too. And if that maternal DNA is from a tumor, its sequencing may reveal cancer-specific chromosomal aberrations. One of the women described in the Belgian study, published in *JAMA Oncology*, had ovarian cancer, while the other two had lymphomas. (One case of lymphoma was too slow-growing to merit treatment.) Such incidental findings are, so far, uncommon: The researchers examined test results from 4000 women and found only the three cancers.

PHOTO: © WATERFRAME/ALAMY

Published by AAAS



Soldiers wore masks at a ceremony to mark South Korea's 60th Memorial Day in Seoul.

PHOTO: LEE JIN-MAN/ASSOCIATED PRESS

INFECTIOUS DISEASES

Amid panic, a chance to learn about MERS

South Korea's explosive outbreak gives scientists fresh opportunities to study the virus

By **Kai Kupferschmidt**, *in Seoul*

Crowds wearing facemasks on Asian city streets, soaring numbers of cases and deaths, rumors and panic. To anyone who remembers the outbreak of severe acute respiratory syndrome (SARS) in 2003, the reports from South Korea last week about another viral disease seemed grimly familiar. But virologists downplay parallels between SARS and the new outbreak of Middle East respiratory syndrome (MERS). With 95 cases and seven deaths as *Science* went to press, it is the biggest MERS outbreak ever outside of Saudi Arabia. Yet the virus doesn't spread as easily as the SARS virus, and it shows no signs of mutating to become more dangerous. There is little doubt that South Korea will bring it under control, says virologist Christian Drosten of the University of Bonn in Germany.

The episode may even have a silver lining: It could aid understanding of MERS, which was discovered only in 2012. In contrast to Saudi Arabia's reticence to let foreign scientists in or share data and samples, South Korea has so far provided regular updates and shared the virus with some outside experts. "I have no doubt that given the quality of Korean science, the country will contribute much new knowledge about the disease," Margaret Chan, director-general of the World Health Organization (WHO), said on Tuesday in a video address to the World Conference of Science Journalists, which was held in Seoul this week.

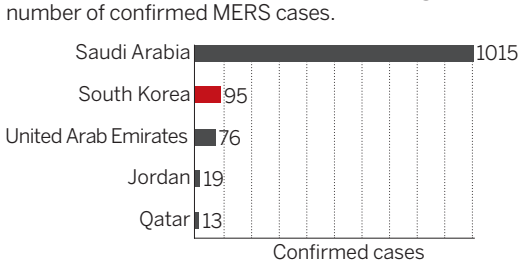
While SARS, a relative of MERS, sickened more than 8000 people around the world before it was stopped in its tracks, MERS has been slower to spread among humans, although it efficiently infects camels, its main host (*Science*, 20 March, p. 1296). But it can spread remarkably fast in hospitals; hospital outbreaks in Saudi Arabia have caused many hundreds of cases. Drosten believes the South Korean outbreak is similar.

The first South Korean patient, who had visited four Middle Eastern countries before flying home, was treated from 15 to 17 May in St. Mary's Hospital in Pyeongtaek. There, he infected the other patient in his room, that patient's son and daughter, and doctors, nurses, and patients in other rooms—more than 30 people altogether, in what researchers call a "superspreading event."

"I assume the index case excreted a lot of coronavirus and contaminated that whole hospital floor," says WooJoo Kim, president of the Korean Society of Infectious Diseases, who is advising the government's MERS response team. Indeed, a survey of dozens of intensive care patients in Saudi Arabia has shown that some have vastly higher amounts of virus in their lungs than others. Kim also suspects that infection control was poor at St. Mary's Hospital, which opened just a few months ago. The patient, who was coughing, was treated in a small room that had an air conditioner but no ventilation. "We are speculating that there is a very high density of virus particles in

MERS's Asian explosion

As of 9 June, South Korea had the second highest number of confirmed MERS cases.



Downloaded from www.sciencemag.org on June 14, 2015

Published by AAAS

the air," says JongKoo Lee, director of the Seoul National University Hospital and former head of the Korea Centers for Disease Control and Prevention.

That doesn't explain why the virus spread so well in a second and third generation of patients, however. One patient infected by the index case spent 3 days in the emergency room of Samsung Medical Center, Kim says, infecting another 36 people so far. Some have speculated that the virus may have mutated to become more transmissible. But the two virus isolates that have been sequenced don't show significant changes from earlier strains, says Marion Koopmans, a virologist at Erasmus MC in Rotterdam, the Netherlands, who has studied them. "There are no obvious red flags," Koopmans says.

The South Korean government has posted numbers of newly diagnosed cases daily. As a result, the outbreak is unfolding "as a live event due to social media," says Peter Ben Embarek, who heads WHO's MERS task force. South Korea has so far quarantined more than 2500 contacts of patients; they are being monitored and tested for MERS if they develop symptoms.

The rapidly climbing numbers have stoked fears, however. Many people have started wearing facemasks; more than a thousand schools and kindergartens have been temporarily closed, and movie theaters and supermarkets are reporting fewer customers. None of that is expected to prevent infections, which seem to occur only in hospitals. Ben Embarek says the government has provided too little information to put the numbers into context. "Numbers are important, but we have to do more than that," he says. The government also fed anxiety by initially refusing to name the affected hospitals.

Another striking aspect of the outbreak is that fewer than 10% of the South Korean patients have died. Until now, the case fatality rate among known MERS patients has been about 40%. Most scientists assumed that to be an overestimate; South Korean authorities may be picking up more mild cases, which may allow for a better estimate of the virus's true lethality.

MERS may reveal other secrets in South Korea, Kim says. Researchers are measuring virus levels of most patients multiple times over the course of their illness, which will help them trace the dynamics of the infection and perhaps understand why some people spread the virus so widely. Scientists also want to look for antibodies in contacts who never became sick, to see whether some who are infected can fight off the disease. "There is a lot to learn," Kim says. ■

PALEONTOLOGY

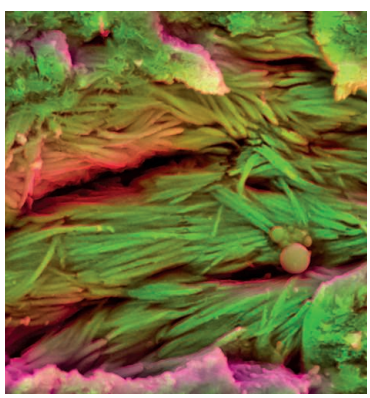
Signs of ancient proteins seen inside dinosaur bones

Can soft tissue survive 75 million years?

By **Robert F. Service**

The cupboards of the Natural History Museum in London hold spectacular dinosaur fossils, from 10-centimeter, serrated *Tyrannosaurus rex* teeth to a 4-meter-long hadrosaur tail. Now, researchers are reporting another spectacular find, buried in eight nondescript fossils from the same collection: what appear to be ancient red blood cells and fibers of ancient protein.

Using new methods to peer deep inside fossils, the study in this week's issue of *Nature Communications* backs up previous, controversial reports of such structures in dinosaur bones. It also suggests that soft tissue preservation may be more common than anyone had guessed. "It's encouraging," especially because the proteins were found in what appear to be the most unremarkable, ordinary bones, says Matthew Collins, an archaeologist and biochemist at the University of York in the United Kingdom. But he and others caution that the team hasn't proven beyond doubt that the structures do contain ancient proteins.



A false-color image of a dinosaur fossil, taken with a scanning electron microscope, shows linear features that look like collagen fibers.

PHOTO: SERGIO BERTAZZO

As early as the 1970s, researchers captured images of what looked like cellular structures inside dinosaur fossils. But did the structures contain actual tissue? Proteins commonly decay hundreds to thousands of years after an organism dies, but in rare cases they have been known to survive up to 3 million years. In a series of studies beginning a decade ago, a team led by North Carolina State University paleontologist Mary Schweitzer reported that they had extracted what appeared to be collagen, the most abundant protein in bone, from a 68-million-year-old *T. rex* fossil. They sequenced fragments of the protein and concluded that it closely matched that of birds, dinosaurs' living descendants (*Science*, 25 March 2005, p. 1852; 13 April 2007, p. 280). But other teams haven't been able to replicate the work, and some suggested that the collagen could be contamination.

The new study, led by materials scientist Sergio Bertazzo and paleontologist Susannah Maidment, both of Imperial College London, has a different strategy for hunting down ancient proteins. Bertazzo, an expert on how living bones incorporate minerals, uses a tool called a focused ion beam to slice through samples, leaving pristine surfaces that are ideal for high-resolution imaging studies. He teamed up with Maidment to apply the technique to eight chunks of dinosaur toe, rib, hip, leg, and claw.

What they found shocked them. Imaging the fresh-cut surfaces with scanning and transmission electron microscopes, "we didn't see bone crystallites" as expected, Maidment says. "What we saw instead was soft tissue. It was completely unexpected. My initial response was these results are not real."

The U.K. team tested more fossils and ran microscopic samples from what appear to be collagen fibers through a mass spectrometer to get the weight of the component molecules. The weights came back as identical to those of the three most common amino acids in collagen, the team reports.

But outsiders, including Schweitzer, say that the weights aren't conclusive proof that the molecules being analyzed are amino acids, or that they came from a dinosaur rather than a contaminant. Results from a different type of mass spectrometer that can sequence the amino acids in a protein fragment could more strongly suggest the existence of collagen and replicate the earlier work, Collins says. Maidment says the team hopes to do such studies soon. If they succeed, the work may spur additional efforts to isolate dinosaur proteins and understand how they differed from those of their modern relatives. ■

Published by AAAS



PHOTO: COURTESY OF ICDP

A decadelong drilling project in northeastern China has penetrated sediments from as early as 100 million years ago.

PALEOCLIMATOLOGY

Dinosaur climate probed

Ancient lake sediments in China record epic temperature swings, biotic turnover before the mass extinction

By **Jane Qiu**, *in Beijing*

Well before an asteroid struck the planet some 66 million years ago, Earth was already in turmoil, a record from an ancient lakebed in northeastern China suggests. Investigators knew from ocean floor sediments that the climate was unstable at the end of the Cretaceous period, when the dinosaurs were making their last stand. But findings from deep drilling in the Songliao Basin, presented at a conference here this spring, show that the climate swings on land were far more drastic, with average annual temperatures going up or down by as much as 20°C over tens of thousands of years—a geological eyeblink. "It certainly wasn't a good time for the dinosaurs," says Robert Spicer, a paleoclimatologist at the Open University in Milton Keynes, U.K.

The findings support a growing consensus that a one-two punch felled the dinosaurs and their contemporaries. Extreme climate fluctuations and tectonic processes that eliminated seaways during the last few million years of the Cretaceous snuffed out some species and hobbled others, the theory holds, before the massive asteroid slammed into the Yucatán Peninsula and finished off about three-quarters of Earth's life forms.

The direst picture yet of the Cretaceous's waning days comes from the Songliao Basin. Covering 260,000 square kilometers, much of the New Zealand–sized swath was a gigantic lake for 80 million years during the Cretaceous. The lakebed's sediments "provide a unique record of what the land environment was like during this turbulent time," says Page Chamberlain, a paleoclimatologist at Stanford University in Palo Alto, California, and a principal investigator of the Songliao International Continental Scientific Drilling Project.

Over the past decade, the drilling team, led by geologist Wang Chengshan of the China University of Geosciences in Beijing, has delved 2.6 kilometers into the basin, below the K-Pg boundary between the Cretaceous and the Paleogene periods. By analyzing oxygen and carbon isotope ratios in the sediment cores, they could trace the seesawing temperatures during the last 6 million years of the Cretaceous, an age known as the Maastrichtian.

Songliao's high latitude likely amplified the fluctuations recorded in the marine records, which tend to blend and blur climate signals. And because the lake sediments accumulated about 10 times faster than the marine sediments did, they offer a finer grained and more precisely dateable picture. But the main selling point of Songliao is the unparalleled continuous record of how the Cretaceous played out on land, says Stephan Graham, a sedimentary geologist at Stanford University, who is also a principal investigator of the project.

The sediments reveal not only the extent of the temperature swings, but also a likely cause. Two major Maastrichtian warming events captured in the Songliao cores—68 million years ago and 66.3 million years ago—coincide with massive eruptions of the Deccan Traps, a volcanic region in present-day India. According to carbon isotope studies, that second warming event was marked by a rapid doubling in atmospheric carbon dioxide. "This was the time when the bulk of Deccan eruptions occurred, which presumably released a massive amount of carbon dioxide," says Zhang Laiming of the China University of Geosciences.

The intense greenhouse effect drove average temperatures to about 22.3°C—compared with 5°C at Songliao today. Adding to the climate turmoil, the warming was interrupted just after the K-Pg boundary by a brief cooling episode, which the team attributes to dust, soot, and aerosols from the Yucatán impact.

As the Maastrichtian climate convulsed, ecosystems changed. The Songliao sediments trapped spores, pollen, algae, and ostracods, or seed shrimp. To the researchers' surprise, some of the species typical of the Paleocene—the geological epoch following the Cretaceous—emerged several million years before the K-Pg boundary. Turnovers in the biota, Wang says, "had already been under way when the asteroid struck."

Paleontologists suspect that dinosaurs were feeling the stress. In a review last August in *The Geological Society of America Special Papers*, paleontologist David Archibald of San Diego State University and colleagues noted that the number of nonavian dinosaur species shrank by half in the last 10 million years of the Cretaceous, with the biggest losses occurring in the Maastrichtian. The Chicxulub impact was, Wang says, "the straw that broke the camel's back." Put another way, Spicer says, "if the asteroid came in on a less stressed system, the effects would not have been so severe."

Having conquered the K-Pg boundary at Songliao, Wang is pressing deeper into the basin—all the way to the Jurassic-Cretaceous boundary about 145 million years ago, a time also marked by climatic havoc, mass extinctions, and species turnovers. Those cores, from as much as 6.4 kilometers below the surface, will span the entire Cretaceous period and, Spicer says, give fresh insights into the world in which the dinosaurs thrived and ultimately died. "You have to look at the bigger picture to fully understand what happened at the boundaries." ■

Downloaded from www.sciencemag.org on June 14, 2015

Published by AAAS

NEUROSCIENCE

Brain implant trials raise ethical concerns

NIH workshop delves into challenges of testing invasive neuromodulation technology

By **Emily Underwood**

In 1980, an 11-year old boy with cerebral palsy had an electrical stimulator implanted into his cerebellum to treat the involuntary muscle contractions that contorted his body. Once the device was switched on, the boy's erratic movements calmed.

Now 46, the man still uses the stimulator, but the device is wearing out. The company that developed it has stopped manufacturing the device, and the electrodes used in the original are no longer available, says neurosurgeon Robert Gross of Emory University in Atlanta, who cares for the patient.

The predicament provides a cautionary tale for neuroscientists, surgeons, and device manufacturers anticipating two new rounds of grants from the National Institutes of Health (NIH) this summer, with a total of about $12 million distributed among seven to 14 awardees. Those grants, the first from NIH's part of President Barack Obama's Brain Research through Advancing Innovative Neurotechnologies (BRAIN) Initiative to test human therapies, will greatly expand clinical experiments with invasive brain devices—and add urgency to the ethical and practical issues they raise.

In recent decades, investigators have developed therapies for depression, Parkinson's disease, deafness, and other conditions that rely on electrodes sending signals into the brain. But moving from laboratory experiments to the clinic has been difficult, and a BRAIN workshop last week at the National Institute of Mental Health (NIMH) in Bethesda, Maryland, focused on ways to remove some obstacles.

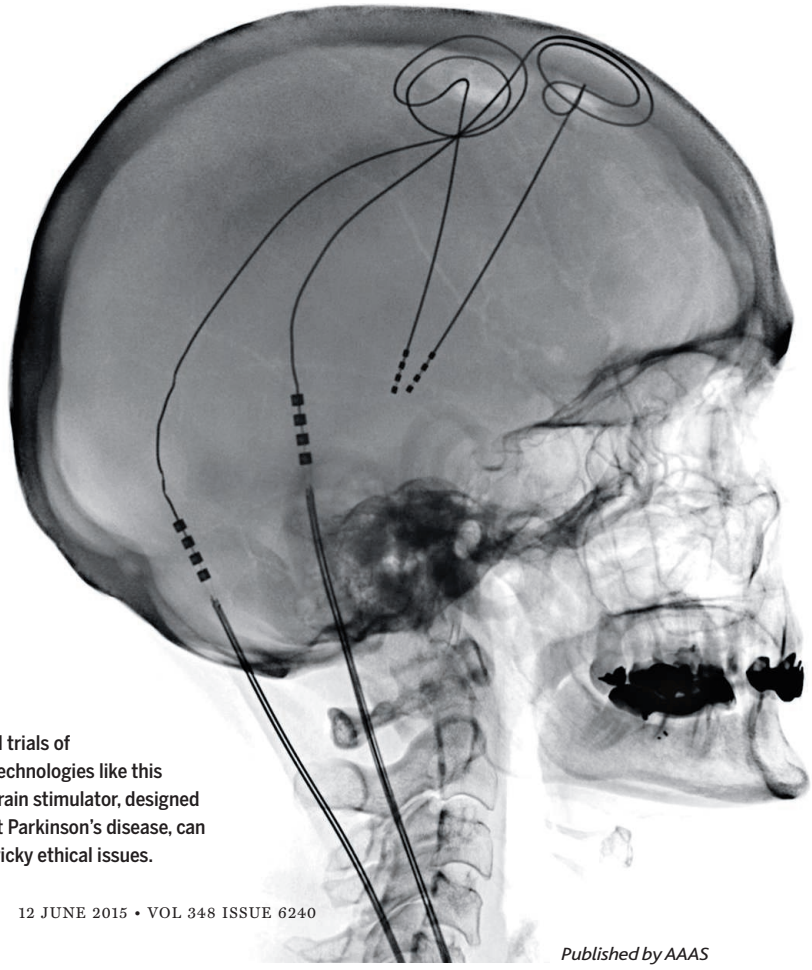
Under current U.S. regulations, for example, researchers must apply for a special exemption from the Food and Drug Administration (FDA) to conduct clinical experiments of neurostimulatory devices and brain-machine interfaces. FDA has sped up its processing time for such permits from more than 440 days to about 100 in recent years, but at the meeting, an FDA representative said the agency aimed to this year reduce its approval time to 30 days. "FDA just got religion. That's amazing," says Thomas Insel, NIMH's director.

NIH aims to remove another barrier that hampers scientific efforts to explore new uses for the few commercially approved invasive brain devices, such as deep brain stimulators for people with Parkinson's disease. The FDA research exemption often requires getting a manufacturer's permission to "unlock" their device's experimental capabilities, such as the frequency and pattern of stimulation a machine can deliver. This essentially makes the companies the "sole arbiters" in determining which experiments are worthwhile, Gross says.

With the new BRAIN grants, however, NIH plans to act as "matchmaker" between researchers and device companies, creating teams that must agree to a common contract specifying intellectual property rights, data sharing, and other tricky matters than can hamper negotiations. Those changes and others should enable investigators to refine brain stimulation therapies, says Kip Ludwig, program director for neural engineering at the National Institute of Neurological Disorders and Stroke in Bethesda, Maryland, and organizer of the meeting. "The truth is we know very little about how even the most successful implantable devices work, and this foundational research is critically necessary to optimize existing therapies, or uncover new therapeutic indications."

Other fields have also confronted the difficulties of experimenting with implanted devices—cardiologists with pacemakers and endocrinologists with insulin pumps, for example. But Hank Greely, a bioethicist at Stanford University in Palo Alto, California, suggests that neuroscientists face special challenges. "We understand the brain much less than we understand the insulin system or heart rhythms," he says, adding, "although you can do great damage with other implants, you are rarely going to change, directly at least, the patient's personality. Even with DBS for Parkinson's disease, we see patients whose personality and behavior changes dramatically with regard to gambling or to sex."

Recent failures of several large clinical trials of deep brain stimulation for depression loomed large over the meeting. In the



Clinical trials of neurotechnologies like this deep brain stimulator, designed to treat Parkinson's disease, can raise tricky ethical issues.

PHOTO: LIVING ART ENTERPRISES/SCIENCE SOURCE

Downloaded from www.sciencemag.org on June 14, 2015

Published by AAAS

United States, companies or institutions sponsoring research are rarely, if ever, required to pay medical costs that trial subjects incur as a result of their participation, Greely points out. "Many people who work in research ethics, including me, think this is wrong," he says.

Even a willing sponsor can do little for a brain implant recipient if the manufacturer goes out of business. The Freehand device from the company NeuroControl is one glaring example, says Warren Grill, a biomedical engineer at Duke University in Durham, North Carolina. The device successfully reactivated paralyzed hands in people with a specific type of nerve damage and was approved by FDA in 1997. In 2001, however, NeuroControl abandoned the technology in order to focus on a therapy for stroke victims. When the company went under, the roughly 250 people who had received the device both during and after trials could no longer access replacements for the fraying wires in their implants.

Some companies try to avoid such unfortunate circumstances by making trial participants agree in advance that an implanted device will be removed at the end of a trial, even if they were seeing benefits. That "seems unfair," says Paul Ford, an ethicist at the Cleveland Clinic in Ohio.

Otherwise, if an investigator wants to ensure that trial participants continue to benefit from the devices used in a study and get proper care and maintenance, they "must play the chess game many, many moves ahead," said Helen Mayberg, a psychiatrist at Emory University, during a workshop panel on ethics. St. Jude Medical, a maker of deep brain stimulation technology, discontinued one large trial for depression in 2013 because of disappointing results. But Mayberg has kept going an independent trial she started 8 years ago of the same electrode device. She believes her data show it helps a large subset of her patients (*Science*, 1 November 2013, p. 548). Moreover, as long as she keeps the trial open, she notes, Medicare and private insurance will cover at least some of her patients' medical costs related to the device.

If such regulatory, ethical, and practical challenges can be sorted out, the new BRAIN grants may kick-start desperately needed technology development, according to some at the meeting. Wireless, flexible, and durable implants that can both pick up and trigger neuronal firing are within reach, they predict. "It has been difficult for me to understand why we are using 1990s technology to put stimulators in people's brains, when you consider how much cellphones and wireless technology have advanced in past 20 years," Insel notes. ■



Susan Larson spends some time with Hercules in her Stony Brook lab.

PHOTO: COURTESY OF SUSAN LARSON

ANIMAL RIGHTS

The scientist behind the 'personhood' chimps

Susan Larson defends her work with two research chimpanzees at the heart of a legal battle

By **David Grimm**

In 2013, the Nonhuman Rights Project filed a series of lawsuits asking courts to recognize four New York chimpanzees as legal persons and free them from captivity. The animal rights group, which hopes to set a precedent for research chimps everywhere, has yet to succeed, but in April a judge ordered Stony Brook University to defend its possession of two of these animals, Hercules and Leo. Last month, the group and the university squared off in court, and the judge is expected to issue a decision soon. But the scientist working with the chimps, anatomist Susan Larson, has remained largely silent until now. In an exclusive interview, Larson talks about her work with these animals and the impact the litigation is having on her studies—and research animals in general. This interview has been edited for clarity and brevity.

Q: Where did Hercules and Leo come from?
A: They were born 8 years ago at the New Iberia Research Center in Louisiana. They were among the last juveniles New Iberia had. We've had them on loan for 6 years.

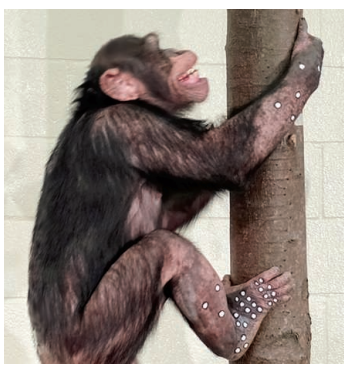
Q: What kind of work do you do with them?
A: We're interested in learning about the evolution of bipedalism by actually looking at what real animals do. Over the past 30 years, we've looked at 17 different species of primates, including 11 chimpanzees. Chimpanzees are the best model because they are so close to us. When we compare how they walk to how we walk, we can feed those data into computer models that may help us understand how early hominids like Lucy moved around. The work we're doing with Hercules and Leo is the most important work we've done.

Q: What do the experiments involve?
A: We do three types of experiments: motion analysis, which involves painting nontoxic white markers on the chimpanzees' limbs so video cameras can accurately track their movements; kinetic analysis, where we look at the forces generated by the animals as they walk over force plates; and electromyography, where fine-wire electrodes inserted into the muscles tell us how they contribute to the motion we're studying. We don't do anything with these chimpanzees that we haven't done on ourselves.

Published by AAAS

Q: Why can't you do this kind of work in a zoo or sanctuary?
A: The work we do requires a lot of time and effort. You need to be able to collect many samples of the same behavior. Animals in zoos and sanctuaries are notoriously unwilling to do what we want them to. Hercules and Leo do everything for a grape or a cherry or a bit of juice.

Q: What are their living conditions?
A: We have a very large facility. It's the equivalent of three moderate-sized bedrooms that are adjacent to each other. They have hammocks, ropes for climbing, and magazines to tear up. We have an animal handler whose job is to keep them comfortable and stimulated. She hides treats in cardboard boxes and gives them plastic toys like airplanes to play with. We try to make their day-to-day lives as interesting as possible. We don't want them to feel threatened or frightened; otherwise we wouldn't get reliable results.


Hercules climbs a tree trunk during a locomotion experiment.

Q: How do you view your relationship with them?
A: I interact with them weekly, but the animal handler has the most direct contact with them. I don't have the bond with them that the animal handler does; she loves them and loves spending time with them. I see them as collaborators, as willing participants in the project. And I respect them. I would never ask them to ride a bicycle or anything goofy like that.

Q: How have perceptions of animal research changed in the decades you have been working with primates?
A: There has been a sea change in attitudes towards chimpanzee research. Oversight has become much stricter, and getting approval to do this work has been harder. The space we have used to be considered vast for these animals; now it's considered average.

In the past, this research wasn't considered controversial; my colleagues used to appear on television programs to talk about their work. Now, my university is very reticent to talk about this research at all. I've been consistently advised never to respond to reporters, even though I don't think there's anything that needs to be concealed. I'm very proud of the work we do, and I feel comfortable with the procedures we use. They worry about us being targeted by animal rights activists, so they think it's better to say nothing than to say something that could be used against you.

Q: What do you make of the movement to turn chimpanzees into legal persons?
A: I think giving them personhood status is a sham. If anyone treats them like people, it's us. We don't treat them like prisoners; we only work with them when they're willing. But we have to be cognizant that these are chimpanzees—not people. They can't provide for themselves; they need human care and protection. They are remarkable animals, and we should respect what they are and what they need. You don't have to pretend something is a person to treat it justly.

Q: How has the litigation affected you?
A: Stony Brook is keeping me out of it. It hasn't changed our protocols, but the university has scrutinized us much more closely. They're not happy about it. I find a lot of what the other side is saying very untrue and hurtful. It's upsetting when someone calls you an evil scientist, or when they say we're causing pain or needless suffering. It's strange to hear people talking about these animals when they don't know who they are.

Q: What's next for Hercules and Leo?
A: Our project is winding up in the next few weeks. After that, it's New Iberia's decision what to do with them. They've said they intend to retire them to a sanctuary. After that, our facility will go dormant.

Q: What do you see as the future of chimp research?
A: The U.S. Fish and Wildlife Service is considering classifying both captive and wild chimpanzees as endangered. NIH [the National Institutes of Health] is saying they're not as useful as animal models. Grant money is very hard to come by, and it's becoming increasingly difficult to meet the regulatory standards. Pretty soon, the kind of work I do will not be possible anymore. We're going to end up with chimpanzees completely cut off from humans; they'll become alien beings. And that makes me sad, because I think there are still a lot of things we can learn from them. ■

MOLECULAR EPIDEMIOLOGY

HIV family trees reveal viral spread

New studies could aid public health efforts

By **Jon Cohen**

The very trait that makes HIV so good at dodging the immune system—and at thwarting efforts to develop an effective vaccine—might also turn out to be an Achilles' heel.

HIV evades immune attack by copying itself at breakneck speed, regularly mutating so that each progeny differs slightly from the parent virus. The pace of change means that the more closely two isolates resemble each other, the more recently they shared a common host—making it possible to track the spread of the virus and design precise interventions to block it. Last week at the New York Academy of Sciences in New York City, researchers, public health specialists, and HIV/AIDS advocates discussed how to exploit the potential of the technique, called phylogenetic analysis—and the thorny ethical and legal issues it raises.

"This is a methodological breakthrough," says epidemiologist William Blattner of the University of Maryland School of Medicine's Institute of Human Virology in Baltimore. The plummeting costs of DNA and RNA sequencing are now allowing it to be applied on a large scale, and early efforts are yielding some surprises about how HIV spreads and when it can most effectively be controlled.

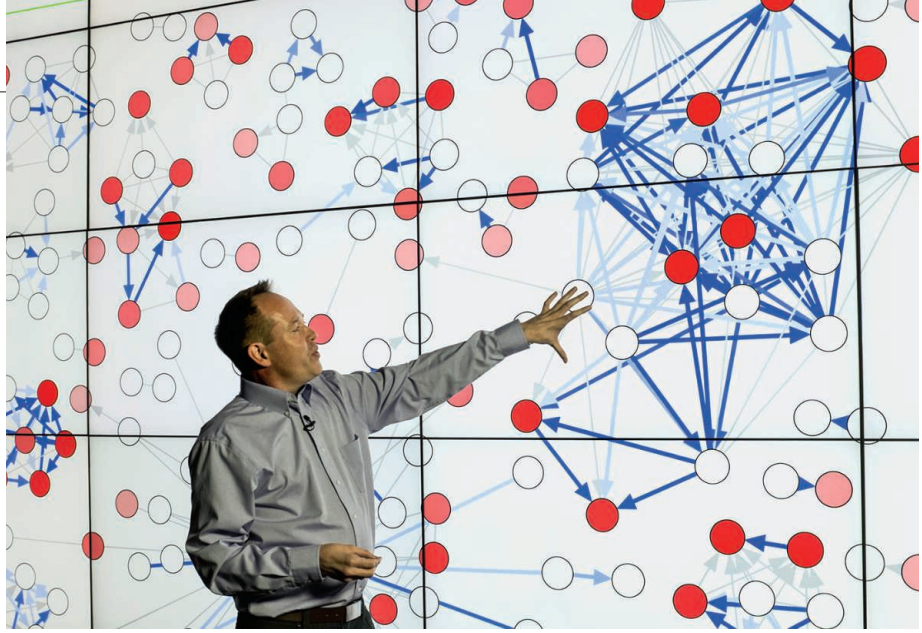
At the heart of the technique is the assumption that if the HIV sequences found in two people differ by less than 1.5%, then they are in a "transmission cluster." This does not prove that one person infected the other—there could have been intermediaries—but their infections are closely linked. Because HIV mutates at a constant rate, researchers can also construct a molecular clock to estimate when the transmission took place. Combining the information from many HIV-infected people in a limited geographical area creates diagrams that resemble airline routing maps, allowing researchers to infer the direction and speed of spread.

One study, by a group led by epidemi-

PHOTO: BRIGITTE DEMES

Downloaded from www.sciencemag.org on June 14, 2015

Published by AAAS



UCSD's Davey Smith and co-workers created an HIV transmission network map, shown here in December 2014, from 15 years of sequence data.

ologist Alexa Oster of the U.S. Centers for Disease Control and Prevention (CDC) in Atlanta, takes advantage of a CDC recommendation that before starting antiretroviral (ARV) treatment, every newly infected person be tested for drug-resistant virus. That requires sequencing HIV, which has enabled CDC to build an anonymized database that includes information such as likely mode of transmission and age.

With researchers from the University of California, San Diego, Oster's team mined HIV sequences from 27 sites around the country. They found that in men who report having sex with men (MSM), that explains the transmission 88% of the time. But surprisingly, Oster said, among men and women who inject drugs, the most common source of infection is not needle sharing but sex involving MSM. Also unexpected: Infections in heterosexual women were more frequently linked to MSM than to heterosexual men.

CDC is now tracking transmission networks of 30 or more people to project whether they will grow by 2020. "If we were able to predict which clusters are going to grow, we would know where we might want to focus prevention efforts," Oster said.

Christophe Fraser, an epidemiologist at Imperial College London, and his colleagues hope to bolster prevention efforts in the Netherlands with their analysis of more than 13,000 HIV sequences from a cohort of predominantly MSM. They identified 106 distinct transmission networks and 883 probable transmitters, 69.2% of whom had undiagnosed infections; diagnosed people on ARV treatment, in contrast, rarely transmitted. What's more, 40% of the probable transmitters had just recently become infected, a time when they are most infectious. Models suggest that treating high-risk people who test negative for HIV with ARVs, a strategy called preexposure prophylaxis, could lead to "substantial reductions in transmission" in the Netherlands, Fraser said.

An ambitious new consortium, the Phylogenetics and Networks for Generalised HIV Epidemics in Africa (PANGEA_HIV), plans to sequence 20,000 full HIV genomes from people who are already participating in other research studies in four sub-Saharan countries. PANGEA_HIV aims to see whether phylogenetics can accurately assess new infection rates. That, in turn, could reveal whether a prevention intervention worked. "If you can use genetic data to see the effect of interventions, it may be much cheaper" than the current method of following an uninfected cohort over time, said PANGEA_HIV collaborator Tulio de Oliveira, a bioinformatics specialist at the Wellcome Trust Africa Centre for Health and Population Studies in Mtubatuba, South Africa.

Speakers stressed the limits of phylogenetic analyses and cautioned that data could potentially be misused. Gay men could be "blamed" for infecting heterosexual women, for example. Several countries criminalize HIV transmission and homosexuality, and some speakers worry that governments could try to acquire confidential information to identify individuals in the studies. "Using this technology does not prove who infected whom: It proves that people were involved in a temporally related transmission cluster," stressed Mark Harrington of Treatment Action Group in New York City. "We don't want to have a bunch of court cases where people are suing because they have biologically similar strains." ■

PHOTO: MALCOLM LINTON

Published by AAAS



Downloaded from www.sciencemag.org on June 14, 2015

BUSINESS DECISIONS

What does it take for an academic scientist to become an entrepreneur? Here are some of their stories

By **Jeffrey Mervis**

For academics, the journey from a discovery to a product can be arduous. But as a culture of entrepreneurship has spread to universities across the country and around the world, aid stations have popped up to ease the way. They come in various forms, including campus competitions to solicit commercially viable ideas, universities establishing their own venture capital funds and "incubators" to nurture startup companies, and programs such as the Innovation Corps (I-Corps) at the National Science Foundation.

"We all know that entrepreneurship is the big buzzword today on campus," says Laura Ray, an engineer at Dartmouth College, who has founded two firms based on her work in acoustics and signal detection and runs a graduate fellowship program in innovation.

Ray's own entrepreneurial learning curve has been steep. Her first company, begun in 2005, was the result of a knock on the door from a university tech transfer official who asked if she had anything that could be taken to market. "We thought he was crazy," Ray recalls—but she was willing to take a shot. Eight years later, a second company grew out of her participation in I-Corps' 10-week boot camp for would-be academic entrepreneurs. "I-Corps opened my eyes," Ray says. "It taught me that you need to know the customer, and your value proposition—that is, how you plan to make money."

Despite those commercial ventures, Ray has remained an academic. And although some scientists leave campus to follow their commercial dreams, most do not. They like research and teaching, for one thing, and may not think they have what it takes to run a

PHOTO: TAY KAY CHIN

Published by AAAS

Chemical engineer Jackie Ying has had to modify MIT's entrepreneurial ethos in building up her Singapore research institute.

company. "If I had quit my [academic] job, I don't know that I would have succeeded," Ray admits. Frances Arnold, a biochemist at the California Institute of Technology in Pasadena, who has founded two biofuel companies, advised several others, and is a member of the National Inventors Hall of Fame, echoes that attitude. "I never chose to do the hard work of being a CEO or a chief technical officer," she says.

Research on entrepreneurship—who does it best, what policies promote it, and how it contributes to economies, for example—is flourishing, as an Insight on page 1200 describes. In one story in our special News section, two venture capitalists describe how they vet scientists' pleas for money; a second Feature gives an inside look at the incubator phenomenon. But first, we offer several stories that illustrate some of the many possible paths from campus to commercialization.



Todd Zion

THE CATALYST AND THE PROTÉGÉ

Todd Zion came to the Massachusetts Institute of Technology (MIT) in Cambridge in 1999 to earn a Ph.D. in chemical engineering. When he went shopping for advisers, Jackie Ying stood out, in part because of a fanatical work ethic that helped her become a full professor at the age of 35. "Some people would never want to work for Jackie, but I was attracted to the idea of working twice as hard as any other lab," says Zion, who spent 2 years after college as a corporate research scientist at Kodak, before deciding he needed a Ph.D. to make his mark.

Ying's business-minded approach—she says that "every grad student should tackle a project not only of tremendous scientific interest, but also of great commercial potential"—also appealed to Zion's nascent interest in becoming an entrepreneur. "I saw people in her lab go off and start a company," he says, "and I'd think, 'Hey, that's something I'd like to do, too.' "

So Zion signed on. Eager to push her already productive lab into the life sciences, Ying asked Zion to see if the same technology her lab had used to make a nanoemulsion to coat the turbines in jet engines could create a platform for delivering insulin to treat diabetes. The idea was to create an insulin-containing polymer that would break down after interacting with glucose in the patient's blood, releasing the insulin as it was needed.

Zion spent 2 years trying to find a material that prevented the insulin from leaking out before he realized that the secret lay in chemically modifying the insulin itself. That discovery led to SmartCells, a company he and Ying co-founded in 2003. Zion and a small team spent another 7 years improving the technology before selling the company for an undisclosed upfront sum to Merck, which is betting that this novel drug-delivery system will one day allow millions of diabetics to discard their pumps, meters, and monitors. The acquisition drew notice because Merck reportedly will pay out more than a half-billion dollars if certain milestones are met; a company representative said last month that a phase I clinical trial in humans has begun.

"Todd was a very good scientist, although he was by no means my best student," Ying says. "But he had very good business acumen. And that's essential in running a company."

For Zion, becoming a full-time entrepreneur was the obvious next step once he realized the value of his discovery. "I suppose that somewhere in the recesses of my subconscious, remaining in academia was a possibility," he says. "But it's hard to go out and be an entrepreneur with a Plan B. You gotta tell yourself that this is the only way the company can move forward, and we're going to make that work."

Zion's business savvy made an impression on Lita Nelsen, the longtime director of MIT's technology licensing office. Biotech startups are common at MIT, she says, but SmartCells stuck in her mind because Zion managed to avoid what she calls "diluting the company." By running a tight operation and not asking for more money than he needed to reach a succession of technical milestones, Zion was able to retain control of the company rather than trade away a lot of equity for cash. That strategy resulted in a huge windfall for Zion, his small team, and a handful of early investors, including MIT, when Merck acquired the company.

Zion immediately spent some of his profits to buy a struggling private Montessori school that his three children were attending. Then, he took some time off. But within a year, Zion reunited with some of his former SmartCells colleagues to start another company. Largely self-funded, Akston Biosciences Corp. is testing technologies for clearing the body of unwanted material implicated in various diseases, like the β amyloid protein that forms abnormal deposits in the brains of Alzheimer's patients.

Ying says that roughly one-quarter of her MIT students have founded companies or gone to work for a startup. But she has chosen not to take that path. "What interests me," Ying says, "is bringing the technology to a certain level where you can spin it off, and then playing an advisory role to make sure that things are running smoothly."

"She's an educator at heart," says Andrey Zarur, who as one of Ying's first graduate students developed the initial technology that Zion later modified to create SmartCells. Now a partner at Kodiak Venture Partners in Boston and CEO of Greenlight Biosciences in Medford, Massachusetts, the latest of 15 companies he has started, Zarur says Ying "would take me with her on visits to companies to get funding for the lab. And I would make the presentation. People thought she was taking advantage of me because she made me do three Ph.D. projects. But I was like, 'Dude, you're crazy. She is preparing me for the life I want to have.' "

> ***"It's hard to go out and be an entrepreneur with a Plan B."***
>
> **Todd Zion**, Akston Biosciences Corp.

By the time Zion launched SmartCells, Ying had left MIT to become the founding director of the Institute for Bioengineering and Nanotechnology (IBN) in Singapore. She says the job gave her a chance to return to her roots—born in Taipei, she grew up in Singapore before coming to the United States as a teenager—and to spread the twin gospels of top-flight research and entrepreneurship that she had learned at MIT.

Her record over the past 12 years suggests she has done exactly that. IBN has generated more than 300 patents, 80 licenses, and eight startup companies. But basic research with commercial potential doesn't just happen, she notes. Faculty members have to buy into the goal—and sometimes they need some help in finding a project with commercial promise. Ying recalls coaxing a scientist who was studying epigenetics to shift to cell and tissue engineering. "She got very interested in that and she wanted to work on liver tissue. But I persuaded her to work on kidneys, because it's a much less crowded area."

Ying also weighed in when the researcher began to think about developing an artificial kidney. "That would take a very long time," she told her. The institute had recently developed new ways to produce stem cells from a person's kidney tumors, so Ying persuaded her colleague to instead turn

ONLINE

For a quiz and more on entrepreneurship, go to http://scim.ag/SCIbiz.

PHOTO: ROB MATHESON/MIT

Published by AAAS

such cells into a toxicity assay for potential cancer drugs. Ying hopes to find partners in the drug, consumer care, and food industries who are interested in developing the in vitro technology, which she says is more efficient than having to use animals.

Overall, she envisions creating a different entrepreneurial model than simply having lab members leave to spin off a technology. "We don't have a steady supply of new students like at MIT," she notes, "so a spinoff can mean losing five or 10 good people" from a staff of 160 researchers and 20 graduate students.

Instead, Ying hopes to find a way for IBN to help nurture new companies without losing all the scientists who did a technology's foundational work. "We will continue to help [the firms] with the research," Ying says, "and maybe they will give us not just royalties but some shares to the people involved. So it would be win-win."



Howard Schulman



Mark Anderson

THE ROUGH ROAD TO A PRODUCT

Howard Schulman has experienced the roller coaster ride familiar to many scientists who try to turn an academic discovery into a drug. More than 2 decades have passed since he and Mark Anderson demonstrated that inhibiting an enzyme Schulman had co-discovered, calmodulin-dependent protein kinase II (CaMKII), could block heart arrhythmias. And for the past 6 years Schulman has been president of Allosteros Therapeutics, a tiny company the two men created to translate their knowledge into helping heart patients. But so far it hasn't happened.

Schulman and Anderson, now director of medicine at Johns Hopkins University School of Medicine in Baltimore, Maryland, began their collaboration in the early 1990s at Stanford University in Palo Alto, California, where Schulman, a molecular pharmacologist, was a professor, and Anderson, an M.D.-Ph.D., was doing a postdoc and medical residency. Their work offered an alternative to antiarrhythmic therapies based on ion channels, a once-popular idea that had proven to cause more harm than good. But Schulman was happily ensconced at Stanford, and Anderson was just beginning his career as a physician-scientist. So instead of commercializing the discovery themselves, the two scientists obtained a use patent on it and hoped that a company would license their work.

It was a long wait.

"Stanford made a minimal effort to find a partner," Schulman says. "They might have done more if I had already been a successful founder or if I had chosen to be more aggressive." Stanford finally struck a deal with a nearby biotech company, Scios Inc.

Scios designated CaMKII inhibition as one of its three lead programs in cardiovascular medicine, and Schulman and Anderson became consultants. But the arm's-length relationship prevented Schulman from using his expertise in medicinal chemistry. "I didn't get to see the compounds or help them on assays," he notes. "It was not an entirely satisfactory relationship." In 2003, Scios was purchased by Johnson & Johnson, and 3 years later the pharma giant shut down its entire preclinical cardiovascular effort, including a gleaming building that housed its research on CaMKII. "So we got the license back," Schulman says.

He and Anderson had continued to work on CaMKII, and so they took matters into their own hands. "It's actually not that hard to start a company," Schulman says. "All you need to do is go on the Web, register it in Delaware, and create a post office box. It doesn't cost very much."

What costs lots of money, of course, is turning a molecular drug target into an actual therapy. The Leducq Foundation, a family philanthropy based in Paris that supports basic research on cardiovascular disease and stroke, was already funding Anderson to lead an international collaboration on CaMKII. As luck would have it, the trust decided to create a philanthropic venture company—a for-profit entity with the mandate to invest in promising treatments against heart disease—just as the two men formed Allosteros.

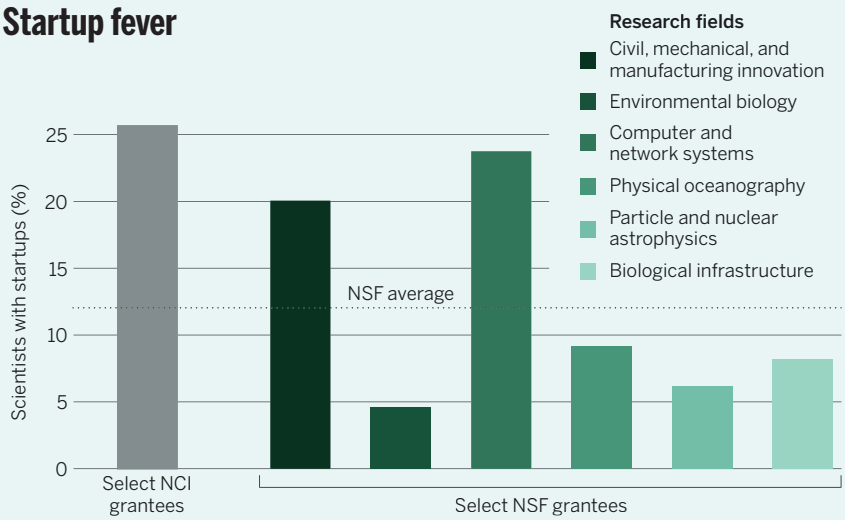
"We competed successfully for seed money," Anderson says. The $1.3 million that Allosteros received enabled Schulman to set up a small lab in nearby Sunnyvale, California, and subsequent federal small business grants and other funding have allowed the company to outsource some needed chemistry work and refine two compounds into potential candidate drugs. This spring, the two men came within a whisker of inking a deal with a major pharma that would have taken those compounds through clinical trials.

"At the last minute, they told us they were no longer interested in heart failure," Schulman says. "Being part of a multibillion-dollar cardiovascular program would have been nice. But not yet."

Schulman remains optimistic that the stars will eventually align for Allosteros. In the meantime, he's trying to maintain a basic science program and has applied for another small business grant.

For Schulman, 66, seeing CaMKII become the basis for a range of heart treatments would establish his credibility as an entrepreneur and fulfill a careerlong urge to help bring a drug to market. For the 55-year-old Anderson, the stakes are not

Startup fever



Few universities track faculty startups, but direct surveys of university scientists reveal a "high prevalence of entrepreneurship," says David Audretsch of Indiana University. He and colleagues asked two groups whether they had ever started a business: 140 scientists who received both a large National Cancer Institute R01 grant and a U.S. patent; and 1899 scientists in six different fields who received National Science Foundation grants. Not all the startups are necessarily related to the scientists' research.

CREDITS: (PHOTOS, TOP TO BOTTOM) MARY COE; BOB STOCKFIELD; (GRAPH) ADAPTED FROM T. T. ALDRIDGE *ET AL.*, *THE JOURNAL OF TECHNOLOGY TRANSFER* **39**, 6 (DECEMBER 2014) © SPRINGER INTERNATIONAL PUBLISHING AG/T. T. ALDRIDGE *ET AL.*, *RESEARCH POLICY* **40**, 8 (OCTOBER 2011)

Published by AAAS

so high. "I think entrepreneurs are people who put their livelihoods at risk by placing bets on a particular business concept," he says. "That's not me. I'm a physician scientist, and I live mostly in a world of mice. Howard's been living Allosteros for 6 years. I still have a day job."


Michael Weiss

THE BUSINESS OF DOING GOOD

Michael Weiss has carved out a successful research career unraveling the complex structure and inner workings of insulin. But Weiss, a biochemistry professor at Case Western Reserve University in Cleveland, Ohio, has more than just an academic interest in understanding the hormone that helps the body regulate blood glucose levels.

In 1980, as a Harvard Medical School student on a travel fellowship across the Middle East and Africa, Weiss was shocked to find out that millions of diabetics in the developing world couldn't manage their disease properly because they lacked access to a version of the hormone that doesn't need to be kept refrigerated. "That problem should be easy to solve by engineering an ultra–heat-stable insulin," he remembers thinking.

It wasn't. It took Weiss nearly 3 decades to come up with a solution, one that relies on single-chain analogs of the natural protein, which has two chains. Since founding Thermalin Diabetes in 2009, Weiss has been simultaneously publishing papers in top journals and getting up to speed on what it takes to make a synthetic form of heat-stable insulin available commercially.

One important lesson came in 2007 from Richard Klausner, then the head of global health programs at the Bill & Melinda Gates Foundation and a friend from Weiss's medical school days. "Rick told me two things: One, you need a business plan that makes sense to Western investors, including how to win FDA [Food and Drug Administration] approval for the drug; and two, don't tell me anything more until Case Western has secured the IP [intellectual property]."

"Those were new words to me," Weiss admits. "I was very naive about business and the commercialization process." Weiss decided to make up for lost time, taking a 2-year sabbatical so he could earn an MBA in 2010—at the age of 53—from Case Western's Weatherhead School of Management.

Weiss also reached into his past to find someone to run the company: Rick Berenson, a college roommate turned venture capitalist. In line with Klausner's advice, Berenson decided to target diabetics in the industrialized world. One niche, he says, is the many people who suffer from a marked insulin resistance and need a large dose of insulin before meals to help manage their bodies' reaction to the glucose. The company's first product is likely to be Fluorolog, an ultraconcentrated, rapid-acting biosynthetic version of insulin. "Insulin is sticky, so you can't just concentrate it," Weiss explains. "So we put fluorine in it so it's not so sticky."

Weiss has raised $11 million from investors and garnered $9 million in grants, mostly federal small business research grants. He needs at least that much again to take just that drug candidate into clinical trials. "I was hoping to do consecutive clinical trials [on several candidates], with several years of really interesting science coming out of all this," Weiss notes. "But the venture capitalists have a different perspective. They want to know how quickly we can create value, and then exit."

Weiss knows that "creating value" will also hasten progress toward solving the problem he encountered on his travels 35 years ago. "I want to move insulin analogs out of the lab—from mice and rats and pigs—and into humans," he says. "And the only way to do that is company creation. I have [entrepreneurial] friends who don't really care what the product is. But my goal has always been to meet the unmet clinical needs of diabetics."


Paul Romer

LOOKING BEYOND ONE'S RESEARCH

Not every company founded by an academic springs from what he or she is studying. For 2 decades, economist Paul Romer probed how a nation's investments in education and research can spur long-term economic growth, an important question in macroeconomics. But in 2001, he left his faculty position at Stanford University to launch a company aimed at solving a very prosaic problem: getting students to do their homework.

Romer had noticed that students in intro economics courses were blowing off homework assignments. And even when the students did do the problem sets, many faculty members couldn't provide much feedback because the classes were so large.

Romer thought that technology could solve the problem. His chance came when Skandia, a Swedish life insurance company, offered to finance an endowed chair at Stanford so he could extend his work on innovation. "Why not fund a new venture instead?" he asked them.

Skandia said yes, and its $11.2 million investment bankrolled Aplia, an educational software company that lets students go online to work on material aligned with their textbooks. The software gives immediate feedback on wrong answers and allows students to participate in interactive group exercises that simulate market conditions—

> ***"As an entrepreneur, you have to be willing to walk away with nothing if you don't succeed."***
>
> **Paul Romer**, New York University

"it's like lab experiments in the natural sciences," Romer explains.

Romer also wanted to fix what he calls a "broken" publishing model: Textbooks were getting more and more expensive, but they weren't helping students master the subject. Aplia offers a menu of online supplemental materials so that students can choose what fits their needs—and their budgets.

Although lacking any formal business experience, Romer chose not to work with Stanford's technology transfer office. Instead, he took a 2-year leave from the university—"they weren't very happy"—that eventually stretched to 6 years. Romer initially hired a CEO to run the company, but he eventually grabbed the reins, believing it necessary to remain "cash positive." At one point he even sold his house and poured the proceeds into the company.

It took Aplia a few years to regain its footing, by which time Romer realized that he missed doing research. "I had proven my original point: It was possible to get students to learn more by doing homework, and to change the textbook-based model of education." So in 2007 he sold the company. Romer's current research focuses on the role of cities as an engine for innovation, and in 2010 he joined the faculty at New York University in New York City, where he directs the Urbanization Project at the Stern business school.

Would he ever want to be an entrepreneur again? "It was very exciting and intellectually stimulating, and the closest friendships I ever had were part of that experience," he says about Aplia.

Starting the firm also taught him an important lesson about entrepreneurship, he says: Don't risk more than you can afford to lose. "Things were touch-and-go for a while—we didn't have much in the bank. As an entrepreneur, you have to be willing to walk away with nothing if you don't succeed." ■

PHOTOS: (LEFT TO RIGHT) JAMIE JANOS; KATHI BAHR

Published by AAAS



Anthony Sun: "Biology is complicated. Plenty of investments have not gone well."

GIVE US YOUR BEST PITCH

Two venture capitalists explain the investor's mindset

By **Jon Cohen**

Some like it risky. In 2014, venture capitalists pumped $8.6 billion into nearly 800 deals with fledgling biotechnology and medical device companies in the United States. It was the biggest cash infusion that the life sciences sector has received from venture capital in 6 years, according to the end-of-the-year analysis in the MoneyTree Report. But most researchers who have great ideas (in *their* minds, anyway) for treatments, preventives, or diagnostics have only a vague notion how to transform their science projects into "value propositions" that can raise the millions needed to commercialize a concept. And fewer still have ever crossed paths with those who hold the purse strings: the venture capitalists, or VCs for short.

VCs invest in scientific ideas they judge as hot, backed by investors such as pension funds and endowments, wealthy families, and "high net worth" individuals. Investors usually require that VC firms put some of their own money on the table, too. They provide guidance to the companies (which often means a seat on the board of directors) and ultimately hope to "exit" with a big windfall in 3 to 5 years, when the startup is gobbled up by a bigger company or goes public.

Although the life sciences have never spawned a Google or an Amazon.com and often require longer term investments than other sectors, life science VCs can reap handsome profits for their backers and themselves: Between 2000 and 2010, investors who exited earned 15% returns, nearly four times the gain in the S&P 500 over that time period, according to an analysis published in the July 2011 issue of *Nature Biotechnology*.

Science spoke with two VCs about their backgrounds and perspectives. Robert Nelsen, based in Seattle, Washington, is a co-founder of ARCH Venture Partners, which has funded more than 160 companies, including Illumina (sequencing), deCODE Genetics (genomics), and, more recently, Juno Therapeutics (cancer immunotherapy). Anthony Sun works across the country in New York City for Aisling Capital, which has a diverse, $1.6 billion portfolio that includes Chimerix (antivirals), Vivus (erectile dysfunction), and ZELTIQ Aesthetics (nonsurgical fat reduction). Nelsen does not have an advanced science degree, while Sun earned an M.D. at Philadelphia's Temple University School of Medicine in 1997. Both went into the venture capital business immediately after finishing a master's in business administration.

Like scientists, VCs have a specialized language, and they can baffle outsiders when they speak of "halo deals" (highly profitable investments that cover shakier ones), "lockup periods" (time windows when investors can't trade shares), and "family offices" (firms that manage investments for groups of wealthy relatives). VCs also have different appetites for risk—some like only early-stage, big gambles, whereas others favor more mature companies that have revenue. *Science* interviewed Nelsen and Sun separately, but their answers, edited for brevity and clarity, are combined here.

PHOTO: DREW GURIAN

Downloaded from www.sciencemag.org on June 14, 2015

Published by AAAS

Q: How did you become a venture capitalist?
R.N.: I kind of fell into it. When I got to the University of Chicago [for an MBA program], I started volunteering for an organization that eventually became ARCH, and I was the first employee. The trustees of the university created it to form a startup infrastructure with Argonne National Labs. They couldn't figure out why all this cool stuff was happening in Boston and California when, of course, everybody at the University of Chicago knew that they were smarter than those guys. Harvard was a vocational school compared to Chicago.
A.S.: I tried to start a small company during my residency program at [the University of Pennsylvania]. Normally, patients on a blood thinner called Coumadin get tested in the hospital, clinic, or the lab [to assess how fast their blood clots]. We were trying to start a company that was going to do Coumadin monitoring based on a portable test. It was a novel concept, but, unfortunately, it was too novel. The hard part wasn't the science: We had a lot of good data. The issue was the business model was fundamentally flawed because insurance companies wouldn't reimburse the concept. I also had no concept of what venture capital was. It's a really opaque entity that doesn't exactly hang a shingle or have a 1-800 line that you can call. So, it was a very eye-opening experience, and I saw that the intersection of business and medicine is a very interesting place to be.

Q: Does a VC in the life sciences need a scientific or medical background?
R.N.: I have a B.A. in biology, but I consider it an advantage, actually, that I don't have an advanced scientific degree. I'm an absorber: I learn my science by talking to a bunch of smart scientists. I've never worked in a lab and I have very thin knowledge in those areas. But the best investors are people who actually know how to bet on people and have a sense of whether the science is good. The people that get lost in the weeds in the science are usually poor investors, because if you ever really thought about how much risk there was in these things, you would never invest in anything. And so you have to do this based on a belief and faith that big problems that people will tell you are not solvable are solvable.
A.S.: For me, being a physician is integral to doing this job. I'm board-certified in internal medicine, so I did see patients and got extensive training. It really helps me know very quickly how a business concept or a company fits into the realm of health care. And being an internal medicine doctor, I've seen and studied all different types of diseases. That's important because sometimes, say, a new diagnostic looks good on paper, but then I remember if that diagnostic test is going to take 40 minutes, that doesn't really fit into the workflow if you spend an average 12 minutes per patient. But you can be a fabulous investor without having an M.D.

Q: What stage do you like investing in?
R.N.: We like early—before there's a company, when there's just a really cool idea. Highest risk and hypothetically highest return.
A.S.: We try to take less risk than most. But no matter how much diligence you do and how well you think you know the science and mitigate the risk, this is biology and biology is complicated. Plenty of investments have not gone well.

Q: What is an investment you made that didn't work out well?
A.S.: We had made an investment in a company called CeNeRx that was doing antidepressants through the monoamine oxidase pathway. We had a drug that had a proven mechanism of action—we even saw that the drug was actually making it into the brain, the site of action. We had all the basic science pieces worked out. But the trial failed.



Robert Nelsen: "The people that get lost in the weeds in the science are usually poor investors."

PHOTO: NATALIE FOBES

R.N.: Xcyte is a great example. We knew that if we took T cells out of humans and expanded them and put them back into humans that really cool things happen. It became the basis for what we call CAR T cells [a type of cancer immunotherapy] now. But it wasn't enough to really cure people then. We were just too early.

Q: How do you get ideas for companies?
R.N.: I kind of avoid conferences. People who go to conferences are chasing old science, actually. If you don't know about it a year ahead of when it's presented at the conference, then you're probably not up to speed on where the technology is. Scientists don't tell other scientists in their fields what they have. But they will tell investors. We mainly go to universities and find out who the top five or 10 smartest people are. You can look at publications, you can look at grant funds, you can look at young investigator awards, and then just ask people. We back good scientific DNA, and we back good management DNA. We put all of them in a room and just see what happens.
A.S.: People bring ideas to us, but oftentimes, the best ideas are ones where we understand there's an unmet need, and then we try to go find solutions for that space. Those, I think, can also be the most rewarding. We generally invest, but on occasion, we form companies ourselves. If you're trying to ride the wave, you're oftentimes already late. You have to look across it and toward the horizon to see what's coming and ride that one.

Q: What are common misconceptions you run into?
R.N.: Most academic scientists don't appreciate how hard it is to make a drug—how complicated it is to take a molecule and make it safe and how much it costs to do all that. There are a few who have been through it before, but it's kind of hard to teach people that. People's emotions also get in the way when it's about their science or money. They can understand that statistically there's a high failure rate. But those failures are other people's drugs, not theirs.
A.S.: For a new entrepreneur coming through, it's hard. And it's not just about the money. Working with the right venture capitalist can help you get there quicker and hopefully with less risk. But it doesn't mean it's going to be easy. I could go and say, "I got funded by so-and-so well-known venture fund" and that's great. It's a huge milestone for any entrepreneur. But it's just the beginning. ■

Published by AAAS

Corrected 12 June 2015; see full text.

GOT A STARTUP? RENT A BENCH

Biotech incubators such as LabCentral are lowering barriers to entrepreneurship

By **Trisha Gura**, *in Cambridge, Massachusetts*

With its cookie-cutter windows and boxy brick exterior, the building here on Main Street could be just another former 19th century warehouse or factory. It's no surprise to learn that passenger railroad cars were once built in its spacious interior. Yet the Cambridge landmark has a history not just of production, but also of innovation. In 1876, it housed the office of Thomas Watson, assistant to Alexander Graham Bell, when the pair made the first two-way long-distance phone call, to Boston. In the 20th century, it was home to Polaroid and the lab of Edwin Land when he invented the instant camera.

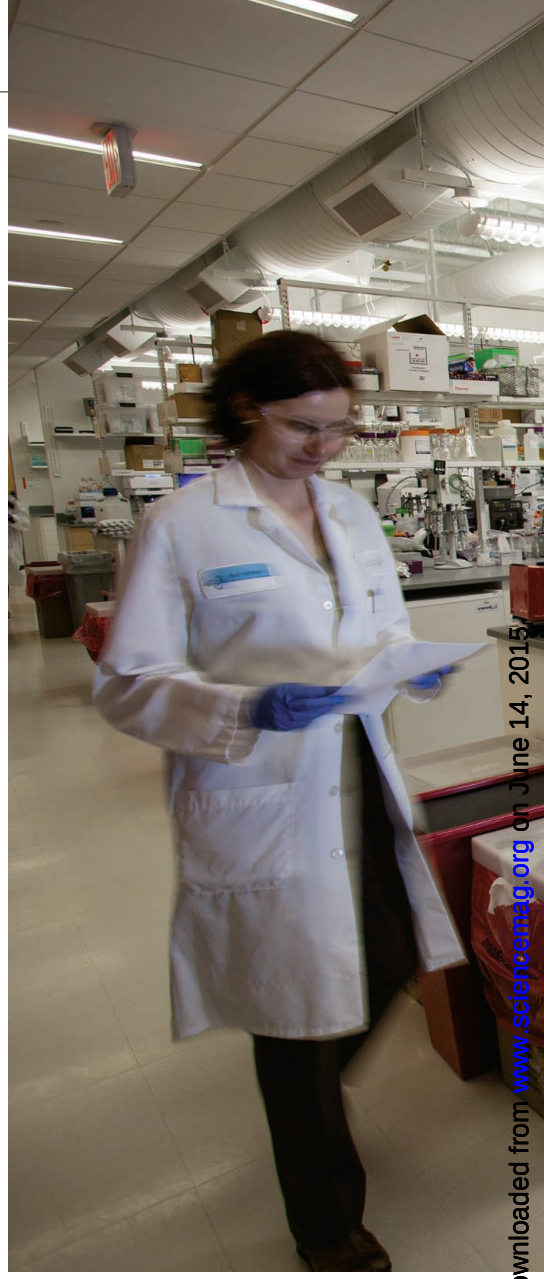
Today, a nonprofit organization called LabCentral has taken up that entrepreneurial heritage. The renovated, 2600-square-meter facility, now owned by the Massachusetts Institute of Technology (MIT) and leased to LabCentral, functions as a life science "incubator" that helps budding biotech firms combat the soaring costs of lab space and equipment in the red-hot Boston-Cambridge region. Any scientist with an idea and ambition can rent a bench and an office, sharing space, services, and high-cost tools with others pursuing their own entrepreneurial dreams. "It is very exciting because we are there at the nascent moment of many really, really cool companies," says molecular biologist Johannes Fruehauf, a LabCentral founder.



Molecular biologist Johannes Fruehauf and investor Peter Parker, two of LabCentral's founders, with Olivier Boss, a tenant at an earlier incubator (*left to right*).

It's also the nascent moment for facilities like LabCentral. Similar incubators are opening up in Cambridge, San Francisco, and other hotbeds of life science entrepreneurship, and startup companies are lining up to rent space. Incubators lower the entry barrier to the entrepreneurial world, foster networking, and serve as showcases of gleaming ideas for venture capitalists and bigger companies to browse. As startup founder Laura Hales, whose company Extend Biosciences was one of LabCentral's first tenants, puts it: "If you start talking to big pharma, you need to show them that you are established. Anyone who walks into this place is immediately impressed. It just speaks for itself."

THE IDEA BEHIND LABCENTRAL dawned in 2006 when Fruehauf's Ph.D. adviser, gastroenterologist Chiang Li at Beth Israel Deaconess Medical Center, launched Cequent Pharmaceuticals, bent on delivering molecular payloads of artificial RNA via genetically engineered bacteria. Backed by $22 million in venture capital and with a staff that quickly swelled to 17 people, Fruehauf chose a space at One Kendall Square, a hub of contemporary buildings in the so-called Boston Innovation Supercluster that encompasses MIT and a slew of life science companies.



He successfully negotiated the lease, renovated and equipped the lab, and jumped through the daunting hurdles of permitting and compliance. But Fruehauf also burned through $1.5 million and 6 months before he or colleagues could even lift a pipette. "In retrospect, it was really a bad use of our capital and time," he says.

Fast-forward a year. Li had sold Cequent to another company for $46 million, and Fruehauf was launching his own enterprise, called ViThera, based on a probiotic technology licensed from a French group. Bankrolled only by his own money—he wanted to stay away from venture capital funding—Fruehauf had to find a cheaper way.

So, he subleased lab space from a Kendall Square–based company called Pervasis, which was downsizing. Then he brought

PHOTOS: PAUL AVIS (2)

Downloaded from www.sciencemag.org on June 14, 2015

Published by AAAS

Corrected 12 June 2015; see full text.



Shannon Pendergrast and Anna Markowska of biotech startup Ymir value the networking opportunities at LabCentral.

in cash by essentially subletting the sublet. Word got out, demand increased, and by January 2011, Fruehauf spun off a new company—eventually called Cambridge Biolabs (CBL)—designed to provide tailor-made, minimal units of lab space for early startup companies.

Olivier Boss was one of his first customers. Coming out of a small biotech company focused on thwarting obesity, Boss and two colleagues launched Energesis Pharmaceuticals to develop a technology based on brown fat, which generates body heat by metabolizing stored fat. Desperately needing access to a lab, Boss initially collaborated with Stephen Farmer, an obesity researcher at the Boston University School of Medicine, but could only work in the laboratories there for academic goals, i.e., to churn out brown fat stem cells for Farmer's studies.

By one standard, the strategy was successful; it gleaned a $90,000 Small Business Technology Transfer (STTR) grant that Boss and Farmer shared. However, Boss still needed to conduct a commercial pilot study. In figuring out where to do that, he found himself in a tricky situation, one encountered by many a potential scientific entrepreneur. "People get in trouble when they start companies around academic technology and continue to use academic resources," Fruehauf says. Many, he adds, end up "fudging things" or conducting "submarine projects" that proceed underneath the university radar.

Boss wanted to do it right. He unearthed "the best option, the only option," he says, when he met Fruehauf in 2010. Then trying to bootstrap ViThera, Fruehauf offered Boss a bench and use of the company's lab facilities for $3000 a month. Boss accepted and in 6 months obtained results that convinced enough people to score a $750,000 STTR grant. He transplanted his brown fat cells into mice, and 3 years later—still renting from Fruehauf at CBL—has won another $1 million in grant money and partnered with pharmaceutical giant Johnson & Johnson on a project that may lead to clinical trials of brown fat therapies in people.

Could he have done it without the incubator? "Absolutely not," Boss says. "That lab space was what we needed. And not just us."

THE SUCCESS OF CBL prompted Fruehauf to gather backers, most notably $5 million from a Massachusetts state life science initiative, to found a second incubator, LabCentral, in the back half of the Main Street landmark. The space is a scientific entrepreneur's dream,

Published by AAAS

 Corrected 12 June 2015; see full text.

replete with cell culture facilities, biosafety level 2 labs, and a dizzying array of gadgets for analyzing cells, DNA, and proteins. A new glass-enclosed entrance has a patio for networking and the interior includes immaculate common spaces—lounges with video games, glass-walled conference rooms, and a well-stocked kitchen with an espresso machine. The place buzzes 24/7—different startup companies even share workbenches in shifts throughout the day and night to save money.

The arrangement is analogous to cloud computing in the information technology world, which gives high-tech entrepreneurs a cheap alternative to purchasing costly computer hardware. LabCentral and other incubators essentially proffer a cloud for life science research. "We dedicated ourselves to breaking down the expensive lab resource into such small increments that any entrepreneurial scientist with a credit card can get going," says Douglas Crawford, associate director of QB3, a University of California (UC) research institute that provides several incubator locations in the San Francisco Bay Area for UC faculty and other scientists.

Incubators offer more than physical facilities. LabCentral, for example, surveys the companies it hosts about other needs—finding the right lawyer, patent attorney, janitorial service—and then farms out the solution. Financial, legal, pharmaceutical, and even waste management companies have lined up at Fruehauf's doors, offering capital, mentorship, and a host of services, at free or reduced costs. Some sponsors figure if they offer their services—such as advice on patent filings—cheaply and early on, the relationship will blossom as early-stage companies grow up and move out.

Besides, what fledgling entrepreneur has the time and money to slog through environmental health and safety compliance? "As a scientist entrepreneur, your time should be exclusively focused on what problem your business can solve and how are you using science to address that," says John McQuillan, CEO and president of Triumvirate Environmental, a LabCentral founding sponsor that provides advice and waste management/environmental services to life science companies. "Any other question ought to be handed over to somebody else."

> *"We are there at the nascent moment of many really, really cool companies."*
>
> **Johannes Fruehauf**, LabCentral

STARTUPS LIKE the approach. LabCentral reached capacity within 6 months of opening in 2014—and now has a long waiting list. Similarly, within a half-year of opening in 2013, QB3 filled one 2230-square-meter incubator with 46 startup companies, most having fewer than five employees. Venture Development Center at the University of Massachusetts, Boston, last year had 104 applicants for a mere three open laboratory spaces (see table). Due to the high demand, it has become common for incubators to be very selective about the companies they host.

The surge of interest may stem, in part, from a major sea change now coursing through the pharmaceutical and biotech industries. Rather than conduct a lot of initial risky research in-house, larger companies are increasingly backing and partnering with startups, particularly at incubators. They are realizing that "a few hundred thousand dollars invested in a three-person company gives huge amount of return on investment," Crawford says.

For big companies searching for new ideas, incubators are a convenient place to look. By attending talks, symposia, and other events at the incubators, the big fish can land the most attractive startups, whether by investing in their technology, funding specific projects, or buying the companies outright. In fact, Pfizer leases part of the Main Street building and sponsors LabCentral for an undisclosed sum—in exchange for picking the recipients of two LabCentral slots.

LabCentral tenants also help each other. Hales and her partner at Extend, virologist Tarik Soliman, for example, partnered up with researchers on the same floor at a company called Advirna. The two startups co-wrote a Small Business Innovation Research grant proposal to tack the vitamin D metabolites developed by Extend onto Advirna's RNAs and so prevent their degradation in the body. The project was funded by the National Institutes of Health.

One might imagine that startups in such close proximity would be rivals. But the environment is more like a close-knit academic laboratory, LabCentral tenants say. "I thought people would be much more secretive," says Shannon Pendergrast, co-founder of Ymir Genomics, which focuses on using RNA in urine as diagnostics for diseases such as cancer. "But it has worked incredibly well."

LabCentral is now building "franchises" in San Diego, California; Chapel Hill, North Carolina; and New York City. Fruehauf is

Start me up

Incubators for biotech firms are popping up around the world, with the Boston and Northern California regions home to some of the most popular—and most successful, in terms of firms "graduated" to bigger sites and money raised by tenants.

	CAMBRIDGE BIOLABS	LABCENTRAL	VENTURE DEVELOPMENT CENTER	QB3 (FIVE SITES)	MASS INNOVATION LABS
Location	Cambridge, MA	Cambridge, MA	University of Massachusetts, Boston	San Francisco, Berkeley, Palo Alto	Cambridge, MA
Year launched	2010	2014	2009	2006–2014	2015
Size (square meters)	325	2600	1670	4600	11,520
Companies present	10	27	19	~85	1 so far
Companies graduated	65	4	42	~40	0
Capital raised by tenants	$360 million (aggregate)	$200 million (2014)	$123 million (aggregate)	$72.7 million (2014)	N/A

Published by AAAS

Corrected 12 June 2015; see full text.



Representatives of the companies working at LabCentral's historic building. The newly renovated facility provides space and facilities for startup companies in the biotech industry.

PHOTO: PAUL AVIS

also consulting with groups in Europe and Japan. He dreams of creating an incubator network, housing some 150 startups throughout the country.

On the West Coast, Crawford's QB3 has expanded to five sites and gets up to a half-dozen queries a week for total space that can hold only 62 companies. In the Boston area, chemist Amrit Chaudhuri and two other co-founders just opened the doors to Mass Innovation Labs, a 11,520-square-meter extravaganza of chemistry and biology space that offers a huge array of services, from DNA sequencing to a small animal facility, which is unique among incubators. According to Chaudhuri, the goal is to service startup companies that outgrow places like LabCentral, as well as academics whose large labs spill over from their university space and pharmaceutical subgroups.

Fruehauf is trying to address that expansion need by conjuring up his next venture: "graduation space" for incubator tenants. That may nest in the Main Street building itself—in 2017, another lease-holder on the second floor is due to move out. Fruehauf wants to emphasize scalable, private labs and offices but still maintain common elements of interaction and events such as lunch workshops with experts.

Kathryn Kosuda is an early LabCentral tenant who now needs a bigger home. A chemist by training, she and three other people she met at Harvard Business School started a firm in 2011 to develop a technology that exploits a silk protein to stabilize vaccines, allowing them to be shipped around the world without refrigeration. But having grown to 10 employees and "incubated" successfully, Vaxess Technologies wants more room soon. "We all joke about how it is going to be very difficult to find a new space," Kosuda says, "because we have set the bar so high with our initial location" at LabCentral.

EARLY ON, some venture capitalists voiced doubts about life science incubators. "They told us we were just creating an intensive care unit for little companies," Crawford says. The idea was that such companies would emerge only to face a dearth of capital, particularly on the heels of the recession prior to 2011.

"Now, people who said that look pretty bad," Crawford says. "There are lots of companies getting public ranking or attracting more and more investors from a more diverse setting."

Last year alone, LabCentral tenants collectively raised $200 million—equal to all biotech earnings in the country of Switzerland, Fruehauf says. In its first 2 years, QB3 Garage, the first and smallest of the Bay Area lineage, hosted six companies, four of which closed venture financing rounds, while a fifth was acquired by Affymetrix for $25 million.

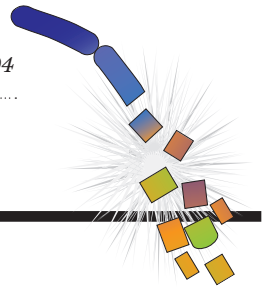
QB3 has been so successful that Crawford was able to tap private backers and found Mission Bay Capital, an $11.3 million seed-stage venture fund that invests in early-stage bioscience companies, three emerging from the QB3 network. He just closed a second fund of $25 million. "I agree there is a limit to these incubators," he says. "But nowhere do I feel that we are approaching it." ■

Trisha Gura is a writer based in Brookline, Massachusetts.

Published by AAAS

Shakedown on fracking *p. 1204*

How cancer chromosomes shatter *p. 1205*



PERSPECTIVES

ENTREPRENEURSHIP

Studying the start-up system

There is seemingly limitless, often breathless, rhetoric championing "innovation" and "entrepreneurship" as keys to harnessing science and technology for economic advancement. More elusive, and illuminating, is solid evidence on features that allow a dynamic technology commercialization ecosystem to thrive. *Science* invited social scientists to highlight insights from their research on what makes entrepreneur-driven systems flourish and how those lessons might inform policies and practices to help make rhetoric reality.

Financing experiments

By **Ramana Nanda**[1,2]† *and* **Matthew Rhodes-Kropf**[1,2]

Venture capital (VC) investors have recently been criticized for no longer financing innovations related to society's "biggest problems." We have shown that two defining features of VC investments are an extremely skewed distribution of outcomes and an inability to tell—up front—which will be successful. VCs therefore learn about the viability of potential investments through a multistage financing process, where each round of funding is tied to results of "experiments" that create information about future prospects (*1*). The value of staging stems from being able to abandon investments partway if information from early experiments is negative. Startups for which experiments are cheaper to run and are more discriminating are more attractive investments. The advent of cloud-computing significantly lowered costs of early experiments for firms in software, Internet, and digital media and shifted funding away from sectors where early experiments cost more and are less discriminating, such as biotechnology and energy production. Advances in simulation technologies, rapid prototyping, and gene sequencing have begun lowering costs of experiments in these sectors, as have platforms, such as Science Exchange, that allow startups to conduct early tests without investing in infrastructure upfront. Nevertheless, entrepreneurs in science-based ventures that are expensive to commercialize can also benefit from setting up experiments that help investors learn about viability early on. Although entrepreneurs are never happy when investors stop funding, structuring early experiments that facilitate such abandonment, by being highly specific (correctly identifying all failures), even if at the expense of sensitivity (correctly identifying every success), can actually help obtain investment in the first place. To increase the chances that innovations focused on society's biggest problems attract sufficient funding, government policy should focus on sectors or stages where the cost and the time to learn is high, thereby making it more difficult for private investors to finance experimentation.

POLICY

REFERENCES

1. W. R. Kerr, R. Nanda, M. Rhodes-Kropf, *J. Econ. Perspect.* **28**, 25 (2014).

10.1126/science.aab4135

Founders and joiners

By **Michael Roach**[3]‡ *and* **Henry Sauermann**[4,2]

Most efforts to promote technology entrepreneurship, such as courses and incubators, focus on potential founders of startup companies. Yet the vast majority of scientists and engineers contribute to entrepreneurship as "joiners"—employees who join founders in their efforts to start companies. We investigated individuals' entrepreneurial interests through a survey of nearly 4200 science and engineering Ph.D. candidates at tier 1 U.S. research universities (*1*), focusing on three questions: How prevalent are interests in joining a startup as an employee versus being a founder? How are joiners different from founders? How do contextual factors shape different entrepreneurial interests? Among the Ph.D.'s surveyed, 46% were interested in joining a startup as an employee, whereas 11% expected to one day start their own company. Compared with Ph.D.'s interested in careers in established firms, founders and joiners share similar preferences for an entrepreneurial work setting, such as a desire for greater autonomy, tolerance for risk, and a desire to commercialize technologies. However, founders are significantly more risk tolerant and have a stronger interest in management, whereas joiners are more interested in functional work activities

[1]*Harvard Business School, Boston, MA 02163, USA.* [2]*National Bureau of Economic Research, Cambridge, MA 02138, USA.* [3]*Cornell University, Ithaca, NY 14850, USA.* [4]*Georgia Institute of Technology, Atlanta, GA 30332, USA.* [5]*School of Management, Polytechnic University of Milan, 20156 Milan, Italy.* [6]*Rice University, Houston, TX 77251, USA.* [7]*Massachusetts Institute of Technology, Cambridge, MA 02139, USA.* [8]*Universitat Pompeu Fabra, 08005 Barcelona, Spain.* [9]*Barcelona GSE, 08005 Barcelona, Spain.* [10]*Banco de España, 08002 Barcelona, Spain.* [11]*Boston University, Boston, MA 02215, USA.* [12]*Hoover Institution, Stanford University, Stanford, CA 94305, USA.* **The opinions in this article are the sole responsibility of the authors and do not necessarily coincide with those of the Banco de España. Corresponding author. E-mail: †rnanda@hbs.edu (R.N.); ‡rmichael.roach@cornell.edu (M.R.); §chiara.franzoni@polimi.it (C.F.); ¶carlos.serrano@upf.edu (C.S.); ‖hochberg@rice.edu (Y.V.H.); #stern@mit.edu (S.S.)*

Published by AAAS

Downloaded from www.sciencemag.org on June 14, 2015



Downloaded from www.sciencemag.org on June 14, 2015

such as research and development (R&D). Preferences for financial income have little relation with interests in entrepreneurship. Together these preferences shape individuals' predispositions toward entrepreneurship, which in turn condition how they respond to factors thought to promote entrepreneurship, such as having a faculty adviser who has founded a company. Individuals with a strong predisposition toward entrepreneurship are most likely to be interested in becoming a founder, whereas those who lack preferences for entrepreneurial job attributes show no interest in founding, regardless of external factors. Individuals with a moderate entrepreneurial predisposition are most susceptible to external factors, which increase their interest in joining a startup as an employee. Efforts to foster technology entrepreneurship should recognize that individuals may respond in different ways; blanket efforts, such as mandated entrepreneurship training, are likely to be inefficient. Programs should also prepare scientists and engineers for a variety of entrepreneurial roles—joiners as well as founders.

ILLUSTRATION: DAVIDE BONAZZI

REFERENCES

1. M. Roach, H. Sauermann, *Manage. Sci.*, 10.1287/mnsc.2014.2100 (2015).

10.1126/science.aab2804

Cash from the crowd

By **Massimo G. Colombo,[5] Chiara Franzoni,[5]§ Cristina Rossi-Lamastra[5]**

Crowdfunding (CF), in which financing for projects is sought via the Internet from large groups of individuals, is a $3.3 billion per year phenomenon. But it's not clear how well CF, typically used for creative arts projects, can be used to finance science and technology ("tech") projects. We analyzed nearly 112 thousand CF campaigns launched on Kickstarter.com through late 2014 (see supplementary materials). The share of tech projects is increasing, from 4% of total projects in 2009 to 8% in 2014. Tech projects have the largest average target budgets ($86,529; nontech average, $18,003). The rate of tech projects that reached their target budget and were funded, 38%, is lower than the overall 58% success rate. Tech projects received 14% of the capital raised through Kickstarter, totaling $139.8 million. Although this is a substantial amount, it is only 3% of the $4.7 billion invested by venture capitalists in high-tech ventures in the United States in 2013. CF also differs qualitatively from other forms of entrepreneurial finance.

Published by AAAS

CF money is not invested in exchange for a financial return but is pledged in the form of product prepurchasing from end users as consumers. This has three important implications. First, CF invites gathering feedback from users during project development, a practice shown to be effective in problem-solving and product-testing in open-source and open-innovation platforms. By cutting development time and failure rates, this feature offers new means for tech transfer. Second, crowdfunders are highly responsive to social exchanges that the entrepreneur uses inside the CF community and beyond (*1*). Third, CF is more suitable when the project outcome is a ready-to-use product that can be offered in exchange for the pledge. This makes CF more suitable for applied projects, which are close to market delivery, but calls into doubt the suitability of CF as a means for funding basic research.

SUPPLEMENTARY MATERIALS

www.sciencemag.org/content/348/6240/1201/suppl/DC1

REFERENCES

1. M. G. Colombo, C. Franzoni, C. Rossi-Lamastra, *Entrep. Theory Pract.* **39**, 75 (2015).

10.1126/science.aab3832

Intangible but bankable

By **Yael V. Hochberg,[6,7,2] Carlos Serrano,[8,9,10]*¶ Rosemarie Ziedonis[11,12]**

Young science and technology companies are often rich in intangibles but lack physical assets and cash flows required to secure a loan. Intangibles, such as patents, are effectively "unbankable" for traditional lenders because of international banking regulations. Intangibles also are often difficult to value and sell. External debt is therefore widely cast as an unlikely way to fund the risky projects of intangibles-rich companies. Despite this conventional wisdom, we uncover a surprisingly active market for "venture lending" to patent-producing U.S. startups in three innovation-intensive sectors: medical devices, semiconductors, and software (*1*). Venture lenders fund such startups in early stages of development, most often alongside VC investors. According to one estimate, venture lenders supply roughly $5 billion in growth capital to startups each year, with funds originating from both regulated banks and specialized lenders. To minimize downside risk, lenders typically require a lien on assets, including intangibles, and record liens involving patents with the U.S. Patent and Trademark Office. Lenders also pay keen attention to the solvency and reputations of VCs backing startups that apply for funding. Among VC-backed startups in our sample, 36% received venture loans. Lending was more prevalent for startups with top-tier VCs and for startups with more "saleable" patents. After the NASDAQ crash of 2000, many VCs faced severe constraints in raising capital, whereas others were flush with recently raised funds. Lenders continued to finance startups backed by less capital-constrained investors but withdrew from otherwise promising projects that may have needed their funds the most. Thus, VCs play a vital intermediary role in lending relations with risky startups. Attempts to stimulate entrepreneurial activity through debt channels alone may have limited economic effects in the absence of well-developed markets for buying and selling patents and infrastructures for equity investing.

REFERENCES

1. Y. V. Hochberg, C. Serrano, R. H. Ziedonis, "Patent collateral, investor commitment, and the market for venture lending" (Working paper 20587, National Bureau of Economic Research, Cambridge, MA, 2014); www.nber.org/papers/w20587.

10.1126/science.aac4837



ILLUSTRATION: DAVIDE BONAZZI

Accelerators and ecosystems

By **Yael V. Hochberg[6,7,2]** | *and* **Daniel C. Fehder[7]**

A new institutional form has emerged in the entrepreneurial ecosystem in recent years: the seed accelerator. These fixed-term cohort-based "boot camps" for startups offer education and mentorship for startup founders and culminate in a "demo day," during which graduates pitch their businesses to potential investors. Many local governments hope to use accelerators to transform their local economies through establishment of startup technology clusters. Evidence of accelerators' efficacy is limited, however, so we examine their effects on regional entrepreneurial ecosystems, particularly provision of venture capital (VC) financing to new startups (*1*). Accelerators emerge in different regions in different years, often for reasons exogenous to the nature of the ecosystem or precisely because of its lacking. This allows us to compare changes in regions that receive an accelerator with similar regions that do not have one. We see a shift in funding for startups in accelerator-treated regions: more deals, more dollars, and more local investment groups. This applies to startups that attend the accelerator and those that do not. Most accelerators focus on software companies, and regions with accelerators shift toward a higher share of early-stage software and information technology–related VC deals (although financing for other industry groups, such as biotechnology, is not necessarily reduced). These patterns hold both for high- and low-ranked accelerators in the annual Seed Accelerator Rankings, which suggests that the funding increase is less about the effect of accelerator programs on companies that attend them and more about what such programs

Published by AAAS



do to encourage latent entrepreneurial activity in the region more generally—providing role models, catalyzing establishment of other ecosystem institutions, and acting as a nexus for startup activity. Although accelerators studied so far focus on software startups, further research will be needed to assess new programs emerging to serve biotech and hardware startups.

REFERENCES AND NOTES

1. D. C. Fehder, Y. V. Hochberg, *Accelerators and the Regional Supply of Venture Capital Investment* (Social Science Research Network, 2014); .http://dx.doi.org/10.2139/ssrn.2518668.

10.1126/science.aab3351

Linking and leveraging

By **Fiona Murray**[7,2] *and* **Scott Stern**[7,2]#

Beyond aspiring to become the "next" Silicon Valley, how can a region leverage innovation-driven entrepreneurship for economic and social progress? Given the poor performance of government support for entrepreneurship, should the job be left to the private sector? Moving beyond the traditional public-private debate, the MIT Regional Entrepreneurship Acceleration Program (REAP) (http://reap.mit.edu) charts a new approach.

REAP builds on an ecosystem framework drawing on recent research highlighting distinct, yet interdependent, roles of innovative capacity (the ability to develop new technology), entrepreneurial capacity (the ability to scale startup businesses), and the economic clusters supporting a region. Rather than focus solely on entrepreneurship (as do many government initiatives) or innovation (often focused on increased R&D investment), REAP builds on evidence that successful regions link the two to establish a comparative advantage through innovation-driven startups.

MIT REAP's 2-year program brings together regional teams of entrepreneurs; risk-capital, corporate, and university leadership; and government. Although this approach is simple to describe, most regions have found it challenging to link high-level stakeholders for sustained effort (and are often surprised by the many connections that are "missing" from their ecosystem). Teams undertake data-driven, regional diagnoses, including assessing strengths and weaknesses in their regional capacities, and benchmark their ecosystem using our novel methodology for measuring entrepreneurial quality through the use of business registration records and predictive analytics (*1*). These insights are turned into action: Teams aim to catalyze their innovation ecosystem in a measurable and sustainable way and build an organization for ongoing regional collective action.

For example, REAP Scotland is leading changes in Scotland's economic-development approach to emphasize entrepreneurial mentoring (an area that had been previously downplayed) and the development of a dynamic network for Scottish entrepreneurs and expatriates (a potential strength that had not previously been leveraged). These initiatives upgrade the region's entrepreneurial capacity in order to match its traditional strength in innovative capacity (see www.hie.co.uk/business-support/entrepreneurship/mit-reap/).

REFERENCES

1. J. Guzman, S. Stern, *Science* **347**, 606 (2015).

10.1126/science.aac5843

Published by AAAS

Downloaded from www.sciencemag.org on June 14, 2015



A fracking wellhead.

SEISMOLOGY

Earthquakes induced by fluid injections

Controlling fluid injection may mitigate the extent of induced earthquakes

By **Francois H. Cornet**

In the early 1960s, the U.S. Army unintentionally triggered some seismic activity by injecting waste fluids into the basement rock beneath the Rocky Mountain Arsenal, near Denver, Colorado (*1*). It is now recognized that an increase in the pressure applied by the fluids that fill fractures and faults at depth balances progressively the normal stress exerted through the rock on these fractures but leaves the shear stress supported by these surfaces unchanged. According to friction laws, when the fluid pressure gets too high and the effective normal stress gets too low, shear motion starts. This motion is generally considered to be mostly seismogenic, that is, to be the source of earthquakes that may reach in some localities magnitudes larger than 5, or even 6, as was observed upon filling the Koyna Dam in India in the early 1960s. Today, the phenomenon of fluid-induced seismicity has become a societal concern wherever injection of large quantity of fluids at depth is involved. On page 1224 of this issue, however, Guglielmi *et al.* (*2*) report that water injected in a natural fault at a depth of 282 m generates nonseismic motion. That is, the ground displacements take place at slow velocities (≈4 μm/s), with only very small microseismic activity.

By injecting water in a 500-m-long fault, Guglielmi *et al.* initiated a shear motion along the fault that reached 0.3 mm together with a larger normal displacement (dilatancy) before the first microseismic event was detected. The onset of microseismic activity was associated with a decrease in the rate of dilatancy. Observations demonstrate that the cumulative seismic displacements account for only a small fraction of the slip occurring on the fault segment. The total released moment is determined to have reached 65×10^9 Nm (equivalent to a 1.17 seismic moment magnitude) and is much larger than the cumulated moment released by micro-earthquakes. Guglielmi *et al.* then discuss whether this aseismic slip was mostly caused by the decrease in fluid pressure induced by dilatancy or whether it was the result of a rate-strengthening behavior of friction (the coefficient of friction increases with slip rate). They conclude that the results are due to an increase in the friction coefficient from an original value of 0.4 to a final value of 0.8 and suggest a logarithmic rate-dependent friction law.

The existence of aseismic slip associated with fluid injections is known. For example, by modeling the measured stress perturbation associated with fluid injection Scotti and Cornet (*3*) concluded that aseismic slip occurred. Calo *et al.* (*4*) referred also to large aseismic slips for interpreting seismic velocity variation linked to change in fluid-injection rate. Cornet *et al.* (*5*) observed large displacements in a borehole after a fluid injection and reported that these displacements were much larger than the shear displacement associated with the largest observed micro-earthquake. However, they could not exclude the possibility that observed displacements resulted from a large number of microseismic events with magnitudes so small that they had gone undetected.

Institut de Physique du Globe de Strasbourg, 5 Rue René Descartes, F 67084 Strasbourg Cedex, France.
E-mail: francois.cornet@unistra.fr

Downloaded from www.sciencemag.org on June 14, 2015

PHOTO: BRENNAN LINSLEY/AP PHOTO/CORBIS

Published by AAAS

The findings reported by Guglielmi *et al.* provide direct observational evidence that aseismic slip does occur. Furthermore, their suggestion of a logarithmic rate dependency of friction provides a possible route to controlling seismicity induced by fluid injections. If aseismic slip could be monitored continuously during fluid injection, then the injection flow rate could be adjusted to keep the slip rate within the range where motion remains aseismic. However, one difficulty is in detecting aseismic slip during deep injections, and an interesting point of the Guglielmi *et al.* paper is their description of a specific in situ observation tool.

An important issue concerns the applicability of these results to greater depths. Indeed, as depth increases, so does the normal stress supported by fractures and faults, and it is not clear yet how the rate dependency of friction varies with the effective normal stress. However, indirect observations of aseismic slip described by Calo *et al.* (*4*) concern fluid injections at 4-km depths, and this suggests that the control of seismicity induced by large fluid injections may be possible for many engineering applications.

Another delicate issue is that raised in regions where the natural stress field is close to instability. It may be feared that even a small stress perturbation close to the ground surface may trigger earthquakes. Yet, interestingly, results observed during a fluid injection through the Philippine fault, which creeps at a rate of 3 cm per year at the location where injection was conducted, demonstrated that no seismic event was triggered on the fault (*6*). Clearly, a better understanding of the friction law is necessary before large-scale applications of Guglielmi *et al.*'s findings become realistic. Their results give credibility to the proposition on earthquake control through proper fluid injection, as was formulated by Griggs after the Denver earthquakes in the late 1960s and presented to an ad hoc panel on earthquake prediction (*7*). ■

REFERENCE

1. J. H. Healy, W. W. Rubey, D. T. Griggs, C. B. Raleigh, *Science* **161**, 1301 (1968).
2. Y. Guglielmi *et al.*, *Science* **348**, 1224 (2015).
3. O. Scotti, F. H. Cornet, *Int. J. Rock Mech. Min. Sci.* **31**, 347 (1994).
4. M. Calo, C. Dorbath, F. H. Cornet, N. Cuenot, *Geophys. J. Int.* **186**, 1295 (2011).
5. F. H. Cornet, J. Helm, H. Poitrenaud, A. Etchecopar, *Pure Appl. Geophys.* **150**, 563 (1997).
6. R. Prioul, F. H. Cornet, C. Dorbath, M. Ogena, E. Ramos, *J. Geophys. Res.* **105** (B6), 13595 (2000).
7. C. B. Raleigh, J. H. Healy, J. D. Bredehoeft, in *Flow and Fracture of Rocks*, H. C. Heard, I. Y. Borg, N. L. Carter, C. B. Raleigh, Eds. (AGU, Washington, 1972), pp. 275–284.

10.1126/science.aab3820

GENETICS

Making heads or tails of shattered chromosomes

Isolation of lagging chromosomes in micronuclei causes catastrophic genome rearrangements

By **Wigard P. Kloosterman**

The human genome is subject to continuous change as a result of spontaneous DNA mutation. Most of the genetic changes are harmless, but occasionally they can disturb normal cell functioning and lead to cancer or congenital diseases. Much of the novel genetic variation that arises in human genomes affects only one or a few nucleotides. However, catastrophic changes of genome structure, termed chromothripsis, can produce a dramatic reorganization of DNA on one or even several chromosomes. A recent study by Zhang *et al.* (*1*) has now revealed a molecular mechanism that causes chromothripsis.

Chromothripsis was discovered as a mutational phenomenon in the genomes of tumors (*2*) and in patients with congenital disease (*3*). The emergence of chromothripsis as an important genomic change in cancer has considerably influenced our thinking of how tumors develop. Rather than a gradual and sequential accumulation of genetic changes, chromothripsis can provoke a sudden change in the cancer genome, with simultaneous effects on multiple genes. Since these initial discoveries, the molecular cause of chromothripsis has been a subject of considerable debate (*4*).

Chromothripsis is marked by massive and clustered chromosomal rearrangements, random joining of broken DNA ends, and a frequent occurrence of deletions (*5*). On the basis of these genomic characteristics, a rearrangement model was proposed that involved massive chromosome shattering by double-stranded DNA breaks, followed by reassembly of the chromosome segments into a new, mosaic chromosome (*2*).

An alternative to the shattering model (*6*) was based on the configuration of rearranged genomes in patients with congenital disease. These showed alternating regions of genome deletion, duplication, and even triplication, suggesting the involvement of aberrant DNA replication. This replicative mode of chromothripsis formation is known as microhomology-mediated break-induced replication (MMBIR). In essence, MMBIR involves a broken replication fork exposing a single-stranded DNA end that reforms a replication fork on a different (remote) DNA template.

Arguably, the most fascinating aspect of chromothripsis is the striking localization of the massive rearrangements to just one or a few chromosomes, which raises the question of how the rest of the genome escapes this catastrophic event. An appealing hypothesis was advanced by the Pellman lab, which had previously studied micronuclei that form around lagging chromosomes that result from chromosome segregation errors (*7*). An isolated chromosome within a micronucleus accumulates

> ***"...chromothripsis can provoke a sudden change in the cancer genome..."***

DNA damage during DNA replication (S phase) and in the G_2 phase of the cell cycle. The damage is associated with the loss of compartmentalization due to collapse of the micronuclear envelope, which reduces normal nuclear functions (*8*). Work by Crasta *et al.* showed that a small fraction of the chromosomes in micronuclei undergo pulverization, suggesting that micronuclei may be the source of chromothripsis (*7*).

However, the question remained whether these pulverized chromosomes in micronuclei assemble into chromosomes with a chromothriptic appearance similar to those observed in the initial genome sequencing studies (*2*, *3*). Answering this question required a combination of cell biological experiments and genomic sequencing. In the current study by Zhang *et al.*, chromosome segregation errors were induced in human epithelial cells after inhibition of the tumor

Department of Medical Genetics, Center for Molecular Medicine, University Medical Center Utrecht, 3584CG Utrecht, Netherlands.
E-mail: w.kloosterman@umcutrecht.nl

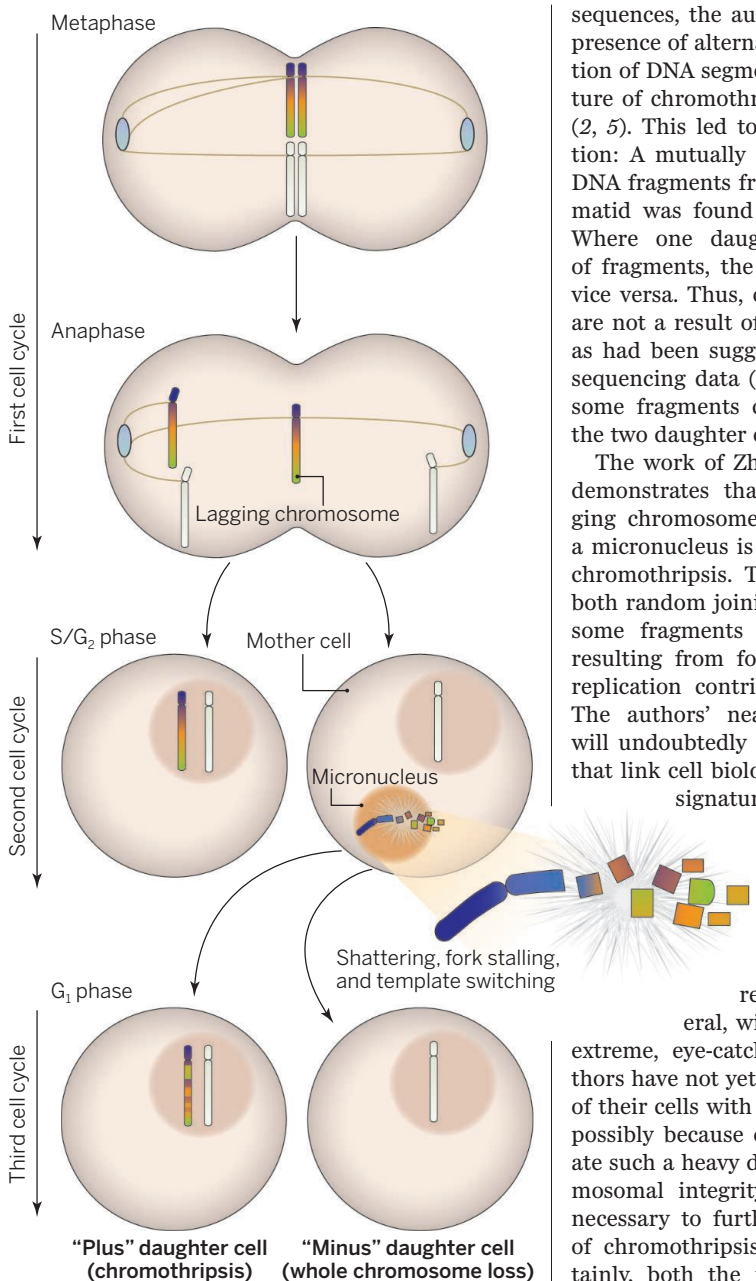
Published by AAAS

Corrected 12 June 2015; see full text.

suppressor p53, the truncation of which is associated with chromothripsis (*9*). The fate of subsequent micronucleated lagging chromosomes was traced using a sophisticated setup of live-cell imaging and single-cell sequencing, termed Look-Seq. The complete genomes of daughters from cells with micronuclei were sequenced. One challenge emerged, namely the identification of the chromosome that was present in the micronucleus of the mother cell. It turned out that the two postmicronuclear daughter cells displayed asymmetry in the number of (at least) one of their chromosomes: either a 2:1 or 3:2 ratio. This was expected because of reduced DNA replication in micronuclei. In each case, the daughter with the higher chromosome number (the "plus" cell) contained the chromosome that was micronucleated in its mother.

A subsequent analysis addressed whether the DNA damage that was observed in micronuclei in the mother cells led to an increase in the number of rearrangements on the chromosome that had passed through a micronucleus. This was indeed observed: First, there was a marked enrichment of rearrangements on the chromosomes with asymmetric chromosome number. Moreover, on the basis of genetic changes that distinguish both homologous chromosomes, it could be inferred that most rearrangements had specifically occurred on the extra chromatid in the plus cell. This suggested that the rearrangements were caused by DNA breakage in the micronucleus of the mother cell. In one of the analyzed cells, two chromosomes had gone through a micronucleus together, and this led to interchromosomal translocations. Also, small circular chromosome fragments were found. These are presumed to be precursors of "double minutes," acentric chromosomes that are a frequent cause of oncogene amplification in human cancer and have been associated with chromothripsis (*2*, *9*).

The genomic characteristics of the complex rearrangements in daughter cells were assessed to gather insight into the rearrangement mechanism. Analysis of the breakpoint junctions—the joints by which broken DNA ends are fused together—frequently showed short stretches of sequence homology (termed microhomology), indicating break repair by alternative end-joining or MMBIR. In addition, occasional chains of short fragments from remote regions on the rearranged chromosome were found, supporting serial template switching by MMBIR (*6*). Besides the breakpoint sequences, the authors also examined the presence of alternating deletion and retention of DNA segments, a characteristic feature of chromothripsis in cancer genomes (*2*, *5*). This led to an interesting observation: A mutually exclusive distribution of DNA fragments from the rearranged chromatid was found for two daughter cells. Where one daughter showed retention of fragments, the other showed loss, and vice versa. Thus, chromothriptic deletions are not a result of loss of DNA fragments, as had been suggested by cancer genome sequencing data (*2*). Instead, the chromosome fragments can be divided between the two daughter cells.



Path of destruction. A chromosome segregation error during cell division produces a lagging chromosome, which ends up in a micronucleus where shattering and rearrangement happen. After cell division, two daughter cells are produced, one of which carries a chromothriptic chromosome.

The work of Zhang *et al.* unequivocally demonstrates that DNA damage of lagging chromosomes within the context of a micronucleus is one mechanism causing chromothripsis. The paper confirms that both random joining of shattered chromosome fragments and template-switching resulting from fork stalling during DNA replication contribute to chromothripsis. The authors' neat experimental system will undoubtedly catalyze new discoveries that link cell biology to genomic mutation signatures.

But there is much more: A new mutational mechanism was discovered that is a potentially widespread source of chromosome rearrangements in general, with chromothripsis as an extreme, eye-catching, outcome. The authors have not yet shown stable outgrowth of their cells with induced chromothripsis, possibly because cells do not easily tolerate such a heavy disturbance of their chromosomal integrity. Outgrowth would be necessary to further understand the role of chromothripsis in tumorigenesis. Certainly, both the mutational process and subsequent selection for viability or advanced growth shape the final configuration of chromothriptic chromosomes in the context of cancer and genetic disease. ■

REFERENCES

1. C.-Z. Zhang, A. Spektor, H. Cornils, J. M. Francis, E. K. Jackson, S. Liu, M. Meyerson, D. Pellman, *Nature* 10.1038/nature14493, (2015).
2. P. J. Stephens *et al.*, *Cell* **144**, 27 (2011).
3. W. P. Kloosterman *et al.*, *Hum. Mol. Genet.* **20**, 1916 (2011).
4. A. J. Holland, D. W. Cleveland, *Nat. Med.* **18**, 1630 (2012).
5. J. O. Korbel, P. J. Campbell, *Cell* **152**, 1226 (2013).
6. P. Liu *et al.*, *Cell* **146**, 889 (2011).
7. K. Crasta *et al.*, *Nature* **482**, 53 (2012).
8. E. M. Hatch, A. H. Fischer, T. J. Deerinck, M. W. Hetzer, *Cell* **154**, 47 (2013).
9. T. Rausch *et al.*, *Cell* **148**, 59 (2012).

10.1126/science.aac5277

Published by AAAS

IMMUNOLOGY

Microbial metabolite triggers antimicrobial defense

Bacteria can activate innate immune responses by releasing a metabolite that enters host cells

By **Sky W. Brubaker** *and* **Denise M. Monack**

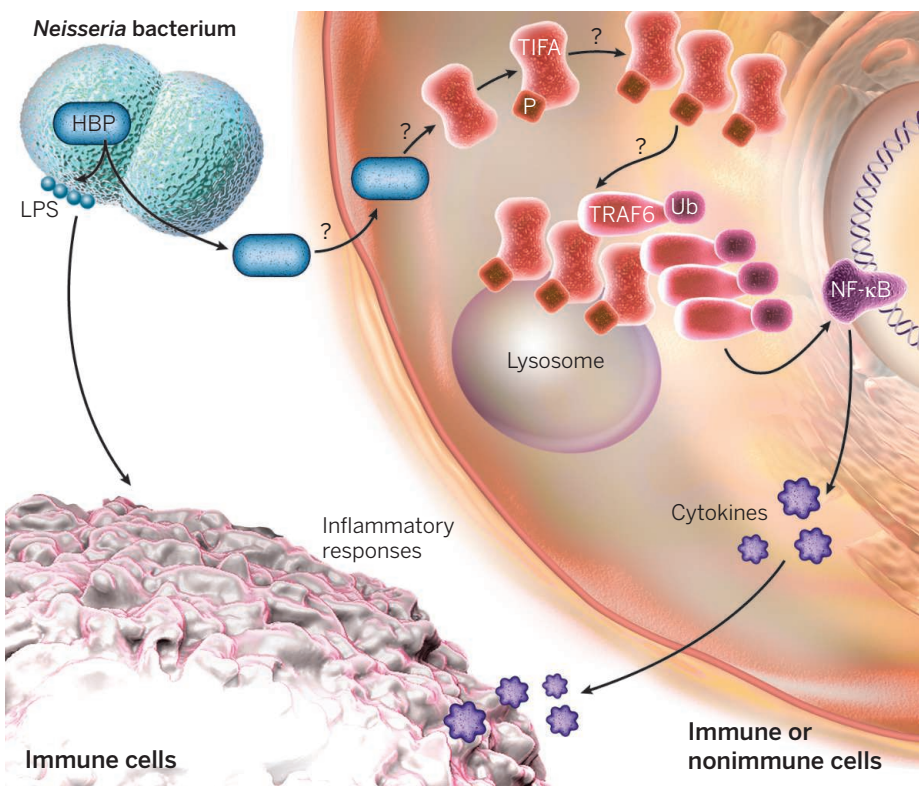
In general, innate immune responses are beneficial to the host. However, under certain circumstances, such as coinfections, these responses may contribute to disease progression. For instance, an initial infection may induce an immune response that renders the host susceptible to a subsequent infection by a different pathogen. For years, it has been understood that *Neisseria gonorrhoeae* and HIV coinfection increase viral shedding and transmission (*1*). However, the molecular mechanisms that control this phenomenon have been unclear. *Neisseria* spp. release a factor that can activate the transcription factor nuclear factor κB (NF-κB) in host cells and drive HIV gene expression (*2*). On page 1251 of this issue, Gaudet *et al.* (*3*) reveal the identity of this bacterial-derived factor, as well as the signaling axis through which it drives innate immune gene expression. This detection pathway may constitute a previously unknown innate immune signaling response with broader implications in microbial defense, as well as the pathogenesis of HIV.

In mammals, host defense and immunity rely heavily on pattern recognition receptors expressed by cells of the innate immune system. When activated, these receptors initiate inflammation at the site of infection and instruct adaptive immune responses (*4*). The receptors recognize conserved motifs of microbial and viral origin that are often referred to as pathogen-associated molecular patterns (PAMPs). Both transcriptional and nontranscriptional responses can take place following PAMP detection; however, the responses mediated by NF-κB are most notable for the production of proinflammatory cytokines. Importantly, HIV utilizes NF-κB for its own expression (*5*). Therefore, innate immune signaling can enhance the replication of HIV in some cases.

Gaudet *et al.* took a genetic and biochemical approach to identify the PAMP released by *Neisseria* spp. as heptose-1,7-bisphosphate (HBP). Interestingly, this monosaccharide belongs to part of the biosynthetic pathway that produces lipopolysaccharide, a membrane component of Gram-negative bacteria and a potent innate immune agonist (*6*). Thus, HBP is a common metabolite among many Gram-negative bacterial species. However, the release of HBP into the extracellular environment by *Neisseria* spp. is unique. Other Gram-negative species require bacterial lysis to liberate HBP and produce an immunostimulatory effect.

Gaudet *et al.* show that either the lysates of Gram-negative bacteria or the supernatants from *Neisseria* spp. that have not been intentionally lysed can induce the activity of NF-κB in immune cells, resulting in a transcriptional profile similar to those associated with other activated innate immune receptors. Importantly, these transcriptional changes depend on HBP. Intracellular delivery of lysates or synthetic HBP into host cells greatly enhanced transcriptional responses, indicating that HBP is detected from within the cell. However, the mechanism by which HBP is transported into the host cell during *Neisseria* spp. infection remains to be determined. Although HBP is actively released from viable *Neisseria* spp., its uptake may be controlled by an unidentified host factor or process.

To characterize the HBP detection pathway in host cells, Gaudet *et al.* performed a genome-wide RNA interference screen and identified TRAF-interacting protein with forkhead-associated domain (TIFA). This protein is a constituent of a cellular signaling pathway controlled by the receptor for the cytokine interleukin-1. TIFA interacts with tumor necrosis factor receptor–associated factor 6 (TRAF6) to activate the transcription factors NF-κB and activator protein 1 (*7*). Treatment of immune or nonimmune cells with HBP triggered several regulatory events that control the activity of TIFA, including tyrosine phosphorylation, the formation of large oligomeric complexes, and the recruitment of phosphorylated oligomers



Antimicrobial defense. During *Neisseria* infection, a bacterial metabolite (HBP) either incorporates into lipopolysaccharide (LPS) or is released. HBP can enter a host cell and initiate TIFA activation, which involves phosphorylation (P), oligomerization, relocalization to lysosomes, and TRAF6 interaction. TRAF6 is activated by ubiquitin (Ub) modification and triggers the canonical NF-κB activation pathway, which drives the expression of innate immune genes (such as cytokines), and HIV replication during coinfection.

ILLUSTRATION: NICOLLE FULLER

Department of Microbiology and Immunology, Stanford School of Medicine, Stanford University, Stanford, CA 94305, USA. E-mail: dmonack@stanford.edu

Downloaded from www.sciencemag.org on June 14, 2015

Published by AAAS

to lysosomes. There, TIFA interacts with TRAF6, which has been modified with ubiquitin. A canonical NF-κB activation pathway is subsequently triggered by oligomers of ubiquitinated TRAF6, which ultimately induces innate immune gene expression (*8*) (see the figure).

The regulators that control this cascade of events will be of interest in future studies. For instance, the identity of the tyrosine kinase that phosphorylates TIFA remains to be determined. Subcellular relocalization of adapter proteins involved in controlling innate immune responses can also be a point of regulation for gene expression (*9*). Therefore, identifying the factors that control TIFA relocalization to lysosomes after HBP treatment will be critical for understanding its regulation. It is also unclear whether an upstream HBP receptor exists, or if TIFA itself is the functional HBP receptor.

Gaudet *et al.* further observed that injection of HBP-containing bacterial supernatants into mice elicited a proinflammatory response, and sublethal *Neisseria meningitides* infection of mice increased antibody titers and immunoglobulin class switching. However, it is unclear whether these responses contribute to the control or elimination of *Neisseria* spp. during infection. Given that *Neisseria* spp. replicate primarily outside of mammalian cells, it will be important to determine, in the context of an infection, which host cells respond to HBP and how HBP gains access to the host cell cytosol.

The bacterial metabolite HBP appears to fit the classical definition of a PAMP because it is not a product of eukaryotic or mammalian cell biology, it is found in a broad class of prokaryotes (Gram-negative bacteria), and it stimulates the production of cytokines that drive inflammation and adaptive immune responses (*10*). However, HBP is not released from other Gram-negative bacteria, and it is unclear whether the response to this metabolite is a general mechanism of antimicrobial defense. Regardless, understanding the TIFA-mediated immune response to HBP may provide insight into therapies for patients coinfected with *N. gonorrhoeae* and HIV. ■

REFERENCES

1. S. R. Galvin, M. S. Cohen, *Nat. Rev. Microbiol.* **2**, 33 (2004).
2. R. J. Malott *et al.*, *Proc. Natl. Acad. Sci. U.S.A.* **110**, 10234 (2013).
3. R. G. Gaudet *et al.*, *Science* **348**, 1251 (2015).
4. N. W. Palm, R. Medzhitov, *Immunol. Rev.* **227**, 221 (2009).
5. J. Hiscott, H. Kwon, P. Génin, *J. Clin. Invest.* **107**, 143 (2001).
6. B. Kneidinger *et al.*, *J. Bacteriol.* **184**, 363 (2002).
7. H. Takatsuna *et al.*, *J. Biol. Chem.* **278**, 12144 (2003).
8. C. K. Ea *et al.*, *Proc. Natl. Acad. Sci. U.S.A.* **101**, 15318 (2004).
9. S. W. Brubaker *et al.*, *Annu. Rev. Immunol.* **33**, 257 (2015).
10. C. A. Janeway Jr., *Quant. Biol* **54**, 1 (1989).

10.1126/science.aac5835

BIOMEDICINE

Bringing PGE_2 in from the cold

A small molecule that prevents the breakdown of a prostaglandin promotes tissue regeneration

By **Garret A. FitzGerald**

Prostaglandins (PGs) are evanescent, locally acting lipids. They are not stored within cells, but are generated when their precursor, arachidonic acid, is mobilized from cellular membranes by rather nonspecific activation of phospholipases. Most cells generate one or two dominant PGs, each with a remarkable diversity of effects. Prostaglandin E_2 (PGE_2) is a vasodilator that acts with other PGs and metabolic products of arachidonic acid to promote pain and inflammation. The development and clinical use of drugs that suppress the production of these PGs has been ongoing for decades, but PGE_2 also has been long recognized to have a role in tissue maintenance and regeneration. Its stable analog, dimethyl PGE_2, is currently being evaluated for use as an adjunct to hematopoietic stem cell transplantation. On page 1223 of this issue, Zhang *et al.* (*1*) report that elevating the capacity of tissues to form PGE_2 by inhibiting 15-hydroxyprostaglandin dehydrogenase (15-PGDH), its major inactivating enzyme, augments the capacity for tissue regeneration in mouse models. So, is it time to bring PGE_2, which we are so used to suppressing, in from the cold?

The biosynthesis of PGs begins with the transformation of arachidonic acid to endoperoxide intermediates by the prostaglandin G/H synthase enzymes, colloquially known as cyclooxygenases (COX-1 and COX-2), the targets of nonsteroidal anti-inflammatory drugs (NSAIDs), including aspirin. These PG endoperoxides are acted on, in turn, by isomerases and synthases to generate PGs of the E, I, D, and F series along with thromboxane A_2. Although some PGs can activate nuclear receptors, the evidence that they do so at concentrations actually formed in biological systems is scant. Suppression of PG formation by NSAIDs relieves pain and inflammation but may also result in cardiovascular and gastrointestinal adverse events, whereas the effectiveness of aspirin is well established in the secondary prevention of cardiovascular disease.

Downstream of the COXs, microsomal PGE synthase-1 (mPGES-1) is the dominant source of PGE_2 biosynthesis. Indeed, recent evidence suggests that in response to a rise in intracellular calcium, a cytosolic phospholipase A_2 translocates to the Golgi, where it associates with COX-2 and mPGES-1 to form a biosynthetic complex that generates PGE_2 (*2*). There has been interest in developing inhibitors of mPGES-1 as an alternative to NSAIDs that might bypass the cardiovascular consequences of NSAIDs, attributable to suppression of COX-2–dependent formation of PGI_2 (*3*). PGE_2 activates four E prostanoid (EP) receptors, two of which (EP2 and EP4) are coupled to adenylate cyclase activation.

Aside from biosynthesis, PGE_2 concentration is determined by the activity of two transporters, multiple drug resistance–associated protein 4 and prostaglandin transporter, which export the lipid from the cell. PGE_2 is also catabolized by 15-PGDH. Loss-of-function mutations in 15-PGDH have been causally implicated in the rare genetic disorder, familial hypertrophic osteoarthropathy–digital clubbing (*4*).

> ***"...the hope is that inhibition of 15-PGDH emerges as a safe and effective therapy..."***

Zhang *et al.* report that elevating PGE_2, either by deleting or inhibiting 15-PGDH, increases hematopoiesis, liver regeneration, and boosts resistance to colitis (inflammation and ulcerations) in mouse models (see the figure). Indeed, a role for PGE_2 in tissue maintenance and expansion was recognized in engraftment studies of epithelial stem cells in zebrafish and mice (*5*, *6*). Administration of PGE_2 to sublethally irradiated mice also accelerates hematopoietic recovery and increases the number of the short-term subtype of hematopoietic stem cells (*7*). Zhang *et al.* show that injecting normal mice, after hematopoietic stem cell transplantation, with the small molecule SW033291, which inhibits 15-PGDH, enhanced neutrophil count recovery. This in-

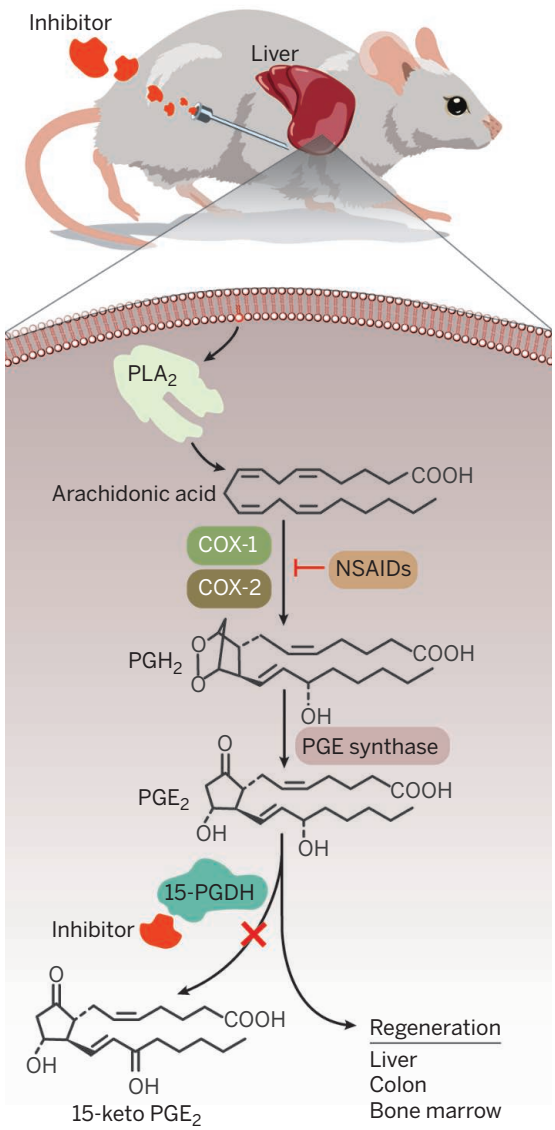
Institute for Translational Medicine and Therapeutics, Perelman School of Medicine, University of Pennsylvania, Philadelphia, PA 19104.
E-mail: garret@exchange.upenn.edu

Published by AAAS

cluded a ~40% increase in a subset of cells (Sca-1$^+$, C-kit$^+$, Lin$^-$) that are enriched for bone marrow stem cells. This effect was also observed in mice genetically engineered to lack 15-PGDH. Treatment of harvested bone marrow cells (from normal, irradiated mice) with SW033291 increased hematopoietic colony formation. The small-molecule inhibitor also increased expression of C-X-C motif chemokine 12 (CXCL12) and stem cell factor (SCF) in nonhematopoietic stem cells that are enriched in bone marrow stroma (referred to as CD45$^-$ cells). CXCL12 and SCF are relevant to stem cell homing and maintenance, processes that are blocked if PGE_2 receptors (EP2 or EP4) expressed by such stromal cells are blocked. Concordant with these observations, Zhang *et al.* found that SW033291 treatment of mice following hematopoietic stem cell transplantation showed a two- to threefold increase in the homing of donor stem cells to recipient marrows. This effect was blocked by treating the recipient mouse with a nonspecific COX inhibitor (indomethacin), an EP4 antagonist (L-161,982), or a CXCL12 antagonist (Plerixafor). Thus, PGE_2 appears to act in vivo in an EP4-dependent manner on nonhematopoietic stromal cells to increase the expression of genes in the recipient marrow that support the homing of the transplanted stem cells. Unlike conventional approaches, like granulocyte–colony–stimulating factor (G-CSF), which does what it says, augmenting PGE_2 concentration appeared not only to be faster and more effective, but also to favor recovery of erythroid and platelet lineages in the irradiated mice. Zhang *et al.* also show that boosting the capacity of colonocytes to form PGE_2 enhances their proliferative capacity and resistance to experimentally induced colitis, and that deletion or inhibition of 15-PGDH enhances liver regeneration after partial hepatectomy.

The results of Zhang *et al.* are provocative, but their translational implications are complicated. Epidemiological studies have long associated NSAID consumption with a reduced risk of a range of cancers (especially for colon). This includes a form of low-dose aspirin without systemic availability, suggesting that a product of activated platelets might increase the expression of COX-2 noted in many cancers (*8*). A modest increase in PGE_2 concentration can activate platelets via their EP3 receptors (*9*). Evidence implicating mPGES-1, EP2, and EP4 in fostering expansion of the cancer stem cell niche and in other aspects of carcinogenesis (*10*) echoes the biosynthetic response system activated to facilitate "desirable" tissue regeneration. Indeed, a loss-of-function mutation in 15-PGDH has been linked to digital clubbing, colon neoplasia, and resistance to the ability of NSAIDs to suppress PGs (*11*). Moreover, tumor cells can activate the COX-2–mPGES-1–PGE_2 synthesis axis in mesenchymal stem cells, which get recruited to the tumor-associated stroma and in turn elicit a mesenchymal stem cell–like phenotype in the carcinoma cells (*12*). An important question is whether the administration of a 15-PGDH inhibitor fosters not just hematopoietic recovery or tissue regeneration in patients treated for lymphoma or liver cancer, but also expansion of the very disease for which they are treated. Whether the risk profile of this approach will differ from that of "conventional" regenerative therapies should also be examined. Indeed, should NSAIDs be used to treat the bone pain evoked by G-CSF? Such observations are a caution to hasten slowly.

The use of a 15-PGDH inhibitor in treating inflammatory disease is also provocative but again, controversial. The anti-inflammatory efficacy of NSAIDs in diseases like arthritis is well established. On the other hand, increased expression and activation of EP4 have been linked to exacerbation of Crohn's disease, an inflammatory condition of the gastrointestinal tract (*13*). Conflicting results have been reported with the use of COX inhibitors in the mouse colitis model—endothelial or myeloid COX-2 restrains the colitis phenotype, but not COX-2 in colonocytes (*14*), which is the site implicated in the beneficial action of 15-PGDH inhibition. Further complicating the issue, the severity of induced colitis is augmented in mice lacking either cytosolic PLA_2 or mPGES-1, whereas colonic tumor burden is somewhat reduced in a mouse model of colon cancer, perhaps due to diversion of the precursor PGH_2 from forming PGE_2 to other PGs instead (*15*). Zhang *et al.* confirm that PGE_2 is a player in the process of tissue regeneration; the hope is that inhibition of 15-PGDH emerges as a safe and effective therapy for this indication. ■



Tissue regeneration. Treating mice with a small-molecule inhibitor of the enzyme 15-PGDH prevents a decrease in PGE_2. This stimulates bone marrow and liver regeneration and prevents colitis in mouse models of disease.

ILLUSTRATION: NICOLLE FULLER

REFERENCES

1. Y. Zhang *et al.*, *Science* **348**, aaa2340 (2015).
2. C. Yuan, W. L. Smith, *J. Biol. Chem.* **290**, 5606 (2015).
3. T. Grosser, Y. Yu, G. A. FitzGerald, *Annu. Rev. Med.* **61**, 17 (2010).
4. S. Uppal *et al.*, *Nat. Genet.* **40**, 789 (2008).
5. T. E. North *et al.*, *Nature* **447**, 1007 (2007).
6. M. D. Castellone, H. Teramoto, B. O. Williams, K. M. Druey, J. S. Gutkind, *Science* **310**, 1504 (2005).
7. J. Hoggatt, P. Singh, J. Sampath, L. M. Pelus, *Blood* **113**, 5444 (2009).
8. D. J. Fitzgerald, G. A. FitzGerald, *Circ. Res.* **112**, 174 (2013).
9. J. E. Fabre *et al.*, *J. Clin. Invest.* **107**, 603 (2001).
10. T. J. Kochel, A. M. Fulton, *Prostaglandins Other Lipid Mediat.* **116-117C**, 99 (2015).
11. K. Guda *et al.*, *Cancer Prev. Res. (Phila.)* **7**, 805 (2014).
12. H. J. Li, F. Reinhardt, H. R. Herschman, R. A. Weinberg, *Cancer Discov.* **2**, 840 (2012).
13. J. Glas *et al.*, *PLOS ONE* **7**, e52873 (2012).
14. T. O. Ishikawa, M. Oshima, H. R. Herschman, *Carcinogenesis* **32**, 417 (2011).
15. D. C. Montrose *et al.*, *Prostaglandins Other Lipid Mediat.* **116-117**, 26 (2015).

10.1126/science.aac5515

Published by AAAS

ATMOSPHERIC SCIENCE

Can climate feel the pressure?

Changes in atmospheric pressure may be an important long-term climate forcing mechanism

By **Daniel J. Peppe**[1] *and* **Dana L. Royer**[2]

Atmospheric carbon dioxide (CO_2) concentrations are widely held to be the main driver of climate change through the Phanerozoic (the past 541 million years), with warm intervals corresponding to high CO_2 concentrations and cold intervals having low CO_2 concentrations (*1*) (see the figure). However, paleoclimate models often cannot match proxy estimates of temperature and precipitation unless unrealistic CO_2 concentrations are prescribed (*2*, *3*). The solution may come from an unexpected direction: atmospheric oxygen (O_2), which is not a greenhouse gas and thus provides no direct greenhouse forcing. On page 1238 of this issue, Poulsen *et al.* (*4*) report model results that identify O_2 as an important climate driver through its contribution to total atmospheric pressure.

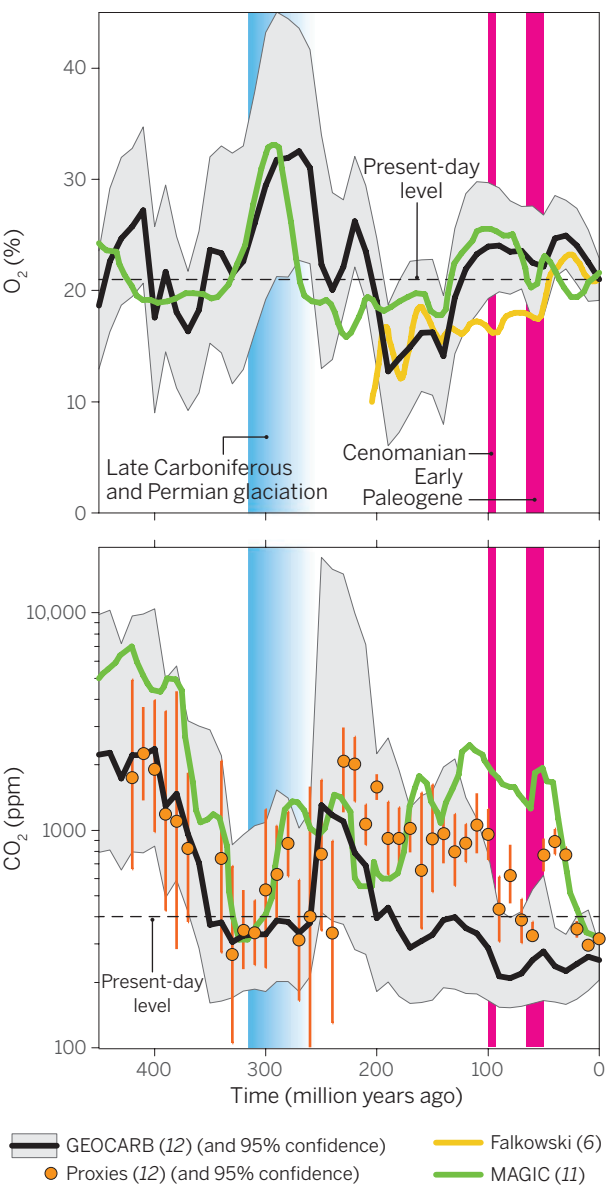
O_2 has varied through the Phanerozoic from ~10 to 35% (see the figure), affecting the evolution and diversification of plants, animals, and insects (*5*, *6*). Yet the possible influence of O_2 on climate has been underappreciated. Poulsen *et al.* show that changes in atmospheric density caused by geologically reasonable variations in O_2 partial pressure affect the scattering of incoming solar radiation. At high atmospheric pressure, shortwave scattering intensifies, leading to a weaker greenhouse forcing and a reduction in atmospheric water vapor, global precipitation, and surface temperatures; at low atmospheric pressure, the reverse patterns are seen. These results mark an important advance in thinking about climate over geologic time and may address a long-standing problem in paleoclimate research: disagreements between model results and proxy reconstructions of climate.

The authors focus on the Cenomanian (100 to 94 million years ago). Climate models for this time period consistently predict lower increases in temperature and moisture than seen in climate proxies, especially at mid- and high latitudes, given that CO_2 concentrations are constrained to between 500 and 2000 ppm (parts per million) by proxies and long-term carbon cycle models (see the figure). Under a scenario in which O_2 is at the low end of the range of estimates (see the figure), these differences between climate models and proxy data largely disappear. The results have important implications for assessing climate during other times in Earth history.

The early Paleogene (66 to 50 million years ago) is one of the best-studied intervals of a hothouse planet, with proxy records indicating very warm and wet conditions in mid-latitude and polar regions (*2*, *7*) and CO_2 levels below 2000 ppm (*1*) (see the figure). Despite decades of intensive research, climate models predict too cool and too dry climates, especially in polar regions (*2*), unless CO_2 concentrations greater than 2500 ppm are used. O_2 during this time was probably between ~15 and 25% (see the figure). If the low-end O_2 estimates are correct (~15%), the reduced density of the atmosphere relative to today would elevate surface temperatures and precipitation, particularly at the poles, likely reducing the model-proxy differences.

During the late Carboniferous and Permian (315 to 255 million years ago), Earth experienced the largest and longest glacial period of the Phanerozoic (*8*), coincident with high O_2 (as much as 35%) and low CO_2 (~350 ppm) (see the figure). Climate models require CO_2 to drop below 560 ppm to initiate ice sheet growth (*8*) and are thus broadly compatible with CO_2 constraints from proxies and long-term carbon cycle models. Nevertheless, climate model results should be revisited in light of Poulsen *et al.*'s findings, because the high-pressure atmosphere at this time likely caused additional

Long-term record of O_2 and CO_2



Poulsen *et al.*'s model results (*4*) indicate that oxygen-driven changes in atmospheric density cause changes in atmospheric water vapor, precipitation, and surface temperature. The model may help provide a mechanism that at least partially explains the cold temperatures during the late Carboniferous and Permian glaciation, when atmospheric pressures were high, as well as the warm temperatures during the Cenomanian and early Paleogene, when atmospheric pressures may have been lower (*6*, *11*, *12*).

[1]*Terrestrial Paleoclimatology Research Group, Department of Geology, Baylor University, Waco, TX 76706, USA.* [2]*Department of Earth and Environmental Sciences, Wesleyan University, Middletown, CT 06459, USA.*
E-mail: daniel_peppe@baylor.edu

Published by AAAS

Downloaded from www.sciencemag.org on June 14, 2015

cooling and reduced precipitation. Additional cooling may provide a mechanism for near-tropical glaciation, because ice in the tropics cannot be modeled using radiative forcing from only CO_2 (*3*).

Both climate modelers and paleoclimate researchers most commonly express CO_2 in terms of volume fraction (such as parts per million by volume, or ppmv). However, if total atmospheric pressure is changing, these CO_2 estimates mean different things in terms of radiative forcing. For example, if the partial pressure of atmospheric CO_2 remains constant but the total atmospheric pressure decreases because of a drop in the partial pressure of atmospheric O_2, CO_2 concentrations (expressed in ppmv) will increase, even though the CO_2 radiative forcing will not have changed. Thus, if climate models prescribe CO_2 ppmv estimates informed from proxies from a time period with a different atmospheric pressure from today's (such as the Carboniferous or early Paleogene; see the figure), the modeled radiative forcing from CO_2 may be incorrect. There would be great benefit to developing a common language for use in modeling and proxy work—for example, reporting whenever possible the sea-level partial pressure of CO_2 along with the total atmospheric pressure of CO_2. Additionally, because all CO_2 proxies have been developed at modern atmospheric pressure, it will be crucial to test the sensitivity of CO_2 proxies at differing atmospheric pressures.

A critical limitation of exploring the climatic effects of Poulsen *et al.*'s model in the geologic past is that paleo-O_2 records are uncertain (see the figure). During the Cenomanian and early Paleogene, O_2 levels may have been lower or higher than today. New O_2 proxies are in development (*9*, *10*), but as with any new proxy system, they must be tested thoroughly. Poulsen *et al.*'s study provides a convincing argument for the importance of developing a robust history of atmospheric O_2. ■

REFERENCES

1. D. Royer, *Treatise Geochem.* **6**, 251 (2014).
2. M. Huber, R. Caballero, *Clim. Past* **7**, 603 (2011).
3. G. S. Soreghan *et al.*, *Geology* **36**, 659 (2008).
4. C. J. Poulsen, C. Tabor, J. D. White, *Science* **348**, 1238 (2015).
5. R. A. Berner, J. M. Vandenbrooks, P. D. Ward, *Science* **316**, 557 (2007).
6. P. G. Falkowski *et al.*, *Science* **309**, 2202 (2005).
7. D. R. Greenwood *et al.*, *Geology* **38**, 15 (2010).
8. I. P. Montañez, C. J. Poulsen, *Annu. Rev. Earth Planet. Sci.* **41**, 629 (2013).
9. I. J. Glasspool, A. C. Scott, *Nat. Geosci.* **3**, 627 (2010).
10. R. Tappert *et al.*, *Geochim. Cosmochim. Acta* **121**, 240 (2013).
11. R. S. Arvidson, F. T. Mackenzie, M. W. Guidry, *Chem. Geol.* **362**, 287 (2013).
12. D. L. Royer, Y. Donnadieu, J. Park, J. Kowalczyk, Y. Goddéris, *Am. J. Sci.* **314**, 1259 (2014).

10.1126/science.aac5264

NANOMATERIALS

Economical routes to colloidal nanocrystals

A new precursor library yields high-quality quantum dots for device applications

By **Zeger Hens**

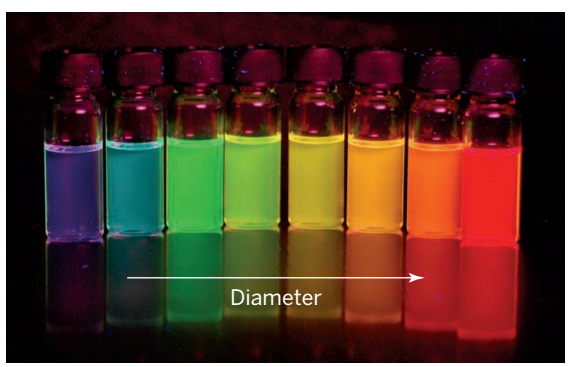
Colloidal semiconductor nanocrystals (NCs) or "quantum dots" offer exquisite control of absorption and emission colors for device applications by tuning their size and shape (*1*). The proliferation of NC applications has been enabled by the "hot-injection" synthesis, which can tightly control the particle size to achieve pure colors (*2*). However, current hot-injection synthesis recipes are largely incompatible with low-cost, large-area remote phosphor applications of NCs. Reagents are too expensive, reaction mixtures too dilute, and conversion yields too low, especially if size tuning is accomplished by adjusting the reaction time. On page 1226 of this issue, Hendricks *et al.* (*3*) report on a radical improvement of the hot-injection synthesis economics of metal sulfide NCs by introducing a library of inexpensive thioureas as reagents.

The hot-injection synthesis is a homogeneous nucleation and growth reaction (*4*) initiated by the rapid mixing of reagents at elevated temperatures in apolar solvents. By stopping growth at a specific time, NCs of different sizes and thus different properties are readily obtained (see the first figure). Hendricks *et al.* introduce substituted thioureas as an alternative sulfur precursor for the formation of metal sulfide NCs, such as sulfides of lead (PbS), cadmium, zinc, and copper, by hot injection. As generic synthesis recipes for most of these NCs have been proposed before (*5*), this result may not seem particularly groundbreaking. However, unlike other approaches, the authors focus on reactions that have nearly quantitative chemical yield.

They manage to control the final NC size by adapting the reactivity of the thioureas through subtle changes of their composition (see the second figure, panel A). This size-tuning scheme relies on the most recent understanding of the several steps that turn injected precursors into NCs, especially the finding that NCs do not form by the separate incorporation of the injected precursors, thiourea and a metal carboxylate. Instead, these precursors react to form the actual solute, and it is the solute supersaturation that initiates the nucleation and drives the growth of NCs (*6*).

This two-step reaction mechanism has important consequences. First, the rate of solute formation sets the rate of solute consumption by nucleation of new nuclei or growth of existing nuclei into larger NCs (see the second figure, panel B). Second, hot-injection synthesis becomes a zero-sum game where solute consumption by growth can only increase at the expense of nucleation. Faster solute formation benefits nucleation, such that more NCs are formed by the time growth arrests nucleation (*7*). If all precursors injected are transformed in more NCs, their size at the end of the reaction will be smaller, which makes for an effective mechanism for size tuning at full yield (*8*).

By proposing an easily implemented chemical approach to adjust the rate of solute formation, Hendricks *et al.* likely make the best possible use of this tuning scheme. The vast possibilities for substitution make for an astonishing range of reactivities and thus a library of precursors fit to synthesize

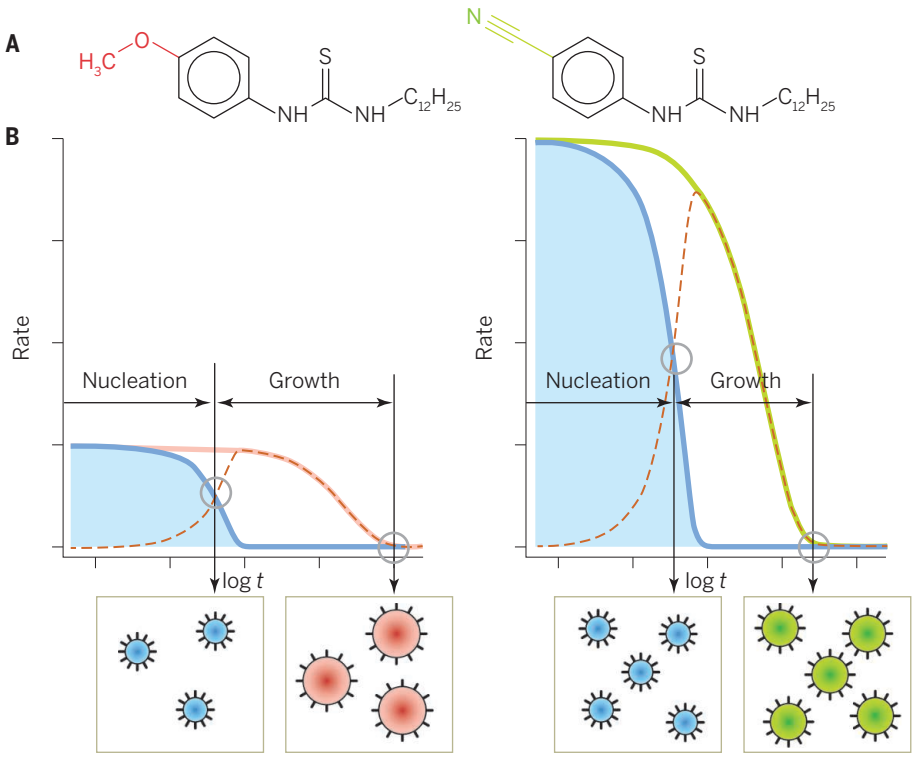


Color shift. Colloidal nanocrystals have size-dependent optical properties. For example, photoluminescence of CdSe nanocrystals shifts from blue to red with increasing diameter.

Physics and Chemistry of Nanostructures and Center for Nano and Biophotonics, Ghent University, B9000 Ghent, Belgium. E-mail: zeger.hens@ugent.be

Published by AAAS

Chemical control of quantum dot growth



The reactivity of substituted thioureas can be tweaked by changing functional groups indicated in (A) as red (low reactivity) and green (high reactivity). In (B), the decomposition rates of the two precursors shown in (A) (the bold red and green curves) dictate the rates of monomer consumption by nucleation (blue curves) and growth (dashed orange curves). These processes are exponentially fast, so rates are plotted against the logarithm of time. When growth overtakes nucleation, the number of final NCs that will be formed from the nuclei (shown in blue) is now fixed; there are fewer nuclei for the slow reaction. At the end of the reaction, the less reactive precursor forms a smaller number of larger NCs (red), whereas the more reactive precursor forms a larger number of NCs that are smaller in size (green).

metal sulfide NCs with a predefined size starting from common chemicals. In this way, the work sets a standard for synthesis schemes of other NC material classes such as metal selenides, phosphides, and arsenides that can make possible large-area, low-cost NC applications such as remote phosphor lighting or solar concentrators (*9*, *10*), thus stressing the importance of finding similarly versatile precursors for these NCs.

Especially for their PbS synthesis, Hendricks *et al.* show that the reaction rate gives them full control over the NC size while maintaining extremely narrow size dispersions (the NCs are all nearly the same size). Thus, the size dispersion is not tightly linked to the reaction rate. Nor is the use of thioureas in itself sufficient to obtain a tight size dispersion. The thiourea-based synthesis of Cu_xS and Cu_2ZnSnS_4 (CZTS), for example, yields quite polydisperse NCs. These findings indicate that, unlike the case for size control, the question as to what factors really determine size dispersion in a hot-injection synthesis remains to be answered. Hence, following Hendricks *et al.* in their pursuit of insight-enabled synthesis economics, understanding and controlling size dispersion in the hot-injection synthesis appears to be an essential next step on the road to affordable, high-quality NCs. ■

REFERENCES

1. M. V. Kovalenko *et al.*, *ACS Nano* **9**, 1012 (2015).
2. C. B. Murray, D. J. Norris, M. G. Bawendi, *J. Am. Chem. Soc.* **115**, 8706 (1993).
3. M. P. Hendricks, M. P. Campos, G. T. Cleveland, I. Jen-La Plante, J. S. Owen, *Science* **348**, 1226 (2015).
4. V. K. LaMer, R. H. Dinegar, *J. Am. Chem. Soc.* **72**, 4847 (1950).
5. H. Zhang, B.-R. Hyun, F. W. Wise, R. D. Robinson, *Nano Lett.* **12**, 5856 (2012).
6. H. Liu, J. S. Owen, A. P. Alivisatos, *J. Am. Chem. Soc.* **129**, 305 (2007).
7. J. S. Owen, E. M. Chan, H. Liu, A. P. Alivisatos, *J. Am. Chem. Soc.* **132**, 18206 (2010).
8. S. Abe, R. K. Čapek, B. De Geyter, Z. Hens, *ACS Nano* **6**, 42 (2012).
9. Y. Shirasaki, G. J. Supran, M. G. Bawendi, V. Bulovic, *Nat. Photonics* **7**, 13 (2013).
10. C. S. Erickson *et al.*, *ACS Nano* **8**, 3461 (2014).

10.1126/science.aab0866

ORGANISMAL BIOLOGY

Visual tracking in the dead of night

Even in dim light, hawkmoths can track the motions of wind-tossed flowers

By **Eric Warrant**

Nocturnal insects live in a dim world. They have brains smaller than a grain of rice, and eyes that are even smaller. Yet, they have remarkable visual abilities, many of which seem to defy what is physically possible (*1*). On page 1245 of this issue, Sponberg *et al.* reveal how one species, the hawkmoth *Manduca sexta*, is able to accurately track wind-tossed flowers in near darkness and remain stationary while hovering and feeding (*2*).

Examples of remarkable visual abilities include the nocturnal central American sweat bee *Megalopta genalis*, which can use learned visual landmarks to navigate from its nest—an inconspicuous hollowed-out twig hanging in the tangled undergrowth—through a dark and complex rainforest to a distant source of nocturnal flowers, and then return (*3*). The nocturnal Australian bull ant *Myrmecia pyriformis* manages similar navigational feats on foot (*4*). Nocturnal South African dung beetles can use the dim celestial pattern of polarized light around the moon (*5*) or the bright band of light in the Milky Way (*6*) as a visual compass to trace out a beeline when rolling dung balls. Some nocturnal insects, like the elephant hawkmoth *Deilephila elpenor*, even have trichromatic color vision (*7*).

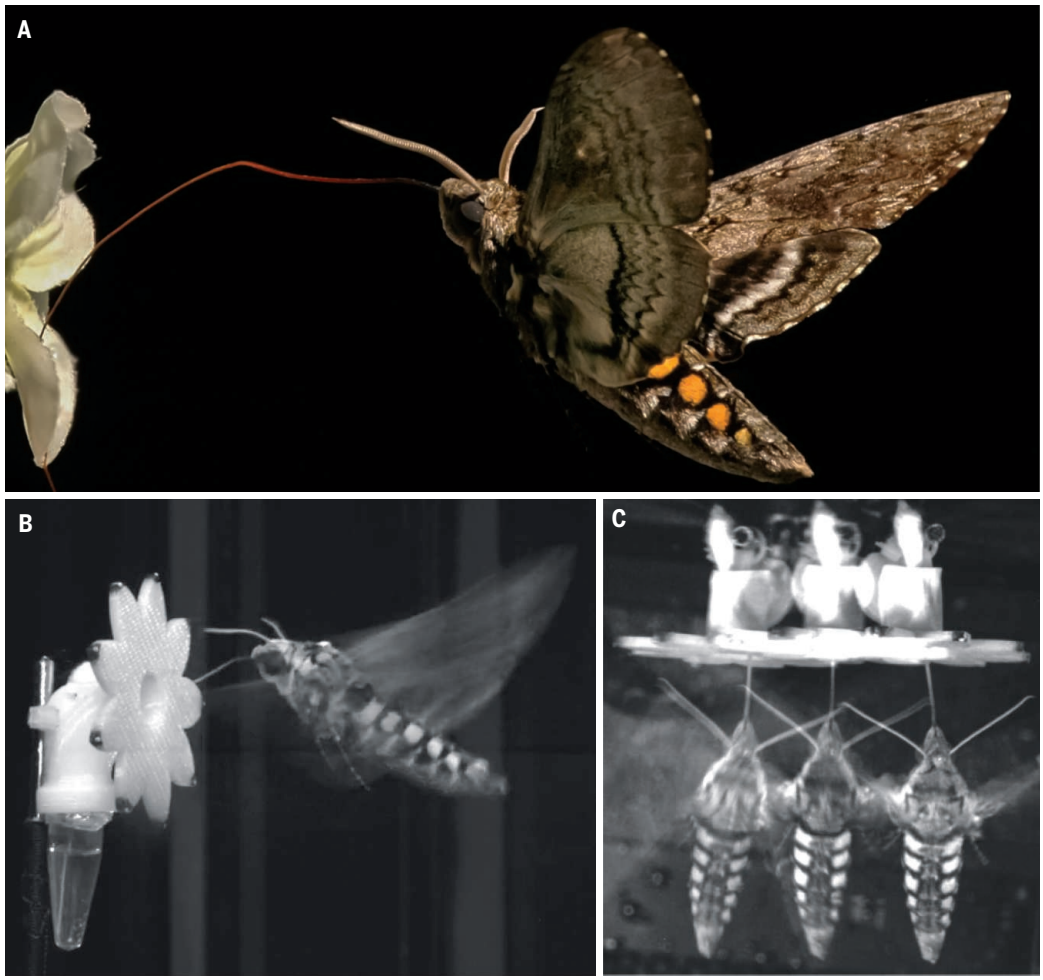
These impressive behavioral feats are likely to depend on specialized neural mechanisms in the brain that sum photons over space and time (*8*, *9*), thus greatly strengthening the visual impression even though each photoreceptor absorbs photons at extremely low rates—in the American cockroach, as few as one photon every 10 s (*10*). Sponberg *et al.* now quantify the extent of these summation strategies for the detection of a moving target: a wind-tossed flower visually tracked by a dusk- and dawn-

Downloaded from www.sciencemag.org on June 14, 2015

Published by AAAS

active hovering hawkmoth that sucks nectar on the wing. It turns out that even though the hawkmoths must compromise tracking accuracy to meet the demands of visual motion detection in dim light, the tracking error remains small exactly over the range of frequencies with which wind-tossed flowers move in the wild. The results reveal a remarkable match between the sensorimotor performance of an animal and the dynamics of the sensory stimulus that it most needs to detect.

To quantify the ability of the hawkmoth *M. sexta* to track a moving flower at two different light levels, one brighter (300 Lux: early dusk) and one dimmer (0.3 Lux: quarter moon), the authors allowed freely flying hawkmoths to locate and feed from a sugar solution reservoir placed at the center of an artificial plastic flower. During experiments, this flower was attached to a motorized arm that moved the flower from side to side in a complex trajectory. The component movement frequencies of this trajectory varied over two orders of magnitude and encompassed the narrower range of frequencies typical of wind-tossed flowers. A hovering moth fed from the flower by extending its proboscis into the reservoir, rapidly flying from side to side to maintain feeding by stabilizing the moving flower in the center of its visual field.



Track and feed. Sponberg and colleagues (*2*) reveal the mechanisms that dusk-active hawkmoths (*M. sexta*) use to track wind-tossed flowers at night while feeding (**A**). The authors use a robotic flower (**B**) that the moth tracks during flight [(**C**); three successive film frames are superimposed]. For a video of the experiments see scim.ag/6239moth.

When Sponberg *et al.* analyzed how well the moth's tracking trajectory matched the flower's movement trajectory, they made two important discoveries. First, the moth tracked the flower remarkably well at either light intensity for flower movement frequencies up to ~2 Hz, but tracking error increased dramatically beyond this frequency, particularly in dim light. Second, the lag between the moth's trajectory and the trajectory of the flower increased in dim light, indicating that visual motion detection had slowed by around 17%. This slowing visual response is consistent with temporal summation, a visual strategy whereby the visual integration time (or "shutter time") is lengthened to increase visual reliability in dim light (*8*, *9*). This strategy has recently been demonstrated in bumblebees flying in dim light (*11*) and has been predicted for nocturnal hawkmoths (*12*). Although temporal summation sacrifices the perception of faster objects, it strengthens the perception of slower ones (*8*, *9*), like the slower movement frequencies (below ~2 Hz) of the robotic flower.

By carefully analyzing the movements of several species of flowers tossed by natural winds—including those favored by hawkmoths—Sponberg *et al.* discovered that their movements were confined to frequencies below ~2 Hz. Thus, despite visual limitations in dim light, the flight dynamics and visual summation strategies of hovering hawkmoths have evolved to perfectly match the movement characteristics of flowers, their only food source.

The implications of the study go far beyond this particular species. It shows how in small animals like hawkmoths, with limited nervous system capacities and stretched energy budgets, the forces of natural selection have matched sensory and motor processing to the most pressing ecological tasks that animals must perform in order to survive. This is done not by maximizing performance in every possible aspect of behavior, but by stripping away everything but the absolutely necessary and honing what remains to perform tasks as accurately and efficiently as possible. ■

Department of Biology, Lund University, 22362 Lund, Sweden. E-mail: eric.warrant@biol.lu.se

PHOTO: PANEL A, ARMIN HINTERWIRTH; PANELS B AND C, SIMON SPONBERG

REFERENCES

1. E. Warrant, M. Dacke, *Annu. Rev. Entomol.* **56**, 239 (2011).
2. S. Sponberg, J. P. Dyhr, R. W. Hall, T. L. Daniel, *Science* **348**, 1245 (2015).
3. E. J. Warrant *et al.*, *Curr. Biol.* **14**, 1309 (2004).
4. S. F. Reid, A. Narendra, J. M. Hemmi, J. Zeil, *J. Exp. Biol.* **214**, 363 (2011).
5. M. Dacke, D.-E. Nilsson, C. H. Scholtz, M. Byrne, E. J. Warrant, *Nature* **424**, 33 (2003).
6. M. Dacke, E. Baird, M. Byrne, C. H. Scholtz, E. J. Warrant, *Curr. Biol.* **23**, 298 (2013).
7. A. Kelber, A. Balkenius, E. J. Warrant, *Nature* **419**, 922 (2002).
8. J. H. Van Hateren, *Vision Res.* **33**, 257 (1993).
9. E. J. Warrant, *Vision Res.* **39**, 1611 (1999).
10. A. Honkanen, J. Takalo, K. Heimonen, M. Vähäsöyrinki, M. Weckström, *J. Exp. Biol.* **217**, 4262 (2014).
11. T. Reber *et al.*, *J. Exp. Biol.* **218**, 1339 (2015).
12. D. C. O'Carroll, E. J. Warrant, *Proc. 7th ISSNIP Conf.*, 119 (2011).

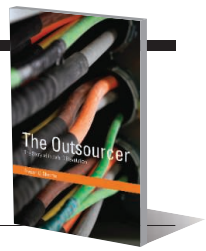
10.1126/science.aab2185

Published by AAAS



The Infosys Global Education Centre in Mysore, India.

The Outsourcer
The Story of India's IT Revolution
Dinesh C. Sharma
MIT Press, 2015. 294 pp.



HISTORY OF SCIENCE

The Indian advantage

A commitment to national self-sufficiency set the stage for the rise of India's information technology industry

By **Somaditya Banerjee**

In a well-written and fast-paced book, Dinesh Sharma examines the history of computing technology in modern India. Sharma argues that the foundations of India's information technology (IT) revolution were laid during the first half of the 20th century, when the country was still under British rule. During this time, leading Indian scientists, including P. C. Mahalanobis and H. J. Bhabha, were working to make their respective institutions—the Indian Statistical Institute (ISI) and the Tata Institute of Fundamental Research (TIFR)—into centers for computer science and technology.

Asia's first data processing computer—custom-built by the British Tabulating Machine Company for ISI—was bought in 1954 under Mahalanobis's aegis to familiarize the institute's engineers with the functioning of a modern computer. In 1958, a fully automatic, electronic digital computer capable of solving mathematical problems, known as Ural, arrived from the Soviet Union.

Meanwhile, researchers at TIFR initiated work on an analog computer capable of solving large mathematical problems related to control systems for nuclear reactors. In 1961, M. G. K. Menon, head of the physics group, visited IBM and UNIVAC in the United States to inquire about the potential purchase of a top-of-the-line computer. (Menon would go on to make electronics a separate entity in the policy-making apparatus of India's central government in the 1970s—a move that would help the country foster indigenous initiatives and curtail the influence of foreign corporations.) Knowing that the Indian government would only be able to subsidize the purchase of one commercial machine, Mahalanobis and Bhabha fought over whether the UNIVAC or the IBM 704 was to be acquired. Bhabha won this battle, and TIFR became the national computing center.

American computer gurus, including Nicholas Metropolis, Norbert Wiener, and Harry Huskey, made important contributions to the Indian computing scene in the 1960s. Their contributions were direct and indirect. Many foreign scientists, including Nobel laureates, were invited to give lecture tours. Some were part of structured programs like the Kanpur Indo-American Program. The computer centers at TIFR and the Indian Institute of Technology at Kanpur were particularly important for helping to build computer awareness and software-writing skills in India during this time.

In 1967, Indira Gandhi, India's first female prime minister, appointed Vikram Sarabhai as the chairman of the Atomic Energy Establishment (AEE), a government-sponsored institution dedicated to nuclear energy research. The AEE was charged with creating a plan for the indigenous production of electronics. That same year, its electronics division was spun off into an independent public enterprise called Electronics Corporation of India Limited (ECIL) in Hyderabad.

IBM contributed to creating a computer culture in the government and in the business community by developing a pool of highly skilled computer professionals in systems engineering, programming, and maintenance in the 1970s. The number of trainees ran into the thousands, as IBM had extensive installations across the country and a robust training program.

In the 1980s, computing technologies that had previously been relegated to the domain of scientists were seamlessly transitioned to common users. This led to a shift away from basic research applications and a burst of activity in the Indian hardware and software market.

By the end of the 1990s, outsourcing had become a multibillion-dollar business for many Indian companies. As software exports grew, "body shopping" (in which local consultancy firms recruited IT workers to work on foreign software projects) became common. Outsourcing became an essential management process in the globalized economy by also creating direct and indirect employment opportunities that ultimately led to the growth of the Indian domestic job sector.

Although this is a magnificent study that addresses the dearth of scholarship on the history of computing outside the Euro-American context, Sharma's monograph shows the entangled histories of computing in India and America.

One may be tempted to dismiss the book's emphasis on elite figures like Nehru and Gandhi as technoscientific elitism; however, it actually serves to highlight how science in postcolonial India functioned very differently from the science conducted during the early 20th century. Although science in colonial India was about the individual brilliance of the "pure scientist" working under a power differential, postcolonial technoscience saw an entangling of the scientist with the emergent nation-state.

India's lasting contribution to the computing industry is mainly in the development of a global service delivery model, which gave birth to the outsourcing industry. This model allowed for the conversion of knowledge and skills into commerce, even when physical infrastructure was lacking. However, this focus on software services has meant that India has not made a significant mark in software products and computer hardware. This may change, though, in years to come, due to an evolving economic environment.

The reviewer is in the Department of History, University of Idaho, Moscow, ID 83844, USA. E-mail: sbanerjee@uidaho.edu

10.1126/science.aab3022

PHOTO: © JAGADEESH NV/EPA/CORBIS

Downloaded from www.sciencemag.org on June 14, 2015

Published by AAAS

AGRICULTURAL SCIENCE

Tomorrow's table

It's time to talk about the future of food

By **Jean L. Steiner**

Confronted with a rapidly increasing global population, sluggish crop yield increases, and uncertainty about the future climate, the agricultural community faces the challenge of doubling crop yields by 2050. However, too often, we focus on increased production per se without adequate consideration of other elements that contribute to food insecurity. Joel K. Bourne's new book, *The End of Plenty*, presents a fascinating narrative about agriculture, population, hunger, and health, spanning decades, that frames the current situation within a historical context. Along the way, he analyzes some of the most complex and contentious issues challenging food supply today.

Bourne opens with this personal note, describing how most people react when he tells them he studied agronomy in college. "When I explain that it's a combination of soil science and plant science for row crop production, their interest wilts. Journalists call this MEGO—short for 'my eyes glaze over.'" Having experienced similar MEGO when describing my own work as an agronomist, I felt compelled to read on.

Throughout the book, Bourne interweaves the legacy of Malthusian demographics—the idea that human populations grow exponentially while food production grows at an arithmetic rate—bringing the "demand" side to the forefront. He also illuminates the historical roots of scientific, policy, and social drivers that have brought us to the current state of food production, hunger, and population. His cogent arguments for addressing what he sees as the root causes of the population explosion—primarily, lack of empowerment of girls and women to determine their own destinies—are compelling. Investments in education for girls, access to family planning information and contraceptives, and equity in access to agricultural knowledge and land are offered as a far more certain path to feeding future populations than relying solely on investments in technologies to increase production.

The "Green Revolution," the term given to the flurry of advances that increased agricultural production in the mid-20th century, is one of the most honored and influential agricultural achievements in history. Bourne tells the history of the revolution along with heart-rending stories of its unintended consequences, including the environmental and health effects of high levels of agrichemical use in developing nations.



Andy Rozendaal harvests nasturtium at CIty Farm, a nonprofit farming venture on the edge of downtown Chicago.

PHOTO: SCOTT OLSON/THINKSTOCK

Improved seeds, fertilizers, and chemicals were part of the equation, but the transformation of agricultural landscapes also hinged on the availability of a secure water supply. Although irrigation has proven to be unsustainable in many regions, resulting in depleted and polluted groundwater supplies, Bourne identifies substantial regions in southeastern India and Africa that have aquifers that could be sustainably developed. He additionally explores opportunities for improving micro-irrigation for small-holder producers and the advances offered by increased water-use efficiency.

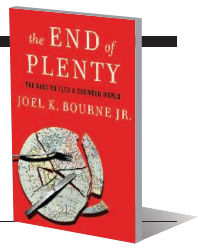
The often-maligned GMO (genetically modified organism) breeding technologies, which have the potential to provide breakthrough advances with broad social benefits, are also highlighted. These include "scuba rice," which can tolerate extended submergence under water (a common problem in rice production regions near sea level), and "golden rice" that produces vitamin A. Bourne also discusses the elusive goal of developing nitrogen-fixing grasses, which could render expensive and damaging nitrogen fertilizers obsolete. He similarly explores constraints and opportunities in concentrated meat production and aquaculture systems.

This book is thoroughly researched, and the extensive index and bibliography will be a useful resource for readers. The informal, journalistic style of the writing is one of its strengths, but occasionally, some of the language used is jarring: the use of the word "zombies" to describe displaced, starving populations, for example, or the phrase "Potbellied Papa … Grandma, Ma and children of all ages" to describe rural populations in Ukraine, or the emphasis on the dialect of a gentleman near Bath Abbey in southeastern England ("'Mowfus?' … 'Never 'erd of 'im'"). However, the book is ultimately extremely sympathetic to the plight of the poor, as well as respectful of the motivations and wisdom of Green Revolution leaders and innovators.

Bourne brings a piercing eye to intransigent problems in food production and alleviation of hunger, leavened by notes of pragmatism and optimism. Although some agronomists will take exception to the provocative lens through which the Green Revolution and some of today's production systems are presented, those who continue will find a challenge to adopt a more holistic approach than has been taken in the past.

The reviewer is president of the American Society of Agronomy. E-mail: jean.steiner@ars.usda.gov

The End of Plenty
The Race to Feed a Crowded World
Joel K. Bourne Jr.
Norton, 2015. 414 pp.



10.1126/science.aab1045

Downloaded from www.sciencemag.org on June 14, 2015

Published by AAAS

LETTERS

Edited by **Jennifer Sills**

Defining the happiness gap

IN THEIR REPORT "Conservatives report, but liberals display, greater happiness" (13 March 2015, p. 1243), S. P. Wojcik *et al.* show that liberals display more cheer in smiles, positive word choice, and use of positive emoticons. The authors explicitly contrast these findings to the allegedly higher happiness levels of conservatives found with self-report scales (*1*). However, as Wojcik *et al*. note, both the size and direction of the effect greatly depend on the type of measurement.

Such variation does not imply that ideological preferences cannot have a substantial effect on happiness in specific circumstances. Indeed, the so-called happiness gap may be context-dependent (*1*–*3*). For instance, a small relationship between conservatism and self-reported life satisfaction emerges in the United States, whereas it is absent in Europe (*1*). Unfortunately, Wojcik *et al.* have only presented U.S. data.

Moreover, their findings are partly based on the public behavior of politicians. Obviously, self-presentation has a strategic component and does not necessarily reflect one's true inner state (*4*). For liberal politicians, smiling is useful indeed, considering that especially left-wing voters prefer friendly and agreeable politicians (*5*).

The negligible main effects indicate that the question of whether liberals or conservatives are happier is rather futile in scientific terms. A more meaningful avenue for future studies would be investigating which contexts and life conditions affect happiness differently for conservatives and liberals (*3*, *6*).

Alain Van Hiel,*Arne Roets, Jasper Van Assche, Dries Bostyn, Jonas De keersmaecker, Tessa Haesevoets, Anne Joosten, Jonas Stadeus, Emma Onraet

Ghent University, Department of Developmental, Personality and Social Psychology, Social Psychology Unit, B-9000, Ghent, Belgium.

*Corresponding author. E-mail: alain.vanhiel@ugent.be

REFERENCES

1. E. Onraet *et al.*, *Pers. Soc. Psychol. Bull.* **39**, 509 (2013).
2. D.R. Mandel, P. Omorogbe, *PLOS One* **9**, e98854 (2014).
3. M. Brandt *et al.*, *Soc. Psychol. Pers. Sci.* **6**, 219 (2015).
4. E. Goffman, *The Presentation of Self in Everyday Life* (Doubleday, Garden City, NY, 1959).
5. A. Roets, A. Van Hiel, *Pers. Indiv. Diff.* **46**, 60 (2009).
6. E. Onraet, A. Van Hiel, *Curr. Dir. Psychol. Sci.* **23**, 35 (2014).



Are conservatives happier than liberals?

Response

IN OUR ANALYSES of more than 6000 political liberals and conservatives, we found that conservatives reported greater life satisfaction than liberals, but that liberals displayed more frequent, more intense, and more genuine happiness in their behavior. We concluded from these findings that whether liberals or conservatives appear happier depends on how happiness is measured.

In their Letter, Van Hiel and colleagues reiterate that our analyses were primarily restricted to American participants. As we outlined in our Report's introduction, we made this decision because liberalism and conservatism have very different, sometimes even oppositional, meanings across different national contexts. Regardless, Van Hiel *et al.*'s specific concern is curious, given that the association between conservatism and self-reported life satisfaction in European samples (r = 0.11) does not appear to be weaker than in North American samples (r = 0.09) (*1*). Equally curious is their concern about the self-presentational components of happiness expression among politicians, given that our FACS analyses were purposefully implemented to differentiate between more and less genuine expressions of happiness, and that our findings replicated in samples of both politicians and the general public.

Van Hiel and colleagues oversimplify our complex pattern of results, mischaracterize our findings as "negligible," and then report that further scientific investigation is "futile." But the relationship between ideology and subjective well-being is more productively and accurately understood as nuanced, and this nuance has both scientific and practical import. Why do measurements of such closely related constructs reveal opposing patterns of results? As revealed in our Report, group differences in self-reported life satisfaction can be driven by differences in self-enhancing styles of self-report (*2*). This finding has important implications for understanding subjective well-being research, given that self-reported life satisfaction is perhaps the most frequently used measure of subjective well-being (*3*, *4*), and given the commonness of comparing self-reported subjective well-being across nonrandomized groups that may differ in self-enhancement (*5*).

In our view, the contradictory patterns of results across measures and methods do not cancel each other out to simply create "equal" levels of happiness. Instead, they provide insight into the complexity involved in the measurement of well-being, as well as in the psychological processes underlying human happiness.

Sean P. Wojcik,[1] Arpine Hovasapian,[1] Jesse Graham,[2] Matt Motyl,[3] Peter H. Ditto[1]

[1]Department of Psychology and Social Behavior, University of California, Irvine, CA 92697, USA. [2]Department of Psychology, University of Southern California, CA 90089, USA. [3]University of Illinois, Chicago, IL 60607, USA.

*Corresponding author. E-mail: swojcik@uci.edu

REFERENCES

1. E. Onraet *et al.*, *Pers. Soc. Psychol. Bull.* **39**, 509 (2013).
2. S. P. Wojcik, P. H. Ditto, *Soc. Psychol. Pers. Sci.* **5**, 825 (2014).
3. E. D. Diener *et al.*, *J. Pers. Assess.* **49**, 71 (1985).
4. W. Pavot, E. Diener, *Psychol. Assess.* **5**, 164 (1993).
5. E. Diener *et al.*, *Psychol. Bull.* **125**, 276 (1999).

Protect researchers from harassment

IT IS DEEPLY troubling that an animal rights extremist campaign will stop an important line of research, and the entire scientific community should be concerned when, yet again, disruptive actions by extremists silence important, well-regulated science ("Researcher drops primate work," News In Brief, 8 May, p. 613). It is unacceptable that researchers worldwide are subject to harassment, threats of violence, illegal taping, and property damage, and we urge aggressive enforcement of laws that protect responsible research, scientific institutions, and scientists.

The Society for Neuroscience has long urged research institutions to be proactive

PHOTO: © MODE IMAGES / ALAMY

Downloaded from www.sciencemag.org on June 14, 2015

Published by AAAS

in identifying and supporting researchers who experience animal rights threats. Nonhuman primate models, the research subject in this case, are critical for advancing scientific understanding of the brain, and to improve the health and well-being of humans and nonhuman species. Research on animals, including nonhuman primates, provides the basis for breakthroughs in the treatment of cancer, heart disease, and devastating infectious diseases like HIV, Ebola, and influenza. Monkey research played a key role in the development of deep-brain stimulation for treating conditions such as Parkinson's disease, depression, and obsessive-compulsive disorder. Biomedical research operates within the laws and guidelines set by multiple oversight bodies to ensure humane treatment of animals.

For neuroscience, this troubling news will only lengthen the time needed to better understand complex neural systems, which are crucial to find treatments for more than 1000 disorders—including addiction, schizophrenia, and Alzheimer's disease—which afflict more than 1 billion people worldwide. We urge the scientific community to make a strong stand about the irreplaceable role of animals in research, and for organizations to sign on to the international statement supporting animal research, found at the International Brain Research Organization (*1*).

Steven E. Hyman[1,2]* and Michael E. Goldberg[3,4]*

[1]President, Society for Neuroscience. [2]Broad Institute, Cambridge, MA 02142-1403, USA. [3]Chair, Society for Neuroscience Committee on Animals in Research. [4]Columbia University, New York, NY 10032-1007, USA.

*Corresponding authors. E-mail: media@sfn.org

REFERENCE

1. International Brain Research Organization, Statement on the Use of Animals in Biomedical Research (http://ibro.info/publications/statement-on-the-use-of-animals-in-biomedical-research/).

TECHNICAL COMMENT ABSTRACTS

Comment on "Principles of ER cotranslational translocation revealed by proximity-specific ribosome profiling"

David W. Reid and Christopher V. Nicchitta

Jan *et al.* (Research Article, 7 November 2014, p. 716) propose that ribosomes translating secretome messenger RNAs (mRNAs) traffic from the cytosol to the endoplasmic reticulum (ER) upon emergence of the signal peptide and return to the cytosol after termination. An accounting of controls demonstrates that mRNAs initiate translation on ER-bound ribosomes and that ribosomes are retained on the ER through many cycles of translation.

Full text at http://dx.doi.org/10.1126/science.aaa7257

Response to Comment on "Principles of ER cotranslational translocation revealed by proximity-specific ribosome profiling"

Calvin H. Jan, Christopher C. Williams, Jonathan S. Weissman

Reid and Nicchitta propose that most cellular translation is carried out by a noncycling pool of endoplasmic reticulum (ER)–associated ribosomes. However, proximity-specific ribosome profiling data place an upper bound of about 7 to 16% on the fraction of cytosolic protein translation carried out by ribosomes accessible to ER-tethered biotin ligases. Moreover, yeast pulse-labeling experiments argue against there being a static population of ER-associated ribosomes.

Full text at http://dx.doi.org/10.1126/science.aaa8299

Comment on "Planetary boundaries: Guiding human development on a changing planet"

Fernando Jaramillo and Georgia Destouni

Steffen *et al.* (Research Article, 13 February 2015, p. 736) recently assessed current global freshwater use, finding it to be well below a corresponding planetary boundary. However, they ignored recent scientific advances implying that the global consumptive use of freshwater may have already crossed the associated planetary boundary.

Full text at http://dx.doi.org/10.1126/science.aaa9629

Response to Comment on "Planetary boundaries: Guiding human development on a changing planet"

Dieter Gerten, Johan Rockström, Jens Heinke, Will Steffen, Katherine Richardson, Sarah Cornell

Jaramillo and Destouni claim that freshwater consumption is beyond the planetary boundary, based on high estimates of water cycle components, different definitions of water consumption, and extrapolation from a single case study. The difference from our analysis, based on mainstream assessments of global water consumption, highlights the need for clearer definitions of water cycle components and improved models and databases.

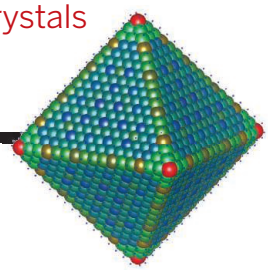
Full text at http://dx.doi.org/10.1126/science.aab0031

Published by AAAS

RESEARCH

Molybdenum doping enhances catalysis and stability of Pt_3Ni nanocrystals

Huang et al., *p. 1230*



IN *SCIENCE* JOURNALS

Edited by **Stella Hurtley**



Human trade in produce promotes the spread of invasive mollusk species

BIOGEOGRAPHY

Emerging patterns in species distribution

Human influences are leading to a shift in the geographical distribution of animal species. Capinha *et al*. compared the distributions of native mollusk species with those introduced to new areas by human activities. The ranges of native species are still broadly constrained by limitations on their capacity for dispersal, whereas those of the introduced aliens are affected more by climate and patterns of human movement. As humans continue to break down barriers to dispersal, more species' distributions will come to be limited by their environmental tolerances. — AMS

Science, this issue p. 1248

CELL DIVISION CYCLE

How cells sense connected chromosomes

Cells have a "checkpoint" that pauses cell division until all chromosomes are properly arranged on the mitotic spindle to allow precise distribution of one copy of each chromosome to each daughter cell. Hiruma *et al*. and Ji *et al*. explain the molecular mechanism by which cells sense that they are ready to divide. The protein kinase MPS1 associates with a protein complex at the kinetochore of the chromosome. Its activity produces signals that pause the cell cycle. When the chromosome becomes properly attached to the mitotic spindle, microtubules of the spindle physically compete for binding to the same site on the kinetochore where MPS1 is bound. Thus, once the kinetochore is properly attached, MPS1 dissociates, the inhibitory signal is lost, and cell division is allowed to proceed. — LBR

Science, this issue pp. 1264 and 1260

CLIMATE CHANGE

Change was in the air

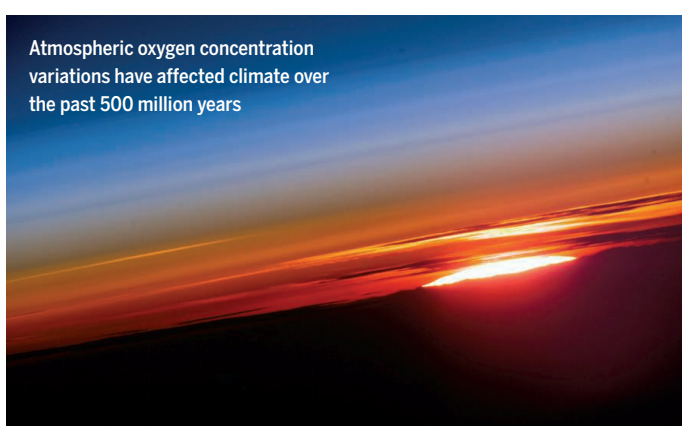
The atmospheric fraction of molecular oxygen gas, O_2, currently at 21%, is thought to have varied between around 35 and 15% over the past 500 million years. Because O_2 is not a greenhouse gas, often this variability has not been considered in studies of climate change. Poulson and Wright show that indirect effects of oxygen abundance, caused by contributions to atmospheric pressure and mean molecular weight, can affect precipitation and atmospheric humidity (see the Perspective by Peppe and Royer). These effects may thus have produced significant changes in the strength of greenhouse forcing by water vapor, surface air temperatures, and the hydrological cycle in the geological past. — HJS

Science, this issue p. 1238; see also p. 1210

NANOMEDICINE

Nanoformulation keeps vein grafts healthy

The MK2i peptide is now in clinical trials aimed at halting inflammation and fibrosis after vein grafting. However, low bioavailability and rapid degradation have slowed MK2i's



Atmospheric oxygen concentration variations have affected climate over the past 500 million years

CREDITS: (TOP TO BOTTOM) HUANG *ET AL.*; © ALENA DUDAEVA /DREAMSTIME; INTERNATIONAL SPACE STATION/NASA

Downloaded from www.sciencemag.org on June 14, 2015

Published by AAAS

clinical translation. Evans *et al.* formulated the MK2i peptide in electrostatically complexed nanoparticles. The resulting MK2i-nanopolyplexes entered both vascular smooth muscle and endothelial cells in human veins. Their delivery reduced proinflammatory cytokine levels, vascular smooth muscle cell migration, and neointima formation (i.e., vessel thickening). In rabbit vein grafts, treatment with MK2i-nanopolyplexes, but not free MK2i, prevented intimal hyperplasia for 1 month after transplant. Thus, nanopolyplexes might improve the utility of vein grafts in the longer term. — MLF

Sci. Transl. Med. **7**, 291ra95 (2015).

BIOENGINEERING

Reconstruction of circadian oscillations

Circadian rhythms are found widely in the tree of life. However, circadian clocks are often difficult to study reductively in their natural organism, in part because of high redundancy within these systems. Silver *et al.* transplanted a circadian clock from a cyanobacterium into a noncircadian organism, *Escherichia coli*. Enabling study in a noncircadian organism opens the opportunity to molecularly dissect the clock and suggests ways to engineer time-dependent biological circuits. — PLY

Sci. Adv. 10.1126.sciadv.1500358 (2015).

INDUCED SEISMICITY

How to observe fault injections in real time

Faults in the ground are known to deform in response to procedures such as wastewater injection that change the pore pressure. Guglielmi *et al.* took a crack at monitoring this process in real time with a controlled fluid injection into an inactive fault (see the Perspective by Cornet). Reactivating the dead fault induced aseismic slip, which triggered small earthquakes. These observations can inform models of how friction is related to slip rate. The technique can also be applied to field-scale monitoring of seismicity-inducing wastewater injections. — BG

Science, this issue p. 1224; see also p. 1204

PHYSIOLOGY

Receptor in the brain controls breathing

Control of breathing in mammals depends primarily not on sensing oxygen, but rather on detecting concentrations of carbon dioxide in the blood. Failure of this system can cause potentially deadly sleep apnias. Taking a hint from insects, which use a heterotrimeric guanine nucleotide–binding protein-coupled receptor (GPCR) to sense carbon dioxide, Kumar *et al*. demonstrate that the GPCR GPR4 is essential to control breathing in mice. GPR4 senses protons generated by the formation of carbonic acid in the blood and works with a pH-sensitive potassium channel called TASK-2 in a set of brain cells that control breathing. — LBR

Science, this issue p. 1255

SOLAR CELLS

Taking in more sun

Most efforts to grow superior films of organic-inorganic perovskites for solar cells have focused on methylammonium lead iodide ($MAPbI_3$). However, formamidinium lead iodide ($FAPbI_3$) has a broader solar absorption spectrum that could ultimately lead to better performance. Yang *et al*. grew high-quality $FAPbI_3$ films by starting with a film of lead iodide and dimethylsulfoxide (DMSO) and then exchanging the DMSO with formamidinium iodide. Their best devices achieved power conversion efficiencies exceeding 20%. — PDS

Science, this issue p. 1234

IN OTHER JOURNALS

Edited by **Sacha Vignieri** *and* **Jesse Smith**



Soil chlorine inventories depend on the species of trees they host

BIOGEOCHEMISTRY

Diving deep into soil's chlorine pool

The density and type of trees in forested ecosystems control the large organic chlorine pool of soils. Chlorine is a trace nutrient for plant growth; however, its distribution is highly variable, even in instances where it was deposited regionally as chloride from the atmosphere. In an experimental forest ecosystem in eastern France, Montelius *et al.* show that tree species controlled total soil chlorine fluxes over 30 years. Coniferous trees, especially Norway spruce, retained organic chlorine and chloride ions in nearby soil more than deciduous trees. The preferential retention or transformation of certain chlorine compounds beyond microbial processes complicates the terrestrial chlorine cycle. — NW

Environ. Sci. Technol. **49**, 4921 (2015).

PHOTO: © IMAGEBROKER/ALAMY

Published by AAAS

ALSO IN *SCIENCE* JOURNALS

Edited by **Stella Hurtley**

ELECTROCHEMISTRY

Molybdenum doping drives high activity

Platinum (Pt) is an effective catalyst of the oxygen reduction reaction in fuel cells but is scarce. One approach to extend Pt availability is to alloy it with more abundant metals such as nickel (Ni). Although these catalysts can be highly active, they are often not durable because of Ni loss. Huang *et al*. show that doping the surface of octahedral Pt_3Ni nanocrystals with molybdenum not only leads to high activity (~80 times that of a commercial catalyst) but enhances their stability. — PDS

Science, this issue p. 1230

NANOMATERIALS

Quality manufacture beats quality control

For semiconductor nanocrystals, tight control over particle size is needed to obtain particles with uniform properties. However, post-synthesis purification methods can be difficult and costly. Hendricks *et al*. present a family of substituted thioureas as a class of chalcogen precursors (see the Perspective by Hens). The rate of reactivity is connected to the specific chemistry of the precursor, making it possible to synthesize metal chalcogenide nanocrystals, such as PbS, with a specific size, narrow size distribution, and full conversion of the reactants. — MSL

Science, this issue p. 1226; see also p. 1211

INSECT FLIGHT

Not too fast and not too slow

Moths are typically active during dawn and dusk when light levels are low and vision is challenging. Slower visual response times can allow for greater light sensitivity, but flying insects are both moving and tracking moving targets, making such tradeoffs potentially problematic. Using a combination of modeling and experiments, Sponberg *et al*. show that moths are able to avoid this potential decrease in visual acuity (see the Perspective by Warrant). This is because the point at which their perception of movement would be compromised is just above the natural frequency at which flowers sway. Thus, insect vision is precisely adapted to the light and movement conditions of their environment. — SNV

Science, this issue p. 1245; see also p. 1212

ECOLOGY

A brave new world with a wider view

Researchers have long attempted to follow animals as they move through their environment. Until relatively recently, however, such efforts were limited to short distances and times in species large enough to carry large batteries and transmitters. New technologies have opened up new frontiers in animal tracking remote data collection. Hussey *et al.* review the unique directions such efforts have taken for marine systems, while Kays *et al.* review recent advances for terrestrial species. We have entered a new era of animal ecology, where animals act as both subjects and samplers of their environments. — SNV

Science, this issue p. 1121, p. 1122

TISSUE REGENERATION

A shot in the arm for damaged tissue

Tissue damage can be caused by injury, disease, and even certain medical treatments. There is great interest in identifying drugs that accelerate tissue regeneration and recovery, especially drugs that might benefit multiple organ systems. Zhang *et al.* describe a compound with this desired activity, at least in mice (see the Perspective by FitzGerald). SW033291 promotes recovery of the hematopoietic system after bone marrow transplantation, prevents the development of ulcerative colitis in the intestine, and accelerates liver regeneration after hepatic surgery. It acts by inhibiting an enzyme that degrades prostaglandins, lipid signaling molecules that have been implicated in tissue stem cell maintenance. — PAK

Science, this issue p. 1223; see also p. 1208

BRAIN NETWORKS

Cooperating brain regions express similar genes

When the brain is at rest, a number of distinct areas are functionally connected. They tend to be organized in networks. Richiardi *et al*. compared brain imaging and gene expression data to build computational models of these networks. These functional networks are underpinned by the correlated expression of a core set of 161 genes. In this set, genes coding for ion channels and other synaptic functions such as neurotransmitter release dominate. — PRS

Science, this issue p. 1241

INNATE IMMUNITY

Detecting Gram-negative bacteria

Invariant molecules specific to different classes of microbes, but not expressed by eukaryotic cells, alert the immune system to a potential invader. Gaudet *et al.* identified one such molecule expressed by a variety of Gram-negative bacteria: the monosaccharide heptose-1,7-bisphosphate (HBP) (see the Perspective by Brubaker and Monack). HBP is an intermediate in the synthesis of lipopolysaccharide, a major component of bacterial cell walls. Rather than alerting the immune system through traditional pathogen detection pathways, such as Toll-like receptors, HBP signals through the host protein TIFA (TRAF-interacting protein with forkhead-associated domain), which activates both innate and adaptive immune responses to control the infection. — KLM

Science, this issue p. 1251; see also p. 1207

SEX DETERMINATION

Manipulating M factor alters mosquito sex

Female mosquitoes feed on blood and in so doing transmit pathogens to millions annually. Although the molecular mechanism for determining sex in many animals is known, the specific factors in mosquitoes have been elusive. This is because sex determination in insects involves a section of the genome that is highly repetitive. Hall *et al*. now identify a male-determining factor (M factor) in *Aedes aegypti*. Manipulation of the M factor produced sex-change phenotypes. Knocking out the gene *Nix* resulted in feminized males, and ectopic expression gave masculinized females. These findings should help to advance strategies for converting female mosquitoes into nonbiting males. — BAP

Science, this issue p. 1268

BIOCHEMISTRY

SUMO switching for degradation

Acute promyelocytic leukemia is caused by a fusion protein, a portion of which is the nuclear protein PML. Arsenic trioxide chemotherapy triggers the degradation of this fusion protein through modification of the PML portion. Fasci *et al.* found that

Published by AAAS

under basal conditions, SUMO2 was constantly added to and removed from a specific lysine residue in PML. In cells exposed to arsenic trioxide, SUMO1, rather than SUMO2, was conjugated to this residue (which the authors called the "switch" residue), leading to the formation of SUMO2 chains on a different lysine residue (the "chain" residue) and the ubiquitylation and breakdown of PML. — WW

Sci. Signal. **8**, ra56 (2015).

Published by AAAS

REVIEW SUMMARY

ECOLOGY

Aquatic animal telemetry: A panoramic window into the underwater world

Nigel E. Hussey, Steven T. Kessel, Kim Aarestrup, Steven J. Cooke, Paul D. Cowley, Aaron T. Fisk, Robert G. Harcourt, Kim N. Holland, Sara J. Iverson,* John F. Kocik, Joanna E. Mills Flemming, Fred G. Whoriskey

BACKGROUND: Global aquatic environments are changing profoundly as a result of human actions; consequently, so too are the ways in which organisms are distributing themselves through space and time. Our ability to predict organism and community responses to these alterations will be dependent on knowledge of animal movements, interactions, and how the physiological and environmental processes underlying them shape species distributions. These patterns and processes ultimately structure aquatic ecosystems and provide the wealth of ecosystem services upon which humans depend. Until recently, the vast size, opacity, and dynamic nature of the aquatic realm have impeded our efforts to understand these ecosystems. With rapid technological advancement over the past several decades, a suite of electronic tracking devices (e.g., acoustic and satellite transmitters) that can remotely monitor animals in these challenging environments are now available. Aquatic telemetry technology is rapidly accelerating our ability to observe animal behavior and distribution and, as a consequence, is fundamentally altering our understanding of the structure and function of global aquatic ecosystems. These advances provide the toolbox to define how future global aquatic management practices must evolve.

ADVANCES: Aquatic telemetry has emerged through technological advances in miniaturization, battery engineering, and software and hardware development, allowing the monitoring of organisms whose habitats range from the poles to the tropics and the photic zone to the abyssal depths. This is enabling the characterization of the horizontal and vertical movements of individuals, populations, and entire communities over scales of meters to tens of thousands of kilometers and over time frames of hours to years and even over the entire lifetimes of individuals. Electronic tags can now be equipped with sensors that measure ambient physical parameters (depth, temperature, conductivity, fluorescence), providing simultaneous monitoring of animals' environments. By linking telemetry with biologgers (e.g., jaw-motion sensors), it is possible to monitor individual feeding events. In addition, other devices on instrumented animals can communicate with one another, providing insights into predator-prey interactions and social behavior. Coupling telemetry with minute nonlethal biopsy allows understanding of how trophic dynamics, population connectivity, and gene-level basis for organismal health and condition relate to movement. These advances are revolutionizing the scope and scales of questions that can be addressed on the causes and consequences of animal distribution and movement.

ON OUR WEB SITE

Read the full article at http://dx.doi.org/10.1126/science.1255642

OUTLOOK: Aquatic animal telemetry has advanced rapidly, yet new challenges present themselves in coordination of monitoring across large-spatial scales (ocean basins), data sharing, and data assimilation. The continued advancement of aquatic telemetry lies in establishing and maintaining accessible and cost-effective infrastructure and in promoting multidisciplinary tagging approaches to maximize cost benefits. A united global network and centralized database will provide the mechanism for global telemetry data and will promote a transparent environment for data sharing that will, in turn, increase global communication, scope for collaboration, intellectual advancement, and funding opportunities. An overarching global network will realize the potential of telemetry, which is essential for advancing scientific knowledge and effectively managing globally shared aquatic resources and their ecosystems in the face of mounting human pressures and environmental change. ■



PHOTO CREDITS: (A) H. PEDERSON; (B) MARINESAVERS.COM; (C) D. LIDGARD; (D) M. POTENSKI

Aquatic telemetry in action. A southern rock lobster (*Jasus edwardsii*) (**A**) and a lemon shark (*Negaprion brevirostris*) (**D**) fitted with acoustic tags are detected and logged by moored receivers (D) or mobile receivers attached to opportunistic platforms or carried by large animals (C). A juvenile green turtle (*Chelonia mydas*) (**B**) fitted with a satellite tag is monitored in real time via orbiting satellites. A grey seal (*Halichoerus grypus*) "bioprobe" (**C**), fitted with intercommunicating acoustic and satellite transmitters, transmits and receives data on animal interactions and ocean conditions.

RELATED ITEMS IN *SCIENCE*

R. Kays *et al.*, Terrestrial animal tracking as an eye on life and planet. *Science* **348**, aaa2478 (2015).

The list of author affiliations is available in the full article online.
*Corresponding author. E-mail: sara.iverson@dal.ca
Cite this article as N. E. Hussey *et al.*, *Science* **348**, 1255642 (2015). DOI:10.1126/science.1255642

Downloaded from www.sciencemag.org on June 14, 2015

REVIEW

ECOLOGY

Aquatic animal telemetry: A panoramic window into the underwater world

Nigel E. Hussey,[1] Steven T. Kessel,[1] Kim Aarestrup,[2] Steven J. Cooke,[3] Paul D. Cowley,[4] Aaron T. Fisk,[1] Robert G. Harcourt,[5] Kim N. Holland,[6] Sara J. Iverson,[7]* John F. Kocik,[8] Joanna E. Mills Flemming,[9] Fred G. Whoriskey[7]

The distribution and interactions of aquatic organisms across space and time structure our marine, freshwater, and estuarine ecosystems. Over the past decade, technological advances in telemetry have transformed our ability to observe aquatic animal behavior and movement. These advances are now providing unprecedented ecological insights by connecting animal movements with measures of their physiology and environment. These developments are revolutionizing the scope and scale of questions that can be asked about the causes and consequences of movement and are redefining how we view and manage individuals, populations, and entire ecosystems. The next advance in aquatic telemetry will be the development of a global collaborative effort to facilitate infrastructure and data sharing and management over scales not previously possible.

Most aquatic life forms—from microscopic bipolar bacteria (*Polaribacter* spp.) to the immense blue whale (*Balaenoptera musculus*)—move, which facilitates countless ecological processes. Animals move to acquire food, avoid predation or adverse conditions, seek out suitable mates, and locate spawning or nursery areas (*1*). Collectively, these movements transport nutrients, biomass, and dynamic energy across distinct ecosystems. Consequently, movements, influenced by environmental context and the physiological, endocrine, and energetic states of individuals, structure populations and ecosystems, maintain ecosystem function, and ultimately determine global aquatic productivity (*2*).

The vastness, complexity, and opacity of aquatic environments have historically impeded our efforts to acquire and process information on animal movements. However, recent advances in remote monitoring devices have revolutionized our capabilities for observation. These evolving and increasingly miniaturized electronic devices not only provide detailed information on the movements of free-ranging animals in space and time, but with the addition of sensors and/or biosampling, can document the ambient conditions surrounding an organism and measure its behavioral and physiological states (*3*). New generations of tracking devices even allow communication among instruments on different individuals, enabling novel insights into social behavior and predator-prey interactions. Aquatic telemetry now provides the tools to understand the causes and consequences of species' movements and their underlying patterns and processes over ecologically meaningful spatial and temporal scales.

[1]Great Lakes Institute for Environmental Research, University of Windsor, 401 Sunset Avenue, Windsor, Ontario N9B 3P4, Canada. [2]National Institute of Aquatic Resources, Technical University of Denmark, Vejlsoevej 39, DK-8600 Silkeborg, Denmark. [3]Fish Ecology and Conservation Physiology Laboratory, Department of Biology and Institute of Environmental Science, Carleton University, 1125 Colonel By Drive, Ottawa, Ontario K1S 5B6, Canada. [4]South African Institute for Aquatic Biodiversity, Private Bag 1015, Grahamstown 6140, South Africa. [5]Department of Biological Sciences, Macquarie University, Sydney, New South Wales 2109, Australia. [6]Hawaii Institute of Marine Biology, University of Hawaii at Manoa, Kane'ohe, HI 96744, USA. [7]Ocean Tracking Network, Department of Biology, Dalhousie University, 1355 Oxford Road, Halifax, Nova Scotia B3H 4R2, Canada. [8]Northeast Fisheries Science Center, National Oceanic and Atmospheric Administration Fisheries, 17 Godfrey Drive, Orono, ME 04473, USA. [9]Department of Mathematics and Statistics, Dalhousie University, 6316 Coburg Road, PO Box 15000, Halifax, Nova Scotia B3H 4R2, Canada.
*Corresponding author. E-mail: sara.iverson@dal.ca

Aquatic telemetry

Historically, the predictable occurrence of where and when valued aquatic animals could be caught (e.g., salmon returning to rivers to spawn, coastally migrating whales) provided the only measure of abundance and movements (*4*). This local or traditional knowledge transitioned to systematic marking of individuals for mark-recapture studies during the early phases of both whaling and fisheries management in the past century (*5*, *6*). These methods documented coarse-scale movement patterns and distributions but were typically limited in resolution (e.g., providing knowledge of only tagging location and recapture site). With the arrival of the technological era, these methods progressed to telemetry (*7*), which involves placing electronic devices ("transmitters" or "tags") on animals that autonomously transmit data to data-logging or relay-receiving stations. Because radio waves do not propagate in salt water, most aquatic telemetry is rooted in two principal approaches: acoustic (*8*) and satellite telemetry (*9*). Acoustically tagged animals are detected and logged by receivers moored at fixed locations that are retrieved periodically or by mobile receivers (e.g., on a pursuit vessel), whereas satellite observations are sent to land-based receivers via orbiting satellites. Electronic tags may be secured externally, inserted into the stomach, or surgically implanted in animals and programmed to record and/or transmit various data types, ranging from simple presence and location to extensive time series records of the animal's movements and environment (e.g., depth, temperature). Although other telemetric tools are available, such as short-range radio telemetry in freshwater environments and passive integrated transponders, we focus here on the two most widely used methods in aquatic ecosystems (acoustic and satellite telemetry). Biologging platforms (*10*) that do not have the capacity for data transmission are excluded from this Review.

Technological advances driving telemetry applications and growth

Telemetry is revolutionizing the discovery of aquatic animal movement, stemming from the groundbreaking acoustic tracks that revealed nightly excursions of scalloped hammerhead sharks (*Sphyrna lewini*) from seamounts into adjacent deep waters (*11*) and the first ARGOS (Advanced Research and Global Observation Satellite) satellite track of a basking shark (*Cetorhinus maximus*) off the west coast of Scotland (*12*). Miniaturization continues to be pivotal in the advancement of aquatic telemetry by expanding both the number of species and the life stages of animals that can be tracked. The smallest acoustic transmitters now weigh less than 1.4 g, enabling the tagging of tiny neonate fish. Similarly, advances in battery technology are allowing longer and more reliable deployments, while sophisticated software developments are providing more detailed movement information and greater data logging and transmitting flexibility. These hardware and software developments and cross-pollination of technologies are fuelling the animal movement ecology revolution.

Acoustic telemetry can now monitor the movements of tagged individuals for periods ranging from days to more than 10 years. Study durations are dictated by battery life, attachment method, and data resolution and/or complexity, allowing measurements of high-resolution continuous movements over small spatiotemporal scales or presence-absence data over vast spatial scales and multiple years (*8*). Acoustic telemetry traditionally depended on the recovery of submerged acoustic receivers or their interrogation by modems, but data can now be telemetered via satellite from remote locations, such as anchored or drifting buoys (*13*) or cabled underwater arrays. Most recently, acoustic receivers have been deployed on large animal carriers (e.g., seals) (*14*) and on ocean gliders, providing mobile platforms

to detect tagged animals; autonomous underwater vehicles can even actively follow them (*15*).

Complementary to acoustic telemetry, satellite tags have evolved to suit the morphological and behavioral traits of the animal carrier, ranging from fish to marine mammals and reptiles. Pop-up archival tags log ambient variables and movements of ocean-roaming animals before popping off, whereupon they float to the surface and transmit data. Real-time satellite tags transmit logged dive behavior and location of tagged animals each time they surface. Satellite tags are bigger than acoustic tags and hence are restricted to larger animals, but they can record fine-scale time series data on the depth, temperature, and location of animals transiting thousands of kilometers. The recent addition of solar power cells and improved attachment designs now permit multiyear observations of individual animals (*16*).

The scale of aquatic telemetry monitoring

The application of aquatic animal telemetry has grown rapidly over the past 30 years, with thousands of studies having been conducted spanning all continents and biomes (Fig. 1). The sixfold increase in aquatic telemetry studies over the past decade (Fig. 1, A to C, and movies S1 and S2) has provided information across diverse taxa (Fig. 1D) that are crucial to ecosystem health, economically important, and/or imperilled (Fig. 1E).

Through the global coverage of the ARGOS satellite system, satellite telemetry can monitor animal movements over vast spatial scales encompassing the open ocean and even in politically unstable regions (Fig. 1B) (*17*). The dependence of acoustic telemetry on fixed receivers that detect transmissions over small distances (<1000 m) has focused the majority of research on coastal, estuarine, and freshwater ecosystems in the developed world (Fig. 1A). This has enabled the study of fine-scale movements of organisms that are too small to equip with satellite tags or where satellite location data are insufficiently precise. However, the rapid expansion of acoustic telemetry arrays in coastal regions and on offshore and mobile platforms now presents the opportunity for cost-effective and large-scale integrated monitoring of large numbers of individuals over the long term.

Movements of aquatic animals in four dimensions

The two-dimensional (2D) horizontal plane of the aquatic world consists of a diverse mosaic of polar to tropical habitats. Horizontal movements of species are subdivided into those that occur within well-defined home ranges and those that take place between two or more distinct habitats, typically referred to as migrations (*18*). Telemetry has allowed accurate estimation of the horizontal space use of a diverse range of organisms from Atlantic cod (*Gadus morhua*) (Fig. 2A) (*19*) to king prawns (*Penaeus plebejus*) (*20*). At localized scales, these data have defined home ranges and core habitat use, delineated species distributions, and identified spawning site fidelity. This has permitted estimation of complex population parameters required for stock assessments, such as both fisheries and natural mortality (*21*). At the

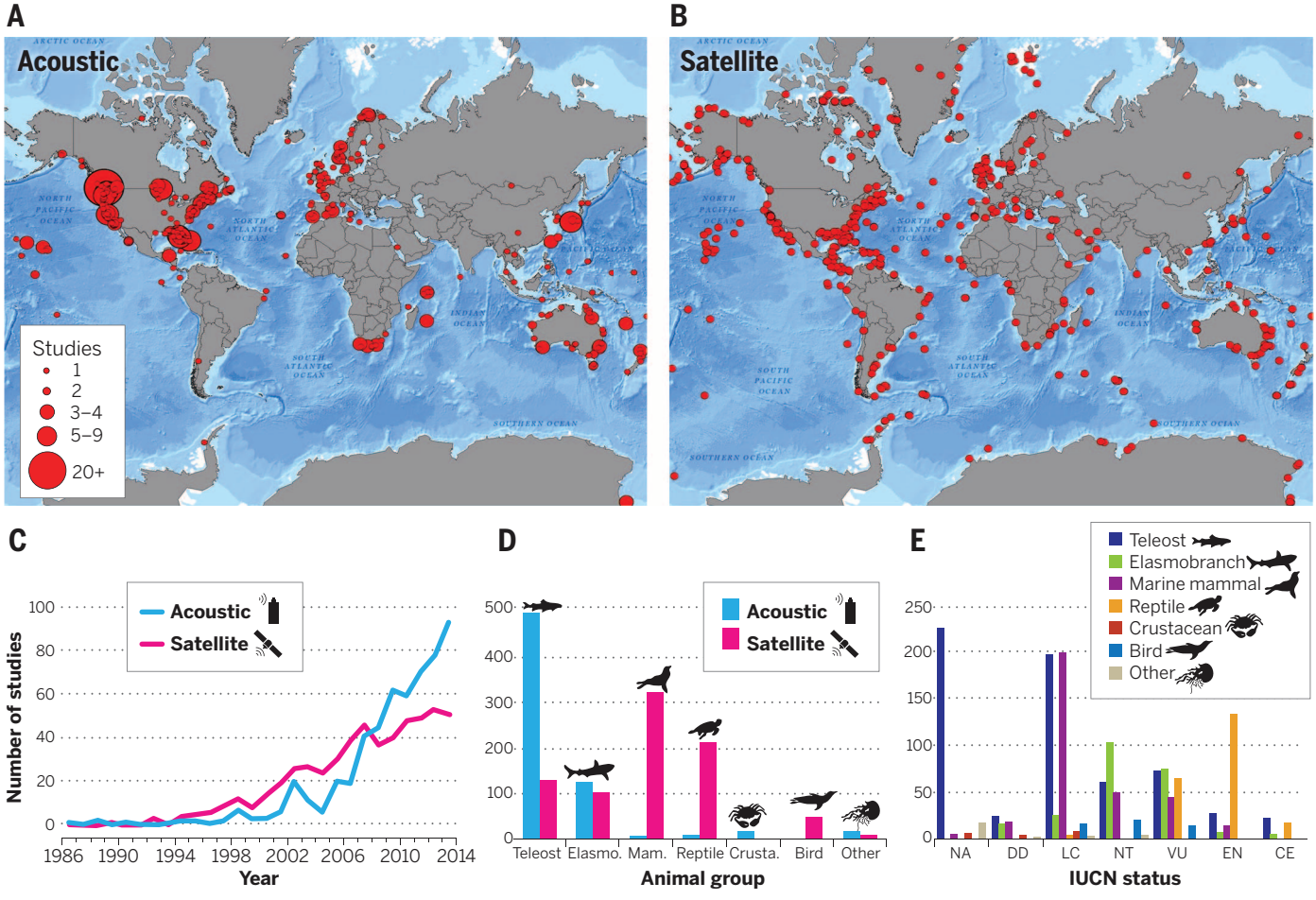


Fig. 1. Global distribution of aquatic telemetry studies. (**A**) Acoustic telemetry studies only. (**B**) Satellite telemetry studies only. (**C**) Increase in number of acoustic and satellite telemetry studies per year since 1986. (**D**) Number of acoustic and satellite telemetry studies by major aquatic animal groups [Elasmo., elasmobranch; Mam., marine mammals (including polar bears); Crusta., crustacean; Bird, flightless marine birds only]. (**E**) Number of acoustic and satellite telemetry studies per major animal group by International Union for Conservation of Nature (IUCN) threat categorization. NA, not assessed; DD, data deficient; LC, least concern; NT, near threatened; VU, vulnerable; EN, endangered; CE, critically endangered. See the associated data repository at DOI: 10.14286/20150203/KESSEL.

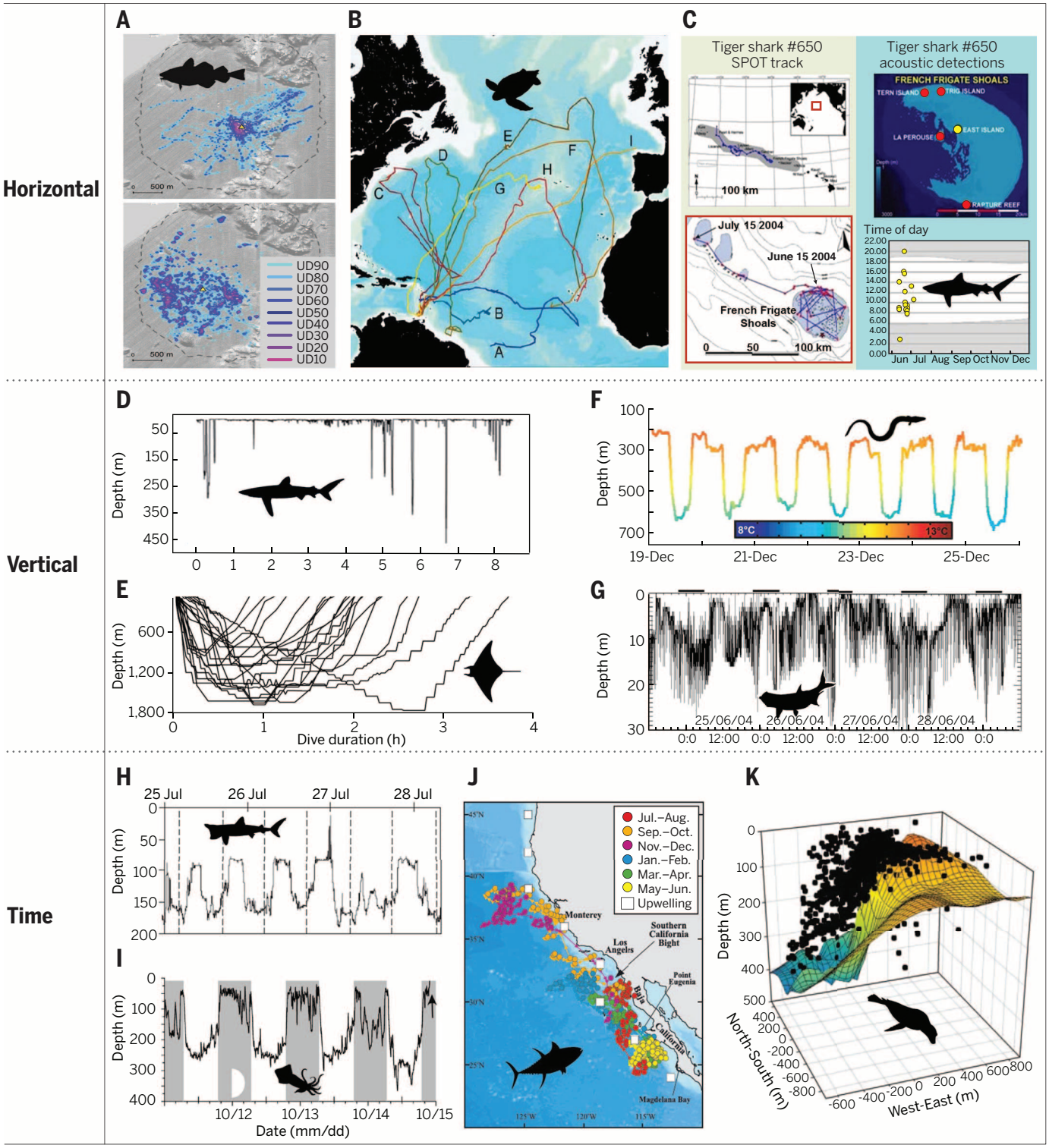


Fig. 2. Aquatic telemetry to understand the movements of animals in four dimensions: horizontal (2D), vertical (depth), and over time. (**A**) Fine-scale utilization distribution (UD) probabilities of Atlantic cod (*G. morhua*) at their spawning grounds, [altered from (*19*)]. (**B**) Transatlantic migrations of individual (A to I) leatherback turtles (*D. coriacea*) [taken from (*23*)]. (**C**) Small- and large-scale movements of tiger sharks (*G. cuvier*) revealed through a combination of satellite and acoustic telemetry [altered from (*29*)]. (**D**) Vertical movement behavior of a blue shark (*P. glauca*) [altered from (*35*)]. (**E**) Varying dive profile patterns of Chilean devil rays (*M. tarapacana*) [taken from (*32*)]. h, hours. (**F**) Oceanic diel migration of a European eel (*A. anguilla*), showing distinct temperature and vertical patterns [altered from (*27*)]. (**G**) Shallow-water dive profile of an Atlantic tarpon (*M. atlanticus*) [taken from (*34*)]. (**H**) Tidal-driven vertical movement patterns of a basking shark (*C. maximus*) [altered from (*40*)]. (**I**) Diel vertical movement patterns of a jumbo squid (*D. gigas*) [taken from (*41*)]. mm/dd, month/day. (**J**) Seasonal spatial utilization patterns by bluefin tuna (*T. orientalis*) [taken from (*43*)]. (**K**) Three-dimensional dive profile of female Weddell seals (*L. weddellii*) [taken from (*47*)] in relation to bathymetry and over two breeding seasons.

macroscale, telemetry has documented species migrations over tens of thousands of kilometers, confirming connectivity between populations at oceanic basin scales. This has revealed the intricacies and previously unanticipated complexity of migratory paths of bluefin tuna (*Thunnus thynnus*) (*22*), unsuspected transoceanic migrations of leatherback turtles (*Dermochelys coriacea*) (Fig. 2B) and white sharks (*Carcharodon carcharias*) (*23*, *24*), and transequatorial migrations of basking sharks (*25*). To date, much work has focused on simply describing these movement patterns, but due to their increasing size, such data sets, in the context of environmental variation, now lend themselves to an understanding of the mechanistic drivers of population structure and connectivity and metapopulation dynamics of species through quantifying emigration and immigration (*26*).

Unexpected horizontal movements of smaller animals are also challenging ideas that animal size dictates the scale of movement. For example, satellite telemetry revealed much of the long-suspected spawning migration of the critically endangered European eel (*Anguilla anguilla*) between Europe and the Sargasso Sea, with individuals measuring <1 m in length moving >1000 km in a few months (*27*). Through our capacity to examine horizontal movements of large numbers of individuals (>20,000 salmon smolts in one study alone in the Columbia River basin) (*28*), we can now begin to tease apart population processes built on individual-level behavior. Combining different telemetry techniques also provides opportunities to simultaneously elucidate movements over multiple scales. For example, fine-scale spatiotemporal movements of tiger sharks (*Galeocerdo cuvier*) seasonally feeding on fledgling albatrosses at a Hawaiian atoll were revealed through implanted acoustic tags, whereas the subsequent dispersal of these sharks over thousands of kilometers was revealed through satellite tags attached to the same individuals (Fig. 2C) (*29*).

Aquatic realms have a third dimension, depth, and a number of important environmental variables—including light level, pressure, temperature, and oxygen and salinity concentrations—vary predictably with depth. These parameters can divide species occurrence (e.g., by adaptive morphology and physiology), but other species can traverse these distinct vertical habitats. Some of the most notable telemetry results have revealed the extent and plasticity of these movements. These include highly dynamic vertical behaviors, from exclusively surface-orientated movements of salmon smolts (<5 m) (*30*) and obligate benthic movements of Greenland halibut (*Reinhardtius hippoglossoides*) (*31*) in the deep ocean (>1000 m) to species that undertake sporadic or prolonged deep diving, repetitive bounce dives, and/or consistent yo-yo movements (Fig. 2, D to G). Very deep dives to ~2000 m by Chilean devil rays (*Mobula tarapacana*) were characterized by two distinct dive profiles: one of rapid descent with slow stepwise ascent potentially related to prey searching and a second where rays rapidly descended and remained at depth (Fig. 2E) (*32*). By combining temperature and depth data derived from sensors integrated in transmitters, environmental profiles of the vertical habitats used by an animal can be compiled (Fig. 2F). These profiles provide explanatory power for the shape and duration of dive behavior observed related to the environment the animal encounters and have revealed behavioral and physiological thermoregulation in the world's largest fish, the whale shark (*Rhincodon typus*) (*33*). Even within shallow-water environments, diverse, highly structured shallow-water dive profiles have been recorded across numerous fish species, such as the Atlantic tarpon (*Megalops atlanticus*) (Fig. 2G) (*34*).

These vertical observations are providing insight into ecological linkages among depth zones and the foraging decisions of aquatic animals. Vertical movements of both pelagic and benthic predators such as blue sharks (*Prionace glauca*) (Fig. 2D) (*35*) and freshwater burbot (*Lota lota*) (*36*) show distinct profiles associated with bioenergetic gains, the vertical structuring of prey resources, predator avoidance, and social behavior. This has stimulated investigations into the occurrence of optimal foraging strategies such as Lévy walks, whereby animals undertake fractal vertical movement trajectories to optimize searching complex and sparsely distributed prey fields (*37*). Synthesizing horizontal and vertical movement data through state-space models to determine resident or directed movement states (*38*) will undoubtedly advance our understanding of foraging decisions, species interactions, and species redistributions under natural and anthropogenic change.

Time provides the fourth dimension within which 3D spatial utilization can be understood. The quality of habitat patches and their associated resources varies over time and is frequently in a state of disequilibrium. Examining how animals optimally synchronize their endogenous biological clocks with geophysical cycles is a critical step to resolving species' temporal distributions (*39*). Geophysical cycles produce predictable changes in the environment animals inhabit, from tidal changes in depth, temperature, and salinity to the contrasting dark and light periods of daily cycles. Tidally induced zooplankton aggregations, for example, are thought to cause the rhythmic dive patterns observed in basking sharks (Fig. 2H) (*40*), whereas many species, including jumbo squid (*Dosidicus gigas*), undertake diel vertical movement patterns related to prey distribution (Fig. 2I) (*41*). Telemetry has been instrumental in deciphering spawning aggregation dynamics of many reef fishes, where lunar cycles elicit spawning activity (*42*). Telemetry has also unveiled seasonal movements of endothermic Pacific bluefin tuna (*Thunnus orientalis*), driven by thermal fronts and strong downwellings that shape prey distributions (Fig. 2J) (*43*). For ectotherms that inhabit seasonally distinct temperate and subtropical zones, telemetry is showing how species use movements to compensate for localized environmental fluctuations. For example, estuarine yellow fin bream (*Acanthopagrus australis*) exhibit intricate behavioral switches, reversing depth distributions and diel activity patterns as a result of heavy rainfall and severe changes in turbidity and salinity (*44*).

The longevity of electronic tags now allows for measures of the consistency, repeatability, and interindividual variation in animal movements over time and, ultimately, during behavioral ontogeny. Through multiyear satellite telemetry of leatherback turtles, fidelity to a single migratory route was identified, providing clear conservation recommendations for a population that has declined by >90% over the past two decades (*45*). Conversely, highly complex and diverse movement patterns among tiger sharks tracked for several years around Hawaii could be explained by partial migrations, with some females moving for reproduction, whereas others undertook localized interisland movements driven by environmental conditions (*46*). Monitoring the spatiotemporal variability in territory use of Weddell seals (*Leptonychotes weddellii*) under ice and its influence on reproductive strategies over multiple consecutive breeding seasons (Fig. 2K) has also been possible (*47*). Coupling long-term telemetry tracking with biological data (e.g., maturity state) and environmental data (remote sensing imagery of sea surface temperature and productivity) will become central for quantifying temporal variation in the occurrence, timing, and destination of animal movements. These approaches will enable the first investigations of the role of memory and cognition in animal movement and navigation in aquatic ecosystems (*48*).

As telemetry data become more available, management strategies are incorporating geophysical cycles, variation in species' life histories, and environmental stochasticity to guide dynamic spatial planning efforts (*49*). For southern bluefin tuna (*Thunnus macoyii*), this approach integrated a habitat model conditioned with temperature-preference data from satellite tags on fish with an open-ocean model to enable near–real-time predictions of fish occurrence. These data were made available to fisheries managers, leading to the implementation of complex dynamic spatial zoning through which managers request data and repeatedly update spatial zoning plans. These advances make it feasible to consider creating spatially dynamic marine reserves that would vary in location annually as a function of predicted environmental conditions and associated animal movement patterns (*50*). Telemetry movement data are also allowing an assessment of the vulnerability of species to different fishing gears (*51*) to understand the post-release behavior and survival of released fishery bycatch (*52*) and to predict collisions between vessels and cetaceans (*53*). Such data will be imperative to inform fishery development and sustainability and to the conservation of vulnerable species.

Scaling from individual to multispecies movements

The movements of individuals of a species form only one component for understanding system-wide ecological organization in aquatic environments. Predators hunt for, locate, and consume their prey, driving direct behavioral responses

(e.g., predation and competition and predator avoidance). Many species are social and can co-occur in aggregations. Monitoring interactions among species and communities and coordinated movements of social groupings mark the critical next steps. The ability of telemetry to capture movement data for almost all aquatic species is a major contribution toward disentangling these interactions and for facilitating spatially explicit ecosystem-based management (*54*).

Telemetry of co-occurring Antarctic and sub-Antarctic fur seals (*Arctocephalus gazella* and *A. tropicalis*), for example, recorded considerable temporal and spatial foraging overlap (*55*) and a lack of resource partitioning. Conversely, sympatric jellyfishes (*56*) and whales (*57*) (Fig. 3A), with known dietary overlap, exhibited contrasting movements to avoid direct resource competition. Simultaneous monitoring of predators and prey can reveal the timing of predation events, such as sperm whales (*Physeter macrocephalus*) feeding on jumbo squid (Fig. 3B) (*58*). Emerging telemetry technologies include animal-borne acoustic-receiver tags that have recorded intra- and interspecific interactions of Galapagos sharks (*Carcharhinus galapagensis*) (*59*), whereas satellite-linked units on seals have documented spatiotemporal patterns of encounters with conspecifics and prey species (*14*). Moreover, abdominally implanted satellite tags equipped with temperature sensors are enabling the first monitoring of aquatic animals over their entire lifetimes. For instance, these tags revealed that some Steller sea lion (*Eumetopias jubatus*) deaths are apparently due to predation by Pacific sleeper sharks (*Somniosus pacificus*) (*60*).

Monitoring of multispecies movement patterns also provides a tool to assess the effectiveness of spatial management practices. So far, telemetry has revealed both successes and failures. Eighteen species of acoustically tagged reef fishes in the Caribbean region showed fidelity to marine protected areas (MPAs). However, three-quarters of the species examined travelled outside their protective limits (*61*). In contrast, telemetry data for five historically overfished snapper and grouper species in the Dry Tortugas islands indicated that the fish stayed primarily in a no-take marine reserve, which should provide sufficient protection for species recovery (Fig. 3C) (*62*). By directly quantifying multispecies movements and home ranges relative to protective boundaries, improvements in the design (e.g., stepping stone MPAs encompassing habitat hotspots) (*63*) and approach (e.g., spatially and temporally flexible closures) (*64*) to MPAs can be made and their limitations fully understood.

The ability of telemetry to resolve multispecies movements over scales much larger than those used in the current spatial management practices, encompassing cross-national and political borders, is a great asset. A foremost example is the Tagging of Pacific Predators (TOPP) program. Coordinated satellite telemetry of 23 apex marine predators—including tunas, pinnipeds, sharks, sea turtles, and cetaceans—documented systematic migration pathways, congener niche separation, and the location of multispecies biodiversity hotspots (*65*). These data, and those from a similar effort in Antarctica (*66*), are unveiling the first oceanscale view of the movement dynamics of entire predator guilds (Fig. 3D). Through characterizing daily, seasonal, and multi-year scales of species movements and interactions, as well as of imperilled species distributions and biodiversity hotspots, these data will be foundational for macroscale marine ecosystem management. Recent predictive modeling of projected climate change scenarios on species-specific core habitat use and basin-scale biodiversity patterns provides one such management application (*67*).

Integrating telemetry with other biological measures

Huey's (*68*) seminal paper established the first framework on the physiological consequences of animal habitat selection, but only through the emergence of telemetry tools can those relationships be empirically tested. Increasingly, physiological approaches are being combined with telemetry to link animal behavior, physiology, movement, and habitat selection (*69*). This allows the prediction of how anthropogenic and climate changes will affect ecosystems, for example, by determining cause and effect relationships and identifying optimal habitats and stressor thresholds for species, populations, and communities. This is achievable with the use of nonlethal tissue sampling (e.g., blood sample, muscle biopsy) of telemetered animals and laboratory experiments linked with telemetry of free-ranging animals (often including sensors that measure acceleration or cardiac activity, for example) (*70*).

Satellite telemetry of salmon sharks (*Lamna ditropis*) documented a subarctic-to-subtropical migration, with animals occupying an extreme thermal range of 2° to 24°C. Subsequent tissue analysis revealed that enhanced expression of specific cardiac proteins enabled exploitation of this thermal range (Fig. 4A) (*71*). In the vertical dimension, tropical bigeye tuna (*Thunnus obesus*) were shown to use behavioral and physiological thermoregulation to allow pursuit of prey into cold and hypoxic deep water, by using warm surface waters to regain body heat (*72*). In salmonids, combining telemetry measurements with laboratory manipulation of their endocrine and neurophysiology revealed links between migration speed, timing, and testosterone concentrations and the mechanisms underlying migration timing and homing in these commercially and culturally important fish (*73*, *74*).

Feeding, energetic requirements, digestive physiology, and body condition are major factors that shape species' movements, distributions, and survival. By linking jaw-attached sensors with satellite telemetry, it was possible to remotely identify individual feeding attempts of free-swimming northern elephant seals (*Mirounga angustirostris*) (Fig. 4B) (*75*). Refined feeding estimates of the planet's largest predatory fish, the white shark, have only been possible by coupling swimming speeds derived from high-resolution movement data with experimental measurements of standard metabolic rate and respiration (Fig. 4C) (*76*). Similarly, the correlation between lipid stores measured using ultrasound and drift dives derived from satellite telemetry has led to reconstruction of a time series of elephant seal body condition over fine spatial and temporal scales (Fig. 4D) (*77*). The miniaturization of archival multi-instrumented biologger devices that incorporate triaxial accelerometers and video and audio capability, coupled with telemetric approaches, provides one of the most exciting avenues for directly relating behavior and physiology to stimuli in the environment (*78*). Remote streaming of these high-sampling–rate and high-resolution data-rich files through rapid data transmission is the next needed evolution in telemetry technology.

Collectively, integration of the tools of telemetry and physiology provides real-world views of animal-environment interactions that directly feed into conservation and management (*79*). For example, biochemical measures of stress responses linked with telemetry can explain and predict mortality rates associated with fishing; examples include salmon bycaught and released from nets (*80*) or sharks released from drum lines (*81*). Telemetry data focused on thermally influenced behavior can be combined with laboratory-based studies on swimming energetics to estimate potential mortality in the face of climate change (*82*). Nonlethal biosampling of tagged barracuda (*Sphyraena barracuda*) revealed differences in habitat use among fish with different levels of ciguatera biotoxin, with implications for human consumption and health (*83*).

The integration of telemetry with molecular genetics will allow us to address questions on population structure and rates and patterns of organism dispersal that will be central for understanding metapopulations and ensuring population resilience. Long-term movements of lemon sharks (*Negaprion brevirostris*) off coastal Florida combined with molecular genetics confirmed connectivity between a seasonal aggregation of migratory adults and juveniles resident in genetically and geographically distinct nurseries (Fig. 4E) (*84*). In the first integrated framework of its kind, biogeographic, genetic, and telemetry data on global turtle populations were used to define regional management units at multiple biological and spatial scales (*85*). Incorporating telemetry with genetics will improve fisheries managers' confidence in stock delineation units. Scaling to ecological genomics provides the next generation of tools to study the genetic basis for organismal health and behavior related to movement. For instance, gene assays have identified key physiological processes that predicted the failure of sockeye salmon during migrations on the high seas (*86*).

Biosampling and the analysis of biochemical tracers—including stable isotopes of carbon and nitrogen, fatty acids, and trace elements in animal tissues—can link movement to an animal's diet and trophic ecology. This approach can elucidate food web dynamics, specifically rates of energy transfer through herbivores to carnivores and nutrient coupling among distinct

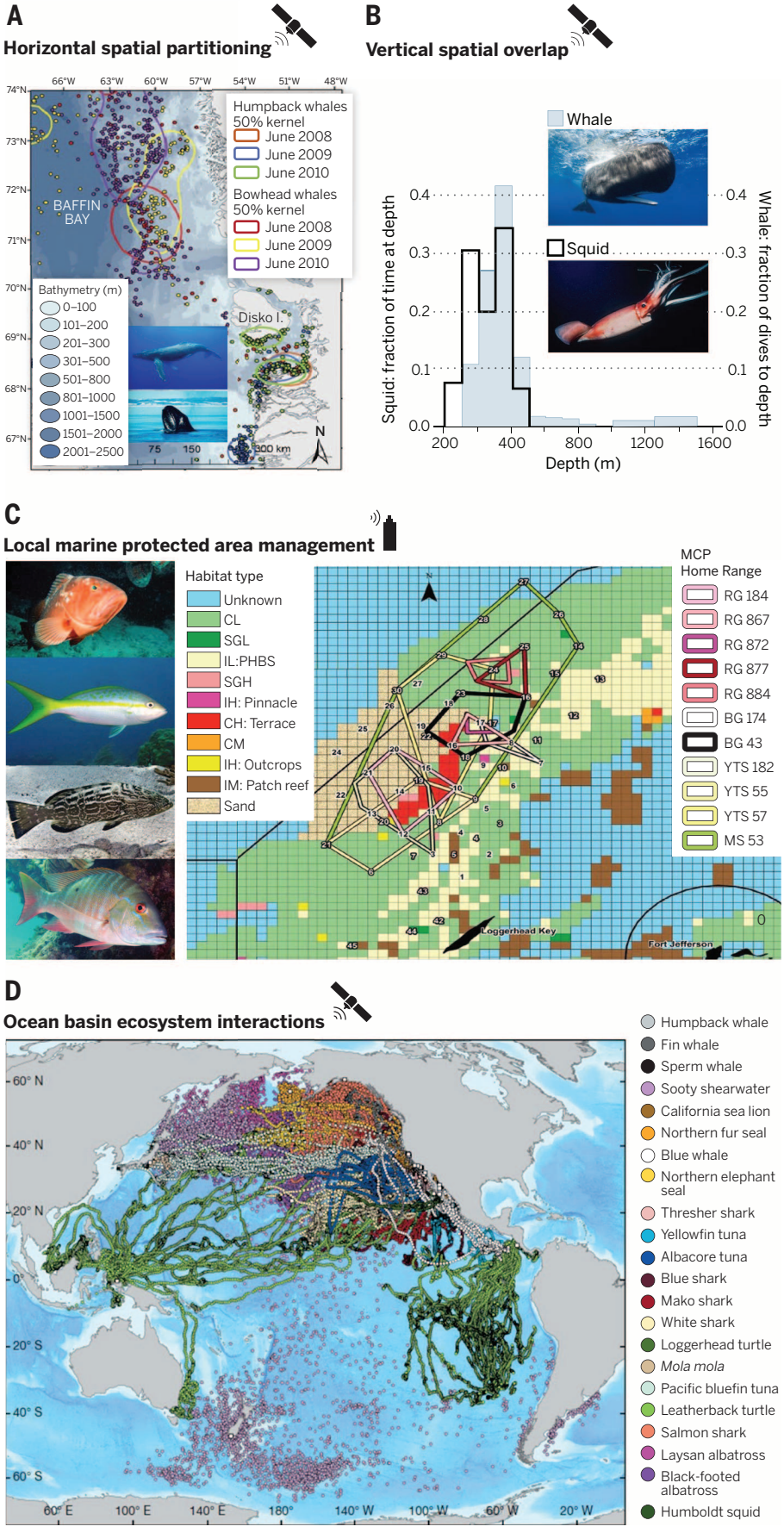


Fig. 3. Multispecies aquatic telemetry studies. (**A**) Spatial partitioning between humpback (*Megaptera novaeangliae*) and bowhead (*Balaena mysticetus*) whales limits resource competition [altered from (*57*)]. (**B**) Spatial overlap between sperm whales (*P. macrocephalus*) and jumbo squid (*D. gigas*) supports predation hypotheses [altered from (*58*)]. (**C**) Home ranges of four exploited teleost fish species (BG, black grouper; MS, mutton snapper; RG, red grouper; YTS, yellowtail snapper) fall within marine reserve boundaries (habitat types: C, contiguous; I, isolated; SG, spur-and-groove; H, high; M, medium; L, low relief; HB, hard bottom; PHBS, patchy HB in sand) [altered from (*62*)]. MCP, minimum convex polygon. (**D**) Long-term tracking of 23 apex predators across the Pacific Ocean [altered from (*65*)]. [Photo credits for (C), starting second from top: G. Carter; C. Estape; J. McEvoy]

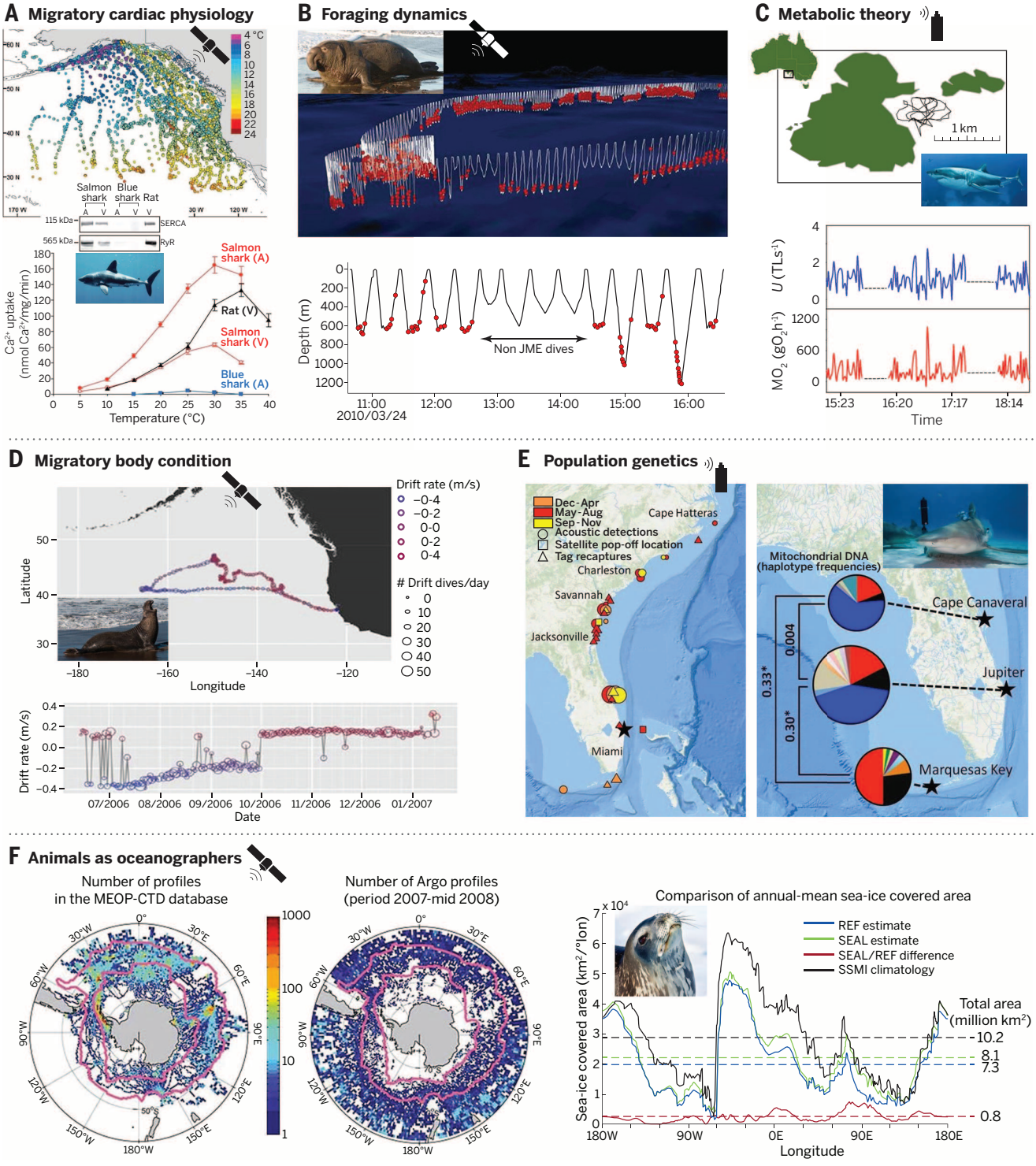


Fig. 4. Multidisciplinary aquatic telemetry approaches. (**A**) Satellite telemetry and tissue analysis reveal the physiological mechanism for spatial distribution of salmon sharks (*L. ditropis*) [altered from (*71*)]. (A) atrium; (V) ventricle. (**B**) Monitoring horizontal and vertical movements of seals and their jaw-motion events (JMEs) to quantify feeding events in northern elephant seals (*M. angustirostris*) [altered from (*75*)]. (**C**) High-resolution localized movements of white sharks (*C. carcharias*) using acoustic telemetry tied with metabolic theory to infer feeding rates [taken from (*76*)]. MO_2 (gO_2h^{-1}), routine metabolic rate; *U* (TLs^{-1}), swimming speed. (**D**) Blubber thickness and drift dive rates derived from satellite telemetry are used to estimate the rate of resource acquisition and the at-sea body condition of free-ranging northern elephant seals [taken from (*77*)]. (**E**) Population ecology of lemon sharks (*N. brevirostris*) on the east coast of the United States investigated using acoustic and satellite telemetry (left) and mitochondrial DNA analysis (right) [altered from (*84*)]. Stars represent tagging location (left) and genetic sampling location (right). (**F**) Improved estimates of the Southern Ocean general circulation using data from seals equipped with conductivity-temperature-depth sensors and satellite transmitters [altered from (*91*)]. MEOP-CTD, marine mammals exploring the oceans pole to pole–conductivity-temperature-depth database; REF, reference state estimate; SEAL, state estimate constrained with Argo and seal telemetry data; SSMI, Special Sensor Microwave Imager satellite observation data. [Photo credits: (A) B. Olsen; (B and D) M. Baird; (E) M. Potenski]

ecosystems. The analysis of these tracers in a large number of individuals, including telemetered animals, allows extrapolation of observations to the population level. Moreover, it can permit a retrospective view of a population's movement patterns and trophic dynamics to examine the effects of climate- and human-induced change. Biochemical tracers combined with telemetry have documented resource partitioning among eared seals (*87*), detected trophic linkages among alligators (*88*), and characterized the effects of tourism-related provisioning (i.e., baiting sharks into areas where divers can view them) on reef sharks (*89*). Telemetry coupled with genetics and/or genomics and biochemical tracers provides cutting-edge opportunities to examine the effects, roles, and evolutionary successes of invasive, commercial, and imperilled species.

Animal oceanographers

Telemetered animals undertaking their daily routines encounter environmental variation and compile data sets with a frequency and over a range of scales that humans could not feasibly collect using conventional tools. Satellite-linked transmitters attached to marine mammals can record time series data on temperature, salinity, fluorescence, light, and partial pressure of oxygen as a function of location and depth in the different water masses that animals encounter (*90*). This approach has proven extremely effective for sampling regions that are logistically challenging and costly to observe, for example, areas under sea ice during fall and winter (*91*).

Data derived from these "animal oceanographers" are now enhancing regional oceanographic models. Transmitters carried by narwhals (*Monodon monoceros*) and beluga whales (*Delphinapterus leucas*) have provided more than 200,000 temperature and salinity profiles of the Arctic Ocean (*92*), whereas transmitters carried by seals and sea lions have provided almost circumpolar oceanographic sampling of the Southern Ocean (Fig. 4F) (*91*). Approximately 70% of all animal oceanographer profiles from this region are from south of 60°S (*93*), with considerable data from south of the Antarctic Circumpolar Current where Argo buoy data are effectively absent due to ice. These data produce hydrographic profiles with high spatial and temporal resolution (2.5 profiles per day, on average). These profiles are improving estimates of Southern Ocean circulation (*91*), revealing upper ocean and coastal processes that affect the basal melting of ice shelves (*94*), and elucidating previously unknown physical properties of upwelling off the southern coast of Australia (*95*).

These successes are encouraging the further development and testing of oceanography-capable telemetry tags on nonmammalian species such as tuna and sharks. Satellite tag measurements of the depth at which blue marlins (*Makaira nigricans*) limit their dives (requiring oxygen concentrations >3.5 ml·liter^{-1}) now allow inferences over the 3D extent of the oxygen minimum zone in the tropical northeast Atlantic (*96*). Animals monitoring their environments have the potential to record these oceanographic data across all biomes, from the poles to the tropics and the photic zone to the abyssal depths. These data will continue to enhance existing ocean-atmosphere observation platforms but will also provide opportunities to improve ocean forecasting.

The future of aquatic telemetry, obstacles to traverse, and relevance for aquatic management and conservation

Aquatic telemetry has revealed distinctive insights into our blue planet, in a range of organisms and over previously unimaginable spatiotemporal scales. It has led to paradigm shifts in our understanding of animal-environment interactions and how aquatic ecosystems are structured. Most importantly, telemetry now provides the opportunity for the development of next-generation aquatic governance frameworks. Traditionally, management of aquatic resources has lagged behind that of the terrestrial realm, where landscape ecology principles are well founded, broadly accepted, and incorporated into management regimes. The terrestrial approach is built on understanding the causes, changes, and ecological functions associated with spatial animal-environment patterns under a nonequilibrium view. Aquatic resource management requires a similar approach, but its adoption has been hindered by a lack of data over relevant spatiotemporal scales. Telemetry can now provide these data, facilitating aquatic-scape approaches for conservation and management, while also bridging the gap between terrestrial and aquatic ecosystems (*97*), inspiring a unified approach to global resource management.

However, addressing global scientific and management questions will require expanded telemetry infrastructure and animal-tagging efforts

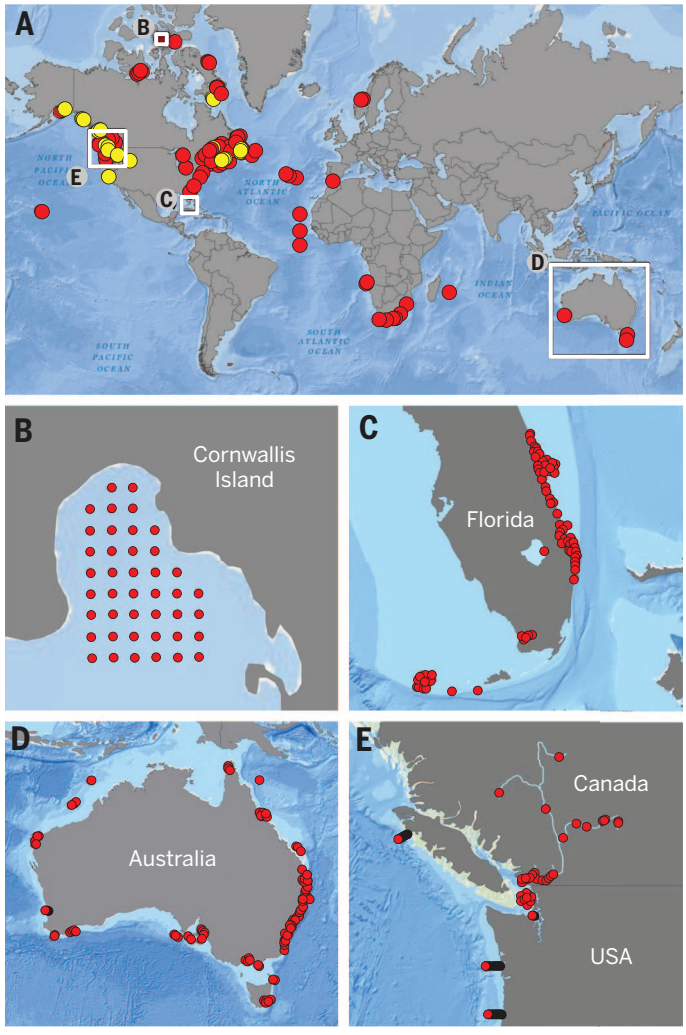


Fig. 5. The network model (or approach) of acoustic telemetry to facilitate monitoring of aquatic species over required ecological and biological scales. (**A**) Global monitoring (OTN global). Red points indicate current receiver stations; yellow points denote proposed receiver stations. Monitoring (**B**) within a 2 km by 3 km high Arctic embayment, (**C**) along the coast of an entire state [Florida Atlantic Coast Telemetry (FACT) array], (**D**) across an entire country coastline [Australian Animal Tagging and Monitoring System (AATAMS) array], and (**E**) trans-boundary between Canada and the United States [Pacific Ocean Shelf Tracking (POST)/OTN array]. In most instances, these network models integrate both acoustic and satellite telemetry approaches.

over scales larger than those previously considered. Industry commitment to advance technologies and ensure compatibility will be imperative. Collaborative research groups are emerging to facilitate sharing of equipment, facilities, and expertise and to foster coordinated data sharing. This "network model" integrates acoustic and satellite telemetry and covers scales from individual bays to coastal shelves that cross national boundaries and, in the case of Australia, an entire continent (Fig. 5). This recognition that aquatic animal movements and the dynamic nature of the physical environment they inhabit transcend geopolitical, economic, and management boundaries is driving the formation of global consortia such as the Ocean Tracking Network (OTN) (*98*) (Fig. 5A) and the Global Tagging of Pelagic Predators (*99*).

The establishment of these global networks raises new challenges over data sharing and will require strategies to address data management, ownership, and public release. Successful models exist in the physical oceanography, ocean chemistry, and molecular genetic domains (e.g., the GenBank archive) (*100*). Varying levels of data sharing are already apparent in current telemetry networks: The early success of animal oceanographers provides one such example (*91*), and centralized telemetry databases are available, such as the Ocean Biogeographic Information System–Spatial Ecological Analysis of Megavertebrate Populations (*101*). Aquatic telemetry may benefit from a single centralized governing body for data archiving and management, similar to the GenBank model that is funded across organizations and continents. This would promote data standardization and would benefit the global research community through increased communication, scope for collaboration, intellectual exposure, and funding opportunities. Recognizing that large spatial gaps in aquatic monitoring currently exist, a concerted effort is needed. This is particularly true in developing countries, where the status of aquatic resources is poorly known and only fragmented management exists yet resources are often exploited by developed nations. An integrated global telemetry approach would substantially improve equitable decision-making at local and international scales and would generate considerable dividends with regard to resource management, commerce, and food security.

Conclusions

Telemetry has profoundly altered and, at times, revolutionized our understanding of the complexities of animal movements and interactions and how these structure aquatic ecosystems. Technological advancements in telemetry and multidisciplinary approaches will continue to promote new avenues of enquiry, growing the knowledge base. Challenges remain in building a unified global network approach that will enable us to meet the upcoming needs in ocean management and to achieve telemetry's potential for deriving and disseminating knowledge on the spatial and temporal scales over which aquatic resources are structured and must be sustainably managed. It is certain that the ocean will continue to change. The global network approach will realize and facilitate an environment for knowledge and the sharing of resources and data. Additionally, through centralized data archiving and the promotion of collaboration across disciplines, this approach will provide great potential for the development and implementation of global aquatic-scape management, as well as for reaction to future changes in aquatic populations and ecosystems dominated by mobile animals.

REFERENCES AND NOTES

1. D. E. Bowler, T. G. Benton, Causes and consequences of animal dispersal strategies: relating individual behavior to spatial dynamics. *Biol. Rev.* **80**, 205–225 (2005).
2. T. R. Parsons, M. Takahashi, B. Hargrave, *Biological Oceanographic Processes* (Elsevier, Amsterdam, 2013).
3. D. P. Costa, G. A. Breed, P. W. Robinson, New insights into pelagic migrations: Implications for ecology and conservation. *Annu. Rev. Ecol. Evol. Syst.* **43**, 73–96 (2012). doi: 10.1146/annurev-ecolsys-102710-145045
4. R. L. Kelly, *The Foraging Spectrum: Diversity in Hunter-Gatherer Lifeways* (Smithsonian Institution Press, Washington, DC, 1995).
5. K. Dahl, *Studier og Forsøk Over Ørret og Ørretvann* (Centraltrykkeriet, Kristiania, Norway, 1917).
6. E. D. Le Cren, A note on the history of mark-recapture population estimates. *J. Anim. Ecol.* **34**, 453–454 (1965). doi: 10.2307/2661
7. G. Arnold, H. Dewar, in *Electronic Tagging and Tracking in Marine Fisheries* (Springer, Dordrecht, 2001), pp. 7–64.
8. M. R. Donaldson *et al*., Making connections in aquatic ecosystems with acoustic telemetry monitoring. *Front. Ecol. Environ* **12**, 565–573 (2014). doi: 10.1890/130283
9. E. L. Hazen *et al*., Ontogeny in marine tagging and tracking science: Technologies and data gaps. *Mar. Ecol. Prog. Ser.* **457**, 221–240 (2012). doi: 10.3354/meps09857
10. C. Rutz, G. C. Hays, New frontiers in biologging science. *Biol. Lett.* **5**, 289–292 (2009). doi: 10.1098/rsbl.2009.0089; pmid: 19324624
11. A. P. Klimley, S. B. Butler, D. R. Nelson, A. T. Stull, Diel movements of scalloped hammerhead sharks, *Sphyrna lewini* griffith and smith, to and from a seamount in the Gulf of California. *J. Fish Biol.* **33**, 751–761 (1988). doi: 10.1111/j.1095-8649.1988.tb05520.x
12. I. Priede, A basking shark (*Cetorhinus maximus*) tracked by satellite together with simultaneous remote sensing. *Fish. Res.* **2**, 201–216 (1984). doi: 10.1016/0165-7836(84)90003-1
13. L. Dagorn *et al*., Satellite-linked acoustic receivers to observe behavior of fish in remote areas. *Aquat. Living Resour.* **20**, 307–312 (2007). doi: 10.1051/alr:2008001
14. D. C. Lidgard, W. D. Bowen, I. D. Jonsen, S. J. Iverson, Predator-borne acoustic transceivers and GPS tracking reveal spatiotemporal patterns of encounters with acoustically tagged fish in the open ocean. *Mar. Ecol. Prog. Ser.* **501**, 157–168 (2014). doi: 10.3354/meps10670
15. C. M. Clark *et al*., Tracking and following a tagged leopard shark with an autonomous underwater vehicle. *J. Field Robot.* **30**, 309–322 (2013). doi: 10.1002/rob.21450
16. M. Domeier, N. Nasby-Lucas, Two-year migration of adult female white sharks (*Carcharodon carcharias*) reveals widely separated nursery areas and conservation concerns. *Anim. Biotelem.* **1**, 2 (2013).
17. S. M. Maxwell *et al*., Using satellite tracking to optimize protection of long-lived marine species: Olive ridley sea turtle conservation in Central Africa. *PLOS ONE* **6**, e19905 (2011). doi: 10.1371/journal.pone.0019905; pmid: 21589942
18. H. Dingle, V. A. Drake, What is migration? *Bioscience* **57**, 113–121 (2007). doi: 10.1641/B570206
19. M. J. Dean, W. S. Hoffman, D. R. Zemeckis, M. P. Armstrong, Fine-scale diel and gender-based patterns in behaviour of Atlantic cod (*Gadus morhua*) on a spawning ground in the Western Gulf of Maine. *ICES J. Mar. Sci.* **71**, 1474–1489 (2014). doi: 10.1093/icesjms/fsu040
20. M. Taylor, A. Ko, Monitoring acoustically tagged king prawns *Penaeus* (*Melicertus*) *plebejus* in an estuarine lagoon. *Mar. Biol.* **158**, 835–844 (2011). doi: 10.1007/s00227-010-1610-6
21. K. H. Pollock, H. Jiang, J. E. Hightower, Combining telemetry and fisheries tagging models to estimate fishing and natural mortality rates. *Trans. Am. Fish. Soc.* **133**, 639–648 (2004). doi: 10.1577/T03-029.1
22. B. A. Block *et al*., Electronic tagging and population structure of Atlantic bluefin tuna. *Nature* **434**, 1121–1127 (2005). doi: 10.1038/nature03463; pmid: 15858572
23. G. C. Hays, V. J. Hobson, J. D. Metcalfe, D. Righton, D. W. Sims, Flexible foraging movements of leatherback turtles across the North Atlantic Ocean. *Ecology* **87**, 2647–2656 (2006). doi: 10.1890/0012-9658(2006)87[2647:FFMOLT]2.0.CO;2; pmid: 17089672
24. R. Bonfil *et al*., Transoceanic migration, spatial dynamics, and population linkages of white sharks. *Science* **310**, 100–103 (2005). doi: 10.1126/science.1114898; pmid: 16210537
25. G. B. Skomal *et al*., Transequatorial migrations by basking sharks in the western Atlantic Ocean. *Curr. Biol.* **19**, 1019–1022 (2009). doi: 10.1016/j.cub.2009.04.019 pmid: 19427211
26. R. A. Cheke, J. A. Tratalos, Migration, patchiness, and population processes illustrated by two migrant pests. *Bioscience* **57**, 145–154 (2007). doi: 10.1641/B570209
27. K. Aarestrup *et al*., Oceanic spawning migration of the European eel (*Anguilla anguilla*). *Science* **325**, 1660 (2009). doi: 10.1126/science.1178120; pmid: 19779192
28. E. L. Rechisky, D. W. Welch, A. D. Porter, M. C. Jacobs-Scott, P. M. Winchell, Influence of multiple dam passage on survival of juvenile Chinook salmon in the Columbia River estuary and coastal ocean. *Proc. Natl. Acad. Sci. U.S.A.* **110**, 6883–6888 (2013). doi: 10.1073/pnas.1219910110; pmid: 23576733
29. C. G. Meyer, Y. P. Papastamatiou, K. N. Holland, A multiple instrument approach to quantifying the movement patterns and habitat use of tiger (*Galeocerdo cuvier*) and Galapagos sharks (*Carcharhinus galapagensis*) at French Frigate Shoals, Hawaii. *Mar. Biol.* **157**, 1857–1868 (2010). doi: 10.1007/s00227-010-1457-x
30. M. D. Renkawitz, T. F. Sheehan, G. S. Goulette, Swimming depth, behavior, and survival of Atlantic salmon postsmolts in Penobscot Bay, Maine. *Trans. Am. Fish. Soc.* **141**, 1219–1229 (2012). doi: 10.1080/00028487.2012.688916
31. I. Peklova, N. E. Hussey, K. J. Hedges, M. A. Treble, A. T. Fisk, Depth and temperature preferences of the deep-water flatfish Greenland halibut *Reinhardtius hippoglossoides* in an Arctic marine ecosystem. *Mar. Ecol. Prog. Ser.* **467**, 193–205 (2012). doi: 10.3354/meps09899
32. S. R. Thorrold *et al*., Extreme diving behaviour in devil rays links surface waters and the deep ocean. *Nat. Commun.* **5**, 4274 (2014). doi: 10.1038/ncomms5274; pmid: 24983949
33. M. Thums, M. Meekan, J. Stevens, S. Wilson, J. Polovina, Evidence for behavioural thermoregulation by the world's largest fish. *J. R. Soc. Interface* **10**, 20120477 (2012). doi: 10.1098/rsif.2012.0477; pmid: 23075547
34. J. Luo, J. S. Ault, Vertical movement rates and habitat use of Atlantic tarpon. *Mar. Ecol. Prog. Ser.* **467**, 167–180 (2012). doi: 10.3354/meps09957
35. N. E. Humphries *et al*., Environmental context explains Lévy and Brownian movement patterns of marine predators. *Nature* **465**, 1066–1069 (2010).pmid: 20531470
36. P. Harrison *et al*., Diel vertical migration of adult burbot: A dynamic trade-off among feeding opportunity, predation avoidance, and bioenergetic gain. *Can. J. Fish. Aquat. Sci.* **70**, 1765–1774 (2013). doi: 10.1139/cjfas-2013-0183
37. D. W. Sims *et al*., Scaling laws of marine predator search behaviour. *Nature* **451**, 1098–1102 (2008). doi: 10.1038/nature06518; pmid: 18305542
38. S. Bestley, I. D. Jonsen, M. A. Hindell, R. G. Harcourt, N. J. Gales, Taking animal tracking to new depths: Synthesizing horizontal-vertical movement relationships for four marine predators. *Ecology* **96**, 417–427 (2015). doi: 10.1890/14-0469.1
39. E. Naylor, Chronobiology: Implications for marine resource exploitation and management. *Sci. Mar.* **69**, 157–167 (2005).
40. E. L. C. Shepard *et al*., Diel and tidal rhythms in diving behaviour of pelagic sharks identified by signal processing of archival tagging data. *Mar. Ecol. Prog. Ser.* **328**, 205–213 (2006). doi: 10.3354/meps328205
41. W. Gilly *et al*., Vertical and horizontal migrations by the jumbo squid *Dosidicus gigas* revealed by electronic tagging. *Mar. Ecol. Prog. Ser.* **324**, 1–17 (2006). doi: 10.3354/meps324001
42. Y. Sadovy, Y. S. de Mitcheson, P. L. Colin, *Reef Fish Spawning Aggregations: Biology, Research and Management* (Springer Science and Business Media, Dordrecht, 2011), vol. 35.

43. T. Kitagawa *et al*., Horizontal and vertical movements of juvenile bluefin tuna (*Thunnus orientalis*) in relation to seasons and oceanographic conditions in the eastern Pacific Ocean. *Fish. Oceanogr.* **16**, 409–421 (2007). doi: 10.1111/j.1365-2419.2007.00441.x
44. N. L. Payne *et al*., Rain reverses diel activity rhythms in an estuarine teleost. *Proc. Biol. Sci.* **280**, 20122363 (2013). doi: 10.1098/rspb.2012.2363; pmid: 23173211
45. G. L. Shillinger *et al*., Persistent leatherback turtle migrations present opportunities for conservation. *PLOS Biol.* **6**, e171 (2008). doi: 10.1371/journal.pbio.0060171; pmid: 18630987
46. Y. P. Papastamatiou *et al*., Telemetry and random-walk models reveal complex patterns of partial migration in a large marine predator. *Ecology* **94**, 2595–2606 (2013). doi: 10.1890/12-2014.1; pmid: 24400511
47. M. A. Hindell, R. Harcourt, J. R. Waas, D. Thompson, Fine-scale three-dimensional spatial use by diving, lactating female Weddell seals *Leptonychotes weddellii*. *Mar. Ecol. Prog. Ser.* **242**, 275–284 (2002). doi: 10.3354/meps242275
48. W. F. Fagan *et al*., Spatial memory and animal movement. *Ecol. Lett.* **16**, 1316–1329 (2013). doi: 10.1111/ele.12165; pmid: 23953128
49. A. J. Hobday, J. R. Hartog, T. Timmiss, J. Fielding, Dynamic spatial zoning to manage southern bluefin tuna (*Thunnus maccoyii*) capture in a multi-species longline fishery. *Fish. Oceanogr.* **19**, 243–253 (2010). doi: 10.1111/j.1365-2419.2010.00540.x
50. S. D. Gaines, S. E. Lester, K. Grorud-Colvert, C. Costello, R. Pollnac, Evolving science of marine reserves: New developments and emerging research frontiers. *Proc. Natl. Acad. Sci. U.S.A.* **107**, 18251–18255 (2010). doi: 10.1073/pnas.1002098107; pmid: 20978212
51. E. Cortés *et al*., Ecological risk assessment of pelagic sharks caught in Atlantic pelagic longline fisheries. *Aquat. Living Resour.* **23**, 25–34 (2010). doi: 10.1051/alr/2009044
52. C. D. Moyes, N. Fragoso, M. K. Musyl, R. W. Brill, Predicting postrelease survival in large pelagic fish. *Trans. Am. Fish. Soc.* **135**, 1389–1397 (2006). doi: 10.1577/T05-224.1
53. H. M. Guzman, C. G. Gomez, C. A. Guevara, L. Kleivane, Potential vessel collisions with Southern Hemisphere humpback whales wintering off Pacific Panama. *Mar. Mamm. Sci.* **29**, 629–642 (2013).
54. J. D. Metcalfe, W. J. Le Quesne, W. W. Cheung, D. A. Righton, Conservation physiology for applied management of marine fish: An overview with perspectives on the role and value of telemetry. *Philos. Trans. R. Soc. London Ser. B* **367**, 1746–1756 (2012). doi: 10.1098/rstb.2012.0017; pmid: 22566680
55. S. A. Robinson, S. G. Goldsworthy, J. Van den Hoff, M. A. Hindell, The foraging ecology of two sympatric fur seal species, *Arctocephalus gazella* and *Arctocephalus tropicalis*, at Macquarie Island during the austral summer. *Mar. Freshw. Res.* **53**, 1071–1082 (2003). doi: 10.1071/MF01218
56. P. E. Moriarty, K. S. Andrews, C. J. Harvey, M. Kawase, Vertical and horizontal movement patterns of scyphozoan jellyfish in a fjord-like estuary. *Mar. Ecol. Prog. Ser.* **455**, 1–12 (2012). doi: 10.3354/meps09783
57. K. L. Laidre, M. P. Heide-Jørgensen, Spring partitioning of Disko Bay, West Greenland, by Arctic and subarctic baleen whales. *ICES J. Mar. Sci.* **69**, 1226–1233 (2012). doi: 10.1093/icesjms/fss095
58. R. Davis *et al*., Diving behavior of sperm whales in relation to behavior of a major prey species, the jumbo squid, in the Gulf of California, Mexico. *Mar. Ecol. Prog. Ser.* **333**, 291–302 (2007). doi: 10.3354/meps333291
59. K. N. Holland, C. G. Meyer, L. C. Dagorn, Inter-animal telemetry: Results from first deployment of acoustic "business card" tags. *Endanger. Species Res.* **10**, 287–293 (2009). doi: 10.3354/esr00226
60. M. Horning, J.-A. E. Mellish, In cold blood: Evidence of Pacific sleeper shark (*Somniosus pacificus*) predation on Steller sea lions (*Eumetopias jubatus*) in the Gulf of Alaska. *Fish Bull.* **112**, 297–310 (2014). doi: 10.7755/FB.112.4.6
61. S. J. Pittman *et al*., Fish with chips: Tracking reef fish movements to evaluate size and connectivity of Caribbean marine protected areas. *PLOS ONE* **9**, e96028 (2014). doi: 10.1371/journal.pone.0096028; pmid: 24797815
62. N. A. Farmer, J. S. Ault, Grouper and snapper movements and habitat use in Dry Tortugas, Florida. *Mar. Ecol. Prog. Ser.* **433**, 169–184 (2011). doi: 10.3354/meps09198
63. S. K. Hooker *et al*., Making protected area networks effective for marine top predators. *Endanger. Species Res.* **13**, 203–218 (2011). doi: 10.3354/esr00322
64. A. Grüss, D. M. Kaplan, S. Guénette, C. M. Roberts, L. W. Botsford, Consequences of adult and juvenile movement for marine protected areas. *Biol. Conserv.* **144**, 692–702 (2011). doi: 10.1016/j.biocon.2010.12.015
65. B. A. Block *et al*., Tracking apex marine predator movements in a dynamic ocean. *Nature* **475**, 86–90 (2011). doi: 10.1038/nature10082; pmid: 21697831
66. B. Raymond *et al*., Important marine habitat off east Antarctica revealed by two decades of multi-species predator tracking. *Ecography* **38**, 121–129 (2015). doi: 10.1111/ecog.01021
67. E. L. Hazen *et al*., Predicted habitat shifts of Pacific top predators in a changing climate. *Nat. Clim. Change* **3**, 234–238 (2013).
68. R. B. Huey, Physiological consequences of habitat selection. *Am. Nat.* **137** (suppl.), S91–S115 (1991). doi: 10.1086/285141
69. S. J. Cooke *et al*., Developing a mechanistic understanding of fish migrations by linking telemetry with physiology, behavior, genomics and experimental biology: An interdisciplinary case study on adult fraser river sockeye salmon. *Fisheries* **33**, 321–338 (2008). doi: 10.1577/1548-8446-33.7.321
70. S. J. Cooke *et al*., Biotelemetry: A mechanistic approach to ecology. *Trends Ecol. Evol.* **19**, 334–343 (2004). doi: 10.1016/j.tree.2004.04.003; pmid: 16701280
71. K. C. Weng *et al*., Satellite tagging and cardiac physiology reveal niche expansion in salmon sharks. *Science* **310**, 104–106 (2005). doi: 10.1126/science.1114616; pmid: 16210538
72. K. N. Holland, R. W. Brill, R. K. Chang, J. R. Sibert, D. A. Fournier, Physiological and behavioural thermoregulation in bigeye tuna (*Thunnus obesus*). *Nature* **358**, 410–412 (1992). doi: 10.1038/358410a0; pmid: 1641023
73. G. Crossin *et al*., Behaviour and physiology of sockeye salmon homing through coastal waters to a natal river. *Mar. Biol.* **152**, 905–918 (2007). doi: 10.1007/s00227-007-0741-x
74. H. Ueda, Homing ability and migration success in Pacific salmon: Mechanistic insights from biotelemetry, endocrinology, and neurophysiology. *Mar. Ecol. Prog. Ser.* **496**, 219–232 (2014). doi: 10.3354/meps10636
75. Y. Naito *et al*., Unravelling the mysteries of a mesopelagic diet: A large apex predator specializes on small prey. *Funct. Ecol.* **27**, 710–717 (2013). doi: 10.1111/1365-2435.12083
76. J. M. Semmens, N. L. Payne, C. Huveneers, D. W. Sims, B. D. Bruce, Feeding requirements of white sharks may be higher than originally thought. *Sci. Rep.* **3**, 1471 (2013). doi: 10.1038/srep01471; pmid: 23503585
77. R. S. Schick *et al*., Estimating resource acquisition and at-sea body condition of a marine predator. *J. Anim. Ecol.* **82**, 1300–1315 (2013). doi: 10.1111/1365-2656.12102; pmid: 23869551
78. K. Evans, M.-A. Lea, T. Patterson, Recent advances in bio-logging science: Technologies and methods for understanding animal behaviour and physiology and their environments. *Deep Sea Res. Part II* **88–89**, 1–6 (2013). doi: 10.1016/j.dsr2.2012.10.005
79. G. T. Crossin, S. J. Cooke, J. A. Goldbogen, R. A. Phillips, Tracking fitness in marine vertebrates: Current knowledge and opportunities for future research. *Mar. Ecol. Prog. Ser.* **496**, 1–17 (2014). doi: 10.3354/meps10691
80. S. M. Wilson, G. D. Raby, N. J. Burnett, S. G. Hinch, S. J. Cooke, Looking beyond the mortality of bycatch: Sublethal effects of incidental capture on marine animals. *Biol. Conserv.* **171**, 61–72 (2014). doi: 10.1016/j.biocon.2014.01.020
81. A. Gallagher, J. Serafy, S. Cooke, N. Hammerschlag, Physiological stress response, reflex impairment, and survival of five sympatric shark species following experimental capture and release. *Mar. Ecol. Prog. Ser.* **496**, 207–218 (2014). doi: 10.3354/meps10490
82. A. P. Farrell *et al*., Pacific salmon in hot water: Applying aerobic scope models and biotelemetry to predict the success of spawning migrations. *Physiol. Biochem. Zool.* **81**, 697–709 (2008). doi: 10.1086/592057; pmid: 18922081
83. A. C. O'Toole, M.-Y. Dechraoui Bottein, A. J. Danylchuk, J. S. Ramsdell, S. J. Cooke, Linking ciguatera poisoning to spatial ecology of fish: A novel approach to examining the distribution of biotoxin levels in the great barracuda by combining non-lethal blood sampling and biotelemetry. *Sci. Total Environ.* **427-428**, 98–105 (2012). doi: 10.1016/j.scitotenv.2011.11.053; pmid: 22560748
84. S. T. Kessel *et al*., Predictable temperature-regulated residency, movement and migration in a large, highly mobile marine predator (*Negaprion brevirostris*). *Mar. Ecol. Prog. Ser.* **514**, 175–190 (2014). doi: 10.3354/meps10966
85. B. P. Wallace *et al*., Regional management units for marine turtles: A novel framework for prioritizing conservation and research across multiple scales. *PLOS ONE* **5**, e15465 (2010). doi: 10.1371/journal.pone.0015465; pmid: 21253007
86. K. M. Miller *et al*., Genomic signatures predict migration and spawning failure in wild Canadian salmon. *Science* **331**, 214–217 (2011). doi: 10.1126/science.1196901; pmid: 21233388
87. J. N. Waite, S. J. Trumble, V. N. Burkanov, R. D. Andrews, Resource partitioning by sympatric Steller sea lions and northern fur seals as revealed by biochemical dietary analyses and satellite telemetry. *J. Exp. Mar. Biol. Ecol.* **416–417**, 41–54 (2012). doi: 10.1016/j.jembe.2012.02.009
88. A. E. Rosenblatt, M. R. Heithaus, Does variation in movement tactics and trophic interactions among American alligators create habitat linkages? *J. Anim. Ecol.* **80**, 786–798 (2011). doi: 10.1111/j.1365-2656.2011.01830.x; pmid: 21418209
89. A. Maljković, I. M. Cote, Effects of tourism-related provisioning on the trophic signatures and movement patterns of an apex predator, the Caribbean reef shark. *Biol. Conserv.* **144**, 859–865 (2011). doi: 10.1016/j.biocon.2010.11.019
90. C. Lydersen *et al*., Salinity and temperature structure of a freezing Arctic fjord—monitored by white whales (*Delphinapterus leucas*). *Geophys. Res. Lett.* **29**, 2119 (2002). doi: 10.1029/2002GL015462
91. F. Roquet *et al*., Estimates of the Southern Ocean general circulation improved by animal-borne instruments. *Geophys. Res. Lett.* **40**, 6176–6180 (2013). doi: 10.1002/2013GL058304
92. J. P. Grist *et al*., Temperature signature of high latitude Atlantic boundary currents revealed by marine mammal-borne sensor and Argo data. *Geophys. Res. Lett.* **38**, L15601 (2011). doi: 10.1029/2011GL048204
93. M. Fedak, The impact of animal platforms on polar ocean observation. *Deep Sea Res. Part II* **88–89**, 7–13 (2013). doi: 10.1016/j.dsr2.2012.07.007
94. L. Padman *et al*., Oceanic controls on the mass balance of Wilkins Ice Shelf, Antarctica. *J. Geophys. Res.* **117**, C01010 (2012). doi: 10.1029/2011JC007301
95. A. D. Lowther, R. G. Harcourt, B. Page, S. D. Goldsworthy, Steady as he goes: At-sea movement of adult male Australian sea lions in a dynamic marine environment. *PLOS ONE* **8**, e74348 (2013). doi: 10.1371/journal.pone.0074348; pmid: 24086338
96. L. Stramma *et al*., Expansion of oxygen minimum zones may reduce available habitat for tropical pelagic fishes. *Nat. Clim. Change* **2**, 33–37 (2012). doi: 10.1038/nclimate1304
97. M. Beger *et al*., Conservation planning for connectivity across marine, freshwater, and terrestrial realms. *Biol. Conserv.* **143**, 565–575 (2010). doi: 10.1016/j.biocon.2009.11.006
98. S. J. Cooke *et al*., Ocean Tracking Network Canada: A network approach to addressing critical issues in fisheries and resource management with implications for ocean governance. *Fisheries* **36**, 583–592 (2011). doi: 10.1080/03632415.2011.633464
99. B. A. Block, D. P. Costa, G. W. Boehlert, R. E. Kochevar, Revealing pelagic habitat use: The tagging of Pacific pelagics program. *Oceanol. Acta* **25**, 255–266 (2002). doi: 10.1016/S0399-1784(02)01212-4
100. D. A. Benson *et al*., GenBank. *Nucleic Acids Res.* **41**, D36–D42 (2013). doi: 10.1093/nar/gks1195; pmid: 23193287
101. P. Halpin *et al*., OBIS-SEAMAP: Developing a biogeographic research data commons for the ecological studies of marine mammals, seabirds, and sea turtles. *Mar. Ecol. Prog. Ser.* **316**, 239–246 (2006). doi: 10.3354/meps316239

ACKNOWLEDGMENTS

Financial and logistical support for this work was provided to the Ocean Tracking Network's International Scientific Advisory Committee through funding from the Canada Foundation for Innovation and the Natural Sciences and Engineering Research Council of Canada. We thank J. Landry and T. Rounds for administrative assistance in assembling the telemetry databases.

SUPPLEMENTARY MATERIALS

www.sciencemag.org/content/348/6240/1255642/suppl/DC1
Movies S1 and S2

10.1126/science.1255642

REVIEW SUMMARY

ECOLOGY

Terrestrial animal tracking as an eye on life and planet

Roland Kays,* Margaret C. Crofoot, Walter Jetz, Martin Wikelski

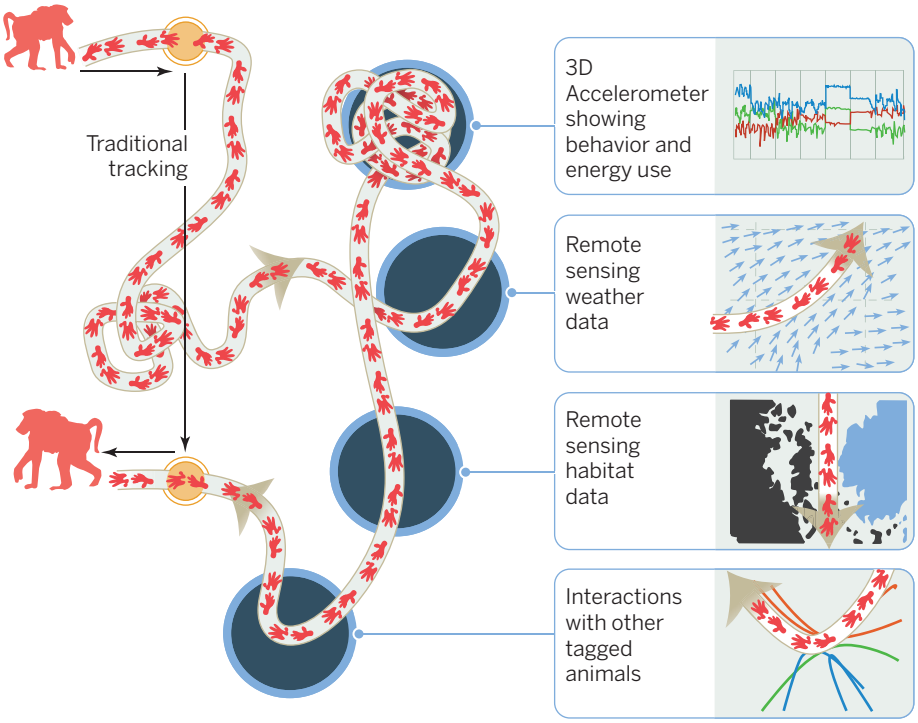
BACKGROUND: The movement of animals makes them fascinating but difficult study subjects. Animal movements underpin many biological phenomena, and understanding them is critical for applications in conservation, health, and food. Traditional approaches to animal tracking used field biologists wielding antennas to record a few dozen locations per animal, revealing only the most general patterns of animal space use. The advent of satellite tracking automated this process, but initially was limited to larger animals and increased the resolution of trajectories to only a few hundred locations per animal. The last few years have shown exponential improvement in tracking technology, leading to smaller tracking devices that can return millions of movement steps for ever-smaller animals. Finally, we have a tool that returns high-resolution data that reveal the detailed facets of animal movement and its many implications for biodiversity, animal ecology, behavior, and ecosystem function.

ADVANCES: Improved technology has brought animal tracking into the realm of big data, not only through high-resolution movement trajectories, but also through the addition of other on-animal sensors and the integration of remote sensing data about the environment through which these animals are moving. These new data are opening up a breadth of new scientific questions about ecology, evolution, and physiology and enable the use of animals as sensors of the environment. High–temporal resolution movement data also can document brief but important contacts between animals, creating new opportunities to study social networks, as well as interspecific interactions such as competition and predation. With solar panels keeping batteries charged, "lifetime" tracks can now be collected for some species, while broader approaches are aiming for species-wide sampling across multiple populations. Miniaturized tags also help reduce the impact of the devices on the study subjects, improving animal welfare and scientific results. As in other disciplines, the explosion of data volume and variety has created new challenges and opportunities for information management, integration, and analysis. In an exciting interdisciplinary push, biologists, statisticians, and computer scientists have begun to develop new tools that are already leading to new insights and scientific breakthroughs.

ON OUR WEB SITE

Read the full article at http://dx.doi.org/10.1126/science.aaa2478

OUTLOOK: We suggest that a golden age of animal tracking science has begun and that the upcoming years will be a time of unprecedented exciting discoveries. Technology continues to improve our ability to track animals, with the promise of smaller tags collecting more data, less invasively, on a greater variety of animals. The big-data tracking studies that are just now being pioneered will become commonplace. If analytical developments can keep pace, the field will be able to develop real-time predictive models that integrate habitat preferences, movement abilities, sensory capacities, and animal memories into movement forecasts. The unique perspective offered by big-data animal tracking enables a new view of animals as naturally evolved sensors of environment, which we think has the potential to help us monitor the planet in completely new ways. A massive multi-individual monitoring program would allow a quorum sensing of our planet, using a variety of species to tap into the diversity of senses that have evolved across animal groups, providing new insight on our world through the sixth sense of the global animal collective. We expect that the field will soon reach a transformational point where these studies do more than inform us about particular species of animals, but allow the animals to teach us about the world. ■



Big-data animal tracking. The red trajectory shows how studies can now track animals with unprecedented detail, allowing researchers to predict the causes and consequences of movements, and animals to become environmental sensors. Multisensor tracking tags monitor movement, behavior, physiology, and environmental context. Geo- and biosciences merge now using a multitude of remote-sensing data. Understanding how social and interspecific interactions affect movement is the next big frontier.

RELATED ITEMS IN *SCIENCE*

N. E. Hussey *et al.*, *Science* **348**, 1255642 (2015).

The list of author affiliations is available in the full article online.
*Corresponding author. E-mail: roland.kays@ncsu.edu
Cite this article as R. Kays *et al.*, *Science* **348**, aaa2478 (2015). DOI: 10.1126/science.aaa2478

Downloaded from www.sciencemag.org on June 14, 2015

REVIEW

ECOLOGY

Terrestrial animal tracking as an eye on life and planet

Roland Kays,[1,2,3*] Margaret C. Crofoot,[3,4,5] Walter Jetz,[6,7] Martin Wikelski[3,5,8]

Moving animals connect our world, spreading pollen, seeds, nutrients, and parasites as they go about the their daily lives. Recent integration of high-resolution Global Positioning System and other sensors into miniaturized tracking tags has dramatically improved our ability to describe animal movement. This has created opportunities and challenges that parallel big data transformations in other fields and has rapidly advanced animal ecology and physiology. New analytical approaches, combined with remotely sensed or modeled environmental information, have opened up a host of new questions on the causes of movement and its consequences for individuals, populations, and ecosystems. Simultaneous tracking of multiple animals is leading to new insights on species interactions and, scaled up, may enable distributed monitoring of both animals and our changing environment.

Movement is a defining characteristic of animals. Animals move to find critical resources such as food and mates and to avoid risk factors such as predators, and their movements are shaped by both evolutionary and ecological processes (*1*). Movement rates and patterns determine abundance and diversity at a given point in time and space, as animals enter and leave a location with speeds that range from as slow as a slug to as fast as a peregrine falcon. Moving animals disperse pollen, seeds, and diseases, and determine the spatiotemporal distribution of herbivory, predation, and many other vital ecological processes, which are valued at many hundreds of billions of dollars per year (*2*). Animal movement thus provides essential insights into patterns of biodiversity, ecological characteristics of individual species, and ecosystem function.

Despite its long history, the study of animal movement has generally fallen toward the margins of ecological research because the data gathered from wild individuals were too sparse to accurately describe these phenomena. Recent generations of tracking devices have removed these constraints, and it is now possible to record the movements of animals nearly continuously through the use of monitors equipped with Global Positioning System (GPS) devices (generally referred to as "tags"). This increased temporal resolution has led to important insights about how and why animals move and offers great potential for future discoveries. The addition of secondary sensors to tags complements the movement data with accelerometry, physiological, or environmental information, providing an integrated view of the animal and its environment.

New technology has brought the study of animal movement into the realm of big data (*3*), and exponential increases in data volumes are expected to continue in the coming decade. For example, a recent 1-month study of the individuals in a baboon troop collected 20 million GPS locations (at 1 Hz) and ~700 million accelerometry records (*4*). In some ways, increased temporal resolution of movement patterns is analogous to the genetic insight provided by DNA sequencers: Animal steps are our base pairs, movement segments are our genes, and combined tracks over an animal's lifetime are analogous to a full genome (*1*). Data describing the entire lifetime of movement by individual animals, and species-wide sampling from multiple populations, are now becoming available (Fig. 1). As in the case of genetics, this avalanche of new data provides the raw material for new insight, but challenges

[1]North Carolina Museum of Natural Sciences, Raleigh, NC, USA. [2]Department of Forestry and Environmental Resources, North Carolina State University, Raleigh, NC, USA. [3]Smithsonian Tropical Research Institute, Balboa, Republic of Panama. [4]Department of Anthropology, University of California, Davis, Davis, CA, USA. [5]Department of Migration and Immuno-Ecology, Max Planck Institute for Ornithology, Radolfzell, Germany. [6]Department of Ecology and Evolutionary Biology, Yale University, New Haven, CT 06520, USA. [7]Department of Life Sciences, Imperial College London, Silwood Park Campus, Ascot SL5 7PY, UK. [8]Department of Biology, University of Konstanz, Konstanz, Germany.
***Corresponding author. E-mail: roland.kays@ncsu.edu**

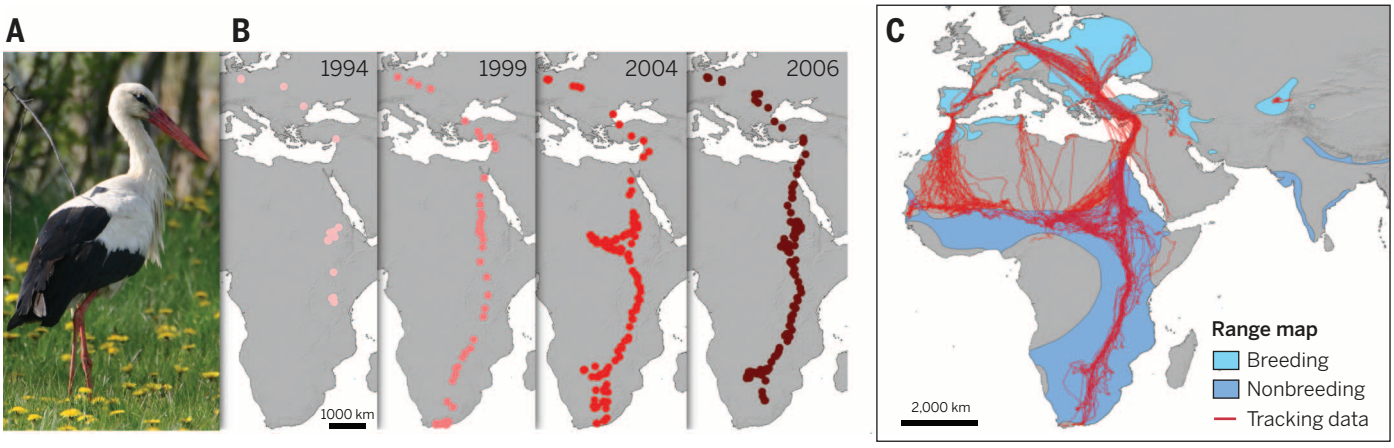


Fig. 1. Lifetime tracks. "Life-tracks" are made possible by solar-powered GPS tags with long life spans, or animals that can be located in real time and recaptured. These maps show detailed tracking data for one individual over its life. "Princess" the white stork (**A**) (*Ciconia ciconia*) was tagged with a GPS tracking device as a 3-year-old, nonreproductive juvenile in Germany in 1994 and was tracked until her death in 2006 (**B**). Four generations of Argos satellite tags were used to track her, and she had to be recaptured and retagged multiple times. Batteries on today's solar-powered tags last much longer. More recent tracking efforts now document the migratory behavior of 11 different populations of storks across their range (**C**), discovering, e.g., unexpected stationary populations in Uzbekistan and new migratory behaviors in Tunisian storks, which cross the Sahara multiple times per year. Because the GPS data collected by these tags can be accessed anywhere in the world, researchers can also document the cause of death for all juvenile storks, as long as they stay in the range of cell phone networks. [Data from (*114*)]

of data management and analysis must first be overcome.

The future of animal tracking will see smaller tags collecting more data, less invasively, on a greater variety of animals. In addition to GPS tags, these could include a series of interconnected sensors to understand internal physiological state and decision-making (*5*), similar to the body-area sensor networks currently being pioneered in human subjects (*6*). Finally, we expect select cases of massive multi-animal tracking to reveal the details of interactions among and within species and also offer distributed monitoring of our changing environment.

Tracking technology: Advances in GPS and sensor technology

Although scientists have been using electronic tags to track animal movement since the 1960s (*7*), data from these early studies were sparse because of the manual labor needed to find and record animal locations. The first automated tracking tags worked with the Argos satellite network but were expensive and relatively inaccurate (*8*). Since the U.S. Department of Defense stopped its policy of degrading the accuracy of civilian GPS receivers in 2000, however, the field of animal tracking has exploded. Large-scale consumer electronics demand has driven the development of smaller batteries and cheaper, more energy-efficient microprocessors, allowing GPS tracking to be an option for most medium- or large-sized vertebrates (Fig. 2). In the last few years, tracking technology has passed important thresholds in both size and temporal resolution of data collection (Fig. 3) and is revolutionizing our understanding of animal ecology.

Locating animals remains the primary objective of most animal tracking studies, although tracking tags now typically incorporate a variety of other sensors to help monitor the animal and its environment. Three-axis accelerometers built into tags can be used to continuously describe behavior and energy use over an animal's entire lifetime (*9*) by measuring fine-scale body movements. Implanted electronics can record heart rate, electroencephalographic (EEG) activity, internal temperature, and other physiological parameters (*10*, *11*). Animal-mounted cameras are also now small enough to be useful on terrestrial mammals and birds, adding new perspective and insight to the motivations of animal movement (*12*).

Data in real time

Real-time acquisition of data on the movement and behavior of tagged animals is fundamentally changing the ways that scientists, managers, and conservation groups use animal-tracking information. Recovering data from animal-borne sensors has been one of the enduring challenges of bio-logging: Until recently, study animals had to be recaptured to access the data stored in their tag's onboard memory. This led to high rates of data loss; for example, 11% of store-on-board GPS tags used in one set of mammal tracking studies were never recovered (*13*), and this statistic is presumably worse for migratory birds.



Fig. 2. Tagging animals with technology. Diverse species require diverse tracking technology and attachment methods, including harnesses, collars, and EEG monitors: (**A**) common cuckoo (*Cuculus canorus*), (**B**) northern tamandua (*Tamandua mexicana*), (**C**) fisher (*Pekania pennanti*), (**D**) great egret (*Ardea alba*), (**E**) three-toed sloth (*Bradypus variegatus*) with a collar and EEG monitor (**F**), lion (*Panthera leo*), (**G**) olive baboon (*Papio anubis*), (**H**) plains zebra (*Equus quagga*), and (**I**) Lyle's flying fox (*Pteropus lylei*).

Furthermore, data logging technology also meant that GPS-tracking studies have necessarily been retrospective.

By taking advantage of existing satellite or cellphone communication networks for remote data download, the current generation of tracking tags allow users to move beyond post hoc analyses of where animals moved and to respond immediately and interactively to changes in their behavior. This is akin to the value of historic weather records versus real-time weather radar data to mountaineers, pilots, or farmers. Wildlife managers, for example, are using GPS tags that send SMS alerts when tagged elephants cross into predefined areas to reduce human–wildlife conflict. These "virtual fences" warn people via text message when specific problem animals are nearby and can help managers and landowners reduce crop raids (*14*). Geofencing also allows automated changes directly to a tag's GPS data collection protocols to adjust sampling frequency at places or times of particular interest, such as initiation of dispersal or migration. Furthermore, live data allow field biologists to immediately backtrack an animal's path and collect additional data, including locating predator kill sites or following snow tracks to identify highway underpass use (*15*). Live data from tagged animals can also provide a powerful tool to engage public interest, involve citizen scientists, and obtain additional data from the field (e.g., Animal Tracker and Global Shark Tracker smartphone applications).

Shrinking tag size

One of the most important factors affecting the increasing utility of tracking tags in ecology has been their miniaturization, which has markedly expanded the range of species studied. Smaller tags can be used on a greater variety of species because biologists usually aim to have tags <5% of the body weight of the animal to minimize their effects on animal behavior and survival (*16*). GPS tags with remote data readout have dropped from 250 to 20 g in about a decade (1 g logging tags are also now available). At the same time, the temporal resolution of these tags has increased by approximately one order of magnitude every 5 years (Fig. 3). However, about 70% of bird species and 65% of mammal species still cannot be tracked while on the move (as opposed to being recaptured to retrieve data loggers), including hundreds of small migratory birds and bats of great conservation concern and ecological importance (*8*). Thus, the continued miniaturization of technology remains a priority for the field, both to increase the number of small species that can be safely tracked and to reduce the impact of tags on all species.

Most modern telemetry devices use the same electronic components as the mass-consumer market and thus have benefited from industry research aimed at decreasing size, increasing computing power, and improving battery technology (*8*). Research focused on consumer electronics is supplemented by groups developing technology specifically for animal tracking. For example, the ICARUS initiative is working to mount a new animal tracking antenna on the International Space Station that would allow smaller tags to send data back through the low-orbit satellite (*17*), and the Sensor Gnome Network is currently managing ~1600 very high frequency (VHF) tracking tags on one standard frequency, reporting the detection of tags at hundreds of locations across North America (*18*).

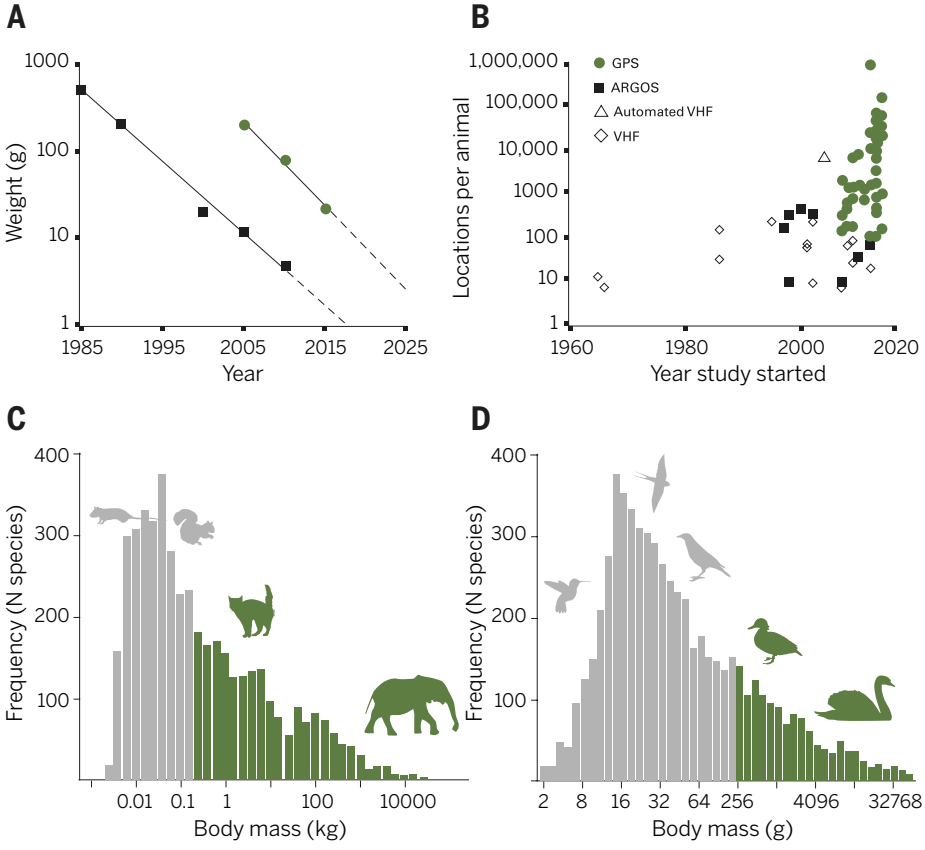


Fig. 3. Smaller and better tags. Rapid technological development has led to not only a decrease in the size of tags over time (**A**) but also a dramatic increase in the amount of data returned from each tagged animal (**B**). VHF tags are conventional "radio-tracking" technology where each animal location is typically collected manually via triangulation, although this process can be automated with base stations (*115*). Argos tags use Doppler shift to locate animals via satellite, which is less accurate than GPS but can presently be done with smaller tags. Data on tag size come from published studies, tag manufacturers websites, and our own data, whereas locations per animals come from 69 studies of birds and mammals (table S1) conducted or collaborated on by the authors. The continued decrease in tag size is essential for tracking the majority of small-mammal (**C**) and bird (**D**) species. Histograms show the body-mass distributions for all known birds and mammals [based on (*7*)], illustrating the proportion of species that can be tracked with GPS accuracy and global data readout with today's technology (15g) (green bars).

Ethics and practicalities of tagging animals

Since the first animal was fitted with an electronic tag, the scientific community has been engaged in an important discussion about ethical standards for this type of research (*19*). There is an inherent risk to each study animal whenever a tracking tag is attached, be it as a collar, harness, or implant. Reducing the negative impacts of these tags is a priority not only for ethical reasons, but also to ensure that the data collected accurately reflect the behavior of the species being studied. Extensive research has shown that the effects of tags on animals are generally undetectable, or low, although there are also examples of severe impacts of particular tag types on particular species (*16*). Animal tracking research is typically regulated by institutional committees (i.e., Institutional Animal Care and Use Committee in the United States) to maintain high standards of animal care, which help drive constant methodological refinements to reduce the risks to animal subjects. The continued miniaturization of tracking tags supports this goal, as adding weight to animals is of primary concern. However, continued refinement of attachment methods is also a priority (*20*).

The ethics of animal tracking is a cost/benefit analysis, and scientists need to consider how they can offset the inherent costs of capture and tagging by extending the benefits of their study. This includes designing studies that maximize the long-term utility of data and addressing issues of important global concern that help confront the conservation challenges these same animals

currently face. Finally, tracking data should be made easily available to policy-makers, conservation organizations, and other scientists via online data repositories such as Movebank, EuroDeer, or WRAM (*21*–*23*). These archives for animal movement data can greatly increase the scientific return on investment and promote animal welfare by reducing the need for new data collection.

Detailed data, diverse questions

Early ecology papers using VHF tracking typically addressed questions of animal home range size and habitat preference (*24*). High-resolution location data and sensor streams allow scientists to consider the ultimate behavioral and ecological mechanisms that underlie these movements, as well as the proximate internal and external factors that direct them (Fig. 4). There has also been a new push to identify the consequences of movement decisions, not only for individual animals, but also for the populations they connect and the ecosystems they move through.

Describing movement and its causes

As the spatial accuracy and temporal resolution of tracking data increase, we can obtain a more process-relevant picture of animal movement. These fine-grain data have opened up new research questions and also forced the development of new metrics and models to describe phenomena and test hypotheses. The advance of "big tracking data" has led to the ultimate vision of highly predictive models of animal movement. Such models are dearly needed by conservation managers working on habitat restoration programs, global change biologists, and intergovernmental agencies trying to predict the movements of problem animals such as desert locusts or queleas (*25*) or diseased animals such as ducks carrying avian influenza (*26*).

The large, continuous data streams from modern GPS tracking tags have revolutionized the study of animal space use, not only through the sheer size of data sets (*3*) but also by revealing an entirely new source of biological information about animal behavior that comes from connecting sequential movement steps. Repeat locations along a movement trajectory are inherently non-independent; traditional analytical approaches attempted to factor out this interdependence before describing an animal's space use (*27*). Modern approaches leverage new biological understanding from this autocorrelation by integrating space and time to test hypotheses about animal movement (*28*). Other approaches use high-resolution movement and accelerometer information to characterize behaviors, providing deeper insight and predictions into why animals visit different areas (*15*).

Deducing habitat preferences remains a priority for many tracking studies. Step-selection

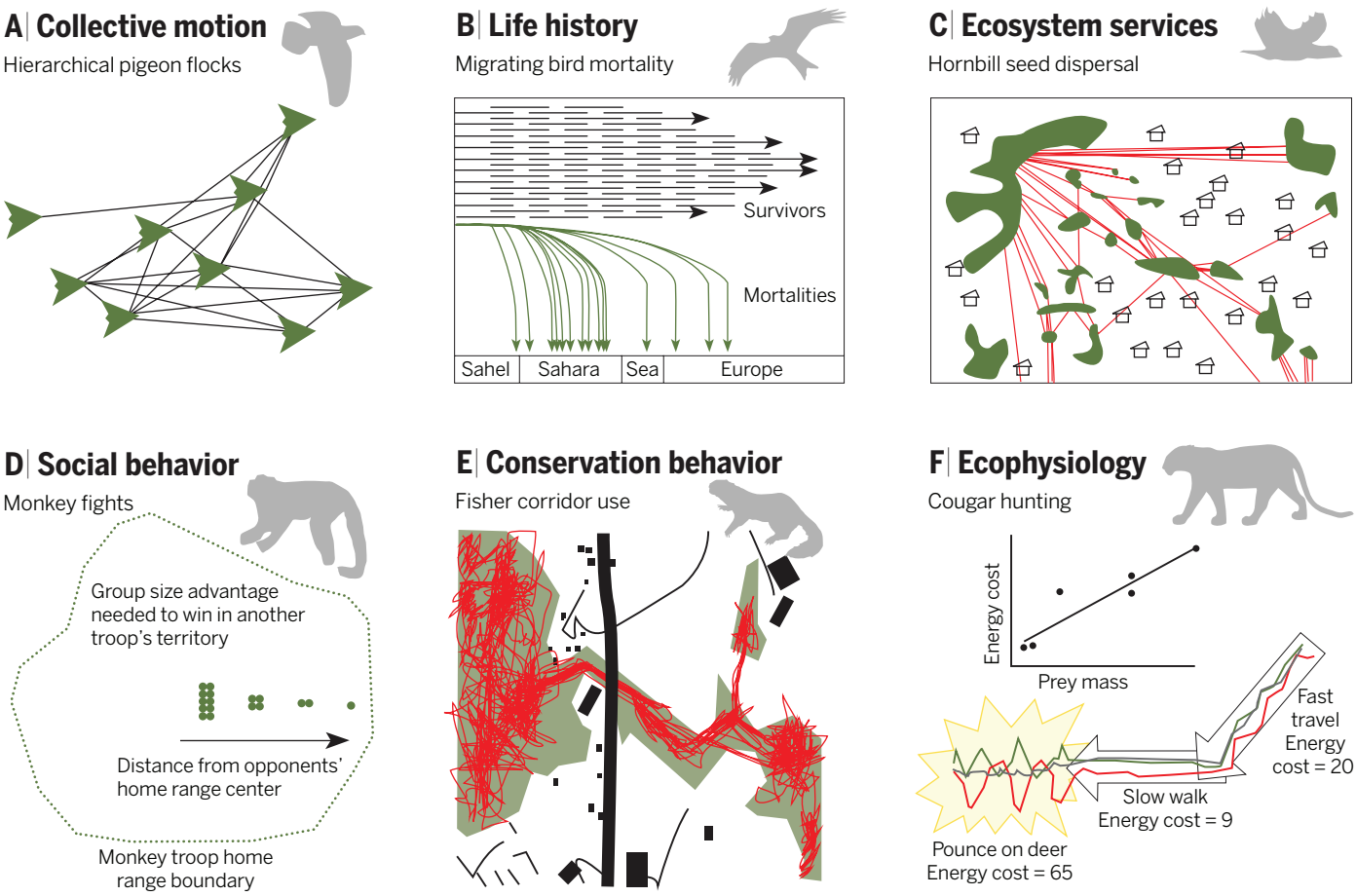


Fig. 4. Discoveries from tracking data. High-resolution animal tracking is leading to important discoveries in a variety of fields. (**A**) Studies of leadership in flocking pigeons documented a consistent hierarchy in following behavior, as representing by the gray lines (*100*). (**B**) Determining where migratory birds died showed that mortality rate was six times higher during migration than during the breeding or wintering grounds and that most of the 15 deaths (green lines) occurred in the Sahara desert (*46*). (**C**) Tracks of large hornbills in South Africa (red lines) showed that they move between scattered fragments of natural vegetation (green patches), moving seeds with them, and highlight the importance of networks of smaller forests acting as stepping stones to connect far-flung larger forests (*116*). (**D**) Simultaneous tracks of competing monkey groups allowed researchers to document the winners and losers of territorial contests and discover a substantial home-field advantage that allows smaller groups to fend off more numerous competing groups closer to the center of their range (*93*). (**E**) Fishers (red lines) moving through suburban Albany, New York, were found to repeatedly use movement corridors to connect smaller forest fragments (green area) into home ranges that were large enough to sustain their hunting needs (*15*). (**F**) Accelerometers combined with GPS tags allowed ecophysiologists to quantify the energy expended (arrows show direction of travel, and colored lines the animal's energy expenditure) by cougars attacking prey and show the cost of targeting large prey (inset graph) (*80*).

functions offer an improvement over traditional compositional analyses by contrasting used against available habitat at each movement step, rather than across an animal's range (*29*). Further development of these methods to integrate over multiple time scales would allow the evaluation of the importance of animal memory in movement decisions (*30*, *31*) and set the stage for major breakthroughs in our understanding of the connections between animal cognition and ecology. Furthermore, the integration of step-selection functions with process-based, mechanistic movement models promises to link the social and environmental context of animal movement decisions to resulting patterns of space use and provide a framework for predicting changes in animal space use following perturbations (*32*).

Another notable advantage of GPS tags with global communication functionality is their ability to track dispersal or exploratory movements of study animals beyond their typical home ranges, information that traditional VHF tracking is usually unable to provide. Continuous, automated tracking can detect extraterritorial prospecting movements in which individuals gather information before making decisions about mating, resource use, or long-distance movements (*33*). Continuous tracking also enables the precise description and study of juvenile dispersal, addressing questions of how young animals make decisions as they move through an environment that is completely foreign, and often hostile. Examples of amazing journeys of young animals that would have otherwise remained undocumented include a wolf that navigated through human-dominated landscapes from Italy to France (*32*) and a leopard that traversed three countries in southern Africa (*34*), demonstrating metapopulation linkages over large scales. If such megadispersals are regular features of a population or species, they can lead to evolutionary diversification, such as in *Buteo* hawks (*35*). Dispersing animals appear to have different habitat preferences than adults, although few studies have tracked enough dispersers to quantify this. Young elk disperse through higher-quality habitat than found in typical adult home ranges (*36*), while dispersing African lions used completely different, and much riskier, habitats than adults (*37*). These differences are critical for models attempting to identify and protect dispersal corridors between populations and should be a priority area for discovery in future GPS tracking studies. Additionally, this line of research could empirically derive the movement metrics needed to evaluate if species will be able to discover and disperse into newly suitable habitats that are rapidly changing with climate (*38*).

Large-scale migration studies are nearly impossible with VHF tags. Early pioneers collected data through a series of cross-country car chases behind tagged birds (*39*) or by flying slowly behind them in light aircraft (*40*). Early satellite tracking provided global coverage for the migration of larger species, but with low-accuracy (±500 m up to ±1000 km) fixes recorded only once every few days. Modern GPS tags with solar panels on migrating birds send location estimates recorded every second streaming live through the phone network (*8*). Maps of migratory flyways can now plot exact routes across continents and identify critical stopover points (*41*) (Fig. 1). Scientists are learning how birds make these amazing flights by integrating data from other sensors, including accelerometers, magnetometers, gyroscopes, pressure and temperature sensors, and even pitot tubes to measure air speed. We can now document birds' flight behavior as if they were airplanes carrying advanced aerospace technology. The results allow for mathematical descriptions of heretofore elusive behaviors such as the dynamic soaring of albatrosses (*42*).

One ultimate goal of the effort to describe animal movement and its causes is to create models that can predict movements from the internal and external conditions an animal faces. Building from the movement ecology framework (*1*), this approach would integrate not only the habitat preferences that have been the focus of most past research, but also parameters reflecting a species' movement abilities, sensory capacities, and memory. Finally, the importance of interactions among animals will need to be addressed, including the intra- and interspecific relationships that tracking studies are just starting to explore. These integrative models will facilitate the testing of mechanistic hypotheses for animal movement and predict how they will respond to our rapidly changing environment.

Consequences of movement for individuals, populations, and ecosystems

Although most traditional movement research has focused on describing patterns and deducing their causes, a new generation of questions are emerging to evaluate the consequences of movement across spatial scales.

Each animal's movements have immediate consequences for its own life and death, making movement a behavioral adaptation subject to evolutionary selection. Few tracking studies simultaneously monitor reproductive fitness and space use; instead, they typically presume that animals' habitat preferences reflect fitness values (*43*). This assumption may be problematic, as one study that did monitor both reproductive output and movement patterns found that the most intensely used habitats were not the best from the perspective of individual fitness, but lower-quality areas that provided a refuge for nonreproductive animals (*44*). Tracking studies have a long history of identifying factors related to animal survival and are the primary way to identify the time, location, and cause of death. A review of mortality in large and medium-sized North American mammals, including over 2000 animals tracked until their death, highlighted the importance of humans (i.e., hunters and cars), which accounted for 52% of mortalities, compared to 35% that fell prey to natural predators (*45*). Satellite technology allows us to monitor mortality of long-distance migrants, which has recently been shown to be much higher during migration (*46*). The cumulative effects of selective survival was noted by Sergio *et al.* (*47*), who showed a slow but steady improvement in migration performance with age, through a combination of differential survival and individual improvements.

When amplified across entire populations, animal movements determine the effect species have on ecosystems, because they determine the spatial distribution of ecological forces like herbivory and predation or because movement itself provides biotic connectivity and associated ecosystem services. Studies of large carnivores offer the best examples of using GPS tracking to map the ecological effects of a species and test their importance. Studies of both temperate and tropical systems have shown that prey avoid areas of high predator activity, especially ambush predators, but that selection of specific habitat features was more important (*48*). Moving animals can also provide ecosystem services by transporting other organisms, acting as vectors for diseases or dispersers for plant seeds and pollen. Because most seeds and pollen are too small to track directly, mechanistic models have been used to quantify seed dispersal, showing how animal movement drives gene flow for plants (*49*).

Given that most new global diseases are zoonotic (i.e., spread through the interaction of wildlife, livestock, and humans), there is extensive interest in understanding the movement of potential disease vectors (*50*). A detailed, mechanistic understanding of the spatiotemporal interactions of wild animals with domestic animals, as well as among each other, is of high global priority (*51*). Similarly, it is essential to recognize that diseased animals could have altered behavior and movement dynamics compared to healthy animals (*52*).

Finally, the movement of immigrant animals provides the genetic linkages necessary to maintain healthy populations, as well as colonizers necessary for establishing new ones. How dispersing animals move through completely foreign landscapes is a key question that has generally been addressed by using tracking to characterize the overall movement and habitat preferences of species, which are then used to extrapolate likely dispersal routes. Although genetic relatedness among populations generally supports these habitat-based predictions (*53*), they would be more robust if they considered actual trajectories of juvenile dispersers, which can differ dramatically from those of adults (*36*, *37*). Integrative studies that quantify habitat use and track the journeys and fates of dispersers are the most compelling. One of the first examples of the metapopulation concept, for example, emerged from a tracking study showing that subpopulations of cougar were separated by expanses of non–cougar habitat, but linked by dispersers (*54*). GPS tracking has also documented the expansion of a species' range through dispersing animals [cougars (*55*)], the impacts of human policies on disperser survival [wolves (*56*)], and the importance of immigrants as genetic rescuers for inbred populations isolated by habitat fragmentation (*57*). We anticipate a surge of research in the next few years highlighting the critical role of dispersing animals for understanding a wide range of ecological phenomena.

New opportunities from integration with remote sensing

The increase in detail of animal movement brought about by improving GPS technology in the last decade has been matched, or even surpassed, by the rapid growth in remotely sensed or modeled products describing the world through which these animals move (Fig. 5). Animal behavior and ecology are intricately linked to environmental conditions that are dynamic in space and time. The ability to more directly and rigorously link up predictors and response offers a powerful avenue for evaluating environmental connections in a hypothesis-testing or predictive framework (*1*, *32*). However, many technical, analytical, and conceptual challenges remain for the successful merging and simultaneous analysis of tracking and environmental data types (*58*).

Plotting animals' positions over a map to see what factors in the environment may affect their locations or movements has always been the first step of any animal tracking study. The individual-specific and continuous nature of high-resolution GPS animal trajectories, when combined with layers describing the environment, provides a unique lens for discovering how specific habitat elements or resources are used daily, seasonally, sequentially, at different life-history stages, and for specific behaviors and purposes (*59*). Using largely categorical habitat characterizations, research to date has helped identify critical habitat patches (*60*); study the impacts of fragmentation or barriers on movement patterns (*61*); model resource use (*62*), connectivity or wildlife corridors (*15*), and critical migratory stop-over or overwintering sites (*63*); or develop predictive models of suitable habitat for animal preservation or reintroduction (*64*). These applications have all been made possible by modeled information on climatic conditions [e.g., (*65*)] and through remote-sensing–based data layers on topography (SRTM: Shuttle Radar Topography Mission) and land cover (GlobCover, MODIS: Moderate Resolution Imaging Spectroradiometer, Landsat), which provide behaviorally and ecologically relevant information at scales from several kilometers down to 30 m.

Compared with spatial habitat information, weather has been integrated into fewer studies of animal movement. Some examples link local movements with information from nearby weather stations, notably so for single events such as migratory onset (*66*). More recently, new tools have allowed the intersections of longer movement paths with meteorological information, providing a continuous characterization of the conditions experienced by animals in three-dimensional space, even as they cross the globe. This has allowed us to estimate the energetic costs or physiological constraints on flight, given temperature or altitude-specific wind conditions (*67*), and identify behavioral strategies such as use of thermal or orographic uplift in flight (*68*). As the availability of temporally well-resolved meteorological layers increases, providing 12- to 3-hourly information at global extent [although still with spatially coarse resolution (*69*)], we expect integration of weather data into movement models to become standard methodology for determining proximate behavioral cues (*69*).

Although challenges for the spatial accuracy of GPS-based animal locations (typically <10 m) remain, especially in closed habitat, these data capture the distribution and environmental niche for a species with accuracy unrivaled by other data types, and are less subject to sampling biases (*70*). At a regional scale, remote-sensing products such as ASTER (Advanced Spaceborne Thermal Emission and Reflection Radiometer) and SPOT (Satellite Pour l'Observation de la Terre) have the potential to match this resolution with information on habitat condition and resources (*71*), and where available, LIDAR (Light Detection and Ranging) and hyperspectral remote-sensing data (*72*) allow us to extend our information to include vegetation structure. Other satellite or aerial survey data, such as those integrated into Google Earth (Quickbird, SPOT, WorldView, IKONOS, RapidEye), offer additional snapshots of meter-level habitat details but usually lack the spectral resolution needed for detailed habitat characterizations and tend to be restricted to small spatio-temporal footprints. A particularly exciting prospect is the increasingly detailed and complete environmental annotation of movement paths. MODIS sensors have the potential to provide global information on greenness and other land-surface attributes down to 8-day or even daily frequency, and researchers have begun to successfully use these to relate movement to resource availability (*73*). Remote-sensing–supported predictions of climate conditions in daily and 1-km resolution (*74*) hold the promise to extend such annotations to ecologically even more meaningful variables.

Given the growth in amount and detail of tracking and remote-sensing data, combined with advances in analysis methods and tools supporting species distribution modeling (*75*) and addressing data nonindependence in habitat analysis (*76*, *77*), we expect to see a future with more integrative modeling of animal location and behavior in multidimensional climate and environment space. The data management challenges for intersecting such fine-grained levels of animal and environmental information are substantial. Fortunately, Web-based infrastructures such as Movebank (*23*, *78*) or Map of Life (*79*) have automated many of the steps needed to access and integrate these data types. Tracking data combined with environmental sensors are thus poised to offer an increasingly thorough, quantitative, and integrative understanding of the environmental underpinning of animal movement and behavior and their reliable prediction in space and time.

New opportunities from multi-individual and multispecies tracking

Multi-sensor tracking tags are not only changing what we know about where animals go, they are also transforming what we know about how animals interact. Rare, and often cryptic, contacts with con- and heterospecifics trigger some of the

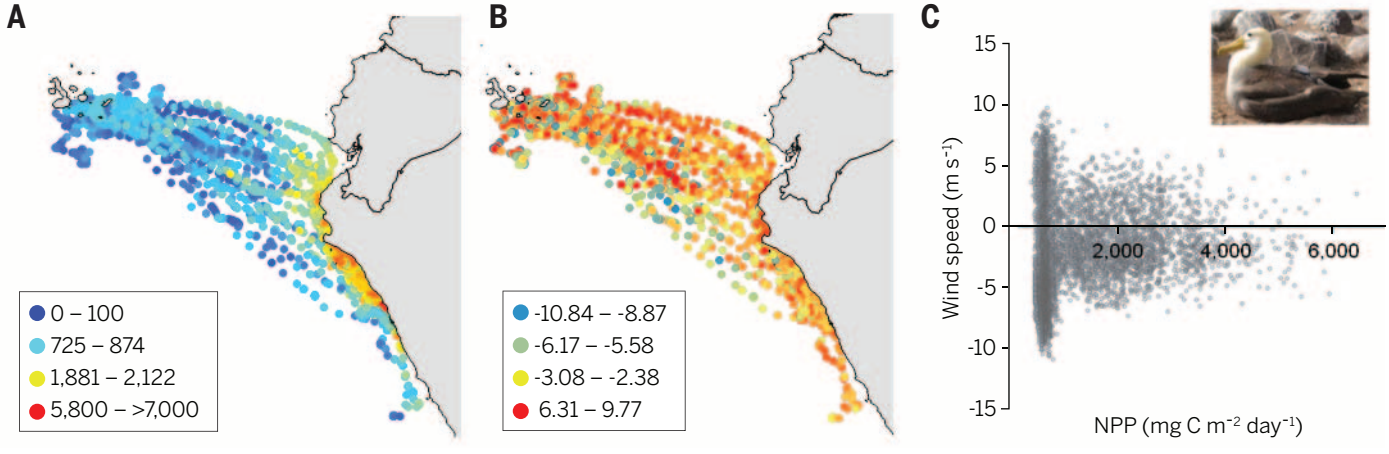


Fig. 5. Tracking animals in environment space. Spatial movements of nine Galapagos Albatross (*Phoebastria irrorata*) from June to September 2008 annotated with net primary productivity (NPP) (from 8-day MODIS ocean productivity) (**A**) and tail-wind data (**B**) (from the National Centers for Environmental Prediction Reanalysis 2 data). (**C**) The same locations in two-dimensional environment space. Birds seek out high-NPP, low-wind foraging areas near the coast, but cross high-wind regions in transit. For details, see (*78*) and movie S1.

most important events in animals' lives, but are often impossible to study with observational techniques. High-resolution, multi-individual GPS-tracking provides new opportunities to "see" such interactions and connect the behavior of individuals to emergent patterns of group, community, and population movement.

Predator-prey interactions are one area where high-resolution animal tracking is already making substantial contributions. A suite of recent studies using GPS in conjunction with accelerometers to track large felids has provided extremely detailed information about the dynamics of predation, documenting the energetics of sit-and-wait (*80*) and active-pursuit hunting strategies (*81*), detailing the locomotor performance of hunting cheetah (*82*), and describing how cheetah pursuit behavior changes depending on prey species (*83*). Simultaneous tracking of caribou, moose, and wolves in anthropogenically disturbed habitats has revealed that the network connectivity of resource patches affects both the spatial dynamics of large herbivores and the hunting strategies of their predators (*84*). Simultaneous tracking has also been used to assess the feeding costs of antipredator behavior (*85*). However, caution is needed when drawing conclusions from such studies, as mismatches between sampling protocols and biological phenomena of interest can complicate inference. For example, while a recent study of wolf–elk interactions concluded that encounters were rare and thus that wolves had little direct influence on elk behavior (*86*), a reanalysis suggested that the interactions were seriously underestimated because the interval between GPS fixes was long relative to the duration of interactions and because uncollared wolves in the population were not properly accounted for (*87*). This example highlights the importance of matching the scale of data collection with the behavior being studied and the value of very high temporal resolution tracking data for interaction studies.

Multi-individual tracking is also shedding light on how competitive dynamics organizes space use and resource access in animal communities. Attraction and avoidance can be inferred from concurrent movements of neighboring animals (*88*, *89*), providing important insight into the behavioral processes underlying the territorial dynamics of individuals (*90*, *91*) and groups (*88*, *92*). For example, simultaneous tracking has revealed that the outcome of competitive interactions between neighboring primate social groups depends more strongly on the location of the encounter than the relative size of the groups and has documented the costs of losing territorial interactions (*93*, *94*, *95*). Although mechanistic home range models provide a framework for investigating how indirect interactions among animals shape patterns of space use [i.e., scent marks (*96*); vocalizations (*97*)], it is less clear how to integrate direct, dynamic interactions such as fights and territorial displays (*98*), and this remains an area of active, and much-needed, research (*99*).

The ability to monitor the movements of many free-ranging animals with submeter accuracy and continuous resolution is also influencing the study of collective animal behavior, allowing data collection to move from the lab into the field. High-resolution tracking of entire pigeon flocks reveals that some individuals have more influence over collective movement decisions than others, leading to strong, consistent leadership hierarchies (*100*). "Rules of interaction" extracted from the correlation structure of the trajectories of pairs of homing individuals suggest that speed, rather than dominance, is the key factor underlying leadership (*101*, *102*). Whole-group GPS tracking is also providing insight into the self-organization of animal groups. Using a herding dog to provoke changes in the geometry of sheep groups, King and colleagues (*103*) show that the selfish-herd effect emerges because individual sheep respond to global, rather than local, cues of group structure when their perceived predation risk increases.

Species' behavioral and ecological characteristics, and how they may respond to environmental change, are affected by plasticity and adaptation set at the individual and population scale (*104*). Foraging behaviors and associated ecological niches have been shown to sometimes exhibit substantial individual differences, with far-reaching ecological and evolutionary consequences (*105*). Multi-individual tracking opens up new opportunities to quantify this individual variation in space use and associated niches for animals in the field and over larger scales than close-observation designs allow. However, collaboration is perhaps as important as improving technology to our understanding of plasticity in animal movement. By using metadata standards and sharing across studies, new questions can be addressed with better statistical power about changes in animal movement over larger temporal and spatial scales (*21*, *106*).

Animal tracking to monitor a changing planet

With global change causing ongoing and accelerating loss of biodiversity, a more mechanistic and detailed understanding of the space requirements and environmental associations of animals is pressing. Tracking data, especially when combined with remote sensing and detailed climate layers, has the potential to play a vital role, complementing biodiversity information gathered from museum or citizen science efforts (*70*). The high-resolution locations from tracking can contribute to essential biodiversity variables addressing species distributions (*107*) and support biodiversity monitoring and assessment as mandated under the Convention on Biological Diversity and the Intergovernmental Platform on Biodiversity and Ecosystem Services. The spatiotemporally detailed and real-time nature of GPS tracking data supports the use of tagged animals as passive sensors of the environment to document how ongoing changes are affecting species' distribution and ecological function. In particular, species with large movements may offer an opportunity to monitor specific biological impacts of ongoing environmental change—for example, if they are found to avoid previously used locations, habitat, or migratory stopover sites.

The roles of tracked animals as sensors of environmental change can extend to more active uses by which animals directly sense the environment. Recent examples include the monitoring of arctic temperatures and vegetation changes during climate change (*108*) and documenting ocean currents (*109*), and in the future may allow for the estimation of altitudinal wind profiles based on bird flight parameters. Tagged animals as sensors could be especially useful as environmental sensing agents in areas plagued by security or logistical difficulties, or for phenomena not directly detectable by remote sensing; for example, the accumulation of migratory European storks migrating in the African Sahel could indicate where desert locust swarms develop each year (Fig. 1). Similarly, animals may even be able to anticipate upcoming natural disasters and change their movements on the basis of this knowledge (*110*, *111*).

Achievements and future vision

Over the last 5 years, the field of animal tracking has climbed a steep trajectory of data and knowledge; we think that it is approaching a transformational point from us learning about animals, to having animals teach us about our world. The concept of animals as in situ sensors of our environment has only begun to be explored in the terrestrial realm, although it has a strong history in marine tracking (*112*). We suggest that a new approach that views animals as naturally evolved sensors of the environment has the potential to help us monitor the planet in completely new ways, especially if coordinated through a massive multi-individual monitoring program. Many of the components for this program are already in use for individual projects, including live data streams, community data standards and sharing frameworks, and tools for environmental data integration (*14*, *23*, *78*). Additional improvement in animal-mounted sensors, especially continuing miniaturization, is still needed to increase the variety of animals that can be tagged and the sensors they can carry, and to further minimize the impact of tags on animals' daily lives (*8*).

A massive multi-individual monitoring program would allow a quorum sensing of our planet (*113*), using a variety of species to tap into the diversity of senses that have evolved in different animal groups. Connecting these individual-level telemetry data with population-level monitoring could identify mechanisms driving population increases or declines, and identify the consequences to the environments in terms of ecosystem services. Ecological forecasting based on predictable animal movements could help us anticipate and mitigate environmental problems. However, documenting unpredictable movements might be just as important—showing how animals adapt to changing conditions in unpredictable ways offers a lens to the future of animal ecology in the Anthropocene.

REFERENCES AND NOTES

1. R. Nathan *et al.*, A movement ecology paradigm for unifying organismal movement research. *Proc. Natl. Acad. Sci. U.S.A.* **105**, 19052–19059 (2008). doi: 10.1073/pnas.0800375105; pmid: 19060196

2. C. Kremen *et al*., Pollination and other ecosystem services produced by mobile organisms: A conceptual framework for the effects of land-use change. *Ecol. Lett.* **10**, 299–314 (2007). pmid: 17355569
3. F. Urbano *et al*., Wildlife tracking data management: A new vision. *Philos. Trans. R. Soc. B Biol. Sci.* **365**, 2177–2185 (2010).
4. J. Li *et al*., Social information improves location prediction in the wild. *AAAI Workshop* (2015).
5. A. L. Vyssotski *et al*., EEG responses to visual landmarks in flying pigeons. *Curr. Biol.* **19**, 1159–1166 (2009). doi: 10.1016/j.cub.2009.05.070; pmid: 19559612
6. M. A. Hanson *et al*., Body area sensor networks: Challenges and opportunities. *Computer* **42**, 58–65 (2009). doi: 10.1109/MC.2009.5
7. R. D. Lord Jr., F. C. Bellrose, W. W. Cochran, Radiotelemetry of the respiration of a flying duck. *Science* **137**, 39–40 (1962). doi: 10.1126/science.137.3523.39; pmid: 17774128
8. E. Bridge *et al*., Technology on the move. *Bioscience* **61**, 689–698 (2011). doi: 10.1525/bio.2011.61.9.7
9. D. D. Brown, R. Kays, M. Wikelski, R. Wilson, A. P. Klimley, Observing the unwatchable through acceleration logging of animal behavior. *Anim. Biotelemetry* **1**, 20 (2013). doi: 10.1186/2050-3385-1-20
10. C. Signer *et al*., A versatile telemetry system for continuous measurement of heart rate, body temperature and locomotor activity in free-ranging ruminants. *Meth. Ecol. Evol.* **1**, 75–85 (2010). doi: 10.1111/j.2041-210X.2009.00010.x; pmid: 22428081
11. N. C. Rattenborg *et al*., Sleeping outside the box: Electroencephalographic measures of sleep in sloths inhabiting a rainforest. *Biol. Lett.* **4**, 402–405 (2008). doi: 10.1098/rsbl.2008.0203; pmid: 18482903
12. R. J. Moll, J. J. Millspaugh, J. Beringer, J. Sartwell, Z. He, A new 'view' of ecology and conservation through animal-borne video systems. *Trends Ecol. Evol.* **22**, 660–668 (2007). doi: 10.1016/j.tree.2007.09.007; pmid: 18006184
13. A. Matthews *et al*., The success of GPS collar deployments on mammals in Australia. *Aust. Mammal.* **35**, 65–83 (2013). doi: 10.1071/AM12021
14. J. Wall, G. Wittemyer, B. Klinkenberg, I. Douglas-Hamilton, Novel opportunities for wildlife conservation and research with real-time monitoring. *Ecol. Appl.* **24**, 593–601 (2014). doi: 10.1890/13-1971.1; pmid: 24988762
15. S. LaPoint, P. Gallery, M. Wikelski, R. Kays, Animal behavior, cost-based corridor models, and real corridors. *Landscape Ecol.* **28**, 1615–1630 (2013). doi: 10.1007/s10980-013-9910-0
16. D. L. Murray, M. R. Fuller, in *Research Techniques in Animal Ecology: Controversies and Consequences*, L. Boitani, T. K. Fuller, Eds. (Columbia Univ. Press, New York, 2000), pp. 15–64.
17. ICARUS Initiative, International Cooperation for Animal Eesearch Using Space, (available at http://icarusinitiative.org.
18. Sensor Gnome (2014), available at www.sensorgnome.org).
19. E. Benson, *Wired Wilderness: Technologies of Tracking and the Making of Modern Wildlife* (John Hopkins Univ. Press, Baltimore, MD, 2010).
20. S. P. Vandenabeele, R. P. Wilson, M. Wikelski, New tracking philosophy for birds. *Front. Ecol. Environ* **11**, 10–12 (2013). doi: 10.1890/13.WB.002
21. F. Cagnacci, F. Urbano, Managing wildlife: A spatial information system for GPS collars data. *Environ. Model. Softw.* **23**, 957–959 (2008). doi: 10.1016/j.envsoft.2008.01.003
22. H. Dettki, M. Brode, I. Clegg, T. Giles, J. Hallgren, Wireless Remote Animal Monitoring (WRAM)—A new international database e-infrastructure for management and sharing of telemetry sensor data from fish and. *Int. Congr. Env. Model. Softw.* **7** (2014).
23. M. Wikelski, R. Kays, Movebank: Archive, analysis and sharing of animal movement data. World Wide Web electronic publication.; www.movebank.org (2010).
24. J. J. Millspaugh *et al*., in *The Wildlife Techniques Manual: Volume 1: Research*, N. J. Silvy, Ed. (Johns Hopkins Univ. Press, Baltimore, MD, ed. 7, 2012), pp. 258–283.
25. R. A. Cheke, J. A. Tratalos, Migration, patchiness, and population processes illustrated by two migrant pests. *Bioscience* **57**, 145 (2007). doi: 10.1641/B570209
26. J. Y. Takekawa *et al*., Migration of waterfowl in the East Asian flyway and spatial relationship to HPAI H5N1 outbreaks. *Avian Dis.* **54** (suppl.), 466–476 (2010). doi: 10.1637/8914-043009-Reg.1; pmid: 20521681
27. S. R. De Solla, R. Bondurianski, R. J. Brooks, Eliminating autocorrelation reduces biological relevance of home range estimates. *J. Anim. Ecol.* **68**, 221–234 (1999). doi: 10.1046/j.1365-2656.1999.00279.x
28. S. Benhamou, L. Riotte-lambert, Beyond the utilization distribution : Identifying home range areas that are intensively exploited or repeatedly visited. *Ecol. Model.* **227**, 112–116 (2012). doi: 10.1016/j.ecolmodel.2011.12.015
29. H. Thurfjell, S. Ciuti, M. S. Boyce, Applications of step-selection functions in ecology and conservation. *Mov. Ecol.* **2**, 4 (2014). doi: 10.1186/2051-3933-2-4; pmid: 25520815
30. W. F. Fagan *et al*., Spatial memory and animal movement. *Ecol. Lett.* **16**, 1316–1329 (2013). doi: 10.1111/ele.12165; pmid: 23953128
31. T. Avgar, R. Deardon, J. M. Fryxell, An empirically parameterized individual based model of animal movement, perception, and memory. *Ecol. Model.* **251**, 158–172 (2013). doi: 10.1016/j.ecolmodel.2012.12.002
32. P. Ciucci, W. Reggioni, L. Maiorano, L. Boitani, Long-Distance dispersal of a rescued wolf from the Northern Apennines to the Western Alps. *J. Wildl. Manage.* **73**, 1300–1306 (2009). doi: 10.2193/2008-510
33. A. Ponchon *et al*., Tracking prospecting movements involved in breeding habitat selection: Insights, pitfalls and perspectives. *Methods Ecol. Evol.* **4**, 143–150 (2013). doi: 10.1111/j.2041-210x.2012.00259.x
34. J. Fattebert, T. Dickerson, G. Balme, R. Slotow, L. Hunter, Long-distance natal dispersal in leopard reveals potential for a three-country metapopulation. *S. Afr. J. Wildl. Res* **43**, 61–67 (2013). doi: 10.3957/056.043.0108
35. K. Bildstein, Raptor migrations in the Neotropics: Patterns, processes, and consequences. *Ornitol. Neotrop.* **15**, 83–99 (2004).
36. J. Killeen *et al*., Habitat selection during ungulate dispersal and exploratory movement at broad and fine scale with implications for conservation management. *Mov. Ecol.* **2**, 15 (2014). doi: 10.1186/s40462-014-0015-4
37. N. B. Elliot, S. A. Cushman, D. W. Macdonald, A. J. Loveridge, The devil is in the dispersers: Predictions of landscape connectivity change with demography. *J. Appl. Ecol.* **51**, 1169–1178 (2014). doi: 10.1111/1365-2664.12282
38. C. A. Schloss, T. A. Nuñez, J. J. Lawler, Dispersal will limit ability of mammals to track climate change in the Western Hemisphere. *Proc. Natl. Acad. Sci. U.S.A.* **109**, 8606–8611 (2012). doi: 10.1073/pnas.1116791109; pmid: 22586104
39. W. W. Cochran, C. G. Kjos, Wind drift and migration of thrushes: A telemetry study. *Ill. Nat. Hist. Surv. Bull.* **33**, 297–330 (1985).
40. M. Wikelski *et al*., Simple rules guide dragonfly migration. *Biol. Lett.* **2**, 325–329 (2006). doi: 10.1098/rsbl.2006.0487; pmid: 17148394
41. F. Qian *et al*., Migration routes and stopover sites of Black-necked Cranes determined by satellite tracking. *J. Field Ornithol.* **80**, 19–26 (2009). doi: 10.1111/j.1557-9263.2009.00201.x
42. G. Sachs, J. Traugott, A. P. Nesterova, F. Bonadonna, Experimental verification of dynamic soaring in albatrosses. *J. Exp. Biol.* **216**, 4222–4232 (2013). doi: 10.1242/jeb.085209; pmid: 24172888
43. J. M. Morales *et al*., Building the bridge between animal movement and population dynamics. *Philos. Trans. R. Soc. Lond. B Biol. Sci.* **365**, 2289–2301 (2010). doi: 10.1098/rstb.2010.0082; pmid: 20566505
44. A. Mosser, J. M. Fryxell, L. Eberly, C. Packer, Serengeti real estate: Density vs. fitness-based indicators of lion habitat quality. *Ecol. Lett.* **12**, 1050–1060 (2009). doi: 10.1111/j.1461-0248.2009.01359.x; pmid: 19708970
45. C. Collins, R. Kays, Causes of mortality in North American populations of large and medium-sized mammals. *Anim. Conserv.* **14**, 474–483 (2011). doi: 10.1111/j.1469-1795.2011.00458.x
46. R. H. G. Klaassen *et al*., When and where does mortality occur in migratory birds? Direct evidence from long-term satellite tracking of raptors. *J. Anim. Ecol.* **83**, 176–184 (2014). doi: 10.1111/1365-2656.12135; pmid: 24102110
47. F. Sergio *et al*., Individual improvements and selective mortality shape lifelong migratory performance. *Nature* **515**, 410–413 (2014). doi: 10.1038/nature13696; pmid: 25252973
48. M. Thaker *et al*., Minimizing predation risk in a landscape of multiple predators: Effects on the spatial distribution of African ungulates. *Ecology* **92**, 398–407 (2011). doi: 10.1890/10-0126.1; pmid: 21618919
49. M. C. Côrtes, M. Uriarte, Integrating frugivory and animal movement: A review of the evidence and implications for scaling seed dispersal. *Biol. Rev. Camb. Philos. Soc.* **88**, 255–272 (2013). doi: 10.1111/j.1469-185X.2012.00250.x; pmid: 23136896
50. S. H. Newman *et al*., Eco-virological approach for assessing the role of wild birds in the spread of avian influenza H5N1 along the Central Asian Flyway. *PLOS ONE* **7**, e30636 (2012). doi: 10.1371/journal.pone.0030636; pmid: 22347393
51. S. H. Newman, J. H. Epstein, L. M. Schloegel, The nature of emerging zoonotic diseases: Ecology, prediction, and prevention. *MLO Med. Lab. Obs.* **37**, 10–11, 14–16, 18–19, quiz 20–21 (2005). pmid: 16156542
52. J. A. van Gils *et al*., Hampered foraging and migratory performance in swans infected with low-pathogenic avian influenza A virus. *PLOS ONE* **2**, e184 (2007). doi: 10.1371/journal.pone.0000184; pmid: 17264886
53. A. B. A. Shafer *et al*., Habitat selection predicts genetic relatedness in an alpine ungulate. *Ecology* **93**, 1317–1329 (2012). doi: 10.1890/11-0815.1; pmid: 22834373
54. L. L. Sweanor, J. A. Logan, M. G. Hornocker, Cougar dispersal patterns, metapopulation dynamics, and conservation. *Conserv. Biol.* **14**, 798–808 (2000). doi: 10.1046/j.1523-1739.2000.99079.x
55. D. J. Thompson, J. A. Jenks, Dispersal movements of subadult cougars from the Black Hills: The notions of range expansion and recolonization. *Ecosphere* **1**, art8 (2010). doi: 10.1890/ES10-00028.1
56. I. Kojola *et al*., Dispersal in an expanding wolf population in Finland. *J. Mammal.* **87**, 281–286 (2006). doi: 10.1644/05-MAMM-A-061R2.1
57. S. P. D. Riley *et al*., Individual behaviors dominate the dynamics of an urban mountain lion population isolated by roads. *Curr. Biol.* **24**, 1989–1994 (2014). doi: 10.1016/j.cub.2014.07.029; pmid: 25131676
58. C. Kuenzer *et al*., Earth observation satellite sensors for biodiversity monitoring: Potentials and bottlenecks. *Int. J. Remote Sens.* **35**, 6599–6647 (2014). doi: 10.1080/01431161.2014.964349
59. J.-M. Gaillard *et al*., Habitat-performance relationships: Finding the right metric at a given spatial scale. *Philos. Trans. R. Soc. Lond. B Biol. Sci.* **365**, 2255–2265 (2010). doi: 10.1098/rstb.2010.0085; pmid: 20566502
60. J. Lenz *et al*., Seed-dispersal distributions by trumpeter hornbills in fragmented landscapes. *Proc. R. Soc. B Biol. Sci.* **278**, 2257–2264 (2010).
61. G. Kerth, M. Melber, Species-specific barrier effects of a motorway on the habitat use of two threatened forest-living bat species. *Biol. Conserv.* **142**, 270–279 (2009). doi: 10.1016/j.biocon.2008.10.022
62. J. D. Forester *et al*., State–space models link elk movement patterns to landscape characteristics in Yellowstone National Park. *Ecol. Monogr.* **77**, 285–299 (2007). doi: 10.1890/06-0534
63. C. Trierweiler *et al*., Migratory connectivity and population-specific migration routes in a long-distance migratory bird. *Proc. R. Soc. Lond. B Biol. Sci.* **281** (2014 doi: 10.1098/rspb.2013.2897
64. T. M. Donovan *et al*., Quantifying home range habitat requirements for bobcats (*Lynx rufus*) in Vermont, USA. *Biol. Conserv.* **144**, 2799–2809 (2011). doi: 10.1016/j.biocon.2011.06.026
65. M. New, M. Hulme, P. Jones, Representing twentieth-century space-time climate variability. Part II: Development of 1901-96 monthly grids of terrestrial surface climate. *J. Clim.* **13**, 2217–2238 (2000). doi: 10.1175/1520-0442(2000)013<2217:RTCSTC>2.0.CO;2
66. N. Sapir, M. Wikelski, R. Avissar, R. Nathan, Timing and flight mode of departure in migrating European bee-eaters in relation to multi-scale meteorological processes. *Behav. Ecol. Sociobiol.* **65**, 1353–1365 (2011). doi: 10.1007/s00265-011-1146-x
67. R. E. Gill *et al*., Extreme endurance flights by landbirds crossing the Pacific Ocean: Ecological corridor rather than barrier? *Proc. Biol. Sci.* **276**, 447–457 (2009). pmid: 18974033
68. G. Bohrer *et al*., Estimating updraft velocity components over large spatial scales: Contrasting migration strategies of golden eagles and turkey vultures. *Ecol. Lett.* **15**, 96–103 (2012). doi: 10.1111/j.1461-0248.2011.01713.x; pmid: 22077120
69. C. Kummerow, W. Barnes, T. Kozu, J. Shiue, J. Simpson, The Tropical Rainfall Measuring Mission (TRMM) sensor package. *J. Atmos. Ocean. Technol.* **15**, 809–817 (1998). doi: 10.1175/1520-0426(1998)015<0809:TTRMMT>2.0.CO;2
70. W. Jetz, J. M. McPherson, R. P. Guralnick, Integrating biodiversity distribution knowledge: Toward a global map of life. *Trends Ecol. Evol.* **27**, 151–159 (2012). doi: 10.1016/j.tree.2011.09.007; pmid: 22019413

71. M. R. Recio, R. Mathieu, M. C. Latham, A. D. M. Latham, P. J. Seddon, Quantifying fine-scale resource selection by introduced European hedgehogs (Erinaceus europaeus) in ecologically sensitive areas. *Biol. Invasions* **15**, 1807–1818 (2013). doi: 10.1007/s10530-013-0410-6
72. S. J. Goetz, M. Sun, S. Zolkos, A. Hansen, R. Dubayah, The relative importance of climate and vegetation properties on patterns of North American breeding bird species richness. *Environ. Res. Lett.* **9**, 034013 (2014). doi: 10.1088/1748-9326/9/3/034013
73. C. Trierweiler *et al*., A Palaearctic migratory raptor species tracks shifting prey availability within its wintering range in the Sahel. *J. Anim. Ecol.* **82**, 107–120 (2013). doi: 10.1111/j.1365-2656.2012.02036.x; pmid: 23137184
74. B. Parmentier *et al*., An assessment of methods and remote-sensing derived covariates for regional predictions of 1 km daily maximum air temperature. *Remote Sens.* **6**, 8639–8670 (2014). doi: 10.3390/rs6098639
75. C. Calenge, The package "adehabitat" for the R software: A tool for the analysis of space and habitat use by animals. *Ecol. Model.* **197**, 516–519 (2006). doi: 10.1016/j.ecolmodel.2006.03.017
76. J. Fieberg, J. Matthiopoulos, M. Hebblewhite, M. S. Boyce, J. L. Frair, Correlation and studies of habitat selection: Problem, red herring or opportunity? *Philos. Trans. R. Soc. Lond. B Biol. Sci.* **365**, 2233–2244 (2010). doi: 10.1098/rstb.2010.0079; pmid: 20566500
77. B. Kranstauber, R. Kays, S. D. Lapoint, M. Wikelski, K. Safi, A dynamic Brownian bridge movement model to estimate utilization distributions for heterogeneous animal movement. *J. Anim. Ecol.* **81**, 738–746 (2012). doi: 10.1111/j.1365-2656.2012.01955.x; pmid: 22348740
78. S. Dodge *et al*., The environmental-data automated track annotation (Env-DATA) system: Linking animal tracks with environmental data. *Mov. Ecol.* **1**, 3 (2013). doi: 10.1186/2051-3933-1-3; pmid: 25709817
79. Map of Life (2014), available at http://mol.org.
80. T. M. Williams *et al*., Instantaneous energetics of puma kills reveal advantage of felid sneak attacks. *Science* **346**, 81–85 (2014). doi: 10.1126/science.1254885; pmid: 25278610
81. D. M. Scantlebury *et al*., Flexible energetics of cheetah hunting strategies provide resistance against kleptoparasitism. *Science* **346**, 79–81 (2014). doi: 10.1126/science.1256424; pmid: 25278609
82. J. W. Wilson *et al*., Cheetahs, *Acinonyx jubatus*, balance turn capacity with pace when chasing prey. *Biol. Lett.* **9**, 20130620 (2013). doi: 10.1098/rsbl.2013.0620; pmid: 24004493
83. A. M. Wilson *et al*., Locomotion dynamics of hunting in wild cheetahs. *Nature* **498**, 185–189 (2013). doi: 10.1038/nature12295; pmid: 23765495
84. N. Courbin, D. Fortin, C. Dussault, R. Courtois, Logging-induced changes in habitat network connectivity shape behavioral interactions in the wolf-caribou-moose system. *Ecol. Monogr.* **84**, 265–285 (2014). doi: 10.1890/12-2118.1
85. F. Barnier *et al*., Diet quality in a wild grazer declines under the threat of an ambush predator. *Proc. Biol. Sci.* **281**, 20140446 (2014). doi: 10.1098/rspb.2014.0446; pmid: 24789903
86. A. D. Middleton *et al*., Linking anti-predator behaviour to prey demography reveals limited risk effects of an actively hunting large carnivore. *Ecol. Lett.* **16**, 1023–1030 (2013). doi: 10.1111/ele.12133; pmid: 23750905
87. S. Creel, J. A. Winnie Jr., D. Christianson, Underestimating the frequency, strength and cost of antipredator responses with data from GPS collars: An example with wolves and elk. *Ecol. Evol.* **3**, 5189–5200 (2013). doi: 10.1002/ece3.896; pmid: 24455148
88. Z. Li, T. Kin, H. Lei, R. Kays, M. C. Crofoot, Attraction and avoidance detection from movements. *Proc. 2014 Int. Conf. Very Large Data Bases*, 157–168 (2013).
89. J. A. Long, T. A. Nelson, S. L. Webb, K. L. Gee, J. A. Long, T. A. Nelson, S. L. Webb, K. L. Gee, A critical examination of indices of dynamic interaction for wildlife telemetry studies. *J. Anim. Ecol.* **83**, 1216–1233 (2014). doi: 10.1111/1365-2656.12198
90. S. Benhamou, M. Valeix, S. Chamaillé-Jammes, D. W. Macdonald, A. J. Loveridge, Movement-based analysis of interactions in African lions. *Anim. Behav.* **90**, 171–180 (2014). doi: 10.1016/j.anbehav.2014.01.030
91. M. Lührs, P. Kappeler, Simultaneous GPS tracking reveals male associations in a solitary carnivore. *Behav. Ecol. Sociobiol.* **67**, 1731–1743 (2013). doi: 10.1007/s00265-013-1581-y
92. L. Alba-Mejia, D. Caillaud, O. Montenegro, P. Sánchez-Palomino, M. Crofoot, Spatiotemporal interactions among three neighboring groups of free-ranging white-footed tamarins (Saguinus leucopus) in Colombia. *Int. J. Primatol.* **34**, 1281–1297 (2013). doi: 10.1007/s10764-013-9740-6
93. M. C. Crofoot, I. C. Gilby, M. C. Wikelski, R. W. Kays, The home field advantage:Interaction location outweighs the competitive advantage of numerical superiority in *Cebus capucinus* intergroup contests. *Proc. Natl. Acad. Sci. U.S.A.* **105**, 577–581 (2008). doi: 10.1073/pnas.0707749105; pmid: 18184811
94. A. C. Markham, S. C. Alberts, J. Altmann, Intergroup conflict: Ecological predictors of winning and consequences of defeat in a wild primate population. *Anim. Behav.* **84**, 399–403 (2012). doi: 10.1016/j.anbehav.2012.05.009; pmid: 22837555
95. M. C. Crofoot, The cost of defeat: Capuchin groups travel further, faster and later after losing conflicts with neighbors. *Am. J. Phys. Anthropol.* **152**, 79–85 (2013). doi: 10.1002/ajpa.22330; pmid: 23900797
96. P. R. Moorcroft, M. A. Lewis, Mechanistic home range analysis. *Monogr. Popul. Biol.* **43**, 208 (2006).
97. J. R. Potts, K. Mokross, M. A. Lewis, A unifying framework for quantifying the nature of animal interactions. *J. R. Soc. Interface* **11**, 20140333 (2014). doi: 10.1098/rsif.2014.0333; pmid: 24829284
98. J. R. Potts, M. A. Lewis, How do animal territories form and change? Lessons from 20 years of mechanistic modelling. *Proc. R. Soc. Lond. B Biol. Sci.* **281** (2014).
99. A. W. Bateman, M. A. Lewis, G. Gall, M. B. Manser, T. H. Clutton-Brock, Territoriality and home-range dynamics in meerkats, *Suricata suricatta* : A mechanistic modelling approach. *J. Anim. Ecol.* **84**, 260–271 (2015). doi: 10.1111/1365-2656.12267
100. M. Nagy, Z. Akos, D. Biro, T. Vicsek, Hierarchical group dynamics in pigeon flocks. *Nature* **464**, 890–893 (2010). doi: 10.1038/nature08891; pmid: 20376149
101. M. Nagy *et al*., Context-dependent hierarchies in pigeons. *Proc. Natl. Acad. Sci. U.S.A.* **110**, 13049–13054 (2013). doi: 10.1073/pnas.1305552110; pmid: 23878247
102. B. Pettit, A. Perna, D. Biro, D. J. T. Sumpter, Interaction rules underlying group decisions in homing pigeons. *J. R. Soc. Interface* **10**, 20130529 (2013). doi: 10.1098/rsif.2013.0529; pmid: 24068173
103. A. J. King *et al*., Selfish-herd behaviour of sheep under threat. *Curr. Biol.* **22**, R561–R562 (2012). doi: 10.1016/j.cub.2012.05.008; pmid: 22835787
104. W. Jetz, K. G. Ashton, F. A. La Sorte, Phenotypic population divergence in terrestrial vertebrates at macro scales. *Ecol. Lett.* **12**, 1137–1146 (2009). doi: 10.1111/j.1461-0248.2009.01369.x; pmid: 19708969
105. D. I. Bolnick *et al*., Why intraspecific trait variation matters in community ecology. *Trends Ecol. Evol.* **26**, 183–192 (2011). doi: 10.1016/j.tree.2011.01.009; pmid: 21367482
106. B. Kranstauber *et al*., The Movebank data model for animal tracking. *Environ. Model. Softw.* **26**, 834–835 (2011). doi: 10.1016/j.envsoft.2010.12.005
107. H. M. Pereira *et al*., Ecology. Essential biodiversity variables. *Science* **339**, 277–278 (2013). doi: 10.1126/science.1229931; pmid: 23329036
108. R. E. van Wijk *et al*., Individually tracked geese follow peaks of temperature acceleration during spring migration. *Oikos* **121**, 655–664 (2012). doi: 10.1111/j.1600-0706.2011.20083.x
109. J. Shamoun-Baranes, W. Bouten, C. Camphuysen, E. Baaij, Riding the tide: Intriguing observations of gulls resting at sea during breeding. *Ibis* **153**, 411–415 (2011). doi: 10.1111/j.1474-919X.2010.01096.x
110. R. A. Grant, T. Halliday, Predicting the unpredictable; evidence of pre-seismic anticipatory behaviour in the common toad. *J. Zool. (Lond.)* **281**, 263–271 (2010). doi: 10.1111/j.1469-7998.2010.00700.x
111. M. Wikelski, U. Mueller, W. A. Heidrich, F. X. Kuemmeth, Disaster alert mediation using nature. (2014) (available at Patent priority EP20120167197 20120508, WO2013167661).
112. N. E. Hussey *et al*., Aquatic animal telemetry across diverse scales: Discovery, applications and relevance. *Science* **348**, 1255642 (2015).
113. I. D. Couzin, Collective cognition in animal groups. *Trends Cogn. Sci.* **13**, 36–43 (2009). doi: 10.1016/j.tics.2008.10.002; pmid: 19058992
114. A. Flack *et al*., MPIO White stork lifetime tracking data. Movebank Data Repository (2015). doi: 10.5441/001/1.78152p3q
115. R. Kays *et al*., Tracking animal location and activity with an automated radio telemetry system in a tropical rainforest. *Comput. J.* **54**, 1931–1948 (2011).
116. T. Mueller, J. Lenz, T. Caprano, W. Fiedler, K. Böhning-Gaese, Large frugivorous birds facilitate functional connectivity of fragmented landscapes. *J. Appl. Ecol.* **51**, 684–692 (2014). doi: 10.1111/1365-2664.12247

ACKNOWLEDGMENTS

B. Carlson, J. Hody, K. Mertes, and J. Perrine read a previous draft and offered constructive comments. S. Dodge helped with data for Fig. 5. Work on this study was supported by NASA Biodiversity Grant NNX11AP72G and NSF grants EF 1232442, DBI 0756920, DBI 0960550, DBI-1262600, BCS 1440755, DEB 1026764, DEB-1441737, and IOS 1250895. The range map for Fig. 1 was provided by BirdLife International and NatureServe and the photograph by M. Kaatz. M. Berger and R. Weinzierl made the animation. Photographs are courtesy of D. Brown, R. Henrik, C. Markham, M. McGaw, K. Thorup, and N. Weber.

SUPPLEMENTARY MATERIALS

www.sciencemag.org/content/348/6240/aaa2478/suppl/DC1
Table S1
Movie S1

10.1126/science.aaa2478

RESEARCH ARTICLE SUMMARY

TISSUE REGENERATION

Inhibition of the prostaglandin-degrading enzyme 15-PGDH potentiates tissue regeneration

Yongyou Zhang,* Amar Desai,* Sung Yeun Yang,* Ki Beom Bae,* Monika I. Antczak,* Stephen P. Fink,* Shruti Tiwari,* Joseph E. Willis, Noelle S. Williams, Dawn M. Dawson, David Wald, Wei-Dong Chen, Zhenghe Wang, Lakshmi Kasturi, Gretchen A. Larusch, Lucy He, Fabio Cominelli, Luca Di Martino, Zora Djuric, Ginger L. Milne, Mark Chance, Juan Sanabria, Chris Dealwis, Debra Mikkola, Jacinth Naidoo, Shuguang Wei, Hsin-Hsiung Tai,† Stanton L. Gerson,†‡ Joseph M. Ready,†‡ Bruce Posner,†‡ James K. V. Willson,†‡ Sanford D. Markowitz†‡

INTRODUCTION: Agents that promote tissue regeneration could be beneficial in a variety of clinical settings, such as stimulating recovery of the hematopoietic system after bone marrow transplantation. Prostaglandin PGE2, a lipid signaling molecule that supports expansion of several types of tissue stem cells, is a candidate therapeutic target for promoting tissue regeneration in vivo. To date, therapeutic interventions have largely focused on targeting two PGE2 biosynthetic enzymes, cyclooxygenase-1 and cyclooxygenase-2 (COX-1 and COX-2), with the aim of reducing PGE2 production. In this study, we take the converse approach: We examine the role of a prostaglandin-degrading enzyme, 15-hydroxyprostaglandin dehydrogenase (15-PGDH), as a negative regulator of tissue repair, and we explore whether inhibition of this enzyme can potentiate tissue regeneration in mouse models.

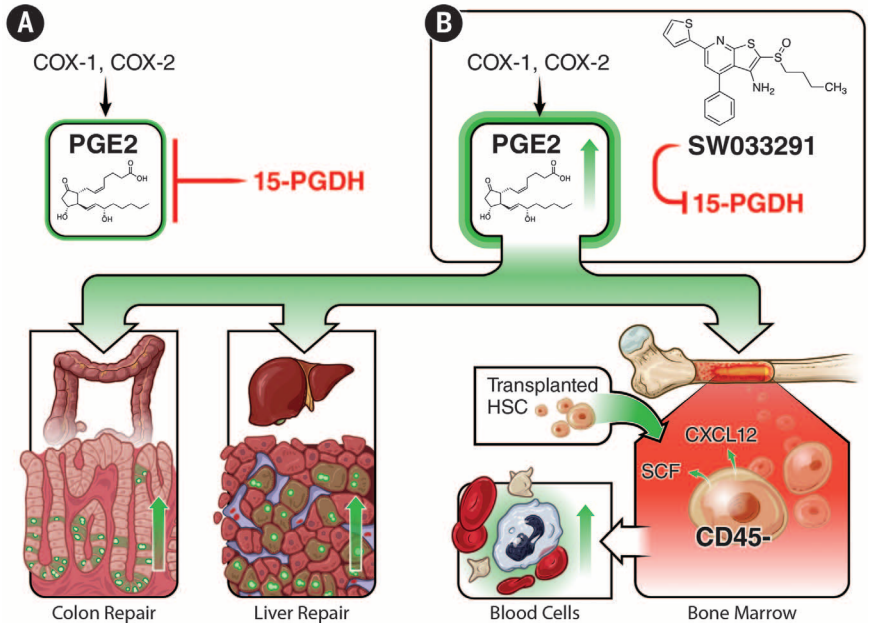
RATIONALE: We used 15-PGDH knockout mice to elucidate the role of 15-PGDH in regulating tissue levels of PGE2 and tissue repair capacity in multiple organs. We then developed SW033291, a potent small-molecule inhibitor of 15-PGDH with activity in vivo. We used SW033291 to investigate the therapeutic potential of 15-PGDH inhibitors in tissue regeneration and to identify a 15-PGDH–regulated hematopoietic pathway within the bone marrow niche.

RESULTS: We found that in comparison with wild-type mice, 15-PGDH–deficient mice display a twofold increase in PGE2 levels across multiple tissues—including bone marrow, colon, and liver—and that they show increased fitness of these tissues in response to damage. The mutant mice also show enhanced hematopoietic capacity, with increased neutrophils, increased bone marrow SKL (Sca-1$^+$ C-kit$^+$ Lin$^-$) cells (enriched for stem cells), and greater capacity to generate erythroid and myeloid colonies in cell culture. The 15-PGDH–deficient mice respond to colon injury from dextran sulfate sodium (DSS) with a twofold increase in cell proliferation in colon crypts, which confers resistance to DSS-induced colitis. The mutant mice also respond to partial hepatectomy with a greater than twofold increase in hepatocyte proliferation, which leads to accelerated and more extensive liver regeneration. SW033291, a potent small-molecule inhibitor of 15-PGDH (inhibitor dissociation constant K_i ~0.1 nM), recapitulates in mice the phenotypes of 15-PGDH gene knockout, inducing increased hematopoiesis, resistance to DSS colitis, and more rapid liver regeneration after partial hepatectomy. Moreover, SW033291-treated mice show a 6-day-faster reconstitution of hematopoiesis after bone marrow transplantation, with accelerated recovery of neutrophils, platelets, and erythrocytes, and greater recovery of bone marrow SKL cells. This effect is mediated by bone marrow CD45$^-$ cells, which respond to increased PGE2 with a fourfold increase in production of CXCL12 and SCF, two cytokines that play key roles in hematopoietic stem cell homing and maintenance.

CONCLUSIONS: Studying mouse models, we have shown that 15-PGDH negatively regulates tissue regeneration and repair in the bone marrow, colon, and liver. Of most direct utility, our observations identify 15-PGDH as a therapeutic target and provide a chemical formulation, SW033291, that is an active 15-PGDH inhibitor in vivo and that potentiates repair in multiple tissues. SW033291 or related compounds may merit clinical investigation as a strategy to accelerate recovery after bone marrow transplantation and other tissue injuries. ■

ON OUR WEB SITE

Read the full article at http://dx.doi.org/10.1126/science.aaa2340



Inhibiting 15-PGDH accelerates tissue repair. (**A**) The enzyme 15-PGDH degrades and negatively regulates PGE2. (**B**) SW033291 inhibits 15-PGDH, increases tissue levels of PGE2, and induces CXCL12 and SCF expression from CD45$^-$ bone marrow cells. This in turn accelerates homing of transplanted hematopoietic stem cells (HSC), generation of mature blood elements, and post-transplant recovery of normal blood counts. Inhibiting 15-PGDH similarly stimulates cell proliferation after injury to colon or liver, accelerating repair of these tissues.

The list of author affiliations is available in the full article online.
*These authors contributed equally to this work.
†These authors contributed equally to this work.
‡Corresponding authors. E-mail: sxm10@cwru.edu (S.D.M.); james.willson@utsouthwestern.edu (J.K.V.W.); slg5@cwru.edu (S.L.G.); joseph.ready@utsouthwestern.edu (J.M.R.); bruce.posner@utsouthwestern.edu (B.P.)
Cite this article as Y. Zhang *et al.*, *Science* **348**, aaa2340 (2015). DOI:10.1126/science.aaa2340

Downloaded from www.sciencemag.org on June 14, 2015

RESEARCH ARTICLE

TISSUE REGENERATION

Inhibition of the prostaglandin-degrading enzyme 15-PGDH potentiates tissue regeneration

Yongyou Zhang,[1]* Amar Desai,[1]* Sung Yeun Yang,[1,2]* Ki Beom Bae,[1,3]* Monika I. Antczak,[4]* Stephen P. Fink,[1]* Shruti Tiwari,[1,5]* Joseph E. Willis,[6,7,5] Noelle S. Williams,[4] Dawn M. Dawson,[6,7] David Wald,[6,7,5] Wei-Dong Chen,[1]† Zhenghe Wang,[6,8] Lakshmi Kasturi,[1] Gretchen A. Larusch,[1] Lucy He,[1]‡ Fabio Cominelli,[1,5] Luca Di Martino,[1] Zora Djuric,[9] Ginger L. Milne,[10] Mark Chance,[11] Juan Sanabria,[12,5] Chris Dealwis,[13] Debra Mikkola,[1] Jacinth Naidoo,[4] Shuguang Wei,[4] Hsin-Hsiung Tai,[14]§ Stanton L. Gerson,[1,6,5]§|| Joseph M. Ready,[4,15]§|| Bruce Posner,[4,15]§|| James K. V. Willson,[15]§|| Sanford D. Markowitz[1,6,5]§||

Agents that promote tissue regeneration could be beneficial in a variety of clinical settings, such as stimulating recovery of the hematopoietic system after bone marrow transplantation. Prostaglandin PGE2, a lipid signaling molecule that supports expansion of several types of tissue stem cells, is a candidate therapeutic target for promoting tissue regeneration in vivo. Here, we show that inhibition of 15-hydroxyprostaglandin dehydrogenase (15-PGDH), a prostaglandin-degrading enzyme, potentiates tissue regeneration in multiple organs in mice. In a chemical screen, we identify a small-molecule inhibitor of 15-PGDH (SW033291) that increases prostaglandin PGE2 levels in bone marrow and other tissues. SW033291 accelerates hematopoietic recovery in mice receiving a bone marrow transplant. The same compound also promotes tissue regeneration in mouse models of colon and liver injury. Tissues from 15-PGDH knockout mice demonstrate similar increased regenerative capacity. Thus, 15-PGDH inhibition may be a valuable therapeutic strategy for tissue regeneration in diverse clinical contexts.

Tissue regeneration is often required during recovery from injury, disease, and certain medical treatments. For example, hematopoietic stem cell (HSC) transplantation, which includes bone marrow transplantation, is a potentially curative therapy for many hematologic malignancies (*1*). However, after HSC transplantation, individuals are at high risk of potentially lethal infections while awaiting regeneration of peripheral blood neutrophils and are also at risk of internal bleeding while awaiting regeneration of platelets (*1*). Therapeutically enhancing hematopoietic tissue regeneration has proved to be challenging. Experimental approaches have principally focused on strategies that use ex vivo treatments to expand the numbers or increase the efficacy of donor hematopoietic stem cells before transplantation (*2*–*4*). In a different disease, ulcerative colitis, tissue damage to the colonic epithelium, in part from immune cells, causes both gastrointestinal bleeding and diarrhea (*5*). Current treatments for ulcerative colitis primarily involve immune suppression; thus far, there are no therapies that potentiate healing and regeneration of the damaged colonic epithelium (*5*). Tissue regeneration is also required after partial hepatic resection for liver cancer or liver metastases, because the patients must regain adequate hepatic function to survive (*6*–*8*).

Prostaglandin PGE2 is a candidate molecule for potentiating regeneration in multiple tissues. PGE2 is a lipid signaling molecule produced by the enzyme activity of cyclooxygenase-1 or cyclooxygenase-2 (COX-1 or COX-2) followed sequentially by that of prostaglandin E synthase (*9*). PGE2 augments Wnt signaling (*10*, *11*), a pathway that is involved in the maintenance of several types of tissue stem cells, including hematopoietic and colon stem cells (*11*, *12*). PGE2, and its more stable analog 16, 16-dimethyl-PGE2 (dmPGE2), expand hematopoietic stem cell numbers in mice and in zebrafish (*11*, *13*, *14*). Murine bone marrow cells and human cord blood stem cells that are treated ex vivo with dmPGE2 show enhanced engraftment when these cells are injected back into recipient mice (*4*, *14*–*17*). dmPGE2 treatment of human cord blood stem cells before their administration in human HSC transplants is currently being tested in clinical trials (*4*). PGE2 similarly supports the expansion of human colon stem cells in cell culture (*18*), and, in a model of murine colitis, colon injury was exacerbated by a COX enzyme antagonist but was ameliorated by treatment with dmPGE2 (*19*).

We hypothesized that alternative potential strategies for increasing PGE2-mediated tissue repair in vivo could be either to increase the synthesis of PGE2 or to inhibit the normally rapid in vivo degradation of PGE2. The enzyme 15-hydroxyprostaglandin dehydrogenase (15-PGDH), which acts in vivo as a negative regulator of prostaglandin levels and activity (*20*–*22*), provides a candidate target. Specifically, 15-PGDH catalyzes the first step in the degradation of prostanoid family molecules, oxidizing the prostanoid 15-hydroxyl group to a ketone and thereby abrogating binding to prostaglandin receptors (*20*). Here, we explore whether pharmacological inhibition of 15-PGDH can potentiate tissue repair in several mouse models of injury and disease.

Results

Genetic deletion or pharmacologic inhibition of 15-PGDH increases tissue PGE2 levels

To confirm that 15-PGDH broadly regulates PGE2 in vivo, we compared PGE2 levels in 15-PGDH knockout (*21*) and wild-type mice, retesting lung (*21*) and colon (*22*) and newly interrogating bone marrow and liver. Although basal PGE2 levels varied by a factor of 5 across these four tissues, the 15-PGDH knockout mice exhibited a consistent twofold increase in PGE2 levels (Fig. 1A). We hypothesized that a chemical inhibitor of 15-PGDH would have a similar effect and, further, would provide a tool to explore 15-PGDH as a therapeutic target for potentiating tissue regeneration.

As a first step in exploring the therapeutic potential of pharmacologically inhibiting 15-PGDH, we conducted a high-throughput screen to identify small-molecule modulators of 15-PGDH enzyme activity. We screened 230,000 synthetic compounds in the University of Texas Southwestern Medical Center chemical library using a cell-based assay designed to identify compounds

[1]Department of Medicine, Case Western Reserve University, Cleveland, OH 44106, USA. [2]Department of Gastroenterology, Haeundae Paik Hospital, Inje University, Busan 612896, South Korea. [3]Department of Surgery, Busan Paik Hospital, and Paik Institute of Clinical Research and Ocular Neovascular Research Center, Inje University, Busan, South Korea. [4]Department of Biochemistry, University of Texas Southwestern Medical Center, Dallas, TX 75390, USA. [5]Case Medical Center, University Hospitals of Cleveland, Cleveland, OH 44106, USA. [6]Case Comprehensive Cancer Center, Case Western Reserve University, Cleveland, OH 44106, USA. [7]Department of Pathology, Case Western Reserve University, Cleveland, OH 44106, USA. [8]Department of Genetics and Genome Sciences, Case Western Reserve University, Cleveland, OH 44106, USA. [9]Department of Family Medicine, University of Michigan, Ann Arbor MI 48109, USA. [10]Department of Pharmacology, Vanderbilt University, Nashville, TN 37232, USA. [11]Proteomics Center, Case Western Reserve University, Cleveland, OH 44106, USA. [12]Department of Surgery, Case Western Reserve University, Cleveland, OH 44106, USA. [13]Department of Pharmacology, Case Western Reserve University, Cleveland, OH 44106, USA. [14]College of Pharmacy, University of Kentucky, Lexington, KY 40536, USA. [15]Simmons Cancer Center, University of Texas Southwestern Medical Center, Dallas, TX 75390, USA.
*These authors contributed equally to this work. †Present name and address: (Wei-Dong) David Chen, Genetics Branch, National Cancer Institute, National Institutes of Health, Bethesda, MD 20892, USA. ‡Present address: Department of Neurological Surgery, Vanderbilt University Medical Center, Nashville, TN 37232, USA. §These authors contributed equally to this work.
||Corresponding author. E-mail: sxm10@cwru.edu (S.D.M.); james.willson@utsouthwestern.edu (J.K.V.W.); slg5@cwru.edu (S.L.G.); joseph.ready@utsouthwestern.edu (J.M.R.); bruce.posner@utsouthwestern.edu (B.P.)

that might bind to and/or alter the stability or amount of 15-PGDH. Positive hits were then further tested to identify functional enzyme inhibitors. This approach identified the small molecule SW033291 (molecular weight 412.59 daltons) as a potent inhibitor of 15-PGDH enzyme activity (Fig. 1G). Initial characterization showed that treating cells with SW033291 decreased cellular 15-PGDH enzyme activity by 85% (fig. S1A). In vitro incubations of this compound with recombinant 15-PGDH protein confirmed that SW033291 is a direct high-affinity inhibitor of 15-PGDH enzyme activity, with an inhibitor dissociation constant K_i^{app} = 0.1 nM (*23*). As expected, the IC_{50} (concentration to inhibit 50% of enzyme activity in vitro) of SW033291 closely approximated 50% of any 15-PGDH concentration tested (e.g., IC_{50} of 1.5 nM SW033291 against 6 nM 15-PGDH) (fig. S1, B to D). SW033291 inhibition of 15-PGDH was noncompetitive versus PGE2 over concentrations up to 40 μM PGE2 (fig. S1E). SW033291 also demonstrated selective high-affinity interaction with 15-PGDH in thermal denaturation assays. Specifically, SW033291 shifted the 15-PGDH melting temperature by 13.5°C (fig. S2) but had no impact on the melting temperature of two other closely related short-chain dehydrogenases (fig. S3). Treatment of A549 cells with SW033291 increased PGE2 levels by 3.5-fold at 500 nM, with 50% of maximal stimulation (EC_{50}) at ~75 nM (fig. S4).

Importantly, mice injected with SW033291 closely phenocopied 15-PGDH knockout mice, with 10 mg per kg of weight (mg/kg) SW033291 inducing a twofold increase in PGE2 levels in bone marrow, colon, lung, and liver (Fig. 1B and fig. S5). Prostaglandins PGD2 and PGF2a are also candidate substrates of 15-PGDH. Basal PGD2 levels were lower than PGE2 levels in all four mouse tissues examined and showed a lesser, although still significant, induction with SW033291 (fig. S6A). PGF2a tissue levels, which were lower still, were mostly unaltered by SW033291 (fig. S6B). We detected no toxicity from chemical inhibition of 15-PGDH in adult mice. Mice injected with SW033291 at 20 mg/kg daily for 7 days showed equivalent daily weights and activity as mice injected with vehicle-control and showed no adverse changes in blood counts or serum chemistry.

15-PGDH inhibition promotes hematopoietic recovery after bone marrow transplantation

The ability of PGE2 to promote hematopoiesis has been documented by two types of experiments: (i) ex vivo treatment of hematopoietic stem cells with dmPGE2 improves stem cell engraftment and consequent survival of mice, and (ii) administration of PGE2 or dmPGE2 to sublethally irradiated mice accelerates hematopoietic recovery and increases numbers of the short-term subtype of hematopoietic stem cells (*11*, *13*–*17*, *24*–*27*). Previous work also revealed that dmPGE2-treated cells have increased levels of cyclic adenosine monophosphate (AMP), increased expression of CXCR4 and survivin, decreased apoptosis, and increased homing to the bone marrow stem cell niche (*11*, *14*–*16*, *24*, *25*, *27*).

To evaluate whether 15-PGDH might regulate these responses, we examined 15-PGDH knockout mice and SW033291-treated wild-type mice. We observed a significant 43% increase in neutrophil counts in 15-PGDH knockout versus wild-type mice (Fig. 1C) and a significant 39% increase in bone marrow SKL (Sca-1$^+$ C-kit$^+$ Lin$^-$) cells

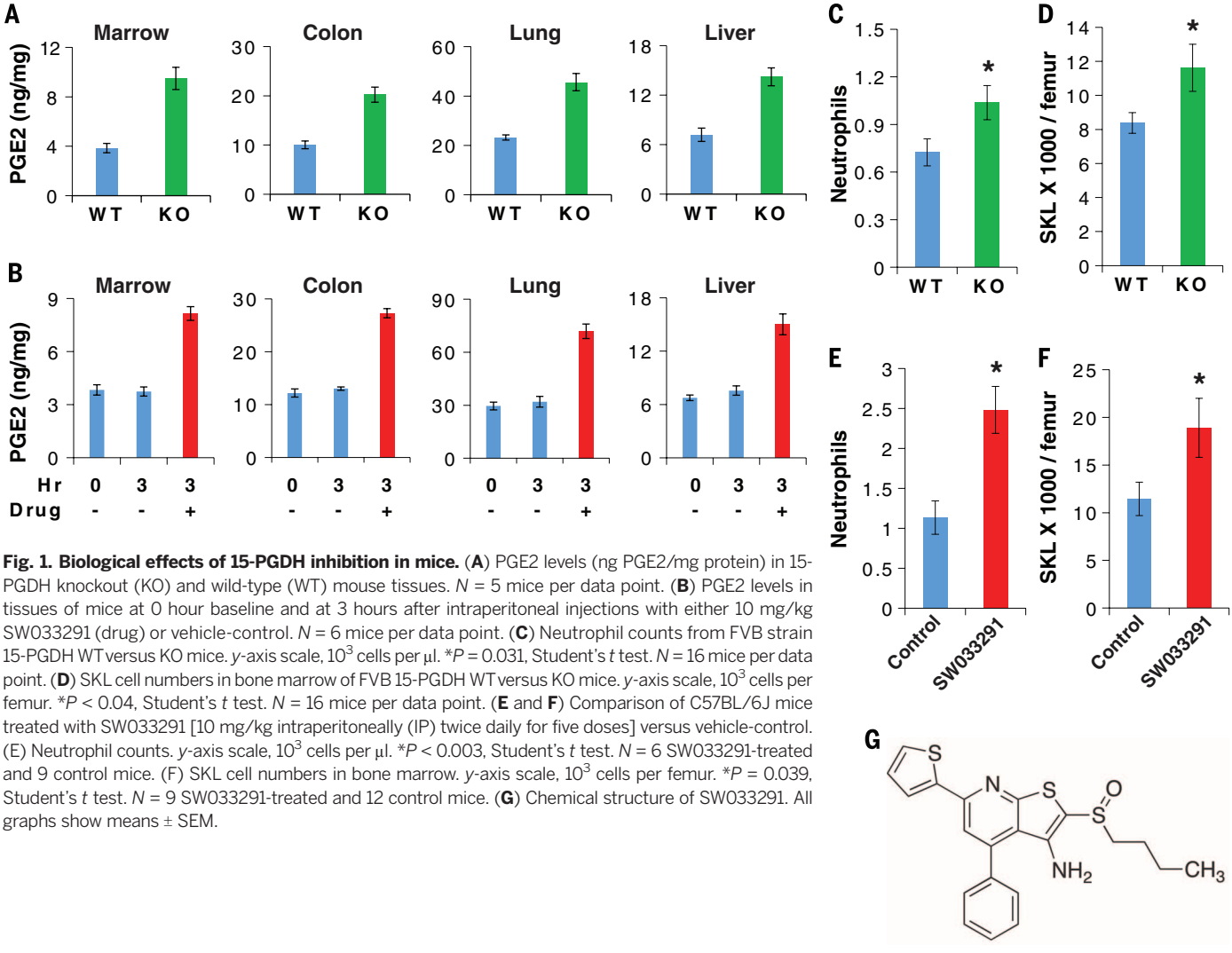


Fig. 1. Biological effects of 15-PGDH inhibition in mice. (**A**) PGE2 levels (ng PGE2/mg protein) in 15-PGDH knockout (KO) and wild-type (WT) mouse tissues. *N* = 5 mice per data point. (**B**) PGE2 levels in tissues of mice at 0 hour baseline and at 3 hours after intraperitoneal injections with either 10 mg/kg SW033291 (drug) or vehicle-control. *N* = 6 mice per data point. (**C**) Neutrophil counts from FVB strain 15-PGDH WT versus KO mice. *y*-axis scale, 10^3 cells per μl. **P* = 0.031, Student's *t* test. *N* = 16 mice per data point. (**D**) SKL cell numbers in bone marrow of FVB 15-PGDH WT versus KO mice. *y*-axis scale, 10^3 cells per femur. **P* < 0.04, Student's *t* test. *N* = 16 mice per data point. (**E** and **F**) Comparison of C57BL/6J mice treated with SW033291 [10 mg/kg intraperitoneally (IP) twice daily for five doses] versus vehicle-control. (E) Neutrophil counts. *y*-axis scale, 10^3 cells per μl. **P* < 0.003, Student's *t* test. *N* = 6 SW033291-treated and 9 control mice. (F) SKL cell numbers in bone marrow. *y*-axis scale, 10^3 cells per femur. **P* = 0.039, Student's *t* test. *N* = 9 SW033291-treated and 12 control mice. (**G**) Chemical structure of SW033291. All graphs show means ± SEM.

(Fig. 1D), which are enriched for bone marrow stem cells. There were no significant differences in counts of other peripheral blood cells, in bone marrow cellularity, or in numbers of bone marrow SLAM (Sca-1$^+$ C-kit$^+$ Lin$^-$ CD48$^-$ CD150$^+$) cells (that are further enriched for bone marrow stem cells) (figs. S7 and S8, A to C). Mice injected with SW033291 for three consecutive days showed similar significant benefits, including a doubling of peripheral neutrophil counts (Fig. 1E and fig. S9), a 65% increase in marrow SKL cells (Fig. 1F), and a 71% increase in marrow SLAM cells (fig. S10, A to C).

In functional assays, bone marrow from 15-PGDH knockout mice and from SW033291-treated mice both showed significant 55% increases in the numbers of hematopoietic colonies generated after plating into methylcellulose (Fig. 2, A and B). Erythroid (BFU-E)– and myeloid (CFU-GM)–type colonies were each significantly increased in assays of marrow from both 15-PGDH knockout mice (fig. S8, D and E) and SW033291-treated mice (fig. S10, D and E). Likewise, ex vivo treatment of harvested bone marrow cells with SW033291 induced a significant 50% increase in hematopoietic colony formation (Fig. 2C), indicating that the compound acts directly on these cells. SW033291 did not increase colony formation of bone marrow from 15-PGDH knockout mice, confirming that the compound acts by directly targeting 15-PGDH (Fig. 2C).

To determine the effects of SW033291 on gene expression, we sorted bone marrow from control and SW033291-treated mice into SKL marked and CD45$^-$ fractions. In CD45$^-$ cells, which are enriched for bone marrow stromal cells, SW033291 treatment induced a greater than fourfold increase in expression of CXCL12 and SCF (Fig. 2, D and E, and fig. S11A). These two cytokines in the hematopoietic niche play key roles in hematopoietic stem cell homing and maintenance (*28*). No changes were seen in expression of CXCR4 or survivin, and JAG1 expression was not detected in either treated or untreated fractions (fig. S11A). In SKL cells, SW033291 had no significant effects on expression of CXCL12, SCF, CXCR4, survivin, or JAG1 (fig. S11B). Induction of CXCL12 and SCF in CD45$^-$ cells was significantly blocked when SW033291 was coadministered to mice together with an antagonist of EP4- or EP2-type PGE2 receptors (Fig. 2, D and E). However, SW033291 fully induced CXCL12 and SCF when coadministered with antagonists of EP1 or EP3 receptors (fig. S11, C and D). As expected for activation of EP2 and EP4 receptors, SW033291 also increased cyclic AMP levels in CD45$^-$ cells (fig. S11E). We conclude that SW033291 increases PGE2 levels within bone marrow and that PGE2 functions through the EP2 and EP4 receptors to induce CXCL12 and SCF.

Having observed that SW033291 treatment increases the expression of cytokines from the hematopoietic niche, we next determined whether SW033291 would affect the ability of the mouse bone marrow to attract and support new hematopoietic stem cells. Accordingly, SW033291 or vehicle-control were administered to mice receiving a bone marrow transplant, and their respective

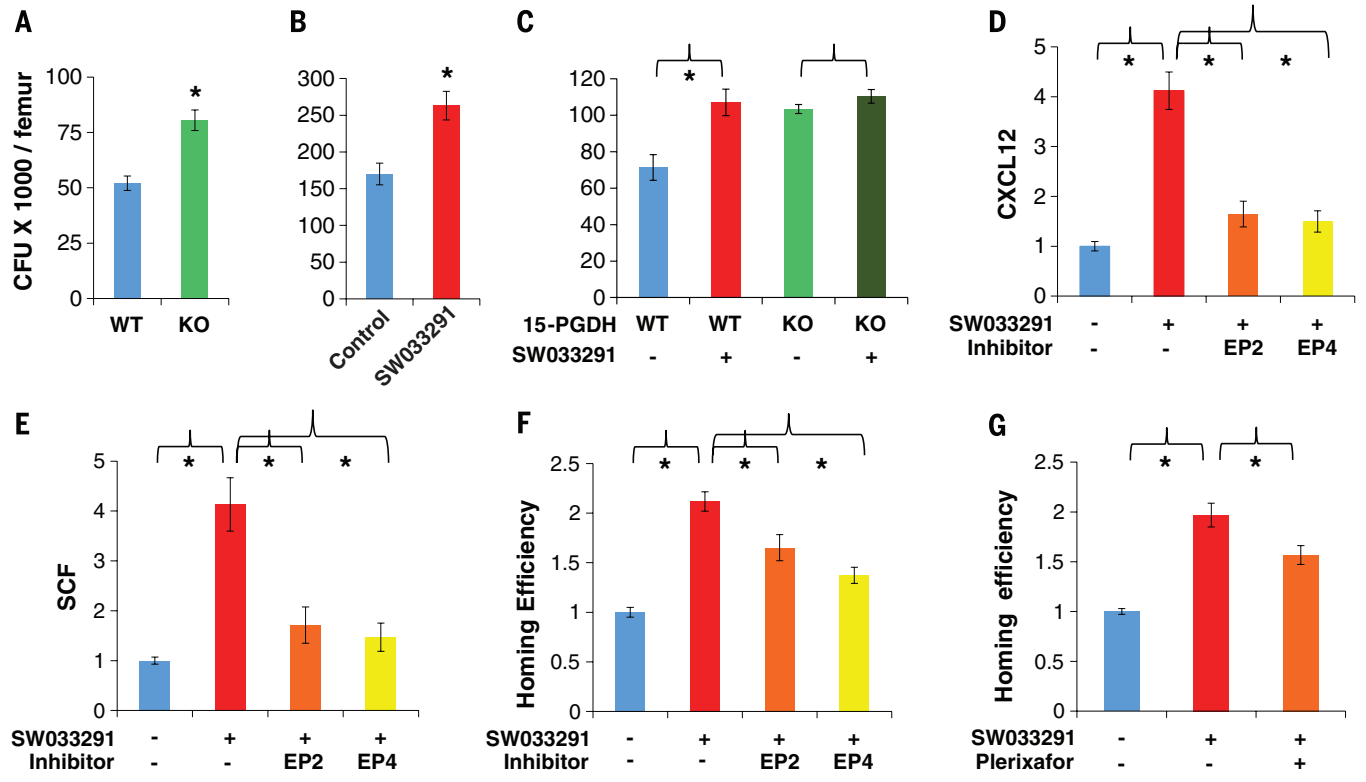


Fig. 2. Effect of 15-PGDH inhibition on bone marrow. (**A** to **C**) The *y* axis graphs comparison of hematopoietic colony-forming units (CFU) generated per femur on day 14 after plating mouse bone marrow cells into methylcellulose with cytokines. (A) Bone marrow from FVB 15-PGDH WT versus KO mice. $N = 4$ mice plated in duplicate per data point. *$P < 0.003$, Student's *t* test. (B) Bone marrow from SW033291-treated (10 mg/kg IP twice daily for 5 doses) versus vehicle-control–treated C57BL/6J mice. $N = 4$ mice plated in duplicate per data point. *$P < 0.009$, Student's *t* test. (C) Bone marrow from FVB WT or KO mice treated ex vivo with SW033291 (+) versus vehicle-control (−). $N = 3$ mice plated in duplicate per data point. *$P < 0.025$, Student's *t* test. (**D** and **E**) Gene induction in CD45$^-$ bone marrow cells from mice treated with SW033291 (+) or with vehicle-control (−) in combination with the EP2 antagonist PF-04418948 (EP2), the EP4 antagonist L-161,982 (EP4), or control diluent (−). $N = 4$ pools of 3 mice each per data point. *$P < 0.02$ compared with mice treated with SW033291 but without an EP receptor antagonist, Student's *t* test. (D) Relative CXCL12 expression. (E) Relative SCF expression. (**F** and **G**) Homing of carboxyfluorescein diacetate succinimidyl ester (CFSE)–labeled donor marrow cells to the bone marrow of irradiated mice, comparing SW033291-treated versus vehicle-control–treated recipient mice. The *y* axis graphs homing efficiency determined as the ratio at 16 hours of percentage of CFSE-labeled cells in the marrows of (SW033291-treated mice)/(vehicle-treated mice). $N = 9$ mice per data point. Graphs show comparison of recipient mice treated with SW033291 (+) or with vehicle-control (−) in combination with control diluent (−) or with the antagonists indicated. (F) EP2 antagonist PF-04418948 (EP2) or EP4 antagonist L-161,982 (EP4). *$P < 0.013$ versus mice receiving only SW033291, Student's *t* test. (G) CXCL12 antagonist Plerixafor. *$P < 0.019$ versus mice receiving only SW033291, Student's *t* test. All graphs show means ± SEM.

abilities to attract new donor marrow cells to the transplant recipient's bone marrow were compared. Transplant recipient mice treated with SW033291 showed a significant two- to threefold increase in the number of donor cells that homed to the recipient's bone marrow (Fig. 2, F and G, and fig. S12). This effect of SW033291 could be blocked by cotreating the transplant recipient mice with an inhibitor of PGE2 generation, an inhibitor of PGE2 signaling, or an antagonist of CXCL12 (that is induced by PGE2). Thus, the increased homing of donor bone marrow cells was significantly blocked when transplant recipient mice were cotreated with SW033291 plus the COX inhibitor indomethacin (fig. S12), the EP4 antagonist L-161,982 (Fig. 2F), or the CXCL12 antagonist Plerixafor (Fig. 2G). An EP2 antagonist produced a weaker, although still significant, block of SW033291 effect (Fig. 2F). The SW033291-induced homing of transplanted donor bone marrow cells is thus driven, at least in part, by the induction of CXCL12 expression in $CD45^-$ nonmyeloid cells that are already resident in bone marrow of recipient mice. Together these results define a pathway in which 15-PGDH inhibition causes an increase in bone marrow PGE2, which in turn induces expression of bone marrow CXCL12 and SCF, cytokines that alter the bone marrow microenvironment to better support the homing of transplanted cells.

To investigate whether 15-PGDH inhibition promotes hematopoietic recovery after a bone marrow transplant, we studied lethally irradiated mice that had been infused with 200,000 strain-matched donor bone marrow cells. Under these conditions, the transplanted cells on their own are insufficient to reconstitute hematopoiesis. We further treated these transplanted mice twice daily with intraperitoneal injections of either SW033291 (5 mg/kg) or vehicle-control, starting immediately after irradiation and continuing for 21 days. The control mice all died between study days 6 and 14 (Fig. 3A). In contrast, all of the SW033291-treated mice survived for more than 30 days (Fig. 3A).

To characterize the hematopoietic recovery induced by SW033291, we examined the compound's effect on mice that were transplanted with 500,000 bone marrow cells. Under these conditions, 63% of vehicle-control–injected mice and all of the SW033291-treated mice survived for 30 days and hence were available for examination. In this experiment, SW033291-treated mice showed significantly accelerated recovery of neutrophils, platelets, and red blood cells (Fig. 3, B to D). On day 12 after transplant, SW033291-treated mice had recovered 535 neutrophils/μl versus 182 neutrophils/μl in controls (Fig. 3B), differences that would likely be meaningful in a clinical setting. On day 18 after transplant, SW033291-treated mice reached 1380 neutrophils/μl versus 646 neutrophils/μl in controls (Fig. 3B). SW033291 thus accelerated neutrophil recovery in mice by nearly 6 days. SW033291-treated mice also showed a significantly accelerated platelet recovery and a significantly less severe platelet nadir (Fig. 3C). For example, on day 8 after transplant, SW033291-treated mice had 77,000 platelets versus 39,500 platelets in controls (Fig. 3C). Again, these differences would likely be meaningful in a clinical setting. SW033291-treated mice also showed accelerated red cell recovery (Fig. 3D). For example, hemoglobin levels on day 12 after transplant were 10.7 g/dL in SW033291-treated mice versus 8.0 g/dL in control mice (Fig. 3D). In humans, these differences would likely translate to lesser need for transfusion support. More rapid recovery of peripheral blood counts in SW033291-treated mice reflected an accelerated and more robust engraftment in the bone marrow, as evidenced by these mice having a 2.4-fold significant increase in SKL bone marrow cells on day 18 after transplant (Fig. 3E). SW033291 effectiveness in accelerating recovery of neutrophils, platelets, and red cells after bone marrow transplant is consistent with this compound increasing generation of both myeloid and erythroid colonies in cell culture assays.

Although systemic administration of PGE2 has been suggested to have potentially negative effects on myelopoiesis (*29*) and on long-term

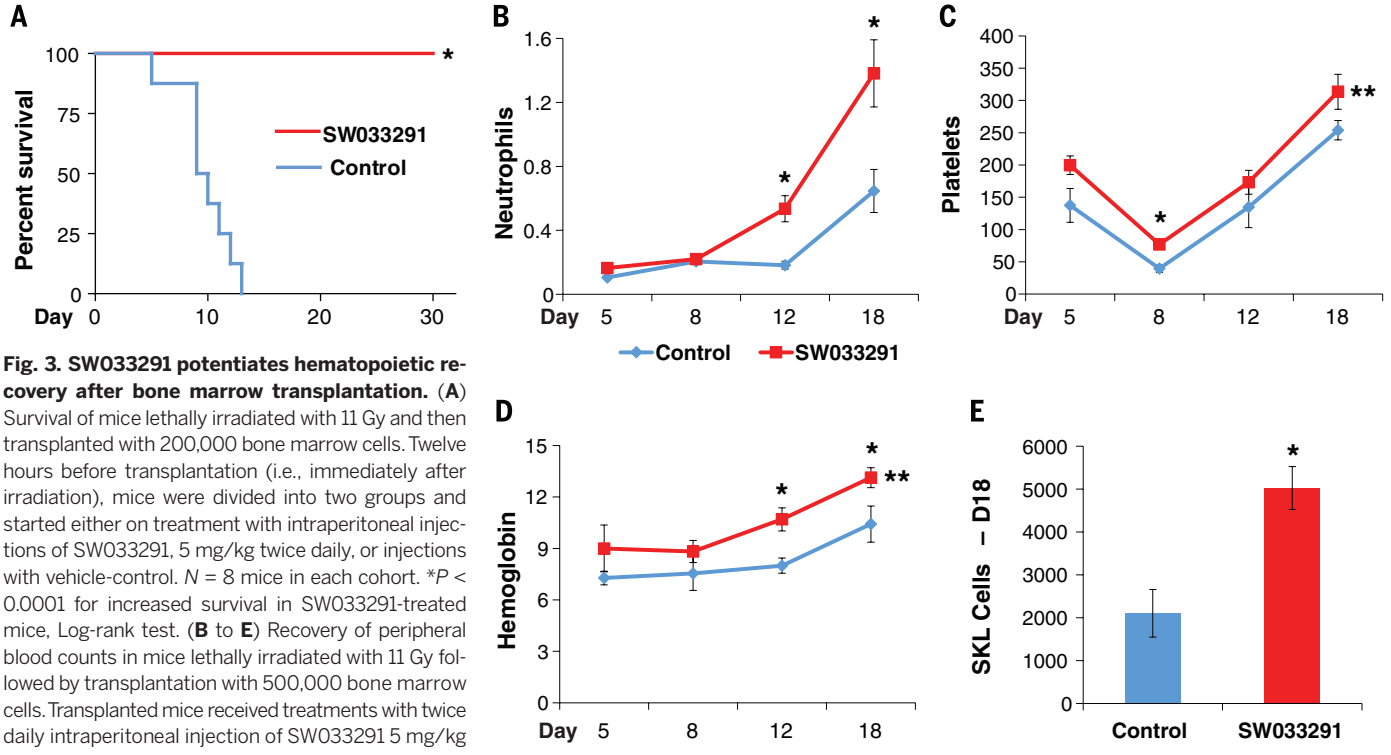


Fig. 3. SW033291 potentiates hematopoietic recovery after bone marrow transplantation. (**A**) Survival of mice lethally irradiated with 11 Gy and then transplanted with 200,000 bone marrow cells. Twelve hours before transplantation (i.e., immediately after irradiation), mice were divided into two groups and started either on treatment with intraperitoneal injections of SW033291, 5 mg/kg twice daily, or injections with vehicle-control. $N = 8$ mice in each cohort. *$P <$ 0.0001 for increased survival in SW033291-treated mice, Log-rank test. (**B** to **E**) Recovery of peripheral blood counts in mice lethally irradiated with 11 Gy followed by transplantation with 500,000 bone marrow cells. Transplanted mice received treatments with twice daily intraperitoneal injection of SW033291 5 mg/kg (SW033291) or vehicle-control (Control). Parallel transplanted cohorts were assayed on posttransplant day 5 (group 1, $N = 4$ control and 4 treated mice), day 8 (group 2, $N = 4$ control and 4 treated mice), and days 12 and 18 (group 3, $N = 8$ control and 10 treated mice, plus two deceased control mice). (B) Neutrophil counts. *y*-axis scale, 10^3 cells per μl. *$P < 0.014$ on days 12 and 18, Student's *t* test. On days 5 and 8, total white blood cell counts are substituted for neutrophil counts because values were too low for meaningful differential counts. (C) Platelet counts. *y*-axis scale, 10^3 cells per μl. *$P < 0.003$ on day 8, Student's *t* test. **$P = 0.005$ for comparison of platelet recovery across days 5 to 18, paired Student's *t* test. (D) Hemoglobin level. *y*-axis scale, g/dL. *$P \leq 0.03$ on days 12 and 18, Student's *t* test. **$P <$ 0.01 for comparison of hemoglobin recovery across days 5 to 18, paired Student's *t* test. (E) Number of SKL bone marrow cells per mouse on day 18 after transplant. Data are means from $N = 8$ control and 10 treated mice. *$P < 0.0013$, Student's *t* test. All graphs show means ± SEM.

hematopoietic stem cells (24), no such adverse effects were seen with SW033291. In particular, in a repeat experiment, 8 of 10 mice transplanted with 500,000 donor bone marrow cells and receiving SW033291 injections for 21 days were alive 7 months later. This was comparable to 7 of 10 mice that were alive after receiving a similar transplant plus injections with vehicle-control. In a second assay to test for any long-term adverse effects of SW033291 on bone marrow stem cells, we harvested bone marrow from transplant recipient mice and challenged its capacity to reconstitute hematopoiesis when retransplanted into a new cohort of irradiated recipient mice. Marrow originating from mice treated with SW033291 during a first transplant could in this manner be serially harvested and repassaged for three successive rounds of harvest, retransplantation, marrow regeneration, and then repeat challenge by reharvest and retransplantation (table S1). In this assay, the marrow harvested from mice receiving SW033291 during the original transplant also showed equal long-term robustness to the marrow harvested from mice injected with vehicle-control during the original transplant, each achieving an 80% success rate in reconstituting hematopoiesis at the third round of serial marrow transfer (table S1). We suggest that the beneficial activity of SW033291 reflects its optimization of the physiology of both dose and route of delivery of PGE2—i.e., that inhibiting 15-PGDH generates increased PGE2 at physiologic levels and directly at tissue sites and avoids the extremes of concentration accompanying administration by exogenous routes.

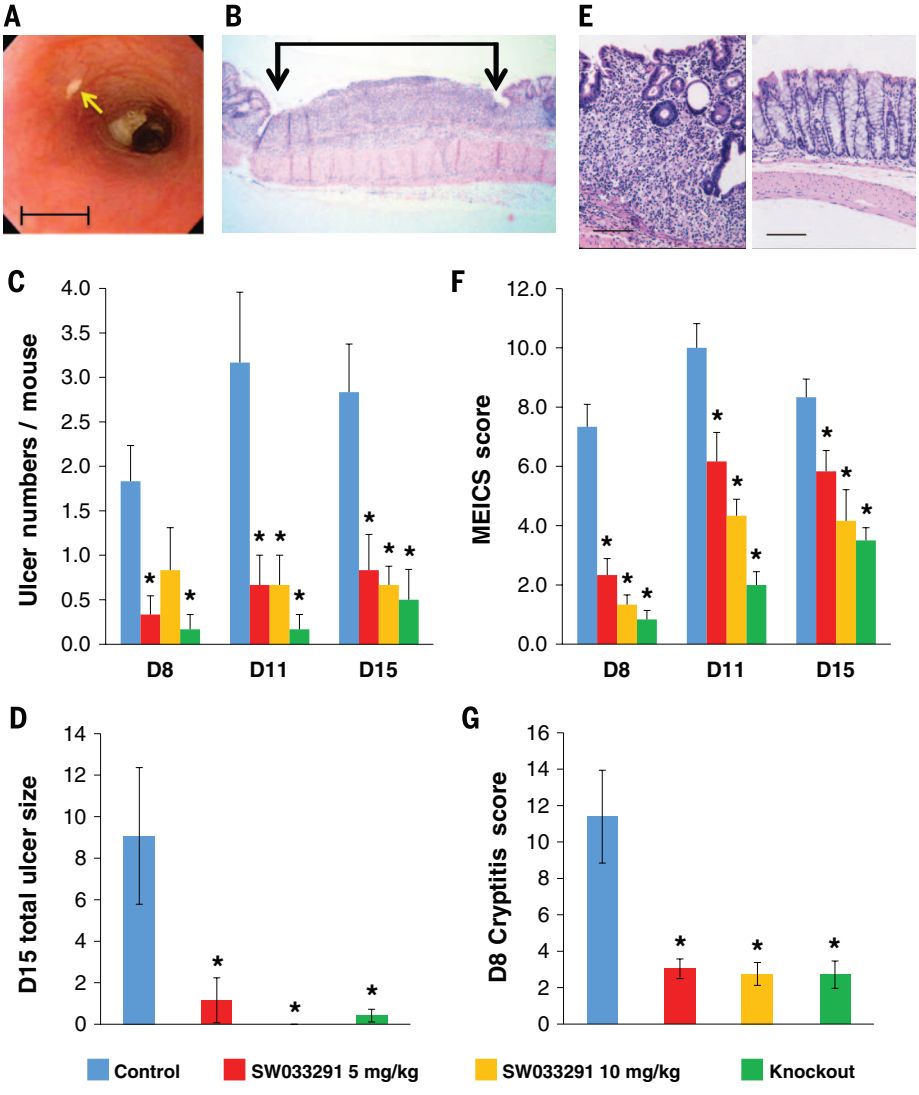


Fig. 4. Inhibition of 15-PGDH protects mice from DSS-induced colitis. (**A**) Colonoscopic view of a DSS-induced colon ulcer (arrow). Scale bar, 1 mm. (**B**) Microscopic image of a DSS-induced colon ulcer (between vertical arrows). Scale bar, 2.3 mm. (**C**, **D**, **F**, and **G**) Effects of administering 7 days (study days 1 through 7) of DSS compared between experimental groups of: vehicle-control–treated mice (blue), SW033291-treated mice (5 mg/kg IP twice daily) (red), SW033291-treated mice (10 mg/kg IP twice daily) (gold), and 15-PGDH knockout mice (green). (C) Graph of mean number of colon ulcers per DSS-treated mouse counted by colonoscopy on study days 8, 11, and 15 (D8, D11, and D15) for vehicle-control–treated mice, SW033291-treated mice (5 mg/kg IP twice daily), SW033291-treated mice (10 mg/kg IP twice daily), and 15-PGDH knockout mice. $N = 6$ mice for each data point. Analysis of variance (ANOVA) $P < 10^{-6}$. $^*P < 0.016$ in daily subgroup comparisons to vehicle-control–treated mice, Student's t test. (D) Graph depicts percentage of total colon length covered by ulcers on study day 15, determined by histomorphometric assessment [as in (B)] for DSS-treated mice in cohorts of: vehicle-control–treated mice ($N = 7$), SW033291-treated mice (5 mg/kg IP twice daily) ($N = 8$), SW033291-treated mice (10 mg/kg IP twice daily) ($N = 8$), and 15-PGDH knockout mice ($N = 9$). ANOVA $P < 0.003$. $^*P < 0.05$ versus vehicle-control-treated mice, Student's t test. (**E**) (Left) Representative photomicrograph of grade 2 cryptitis and mucosal thickening (on a 0 to 4 scale). (Right) Normal colon. Scale bars, 100 μm. (F) Graph of mean murine endoscopic index of colitis severity score (MEICS) in same mice as in (C). ANOVA $P < 10^{-6}$. $^*P < 0.024$ in daily comparisons to vehicle-control–treated mice, Student's t test. (G) Graph of mean total colon cryptitis score (0 to 16 scale) on study day 8 for DSS-treated mice in cohorts of vehicle-control–treated mice ($N = 7$), SW033291-treated mice (5 mg/kg IP twice daily) ($N = 8$), SW033291-treated mice (10 mg/kg IP twice daily) ($N = 8$), and 15-PGDH knockout mice ($N = 6$). ANOVA $P < 0.0005$. $^*P < 0.022$ versus vehicle-control–treated mice, Student's t test. All graphs show means ± SEM.

15-PGDH inhibition protects mice from colitis

To determine whether inhibiting 15-PGDH would promote regeneration in other tissues in which 15-PGDH inhibition increases PGE2, we examined the effects of 15-PGDH blockade in colons of mice treated for 7 days with oral dextran sodium sulfate (DSS), an agent that induces colonic ulcerations similar to those found in human ulcerative colitis (30) (Fig. 4, A and B). Mice treated daily with SW033291 and 15-PGDH knockout mice both showed marked resistance to DSS-induced colitis when compared with wild-type mice receiving vehicle-control. With either chemical or genetic ablation of 15-PGDH, there were 70% fewer colon ulcers counted on colonoscopy (Fig. 4C, days 11 and 15) and 87% less total area of ulcerated colon mucosa as measured by histomorphometry (Fig. 4D). SW033291-treated and 15-PGDH knockout mice showed marked suppression of mucosal inflammation by colonoscopic grading [murine endoscopic index of colitis severity (MEICS) score] (31) (Fig. 4F) and by histological cryptitis score (32) (Fig. 4, E and G). SW033291-treated (figs. S13A and S14A) and 15-PGDH knockout mice (fig. S14A) also show marked suppression of colitis symptoms, with significantly less diarrhea and rectal bleeding, as assessed by disease activity index (DAI) (32). SW033291-treated (figs. S13B and S14B) and 15-PGDH knockout mice (fig. S14B) also showed significantly less weight loss, with SW033291 protection increasing with increasing dose. SW033291-treated and 15-PGDH knockout mice also showed significant protection from colitis-induced colon shortening (fig. S15). Finally, SW033291-treated mice displayed a significant reduction in the levels of colitis-associated inflammatory cytokines, including tumor necrosis

factor, interleukin-1 (IL-1) beta, interferon gamma, IL-2, chemokine (C-C motif) ligand 2 (CCL2), and CCL4 (fig. S16).

To identify the cellular mediators responsible for the protective effect of 15-PGDH inhibition, we constructed chimeric mice from 15-PGDH wild-type mice that received bone marrow transplants from either 15-PGDH wild-type or 15-PGDH knockout marrow donors. The two groups of chimeric mice showed identical susceptibility to DSS-induced colitis as measured by disease activity, weight loss, and total percentage of ulcerated mucosa (figs. S17 and S18). These results suggest that colitis protection is due to inhibition of 15-PGDH in colonocytes, which are the primary site of 15-PGDH expression in the colon (*33*), rather than to inhibition of 15-PGDH in bone marrow–derived cells.

To further characterize the mechanism by which 15-PGDH inhibition protects the colon epithelium, we assessed the effects of SW033291 on cell proliferation in the colon crypts. On day 8, after 7 days of oral DSS treatment, wild-type mice receiving concurrent injections with vehicle-control showed significant suppression of bromodeoxyuridine (BrdU) incorporation in colonic crypts (Fig. 5 and fig. S19). In contrast, day 8 BrdU incorporation was increased 2.5-fold in SW033291-treated animals (Fig. 5, A and B, 10 mg/kg SW033291) and increased 2.4-fold in 15-PGDH knockout mice (Fig. 5, A and C). Immunofluorescence staining for cleaved caspase 3 showed only scattered apoptotic cells, and these were present in similar amounts in control and SW033291-treated mice. Thus, 15-PGDH inhibition appears to confer protection primarily by helping maintain colonocyte proliferation in the DSS-damaged mucosa.

15-PGDH inhibition promotes liver regeneration

We next examined the effects of 15-PGDH inhibition on regeneration in the liver. Inhibiting 15-PGDH increases PGE2 levels in this organ (Fig. 1, A and B) and, provocatively, COX-2 inhibitors antagonize regrowth of the liver after surgery (*11*, *34*, *35*). We found that after resection of two-thirds of the liver mass (*35*), both 15-PGDH knockout mice and SW033291-treated wild-type mice showed a markedly increased rate and extent of liver regeneration as compared with wild-type mice treated with vehicle-control (Fig. 6, A to C). Although the 15-PGDH knockout and wild-type mice had equal preoperative liver weights, the knockout mice attained 28% and 40% greater total liver weight than controls on postoperative days 3 and 4, respectively (Fig. 6, A and B). Liver regeneration was similarly greater in SW033291-treated mice, which attained higher liver weights than controls on each of postoperative days 2 to 7 (Fig. 6C). Between postoperative days 1 to 7, SW033291-treated mice regenerated 77% greater new liver weight (0.48 g increase) than did controls (0.27 g increase) (Fig. 6C). Hepatocytes in SW033291-treated mice displayed a burst of proliferation on postoperative day 2: 40% of hepatocytes showed labeling with BrdU in treated mice versus 16% in vehicle-control–treated mice (Fig. 6, D to F).

Consistent with SW033291 up-regulating prostaglandin signaling, regenerating livers of SW033291-treated mice showed 36 to 55% higher levels of cyclic AMP from postoperative days 1 to 3 ($P < 0.002$, Student's t test) (fig. S20). However, we did not find differences between livers of SW033291-treated versus control mice in other downstream signaling targets, including levels of beta-catenin protein; nuclear localization of beta-catenin; and levels of phosphorylation at cAMP-dependent protein kinase target sites on CREB serine 133, beta-catenin serine 675, and beta-catenin serine 552 (*10*, *11*).

Discussion

In summary, we have shown that 15-PGDH negatively regulates tissue regeneration and repair in the bone marrow, the colon, and the liver. Although bone marrow, colon, and liver each demonstrate very different tissue architectures, in each of these tissues this function of 15-PGDH is conserved, suggesting a biological generality of this pathway. PGE2 and dmPGE2 show activities that favor tissue regeneration when used to treat cells in culture and when administered to animals in pharmacological doses (*11*, *13*–*16*, *18*, *24*–*27*). Our findings further imply that in normal in vivo physiology, prostaglandins play a widespread homeostatic role in the maintenance and repair of injury across multiple body tissues. Indeed, a doubling of tissue PGE2 levels can markedly potentiate tissue repair. Of most direct utility, our observations identify 15-PGDH as a therapeutic target and provide a chemical formulation, SW033291, that is an active 15-PGDH inhibitor in vivo and that potentiates repair in multiple tissues.

Inhibitors of 15-PGDH, such as SW033291, may have applicability to human HSC transplantation by potentially increasing transplant safety and reducing the required time of hospitalization (*1*). The mechanism of SW033291, which activates the bone marrow niche of transplant recipients, is distinct from the effect of treating donor hematopoietic stem cells ex vivo with dmPGE2. Ex vivo treatment with dmPGE2 instead activates the donor stem cells, for example by up-regulating donor cell expression of CXCR4 (the CXCL12 receptor) (*15*, *16*). These previous and current studies together thus identify, respectively, two independent PGE2-responsive pathways for potentiating HSC transplants, one targeted by the ex vivo dmPGE2 treatment of donor hematopoietic stem

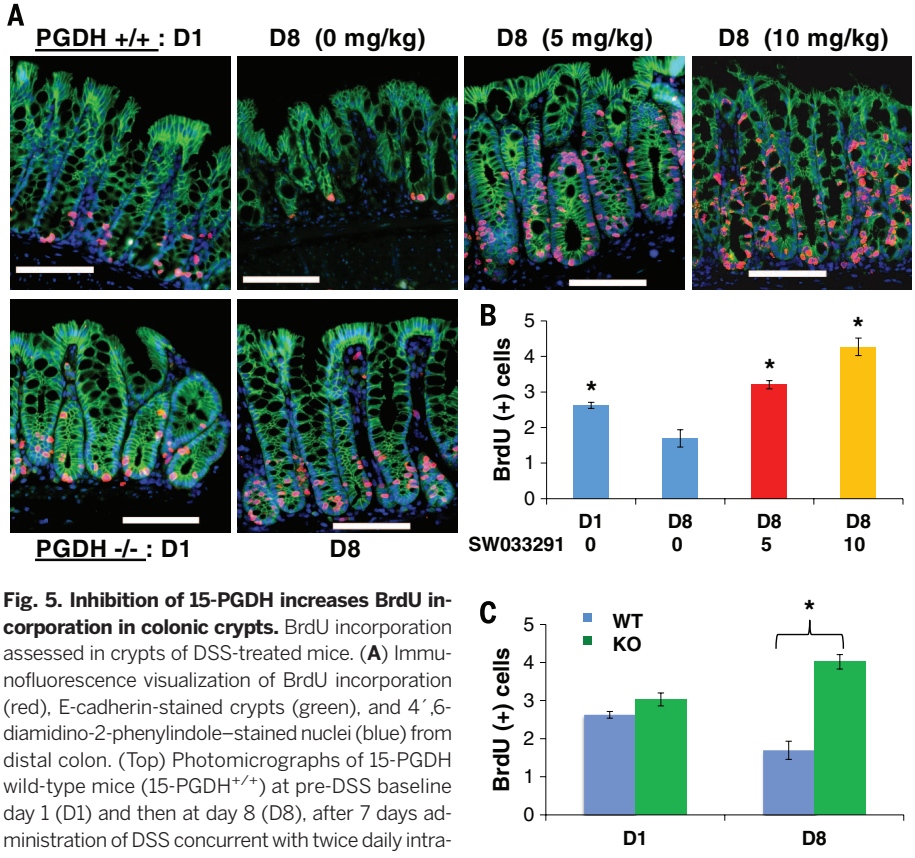


Fig. 5. Inhibition of 15-PGDH increases BrdU incorporation in colonic crypts. BrdU incorporation assessed in crypts of DSS-treated mice. (**A**) Immunofluorescence visualization of BrdU incorporation (red), E-cadherin-stained crypts (green), and 4′,6-diamidino-2-phenylindole–stained nuclei (blue) from distal colon. (Top) Photomicrographs of 15-PGDH wild-type mice (15-PGDH$^{+/+}$) at pre-DSS baseline day 1 (D1) and then at day 8 (D8), after 7 days administration of DSS concurrent with twice daily intraperitoneal injections with either 0, 5, or 10 mg/kg SW033291. (Bottom) Photomicrographs of 15-PGDH knockout (15-PGDH$^{-/-}$) mice at D1, and D8 upon completion of DSS. Scale bars, 50 μm. (**B**) Graphical plots of average number of BrdU-positive cells per crypt in mice from top panel of (A). $N = 6$ mice for day 1 and $N = 8$ mice for each day 8 data point. ANOVA $P < 0.0001$. *$P < 0.013$ versus day 8 mice injected with 0 mg/kg SW033291 (i.e., vehicle-control), Student's t test. (**C**) Graphical plots of average number of BrdU-positive cells per crypt in day 1 (D1) baseline and day 8 (D8) DSS-treated mice that are 15-PGDH WT versus 15-PGDH (KO). $N = 6$ to 8 mice per group. ANOVA $P < 0.0001$. *$P < 3 \times 10^{-5}$, Student's t test. All graphs show means ± SEM.

cells and the other by in vivo SW033291 administration to HSC transplant recipients. The use of granulocyte colony-stimulating factor to assist neutrophil recovery after HSC transplant provides one precedent for the therapeutic utility of tissue regeneration approaches (*36*, *37*). Distinguishing features of SW033291 are that in addition to accelerating neutrophil recovery (by a different approach), this 15-PGDH inhibitor accelerates regeneration of platelets and red blood cells and also expands the numbers of more primitive bone marrow SKL cells. We anticipate that 15-PGDH inhibitors would potentiate bone marrow regeneration after HSC transplants that employ either autologous or allogeneic derived stem cells, which are most often harvested from the donor's peripheral blood (*1*). Because SW033291 also enables successful murine bone marrow reconstitution from a reduced inoculum of marrow cells, SW033291 may additionally have applicability to HSC transplants that use human umbilical cord blood stem cells, in which numbers of donor cells are limited by supply and expense (*2*, *3*).

Inhibitors of 15-PGDH, such as SW033291, may also have applicability to treatment of human ulcerative colitis. Mucosal healing is increasingly recognized as an important therapeutic goal in the treatment of this disease (*5*, *38*). The activity of SW033291 in stimulating colon epithelial regeneration in the mouse DSS colitis model suggests potential applicability to this treatment need. Inhibitors of 15-PGDH, such as SW033291, may also have therapeutic applicability to patients undergoing surgical resection of primary liver tumors or of colon cancers metastatic to the liver. In both these cases, the patient's eligibility for surgery is limited by the requirement that the postoperative liver remnant be sufficient to enable regenerating an adequate liver mass (*6*–*8*).

Previous studies from our group indicated that 15-PGDH shows tumor suppressor activity in colon cancer but that many individuals have low 15-PGDH expression levels in their colonic mucosa (*22*, *39*–*41*). The current observations suggest that one explanation for this paradox may be that in certain biological contexts, such as in bowel injury, low levels of colonic 15-PGDH may provide a biological advantage by potentiating faster organ recovery. More generally, this study provides an example in which the regulated and short-term inhibition of a tumor suppressor gene may provide therapeutic utility without adverse effect, particularly in a disease context in which tissue repair is the immediate medical goal.

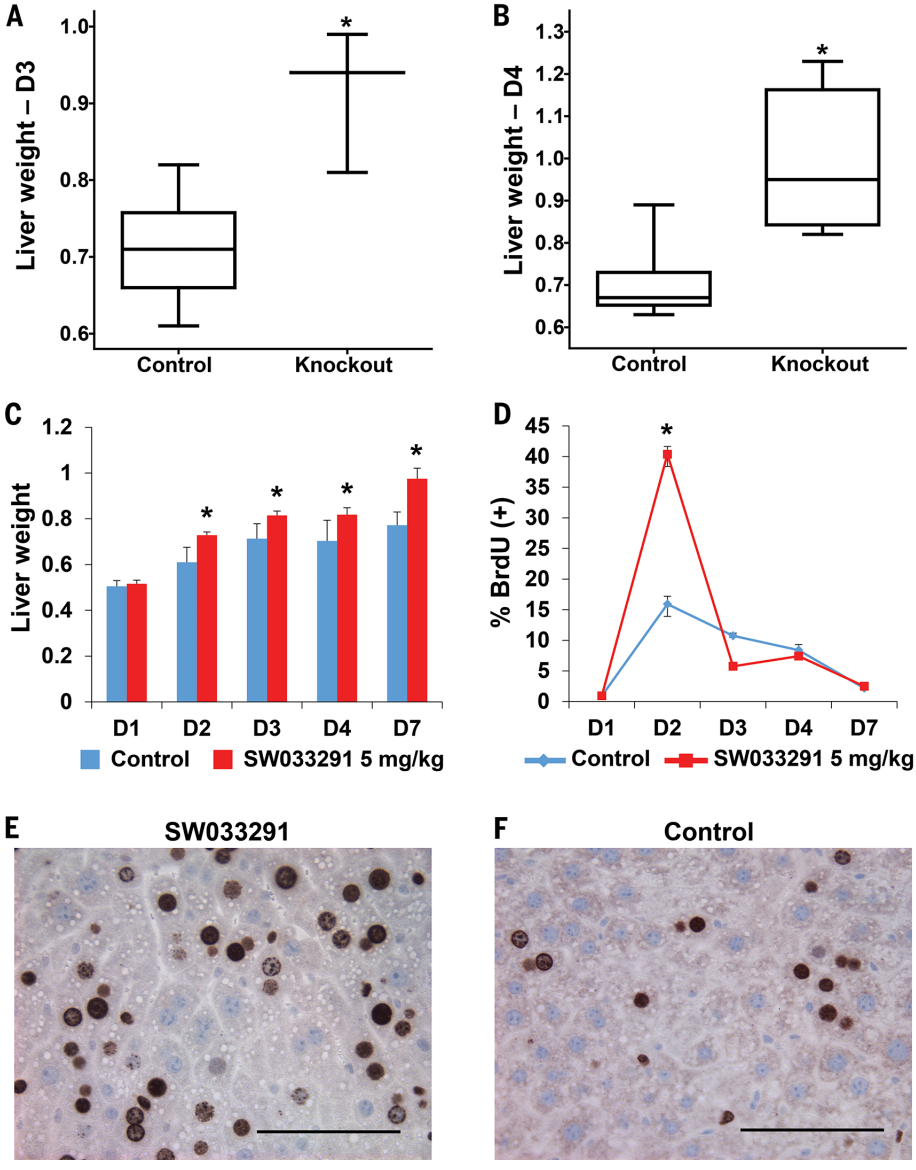


Fig. 6. Liver regeneration in mice after partial hepatectomy. (**A** and **B**) Box plots of regenerated liver weight (grams) attained after partial hepatectomy in control and 15-PGDH knockout mice. (A) Postoperative day 3 (D3). N = 10 control mice and 3 knockout mice. *P < 0.0014, Student's t test. (B) Postoperative day 4 (D4) N = 10 control mice and 6 knockout mice. *P < 0.0005, Student's t test. (**C**) Total liver weight (grams) attained after partial hepatectomy (y axis) in mice injected intraperitoneally twice daily with vehicle-control or SW033291 at 5 mg/kg across postoperative days 1 to 7 (D1 to D7). Each value is mean of N = 10 mice. *P < 0.011, Student's t test. (**D** to **F**) BrdU incorporation after partial hepatectomy. (D) Percentage of BrdU-positive cells (y axis) in vehicle-control–treated versus SW033291-treated mice on postoperative days 1 to 7 (D1 to D7) (x axis). Each value is the mean of from 6 to 10 mice. Error bars are smaller than symbols at nearly all data points. *$P < 1.0 \times 10^{-17}$ for postoperative day 2 comparison of SW033291-treated and control mice, Student's t test. [(E and (F)] Representative high-powered micrograph fields of BrdU staining hepatocytes on postoperative day 2 in SW033291-treated mice (E) and vehicle-control–treated mice (F). Scale bar, 100 μm. All graphs show means ± SEM.

REFERENCES AND NOTES

1. E. A. Copelan, Hematopoietic stem-cell transplantation. *N. Engl. J. Med.* **354**, 1813–1826 (2006). doi: 10.1056/NEJMra052638; pmid: 16641398
2. M. Norkin, H. M. Lazarus, J. R. Wingard, Umbilical cord blood graft enhancement strategies: Has the time come to move these into the clinic? *Bone Marrow Transplant.* **48**, 884–889 (2013). doi: 10.1038/bmt.2012.163; pmid: 22941377
3. I. Fares *et al.*, Pyrimidoindole derivatives are agonists of human hematopoietic stem cell self-renewal. *Science* **345**, 1509–1512 (2014). doi: 10.1126/science.1256337; pmid: 25237102
4. C. Cutler *et al.*, Prostaglandin-modulated umbilical cord blood hematopoietic stem cell transplantation. *Blood* **122**, 3074–3081 (2013). doi: 10.1182/blood-2013-05-503177; pmid: 23996087
5. S. Danese, C. Fiocchi, Ulcerative colitis. *N. Engl. J. Med.* **365**, 1713–1725 (2011). doi: 10.1056/NEJMra1102942; pmid: 22047562
6. A. B. Benson 3rd *et al.*, NCCN clinical practice guidelines in oncology: Hepatobiliary cancers. *J. Natl. Compr. Canc. Netw.* **7**, 350–391 (2009). pmid: 19406039
7. M. S. Tsai *et al.*, Clinicopathological features and prognosis in resectable synchronous and metachronous colorectal liver metastasis. *Ann. Surg. Oncol.* **14**, 786–794 (2007). doi: 10.1245/s10434-006-9215-5; pmid: 17103254
8. M. Hayashi *et al.*, Clinicopathological analysis of recurrence patterns and prognostic factors for survival after hepatectomy for colorectal liver metastasis. *BMC Surg.* **10**, 27 (2010). doi: 10.1186/1471-2482-10-27; pmid: 20875094
9. J. R. Brown, R. N. DuBois, COX-2: A molecular target for colorectal cancer prevention. *J. Clin. Oncol.* **23**, 2840–2855 (2005). doi: 10.1200/JCO.2005.09.051; pmid: 15837998
10. M. D. Castellone, H. Teramoto, B. O. Williams, K. M. Druey, J. S. Gutkind, Prostaglandin E2 promotes colon cancer cell growth through a Gs-axin-beta-catenin signaling axis. *Science* **310**, 1504–1510 (2005). doi: 10.1126/science.1116221; pmid: 16293724

11. W. Goessling *et al*., Genetic interaction of PGE2 and Wnt signaling regulates developmental specification of stem cells and regeneration. *Cell* **136**, 1136–1147 (2009). doi: 10.1016/j.cell.2009.01.015; pmid: 19303855
12. N. Barker *et al*., Identification of stem cells in small intestine and colon by marker gene Lgr5. *Nature* **449**, 1003–1007 (2007). doi: 10.1038/nature06196; pmid: 17934449
13. B. J. Frisch *et al*., In vivo prostaglandin E2 treatment alters the bone marrow microenvironment and preferentially expands short-term hematopoietic stem cells. *Blood* **114**, 4054–4063 (2009). doi: 10.1182/blood-2009-03-205823; pmid: 19726721
14. T. E. North *et al*., Prostaglandin E2 regulates vertebrate haematopoietic stem cell homeostasis. *Nature* **447**, 1007–1011 (2007). doi: 10.1038/nature05883; pmid: 17581586
15. J. Hoggatt, P. Singh, J. Sampath, L. M. Pelus, Prostaglandin E2 enhances hematopoietic stem cell homing, survival, and proliferation. *Blood* **113**, 5444–5455 (2009). doi: 10.1182/blood-2009-01-201335; pmid: 19324903
16. W. Goessling *et al*., Prostaglandin E2 enhances human cord blood stem cell xenotransplants and shows long-term safety in preclinical nonhuman primate transplant models. *Cell Stem Cell* **8**, 445–458 (2011). doi: 10.1016/j.stem.2011.02.003; pmid: 21474107
17. J. Hoggatt, K. S. Mohammad, P. Singh, L. M. Pelus, Prostaglandin E2 enhances long-term repopulation but does not permanently alter inherent stem cell competitiveness. *Blood* **122**, 2997–3000 (2013). doi: 10.1182/blood-2013-07-515288; pmid: 24047650
18. P. Jung *et al*., Isolation and in vitro expansion of human colonic stem cells. *Nat. Med.* **17**, 1225–1227 (2011). doi: 10.1038/nm.2470; pmid: 21892181
19. K. Kabashima *et al*., The prostaglandin receptor EP4 suppresses colitis, mucosal damage and CD4 cell activation in the gut. *J. Clin. Invest.* **109**, 883–893 (2002). doi: 10.1172/JCI0214459; pmid: 11927615
20. H. H. Tai, C. M. Ensor, M. Tong, H. Zhou, F. Yan, Prostaglandin catabolizing enzymes. *Prostaglandins Other Lipid Mediat.* **68-69**, 483–493 (2002). doi: 10.1016/S0090-6980(02)00050-3; pmid: 12432938
21. K. G. Coggins *et al*., Metabolism of PGE2 by prostaglandin dehydrogenase is essential for remodeling the ductus arteriosus. *Nat. Med.* **8**, 91–92 (2002). doi: 10.1038/nm0202-91; pmid: 11821873
22. S. J. Myung *et al*., 15-Hydroxyprostaglandin dehydrogenase is an in vivo suppressor of colon tumorigenesis. *Proc. Natl. Acad. Sci. U.S.A.* **103**, 12098–12102 (2006). doi: 10.1073/pnas.0603235103; pmid: 16880406
23. R. A. Copeland, *Enzymes. A Practical Introduction to Structure, Mechanism, and Data Analysis* (Wiley-VCH, New York, 2000), pp. 305–317.
24. E. J. Hagedorn, E. M. Durand, E. M. Fast, L. I. Zon, Getting more for your marrow: Boosting hematopoietic stem cell numbers with PGE2. *Exp. Cell Res.* **329**, 220–226 (2014). doi: 10.1016/j.yexcr.2014.07.030; pmid: 25094063
25. L. M. Pelus, J. Hoggatt, P. Singh, Pulse exposure of haematopoietic grafts to prostaglandin E2 in vitro facilitates engraftment and recovery. *Cell Prolif.* **44** (suppl. 1), 22–29 (2011). doi: 10.1111/j.1365-2184.2010.00726.x; pmid: 21481039
26. R. L. Porter *et al*., Prostaglandin E2 increases hematopoietic stem cell survival and accelerates hematopoietic recovery after radiation injury. *Stem Cells* **31**, 372–383 (2013). doi: 10.1002/stem.1286; pmid: 23169593
27. C. M. Hoffman, L. M. Calvi, Minireview: Complexity of hematopoietic stem cell regulation in the bone marrow microenvironment. *Mol. Endocrinol.* **28**, 1592–1601 (2014). doi: 10.1210/me.2014-1079; pmid: 25083740
28. S. J. Morrison, D. T. Scadden, The bone marrow niche for haematopoietic stem cells. *Nature* **505**, 327–334 (2014). doi: 10.1038/nature12984; pmid: 24429631
29. L. M. Pelus, H. E. Broxmeyer, J. I. Kurland, M. A. Moore, Regulation of macrophage and granulocyte proliferation. Specificities of prostaglandin E and lactoferrin. *J. Exp. Med.* **150**, 277–292 (1979). doi: 10.1084/jem.150.2.277; pmid: 313430
30. I. Okayasu *et al*., A novel method in the induction of reliable experimental acute and chronic ulcerative colitis in mice. *Gastroenterology* **98**, 694–702 (1990). pmid: 1688816
31. C. Becker *et al*., In vivo imaging of colitis and colon cancer development in mice using high resolution chromoendoscopy. *Gut* **54**, 950–954 (2005). doi: 10.1136/gut.2004.061283; pmid: 15951540
32. H. S. Cooper, S. N. Murthy, R. S. Shah, D. J. Sedergran, Clinicopathologic study of dextran sulfate sodium experimental murine colitis. *Lab. Invest.* **69**, 238–249 (1993). pmid: 8350599
33. M. Yan *et al*., 15-Hydroxyprostaglandin dehydrogenase, a COX-2 oncogene antagonist, is a TGF-beta-induced suppressor of human gastrointestinal cancers. *Proc. Natl. Acad. Sci. U.S.A.* **101**, 17468–17473 (2004). doi: 10.1073/pnas.0406142101; pmid: 15574495
34. D. A. Rudnick, D. H. Perlmutter, L. J. Muglia, Prostaglandins are required for CREB activation and cellular proliferation during liver regeneration. *Proc. Natl. Acad. Sci. U.S.A.* **98**, 8885–8890 (2001). doi: 10.1073/pnas.151217998; pmid: 11447268
35. C. Mitchell, H. Willenbring, A reproducible and well-tolerated method for 2/3 partial hepatectomy in mice. *Nat. Protoc.* **3**, 1167–1170 (2008). doi: 10.1038/nprot.2008.80; pmid: 18600221
36. L. J. Bendall, K. F. Bradstock, G-CSF: From granulopoietic stimulant to bone marrow stem cell mobilizing agent. *Cytokine Growth Factor Rev.* **25**, 355–367 (2014). doi: 10.1016/j.cytogfr.2014.07.011; pmid: 25131807
37. D. Metcalf, Hematopoietic cytokines. *Blood* **111**, 485–491 (2008). doi: 10.1182/blood-2007-03-079681; pmid: 18182579
38. G. R. Lichtenstein, P. Rutgeerts, Importance of mucosal healing in ulcerative colitis. *Inflamm. Bowel Dis.* **16**, 338–346 (2010). doi: 10.1002/ibd.20997; pmid: 19637362
39. M. Yan *et al*., 15-Hydroxyprostaglandin dehydrogenase inactivation as a mechanism of resistance to celecoxib chemoprevention of colon tumors. *Proc. Natl. Acad. Sci. U.S.A.* **106**, 9409–9413 (2009). doi: 10.1073/pnas.0902367106; pmid: 19470469
40. S. P. Fink *et al*., Aspirin and the risk of colorectal cancer in relation to the expression of 15-hydroxyprostaglandin dehydrogenase (HPGD). *Sci. Transl. Med.* **6**, 233re2 (2014). doi: 10.1126/scitranslmed.3008481; pmid: 24760190
41. C. L. Thompson *et al*., Genetic variation in 15-hydroxyprostaglandin dehydrogenase and colon cancer susceptibility. *PLOS ONE* **8**, e64122 (2013). doi: 10.1371/journal.pone.0064122; pmid: 23717544

ACKNOWLEDGMENTS

We thank the members of the University of Texas Southwestern High-Throughput Screening (HTS) Core facility for their support of the high-throughput screen; A Dannenberg, D. Montrose, and M. Datt for helpful scientific discussions; and K. Lingas, B. Maitra, and J. Ren for helpful technical support. This work was funded by NIH grants P50 CA150964 (S.D.M.), P30 CA043703 (S.L.G.), R25CA148052 (Y.Z.), U54HL119810 (Paul DiCorleto), 1P01CA95471-09 (Steven McKnight and J.M.R.), and 5P30 CA142543-03 [The Simmons Cancer Center (J.K.V.W.)], which support the University of Texas Southwestern HTS Core Facility; P50 CA130810 (Dean Brenner); P30 DK097948 (F.C.); a Scholar Innovator Award from the Harrington Discovery Institute (S.D.M.); grants from the Marguerite Wilson Foundation (S.D.M.), Inje University (S.Y.Y. and K.B.B.), and National Research Foundation, Ministry of Science, ICT and Future Planning of Korea 2014002213 (K.B.B); the Welch Foundation (I-1612, J.M.R.); Cancer Prevention Research Institute of Texas (RP110708); a medical research fellowship from the Howard Hughes Medical Institute (L.H.); and gifts from the Leonard and Joan Horvitz Foundation (S.D.M) and the Richard Horvitz and Erica Hartman-Horvitz Foundation (S.D.M.). Case Western Reserve University, the University of Texas, and the University of Kentucky have filed patent applications (PCT/US2013/036790 and PCT/US2013/036790) related to SW033291 and other 15-PGDH inhibitors and their use in the treatment of disease.

SUPPLEMENTARY MATERIALS

www.sciencemag.org/content/348/6240/aaa2340/suppl/DC1
Materials and Methods
Figs. S1 to S20
Table S1
References (*42*–*46*)

5 November 2014; accepted 19 April 2015
10.1126/science.aaa2340

REPORTS

INDUCED SEISMICITY

Seismicity triggered by fluid injection–induced aseismic slip

Yves Guglielmi,[1]* Frédéric Cappa,[2,3] Jean-Philippe Avouac,[3]† Pierre Henry,[1] Derek Elsworth[4]

Anthropogenic fluid injections are known to induce earthquakes. The mechanisms involved are poorly understood, and our ability to assess the seismic hazard associated with geothermal energy or unconventional hydrocarbon production remains limited. We directly measure fault slip and seismicity induced by fluid injection into a natural fault. We observe highly dilatant and slow [~4 micrometers per second (μm/s)] aseismic slip associated with a 20-fold increase of permeability, which transitions to faster slip (~10 μm/s) associated with reduced dilatancy and micro-earthquakes. Most aseismic slip occurs within the fluid-pressurized zone and obeys a rate-strengthening friction law $\mu = 0.67 + 0.045\ln\left(\frac{v}{v_0}\right)$ with v_0 = 0.1 μm/s. Fluid injection primarily triggers aseismic slip in this experiment, with micro-earthquakes being an indirect effect mediated by aseismic creep.

Injection of fluid into the crust can generate seismicity, with source mechanisms similar to natural earthquakes and occasionally large enough to cause damage (*1*–*6*). Induced seismicity is generally regarded as a manifestation of the effective stress principle, where the increase in pore pressure reduces the effective normal stress and brings a preexisting fault or intact rock mass to failure (*7*). Seismic slip requires failure to result in unstable slip, meaning that the resistance to sliding must decrease faster than the elastic unloading associated with fault slip. If a fault strengthens during slip, only aseismic creep should be possible. Only faults that weaken during sliding can, in principle, yield unstable slip. In general, the presence of fluids could either favor seismic slip, through thermal pressurization (*8*), or might impede seismic slip by a variety of other processes. In particular, dilatancy during slip could restrengthen the fault due to the resulting drop of pore pressure (*9*). Current models of earthquake nucleation (*10*) imply that slip becomes stable when the pore pressure approaches lithostatic, because the condition for stability (*10*) is then always reached. For slip to be unstable on a rate-weakening fault, the stiffness must be smaller than a critical value that has the effective normal stress at the numerator (*10*). If the effective normal stress goes to zero as pore pressure approaches lithostatic, this condition can never be met; slip should then be stable. Conditional stability might explain why aseismic slip has been inferred in some case studies (*4*, *11*, *12*). In reality, fault slip is coupled with fluid flow, and assessing whether seismic or aseismic slip should result from a fluid injection is a challenge.

We monitor a natural but initially inactive fault stimulated through a high-pressure injection of water, taking advantage of an instrument—the step-rate injection method for fracture in situ properties (SIMFIP) probe (*13*)—that allows the simultaneous measuring of fault-normal displacements, fault-parallel displacements, and fluid pressure. We selected a preexisting fault cutting through a carbonate formation accessible for examination and instrumentation thanks to an underground experimental facility located in southeastern France at a depth of 0 to 518 m (*14*). The fault is at least ~500 m long and trends 30°N 70°W. It cuts through porous grainstone carbonate layers (inner-platform Rudists' rich facies), with strike-slip to normal cumulated

[1]Centre de Recherche et d'Enseignement de Géosciences de l'Environnement (UMR7330), University of Aix-Marseille, CNRS, IRD, 13545 Aix-en-Provence, France. [2]Géoazur (UMR 7329), University of Nice Sophia-Antipolis, CNRS, IRD, Côte d'Azur Observatory, 06560 Sophia-Antipolis, France. [3]Geological and Planetary Sciences, California Institute of Technology, Pasadena, CA 91125, USA. [4]Energy and Mineral Engineering and Geosciences, Earth and Mineral Sciences Energy Institute and G3 Center, Pennsylvania State University, University Park, PA 16802, USA.
*Corresponding author. E-mail: guglielmi@cerege.fr †Present address: Department of Earth Sciences, University of Cambridge, Cambridge, CB3 OEZ, UK.

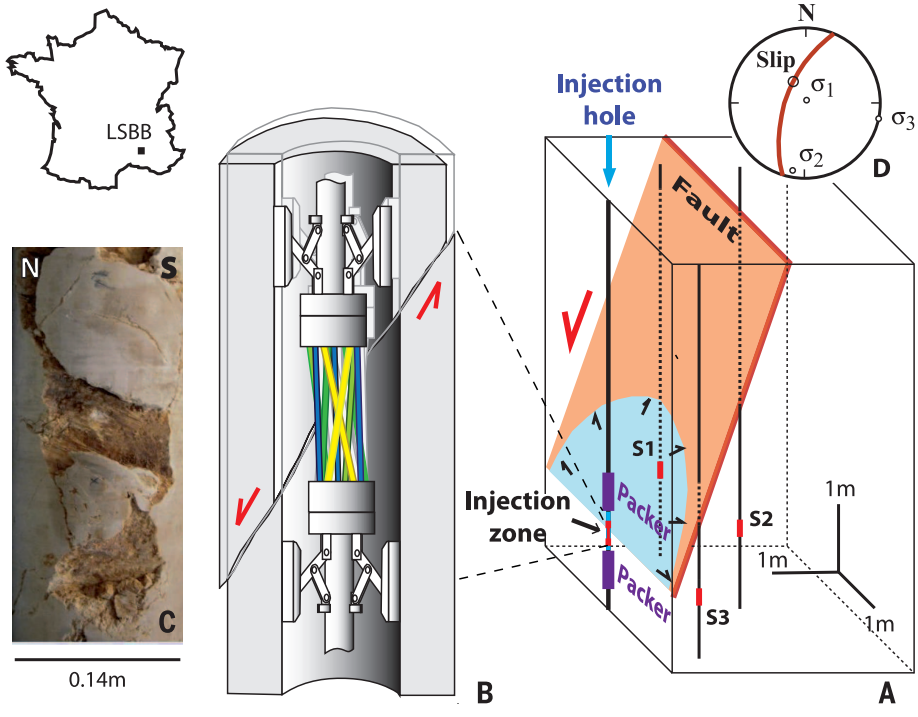


Fig. 1. Experiment setting. (**A**) Location of the injection interval and the seismometers (S1 to S3) in and around the fault plane. The experiment took place at a depth of 282 m below the Earth's surface, in cretaceous limestone of the southeast France sedimentary basin. (**B**) Schematic representation of the SIMFIP probe displacement sensor. Deformation of the linkage tubes (colored in yellow, green, and blue) captures the relative displacement of the anchors clamped on the borehole wall in each fault compartment (*16*). (**C**) Core from the main slip plane of the fault showing slickensided surfaces, breccia/gouge-rich zones, and a fractured damage zone. (**D**) Stereographic view of the state of principal stresses, the fault plane, and the fault-parallel slip vector induced by the experiment.

Downloaded from www.sciencemag.org on June 14, 2015

slip of a few meters. The fault zone consists of subparallel fractures to 1- to 10-m length and discontinuous thin breccias (*15*). The in situ temperature at the location of the injection was 12.5°C and did not vary during the experiment. We therefore ignore thermal effects. We drilled a vertical well intersecting the fault at a depth of 282 m. Based on initial in situ measurements, the fault zone has an average initial permeability of 0.07×10^{-10} m^2 and a bulk modulus of 10 to 17 GPa that are a factor of 25 higher and 2 to 5 lower than the surrounding host rock, respectively (*16*). We injected water into a 1.5-m-long chamber between two inflatable packers spanning the fault zone (Fig. 1A). We injected a total of 950 liters of water with step-increasing rates while monitoring pressure, flowrate, fault movement in both shear and dilation (Fig. 1B), and seismicity (*16*) (fig. S1). We estimated the state of stress from hydraulic tests on preexisting fractures conducted at two different depths in adjacent boreholes using the hydraulic testing of preexisting fractures (HTPF) protocol (*17*) and taking into account topographic stresses. The maximum principal stress σ_1 = 6 MPa is subvertical and dips 80°S; σ_2 = 5 MPa is subhorizontal and strikes 0°N 20°E; and σ_3 = 3 MPa is subhorizontal and strikes 0°N 110°E (Fig. 1D).

Slip initiated at a pressure of about 1.5 MPa (S_0 in Fig. 2) with fault-parallel slip approximately parallel to the shear stress on the fault plane (Fig. 1C), consistent with reactivation by shear failure. No seismic event was detected until about 0.3 mm of fault slip, about 1100 s into the experiment. During this first stage, the dilation rate was around 6 μm/s and exceeded the fault slip rate, which was on the order of 4 μm/s. The dilation rates fell to about 20% of the slip rate approximately at the onset of seismicity. The slip rate increased to about 23 μm/s. The seismicity consists of impulsive micro-earthquakes and tremors (fig. S1), as is observed in injection experiments elsewhere (*18*). About 80 seismic events were generated at an average rate of 15 events per min. Half of these events occurred between 1100 and 1190 s before acceleration of fault slip (Fig. 2), and the transition from aseismic to seismic slip was not associated with any pressure variation (point S_S in Fig. 2). Both observations demonstrate that the majority of the seismic sources are located a few meters away from the injection point and may account for only a small fraction of the slip occurring on the fault segment where the fluid pressurization is occurring.

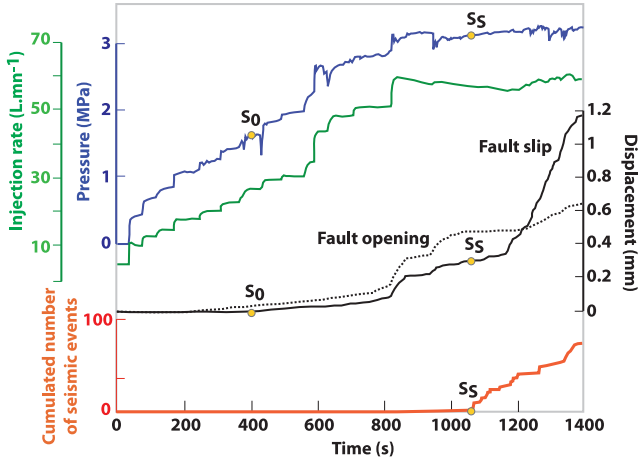


Fig. 2. Fault movements and seismicity induced over time by fluid injection. Temporal evolution of fluid pressure (blue), injection rate (green), fault slip (solid black line), normal displacement (dashed black line), and cumulative number of induced earthquakes (red) during the 1400-s-long injection. Slip initiates at S_0 = 400 s as pressure is increased to 1.5 MPa; seismicity initiates at S_s = 1100 s while there is no notable pressure variation.

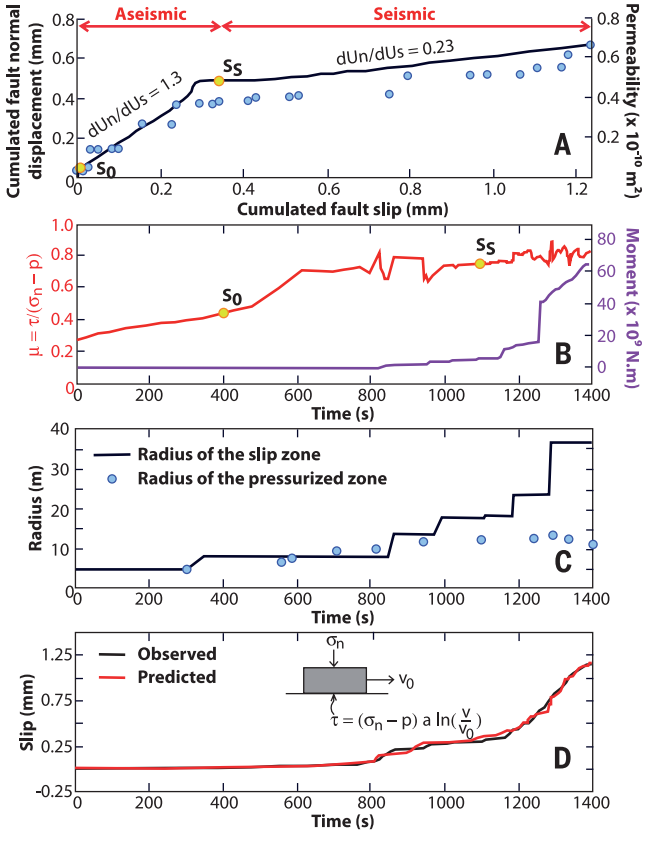


Fig. 3. Estimation of fault permeability and friction law from the in situ hydromechanical data. (**A**) Observed cumulative fault-normal displacement and modeled permeability (blue circles) versus observed fault slip (black). (**B**) Friction (orange), calculated based on the measurements of the initial stress and fault slip, and moment release (purple) derived from fault slip. (**C**) Comparison of the estimated radius of the sliding zone and of the pressurized zone. (**D**) Comparison of observed (black) and modeled (red) fault slip for the best-fitting rate-dependent friction law. The best-fitting friction law of the form $\mu = \mu_0 + a\ln(v/v_0)$ has μ_0 = 0.67 and a = 0.0447, for a reference sliding velocity of $v_0 = 10^{-7}$ m/s.

The observation that the fault opens during the injection implies that permeability varies in close relation to the evolution of fluid pressure, as suggested in theoretical and experimental studies (*19*, *20*). We used hydromechanical modeling (*21*) to determine the evolution of fault permeability (*16*). Our results show a 14-fold increase of the fault permeability from 0.07 to 1.0×10^{-10} m^2 during the aseismic period, representing about 70% of the cumulative permeability increase (20-fold) during the injection (Fig. 3A). This permeability increase probably results from the opening of fractures during sliding, possibly reflecting the roughness of the fracture walls and/or cataclasis of the fault rock and associated microcrack dilatation in the early stages of failure. The model indicates that the pressurized zone (defined here as the zone where the pore pressure exceeds 0.5 MPa) increases to about 12 m during the initial stage of completely aseismic slip (Fig. 3C).

We use our measurements to estimate the friction law and to determine whether aseismic slip is primarily due to rate-strengthening behavior or whether it is due to fluid pressurization bringing the fault zone to the domain of conditional stability. We approximate the sliding zone by a circular crack and assume quasistatic equilibrium with a complete shear stress drop [justified by the net opening of the fractures and following (*22*)]. This simple model ignores the pore-pressure gradient and viscous forces associated with fluid flow. With these assumptions, it is possible to calculate the crack radius as a function of time (Fig. 3C and fig. S3A), as well as the changes of shear and normal stresses associated with fault slip and dilation (*16*) (fig. S3, B and C).

The model yields an accumulated moment at the end of the experiment of $M_0 = 65 \times 10^9$ Nm, (equivalent to a moment magnitude M_w = 1.17), far larger than the moment released by the incremental microseismicity, which was estimated to be lower than −2 in magnitude; so slip is

mostly aseismic in this experiment (Fig. 3B). Micro-earthquakes are triggered only when the estimated size of the slip zone exceeds the pressurized zone (Fig. 3C), suggesting that they occur off the pressurized zone. However, they might occur within the sliding zone or be triggered off the sliding area by static stress increase. Aftershocks might relate to afterslip in a similar way (*23*).

The ratio of the shear stress to the effective normal stress increases from about 0.4 to about 0.8 and indicates a friction between 0.6 and 0.8 once slip becomes notable (fig. S4). Qualitatively, this evolution correlates with slip rate better than with slip. The data suggest a logarithmically varying, rate-dependent friction, as frequently observed in laboratory measurements of rock friction (*24*) or derived from studies of afterslip following large earthquakes (*23*, *25*). We tested such a law based on a simple one-dimensional model (*16*). The model, which involves only two adjustable parameters, qualitatively fits the observations well (Fig. 3D). We determine the friction $\mu_0 = 0.67$ (+/−0.05) at a reference velocity of $v_0 = 0.1\ \mu m/s$, with a rate dependency of $a = \frac{\partial \mu}{\partial \ln v} = 0.0447$ (± 0.005). We also tested rate-and-state friction laws (*16*) but found that the improvement was irrelevant in view of the uncertainties of the measurements. The friction coefficient increases to about 0.7 for slip rates of 1 to 20 μm/s. Similar values have been measured in the laboratory on faults formed in limestone and at comparable sliding rates (*26*–*28*). These laboratory experiments also show a rate-strengthening behavior at temperatures less than 100°C but a rate dependency at steady-state typically one order of magnitude lower than the value we obtained.

The aseismic behavior triggered by the fluid injection in this experiment is apparently due to an intrinsically rate-strengthening behavior, rather than to conditional stable creep of a rate-weakening fault. However, the seismicity, which was probably triggered outside the pressurized zone, requires some areas to allow earthquake nucleation, hence weakening during deformation. This observation is an indication that the frictional properties are likely heterogeneous, as supported by the observations of the main slip surface that displays gouge-rich zones and slickensided areas cutting solid rock (Fig. 1C). During the injection, the effective behavior is rate-strengthening. This behavior is possibly due to the fault zone being rate-strengthening on average, with the gouge-rich zones being possibly more rate-strengthening than the zones where the fault cuts solid rock (*27*) or because the rate-weakening asperities are brought to conditional stability by the increase in pore pressure. This interpretation could explain why seismicity is observed only when the crack radius has become larger than the radius of the pressurized zone. Our results prove unambiguously that fluid injection can trigger primarily aseismic slip, with seismicity induced as a secondary effect. This is observed in the context of our experiment, which is characterized by a particularly low effective normal stress. Thus, our results may be of particular relevance to seismic activity triggered at shallow depth by human-induced injections and shallow aseismic slip. Mechanism observed in this experiment could also be of relevance to explain natural processes at greater depth, such as deep afterslip, slow-slip events, and tremors.

REFERENCES AND NOTES

1. C. B. Raleigh, J. H. Healy, J. D. Bredehoeft, *Science* **191**, 1230–1237 (1976).
2. W. L. Ellsworth, *Science* **341**, 1225942 (2013).
3. C. Nicholson, R. L. Wesson, *Pure Appl. Geophys.* **139**, 561–578 (1992).
4. F. H. Cornet, H. Helm, H. Poitrenaud, A. Etchecopar, *Pure Appl. Geophys.* **150**, 563–583 (1997).
5. C. Nicholson, R. L. Wesson, Earthquake hazard associated with deep well injection: A report to the U.S. Environmental Protection Agency. *U.S. Geol. Surv. Bull.* 1951 (1990); http://pubs.usgs.gov/bul/1951/report.pdf.
6. E. Majer *et al.*, *Geothermics* **36**, 185–222 (2007).
7. M. K. Hubbert, W. W. Rubey, *Geol. Soc. Am. Bull.* **79**, 115–166 (1959).
8. H. Noda, N. Lapusta, *Nature* **493**, 518–521 (2013).
9. P. Segall, J. Rice, *J. Geophys. Res.* **100**, 22155–22171 (1995).
10. C. Scholz, *Nature* **391**, 37–42 (1998).
11. S. Bourouis, P. Bernard, *Geophys. J. Int.* **169**, 723–732 (2007).
12. M. Zoback, A. Kohli, I. Das, M. McClure, The importance of slow slip on faults during hydraulic fracturing stimulation of shale gas reservoirs, SPE 155476, Society of Petroleum Engineers, Americas Unconventional Resources Conference, Pittsburgh, PA, 5 to 7 June 2012.
13. Y. Guglielmi *et al.*, *Rock Mech. Rock Eng.* **47**, 303–311 (2014).
14. Laboratoire Souterrain à Bas Bruit, www.lsbb.eu
15. P. Jeanne, Y. Guglielmi, J. Lamarche, F. Cappa, L. Marie, *J. Struct. Geol.* **44**, 93–109 (2012).
16. Materials and methods are available as supplementary materials on *Science* Online.
17. B. C. Haimson, F. H. Cornet, *Int. J. Rock Mech. Min. Sci.* **40**, 1011–1020 (2003).
18. I. Das, M. Zoback, *Leading Edge (Tulsa Okla.)* **30**, 778–786 (2011).
19. J. Rutqvist, O. Stephansson, *Hydrol. J.* **11**, 7–40 (2003).
20. F. Cappa, Y. Guglielmi, J. Virieux, *Geophys. Res. Lett.* **34**, L05301 (2007).
21. F. Cappa, J. Rutqvist, *Int. J. Greenh. Gas Control* **5**, 336–346 (2011).
22. O. Scotti, F. H. Cornet, *Int. J. Rock Mech. Min. Sci. Geomech. Abstr.* **31**, 347–358 (1994).
23. H. Perfettini, J. P. Avouac, *J. Geophys. Res.* **109**, B02304 (2004).
24. C. Marone, *Annu. Rev. Earth Planet. Sci.* **26**, 643–696 (1998).
25. C. Marone, C. Scholtz, R. Bilham, *J. Geophys. Res.* **96** (B5), 8441–8452 (1991).
26. T. Tesei, C. Collettini, M. R. Barchi, B. M. Carpenter, G. Di Stefano, *Earth Planet. Sci. Lett.* **408**, 307–318 (2014).
27. B. M. Carpenter, M. M. Scuderi, C. Collettini, C. Marone, *J. Geophys. Res. Solid Earth* **119**, 9062–9076 (2014).
28. B. A. Verberne, C. R. He, C. J. Spiers, *Bull. Seismol. Soc. Am.* **100** (5B), 2767–2790 (2010).

ACKNOWLEDGMENTS

The experimental work was funded by the Agence Nationale de la Recherche (ANR) Captage de CO_2 through the HPPP-CO_2 project and by PACA through the PETRO-PRO project. The rate-and-state fault models for this study were supported by the French Academy of Sciences, the California Institute of Technology Tectonics Observatory, and the ANR HYDROSEIS under contract ANR-13-JS06-0004-01. We thank the SITES S.A.S. engineers H. Caron, C. Micollier, R. Blin, and H. Lançon, and the Petrometalic S.A. engineer J. B. Janovczyk, who jointly developed and operated the probe that enabled this experiment. We also thank the Laboratoire Souterrain à Bas Bruit (LSBB) engineers' team for their technical support during the installation of the experiment in one of the LSBB boreholes (www.lsbb.eu). Experimental data are available in the supplementary materials.

SUPPLEMENTARY MATERIALS

www.sciencemag.org/content/348/6240/1224/suppl/DC1
Materials and Methods
Figs. S1 to S6
References (*29*–*32*)
Database S1

3 March 2015; accepted 9 May 2015
10.1126/science.aab0476

NANOMATERIALS

A tunable library of substituted thiourea precursors to metal sulfide nanocrystals

Mark P. Hendricks, Michael P. Campos, Gregory T. Cleveland, Ilan Jen-La Plante, Jonathan S. Owen*

Controlling the size of colloidal nanocrystals is essential to optimizing their performance in optoelectronic devices, catalysis, and imaging applications. Traditional synthetic methods control size by terminating the growth, an approach that limits the reaction yield and causes batch-to-batch variability. Herein we report a library of thioureas whose substitution pattern tunes their conversion reactivity over more than five orders of magnitude and demonstrate that faster thiourea conversion kinetics increases the extent of crystal nucleation. Tunable kinetics thereby allows the nanocrystal concentration to be adjusted and a desired crystal size to be prepared at full conversion. Controlled precursor reactivity and quantitative conversion improve the batch-to-batch consistency of the final nanocrystal size at industrially relevant reaction scales.

The tunable electronic properties of nanometer scale crystals have inspired many synthetic methods that control crystal size and shape with extraordinary fidelity. Modern metal chalcogenide quantum dots, in particular, can be synthesized with a size that varies by less than a layer of surface atoms across the distribution. This precise control is afforded by the homogeneous nucleation and growth mechanism first described by LaMer and Dinegar to follow a three-phase sequence shown in Fig. 1A (*1*). In this mechanism, nucleation only occurs

during a brief period of time when crystal monomers ($[ME]_i$) reach a so-called "critical concentration." Modern syntheses achieve these conditions by using nanocrystal precursors that slowly convert to crystal monomers at a rate that limits the crystallization steps (Fig. 1B) (*2*–*4*). The precursor conversion reaction kinetics, therefore, plays a central role in the nucleation and growth process. In particular, the rate of monomer supply to the crystallization medium during nucleation determines the number of nanocrystals produced (*3*, *5*–*8*). Moreover, if conversion kinetics can be precisely tuned, the number of nanocrystals can be used to control the size at full conversion.

The most widely used sulfide precursors include *bis*(trimethylsilyl) sulfide [$(TMS)_2S$], phosphine sulfides ($R_3P{=}S$, where R indicates an alkyl or aryl group), and hydrogen sulfide produced by heating elemental sulfur in alkane or amine solvents (*9*). Depending on the conditions of the crystallization, a precursor is selected that provides the necessary rate of monomer supply. For example, $(TMS)_2S$ typically reacts rapidly with metal salts, allowing it to be used near room temperature; however, the rapid reactivity can lead to mixing limitations during the injection step that hinder the reaction scale. $R_3P{=}S$ derivatives, on the other hand, typically react sluggishly until ~300°C and produce low reaction yields. Although reactions of elemental sulfur with alkanes and amines are more versatile and can be used at intermediate temperatures, their conversion reactions follow ill-defined radical pathways that are difficult to control and sensitive to the presence of impurities. Further, sulfur-containing by-products contribute to batch-to-batch variability and have detrimental effects on nanocrystal properties. Recently, several phosphine chalcogenides and dichalcogenides have been investigated whose conversion kinetics depends on the organic substituents (*10*, *11*). These compounds show promise for tuning nanocrystal size and shape, but few are commercially available and others require involved, multistep syntheses.

We report a library of inexpensive and air-stable substituted thioureas whose conversion reactivity can be finely tuned over many orders of magnitude by adjusting the organic substituents (Fig. 2). The widely tunable reactivity allows an optimum chalcogen precursor to be matched with the reactivity of a metal complex at a desired reaction temperature. By controlling the monomer supply kinetics, we adjusted the extent of nucleation in syntheses of lead sulfide, cadmium sulfide, zinc sulfide, and copper sulfide nanocrystals and reliably prepared a desired size with a narrow size distribution and in quantitative yield.

Multigram quantities of air-stable *N,N′*-disubstituted and *N,N,N′*-trisubstituted thioureas are obtained in quantitative yields via a one-step "click" reaction between inexpensive, commercially available substituted isothiocyanates and primary or secondary amines (Fig. 2A). Based on the number of commercially available starting materials, we estimate that 10^3 to 10^4 structures can be accessed in a single step. In most cases, the electrophilicity of isothiocyanates makes the reaction with amines rapid at room temperature, allowing *N,N′*-diaryl; *N,N′*-dialkyl; mixed *N*-alkyl-*N′*-aryl; and *N,N,N′*-trialkylthiourea structures to be prepared (**1** to **11**).

The thiourea conversion reactivity depends on the number of substituents and their electronic and steric properties. The rate decreases as the number of substituents increases: Tetrasubstituted thioureas convert most slowly, followed by trisubstituted and then disubstituted derivatives. Thus, the substitution pattern can be used to optimize monomer supply kinetics at the desired crystallization temperature. For example, monodisperse lead sulfide nanocrystals can be synthesized from lead oleate and reactive disubstituted thioureas at temperatures from 90° to 150°C (Fig. 2D). However, monodisperse CdS nanocrystals require higher temperature conditions (150° to 250°C), where disubstituted thioureas convert at a rate that is limited by mixing during the injection. Instead, less-reactive *N,N,N′*- trialkylthioureas (**9** to **11**) or *N,N,N′,N′*-tetramethylthiourea (**12**) were found to have the appropriate conversion reactivity (fig. S1). Monodisperse zinc sulfide nanocrystals could also be obtained, but only at high temperatures (≥240°C) (fig. S2). However, the lower reactivity of zinc oleate compared with cadmium oleate allows more-reactive disubstituted thioureas to be used. In each case, the conversion reactivity could be optimized to induce nucleation shortly after injection at the temperature needed to obtain narrow size distributions. In this manner, a wide variety of metal sulfides could be synthesized—including photoluminescent core-shell nanocrystals (CdSe/CdS/ZnS), plasmonic nanocrystals ($Cu_{2-x}S$), catalyst materials (NiS), complex compound semiconductors ($CuZnSnS_4$), and one-dimensional (1D) and 2D anisotropic nanostructures (CdS nanorods, SnS nanosheets)—across a diverse set of growth media, including amine, carboxylate, and phosphonate surfactant mixtures (figs. S3 to S10).

In addition to matching the demands of the crystallization and co-reactants, tunable monomer supply can control the number of nanocrystals and thereby define a desired size after 100% yield is reached. We demonstrate this principle by optimizing an inexpensive synthesis of lead sulfide nanocrystals with diameters from 2.5 to 7.2 nm [wavelength $\lambda_{max}(1S_e - 1S_h)$ = 850 to 1800 nm, full width at half maximum (FWHM) = 30 to 160 meV] on multigram scales and in quantitative yield [as determined by the final absorbance at λ = 400 nm, where the extinction is proportional to the concentration of lead sulfide formula units within nanocrystals (*12*)] (Fig. 2D and fig. S11). To ensure highly reproducible reactivity, 100-g batches of pure, hydroxide-free lead oleate were prepared by dissolving lead oxide in trifluoroacetic anhydride solution and neutralizing the lead trifluoroacetate product with oleic acid and triethylamine (Fig. 2B and fig. S12). *N,N′*-disubstituted thioureas (**1** to **8**) react with lead oleate at temperatures at or below 150°C, providing access to colloidal PbS nanocrystals with linewidths of the $1S_e - 1S_h$ absorption that are among the narrowest reported, including at sizes relevant for PbS solar cells (*13*, *14*). Concentrated conditions also proved accessible, allowing up to 6 g of nanocrystals to be prepared in 150 ml of solvent with a high degree of reproducibility. Figure 2E shows the results of nine syntheses conducted using *N,N′*-diphenylthiourea (**2**) and six syntheses conducted using *N*-dodecyl-*N′*-phenylthiourea (**3d**) that produce between 0.2 and 6 g of nanocrystals. Within one set of conditions, a final size and size distribution are reliably obtained (Fig. 2E and fig. S13). Moreover, little change in the final size and size distribution is observed as the scale, concentration, and stoichiometry are varied (10 to 150 ml, 25 to 100 mM, 1.2:1 to 3:1 Pb:S) (Fig. 2E and fig. S13). The reproducibility and monodispersity are unusual given the high nanocrystal concentrations (up to 0.12 mM), illustrating the reliability and homogeneity provided by well-defined lead and thiourea precursors.

To determine the relationship between conversion reactivity and the final size, we monitored the kinetics of lead sulfide formation in situ by tracking the absorbance at λ = 400 nm. Lead sulfide formation approaches 100% yield within a few minutes and can be approximated by a single exponential process (fig. S15), from which rate constants [k_{obs}(**1**) to k_{obs}(**8**) (s^{-1})] are extracted. By normalizing k_{obs}(**1**) through k_{obs}(**8**) to the rate constant of the slowest precursor [k_{obs}(**8**)], we determined relative first-order rate constants

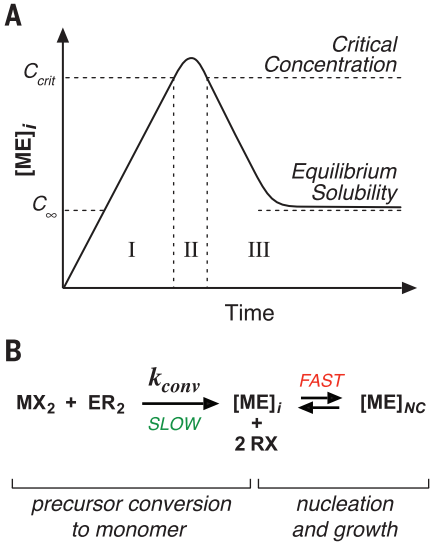
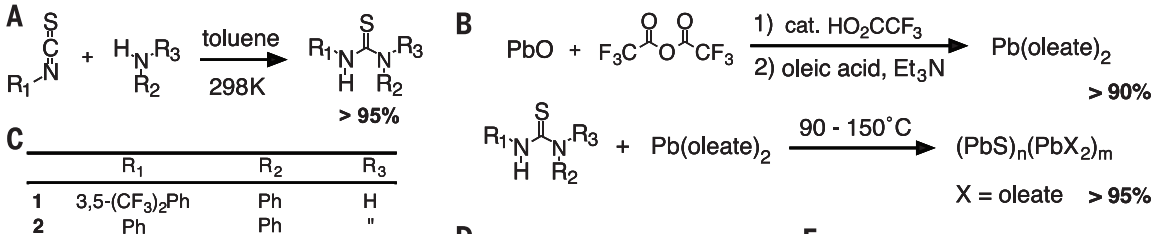


Fig. 1. The mechanism of precursor-limited homogeneous nucleation and growth of colloidal metal chalcogenide nanocrystals. (**A**) The time evolution of the monomer concentration as described by LaMer and Dinegar, where monomer supersaturation (I) precedes crystal nucleation (II) and is followed by growth (III). (**B**) Metal and chalcogen precursors (MX_2, ER_2) react and supply monomers ($[ME]_i$) to the growth medium at a rate that limits the crystallization.

Department of Chemistry, Columbia University, New York, NY 10027, USA.
*Corresponding author. E-mail: jso2115@columbia.edu



C

	R_1	R_2	R_3
1	3,5-$(CF_3)_2$Ph	Ph	H
2	Ph	Ph	"
3a	4-CN-Ph	$C_{12}H_{25}$	"
3b	4-CF_3-Ph	"	"
3c	4-Cl-Ph	"	"
3d	Ph	"	"
3e	4-Me-Ph	"	"
3f	4-MeO-Ph	"	"
4	Ph	C_6H_{13}	"
5	*t*-butyl	$C_{12}H_{25}$	"
6	*i*-propyl	"	"
7	cyclohexyl	"	"
8	C_6H_{13}	"	"
9	C_6H_{13}	C_4H_9	C_4H_9
10	"	C_8H_{17}	C_8H_{17}
11	Ph	C_4H_9	C_4H_9

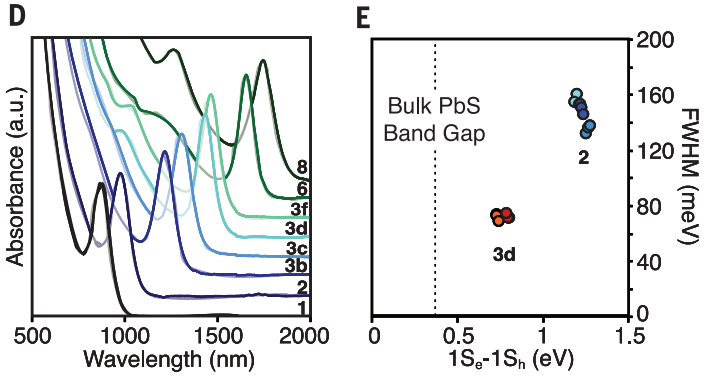
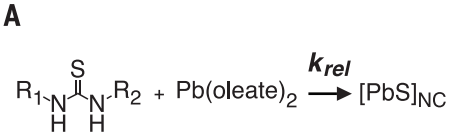


Fig. 2. A library of thioureas can be accessed in a single step and used to prepare PbS nanocrystals with highly reproducible control over the final size. (**A**) Synthesis of substituted thiourea precursors. (**B**) Synthesis of lead oleate from lead oxide and synthesis of PbS nanocrystals from substituted thioureas and lead oleate. Et, ethyl group. (**C**) Table of substituted thiourea precursor structures. Me, methyl; Ph, phenyl. (**D**) Ultraviolet–visible–near-infrared absorption spectra of PbS nanocrystals synthesized using substituted thioureas: **1** and **2** (95°C); **3b**, **c**, **d**, and **f** (120°C); **6** and **8** (150°C). a.u., arbitrary units. (**E**) Results of a reproducibility study showing the nanocrystal diameter and relative size distribution of three reactions for two different precursors (**2** and **3d**). The varying shades of dot color represent differing reaction scale, concentration, or amount of excess lead oleate used in the reaction. See fig. S14 for detailed reaction conditions.



C

	R_1	R_2	T(°C)	k_{rel}
1	3,5-CF_3-Ph	Ph	90	**4000**
2	Ph	Ph	90	**1100**
3a	*p*-CN-Ph	$C_{12}H_{25}$	120	**200**
3b	*p*-CF_3-Ph	$C_{12}H_{25}$	90, 120	**91**
3c	*p*-Cl-Ph	$C_{12}H_{25}$	120	**45**
3d	Ph	$C_{12}H_{25}$	120	**21**
3e	*p*-Me-Ph	$C_{12}H_{25}$	120	**16**
3f	*p*-OMe-Ph	$C_{12}H_{25}$	120, 150	**11**
5	*t*-butyl	$C_{12}H_{25}$	150	**19**
6	*i*-propyl	$C_{12}H_{25}$	150	**2.6**
7	cyclohexyl	$C_{12}H_{25}$	150	**2.3**
8	hexyl	$C_{12}H_{25}$	150	**1**

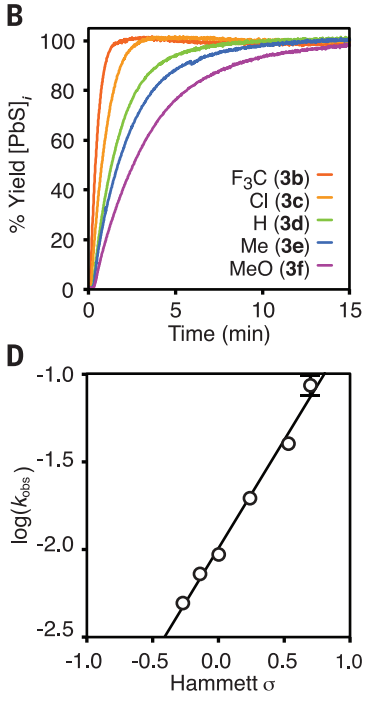


Fig. 3. The reaction of disubstituted thioureas with lead oleate in hexadecane and diphenyl ether follows single exponential kinetics, allowing the conversion rate constants to be quantitatively compared. (**A**) Schematic of PbS formation reaction used to measure conversion kinetics at 90° to 150°C. (**B**) Kinetics of lead sulfide formation as measured in situ by the absorbance at λ = 400 nm. (**C**) Effect of thiourea substitution pattern on the relative thiourea conversion rate constants [k_{rel}(**1**) to k_{rel}(**8**), e.g., k_{rel}(**7**) = k(**7**)/k(**8**)]. The wide range of reactivity requires that kinetics are measured at multiple temperatures. To account for the temperature dependence of the conversion rate constant, **3b** and **3f** were measured at two temperatures, and the change in rate constant was used to normalize the relative rate constants of the respective temperatures {e.g., k_{rel}(**3b**) = [k(**3b**)$^{120°C}$/k(**8**)$^{150°C}$] × [k(**3f**)$^{150°C}$/k(**3f**)$^{120°C}$]}. (**D**) Hammett plot illustrating the well-defined relationship between the electronic structure of the thiourea and the rate of lead sulfide formation.

[k_{rel}(**1**) to k_{rel}(**8**)] across a range of temperatures (90° to 150°C), allowing the reactivity to be quantitatively compared over more than three orders of magnitude (Fig. 3C). These measurements show a well-defined dependence of the conversion reactivity on the thiourea structure that is defined by the substituents.

Within the disubstituted thiourea derivatives, the conversion rate constants decrease over three orders of magnitude upon replacing electron-withdrawing aryl substituents with alkyl substituents. Thus, *N*,*N*′-diarylthioureas such as *N*-(3,5-*bis*-trifluoromethylphenyl)-*N*′-phenylthiourea (**1**) convert most rapidly, whereas *N*,*N*′-di-*n*-alkylthioureas (**8**) react 4000-fold more slowly. Similar reactivity trends were found with cadmium oleate (fig. S16). Mixed *N*-alkyl-*N*′-aryl variants showed intermediate reactivity toward lead oleate that can be finely adjusted by appending electron withdrawing or donating substituents on the aromatic ring. The conversion rate constants of para-substituted *N*-*p*-X-phenyl-*N*′-*n*-dodecylthioureas (**3a** to **3f**, where X = CN, CF3, Cl, H, Me, MeO) increase by a factor of 20 as the para-substituent becomes increasingly electron withdrawing. The logarithms of the observed first-order rate constants are plotted versus the Hammett sigma parameter of the para-substituent in Fig. 3D (*15*). A linear relationship is observed, demonstrating the well-behaved dependence of conversion kinetics on the thiourea acidity.

A large positive slope (ρ = 1.3) indicates a buildup of negative charge during the conversion reaction. These results can be explained by rate-limiting deprotonation of the thiourea or nucleophilic attack on the thiocarbonyl carbon. Conversion of **3d** is faster in the presence of tri-*n*-butylamine and slower when oleic acid

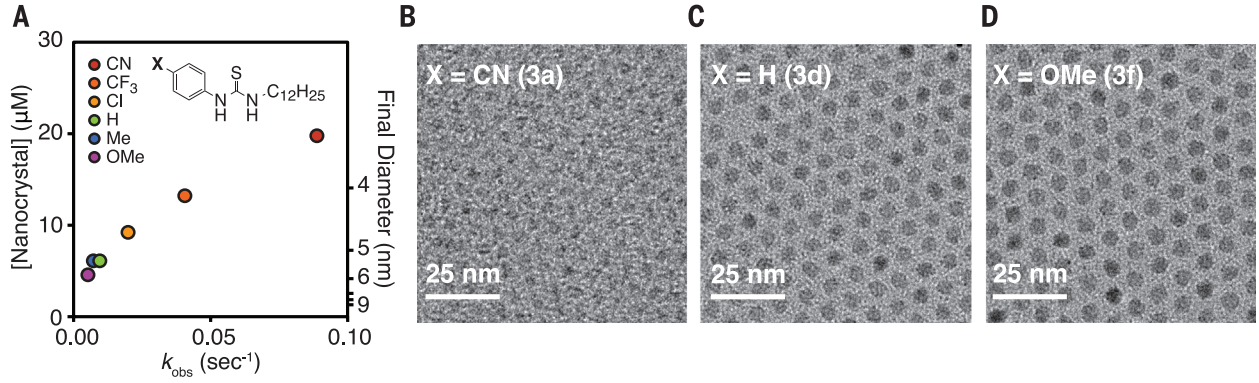


Fig. 4. Increasing thiourea conversion reactivity produces a higher nanocrystal concentration and a smaller final nanocrystal diameter. (**A**) Nanocrystal concentration and final diameter plotted versus the rate constant of lead sulfide formation (k_{obs}) for **3a** to **3f** ($[Nanocrystal]_t \propto [PbS]_t/(r_t^3)$, where t is time and r is the nanocrystal radius at time t). (**B** to **D**) Transmission electron micrographs of PbS nanocrystals synthesized under reaction conditions used for kinetics experiments (**3a**, **3d**, and **3f**).

is present, both of which suggest that deprotonation of the thiourea precedes the formation of lead sulfide. Deprotonation of thiourea in water is known to speed its hydrolysis to cyanamide (*16*). Increasing steric bulk of the thiourea substituents also speeds the rate of conversion (**5** to **8**); the increased bulk may accelerate elimination of lead sulfide from an intermediate lead thioureate complex formed by deprotonation of a lead-bound thiourea. Although detailed work is required to determine the precise conversion mechanism, these observations highlight the importance of the microscopic steps leading to the rate-determining precursor conversion step, which vary depending on the surfactants used as well as the nature of the metal co-reactant.

The nanocrystal concentrations obtained from **3a** to **3f** are plotted versus k_{obs} in Fig. 4A, where an eightfold increase in the conversion rate leads to a fourfold increase in the nanocrystal concentration. The finely tuned monomer supply kinetics controls the extent of nucleation, because the rate of Ostwald ripening is negligibly slow under these conditions (Fig. 4A and fig. S17). A similar dependence is observed in studies of zinc sulfide, copper sulfide, nickel sulfide, and cadmium sulfide nanocrystals (figs. S2, S4, S5, and S16). Tuning the precursor reactivity can also be used to finely control the aspect ratio of CdS nanorods; thioureas of decreasing reactivity (**3f**, **9**, and **12**) lead to a systematic increase in the volume and rod aspect ratio, a trend that results from the lower nanocrystal concentration produced by slower conversion kinetics (figs. S7 to S9) (*17*).

Previous experimental and theoretical work on cadmium selenide and silver halides reported a similar correlation between the concentration of nanocrystals and the precursor conversion rate during nucleation (*3*, *5*–*7*, *18*). The correlation results from a nucleation process that continues until the collective consumption of monomers by growing nuclei exceeds monomer production by precursor conversion. At this point, the concentration of nuclei is sufficiently high to cause the supersaturation to drop and the nucleation process to end. A "critical" dependence of the nucleation rate on monomer supersaturation, like the one predicted by classical nucleation theory, is expected to produce a linear relationship between the nanocrystal concentration and the precursor conversion rate during nucleation (*5*, *6*). However, a subcritical dependence can be observed in Fig. 4A that will require more accurate models of nucleation to explain. Nonetheless, the smooth correlation between precursor conversion rate and nanocrystal concentration can be used to predictably obtain a desired nanocrystal size.

Controlling the final size with the precursor reaction rate rather than modifying the crystallization medium (e.g., reaction temperature, solvent, and surfactant concentration), or limiting the conversion, greatly simplifies the nanocrystal composition because both the starting materials as well as the reaction by-products can bind the nanocrystals (*19*). Although the thiourea conversion by-products were not found to bind the nanocrystals in this case (fig. S18), cadmium and lead oleate precursors are known to reversibly bind and passivate nanocrystal surfaces, and their coverage may depend on the concentration of these complexes remaining after conversion (*20*).

Tuning size with precursor reactivity and running reactions to full conversion allows the final ratio of lead sulfide product and unconverted lead oleate to be determined by the amounts of reactants used. This advance enables a standard purification procedure to be optimized to reproducibly control the final oleate ligand shell and nanocrystal stoichiometry. Moreover, by using preformed lead oleate, syntheses run at or below 120°C can be conducted in low-boiling solvents like 1-octene that are conveniently distilled under vacuum after completion of the synthesis. This reduces the volume of solvent used during the isolation and facilitates large-scale reactions. For example, nanocrystals with a 3.4-nm diameter were synthesized on a 3-g scale from a 1.5:1 lead oleate–to–**2** mixture and isolated with 5.7 oleates per square nanometer of surface area, from which we estimate a Pb:S ratio of 1.26. Larger nanocrystals (6.5 nm) with a lower surface area–to–volume ratio were synthesized on a 6-g scale with a lower lead oleate–to–**3d** ratio (1.2:1) and isolated with 2.9 oleates nm^{-2}, from which we estimate a Pb:S ratio of 1.07 (fig. S18). In both cases, the purification is greatly simplified compared with methods where the conversion is limited. Rather than removing a large excess of unreacted metal precursor—a process that is complicated by the polymeric structures and low solubilities of zinc, cadmium, and lead carboxylates, phosphonates, and halides—a desired amount of remaining metal precursor can be chosen by the starting metal-to-sulfur ratio. Thus, obtaining a desired size at complete conversion is an important step toward reproducibly defining the surface structure and optoelectronic properties at large reaction scales.

Tailoring precursor reactivity will greatly advance our ability to rationally design high-performance materials and to relate atomic structure to nanocrystal function. In particular, highly reproducible syntheses of PbS nanocrystals with narrow size distributions and well-defined surface chemistry can advance the systematic development of solution-processed nanocrystal photovoltaics. Tunable sulfide precursors will also advance the synthesis of complex metal chalcogenide alloys and heterostructures used in solid-state lighting and luminescent displays. More broadly, these results highlight the value of rationally controlling the nanocrystal synthesis mechanism to obtain a desired nanocrystal product in high yields and with a high degree of batch-to-batch consistency.

REFERENCES AND NOTES

1. V. K. LaMer, R. H. Dinegar, *J. Am. Chem. Soc.* **72**, 4847–4854 (1950).
2. H. Liu, J. S. Owen, A. P. Alivisatos, *J. Am. Chem. Soc.* **129**, 305–312 (2007).
3. J. S. Owen, E. M. Chan, H. Liu, A. P. Alivisatos, *J. Am. Chem. Soc.* **132**, 18206–18213 (2010).
4. M. P. Hendricks, B. M. Cossairt, J. S. Owen, *ACS Nano* **6**, 10054–10062 (2012).
5. T. Sugimoto, F. Shiba, T. Sekiguchi, H. Itoh, *Colloids Surf. A Physicochem. Eng. Asp.* **164**, 183–203 (2000).
6. T. Sugimoto, F. Shiba, *Colloids Surf. A Physicochem. Eng. Asp.* **164**, 205–215 (2000).
7. S. Abe, R. K. Čapek, B. De Geyter, Z. Hens, *ACS Nano* **6**, 42–53 (2012).

8. J. Y. Rempel, M. G. Bawendi, K. F. Jensen, *J. Am. Chem. Soc.* **131**, 4479–4489 (2009).
9. R. García-Rodríguez, M. P. Hendricks, B. M. Cossairt, H. Liu, J. S. Owen, *Chem. Mater.* **25**, 1233–1249 (2013).
10. T. P. A. Ruberu *et al.*, *ACS Nano* **6**, 5348–5359 (2012).
11. Y. Guo, S. R. Alvarado, J. D. Barclay, J. Vela, *ACS Nano* **7**, 3616–3626 (2013).
12. I. Moreels *et al.*, *ACS Nano* **3**, 3023–3030 (2009).
13. M. C. Weidman, M. E. Beck, R. S. Hoffman, F. Prins, W. A. Tisdale, *ACS Nano* **8**, 6363–6371 (2014).
14. C.-H. M. Chuang, P. R. Brown, V. Bulović, M. G. Bawendi, *Nat. Mater.* **13**, 796–801 (2014).
15. C. D. Ritchie, W. F. Sager, *Prog. Phys. Org. Chem.* **2**, 323–400 (1964).
16. G. Marcotrigiano, G. Peyronel, R. Battistuzzi, *J. Chem. Soc. Perkin Trans. 2* **1972**, 1539 (1972).
17. F. Wang, W. Buhro, *J. Am. Chem. Soc.* **134**, 5369–5380 (2012).
18. G. G. Yordanov, C. D. Dushkin, E. Adachi, *Colloids Surf. A Physicochem. Eng. Asp.* **316**, 37–45 (2008).
19. D. Zherebetskyy *et al.*, *Science* **344**, 1380–1384 (2014).
20. N. C. Anderson, M. P. Hendricks, J. J. Choi, J. S. Owen, *J. Am. Chem. Soc.* **135**, 18536–18548 (2013).

ACKNOWLEDGMENTS

Precursor design and kinetics studies were supported by the Center for Re-Defining Photovoltaic Efficiency Through Molecule Scale Control, an Energy Frontier Research Center funded by the U.S. Department of Energy, Office of Science, Office of Basic Energy Sciences, under award no. DE-SC0001085. Large-scale syntheses and surface chemistry measurements were supported by the Department of Energy under grant no. DE-SC0006410. The authors thank A. N. Beecher and E. Auyeung for assistance with transmission electron microscopy, which was carried out in part at the New York Structural Biology Center, supported by Empire State Development's Division of Science, Technology and Innovation and the National Center for Research Resources, NIH, grant no. C06 RR017528-01-CEM. We also thank E. Busby and M. Sfier for assistance with near-infrared (NIR) photoluminescence, which was carried out in part at the Center for Functional Nanomaterials, Brookhaven National Laboratory, Office of Basic Energy Sciences, under contract no. DE-AC02-98CH10886. Z. M. Norman is thanked for assistance with Fourier transform–infrared spectroscopy studies and A. S. R. Chesman for helpful advice concerning the synthesis and characterization of copper zinc tin sulfide. A series of patent applications on this subject have been filed.

SUPPLEMENTARY MATERIALS

www.sciencemag.org/content/348/6240/1226/suppl/DC1
Materials and Methods
Figs. S1 to S20
References (*21*–*27*)

13 November 2014; accepted 1 May 2015
10.1126/science.aaa2951

ELECTROCHEMISTRY

High-performance transition metal–doped Pt_3Ni octahedra for oxygen reduction reaction

Xiaoqing Huang,[1,2]*† Zipeng Zhao,[1,2]* Liang Cao,[3] Yu Chen,[1,2] Enbo Zhu,[1,2] Zhaoyang Lin,[4] Mufan Li,[4] Aiming Yan,[5,6,7] Alex Zettl,[5,6,7] Y. Morris Wang,[8] Xiangfeng Duan,[2,4] Tim Mueller,[9]‡ Yu Huang[1,2]‡

Bimetallic platinum-nickel (Pt-Ni) nanostructures represent an emerging class of electrocatalysts for oxygen reduction reaction (ORR) in fuel cells, but practical applications have been limited by catalytic activity and durability. We surface-doped Pt_3Ni octahedra supported on carbon with transition metals, termed *M*-Pt_3Ni/C, where *M* is vanadium, chromium, manganese, iron, cobalt, molybdenum (Mo), tungsten, or rhenium. The Mo-Pt_3Ni/C showed the best ORR performance, with a specific activity of 10.3 mA/cm^2 and mass activity of 6.98 A/mg_{Pt}, which are 81- and 73-fold enhancements compared with the commercial Pt/C catalyst (0.127 mA/cm^2 and 0.096 A/mg_{Pt}). Theoretical calculations suggest that Mo prefers subsurface positions near the particle edges in vacuum and surface vertex/edge sites in oxidizing conditions, where it enhances both the performance and the stability of the Pt_3Ni catalyst.

Proton-exchange membrane (PEM) fuel cells use reactions between the fuel (such as hydrogen or alcohols) at the anode and the oxidant (molecular oxygen) at the cathode (*1*–*3*). Both cathode and anode reactions need catalysts to lower their electrochemical overpotential for high-voltage output, and so far, platinum (Pt) has been the universal choice (*4*–*6*). To fully realize the commercial viability of fuel cells, the following challenges, which may not be strictly independent of one another, need to be simultaneously addressed: the high cost of Pt, the sluggish kinetics of the oxygen reduction reaction (ORR), and the low durability of the catalysts (*7*–*11*).

Alloying Pt with a secondary metal reduces the usage of scarce Pt metal while at the same time improving performance as compared with that of pure Pt on mass activity (*12*–*15*), which has led to the development of active and durable Pt-based electrocatalysts with a wide range of compositions (*16*–*20*). However, although studies so far have led to a considerable increase in ORR activity, the champion activity as observed on bulk $Pt_3Ni(111)$ surface has not been matched in nanocatalysts (*21*–*25*), indicating room for further improvement. At the same time, one noted major limitation of Pt-Ni nanostructures is their low durability. The Ni element in these nanostructures leaches away gradually under detrimental corrosive ORR conditions, resulting in rapid performance losses (*23*–*27*). Thus, synthesizing Pt-based nanostructures with simultaneously high catalytic activity and durability remains an important open challenge (*28*).

Because surface and near-surface features of a catalyst have a strong influence on its catalytic performance, we adopted a surface engineering strategy to further explore and enhance the performance of $Pt_3Ni(111)$ nanocatalysts. We specifically focused our efforts on Pt_3Ni-based nanocatalysts because the bulk extended $Pt_3Ni(111)$ surface has been shown to be one of the most efficient catalytic surfaces for the ORR. On the basis of the control over dopant incorporation of various transition metals onto the surface of dispersive and octahedral Pt_3Ni/C (termed as *M*-Pt_3Ni/C, where *M* = V, Cr, Mn, Fe, Co, Mo, W, or Re), we have developed ORR catalysts that exhibit both high activity and stability. In particular, our Mo-Pt_3Ni/C catalyst has high specific activity (10.3 mA/cm^2), high mass activity (6.98 A/mg_{Pt}), and substantially improved stability for 8000 potential cycles.

We prepared highly dispersed Pt_3Ni octahedra on commercial carbon black by means of an efficient one-pot approach without using any bulky capping agents, which used platinum(II) acetylacetonate [$Pt(acac)_2$] and nickel(II) acetylacetonate [$Ni(acac)_2$] as metal precursors, carbon black as support, *N*,*N*-dimethylformamide (DMF) as solvent and reducing agent, and benzoic acid as the structure-directing agent (fig. S1A). The surface doping for the Pt_3Ni/C catalyst was initiated by the addition of dopant precursors, $Mo(CO)_6$, together with $Pt(acac)_2$ and $Ni(acac)_2$ into a suspension of Pt_3Ni/C in DMF, and the subsequent reaction at 170°C for 48 hours (fig. S1B). The transmission electron microscopy (TEM) and high-angle annular dark-field scanning TEM (HAADF-STEM) images of the Pt_3Ni/C and Mo-Pt_3Ni/C catalysts (Fig. 1, A and B, and fig. S2) revealed highly dispersive octahedral nanocrystals (NCs) in both samples, which were substantially uniform in size, averaging 4.2 ± 0.2 nm in

[1]Department of Materials Science and Engineering, University of California, Los Angeles, CA 90095, USA. [2]California NanoSystems Institute (CNSI), University of California, Los Angeles, CA 90095, USA. [3]Department of Physics and Astronomy, Johns Hopkins University, Baltimore, MD 21218, USA. [4]Department of Chemistry and Biochemistry, University of California, Los Angeles, CA 90095, USA. [5]Department of Physics and Center of Integrated Nanomechanical Systems, University of California, Berkeley, CA 94720, USA. [6]Materials Sciences Division, Lawrence Berkeley National Laboratory, Berkeley, CA 94720, USA. [7]Kavli Energy NanoSciences Institute at the University of California, Berkeley, and the Lawrence Berkeley National Laboratory, Berkeley, CA 94720, USA. [8]Physical and Life Sciences Directorate, Lawrence Livermore National Laboratory (LLNL), Livermore, CA 94550, USA. [9]Department of Materials Science and Engineering, Johns Hopkins University, Baltimore, MD 21218, USA.
*These authors contributed equally to this work. †Present address: College of Chemistry, Chemical Engineering and Materials Science, Soochow University, 215123 Suzhou, China. ‡**Corresponding author. E-mail: tmueller@jhu.edu (T.M.); yhuang@seas.ucla.edu (Y.H.)**

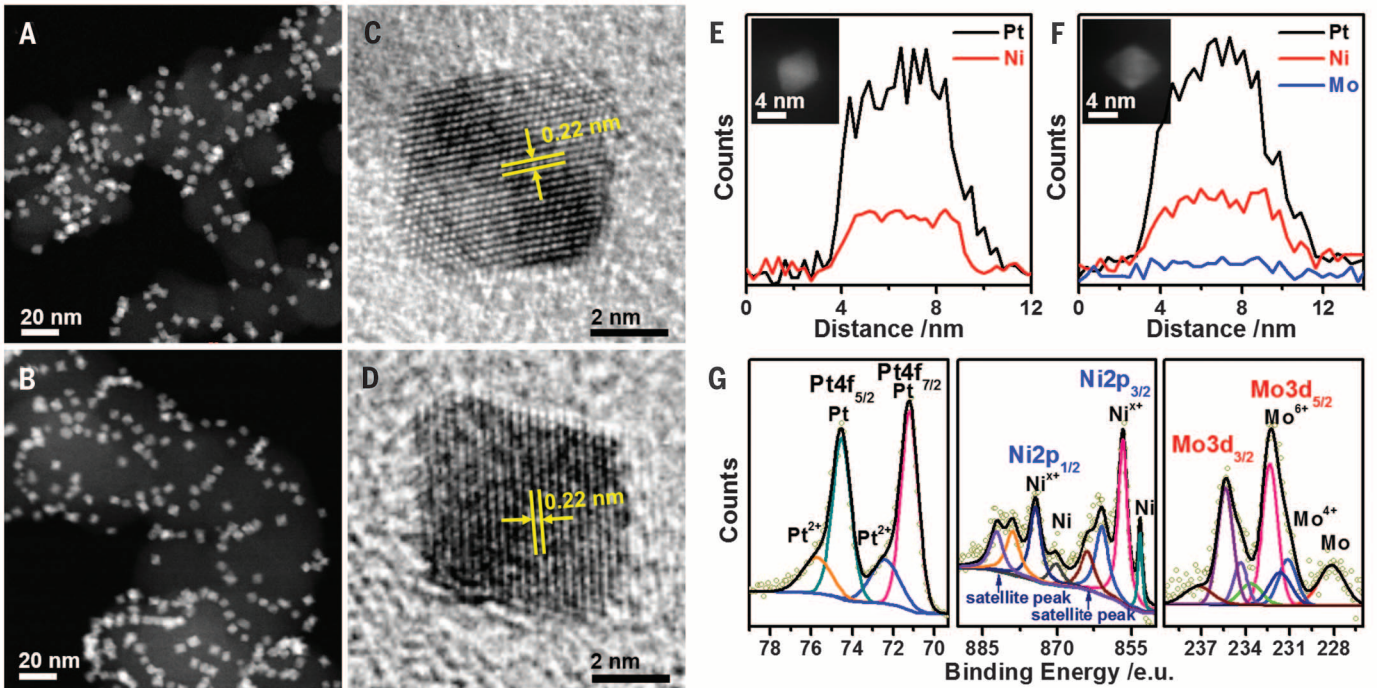


Fig. 1. Schematic illustration of the fabrication process and the structure analyses for the transition metal–doped Pt_3Ni/C catalysts. (**A** and **B**) Representative HAADF-STEM images of the (A) Pt_3Ni/C and (B) Mo-Pt_3Ni/C catalysts. (**C** and **D**) HRTEM images on individual octahedral (C) Pt_3Ni/C and (D) Mo-Pt_3Ni/C nanocrystals. (**E** and **F**) EDS line-scanning profile across individual (E) Pt_3Ni/C and (F) Mo-Pt_3Ni/C octahedral nanocrystals. (**G**) Pt, Ni, and Mo XPS spectra for the octahedral Mo-Pt_3Ni/C catalyst.

edge length. High-resolution TEM (HRTEM) images taken from individual octahedra showed a single-crystal structure with well-defined fringes (Fig. 1, C and D) and an edge lattice spacing of 0.22 nm, which is consistent with that expected for face-centered cubic (fcc) Pt_3Ni.

For Pt_3Ni, powder x-ray diffraction (PXRD) patterns of the colloidal products displayed typical peaks that could be indexed as those of fcc Pt_3Ni (fig. S3) (*29*, *30*), and the Pt/Ni composition of 74/26 was confirmed by means of both inductively coupled plasma atomic emission spectroscopy (ICP-AES) and TEM energy-dispersive x-ray spectroscopy (TEM-EDS) (fig. S4 and table S1). Composition line-scan profiles across octahedra obtained by means of HAADF-STEM-EDS for Pt_3Ni/C (Fig. 1E) and Mo-Pt_3Ni/C (Fig. 1F) showed that all elements were distributed throughout the NCs (Fig. 1, E and F). For the doped NCs, x-ray photoelectron spectroscopy (XPS) shows the presence of Pt, Ni, and Mo in the catalyst (Fig. 1G). The Ni 2p and Pt 4f XPS spectra of the Mo-Pt_3Ni/C catalyst showed that the majority of the surface Ni was in the oxidized state and that the surface Pt was mainly in the metallic state, which were consistent with a recent Pt-Ni catalysts–based study (*28*). Mo exhibits mainly Mo^{6+} and Mo^{4+} states, which is in agreement with previous studies of PtMo nanoparticles (*31*). The overall molar ratio for Pt, Ni, and Mo obtained from ICP-AES was 73.4:25.0:1.6.

To assess ORR catalytic activity, we used cyclic voltammetry (CV) to evaluate the electrochemically active surface areas (ECSAs). Our catalysts were loaded (with the same Pt mass loading) onto

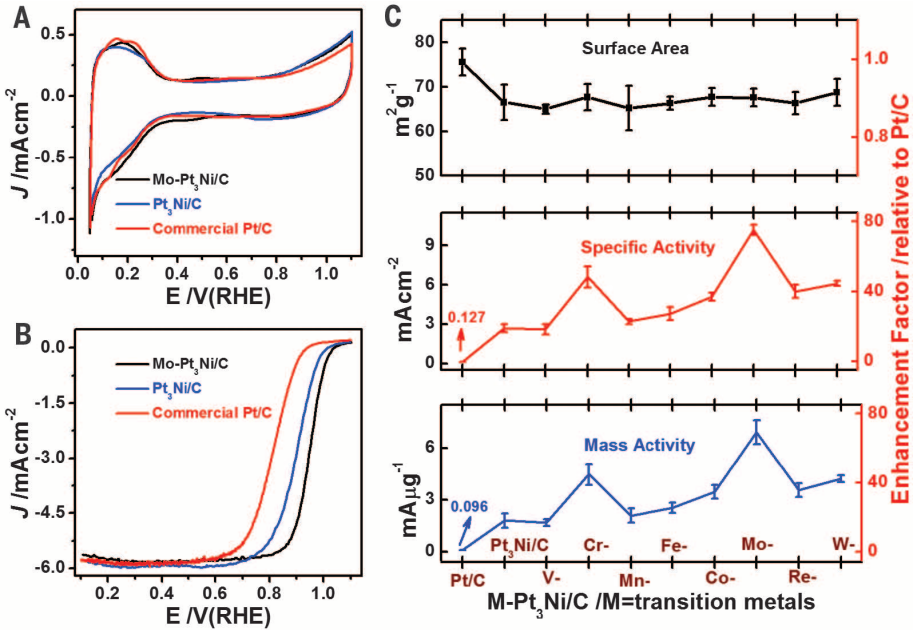


Fig. 2. Electrocatalytic properties of high-performance transition metal–doped octahedral Pt_3Ni/C catalysts and a commercial Pt/C catalyst. (**A**) Cyclic voltammograms of octahedral Mo-Pt_3Ni/C, octahedral Pt_3Ni/C, and commercial Pt/C catalysts recorded at room temperature in N_2-purged 0.1 M $HClO_4$ solution with a sweep rate of 100 mV/s. (**B**) ORR polarization curves of octahedral Mo-Pt_3Ni/C, octahedral Pt_3Ni/C, and commercial Pt/C catalysts recorded at room temperature in an O_2-saturated 0.1 M $HClO_4$ aqueous solution with a sweep rate of 10 mV/s and a rotation rate of 1600 rotations per min (rpm). (**C**) The electrochemically active surface area (ECSA, top), specific activity (middle), and mass activity (bottom) at 0.9 V versus RHE for these transition metal–doped Pt_3Ni/C catalysts, which are given as kinetic current densities normalized to the ECSA and the loading amount of Pt, respectively. In (A) and (B), current densities were normalized in reference to the geometric area of the RDE (0.196 cm^2).

glassy carbon electrodes. A commercial Pt/C catalyst [20 weight percent (wt %) Pt on carbon black; Pt particle size, 2 to 5 nm] obtained from Alfa-Aesar was used as a baseline catalyst for comparison (fig. S5). The CV curves on these different catalysts are compared in Fig. 2A. We calculated the ECSA by measuring the charge collected in the hydrogen adsorption/desorption region (between 0.05 and 0.35 V) after double-layer correction and assuming a value of 210 $\mu C/cm^2$ for the adsorption of a hydrogen monolayer. The octahedral Pt_3Ni/C and Mo-Pt_3Ni/C catalysts display similar and high ECSAs of 66.6 and 67.5 m^2/g_{Pt}, respectively, which is comparable with that of the commercial Pt/C catalyst (75.6 m^2/g_{Pt}) (Fig. 2C, top).

The ORR polarization curves for the different catalysts, which were normalized by the area of the glassy carbon area (0.196 cm^2), are shown in Fig. 2B. The polarization curves display two distinguishable potential regions: the diffusion-limiting current region below 0.6 V and the mixed kinetic-diffusion control region between 0.6 and 1.1 V. We calculated the kinetic currents from the ORR polarization curves by considering the mass-transport correction (*32*). In order to compare the activity for different catalysts, the kinetic currents were normalized with respect to both ECSA and the loading amount of metal Pt. As shown in Fig. 2C, the octahedral Mo-Pt_3Ni/C exhibits a specific activity of 10.3 mA/cm^2 at 0.9 V versus a reversible hydrogen electrode (RHE). In contrast, the specific activity of the undoped Pt_3Ni/C catalyst is ~2.7 mA/cm^2. On the basis of the mass loading of Pt, the mass activity of the Mo-Pt_3Ni/C catalyst was calculated to be 6.98 A/mg_{Pt}. The specific activity of the Mo-Pt_3Ni/C catalyst represents an improvement by a factor of 81 relative to the commercial Pt/C catalyst, whereas the mass activity of the Mo-Pt_3Ni/C catalyst achieved a 73-fold enhancement. To compare the activities of our catalysts with the state-of-the-art reported Pt-Ni catalysts, we also calculated the catalytic activities of our catalysts at 0.95 V and with the ECSA calculated with the CO stripping method. Whether we calculated at 0.90 or 0.95 V or used the ECSA based on Hupd and/or CO stripping, both the specific activity and the mass activity of the Mo-Pt_3Ni/C (fig. S6) are higher than those of the state-of-the-art Pt-Ni catalysts (*21*, *24*), including the recently reported Pt-Ni nanoframes catalyst (Table 1 and table S2) (*28*).

Because Mo-Pt_3Ni/C exhibited an exceptional activity toward ORR, we further examined the doping effects for Pt_3Ni/C modified by other transition metals. Pt_3Ni/C catalysts doped with seven other transition metals—V, Cr, Mn, Fe, Co, W, or Re—were synthesized in a similar fashion with metal carbonyls (figs. S7 and S8 and table S1; details are available in the supplementary materials), and their catalytic activity toward the ORR was tested under the same conditions (Fig. 2C; individual sample measurements are available in fig. S9). The ECSAs of these transition metal–doped Pt_3Ni/C catalysts were all similar (Fig. 2C, top), but variable ORR activities were observed for differently doped Pt_3Ni/C catalysts. None of the other dopants resulted in a catalyst with activity as high as that of the Mo-Pt_3Ni/C (Fig. 2C, middle). The change of mass activities in various *M*-doped Pt_3Ni/C catalysts was also similar to that of the specific activities (Fig. 2C, bottom), with Mo-Pt_3Ni/C showing the highest activity.

We further evaluated the electrochemical durability of the Mo-Pt_3Ni/C catalyst using the accelerated durability test (ADT) between 0.6 and 1.1 V (versus RHE, 4000 and 800 cycles) in O_2-saturated 0.1 M $HClO_4$ at a scan rate of 50 mV/s. The Pt_3Ni/C catalyst was used as a baseline catalyst

Table 1. Performance of Mo-Pt_3Ni/C catalyst and several representative results with high performance from recent published works. NA, not availlable.

	Catalyst	Based on H_{upd}					Based on CO stripping		
		ECSA (m^2/g_{Pt})	Specific activity (mA/cm^2)		Mass activity (A/mg_{Pt})		ECSA (m^2/g_{Pt})	Specific activity (mA/cm^2)	
			@ 0.9 V	@ 0.95 V	@ 0.9 V	@ 0.95 V		@ 0.9 V	@ 0.95 V
This work	Mo-Pt_3Ni/C	67.7	10.3	2.08	6.98	1.41	83.9	8.2	1.74
This work	Pt_3Ni/C	66.6	2.7	0.55	1.80	0.37	81.9	2.2	0.45
(*53*)	PtNi/C	50	3.14	NA	1.45	NA	NA	NA	NA
(*24*)	PtNi/C	48	3.8	NA	1.65	NA	NA	NA	NA
(*21*)	$PtNi_{2.5}/C$	21	NA	NA	3.3	NA	31	NA	NA
(*28*)	Pt_3Ni/C nanoframes	NA	NA	NA	5.7	0.97	NA	NA	1.48

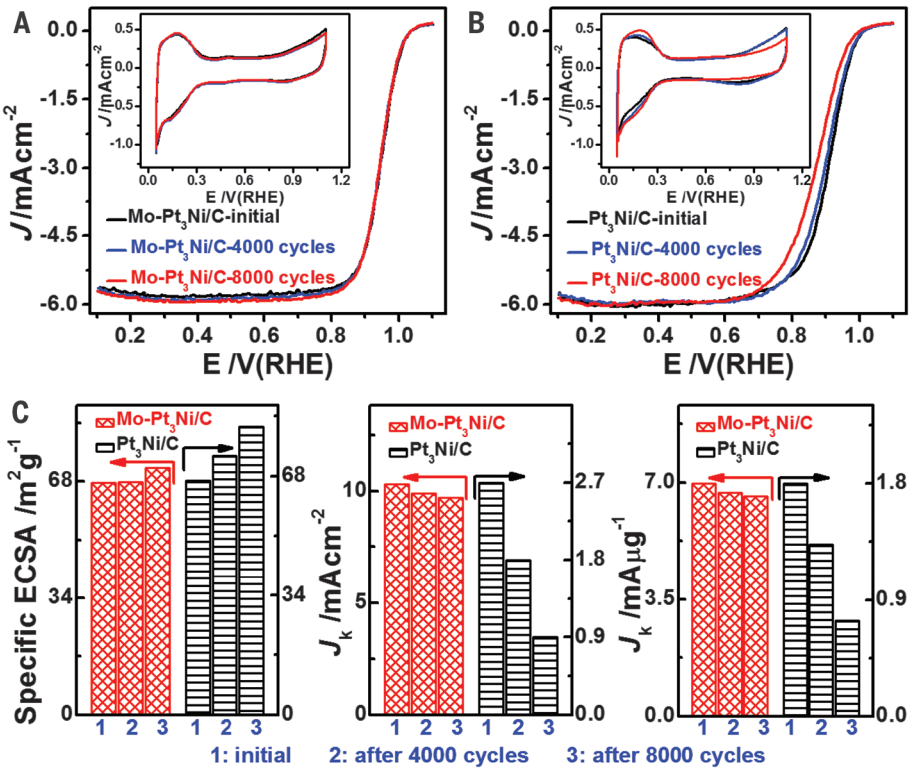


Fig. 3. Electrochemical durability of the high-performance octahedral Mo-Pt_3NiCo/C catalyst and octahedral Pt_3Ni/C catalyst. (**A** and **B**) ORR polarization curves and (inset) corresponding cyclic voltammograms of (A) the octahedral Mo-Pt_3Ni/C catalyst and (B) the octahedral Pt_3Ni/C catalyst before, after 4000, and after 8000 potential cycles between 0.6 and 1.1 V versus RHE. (**C**) The changes of ECSAs (left), specific activities (middle), and mass activities (right) of the octahedral Mo-Pt_3Ni/C catalyst and octahedral Pt_3Ni/C catalyst before, after 4000, and after 8000 potential cycles. The durability tests were carried out at room temperature in O_2-saturated 0.1 M $HClO_4$ at a scan rate of 50 mV/s.

for comparison. After 4000 and 8000 potential cycles, the Mo-Pt_3Ni/C catalyst largely retained its ECSA and activity (Fig. 3A), exhibiting only 1- and 3-mV shifts for its half-wave potential, respectively. And after 8000 cycles, the activity of the Mo-Pt_3Ni/C catalyst was still as high as 9.7 mA/cm^2 and 6.6 A/mg_{Pt} (Fig. 3C), showing only 6.2 and 5.5% decreases from the initial specific activity and mass activity, respectively. On the other hand, the undoped Pt_3Ni/C catalyst was unstable under the same reaction conditions. Its polarization curve showed a 33-mV negative shift after durability tests (Fig. 3B), and the Pt_3Ni/C retained only 33 and 41% of the initial specific activity and mass activity, respectively, after 8000 cycles (Fig. 3C). The morphology and the composition of the electrocatalysts after the durability change were further examined. As shown in fig. S4, although the size of the Pt_3Ni/C octahedra were largely maintained, their morphologies became more spherical. This change of the morphology likely resulted from the Ni loss after the potential cycles, as confirmed by means of EDS and XPS analyses (the Pt/Ni composition ratio changed from 74.3/25.7 to 88.1/11.9) (figs. S4 and S10). In contrast, the corresponding morphology of the Mo-Pt_3Ni/C catalyst largely maintained the octahedral shape, and the composition change was negligible (from 73.4/25.0/1.6 to 74.5/24.0/1.5).

To investigate the cause of the enhanced durability of the Mo-Pt_3Ni/C catalysts, cluster expansions of Pt-Ni-Mo NCs were used in Monte Carlo simulations (*33*–*35*) to identify low-energy NC and (111) surface structures for computational analysis (details of our calculations are provided in the supplementary materials). In vacuum, the equilibrium structures predicted by the cluster expansion have a Pt skin, with Mo atoms preferring sites in the second atomic layer along the edges connecting two different (111) facets (Fig. 4, A and B, and fig. S11). Density functional theory (DFT) (*36*) calculations indicate that in vacuum, the subsurface site is preferable to the lowest-energy neighboring surface site, but in the presence of adsorbed oxygen, there is a strong driving force for Mo to segregate to the surface, where it was found to be most stable on a vertex site. This suggests the formation of surface Mo-oxide species, which is consistent with our XPS measurements. Our calculations indicate that the formation of surface Mo-oxide species may contribute to improved stability by "crowding out" surface Ni. Our computational prediction that Mo favors sites near the particle edges and vertices is consistent with the dopant distributions for Fe shown in our STEM electron energy loss spectroscopy (EELS) line scan results (fig. S12).

Our calculations suggest that doping the NCs with Mo directly stabilizes both Ni and Pt atoms against dissolution and may inhibit diffusion through the formation of relatively strong Mo-Pt and Mo-Ni bonds. Calculations on a representative nanoparticle with dimensions and composition comparable with those observed experimentally (fig. S13) indicate that a Mo on an edge or vertex site increases the energy required to remove a Pt atom from a neighboring edge or vertex site by an average of 362 meV, with values ranging from 346 to 444 meV, and to remove a Ni atom by an average of 201 meV, with values ranging from 160 to 214 meV. These predictions are consistent with our ADT results (fig. S14). The evidence that Mo may have a stabilizing effect on undercoordinated sites suggests that Mo atoms may also pin step edges on the surface, inhibiting the dissolution process.

Although the exact mechanisms by which the surface-doped Pt_3Ni shows exceptional catalytic performance demand more detailed studies, local changes in oxygen binding energies provide a possible explanation for some of the observed increase in specific activity. A Sabatier volcano of ORR catalysts predicts that ORR activity will be maximized when the oxygen binding energy is ~0.2 eV less than the binding energy on Pt(111) (*37*). Our calculations indicate that sites near the particle edge bind oxygenated species too strongly, such as in Pt(111), and sites near the facets of the particles bind oxygenated species too weakly, such as in Pt_3Ni(111) (Fig. 4C). However, compared with the undoped NC, the oxygen binding energies in the doped NC near the Mo atoms are decreased by up to 154 meV, and binding energies at sites closer to the center of the (111) facet are increased by up to 102 meV (Fig. 4D). Thus, if Mo migrates to the thermodynamically favored sites near the particle edges, it may shift the oxygen binding energies at these sites closer to the peak of the volcano plot. Similarly, Mo doping may increase the oxygen binding energies at sites closer to the center of the (111) facet that bind oxygen too weakly. As a result of these shifts, some sites may become highly active for catalysis. Together, our studies demonstrate that by engineering the surface structure of the octahedral Pt_3Ni nanocrystal, it is possible to fine-tune the chemical and electronic properties of the surface layer and hence modulate its catalytic activity.

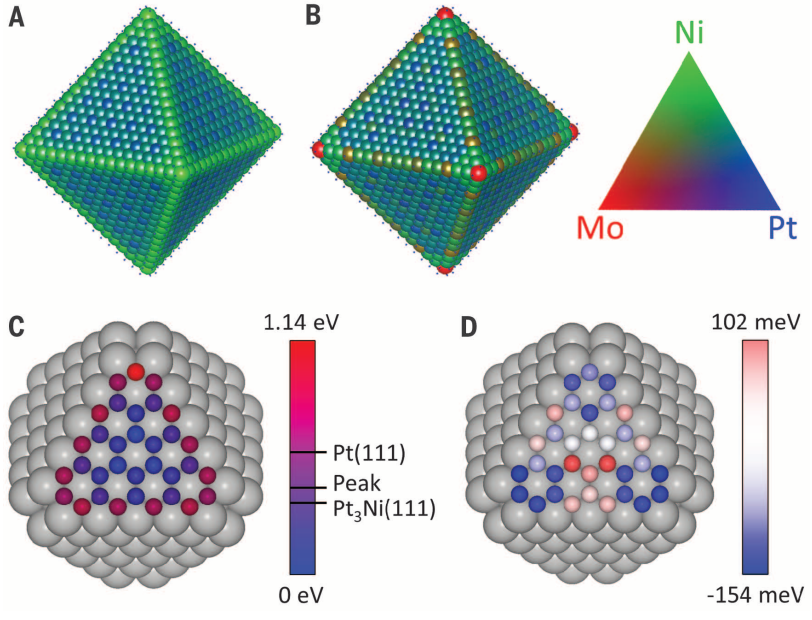


Fig. 4. Computational results. (**A** and **B**) The average site occupancies of the second layer of (A) the $Ni_{1175}Pt_{3398}$ NC and (B) the $Mo_{73}Ni_{1143}Pt_{3357}$ NC at 170°C as determined by means of a Monte Carlo simulation. Occupancies are indicated by the color triangle on the right. Small spheres represent the atoms in the outer layer. (**C**) The calculated binding energies for a single oxygen atom on all fcc and hcp sites on the (111) facet of the $Mo_6Ni_{41}Pt_{178}$ NC, relative to the lowest binding energy. Gray spheres represent Pt, and colored spheres represent oxygen sites. Three binding energies are provided for reference: the calculated binding energy on the fcc site of a pure Pt (111) surface, the binding energy corresponding to the peak of the Sabatier volcano (*37*), and the binding energy on a Pt_3Ni(111) surface. (**D**) The change in binding energies when a $Ni_{47}Pt_{178}$ NC is transformed to a $Mo_6Ni_{41}Pt_{178}$ NC by the substitution of Mo on its energetically favored sites in the second layer below the vertices.

REFERENCES AND NOTES

1. Y. Bing, H. Liu, L. Zhang, D. Ghosh, J. Zhang, *Chem. Soc. Rev.* **39**, 2184–2202 (2010).
2. D. S. Su, G. Sun, *Angew. Chem. Int. Ed. Engl.* **50**, 11570–11572 (2011).
3. Z. W. Chen, D. Higgins, A. P. Yu, L. Zhang, J. J. Zhang, *Energy Environ. Sci.* **4**, 3167–3192 (2011).
4. J. Y. Chen, B. Lim, E. P. Lee, Y. N. Xia, *Nano Today* **4**, 81–95 (2009).
5. J. Wu, H. Yang, *Acc. Chem. Res.* **46**, 1848–1857 (2013).
6. N. S. Porter, H. Wu, Z. Quan, J. Fang, *Acc. Chem. Res.* **46**, 1867–1877 (2013).
7. H. A. Gasteiger, S. S. Kocha, B. Sompalli, F. T. Wagner, *Appl. Catal. B* **56**, 9–35 (2005).
8. F. A. de Bruijn, V. A. T. Dam, G. J. M. Janssen, *Fuel Cells* **8**, 3–22 (2008).
9. J. Greeley *et al.*, *Nat. Chem.* **1**, 552–556 (2009).
10. H. A. Gasteiger, N. M. Marković, *Science* **324**, 48–49 (2009).
11. J. K. Nørskov, T. Bligaard, J. Rossmeisl, C. H. Christensen, *Nat. Chem.* **1**, 37–46 (2009).
12. V. R. Stamenkovic *et al.*, *Nat. Mater.* **6**, 241–247 (2007).
13. V. R. Stamenkovic *et al.*, *Science* **315**, 493–497 (2007).

14. A. S. Aricò, P. Bruce, B. Scrosati, J. M. Tarascon, W. van Schalkwijk, *Nat. Mater.* **4**, 366–377 (2005).
15. S. Guo, S. Zhang, S. Sun, *Angew. Chem. Int. Ed. Engl.* **52**, 8526–8544 (2013).
16. J. Wu, A. Gross, H. Yang, *Nano Lett.* **11**, 798–802 (2011).
17. J. Zhang, J. Fang, *J. Am. Chem. Soc.* **131**, 18543–18547 (2009).
18. Y. Kang, C. B. Murray, *J. Am. Chem. Soc.* **132**, 7568–7569 (2010).
19. Y. Wu, S. Cai, D. Wang, W. He, Y. Li, *J. Am. Chem. Soc.* **134**, 8975–8981 (2012).
20. D. Wang *et al.*, *Nat. Mater.* **12**, 81–87 (2013).
21. S. I. Choi *et al.*, *Nano Lett.* **13**, 3420–3425 (2013).
22. J. Zhang, H. Yang, J. Fang, S. Zou, *Nano Lett.* **10**, 638–644 (2010).
23. X. Huang *et al.*, *Adv. Mater.* **25**, 2974–2979 (2013).
24. C. Cui, L. Gan, M. Heggen, S. Rudi, P. Strasser, *Nat. Mater.* **12**, 765–771 (2013).
25. M. K. Carpenter, T. E. Moylan, R. S. Kukreja, M. H. Atwan, M. M. Tessema, *J. Am. Chem. Soc.* **134**, 8535–8542 (2012).
26. J. Snyder, I. McCue, K. Livi, J. Erlebacher, *J. Am. Chem. Soc.* **134**, 8633–8645 (2012).
27. H. Zhu, S. Zhang, S. Guo, D. Su, S. Sun, *J. Am. Chem. Soc.* **135**, 7130–7133 (2013).
28. C. Chen *et al.*, *Science* **343**, 1339–1343 (2014).
29. K. Ahrenstorf *et al.*, *Small* **3**, 271–274 (2007).
30. Y. Wu *et al.*, *Angew. Chem. Int. Ed. Engl.* **51**, 12524–12528 (2012).
31. Z. Liu *et al.*, *J. Am. Chem. Soc.* **131**, 6924–6925 (2009).
32. B. Lim *et al.*, *Science* **324**, 1302–1305 (2009).
33. J. M. Sanchez, F. Ducastelle, D. Gratias, *Physica A* **128**, 334–350 (1984).
34. N. Metropolis, A. W. Rosenbluth, M. N. Rosenbluth, A. H. Teller, E. Teller, *J. Chem. Phys.* **21**, 1087–1092 (1953).
35. T. Mueller, G. Ceder, *Phys. Rev. B* **80**, 024103 (2009).
36. W. Kohn, L. J. Sham, *Phys. Rev.* **140** (4A), A1133–A1138 (1965).
37. J. Rossmeisl, G. S. Karlberg, T. Jaramillo, J. K. Nørskov, *Faraday Discuss.* **140**, 337–346 (2009).
38. K. Momma, F. Izumi, *J. Appl. Cryst.* **41**, 653–658 (2008).

ACKNOWLEDGMENTS

We acknowledge support from the National Science Foundation (NSF) through award DMR-1437263 on catalysis studies and the Office of Naval Research (ONR) under award N00014-15-1-2146 for synthesis efforts. Computational studies were supported by the NSF through award DMR-1352373 and using computational resources provided by Extreme Science and Engineering Development Environment (XSEDE) through awards DMR130056 and DMR140068. Atomic-scale structural images were generated by using VESTA (*38*). We thank the Director, Office of Energy Research, Office of Basic Energy Sciences, Materials Sciences and Engineering Division, of the U.S. Department of Energy under contract DE-AC02-05CH11231, under the sp^2-bonded materials program, for TEM analytical measurements performed at the National Center for Electron Microscopy at the Lawrence Berkeley National Laboratory. X.D. acknowledges support from the U.S. Department of Energy, Office of Basic Energy Sciences, Division of Materials Science and Engineering through award DE-SC0008055. The work at LLNL was performed under the auspices of the U.S. Department of Energy under contract DE-AC52-07NA27344. A.Y. and A.Z. received additional support from NSF grant EEC-083219 within the Center of Integrated Nanomechanical Systems. We also thank the Electron Imaging Center of Nanomachines at CNSI for TEM support.

SUPPLEMENTARY MATERIALS

www.sciencemag.org/content/348/6240/1230/suppl/DC1
Materials and Methods
Figs. S1 to S17
Tables S1 to S2
References (*39*–*53*)

8 February 2015; accepted 4 May 2015
10.1126/science.aaa8765

SOLAR CELLS

High-performance photovoltaic perovskite layers fabricated through intramolecular exchange

Woon Seok Yang,[1]* Jun Hong Noh,[1]* Nam Joong Jeon,[1] Young Chan Kim,[1] Seungchan Ryu,[1] Jangwon Seo,[1] Sang Il Seok[1,2]†

The band gap of formamidinium lead iodide ($FAPbI_3$) perovskites allows broader absorption of the solar spectrum relative to conventional methylammonium lead iodide ($MAPbI_3$). Because the optoelectronic properties of perovskite films are closely related to film quality, deposition of dense and uniform films is crucial for fabricating high-performance perovskite solar cells (PSCs). We report an approach for depositing high-quality $FAPbI_3$ films, involving $FAPbI_3$ crystallization by the direct intramolecular exchange of dimethylsulfoxide (DMSO) molecules intercalated in PbI_2 with formamidinium iodide. This process produces $FAPbI_3$ films with (111)-preferred crystallographic orientation, large-grained dense microstructures, and flat surfaces without residual PbI_2. Using films prepared by this technique, we fabricated $FAPbI_3$-based PSCs with maximum power conversion efficiency greater than 20%.

The tremendous improvements in device architecture (*1*–*3*), high-quality film formation methodologies (*4*–*6*), and compositional engineering of perovskite materials (*7*–*9*) over the past 3 years have led to rapid improvements in the power conversion efficiency (PCE) of perovskite solar cells (PSCs). Although solar-to-electric PCEs of up to 18% have been reported for PSCs (*10*), developing technologies further to achieve PCEs near theoretical values (>30%) continues to be an important challenge in making the solar cell industry economically competitive.

Formamidinium lead iodide ($FAPbI_3$) is a perovskite material that can potentially provide better performance than methylammonium lead iodide ($MAPbI_3$) because of its broad absorption of the solar spectrum. In addition, $FAPbI_3$ with the n-i-p architecture (the n-side is illuminated with solar radiation) exhibits negligible hysteresis with sweep direction during current-voltage measurements (*8*–*13*). However, it is more difficult to form stable perovskite phases and high-quality films with $FAPbI_3$ than with $MAPbI_3$. Various methodologies such as sequential deposition (*4*), solvent engineering (*5*), vapor-assisted deposition (*14*), additive-assisted deposition (*15*, *16*), and vacuum evaporation (*6*) can now produce high-quality films of $MAPbI_3$ with flat surfaces and complete surface coverage by controlling its rapid crystallization behavior and have led to substantial improvements in the PCE of $MAPbI_3$-based PSCs.

Among these methodologies, two-step sequential deposition and solvent engineering are representative wet processes that can yield perovskite films for high-performance PSCs. In the sequential deposition process, a thin layer of PbI_2 is deposited on the substrate; methylammonium iodide (MAI) or formamidinium iodide (FAI) is then applied to the predeposited PbI_2 to enable conversion to the perovskite phase. This process involves crystal nucleation and growth of the perovskite phase because of solution-phase or solid-state reaction between PbI_2 and an organic iodide such as MAI or FAI (*4*, *13*, *17*, *18*). However, the sequential reaction of organic iodides with PbI_2 that occurs from the surface to the inner crystalline regions of PbI_2 has been ineffective in producing high-performance perovskite films that are >500 nm in thickness because of incomplete conversion of PbI_2, peeling off of the perovskite film in solution, and uncontrolled surface roughness. In contrast, the solvent-engineering process uses the formation of intermediate phases to

[1]Division of Advanced Materials, Korea Research Institute of Chemical Technology, 141 Gajeong-Ro, Yuseong-Gu, Daejeon 305-600, Korea. [2]Department of Energy Science, Sungkyunkwan University, Suwon 440-746, Korea.
*These authors contributed equally to this work. **†Corresponding author. E-mail: seoksi@krict.re.kr**

Table 1. Comparison of layer thickness before and after $FAPbI_3$ phase is formed by conventional and intramolecular exchange process (IEP). The thin PbI_2 and PbI_2(DMSO) layers were deposited on a fused quartz glass, and their layer thickness was measured by alpha-step IQ surface profiler.

Method	Before	After
Conventional process (PbI_2)	290 nm	570 nm
IEP [PbI_2(DMSO)]	510 nm	560 nm

retard the rapid reaction between PbI_2 and organic iodide in the solution. Although this process has been successfully used to form dense and uniform $MAPbI_3$ layers, it has not been explored for $FAPbI_3$ (*5*).

To deposit a uniform and dense $FAPbI_3$ layer, Snaith *et al.* added a small amount of aqueous hydrogen iodide (HI) to a solution mixture containing PbI_2, FAI, and dimethylformamide (DMF) (*11*). Very recently, Zhao *et al.* reported the deposition of highly uniform and fully covered $FAPbI_3$ films using FAI and $HPbI_3$, which is formed by the reaction of PbI_2 and HI in DMF (*19*). The HI in the PbI_2 layers retards the rapid reaction between FAI and PbI_2. In addition, the release of HI from PbI_2 at high temperatures allows the formation of a $FAPbI_3$ layer by solid-state reaction with the neighboring FAI molecules. Stated differently, this process can be regarded as the transformation of PbI_2-HI-FAI into $FAPbI_3$, similar to the formation of $MAPbI_3$ via the PbI_2–dimethylsulfoxide (DMSO)–MAI phase in the solvent-engineering process (*5*).

However, we observed that the solvent-engineering process, which is effective for depositing dense and uniform $MAPbI_3$ layers, yields $FAPbI_3$ layers with pinholes and a rough surface. Although aspects of $FAPbI_3$ film quality, including coverage and uniformity on the substrate, have

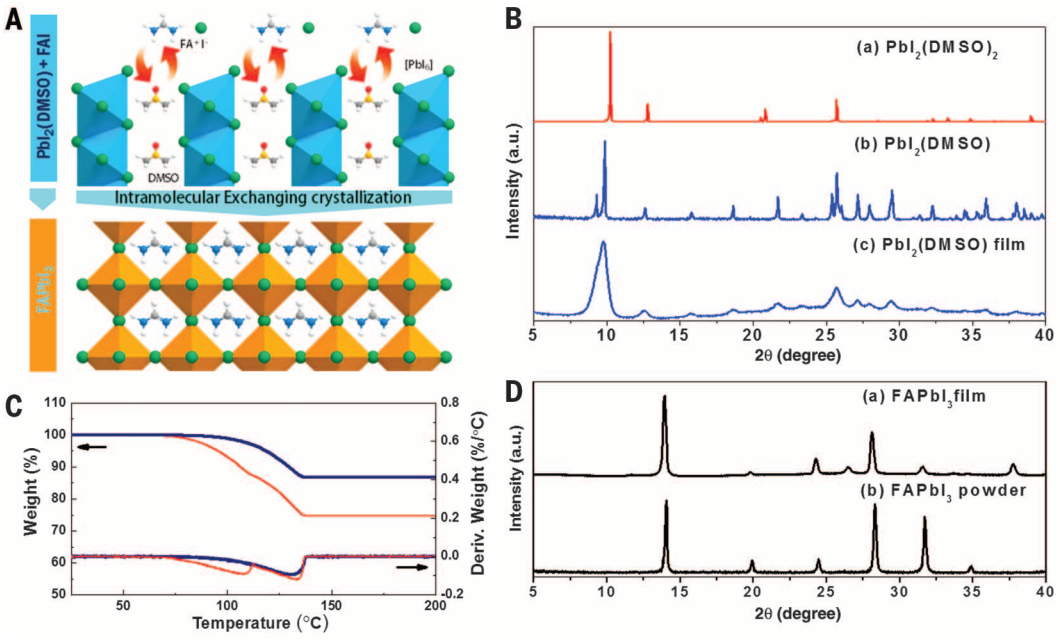


Fig. 1. PbI_2 complex formation and x-ray diffraction. (**A**) Schematics of $FAPbI_3$ perovskite crystallization involving the direct intramolecular exchange of DMSO molecules intercalated in PbI_2 with formamidinium iodide (FAI). The DMSO molecules are intercalated between edge-sharing [PbI_6] octahedral layers. (**B**) XRD patterns of (a) as-prepared $PbI_2(DMSO)_2$ powders, (b) vacuum-annealed PbI_2(DMSO) powders, and (c) as-deposited film on fused quartz substrate using PbI_2(DMSO) complex solution. (**C**) TGA of $PbI_2(DMSO)_2$ (red line) and PbI_2(DMSO) (dark blue line). (**D**) XRD patterns of (a) as-formed film of $FAPbI_3$ by IEP, and (b) $FAPbI_3$ powder.

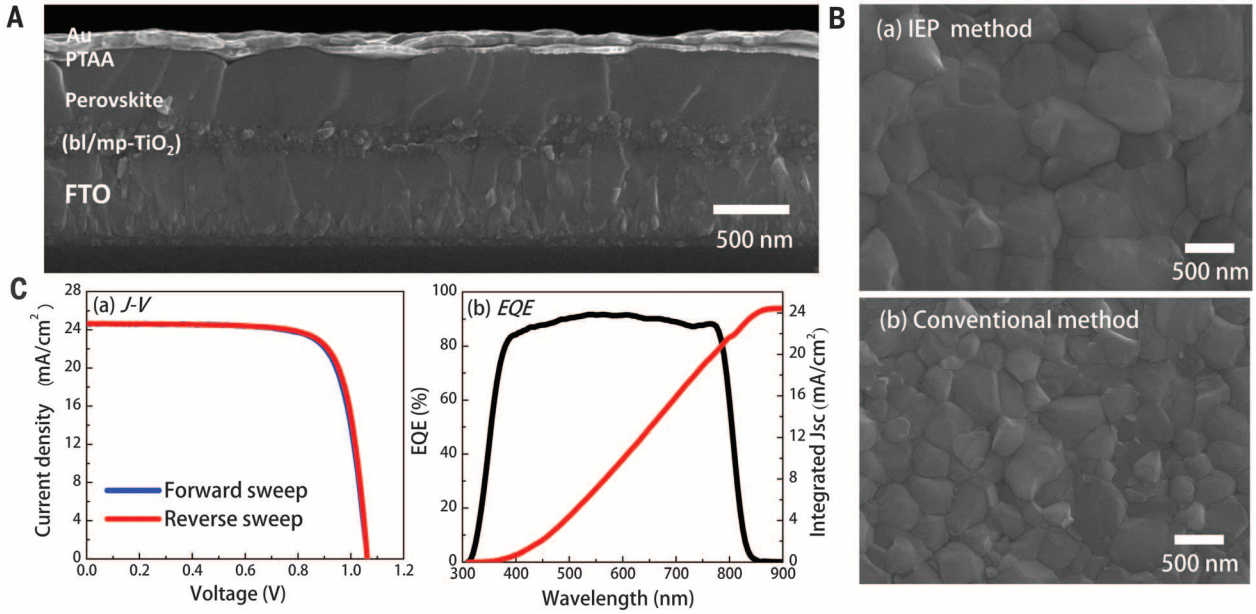


Fig. 2. SEM observations and *J-V* and EQE measurements. (**A**) Cross-sectional FESEM image of the device consisting of FTO-glass/bl-TiO_2/mp-TiO_2/perovskite/PTAA/Au. (**B**) The comparison of FESEM surface images of $FAPbI_3$-based layer formed on mp-TiO_2 by IEP and conventional method. (**C**) (a) *J-V* curves of best device measured with a 40-ms scanning delay in reverse (from 1.2 V to 0 V) and forward (from 0 V to 1.2 V) modes under standard AM 1.5G illumination, and (b) EQE spectra for best device and integrated J_{SC}.

been improved, the performance of $FAPbI_3$ solar cells still lags behind that of $MAPbI_3$-based PSCs (*8*), implying that more sophisticated deposition techniques are necessary for fabricating high-quality, thick $FAPbI_3$ films (>500 nm) that would enable sufficient absorption up to a wavelength of 840 nm.

As expected from the conversion of PbI_2(DMSO)-MAI to $MAPbI_3$ (*5*), the DMSO molecules intercalated in PbI_2 can be easily replaced by external FAIs because of their higher affinity toward PbI_2 relative to DMSO; the FAI molecules experience ionic interactions, whereas DMSO participates in van der Waals interactions (*5*, *20*). Highly uniform and dense predeposited PbI_2-DMSO layers could be directly converted to $FAPbI_3$ because the inorganic PbI_2 framework would be retained. $FAPbI_3$ crystallization by the intramolecular exchange process (IEP) of DMSO intercalated in PbI_2 with FAI was schematically shown in Fig. 1A. The intramolecular exchange between DMSO and FAI can be described as

$$PbI_2\text{-DMSO} + FAI \rightarrow PbI_2\text{-FAI} + DMSO \uparrow (\text{removal}) \quad (1)$$

and does not induce volume expansion, unlike the $FAPbI_3$ formed with FAI intercalating into pristine PbI_2 (discussed below), because the molecular sizes of DMSO and FAI are similar.

In this work, we report on the synthesis of a PbI_2(DMSO) precursor with excellent capabilities for molecular exchange with FAI at low temperatures during the spinning process, as well as the fabrication of highly efficient $FAPbI_3$-based PSCs with certified PCEs exceeding 20%. To synthesize the PbI_2(DMSO) precursors, we obtained precipitates by pouring toluene as a nonsolvent into 1.0 M PbI_2 solution dissolved in DMSO. The x-ray diffraction (XRD) pattern of the resulting complex [Fig. 1B(a)] matched that of the $PbI_2(DMSO)_2$ phase (*5*, *20*). The as-prepared $PbI_2(DMSO)_2$ was then annealed at 60°C for 24 hours in vacuum to obtain PbI_2(DMSO) by removal of 1 mol DMSO. The XRD pattern of the vacuum-annealed powder [Fig. 1B(b)] did not match that of $PbI_2(DMSO)_2$, implying that the $PbI_2(DMSO)_2$ transformed into a different phase by releasing some DMSO molecules. The content of DMSO in the as-annealed powder was estimated by thermogravimetric analysis (TGA). TGA was suitable for this purpose because the only volatile species in the powder was DMSO. The TGA results of the $PbI_2(DMSO)_2$ and PbI_2(DMSO) complexes are shown in Fig. 1C. The $PbI_2(DMSO)_2$ complex exhibited a two-step decomposition process with weight loss of 12.6% at each step, whereas the vacuum-annealed PbI_2(DMSO) complex showed a single-step decomposition. The decomposition of both the complexes was completed at the same temperature (138.6°C). The powders obtained by vacuum-annealing $PbI_2(DMSO)_2$ complex at 60°C can be regarded as one of the most thermodynamically stable forms among the various crystalline PbI_2(DMSO)-based complexes, which are similar to those of $PbBr_2$(DMSO) and $PbCl_2$(DMSO) (*21*). The DMSO content of the vacuum-annealed PbI_2(DMSO) complex was also checked by elemental analysis, which yielded H = 1.0% (1.1%); and C = 4.1% (4.4%), where the values expressed in parentheses indicate the theoretical mass percent for a given element in $C_2H_6SOPbI_2$.

To fabricate $FAPbI_3$-based PSCs through IEP between DMSO and FAI (MABr) using predeposited PbI_2(DMSO) layers and a FAI (MABr) solution, we first confirmed that the PbI_2(DMSO) phase was retained even after spin-coating with the PbI_2(DMSO) precursor dissolved in DMF. The XRD pattern for film coated on a fused silica substrate was compared with that of the initial precursor. As seen in Fig. 1B(c), the XRD pattern for the as-coated film was consistent with that of the PbI_2(DMSO) complex powder, although its crystallinity was lower. The as-coated PbI_2(DMSO) film also had a flat and dense surface, as shown in the field emission scanning electron microscopy (FESEM) image in fig. S1 (*22*). Next, we investigated the formation of mixed $FAPbI_3/MAPbBr_3$ by IEP. We recently reported that the coexistence of MA/FA/I/Br in the PbI_2 skeleton improved the phase stability of $FAPbI_3$ (*10*). The formation of mixed $FAPbI_3/MAPbBr_3$ layers via IEP was controlled by coating the solution mixture with different weight ratios of MABr to FAI, dissolved in isopropyl alcohol, on the predeposited PbI_2(DMSO) layers (see below). It is evident from Fig. 1D(a) that well-crystallized $FAPbI_3$-based films were formed by IEP. The XRD pattern for the $FAPbI_3$ film derived from the PbI_2(DMSO) complex film exhibits dominant (−111) and (−222) diffraction peaks at 13.9° and 28.1°, respectively, corresponding to the $FAPbI_3$ trigonal perovskite phase (*P3m1*), in contrast with the XRD patterns of the $FAPbI_3$ powder [Fig. 1D(b)] (*13*). The intensity ratio of the (−123) peak at 31.5° to the (−222) peak at 28.1° was 0.05. This value was much smaller than the corresponding intensity ratios (0.8) for the $FAPbI_3$ powder. Thus, IEP leads to high-quality pure $FAPbI_3$–based films with preferred orientation along the [111] axis.

Figure S2 (*22*) presents the current density–voltage (*J-V*) curves measured under standard AM 1.5G (air mass 1.5 global) illumination, as well as the external quantum efficiency (EQE) spectra of the fabricated cells with $FAPbI_3$-based layers fabricated with various amounts of MABr (0 to 20 wt%). The onset wavelength in the EQE spectra near 830 nm showed a nonlinear blue shift with increasing amounts of MABr, indicating that there is unsymmetrical competition between FAI and MABr in forming

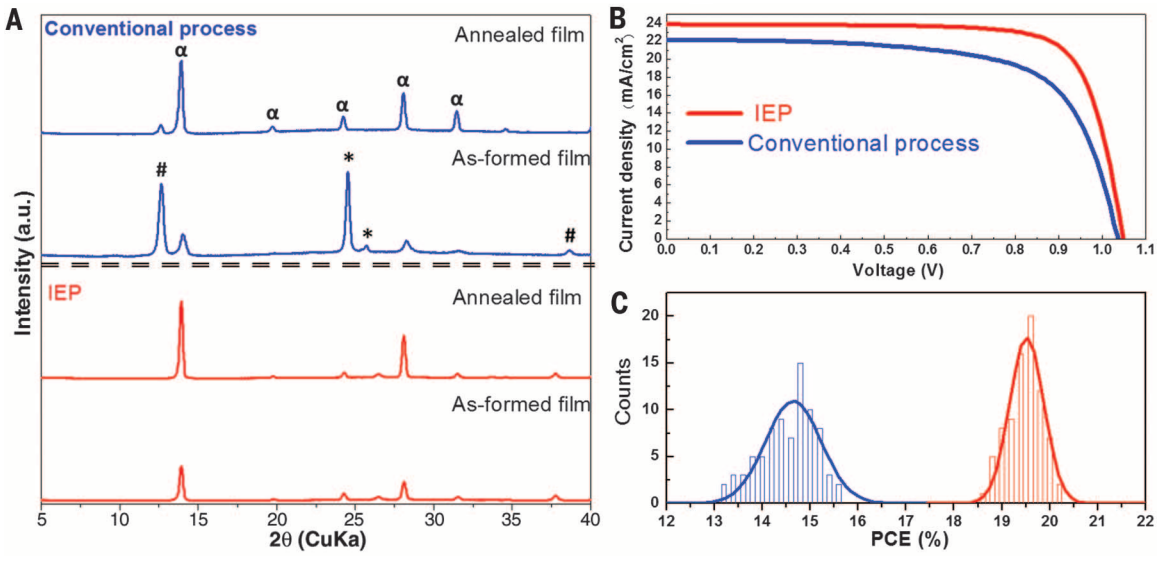


Fig. 3. Comparison of x-ray diffractions, performance, and reproducibility between IEP and conventional process. (**A**) XRD patterns of as-formed and annealed film for $FAPbI_3$-based layers formed by IEP (red line) and conventional (blue line) process. α, #, and * denote the identified diffraction peaks corresponding to the $FAPbI_3$ perovskite phase, PbI_2, and FAI, respectively. (**B**) Representative *J-V* curves for $FAPbI_3$-based cells fabricated by IEP and conventional process. (**C**) Histogram of solar cell efficiencies for each 66 $FAPbI_3$-based cells fabricated by IEP and conventional process.

the $FAPbI_3$-$MAPbBr_3$ perovskite phase through an intramolecular exchange reaction. Nonetheless, the highest PCE of 19.2% was achieved for the film fabricated from a FAI solution containing 15 wt% MABr. To accurately determine the composition of the $FAPbI_3$-based layer, we investigated the lattice parameter using XRD and the band gap using the EQE for the film showing the best performance. Figure S3 (*22*) shows the pseudocubic lattice parameter for $(FAPbI_3)_{1-x}(MAPbBr_3)_x$ as a function of x, in which the composition was controlled by a previously reported method (*10*). In this study, the pseudocubic lattice parameter of the $FAPbI_3$/$MAPbBr_3$ film fabricated by IEP with a FAI solution containing 15 wt% MABr is 6.348 Å. As indicated in fig. S4 (*22*), the lattice parameter can be assigned as x = ~5, corresponding to $(FAPbI_3)_{0.95}(MAPbBr_3)_{0.05}$. This result is in agreement with the value estimated using the band gap (1.49 eV) from EQE [fig. S3 (*22*)], because pure $FAPbI_3$ has a band gap of 1.47 eV and $(FAPbI_3)_{0.85}(MAPbBr_3)_{0.15}$ has a band gap of 1.55 eV (*10*). Fortunately, the simultaneous introduction of both MA^+ cations and Br^- anions in $FAPbI_3$ even after incorporating 5 mol% of $MAPbBr_3$ serves to stabilize the perovskite phase (*10*).

After comparing the absorption coefficients of $FAPbI_3$ and $MAPbI_3$ at wavelengths beyond 800 nm, we noted that the thickness of a $FAPbI_3$ layer needed to be higher than the optimal thickness of a typical perovskite layer with a band gap of ~1.55 eV (300 to 400 nm) to guarantee full light harvesting around 800 nm (*21*, *23*). We deposited $FAPbI_3$-based layers with thickness of ~500 nm, and fabricated devices consisting of fluorine-doped tin oxide (FTO)–glass/barrier layer (bl)-TiO_2/mesoporous (mp)-TiO_2/perovskite/polytriarylamine (PTAA)/Au (n-i-p architecture), as shown in the cross-sectional FESEM image of Fig. 2A. FESEM plane-view images of the device with film derived from PbI_2(DMSO) complex and PbI_2 films are shown in Fig. 2B. The $FAPbI_3$ film derived from PbI_2(DMSO) exhibited a dense and well-developed grain structure with larger grains than the $FAPbI_3$ film derived from PbI_2. Figure 2C(a) shows the *J-V* curves measured via reverse and forward bias sweep for one of the best-performing solar cells. The devices we fabricated also showed no hysteresis. Here, we believe that the hysteresis is highly dependent on the perovskite materials ($FAPbI_3$ or $MAPbI_3$) and cell architecture (n-i-p or p-i-n), although the ferroelectric properties of the perovskite itself are more likely to be the origin of the hysteresis in PSCs (*24*, *25*). Thus, $FAPbI_3$-based PSCs with n-i-p architecture show negligible hysteresis between the reverse and the forward scan in the *I-V* characteristics. In contrast, $FAPbI_3$-based cells consisting of FTO/NiO/perovskite/PCBM/LiF/Al (p-i-n architecture) showed very strong hysteresis [fig. S4 (*22*)]. Values of short-circuit current density (J_{SC}), open-circuit voltage (V_{OC}), and fill factor (*FF*) determined from the *J-V* curves were 24.7 mA cm^{-2}, 1.06 V, and 77.5%, respectively, and correspond to a PCE of 20.2% under standard AM 1.5G illumination. Figure 2C(b) shows the EQE spectrum and integrated J_{SC} for one of the best-performing solar cell. The high J_{SC} is attributed to a very broad EQE plateau of >85% in the illumination wavelength range of 400 to 780 nm and broad light-harvesting up to a long wavelength of 840 nm, owing to the relatively low band gap (1.47 eV) of $FAPbI_3$. The J_{SC} value (24.4 mA cm^{-2}) obtained by integrating EQE spectrum agreed well with that derived from the *J-V* measurement. The PCE of the best-performing cell (20.2%) was certified by the standardized method in the PV calibration laboratory, which confirmed a PCE of 20.1% under AM 1.5 G full-Sun illuminations [fig. S5 (*22*)].

To gain more insight into the enhanced performance of the $FAPbI_3$-based PSCs, we compared the properties of the films fabricated by IEP with those obtained from a conventional sequential process. A sequential reaction such as interdiffusion between FAI/MAI and PbI_2 through thermal annealing in organic iodide/PbI_2 multilayer films has been used to form perovskite $FAPbI_3$/$MAPbI_3$ films from inorganic PbI_2 films in the conventional process (*17*, *18*). Thus, considerable volume expansion occurs in the sequential deposition process based on PbI_2 because of the growth of perovskite crystals with the insertion of organic iodides into PbI_2 skeleton (*14*, *23*). As expected, an initial PbI_2 film with thickness of ~290 nm was doubled to 570 nm for the film formed by the reaction of PbI_2 with FAI [Table 1 and fig. S6 (*22*)].

In contrast, the change in thickness observed by the application of the FAI (MABr) solution to the predeposited PbI_2(DMSO) film was negligible. In fact, the reaction between FAI (MABr) and PbI_2(DMSO) was completed within 1 min during spin-coating and the $FAPbI_3$ perovskite phase was formed without sequential annealing. However, in a conventional process using PbI_2 films, annealing at high temperature is required to achieve interdiffusion. Figure 3A compares XRD patterns for as-formed and annealed films by IEP and conventional process from PbI_2(DMSO) complex film and PbI_2 film, respectively; there is no appreciable difference in XRD patterns between as-formed and annealed film. This result confirms that the $FAPbI_3$-based layer is formed by the IEP of DMSO and FAI (MABr) without additional annealing process. In addition, such an exchange can considerably favor crystallization into perovskite, compared to conventional interdiffusion from PbI_2, and led to an increase in the XRD peaks intensity after annealing at 150°C for 20 min. However, the as-formed film with PbI_2 showed XRD patterns assigned to PbI_2, FAI, and $FAPbI_3$, and a (002) peak at 12.5° corresponding to the PbI_2 still remained after annealing at same temperature and time with IEP. In particular, the $FAPbI_3$ film prepared by IEP shows preferred orientation in the (111) direction compared to $FAPbI_3$ film annealed after preparing it by conventional process.

The advantages of IEP become further apparent upon comparing the *J-V* curves and PCEs of $FAPbI_3$-based devices derived from PbI_2(DMSO) complex films and conventional PbI_2 films (Fig. 3, B and C). The devices based on $FAPbI_3$ fabricated from PbI_2(DMSO) showed superior PCEs with smaller deviations in the value, compared to those prepared from conventional PbI_2 films. High-efficiency solar cells with average PCEs of >19% could be produced with a high degree of reproducibility by using the IEP. This study provides an effective protocol for fabricating efficient and cost-effective inorganic-organic hybrid heterojunction solar cells.

REFERENCES AND NOTES

1. J. H. Heo *et al.*, *Nat. Photonics* **7**, 486–491 (2013).
2. H.-S. Kim *et al.*, *Sci. Rep.* **2**, 591 (2012).
3. M. M. Lee, J. Teuscher, T. Miyasaka, T. N. Murakami, H. J. Snaith, *Science* **338**, 643–647 (2012).
4. J. Burschka *et al.*, *Nature* **499**, 316–319 (2013).
5. N. J. Jeon *et al.*, *Nat. Mater.* **13**, 897–903 (2014).
6. M. Liu, M. B. Johnston, H. J. Snaith, *Nature* **501**, 395–398 (2013).
7. J. H. Noh, S. H. Im, J. H. Heo, T. N. Mandal, S. I. Seok, *Nano Lett.* **13**, 1764–1769 (2013).
8. J. W. Lee, D. J. Seol, A. N. Cho, N. G. Park, *Adv. Mater.* **26**, 4991–4998 (2014).
9. N. Pellet *et al.*, *Angew. Chem. Int. Ed.* **53**, 3151–3157 (2014).
10. N. J. Jeon *et al.*, *Nature* **517**, 476–480 (2015).
11. G. E. Eperon *et al.*, *Energy Environ. Sci.* **7**, 982–988 (2014).
12. T. M. Koh *et al.*, *J. Phys. Chem. C* **118**, 16458–16462 (2014).
13. S. Pang *et al.*, *Chem. Mater.* **26**, 1485–1491 (2014).
14. Q. Chen *et al.*, *J. Am. Chem. Soc.* **136**, 622–625 (2014).
15. P. W. Liang *et al.*, *Adv. Mater.* **26**, 3748–3754 (2014).
16. Y.-J. Jeon *et al.*, *Sci. Rep.* **4**, 6953 (2014).
17. J. H. Im, I. H. Jang, N. Pellet, M. Grätzel, N. G. Park, *Nat. Nanotechnol.* **9**, 927–932 (2014).
18. Y. Wu *et al.*, *Energy Environ. Sci.* **7**, 2934–2938 (2014).
19. F. Wang, H. Yu, H. Xu, N. Zhao, *Adv. Funct. Mater.* **25**, 1120–1126 (2015).
20. H. Miyamae, Y. Numahata, M. Nagata, *Chem. Lett.* **9**, 663–664 (1980).
21. J. Selbin, W. Bull, L. Holmes Jr., *J. Inorg. Nucl. Chem.* **16**, 219–224 (1961).
22. See supplementary materials on *Science* Online.
23. L. Hu *et al.*, *ACS Photonics* **1**, 547–553 (2014).
24. H. J. Snaith *et al.*, *J. Phys. Chem. Lett.* **5**, 1511–1515 (2014).
25. J. M. Frost *et al.*, *Nano Lett.* **14**, 2584–2590 (2014).

ACKNOWLEDGMENTS

Supported by the Global Research Laboratory Program, the Global Frontier R&D Program on Center for Multiscale Energy System funded by the National Research Foundation in Korea, and a grant from the KRICT 2020 Program for Future Technology of the Korea Research Institute of Chemical Technology and SKKU-KRICT DRC program.

SUPPLEMENTARY MATERIALS

www.sciencemag.org/content/348/6240/1234/suppl/DC1
Materials and Methods
Figs. S1 to S6

14 February 2015; accepted 30 April 2015
Published online 21 May 2015;
10.1126/science.aaa9272

CLIMATE CHANGE

Long-term climate forcing by atmospheric oxygen concentrations

Christopher J. Poulsen,[1]* Clay Tabor,[1] Joseph D. White[2]

The percentage of oxygen in Earth's atmosphere varied between 10% and 35% throughout the Phanerozoic. These changes have been linked to the evolution, radiation, and size of animals but have not been considered to affect climate. We conducted simulations showing that modulation of the partial pressure of oxygen (pO_2), as a result of its contribution to atmospheric mass and density, influences the optical depth of the atmosphere. Under low pO_2 and a reduced-density atmosphere, shortwave scattering by air molecules and clouds is less frequent, leading to a substantial increase in surface shortwave forcing. Through feedbacks involving latent heat fluxes to the atmosphere and marine stratus clouds, surface shortwave forcing drives increases in atmospheric water vapor and global precipitation, enhances greenhouse forcing, and raises global surface temperature. Our results implicate pO_2 as an important factor in climate forcing throughout geologic time.

On geological time scales, Earth's atmospheric oxygen concentration is regulated by burial of organic carbon and pyrite, which adds O_2 to the atmosphere, and oxidative weathering, which removes it (*1*). Long-term imbalances in these processes have caused pO_2 to vary on the order of 1% on million-year time scales. Charcoal evidence of fire deposited in sediments suggests that O_2 abundances have remained within the fire window, approximately 13 to 35%, since at least the Silurian (~420 million years ago) (*2*). Estimates of the evolution of pO_2 through the Phanerozoic have been made using geochemical models of carbon and sulfur cycles (*1*, *3*–*7*) and proxy methods based on abundances of charcoal in wetland environments (*8*) and stable carbon isotopes of plant resins and ambers (*9*). These reconstructions differ substantially, with some indicating that pO_2 was essentially at or above modern levels for most of the past 300 million years (*5*, *6*, *8*) and others indicating substantial variations, including a long-term rise from levels as low as 10 to 11% in the Mesozoic to modern values (*1*, *3*, *4*, *7*, *9*).

In the current atmosphere, oxygen (O_2) constitutes approximately 20.95% of air by volume, with nitrogen (N_2) and argon (Ar) contributing 78.09% and 0.93%, respectively. As a result of this composition, dry air has a mean molecular weight of 28.97 g/mol, a typical density at sea level of ~1.2 kg/m^3, and a mean sea-level pressure of 101.3 kPa. Changes to atmospheric pO_2 of several percent, assuming no change in the amounts of other constituents, have a substantial effect on atmospheric density, molecular weight, and pressure (Table 1).

Unlike greenhouse gases, O_2 is inactive in the infrared band, contributes weakly to the radiative forcing of the atmosphere, and is not considered an important factor in climate forcing (*10*). However, through its influence on atmospheric density, O_2 directly influences solar optical depth (τ_α), a measure of atmospheric opacity, by absorption and scattering of solar radiation. In its simplest form, the solar optical depth is expressed as

$$\tau(z) = k\rho\Delta z \quad (1)$$

where k (m^2/kg) represents a mass absorption coefficient, ρ (kg/m^3) is the density of the absorber, and Δz (m) is the thickness of the atmosphere. Following Beer's law, the fraction of solar radiation (I) that passes through the atmosphere is related to the top-of-atmosphere (TOA) intensity I_0 and optical depth by

$$I = I_0 \exp(-\tau) \quad (2)$$

In the modern atmosphere, ~23% of the total incoming radiation (~79 W m^{-2}) is scattered to space by air molecules and water droplets in clouds (*11*). In an atmosphere with less O_2, collisions between photons and air molecules are less common, reducing scattering. Using Eqs. 1 and 2 and assuming a 22.5% decrease in total air density with a decline in O_2 from 21% to 10% (Table 1), total scattering is estimated to decrease by ~16 W m^{-2}.

Here, we quantified the effect of changing pO_2 on global climate with the use of an atmospheric global climate model (GCM) to account for changes in atmospheric density, mass, and molecular weights (Table 1 and supplementary materials). In doing so, we maintained the partial pressures of other atmospheric constituents (N_2, Ar, CH_4, N_2O, and CO_2, except as indicated) at constant values. We focused on simulations of the Cenomanian, a mid-Cretaceous stage characterized by high pCO_2 [e.g., (*12*)] and the warmest conditions of the past ~100 million years (*13*). Paleo-pO_2 estimates inferred from stable-isotope carbon compositions indicate that the atmospheric percentage of O_2 was as low as 10 to 11% during this interval (*7*, *9*), with one biogeochemical model indicating levels as high as 32.5% (*6*). We developed a series of simulations with O_2 abundance varying between 5% and 35%, which captures the full range of both Cretaceous and Phanerozoic pO_2 values estimated by geochemical modeling and proxy techniques, and pCO_2 varying between preindustrial (280 ppmv) and 8 times preindustrial levels (2240 ppmv).

Varying pO_2 in our simulations alters both TOA and surface radiative forcing. In the simulation with 1120 ppmv pCO_2, approximately the median value of Cenomanian pCO_2 proxy estimates [e.g., (*12*)], the global TOA shortwave forcing increases by 3.4 W m^{-2} with a decrease in O_2 from 21 to 10% and is balanced by an increase in outgoing TOA longwave radiation. The equilibrium TOA shortwave forcing response is consistent with a reduction in outgoing shortwave radiation by Rayleigh scattering but is less than anticipated from our scaling estimate because of climate feedbacks. To demonstrate this, we ran a Cenomanian simulation with 10% O_2 branched from an equilibrium 21% O_2 simulation (see supplementary materials). The initial 1-day difference in the total atmospheric scattering, 23.5 W m^{-2}, is similar in magnitude to our scaling estimate, with increases in clear-sky and cloud surface shortwave forcing of 4.5 W m^{-2} and 19 W m^{-2}, respectively. The increase in cloud shortwave forcing is greater than anticipated from a reduction in scattering alone because the cloud fraction initially decreases by 10.5%

Table 1. Dry atmospheric conditions under variable O_2 levels. Atmospheric pN_2 and pAr are fixed at modern values; M_v/M_a is the ratio of the molecular weight of water to the molecular weight of dry air.

O_2 concentration	Density of dry air (kg m^{-3})	Molecular weight of dry air (g/mol)	Sea-level pressure (kPa)	M_v/M_a
5%	0.88	28.33	84.24	0.636
10%	1.00	28.52	88.92	0.632
15%	1.12	28.72	94.15	0.627
21%	1.29	28.97	101.30	0.622
30%	1.60	29.30	114.32	0.615
35%	1.81	29.49	123.12	0.611

[1]Department of Earth and Environmental Sciences, University of Michigan, Ann Arbor, MI 48109, USA. [2]Department of Biology, Baylor University, Waco, TX 76798, USA.
*Corresponding author. E-mail: poulsen@umich.edu

Downloaded from www.sciencemag.org on June 14, 2015

as a result of the instantaneous decrease in atmospheric pressure and relative humidity. The large, instantaneous increase in shortwave forcing with a reduction in O_2 drives an increase in surface latent heat flux of a similar magnitude, leading to increases in atmospheric humidity and a rebound in cloud fraction (fig. S1). As atmospheric humidity and cloud fractions rise, total shortwave scattering increases and surface and TOA shortwave forcing falls.

Under equilibrium conditions, the global net (shortwave + longwave) absorbed surface radiation is greater by 8.4 W m^{-2} under 10% O_2 than under 21% O_2. Of this total, an increase in shortwave radiative forcing accounts for 4.8 W m^{-2} and consists of an increase in total cloud shortwave forcing of 5.7 W m^{-2} and a decrease in clear-sky shortwave forcing of 0.85 W m^{-2}. The increase in cloud forcing arises from a ~7% reduction in cloud liquid water content, causing clouds to be optically thinner and more transparent to incoming shortwave radiation, and a ~9% reduction in low-level marine stratus clouds associated with increased instability and convective activity due to enhanced surface shortwave forcing. The reduction in clear-sky shortwave forcing results from an increase in total atmospheric moisture of ~25%, which increases clear-sky scattering.

In addition to the increases in surface shortwave forcing, the downward longwave radiation at the surface increases by 3.6 W m^{-2}. Clear-sky longwave forcing increases by 9.2 W m^{-2} as a result of infrared absorption and emission by water vapor, and cloudy-sky longwave forcing decreases by 5.6 W m^{-2} primarily as a result of a decrease in stratus cloud fraction. The net increase in surface radiation is balanced by an increase in surface latent heat flux by 9.8 W m^{-2} and a small reduction in the surface sensible heat flux.

Single-column radiative transfer model experiments substantiate our GCM results: In the absence of increases in atmospheric humidity, surface clear-sky radiation increases under low O_2 conditions. Enhanced atmospheric humidity reduces the net clear-sky shortwave forcing and raises surface longwave radiation. And finally, changes in the cloud optical depth and cloud fraction increase surface shortwave forcing and decrease longwave forcing (fig. S2).

The increases in surface radiative forcing and compensation by the latent heat flux with decreasing pO_2 lead to substantial increases in global surface precipitation rates and temperature (Fig. 1). Under 1120 ppmv pCO_2, global mean annual precipitation rates (P) range from 1.11 m/year (35% O_2) to 1.27 m/year (21% O_2) and 1.40 m/year (10% O_2). Precipitation rates generally increase, except in subtropical regions (~30° latitude), with a decrease in pO_2 (Fig. 2, B and C). These precipitation anomalies reflect greater surface evaporation rates and vapor amounts, as well as enhanced vapor export from subtropical regions under reduced pO_2.

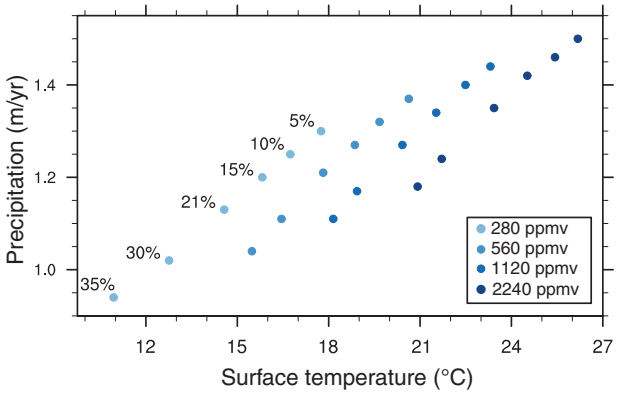


Fig. 1. Simulated global annual surface temperature (°C) versus precipitation rate (m/year) under variable pCO_2 and pO_2. Solid circles represent 20-year means from each run averaged over model years 41 to 60. CO_2 (280, 560, 1120, and 2240 ppm) is indicated by the color of the solid circles, with higher values represented by darker shades. O_2 ranges sequentially from 5 to 35% (as shown) for each set of pCO_2 experiments.

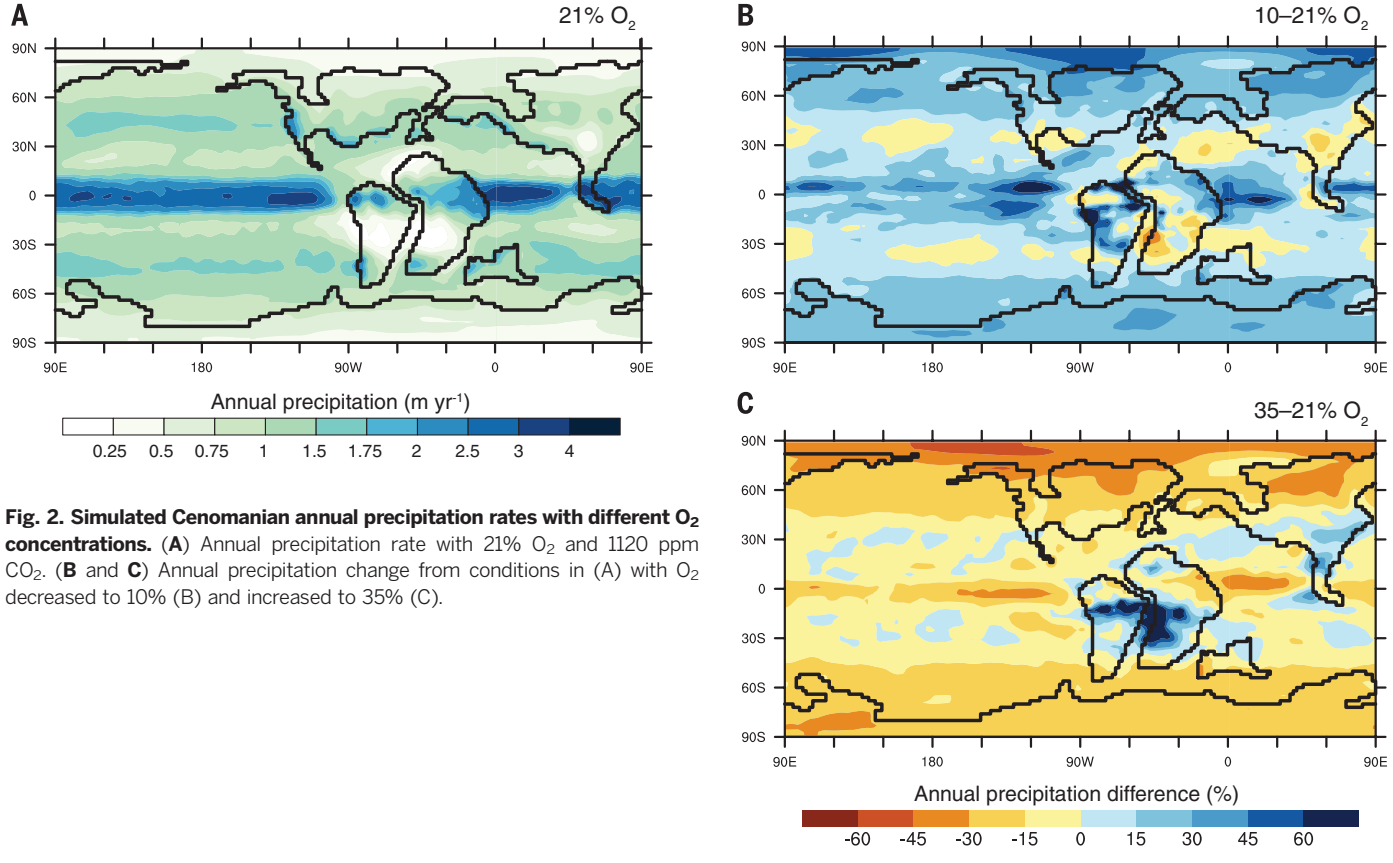


Fig. 2. Simulated Cenomanian annual precipitation rates with different O_2 concentrations. (**A**) Annual precipitation rate with 21% O_2 and 1120 ppm CO_2. (**B** and **C**) Annual precipitation change from conditions in (A) with O_2 decreased to 10% (B) and increased to 35% (C).

Enhanced latent heat fluxes raise global-average precipitable water amounts (q) from 4.9 kg/m^2 (35% O_2) to 6.1 kg/m^2 (21% O_2) and 7.6 kg/m^2 (10% O_2). Although atmospheric humidity increases, the total mass flux of water, approximated as $M \approx P/q$ (*14*), decreases by ~19% as O_2 decreases from 35% to 10%, consistent with a simulated decrease in mean vertical velocities (fig. S3) and with previous studies that describe slowdown of atmospheric circulation with global warming [e.g., (*15*)].

Global surface temperatures also increase with decreasing pO_2 (Fig. 1) and, under 1120 ppmv CO_2, range from 18.2°C (35% O_2) to 22.5°C (10% O_2), yielding differences of −2.3°C and +2.1°C relative to those under current pO_2. Surface temperature differences are regionally amplified by feedbacks (Fig. 3, B and C). Under 10% O_2, reductions in Northern Hemisphere snow and sea ice decrease surface albedo by up to 0.25, causing polar warming. Over subtropical continents, enhanced radiative forcing over arid surfaces with low soil moisture enhances sensible heating of the surface. In addition, reductions by up to 15% in low-level marine stratus clouds along the equator reduce reflected shortwave radiation at the surface, leading to additional warming.

The climate sensitivity to modulation of pO_2 is distinctly different from that of pCO_2. A doubling of pCO_2 in the GCM leads to average increases in radiative forcing, surface temperature, and precipitation of 6.2 W m^{-2}, 3.0 K, and 7.6 cm/year, yielding temperature and precipitation sensitivities of 0.48 K per W m^{-2} and 1.2 cm/year per W m^{-2}, respectively. The precipitation sensitivity is much higher for pO_2 than for pCO_2 (fig. S4) for two reasons. First, solar forcing provides a larger surface forcing than greenhouse forcing. For each W m^{-2} in total radiative forcing, surface forcing increases by 2.1 W m^{-2} and 0.63 W m^{-2} for changes in pO_2 and pCO_2, respectively. Second, because CO_2 decreases radiative cooling, it is less effective than solar forcing in driving changes in global precipitation [e.g., (*16*)]. The temperature sensitivity to pO_2 is lower than that for pCO_2 at low pO_2 and greater at higher pO_2 (fig. S4). The variability in temperature sensitivity to pO_2 is at least partly due to a lapse rate feedback. Under low pO_2, enhanced latent heat fluxes and convection moisten the troposphere, leading to warming throughout the column but preferentially in the mid- and upper troposphere (fig. S5). As a consequence of this warming profile, infrared emission to space is enhanced, reducing greenhouse forcing.

Atmospheric CO_2 is widely considered to be the primary driver of Phanerozoic climate change; this view is supported by the coincidence of low proxy pCO_2 with cold climates and of high proxy pCO_2 with warm climates (*17*). Paleoclimate modeling has demonstrated, however, that proxy levels of pCO_2 alone are not sufficient to fully explain past warm climates, particularly those of the mid-Cretaceous and early Paleogene. Paleoclimate models generally predict high-latitude temperatures that are too low, causing too-large equator-to-pole gradients (*12*, *18*–*21*). The low pO_2 (~10% O_2) estimated for the Mesozoic and early Paleogene (*7*, *9*) would have contributed to the high-latitude warming of these greenhouse periods (Fig. 3B).

Less well recognized but equally problematic is the underestimate by paleoclimate models of precipitation rates during greenhouse periods [e.g., (*20*)]. A variety of proxies, including lithologic indicators [e.g., (*22*, *23*)], geochemical proxies [e.g., (*24*, *25*)], and leaf analyses of paleoflora (*26*–*30*), indicate that mid- and high-latitude continents of the mid-Cretaceous and early Paleogene were more humid than at present. Although sparse and associated with high analytical uncertainty (*28*), mid-Cretaceous proxy precipitation rates based on leaf area analysis of fossil leaves from Alaska and northern Siberia typically exceed >1000 mm/year (*26*, *30*). Low pO_2 may help to account for such high values. In our Cenomanian simulations, mean annual precipitation rates in these high-latitude regions increase by up to 45% with a decrease in pO_2 from current values to 10% O_2 (Fig. 2B). Simulated precipitation rates increase further to values at or approaching 1000 mm/year with 10% O_2 and 2240 ppm CO_2, values well within the uncertainty range of proxy estimates (fig. S6 and table S3). Finally, in our simulations, the combination of low pO_2 and high pCO_2 causes temperate forests to expand their range to high

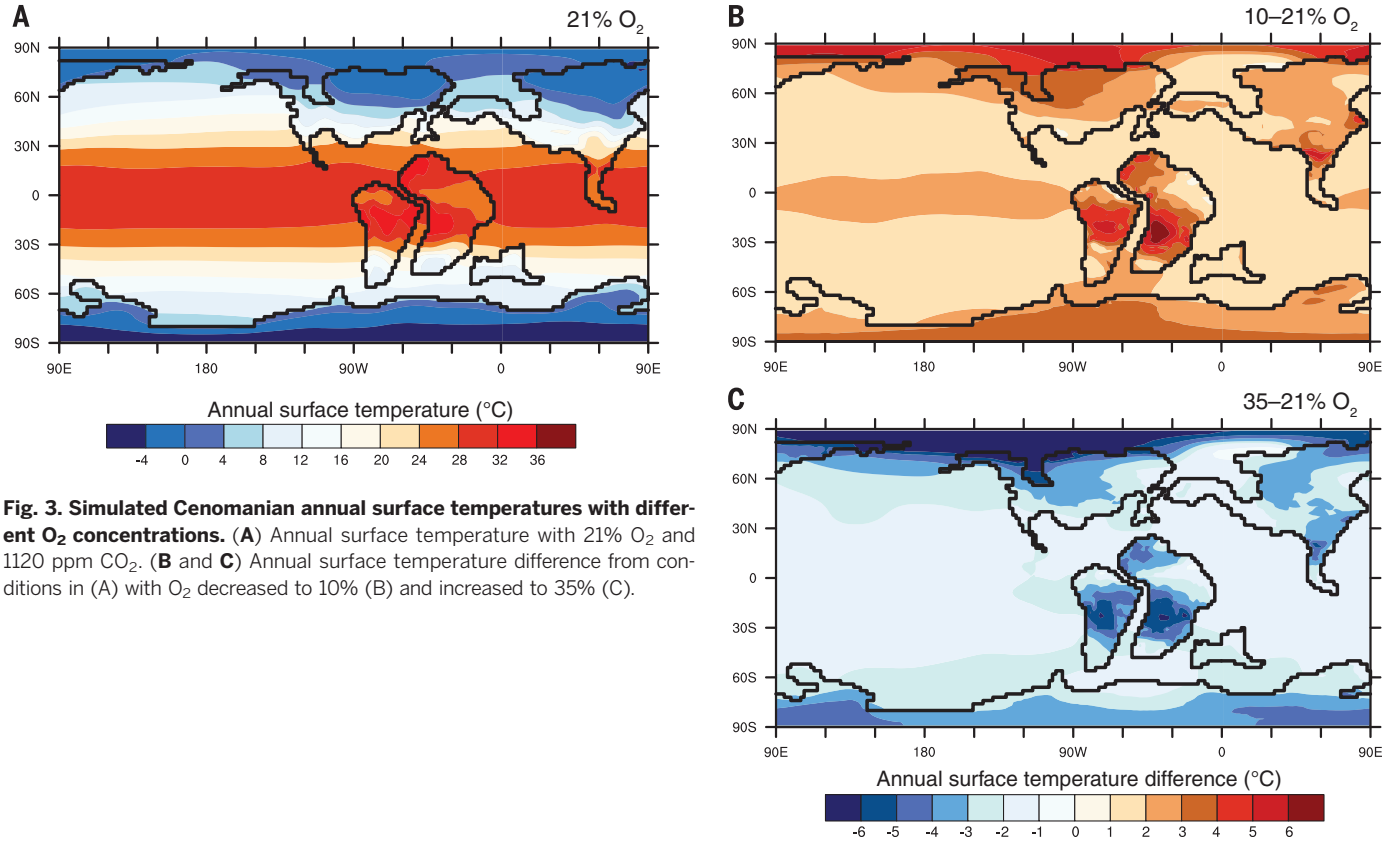


Fig. 3. Simulated Cenomanian annual surface temperatures with different O_2 concentrations. (**A**) Annual surface temperature with 21% O_2 and 1120 ppm CO_2. (**B** and **C**) Annual surface temperature difference from conditions in (A) with O_2 decreased to 10% (B) and increased to 35% (C).

latitudes, consistent with paleobotanical evidence (*31*–*33*) (fig. S7).

Our results for the mid-Cretaceous are broadly applicable throughout Earth history and demonstrate that variations in atmospheric mass, whether through changes in pO_2 or other constituents (i.e., pN_2), were an important factor in climate forcing on geological time scales that must be included in paleoclimate models. We also note the broad inverse correlation between some pO_2 records [e.g., (*1*, *9*)] and global climate change during the Phanerozoic; we speculate that, to the extent that atmospheric pO_2 and pCO_2 have been linked through photosynthetic productivity and organic carbon burial, O_2 may have amplified CO_2-driven climate change.

REFERENCES AND NOTES

1. R. A. Berner, *Geochim. Cosmochim. Acta* **70**, 5653–5664 (2006).
2. A. C. Scott, I. J. Glasspool, *Proc. Natl. Acad. Sci. U.S.A.* **103**, 10861–10865 (2006).
3. R. A. Berner, D. E. Canfield, *Am. J. Sci.* **289**, 333–361 (1989).
4. R. A. Berner, *Am. J. Sci.* **309**, 603–606 (2009).
5. R. S. Arvidson, F. T. Mackenzie, M. Guidry, *Am. J. Sci.* **306**, 135–190 (2006).
6. N. M. Bergman, T. M. Lenton, A. J. Watson, *Am. J. Sci.* **304**, 397–437 (2004).
7. P. G. Falkowski *et al*., *Science* **309**, 2202–2204 (2005).
8. I. J. Glasspool, A. C. Scott, *Nat. Geosci.* **3**, 627–630 (2010).
9. R. Tappert *et al*., *Geochim. Cosmochim. Acta* **121**, 240–262 (2013).
10. IPCC, *Climate Change 2013: The Physical Science Basis. Contribution of Working Group I to the Fifth Assessment Report of the Intergovernmental Panel on Climate Change* (Cambridge Univ. Press, New York, 2013).
11. K. E. Trenberth, J. T. Fasullo, J. Kiehl, *Bull Am. Meteorol. Soc.* **90**, 311–323 (2009).
12. K. L. Bice *et al*., *Paleoceanography* **21**, PA2002 (2006).
13. O. Friedrich, R. D. Norris, J. Erbacher, *Geology* **40**, 107–110 (2012).
14. I. M. Held, B. J. Soden, *J. Clim.* **19**, 5686–5699 (2006).
15. G. A. Vecchi, B. J. Soden, *J. Clim.* **20**, 4316–4340 (2007).
16. M. R. Allen, W. J. Ingram, *Nature* **419**, 224–232 (2002).
17. D. L. Royer, *Geochim. Cosmochim. Acta* **70**, 5665–5675 (2006).
18. E. Barron, *Earth Sci. Rev.* **19**, 305–338 (1983).
19. C. J. Poulsen, *Nature* **432**, 814–815 (2004).
20. J. Zhou, C. J. Poulsen, N. Rosenbloom, C. Shields, B. Briegleb, *Clim. Past* **8**, 565–576 (2012).
21. M. Huber, R. Caballero, *Clim. Past* **7**, 603–633 (2011).
22. G. Ludvigson *et al*., *Geology* **26**, 1039 (1998).
23. H. Hasegawa *et al*., *Clim. Past* **8**, 1323–1337 (2012).
24. T. White, L. Gonzalez, G. Ludvigson, C. Poulsen, *Geology* **29**, 363 (2001).
25. A. H. Jahren, L. Sternberg, *Geology* **31**, 463–466 (2003).
26. A. Herman, R. Spicer, *Nature* **380**, 330–333 (1996).
27. D. R. Greenwood, J. F. Basinger, R. Y. Smith, *Geology* **38**, 15–18 (2010).
28. D. J. Peppe *et al*., *New Phytol.* **190**, 724–739 (2011).
29. P. A. Hayes, J. E. Francis, D. J. Cantrill, J. A. Crame, Palaeoclimate analysis of Late Cretaceous angiosperm leaf floras, James Ross Island, Antarctica. *Geol. Soc. London Spec. Pub. 258*, 49–62 (2006).
30. R. A. Spicer, A. B. Herman, *Palaeogeogr. Palaeoclimatol. Palaeoecol.* **295**, 423–442 (2010).
31. R. Spicer, J. Parrish, *Geology* **14**, 703–706 (1986).
32. E. Peralta-Medina, H. J. Falcon-Lang, *Geology* **40**, 219–222 (2012).
33. J. E. Francis, I. Poole, *Palaeogeogr. Palaeoclimatol. Palaeoecol.* **182**, 47–64 (2002).

ACKNOWLEDGMENTS

Supported by NSF Sedimentary Geology and Paleobiology Program grant FO35175 and NSF Marine Geology and Geophysics grant FO33663. We thank R. Feng, R. Fiorella, I. Montañez, and three anonymous reviewers for discussion of and comments on this work. The model data are available at www.ncdc.noaa.gov/data-access/paleoclimatology-data/contributing.

SUPPLEMENTARY MATERIALS

www.sciencemag.org/content/348/6240/1238/suppl/DC1
Materials and Methods
Supplementary Text
Figs. S1 to S7
Tables S1 to S3
References (*34*–*39*)

2 September 2014; accepted 5 May 2015
10.1126/science.1260670

BRAIN NETWORKS

Correlated gene expression supports synchronous activity in brain networks

Jonas Richiardi,[1,2]*† Andre Altmann,[1]† Anna-Clare Milazzo,[3,1] Catie Chang,[4] M. Mallar Chakravarty,[5,6] Tobias Banaschewski,[7] Gareth J. Barker,[8] Arun L.W. Bokde,[9] Uli Bromberg,[10] Christian Büchel,[10] Patricia Conrod,[8,11] Mira Fauth-Bühler,[12] Herta Flor,[13] Vincent Frouin,[14] Jürgen Gallinat,[15] Hugh Garavan,[9,16] Penny Gowland,[17] Andreas Heinz,[15] Hervé Lemaître,[18,19] Karl F. Mann,[12] Jean-Luc Martinot,[18,19] Frauke Nees,[13] Tomáš Paus,[20,21] Zdenka Pausova,[22] Marcella Rietschel,[23] Trevor W. Robbins,[24] Michael N. Smolka,[25] Rainer Spanagel,[26] Andreas Ströhle,[15] Gunter Schumann,[8,27] Mike Hawrylycz,[28] Jean-Baptiste Poline,[29] Michael D. Greicius,[1]* IMAGEN consortium‡

During rest, brain activity is synchronized between different regions widely distributed throughout the brain, forming functional networks. However, the molecular mechanisms supporting functional connectivity remain undefined. We show that functional brain networks defined with resting-state functional magnetic resonance imaging can be recapitulated by using measures of correlated gene expression in a post mortem brain tissue data set. The set of 136 genes we identify is significantly enriched for ion channels. Polymorphisms in this set of genes significantly affect resting-state functional connectivity in a large sample of healthy adolescents. Expression levels of these genes are also significantly associated with axonal connectivity in the mouse. The results provide convergent, multimodal evidence that resting-state functional networks correlate with the orchestrated activity of dozens of genes linked to ion channel activity and synaptic function.

Brain activity at rest exhibits intrinsic low-frequency synchronization between anatomically distinct brain regions (*1*). When observed with functional magnetic resonance imaging (fMRI), this coherence between regions (functional connectivity) defines 15 to 20 brain networks associated with such canonical functions as vision, language, episodic memory, and spatial attention (*2*–*4*). These functional networks are disrupted in several neurodegenerative and neuropsychiatric diseases (*5*) and may constitute the maps followed by neurodegenerative diseases marching, trans-synaptically, across the brain (*6*). Although it has been shown that connectivity within the default-mode network (DMN) (*7*) and topological measures of whole-brain networks (*8*) are heritable, the set of genes promoting functional connectivity remains unknown. To pursue this question, we applied a network modeling approach to both neuroimaging and gene expression data.

Using resting-state fMRI data from 15 healthy right-handed subjects (eight females, age range 18 to 29 years), we computed 14 well-known and reproducible functional networks (fig. S1) (*9*) by using independent component analysis (ICA). We then mapped samples from the Allen Institute for Brain Science (AIBS) human microarray data set (six subjects, two contributed both hemispheres, four contributed one hemisphere, one female, age range 24 to 57 years, totaling 3702 brain samples) (table S1) (*10*) to these networks by using normalized Montreal Neurological Institute (MNI) coordinates. To avoid biases due to gross transcriptional dissimilarities in different brain regions, we excluded basal ganglia, cerebellum, and deep gray matter (including hippocampus), leaving only cortex samples (data file S1). This removed the basal ganglia network, leaving 13 networks. Of 1777 cortex samples, 501 were mapped to the 13 functional networks, and 1276 to "non-network" regions of the brain. We focused the analysis on four large nonoverlapping networks: dorsal default-mode (dDMN), salience, sensorimotor, and visuospatial (Fig. 1A), comprising 241 samples total. These four networks were chosen because they are well characterized in the imaging literature (*2*, *11*–*14*),

consist of noncontiguous regions in both hemispheres, and have adequate coverage in the AIBS data (Fig. 1B).

We used the transcriptional similarity of gene expression profiles between brain tissue samples to define correlated gene expression networks. In mouse brains, transcriptional similarity reflects cytoarchitecture (*15*), but in human brains, the differences are more subtle across the neocortex (*10*). As opposed to gene coexpression networks, which quantify gene-gene relationships across tissue samples (*16*), a correlated gene expression network quantifies tissue-tissue relationships across genes. Nodes were defined by brain tissue samples (Fig. 1B); edges were weighted by similarity between vectors of gene expression values at each sample. After preprocessing and assigning one probe for each of the 16,906 genes (data file S2) (*17*), we measured expression similarity by means of Pearson correlation (*17*), setting negative correlations to zero. Then we asked whether there are observable genetic correlates for the functional network organization: Are gene expression correlations in functionally grouped regions higher than can be expected by chance?

We defined the strength fraction in functional networks as a measure of the relationship between correlated gene expression within and outside the set of functional networks of interest. Denoting W the sum of all edge weights within all functional networks, W_i the sum of weights within the four functional networks of interest, and T the brain graph's total strength (sum of all edge weights linking the full 1777-nodes graph), the strength fraction is $S = W_i/(T - W)$. Higher values of S mean that the samples in the set of functional networks are more similar to each other, relative to the remaining brain regions (fig. S2). We assessed significance using permutation testing (*18*), randomly reshuffling 10,000 times the sample-to-network assignment in the full 1777-nodes graph. In addition to considering only cortex samples, so as to avoid biasing results toward similar tissues (*10*), before computation we removed edges linking two samples belonging to the same tissue class [defined by means of regional ontology (fig. S3 and table S4)]. Grouping gene expression samples according to functional networks yielded a higher strength fraction than that of other groupings of samples; the spatial organization of functional networks corresponded to regions that have more highly correlated gene expression than expected by chance ($P < 10^{-4}$). Given that we used only cortical samples, that we removed edges linking tissues of the same class, and that functional networks are spatially distributed, this finding cannot emerge from spatial proximity or gross tissue similarity.

We next sought to identify which genes, specifically, drive the relationship between correlated gene expression and functional networks. We computed the marginal influence of each gene on strength fraction of all four functional networks together (*17*) and ranked genes across all six different two-way splits of the six subjects (*17*). Then, we computed list overlap statistics (*19*) between the two brain subgroups at a false discovery rate (FDR) of 5%. Combining results from six splits, the final list was obtained via stability selection (*20*), selecting genes that appear in the majority of splits (four or more out of six). This resulted in a consensus list of 136 genes (table S2).

We validated our findings in vivo (supplementary text) using paired genome-wide single-nucleotide polymorphism (SNP) data and resting state fMRI (rs-fMRI) recordings in $n = 259$ 14-year-olds (126 females) from the IMAGEN database (*21*), which has more subjects, but not all were usable (data file S3) (*17*). The strength fraction for the combined four networks in the rs-fMRI data was computed for every subject (as in the AIBS gene expression data) and used as a quantitative imaging phenotype in a genome-wide association study (GWAS) (fig. S4), correcting for several covariates, including motion. We computed a z statistic (*22*) for the enrichment of P values in the consensus list. Genetic variation in the consensus list was significantly associated with in vivo rs-fMRI strength fraction ($z = 2.55$, $P = 0.006$). Thus, not only gene expression levels but also common polymorphisms in the consensus genes were related to the strength of functional networks. Subjects at both ends of the spectrum of multilocus genetic scores [representing the multiallelic effect of the genes in the consensus list on the functional connectivity phenotype (*17*)] showed definite differences in functional connectivity strength mostly within the functional networks themselves, but also between the functional networks (Fig. 2 and fig. S5).

We next investigated the relationship between our gene list and the connectivity of axonal projections underlying functional networks. We used the Allen Institute mouse brain atlas (*15*), which offers finely sampled whole-genome expression data, together with a recent mesoscale model of mouse connectivity derived from the Allen Mouse Brain Connectivity Atlas (AMBCA) (*23*). To match human data, we focused on the mouse isocortex and used a 38-region parcellation (Fig. 3A) (*23*). With 57 mouse orthologs for our consensus gene list, we obtained a correlated gene expression network, representing transcriptional similarity between these 38 regions. We computed a normalized, symmetric connectivity matrix from the significant connections in the ipsilateral connectivity model of the AMBCA (*17*). We tested the association between the mouse connectivity graph and transcriptional similarity graph (Fig. 3, B and C) using a modified Mantel procedure; we randomly selected gene subsets of the same size as our ortholog consensus list 10,000 times in order to obtain a null distribution. The correlation between transcriptional similarity in these 38 mesoscale isocortex regions and their axonal connectivity was significantly higher when using our list than expected by chance ($P = 0.011$, or $P = 0.022$ when using the contralateral connectivity model).

Last, we categorized the consensus gene list using Gene Ontology (GO) by computing statistical overrepresentation for Biological Processes (BP), Cellular Component (CC), and Molecular Function (MF) with the Database for Annotation, Visualization, and Integrated Discovery (DAVID) 6.7 (*24*). The only significant MF annotation [$P < 0.05$, Benjamini-Hochberg False Discovery Rate (FDR_{BH})–corrected] related to ion transport. No BP annotation was significant. Four out of six significant CC annotations ($P < 0.03$ FDR_{BH}) concerned ion channels, in particular involving sodium channels such as SCN4B or receptors such as GABRA5 (full annotation list is available in tables S5 and S6). Significant associations with nine diseases, including Alzheimer's disease and schizophrenia

[1]Functional Imaging in Neuropsychiatric Disorders Laboratory, Department of Neurology and Neurological Sciences, Stanford University, Stanford, CA, USA. [2]Laboratory of Neurology and Imaging of Cognition, Department of Neuroscience, University of Geneva, Geneva, Switzerland. [3]The War Related Illness and Injury Study Center, VA Palo Alto Health Care System, Palo Alto, CA, USA. [4]Advanced MRI Section, Laboratory of Functional and Molecular Imaging, National Institute of Neurological Disorders and Stroke, National Institutes of Health, Bethesda, MD, USA. [5]Cerebral Imaging Centre, Douglas Mental Health University Institute, Montreal, Canada. [6]Departments of Psychiatry and Biomedical Engineering, McGill University, Montreal, Canada. [7]Department of Child and Adolescent Psychiatry, Central Institute of Mental Health, Medical Faculty Mannheim, Heidelberg University, Mannheim, Germany. [8]Institute of Psychiatry, Psychology and Neuroscience, King's College London, London, UK. [9]Institute of Neuroscience, Trinity College Dublin, Dublin, Ireland. [10]Universitaetsklinikum Hamburg Eppendorf, Hamburg, Germany. [11]Department of Psychiatry, Université de Montréal, Centre Hospitalier Universitaire (CHU) Ste Justine Hospital, Montréal, Canada. [12]Department of Addictive Behaviour and Addiction Medicine, Central Institute of Mental Health, Medical Faculty Mannheim, Heidelberg University, Mannheim, Germany. [13]Department of Cognitive and Clinical Neuroscience, Central Institute of Mental Health, Medical Faculty Mannheim, Heidelberg University, Mannheim, Germany. [14]Neurospin, Commissariat à l'Energie Atomique et aux Energies Alternatives, Paris, France. [15]Department of Psychiatry and Psychotherapy, Campus Charité Mitte, Charité–Universitätsmedizin Berlin, Berlin, Germany. [16]Departments of Psychiatry and Psychology, University of Vermont, Burlington, VT, USA. [17]School of Physics and Astronomy, University of Nottingham, Nottingham, UK. [18]Institut National de la Santé et de la Recherche Médicale, INSERM Unit 1000 "Neuroimaging and Psychiatry," University Paris Sud, Orsay, France. [19]INSERM Unit 1000 at Maison de Solenn, Assistance Publique Hôpitaux de Paris (APHP), Cochin Hospital, University Paris Descartes, Sorbonne Paris Cité, Paris, France. [20]Rotman Research Institute, University of Toronto, Toronto, Canada. [21]School of Psychology, University of Nottingham, Nottingham, UK. [22]The Hospital for Sick Children, University of Toronto, Toronto, Canada. [23]Department of Genetic Epidemiology in Psychiatry, Central Institute of Mental Health, Medical Faculty Mannheim, Heidelberg University, Mannheim, Germany. [24]Behavioural and Clinical Neuroscience Institute and Department of Psychology, University of Cambridge, Cambridge, UK. [25]Department of Psychiatry and Psychotherapy, and Neuroimaging Center, Technische Universität Dresden, Dresden, Germany. [26]Department of Psychopharmacology, Central Institute of Mental Health, Faculty of Clinical Medicine Mannheim, Mannheim, Germany. [27]Medical Research Council (MRC) Social, Genetic and Developmental Psychiatry (SGDP) Centre, London, UK. [28]Allen Institute for Brain Science, Seattle, WA, USA. [29]Helen Wills Neuroscience Institute, University of California Berkeley, Berkeley, CA, USA.

***Corresponding author. E-mail: jonas.richiardi@unige.ch (J.R.); greicius@stanford.edu (M.D.G.)** †These authors contributed equally to this work. ‡IMAGEN consortium (www.imagen-europe.com) authors and affiliations are listed in the supplementary materials.

($P < 0.05$ FDR_{BH}), which are network disorders, were also found (table S10). We validated annotations in vivo on IMAGEN data by restricting the analysis to these seven significant GO terms. Genetic variation in all but 1 GO term was significantly associated with in vivo functional connectivity ($z > 4.02$, $P < 2.8 \times 10^{-5}$ uncorrected) (table S9). Using a mouse transcriptome database (*25*), we also found that 39 mouse orthologs from our list were significantly enriched in neurons, 19 in astrocytes, and 14 in oligodendrocytes (76 were not significantly overexpressed in any of these three cell types). This suggests that the relationship between gene expression and spatial organization into functional networks may be due to neuronal processes more than to support cell or white-matter processes.

Functional networks are fundamental to many brain processes in humans. Here, we show that network strength was correlated with the expression of genes tightly linked to synaptic function. The preservation of the association between functional networks and gene expression across the lifespan (IMAGEN, 14-year-olds; AIBS, 24- to 55-year-olds) is remarkable and could be partly explained by the relative stabilization of interregional transcriptional similarity from adolescence onwards (*26*). Genes in our list may also play a role in certain diseases; some are implicated in brain disorders such as Alzheimer's and schizophrenia (*27*), whose pathogenesis is thought to relate, in part, to aberrant connectivity. Beyond humans, it appears that similar mechanisms extend to lower animals because our list is significantly associated with mouse neural connectivity, and several gene functions from our list were found in a study examining genes supporting neural connectivity in rodents (tables S3, S7, and S8) (*28*). Thus, our results show that across

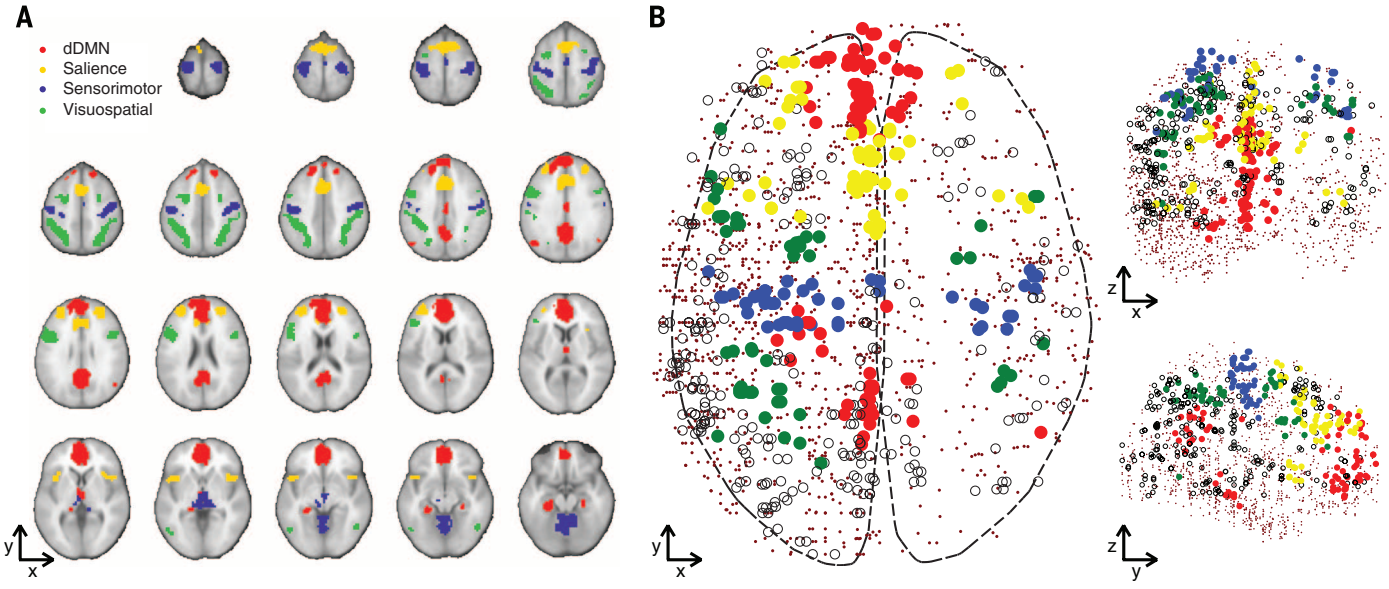


Fig. 1. Functional networks in MRI and gene expression data. (**A**) The four functional networks of interest. Red, dorsal default mode; yellow, salience; green, visuospatial; blue, sensorimotor. (**B**) AIBS brain samples assigned to their corresponding functional network. Solid circles are samples assigned to the four networks of interest, open circles show samples in the nine other networks, and dots show non-network AIBS samples.

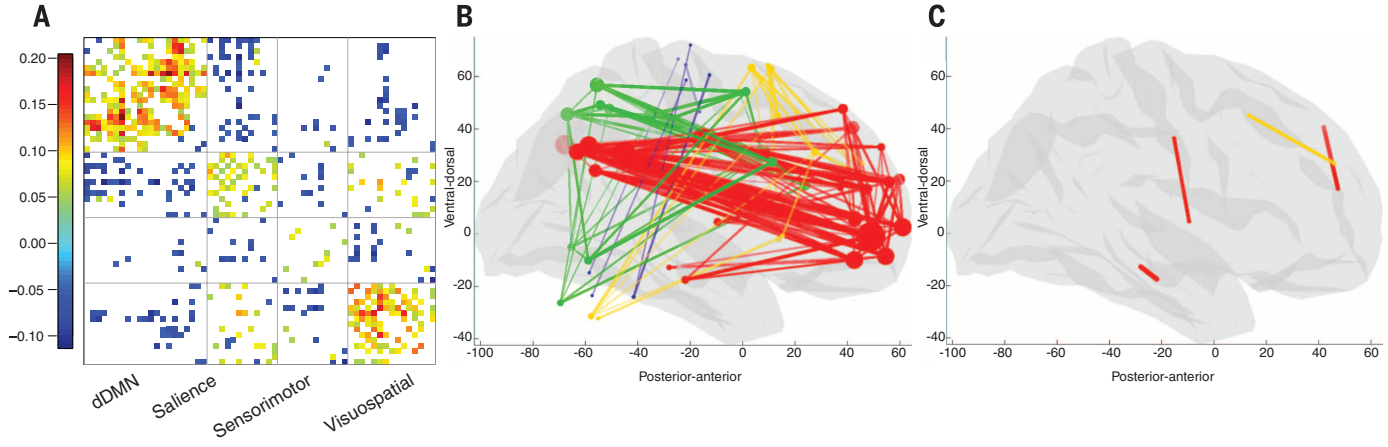


Fig. 2. In vivo functional connectivity differences related to the consensus gene list. Difference in in vivo functional connectivity between the averages of the top 20 and the bottom 20 subjects in IMAGEN, ranked by genotype score with respect to the consensus list of genes. (**A**) Difference matrix sorted by functional network (correlation differences smaller than |0.05| are not shown). Positive values indicate connections that are stronger in high genotype score subjects, and negative values indicate the opposite. Connections are mostly increased within functional networks, but also between some functional networks. (**B**) MNI space sagittal view of within-network connections that are stronger in high-genotype-score subjects. Regions (disks) are coded according to the functional network they belong to: red, dorsal default mode; yellow, salience; green, visuospatial; blue, sensorimotor. Connections (lines) are color-coded to their functional networks. (**C**) Same, for connections that are stronger in low-genotype-score subjects. The majority of connections are strengthened in high-genotype-score subjects.

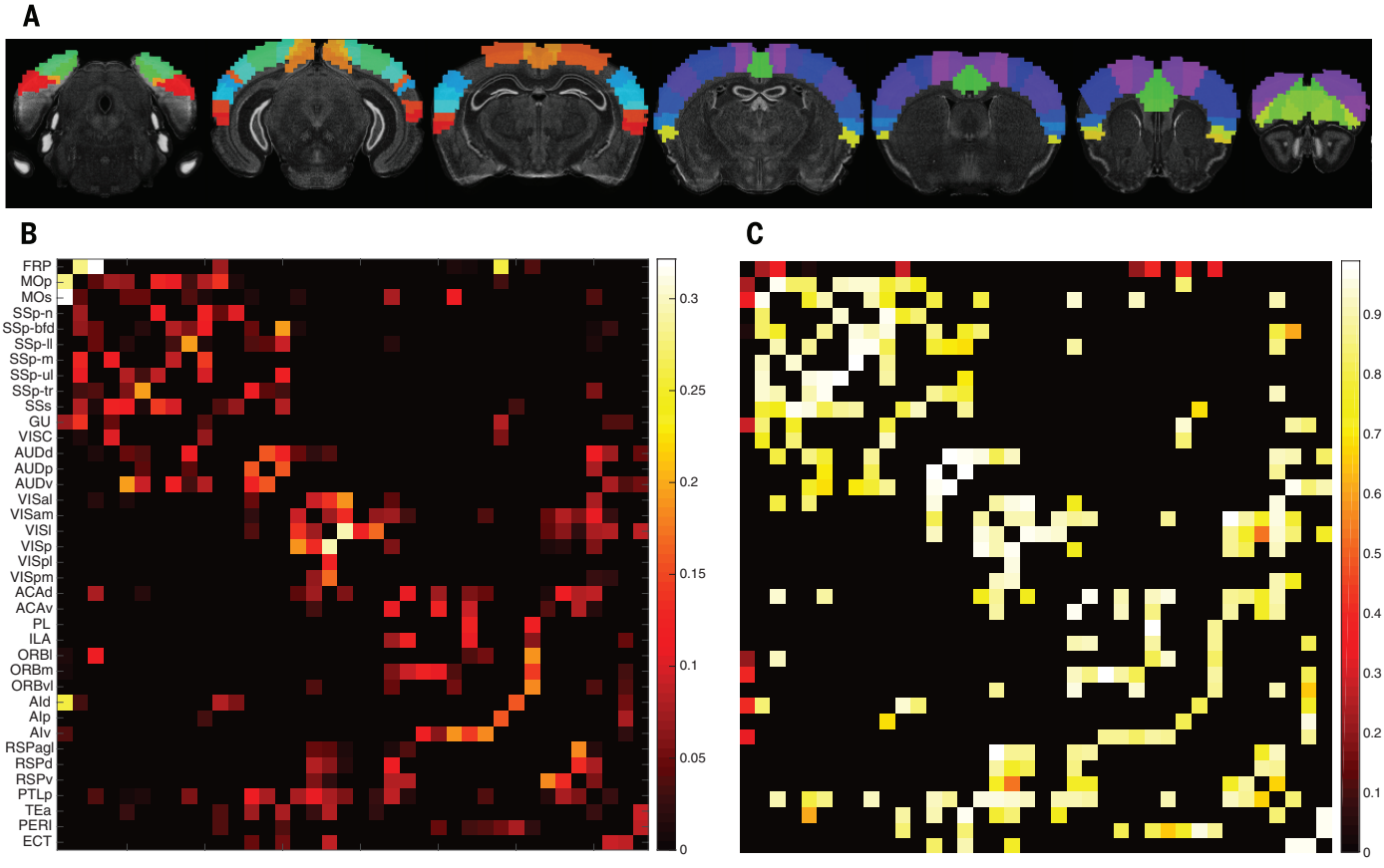


Fig. 3. Mouse mesoscale connectivity and transcriptional similarity. (**A**) Mouse isocortex parcellated into 38 regions (*23*). (**B**) Corresponding symmetrized, thresholded, and normalized ipsilateral axonal connectivity weights. (**C**) Transcriptional similarity (genetic correlation), using our consensus list of genes.

developmental stages and species, functional connectivity in brain networks is integrally linked to the machinery of synaptic communication.

REFERENCES AND NOTES

1. M. D. Fox, M. E. Raichle, *Nat. Rev. Neurosci.* **8**, 700–711 (2007).
2. S. M. Smith *et al.*, *Proc. Natl. Acad. Sci. U.S.A.* **106**, 13040–13045 (2009).
3. R. M. Birn, *Neuroimage* **62**, 864–870 (2012).
4. Z. Shehzad *et al.*, *Cereb. Cortex* **19**, 2209–2229 (2009).
5. M. D. Fox, M. Greicius, *Front. Syst. Neurosci.* **4**, 19 (2010).
6. W. W. Seeley, R. K. Crawford, J. Zhou, B. L. Miller, M. D. Greicius, *Neuron* **62**, 42–52 (2009).
7. D. C. Glahn *et al.*, *Proc. Natl. Acad. Sci. U.S.A.* **107**, 1223–1228 (2010).
8. A. Fornito *et al.*, *J. Neurosci.* **31**, 3261–3270 (2011).
9. W. R. Shirer, S. Ryali, E. Rykhlevskaia, V. Menon, M. D. Greicius, *Cereb. Cortex* **22**, 158–165 (2012).
10. M. J. Hawrylycz *et al.*, *Nature* **489**, 391–399 (2012).
11. D. Mantini, M. G. Perrucci, C. Del Gratta, G. L. Romani, M. Corbetta, *Proc. Natl. Acad. Sci. U.S.A.* **104**, 13170–13175 (2007).
12. N. U. F. Dosenbach *et al.*, *Proc. Natl. Acad. Sci. U.S.A.* **104**, 11073–11078 (2007).
13. Y. Golland, P. Golland, S. Bentin, R. Malach, *Neuropsychologia* **46**, 540–553 (2008).
14. S. D. Roosendaal *et al.*, *Brain* **133**, 1612–1621 (2010).
15. L. Ng *et al.*, *Nat. Neurosci.* **12**, 356–362 (2009).
16. B. Zhang, S. Horvath, *Stat. Appl. Genet. Mol. Biol.* **4**, e17 (2005).
17. Materials and methods are available as supplementary materials on *Science* Online.
18. J. Richiardi, A. Altmann, M. Greicius, in *Proceedings of the 3rd International Workshop on Pattern Recognition in NeuroImaging (PRNI)* (PRNI, Philiadelphia, 2013), pp. 70–73.
19. L. Natarajan, M. Pu, K. Messer, *Ann. Appl. Stat.* **6**, 521–541 (2012).
20. N. Meinshausen, P. Bühlmann, *J. R. Stat. Soc. Series B Stat. Methodol.* **72**, 417–473 (2010).
21. G. Schumann *et al.* IMAGEN consortium, *Mol. Psychiatry* **15**, 1128–1139 (2010).
22. D. Nam, J. Kim, S.-Y. Kim, S. Kim, *Nucleic Acids Res.* **38** (Web Server), W749–W754 (2010).
23. S. W. Oh *et al.*, *Nature* **508**, 207–214 (2014).
24. W. Huang, B. T. Sherman, R. A. Lempicki, *Nat. Protoc.* **4**, 44–57 (2009).
25. J. D. Cahoy *et al.*, *J. Neurosci.* **28**, 264–278 (2008).
26. M. Pletikos *et al.*, *Neuron* **81**, 321–332 (2014).
27. A. Heck *et al.*, *Neuron* **81**, 1203–1213 (2014).
28. L. Wolf, C. Goldberg, N. Manor, R. Sharan, E. Ruppin, *PLOS Comput. Biol.* **7**, e1002040 (2011).

ACKNOWLEDGMENTS

We thank C.-K. Lee for help with AIBS data normalization and C. Quairiaux for help with mouse brain anatomy. Functional networks imaging data are at http://findlab.stanford.edu/functional_ROIs.html. Human microarray data are at http://human.brain-map.org. IMAGEN data are available by application to consortium coordinator G. Schumann (http://imagen-europe.com) after evaluation according to an established procedure. Mouse gene expression data are at http://mouse.brain-map.org. Connectivity model data are from (*23*). J.R. is supported by a Marie Curie Fellowship from the European Union (299500). M.D.G. is supported by grants from the Feldman Family Foundation and the National Institutes of Health (RO1NS073498). This work received additional support from the following sources: the European Union-funded FP6 Integrated Project IMAGEN (Reinforcement-related behavior in normal brain function and psychopathology) (LSHM-CT- 2007-037286), the FP7 projects IMAGEMEND (602450; IMAging GEnetics for MENtal Disorders) and MATRICS (603016), the Innovative Medicine Initiative Project EU-AIMS (115300-2), a Medical Research Council Programme Grant "Developmental pathways into adolescent substance abuse" (93558), the Swedish funding agency FORMAS, the Medical Research Council and the Wellcome Trust (Behavioral and Clinical Neuroscience Institute, University of Cambridge), the National Institute for Health Research (NIHR) Biomedical Research Centre at South London and Maudsley NHS Foundation Trust and King's College London, the Bundesministerium für Bildung und Forschung (BMBF; grants 01GS08152, 01EV0711, eMED SysAlc01ZX1311A, and Forschungsnetz AERIAL), the Deutsche Forschungsgemeinschaft (DFG; grants FOR 1617, EXC 257, SM 80/7-1, SM 80/7-2, and SFB 940/1), the U.S. National Institutes of Health (Axon, Testosterone and Mental Health during Adolescence; RO1 MH085772-01A1), Eranet–Neuron grant (project AF12-NEUR0008-01 - WM2NA), MILDECA, Fondation pour la Recherche Médicale, NIH Consortium grant U54 EB020403, which is supported by a cross-NIH alliance that funds Big Data to Knowledge Centers of Excellence, and the Allen Institute for Brain Science.

SUPPLEMENTARY MATERIALS

www.sciencemag.org/content/348/6240/1241/suppl/DC1
Materials and Methods
Supplementary Text
Figs. S1 to S5
Tables S1 to S10
IMAGEN Consortium Author List
References (*29*–*55*)
Data Files S1 to S3

12 May 2014; accepted 7 May 2015
10.1126/science.1255905

INSECT FLIGHT

Luminance-dependent visual processing enables moth flight in low light

Simon Sponberg,[1,2]* Jonathan P. Dyhr,[1,3] Robert W. Hall,[1] Thomas L. Daniel[1]

Animals must operate under an enormous range of light intensities. Nocturnal and twilight flying insects are hypothesized to compensate for dim conditions by integrating light over longer times. This slowing of visual processing would increase light sensitivity but should also reduce movement response times. Using freely hovering moths tracking robotic moving flowers, we showed that the moth's visual processing does slow in dim light. These longer response times are consistent with models of how visual neurons enhance sensitivity at low light intensities, but they could pose a challenge for moths feeding from swaying flowers. Dusk-foraging moths avoid this sensorimotor tradeoff; their nervous systems slow down but not so much as to interfere with their ability to track the movements of real wind-blown flowers.

Most animals rely on vision to maneuver through complex environments. Similarly, many engineered systems use machine vision to sense their surroundings. Yet all biological or synthetic visual systems operating in natural environments must deal with high variability in ambient light intensity. Animals can encounter light intensities that vary over 10 billion–fold within a single day (*1*–*3*). Low-light specializations can extend an animal's sensory capabilities but frequently produce tradeoffs, (such as increased sensitivity but reduced resolution) (*4*–*6*). Revealing the mechanisms that enable nervous systems to adapt to this vast range of light, as well as their functional tradeoffs, are fundamental to understanding the versatility of vision.

We investigated visual processing in dim light—and its functional consequences—in the hawkmoth *Manduca sexta*, an agile flyer that extracts nectar from moving flowers while hovering even in very dim light (Fig. 1A) (*7*–*9*). The moth's compound eye has an adjustable pseudopupil that allows a large number of the highly refractive eye facets (ommatidia) to deliver light to a single photoreceptor in low light, thereby increasing sensitivity (*1*, *2*). Early in visual processing, neurons may also pool inputs from multiple photoreceptors providing spatial summation of light (*1*, *10*). These spatial adjustments improve sensitivity, but they are insufficient to account for the range of low-light sensitivity exhibited by neurons in the moth's visual system (*10*). A hypothesized complementary mechanism is that moths may progressively slow their visual processing as light intensity (luminance) decreases (*1*, *10*, *11*). In effect, as light diminishes, moths might temporally integrate light for a longer period of time, in addition to summing over larger spatial regions (Fig. 1B) (*10*, *12*). This luminance-dependent neural processing predicts a tradeoff: The increased sensitivity that comes with increased processing time should also slow motion detection. This predicts that moths should lag behind the motion of objects that they are visually tracking. Because moths track and feed from moving flowers (*7*–*9*), we can test not only whether the moth's motion response is slowed, but also what potential tradeoffs this poses for tracking natural flower movements.

We used robotic artificial flowers to explore the moth's behavior under different light levels (Fig. 1, A and C, and movies S1 and S2) (*13*). Moths tracked flowers moving side-to-side with a linear combination of sinusoidal trajectories with frequencies spanning two orders of magnitude (0.2 to 20 Hz, Fig. 1, D to F) (*14*, *15*). Hovering and maneuvering in midair is demanding, inherently unstable, and energetically costly (*9*, *16*, *17*). Nonetheless, moths are able to track and feed from moving flowers even at 14 Hz (Figs. 1E and 2A). In contrast to tethered moths (open-loop) tracking visual images (*18*), flower tracking by freely flying (closed-loop) moths is highly linear (coherence in Fig. 1E; explicit test in fig. S2).

Moths lag farther behind flower movement in dim moonlight [0.3 lux (lx)] than in the brighter light of early dusk (300 lx), as predicted for a slowing visual system (Fig. 2B; $F = 46.3$, df = 349, $P < 0.0001$). At both light levels, moths produce the largest motions (highest gain) to flower movements at intermediate frequencies (1- to 2-Hz bandpass, Fig. 2A and fig. S1). However, in low light they begin overshooting the flower (gain > 1, which is 0 dB) (all frequencies: $F = 16.4$, df = 349, $P < 0.0001$; at 1.7 Hz: $t = 4.5$, df = 20.5, $P = 0.0002$). Because the mechanics of flight are the same at both light levels, the differences in tracking must arise because the moth relies on a luminance-dependent neural process.

To quantify the change in processing time, we can estimate a single time constant from the phase response at each light level (Fig. 2B). Overall, the moth's tracking response is 17% slower in dim moonlight than at early dusk: 83.3 ± 2.4 ms as compared to 71.5 ± 3.5 ms, respectively (mean ± SEM; Fig. 2, B and C; $t = 2.82$; df = 21; $P = 0.01$). We obtained similar results when we considered only frequencies below 10 Hz, which was the highest frequency that all individual moths could track (67.2 ± 3.1 and 80.6 ± 3.3 ms; Fig. 2D).

Next we tested whether the slower tracking responses were consistent with a luminance-dependent delay within the moth's visual system. Moths track flowers in closed loop, meaning that their visual input is the difference between their own motion and the flower's (visual "error"; fig. S3) (*13*, *15*). We applied a luminance-dependent delay to the visual response within this closed feedback loop (fig. S3) (*15*). From this, we predicted the moth's response in low light, $\hat{L}(s)$, for each frequency component of the flower's movement (defined by the Laplace variable s). This prediction (Fig. 2, light blue lines) depends only on the measured high-luminance response, $H(s)$, and a single parameter τ, representing the difference in processing time (delay) between the two light levels

$$\hat{L}(s) = \frac{e^{-s\tau}[H(s)/(1 - H(s))]}{1 + e^{-s\tau}[H(s)/(1 - H(s))]} \quad (1)$$

A delay (τ) of 10.4 ms best fits the change in response from the bright to dim light levels. This single parameter captures the empirical phase differences as well as the overshooting that occurs under low light (Fig. 2, E and F). Hence, the hypothesized luminance-dependent visual processing in the moth's nervous system can account for the differences in the closed-loop tracking response at different light intensities.

The above model treats the change in processing as a single time delay. Changes in spatial processing are likely to help shape the moth's tracking response, especially the gain (*10*, *19*). Temporal processing might also be distributed across multiple regions of the visual system, including in the photoreceptors and motion detection circuits (*1*, *10*, *19*). Most importantly, insect motion detection itself is thought to arise by the correlation of adjacent photoreceptors (*20*, *21*), and the process of correlation is nonlinear. What remains unclear is how these more complicated processes would affect moth motion lag if their time constants were luminance-dependent. To be consistent with our simplified models, a more detailed model would need to produce a lag in its input-output relationship that increases linearly with the time constant inside the model. To test for this relationship, we implemented a longstanding model proposed for visual motion detection, the elaborated Hassenstein-Reichardt (HR) correlator (see the supplementary text). We simulated this model's response to an oscillating visual input and explored how this response depends on the

[1]Department of Biology, University of Washington, Seattle, WA 98195, USA. [2]School of Physics and School of Applied Physiology, Georgia Institute of Technology, Atlanta, GA 30332, USA. [3]Department of Biology, Northwest University, Kirkland, WA 98033, USA.
*Corresponding author. E-mail: sponberg@physics.gatech.edu

Downloaded from www.sciencemag.org on June 14, 2015

model's time constants. (*10*, *12*, *20*, *21*). These simulations show that the phase shifts we observed in experiments are consistent with the HR model of insect visual processing, as well as with simple closed-loop delay models (fig. S5).

In all these analyses, a simple luminance delay term accounts for the closed-loop response (Fig. 2, E and F). The increased phase lag in low light supports the hypothesized luminance-dependent visual processing. However, in order to consider overall tracking performance, we cannot consider phase lags and gain separately, because they each describe only one aspect of the response. To accomplish our second aim of assessing a potential performance tradeoff, we combined gain and phase into one metric of tracking error (ε). Specifically, we used the distance in the complex plane between the moth's responses and the ideal tracking conditions (gain = 1, phase = 0°; fig. S4) (*13*, *14*)

$$\varepsilon = \|H(s) - (1 + 0i)\| \qquad (2)$$

where $i = \sqrt{-1}$.

Although tracking performance depends on light intensity, the effect is frequency-dependent and separates into three distinct frequency bands (Fig. 3A). Below 1.7 Hz, tracking error is relatively low (ε < 1) and does not differ between high- and low-luminance conditions (F = 0.49, df =137, P = 0.48). However, tracking error increases rapidly at higher frequencies, even when gain remains high. This is because the moth is more than 90° out of phase with the flower between 1.7 and 8 Hz. In this frequency band, moths track significantly worse in low light (F = 17.6, df =192, P < 0.0001). However, at the very highest frequencies (>8 Hz), tracking error reverts toward unity because the gain is very small.

Counterintuitively, moths are still much more likely to forage and track moving flowers in dim light levels, despite poorer tracking performance (higher ε; Fig. 3B). This suggests that moths incur worse performance in order to obtain the increased sensitivity afforded by luminance-dependent neural processing. However, moths might avoid this

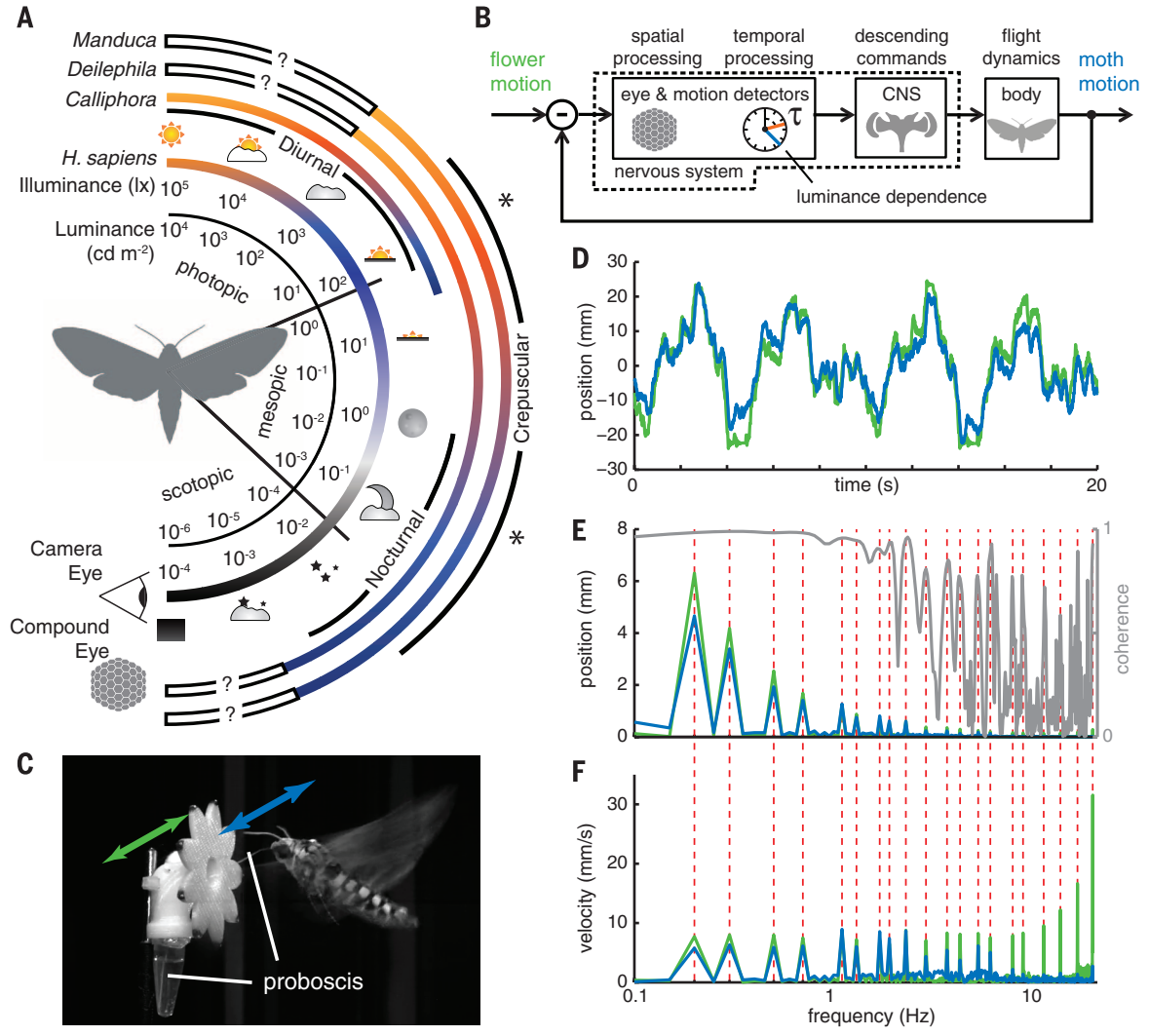


Fig. 1. The effect of light intensity on moths tracking robotic flowers. (**A**) Human photoreceptors, like those of all animals, are capable of detecting even single photons (*28*). However, human color vision (colored arc), as well as our ability to resolve motion and spatial detail, deteriorates below the photopic visual threshold (1 to 10 cd m^{-2}) corresponding to light levels at dusk (*11*, *29*). This is also true for diurnal insects such as the blowfly *Calliphora* (*30*). Human scotopic vision (gray arc) is strictly monochromatic (*29*). The hawkmoth *Deilephila* is truly nocturnal, with color vision throughout much of the scotopic range (*2*). [In (A), "*" indicates experimental light levels. "?" indicates that data are not available.] *Manduca* is crepuscular and is hypothesized to adjust its visual processing (**B**) in order to visually track flowers over its large range of light intensity (>10^6 cd m^{-2}) (*10*, *27*). (CNS, central nervous system.) Robotic, three-dimentional printed flowers generated repeatable moth flight maneuvers (**C**) (movies S1 and S2). We moved the flowers with a trajectory of many superimposed sinewaves to sample many of the frequencies of movement simultaneously (**D**). Fourier transformations (**E** and **F**) of the flower's (green) and moth's (blue) movements show high coherence [(E), gray line], which is the normalized cross-power spectral density (*18*, *24*). Flower movements were prescribed to have equal peak velocities at each frequency (F), which helps avoid saturation in the moth's ability to track.

tradeoff if the flowers they track only move at frequencies below ~2 Hz, below where the performance tradeoff occurs.

We filmed five species of hawkmoth-pollinated flowers in natural wind (see the supplementary text, fig. S6, and movie S3) and found that these flowers move at frequencies where the moth does not suffer a performance cost for tracking in dim moonlight conditions. The vast majority (94%) of motion in all the flowers measured was at frequencies below 1.7 Hz (Fig. 3, C and D, and fig. S6). So whereas moths benefit from the increased sensitivity of slower visual processing in low light, they also avoid negative consequences, because natural flowers usually oscillate in the wind at speeds below those that incur a performance tradeoff.

This matching of frequencies between pollinator vision and flower movement indicates that the relationship between the two organisms probably constrains the slowing of neural processing in variable light conditions. Notably, moths' tracking error increases dramatically above the frequencies of normal flower motion, regardless of light level (Fig. 3C). When the robotic flower moved at frequencies above 2 Hz, the moth would have tracked better by remaining stationary ($\varepsilon > 1$; Fig. 3, A and D). If moths' visual processing was even slower, they would begin to experience adverse tracking performance in

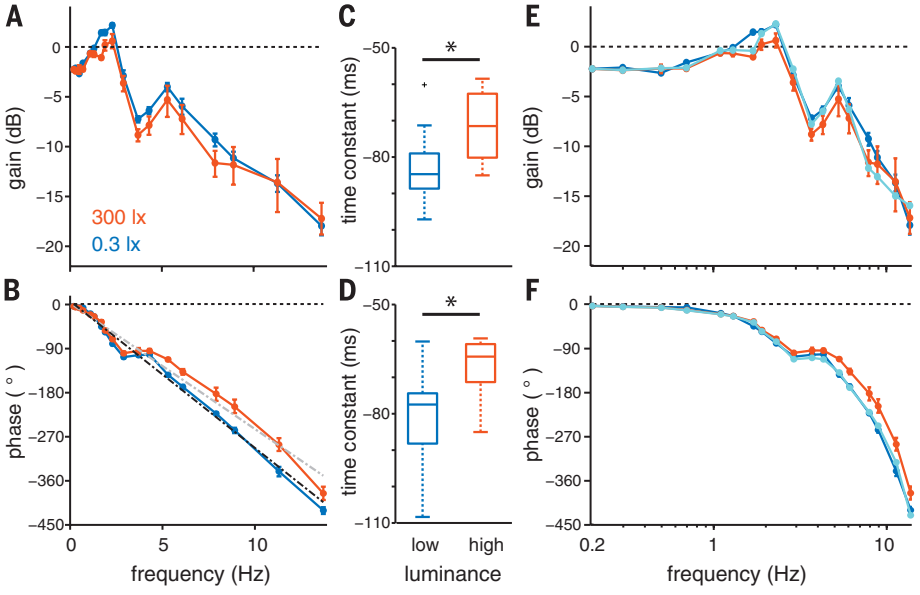


Fig. 2. Visual processing slows in low light. The relative amplitudes of moth and flower give the tracking gain (**A**), and their relative timing gives the phase difference (**B**) with means ± 95% confidence intervals (CIs). The qualitative shape of the response is consistent with the drift-compensation response in the diurnal hawkmoth *Macroglossum* (*8*). Regressing phase onto frequency [(B), dash-dotted lines] estimates the best-fit time constant across all frequencies (**C**) or just those <10 Hz (**D**). We created a prediction for the low-luminance response (light blue) from a closed-loop model of the high-luminance response (orange) with a delayed sensory gain (fig. S3). This prediction successfully captures the overshooting (**E**) and phase shift (**F**) evident in the actual low-light response (dark blue) replotted from (A) and (B) on a log axis.

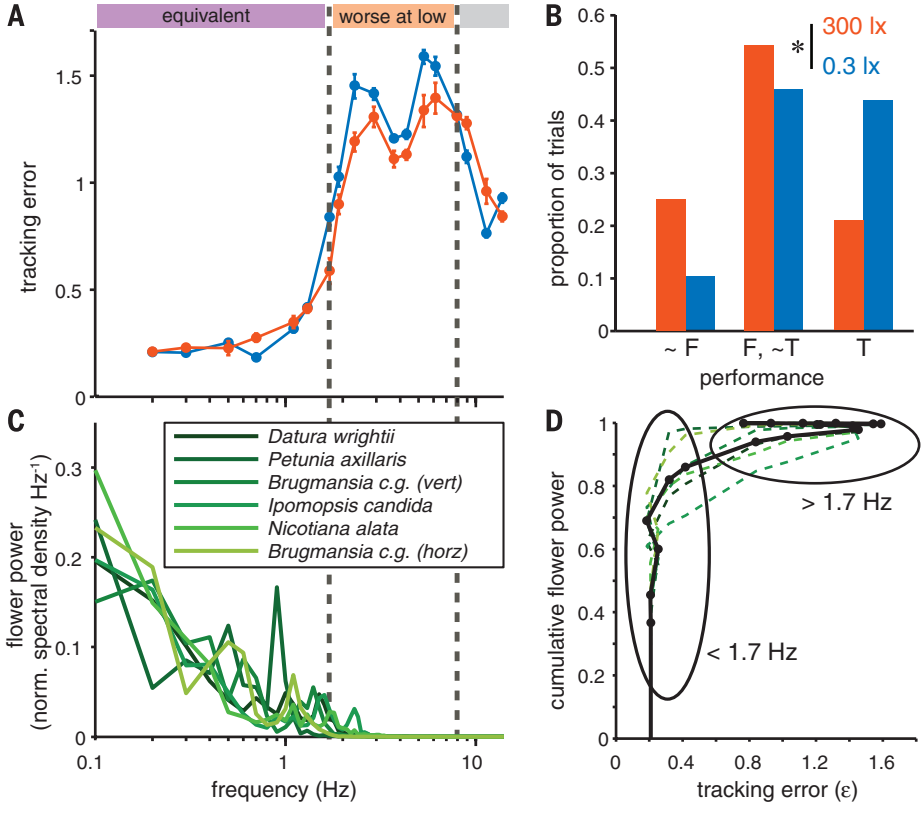


Fig. 3. Tracking performance and real flower movements. Tracking error [(**A**), mean ± 95% CI] is a function of frequency for both luminance conditions. Three distinct frequency bands result, denoted by dashed lines. Behavioral performance of moths (**B**) was scored as no flight (~F); flight, but not tracking (F, ~T); or flight and tracking (T). The power spectra (**C**) of hawkmoth-pollinated flowers blowing in breezes from 0.1 to 2.7 m/s are normalized to the total power. 94% of the cumulative power in the flower's movement (black: mean) occurs in frequencies below 1.7 Hz, where $\varepsilon \approx 0.2$ to 0.4 (**D**).

the frequency band where natural flowers move. One reason moths might rely on both temporal and spatial adjustments to deal with low light (*10*) is to limit the costs to both motion-tracking performance and spatial resolution.

The frequencies with which a moth can maneuver could provide a selective pressure on the biomechanics of flowers to avoid producing floral movements faster than those that the moth can track in low light (*22*). The converse interaction—flower motions selecting on the moth—could also be important, suggesting a coevolutionary relationship between pollinator and plant that extends beyond color, odor, and spatial features (*23*) to include motion dynamics.

The emerging use of system identification to connect open- and closed-loop experiments (*6*, *14*, *15*, *18*, *24*, *25*) provides a useful paradigm for exploring sensorimotor strategies in many systems. Robotic models enable rapid, repeatable experiments that extract critical features of the biological system (*26*) and extend the physical modeling toolkit that has been useful for teasing apart pollinator-plant interactions (*7*, *9*, *23*). Here the robotic flower enabled us to test predictions about closed-loop behavior from open-loop electrophysiological results and models of neural processing (*6*, *15*).

The dual demands of acquiring reliable sensory information and maintaining motor performance are a general challenge, especially for animals such as *Manduca*, which operate in impoverished sensory environments (*4*–*6*, *27*) and on the edge of flight instability (*6*, *25*). Matching the requirements of the motor system to constraints imposed by the dynamics of the environment can provide strategies that enable more extreme sensory performance while averting tradeoffs in motor performance.

REFERENCES AND NOTES

1. E. J. Warrant, *Vision Res.* **39**, 1611–1630 (1999).
2. A. Kelber, A. Balkenius, E. J. Warrant, *Nature* **419**, 922–925 (2002).
3. E. Warrant, M. Dacke, *Annu. Rev. Entomol.* **56**, 239–254 (2011).
4. J. C. Theobald, M. M. Coates, W. T. Wcislo, E. J. Warrant, *J. Exp. Biol.* **210**, 4034–4042 (2007).
5. D. C. O'Carroll, N. J. Bidwell, S. B. Laughlin, E. J. Warrant, *Nature* **382**, 63–66 (1996).
6. N. J. Cowan *et al.*, *Integr. Comp. Biol.* **54**, 223–237 (2014).
7. W. M. Farina, D. Varjú, Y. Zhou, *J. Comp. Physiol. A Neuroethol. Sens. Neural Behav. Physiol.* **174**, 239–247 (1994).
8. W. M. Farina, D. Kramer, D. Varjú, *J. Comp. Physiol. A Neuroethol. Sens. Neural Behav. Physiol.* **176**, 551–562 (1995).
9. J. D. H. Sprayberry, T. L. Daniel, *J. Exp. Biol.* **210**, 37–45 (2007).
10. D. C. O'Carroll, E. J. Warrant, *Proc. 7th ISSNIP Conf.*, 119–124 (2011).
11. E. Warrant, *J. Comp. Physiol. A Neuroethol. Sens. Neural Behav. Physiol.* **190**, 765–789 (2004).
12. A. Borst, S. Bahde, *Biol. Cybern.* **55**, 59–69 (1986).
13. See the supplementary materials and methods.
14. E. Roth, K. Zhuang, S. A. Stamper, E. S. Fortune, N. J. Cowan, *J. Exp. Biol.* **214**, 1170–1180 (2011).
15. E. Roth, S. Sponberg, N. J. Cowan, *Curr. Opin. Neurobiol.* **25**, 54–62 (2014).
16. T. L. Hedrick, B. Cheng, X. Deng, *Science* **324**, 252–255 (2009).
17. K. Y. Ma, P. Chirarattananon, S. B. Fuller, R. J. Wood, *Science* **340**, 603–607 (2013).
18. S. P. Windsor, R. J. Bomphrey, G. K. Taylor, . *J. R. Soc. Interface* **11**, 20130921 (2014).
19. J. H. van Hateren, *Nature* **360**, 68–70 (1992).
20. B. Hassenstein, W. Reichardt, *Z. Naturforsch. B* **11**, 513–524 (1956).
21. J. P. H. van Santen, G. Sperling, *J. Opt. Soc. Am. A* **2**, 300–321 (1985).
22. J. D. H. Sprayberry, M. Suver, *Arthropod-Plant Interact.* **5**, 263–268 (2011).
23. A. Dafni, M. Lehrer, P. G. Kevan, *Biol. Rev. Camb. Philos. Soc.* **72**, 239–282 (1997).
24. M. S. Madhav, S. A. Stamper, E. S. Fortune, N. J. Cowan, *J. Exp. Biol.* **216**, 4272–4284 (2013).
25. J. P. Dyhr, K. A. Morgansen, T. L. Daniel, N. J. Cowan, *J. Exp. Biol.* **216**, 1523–1536 (2013).
26. A. J. Ijspeert, *Science* **346**, 196–203 (2014).
27. J. C. Theobald, E. J. Warrant, D. C. O'Carroll, *Proc. R, Soc. B* **277**, 853–860 (2010).
28. F. Rieke, D. A. Baylor, *Biophys. J.* **75**, 1836–1857 (1998).
29. A. Kelber, L. S. Roth, *J. Exp. Biol.* **209**, 781–788 (2006).
30. E. J. Warrant, in *Ecology of Sensing*, F. G. Barth, A Schmid, Eds. (Springer, Berlin, 2001), pp. 187–213.

ACKNOWLEDGMENTS

J. Riffell kindly provided the artificial *Datura wrightii* scent. We are also grateful for valuable contributions from J. Lockey, M. Salcedo, S. Kazi, A. Molback, A. Hinterwirth, A. Mountcastle, E. Roth, and N. Cowan. Data are available on Dryad, accession no. 10.5061/dryad.jd7b9. This project was supported by the Komen Endowed Chair, an Air Force Research Laboratory grant (FA8651-13-1-0004), an Office of Naval Research Multi University Research Initiative grant (N00014-10-1-0952), an Army Research Office grant (W911NF-13-1-0435), and an Air Force Office of Scientific Research grant (FA9550-14-1-0398) to T.L.D, and by NSF fellowship DBI-1103768 to J.P.D.

SUPPLEMENTARY MATERIALS

www.sciencemag.org/content/328/6240/1245/suppl/DC1
Materials and Methods
Supplementary Text
Figs. S1 to S6
Tables S1
References (*31*–*65*)
Movies S1 to S3

26 November 2014; accepted 29 April 2015
10.1126/science.aaa3042

BIOGEOGRAPHY

The dispersal of alien species redefines biogeography in the Anthropocene

César Capinha,[1,2]* Franz Essl,[3] Hanno Seebens,[4] Dietmar Moser,[3] Henrique Miguel Pereira[1,5,6]

It has been argued that globalization in human-mediated dispersal of species breaks down biogeographic boundaries, yet empirical tests are still missing. We used data on native and alien ranges of terrestrial gastropods to analyze dissimilarities in species composition among 56 globally distributed regions. We found that native ranges confirm the traditional biogeographic realms, reflecting natural dispersal limitations. However, the distributions of gastropods after human transport are primarily explained by the prevailing climate and, to a smaller extent, by distance and trade relationships. Our findings show that human-mediated dispersal is causing a breakdown of biogeographic barriers, and that climate and to some extent socioeconomic relationships will define biogeography in an era of global change.

The reduced similarity in species composition between distant locations is one of the most noticeable patterns in nature (*1*–*3*). Dispersal limitation is at the heart of this pattern, either simply because of the accessibility of nearby locations or because environmental factors of ecophysiological importance tend to be spatially autocorrelated within the range of natural dispersal (*4*). Notwithstanding, human trade and travel have been transgressing natural barriers to dispersal (*5*), and increasing numbers of species are becoming established in places far away from their native range (*6*, *7*). Ultimately, this may cause the breakdown of the "classical" biogeographic regions (*8*)—mainly determined by dispersal barriers and historical factors such as continental drift or paleoclimates—and the emergence of new biogeographic arrangements determined primarily by environmental requirements and by geographic patterns in human transport pathways.

In recent centuries, and particularly during the past few decades, transport pathways have intensified in frequency and extended worldwide (*5*, *9*). This accelerates the speed at which species colonize suitable areas across the globe and inherently contributes to the homogenization of species assemblages at a global scale (*10*–*12*). Niche theory and metacommunity theory suggest that the

[1]CIBIO/InBIO, Centro de Investigação em Biodiversidade e Recursos Genéticos, Cátedra REFER-Biodiversidade, Universidade do Porto, Campus Agrário de Vairão, 4485-661 Vairão, Portugal. [2]Zoologisches Forschungsmuseum Alexander Koenig, Museumsmeile Bonn, 53113 Bonn, Germany. [3]Division of Conservation Biology, Vegetation and Landscape Ecology, Faculty Centre of Biodiversity, University of Vienna, 1030 Vienna, Austria. [4]Institute for Chemistry and Biology of the Marine Environment (ICBM), University of Oldenburg, 26111 Oldenburg, Germany. [5]German Centre for Integrative Biodiversity Research (iDiv) Halle-Jena-Leipzig, 04103 Leipzig, Germany. [6]Institute of Biology, Martin Luther University Halle-Wittenberg, 06108 Halle (Saale), Germany.
***Corresponding author. E-mail: ccapinha@cibio.up.pt**

breakdown of geographic dispersal barriers will allow species to progressively occupy their potential environmental niche (*2*, *13*, *14*), although other factors, such as the biotic composition of the receiving communities, may also play a role (*15*). This dispersal release should give rise to coherent spatial units reflecting environmental similarities among regions, and climatic similarities in particular (*16*, *17*). Despite a strong theoretical rationale, clear evidence of a global, climate-filtered, biogeographic regionalization originated by human activity is still lacking.

Here, we report the results of a global-scale analysis comparing the biogeographic patterns of terrestrial alien gastropods before and after dispersal by humans. In contrast to most previous studies of biotic homogenization, our analysis is global and therefore particularly appropriate to test the climate filter hypothesis. Regional studies capture only a fraction of worldwide climatic variation and are thus more likely to miss climatic signals. We also expect that increases in distributional equilibrium with climate should be particularly apparent for terrestrial gastropods because they are frequently introduced over long distances by means of trade (*18*, *19*).

We collected national and subnational species lists of alien terrestrial gastropods, here defined as established alien species originating from human introductions after 1500 CE. We found data for regions across all continents except Antarctica, representing most of the major climatic types and biogeographic realms of the world (fig. S1 and table S1). For each alien species, we also identified from the literature those regions in our data set that belong to their native range (fig. S2) (*20*). For simplicity, native range was defined as any location in which the species occurred before 1500 CE. This eventually may have led to the inclusion of a few locations to which the species were introduced earlier; however, those introductions have likely occurred within biogeographic realms (*5*, *9*). Our alien distribution data set contained 802 occurrence records spread across 56 countries and subnational entities (e.g., federal states, islands), for a total of 175 species. The native distribution data set represented a subset of 140 species and 45 countries and subnational entities and contained 703 occurrence records.

We quantified pairwise compositional dissimilarity of the species lists in two ways: (i)

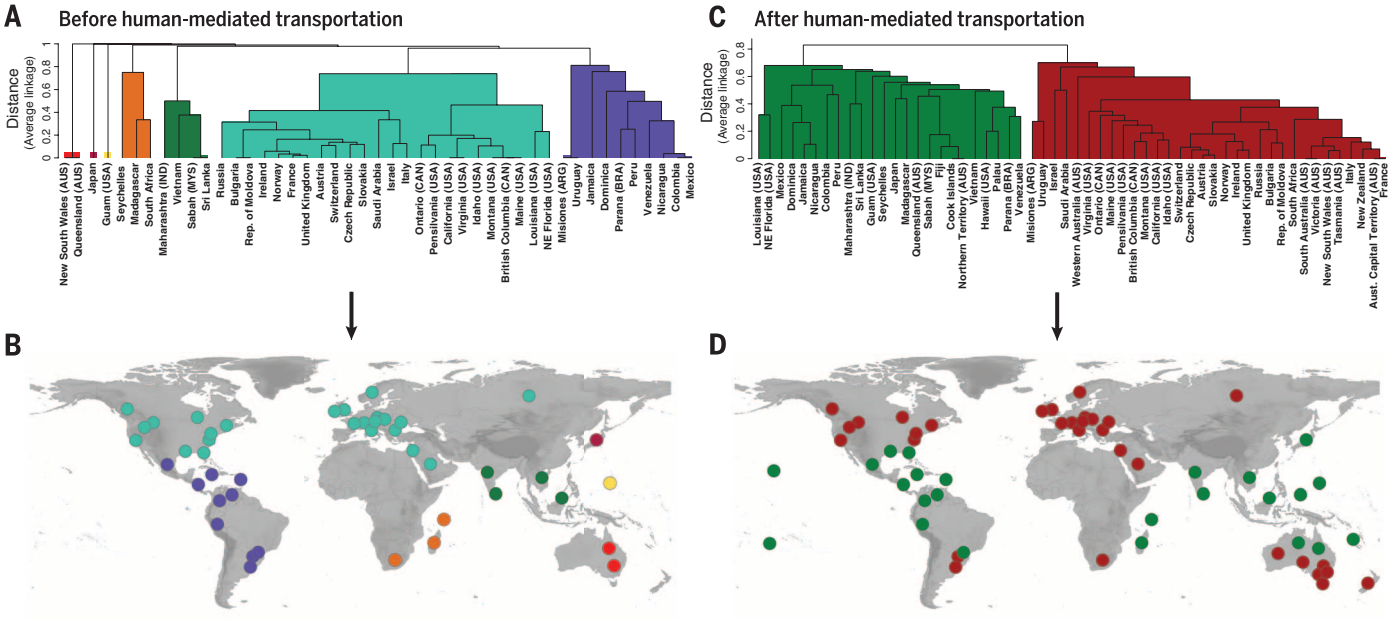


Fig. 1. Dendrogram and map of compositional similarities among lists of alien terrestrial gastropods. (**A** and **B**) Before dispersal by humans. (**C** and **D**) After dispersal by humans. Compositional dissimilarity was measured by the β_{sim} index. Clusters were built through the minimization of the average compositional dissimilarity of one location to the others [i.e., UPGMA (unweighted pair group method with arithmetic mean) grouping]. Colors indicate main clusters identified by the dendrogram and their corresponding locations in the world map.

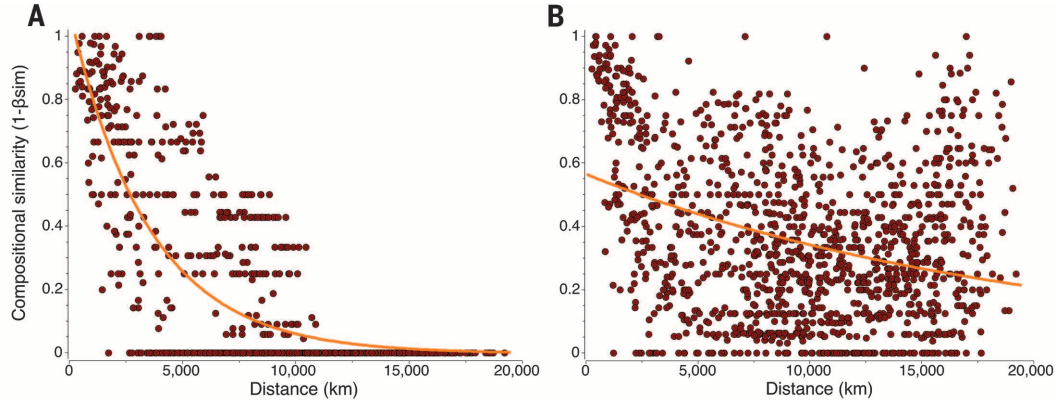


Fig. 2. Relationship between compositional similarities of lists of alien terrestrial gastropods and geographical distances. (**A**) In native ranges. (**B**) In current ranges. Compositional similarities were measured by $1 - \beta_{sim}$. Relationship of compositional similarity for species in their native ranges was assessed on the basis of 990 unique pairs of 45 countries and subnational entities. Relationship for species in their current ranges is based on 1540 unique pairs of 56 countries and subnational entities. Model fits of exponential decay of compositional similarity with increasing distance are shown (orange). Model coefficients are provided in the text; tests of significance were obtained by comparison with distribution of coefficients generated from 1000 permutations of the matrix of compositional similarities.

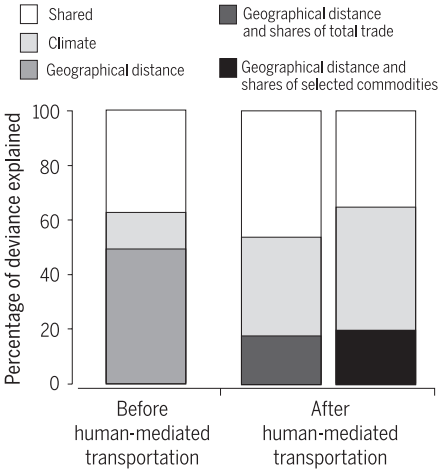


Fig. 3. Proportion of deviance explained in compositional dissimilarity of lists of alien terrestrial gastropods. Proportions are given for species in native ranges (i.e., before dispersal by humans; left bar) and for species in current ranges (i.e., after dispersal by humans; middle and right bars) and represent deviance that is explained by (i) climate- and dispersal-related predictors combined (white), (ii) climate alone (lighter gray), (iii) geographical distance alone (representing natural dispersal; mid-gray), and (iv) geographical distance and trade shares (representing anthropogenic dispersal) combined (darker gray and black). Climate is characterized by prevailing values of four variables: annual mean temperature, temperature seasonality, annual precipitation, and precipitation seasonality.

using only the native distribution, representing the spatial arrangement before human-mediated dispersal, and (ii) using both native and alien distribution, representing their current distribution. Dissimilarity was measured by the β_{sim} index (figs. S3 and S4). This is a standard metric in biogeographic studies (*3*, *21*) because it accounts for differences in species richness. For each of the two dissimilarity matrices, we used an agglomerative hierarchical clustering algorithm (table S3) and nonmetric multidimensional scaling to analyze compositional dissimilarities among the lists (*20*).

Results from both analyses show that native-only distributions reflect "classical" broad-scale biogeographic patterns, which arose over geological time scales (Fig. 1A and fig. S5). For example, faunas located in the Australian, African, Oriental, Neotropical, and Holarctic biogeographic realms become clearly differentiated (Fig. 1, A and B) (*1*–*3*). Moreover, the compositional similarity (i.e., $1 - \beta_{sim}$) distinctly decreases with increasing geographical distance, indicating that dispersal limitations largely control these patterns (Fig. 2A, exponential decay rate of compositional similarity per 1000 km = −0.29, $P < 0.001$). Highly similar species compositions ($1 - \beta_{sim} > 0.5$) do not occur at distances greater than ~6500 km, and none of the represented species are shared beyond ~11,000 km.

Combining the native and alien distributions of gastropods changes the grouping patterns: Species lists from temperate regions cluster into one group, while lists from tropical and subtropical regions cluster into another group (Fig. 1, C and D, and fig. S6). For example, regions in temperate North America (e.g., Virginia, California, British Columbia) have, on average, a higher proportion of species shared with sites in other temperate but distant regions of the world, such as Europe, New Zealand, southern Australia, or South Africa, than with "nearby" (sub)tropical regions such as Florida, Louisiana, México, or Jamaica. This bipartite division of species compositions into two latitudinal biogeographic regions—a (sub)tropical belt and a region composed by temperate to arctic areas in both hemispheres (Fig. 1D) (*2*)—suggests a reorganization of species distributions constrained only by climate. Within each of these broad regions, compositional differences and geographical proximity remain associated (see subclusters in Fig. 1C); however, at the global scale, the arrival of aliens leads to the weakening of the distance decay of similarity (Fig. 2B, exponential decay rate of compositional similarity per 1000 km = −0.05, $P < 0.001$) and to the occurrence of highly similar species compositions ($1 - \beta_{sim} > 0.5$) along the whole range of geographical distances (i.e., up to ~19,000 km).

To explicitly test for the role of climate in shaping biogeographic changes, we tested climate as a predictor for compositional dissimilarity before and after human-mediated dispersal. For species in native ranges (i.e., before human transportation), we compared the explanatory power of climate (as represented by prevailing values of annual means and seasonality of temperature and precipitation) (*20*) with that of geographical distances (which we assume to represent dispersal limitations) (*4*). For the analysis of combined native and alien distributions (i.e., after human dispersal), we additionally accounted for the role of anthropogenic dispersal. Because global patterns of introduction of terrestrial gastropods are primarily determined by commodity trading (*18*, *19*), we used bilateral trade shares as proxy. We calculated this variable in two alternative ways: (i) considering all traded commodities (a general indicator of trade integration among the countries), and (ii) considering only those commodities that are known vectors of gastropods (e.g., household tiles, live plants, or fresh vegetables and fruits for consumption) (*18*, *20*). Because bilateral trade data are not available for most subnational entities, the tests were performed using country-level data representative of the biogeographic groupings identified above (figs. S7 to S12) (*20*).

Monte Carlo permutation of generalized dissimilarity models (*22*) shows that climate and geographical distance are both significant predictors of native-range compositional dissimilarities ($P < 0.001$) (*20*), accounting together for about 61% of total deviance. However, the partitioning into unique and shared components of the factors (*20*) reveals that the unique explanatory power of geographical distance (representing dispersal limitation) is much greater (proportion of total explained deviance = 49.5%) than that of climate (proportion of total explained deviance = 13.3%) (Fig. 3). In contrast, for the current distribution of gastropods (i.e., including both native and alien ranges), climate rather than dispersal becomes the most important predictor. More specifically, when used jointly, both climate- and dispersal-related variables (i.e., geographical distances and trade shares) are significant predictors of current patterns of compositional dissimilarity ($P < 0.001$), accounting for about 63% of its total deviance. But the unique contribution of climate to the total explained is now about 2 to 2.3 times that of the unique contribution of dispersal (climate = 36.4% and dispersal represented by geographical distance and shares of total trade = 17.5%; climate = 45.1% and dispersal represented by geographical distance and shares of selected commodities = 19.6%) (Fig. 3). We cannot exclude the possibility that anthropogenic dispersal pathways that covary with climate (*23*) may also have contributed to the formation of this pattern; however, the reduced relative influence of dispersal-related variables in explaining current distribution patterns suggests that this process, if causative, is of moderate importance.

Signs of ongoing and intensifying biodiversity change are increasingly ubiquitous (*24*, *25*). Still, a recent global analysis of monitoring studies found no significant changes in local species richness, but instead a strong temporal species turnover (*6*). Human-mediated dispersal of species has already caused substantial biotic intermixing worldwide (*12*, *26*, *27*) and may contribute to this turnover. Biotic intermixing is predicted to continue or even intensify in the future (*5*, *28*). The resulting "biogeography of the Anthropocene" defies physical boundaries and reduces compositional dissimilarities among distant regions (*7*). However, our results suggest that instead of a progression toward a uniform biosphere, ecophysiological limitations will cause a higher prevalence of biotic homogenization among areas sharing similar environments. Our results also suggest that homogenization will be greater among regions that have intense trade relations and that are closely located. These novel species assemblages will be dominated by relatively few but widespread alien species, which mostly consist of competitive generalists (*10*). This profound biogeographic reorganization will put additional pressure on native biota [e.g., (*29*)]. A recent international assessment has shown that the rate of alien introduction events shows no signs of abating (*30*). Renewed efforts are needed to slow biotic homogenization if the targets of the Convention on Biological Diversity for 2020 are to be met (*30*).

REFERENCES AND NOTES

1. A. R. Wallace, *The Geographical Distribution of Animals* (Cambridge Univ. Press, Cambridge, 1876).
2. C. B. Cox, P. D. Moore, *Biogeography: An Ecological and Evolutionary Approach* (Blackwell, Malden, MA, ed. 7, 2005).
3. B. G. Holt *et al.*, *Science* **339**, 74–78 (2013).

4. J. C. Nekola, P. S. White, *J. Biogeogr.* **26**, 867–878 (1999).
5. P. E. Hulme, *J. Appl. Ecol.* **46**, 10–18 (2009).
6. M. Dornelas *et al.*, *Science* **344**, 296–299 (2014).
7. M. R. Helmus, D. L. Mahler, J. B. Losos, *Nature* **513**, 543–546 (2014).
8. C. S. Elton, *The Ecology of Invasions by Plants and Animals* (Univ. of Chicago Press, Chicago, 1958).
9. F. di Castri, in *Biological Invasions: A Global Perspective*, J. A. Drake *et al.*, Eds. (Wiley, Chichester, UK, 1989), pp. 1–30.
10. M. L. McKinney, J. L. Lockwood, *Trends Ecol. Evol.* **14**, 450–453 (1999).
11. P. Cassey, T. M. Blackburn, J. L. Lockwood, D. F. Sax, *Oikos* **115**, 207–218 (2006).
12. S. Villéger, S. Blanchet, O. Beauchard, T. Oberdorff, S. Brosse, *Proc. Natl. Acad. Sci. U.S.A.* **108**, 18003–18008 (2011).
13. J. Soberón, *Ecol. Lett.* **10**, 1115–1123 (2007).
14. M. A. Leibold, E. P. Economo, P. Peres-Neto, *Ecol. Lett.* **13**, 1290–1299 (2010).
15. W. Thuiller *et al.*, *Divers. Distrib.* **16**, 461–475 (2010).
16. A. T. Peterson, *J. Biogeogr.* **38**, 817–827 (2011).
17. B. Petitpierre *et al.*, *Science* **335**, 1344–1348 (2012).
18. D. Robinson, G. Davis, *Malacologia* **41**, 413–438 (1999).
19. R. H. Cowie, in *Encyclopedia of Biological Invasions*, D. Simberloff, M. Rejmánek, Eds. (Univ. of California Press, Berkeley, 2011), pp. 634–643.
20. See supplementary materials on *Science* Online.
21. H. Kreft, W. Jetz, *J. Biogeogr.* **37**, 2029–2053 (2010).
22. S. Ferrier, G. Manion, J. Elith, K. Richardson, *Divers. Distrib.* **13**, 252–264 (2007).
23. H. Seebens, M. T. Gastner, B. Blasius, *Ecol. Lett.* **16**, 782–790 (2013).
24. H. M. Pereira, L. M. Navarro, I. S. Martins, *Annu. Rev. Environ. Resour.* **37**, 25–50 (2012).
25. D. P. Tittensor *et al.*, *Science* **346**, 241–244 (2014).
26. M. Winter *et al.*, *Proc. Natl. Acad. Sci. U.S.A.* **106**, 21721–21725 (2009).
27. B. Baiser, J. D. Olden, S. Record, J. L. Lockwood, M. L. McKinney, *Proc. R. Soc B* **279**, 4772–4777 (2012).
28. F. Essl *et al.*, *Proc. Natl. Acad. Sci. U.S.A.* **108**, 203–207 (2011).
29. L. Gibson *et al.*, *Science* **341**, 1508–1510 (2013).
30. P. W. Leadley *et al.*, "Progress towards the Aichi Biodiversity Targets: An assessment of biodiversity trends, policy scenarios and key actions" (Convention on Biological Diversity, 2014); www.cbd.int/doc/publications/cbd-ts-78-en.pdf.

ACKNOWLEDGMENTS

We thank the many researchers who provided information on the native and current distribution of the species, particularly B. Roth, D. Herbert, D. Robinson, G. Stuffle, H. Kappes, J. Ablett, J. Gerlach, K. Hayes, O. Griffiths, R. Preece, R. Forsyth, S. Martin, T.-S. Liew, and T. A. Pearce. We highly appreciate the comments and suggestions of three anonymous reviewers. All sources of species distribution data used in this study are listed in the supplementary materials. Climate and trade data are freely available in the WorldClim (www.worldclim.org) and the UN Comtrade (http://comtrade.un.org) online databases, respectively. Supported by a postdoctoral grant from the Portuguese Foundation for Science and Technology (FCT/MCTES) and POPH/FSE (EC) grant SFRH/BPD/84422/2012 (C.C.), the Austrian Climate and Energy Fund (project no. KR11ACOK00355, SpecAdapt) (F.E.), the German VW-Foundation (H.S.), the German Centre for Integrative Biodiversity Research (iDiv) Halle-Jena-Leipzig funded by German Research Foundation grant FZT 118 (H.M.P.), and Cátedra-REFER-Biodiversidade.

SUPPLEMENTARY MATERIALS

www.sciencemag.org/content/348/6240/1248/suppl/DC1
Materials and Methods
Figs. S1 to S14
Tables S1 to S3
References (*31*–*112*)

10 February 2015; accepted 6 May 2015
10.1126/science.aaa8913

INNATE IMMUNITY

Cytosolic detection of the bacterial metabolite HBP activates TIFA-dependent innate immunity

Ryan G. Gaudet,[1] Anna Sintsova,[1] Carolyn M. Buckwalter,[1] Nelly Leung,[1] Alan Cochrane,[1] Jianjun Li,[2] Andrew D. Cox,[2] Jason Moffat,[1,3] Scott D. Gray-Owen[1]*

Host recognition of pathogen-associated molecular patterns (PAMPs) initiates an innate immune response that is critical for pathogen elimination and engagement of adaptive immunity. Here we show that mammalian cells can detect and respond to the bacterial-derived monosaccharide heptose-1,7-bisphosphate (HBP). A metabolic intermediate in lipopolysaccharide biosynthesis, HBP is highly conserved in Gram-negative bacteria, yet absent from eukaryotic cells. Detection of HBP within the host cytosol activated the nuclear factor κB pathway in vitro and induced innate and adaptive immune responses in vivo. Moreover, we used a genome-wide RNA interference screen to uncover an innate immune signaling axis, mediated by phosphorylation-dependent oligomerization of the TRAF-interacting protein with forkhead-associated domain (TIFA) that is triggered by HBP. Thus, HBP is a PAMP that activates TIFA-dependent immunity to Gram-negative bacteria.

The mammalian innate immune system detects microbes by recognizing pathogen-associated molecular patterns (PAMPs) that are absent from the host yet broadly conserved among classes of microbes (*1*, *2*). However, in many cases, the specific microbial patterns responsible for inducing protective immunity are unclear, suggesting that additional PAMPs may exist that alert the immune system to the nature of a pathogen.

The human pathogens *Neisseria meningitidis* and *Neisseria gonorrhoeae* release a heat-resistant molecule that activates the transcription factor nuclear factor κB (NF-κB) in human embryonic kidney (HEK) 293T and Jurkat T cells—cell types whose ability to respond to PAMPs was thought limited to detection of flagellin by Toll-like receptor 5 (TLR5) (*3*). We previously showed that the *Neisseria* gene *hldA* was required for this molecule's production (*3*). HldA catalyzes the second step in the adenosine 5′-diphosphate (ADP)–heptose biosynthetic pathway, which supplies the precursor for heptose residues found within the inner core of lipopolysaccharide (LPS) (fig. S1A). We tentatively identified a heptose-containing metabolite downstream of HldA as the activating molecule (*3*), yet the specific identity of the active conformation remained unknown. Therefore, we took a genetic approach and examined the ability of culture supernatants from bacterial mutants of the ADP-heptose pathway to activate NF-κB. Although HldA was essential, the ensuing enzymes in the pathway were not (Fig. 1A), indicating that the product of HldA, D-*glycero*-D-*manno*-heptose-1,7-bisphosphate (HBP), was both necessary and sufficient for NF-κB activation. Both Δ*gmhB* and Δ*hldA N. meningitidis* display the "deep-rough" phenotype (*4*), possessing a truncated, heptose-less lipooligosaccharide (LOS) (Fig. 1B), which indicates that the proinflammatory ability of HBP is independent of the incorporation of heptose into the LOS. To confirm this notion, we enzymatically synthesized and purified HBP from sedoheptulose-7-phosphate, using recombinant GmhA and HldA. The reaction product potently stimulated NF-κB only when the substrate and both enzymes were supplied (Fig. 1C), and the activity decreased when the downstream phosphatase GmhB was added (Fig. 1D). Finally, we performed mass spectrometry to show that the proinflammatory product of the GmhA-HldA reaction was indeed HBP (fig. S1, B and C). Thus, HBP is the innate immune agonist shed by *Neisseria*.

Transcriptome analysis identified primarily NF-κB target genes as induced by HBP in Jurkat cells (fig. S2A). The kinetics of HBP-induced transcription and NF-κB activation was slower than stimulation with flagellin or tumor necrosis factor–α (TNFα), both of which signal extracellularly (fig. S2, B to D). Therefore, we considered whether HBP required entry into the host cytosol to signal. Indeed, using reversible digitonin permeabilization (*5*) to deliver HBP-containing supernatants into the cytosol of Jurkat 1G5 cells, which harbor an NF-κB–dependent HIV long terminal repeat (LTR)–luciferase construct (*6*), increased luciferase activity, whereas TLR5 activation was unaffected (Fig. 1E). Moreover, an inhibitor of the guanosine triphosphatase dynamin (*7*) attenuated the NF-κB response to HBP (fig. S3A), indicating that HBP can enter cells via dynamin-dependent endocytosis. HBP enhanced signaling by TLR ligands in THP-1 macrophages, yet did not induce inflammatory cell death (fig. S3, B to D). Finally, HBP induced proinflammatory cytokine production from primary human immune and nonimmune cells (fig. S4, A to C).

The ADP-heptose biosynthetic pathway is highly conserved among Gram-negative bacteria (*8*)

[1]Department of Molecular Genetics, University of Toronto, Toronto, Canada M5S 1A8. [2]Vaccine Program, National Research Council, Ottawa, ON, Canada K1A 0R6. [3]Donnelly Centre and Banting and Best Department of Medical Research, University of Toronto, Toronto, Canada M5S 3E1.
***Corresponding author. E-mail: scott.gray.owen@utoronto.ca**

yet is absent in eukaryotic cells. Moreover, a complete pathway is essential for virulence in a number of bacterial species (*9*–*11*). Therefore, we hypothesized that HBP represented an unrecognized PAMP. However, being a cytosolic bacterial metabolite, HBP signaling by other non-*Neisseria* bacteria would only be apparent if HBP was first liberated from the bacterial cytosol. To test this hypothesis, we transfected soluble lysates from different bacterial genera into 293T cells containing an NF-κB reporter. Gram-negative lysates, with the exception of *Moraxella*, one of the few Gram-negatives that lack the ADP-heptose pathway (*12*), potently activated NF-κB, whereas Gram-positive lysates did not (Fig. 1F). Other than *Neisseria*, which release HBP, NF-κB activation depended on bacterial lysis, as whole bacteria showed no activity. The two known Gram-negative–specific PAMPs cannot account for this activity, as 293T cells were refractory to LPS and only weakly responsive to diaminopimelate (DAP)–containing NOD1 agonists (Fig. 1F). Indeed, overexpression of NOD1 slightly reduced the response to bacterial lysates and HBP (fig. S5), suggesting that an unknown PAMP was activating NF-κB. This activity was directly attributable to the presence of HBP, as disruption of the ADP-heptose pathway upstream of HBP in *Escherichia coli* or *N. meningitidis* abrogated NF-κB activation (Fig. 1G). Alternatively, disrupting the pathway downstream of HBP increased lysate-mediated NF-κB activation (fig. S6). Moreover, *E. coli* that overproduce HBP are more readily detected by the host, as lysates from wild-type *E. coli* that overexpress *Neisseria* HldA, but not the other enzymes in the pathway, increased NF-κB activation by more than 100-fold (Fig. 1H).

In the context of a natural infection, a probable source for bacterial lysis and HBP release would be within the lysosome following phagocytosis. To test this idea, we treated MyD88- and TRIF-deficient THP-1 macrophages (fig. S7) with serum-opsonized HBP-proficient or -deficient *E. coli* of the same LPS phenotype (Fig. 1B). Whereas all three *E. coli* mutants were internalized and degraded at a similar rate (fig. S8), HBP-proficient *E. coli* (Δ*waaC*) induced more interleukin-6 (IL-6) production and proinflammatory transcription than HBP-deficient *E. coli* (Δ*gmhA*, Δ*hldE*) without affecting interferon-β production or cell death (Fig. 1I and fig. S9). Inhibiting phagocytosis with cytochalasin D, or lysosomal acidification with chloroquine, abrogated the effect (Fig. 1I). Thus, HBP liberation during bacterial lysis within the phagolysosome promotes inflammation.

To investigate the HBP-detection pathway, we conducted a genome-wide RNA interference (RNAi) screen using an HIV-based reporter cell line that we designed to take advantage of the TAT-dependent, bifurcating phenotype of the HIV LTR (fig. S10). *RelA* and *Nfκb1*, which are required for HBP-mediated LTR transactivation (*3*), were identified as hits validating the screen (Fig. 2A). Top hits were subjected to a secondary screen assessing the respective proteins' involvement in other NF-κB pathways, specifically TLR5 and TNF receptor (TNFR). The top-scoring gene whose depletion by two different short hairpin RNAs (shRNAs) exclusively affected HBP signaling was TRAF-interacting protein with forkhead-associated domain (TIFA) (Fig. 2B), a ubiquitously expressed cytoplasmic protein that is conserved in vertebrates and activates NF-κB when overexpressed (*13*, *14*). TIFA silencing abolished the proinflammatory transcriptional response in Jurkat cells induced by HBP but not flagellin or TNFα (fig. S11), and abrogated both HBP and Gram-negative lysate-mediated NF-κB activation in 293T cells, a phenotype rescued by ectopic TIFA expression (Fig. 2C). Furthermore, clustered regularly interspaced short palindromic repeats (CRISPR)/Cas9-mediated knockout of *Tifa* in 293T cells abolished HBP and *E. coli*–mediated NF-κB activation (Fig. 2D). Conversely, ectopic expression of TLR2 or NOD1 rendered $Tifa^{-/-}$ cells responsive to Pam3CSK4 or C12-iE-DAP, respectively, distinguishing the TIFA-dependent pathway from the TLR and NLR pathways. In

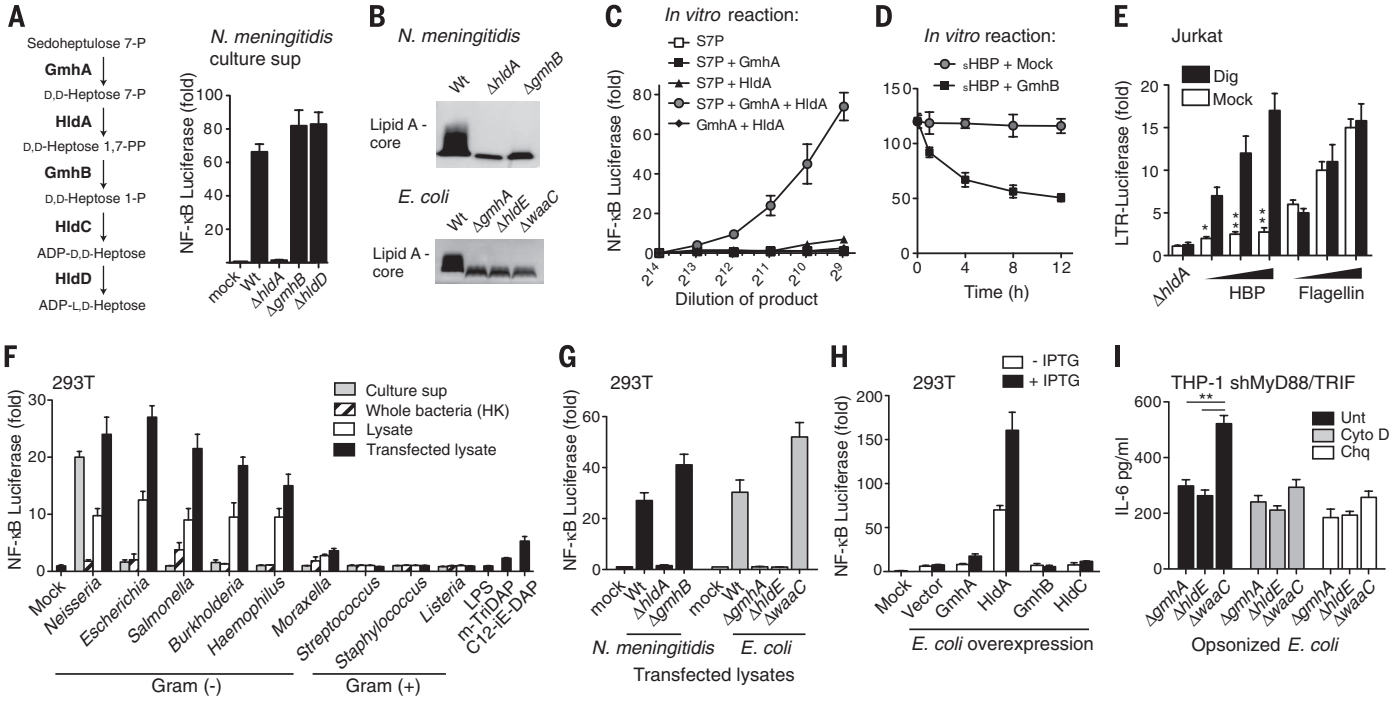


Fig. 1. Cytosolic detection of HBP activates NF-κB. (**A**) NF-κB luciferase activity in 293T cells treated with supernatants from *N. meningitidis* mutants lacking the indicated gene in the ADP-heptose biosynthetic pathway depicted on the left. (**B**) Silver stain of LOS or LPS extracts from *N. meningitidis* or *E. coli* of the indicated genotypes. (**C** and **D**) NF-κB activity in 293T cells treated with the product of in vitro reactions containing combinations of sedoheptulose-7-phosphate (S7P), recombinant GmhA, and/or HldA (C), with or without GmhB (D). (**E**) HIV LTR-luciferase activity in Jurkat T cells treated with HBP-containing or -deficient (Δ*hldA*) supernatants or flagellin, in the presence or absence of the permeabilizing agent digitonin (Dig). (**F** to **H**) NF-κB activity in 293T cells treated with the indicated bacterial fraction (F), transfected with lysates from *N. meningitidis* or *E. coli* of the indicated genotype (G), or treated with lysates of wild-type *E. coli* expressing the indicated *N. meningitidis* enzyme with or without isopropyl-β-D-thiogalactopyranoside (IPTG) (H). (**I**) IL-6 production at 24 hours in THP-1 macrophages expressing shRNAs targeting MyD88 and TRIF, pretreated with dimethyl sulfoxide (Unt), cytochalasin D (Cyto D), or chloroquine (Chq) and infected for 1 hour with *E. coli* of the indicated genotype opsonized with heat-inactivated human serum. Data represent ≥3 independent experiments. Error bars are ±SEM. *$P < 0.05$, ** $P < 0.01$ by analysis of variance (ANOVA).

THP-1 macrophages, TIFA knockdown prevented the HBP-dependent increase in IL-6 after phagocytosis of *E. coli* Δ*waaC* (Fig. 2E). The TIFA requirement was specific to HBP, as TIFA was dispensable for responding to a variety of other PAMPs (Fig. 2F). Finally, HBP detection was independent of other innate immune pathways, as silencing of MyD88, RIP2, STING, or MAVS (*15*–*18*) had no effect on HBP-induced cytokine production (Fig. 2F and fig. S12). Thus, TIFA is uniquely essential for HBP detection.

TIFA overexpression activates NF-κB via the ubiquitin ligase TRAF6 (*14*, *19*), yet a role for TIFA in cellular physiology has remained elusive. Therefore, we asked whether HBP had an effect on the TIFA-TRAF6 interaction, previously reported as constitutive (*14*). We found that in cell lines in which TIFA was depleted and stably complemented with TIFA-1XFLAG, the TIFA-TRAF6 interaction was inducible by HBP (Fig. 2G). Immunostaining revealed that TIFA colocalized with TRAF6 in distinct foci after treatment with HBP (Fig. 2H). The formation of large oligomeric TRAF6 complexes is required to activate its E3 ubiquitin ligase activity and occurs after its recruitment to TLR or IL-1R signalosomes (*20*). Indeed, ubiquitin could be detected in both the *N. gonorrhoeae*-infected, and HBP-induced, TIFA-TRAF6 complex (Fig. 2I). Ubiquitination was TIFA-dependent, as silencing TIFA abolished HBP-mediated TRAF6 ubiquitination (Fig. 2J). TRAF6 is recruited to the TLR signalosomes by the IL-1 receptor–associated kinase (IRAK)

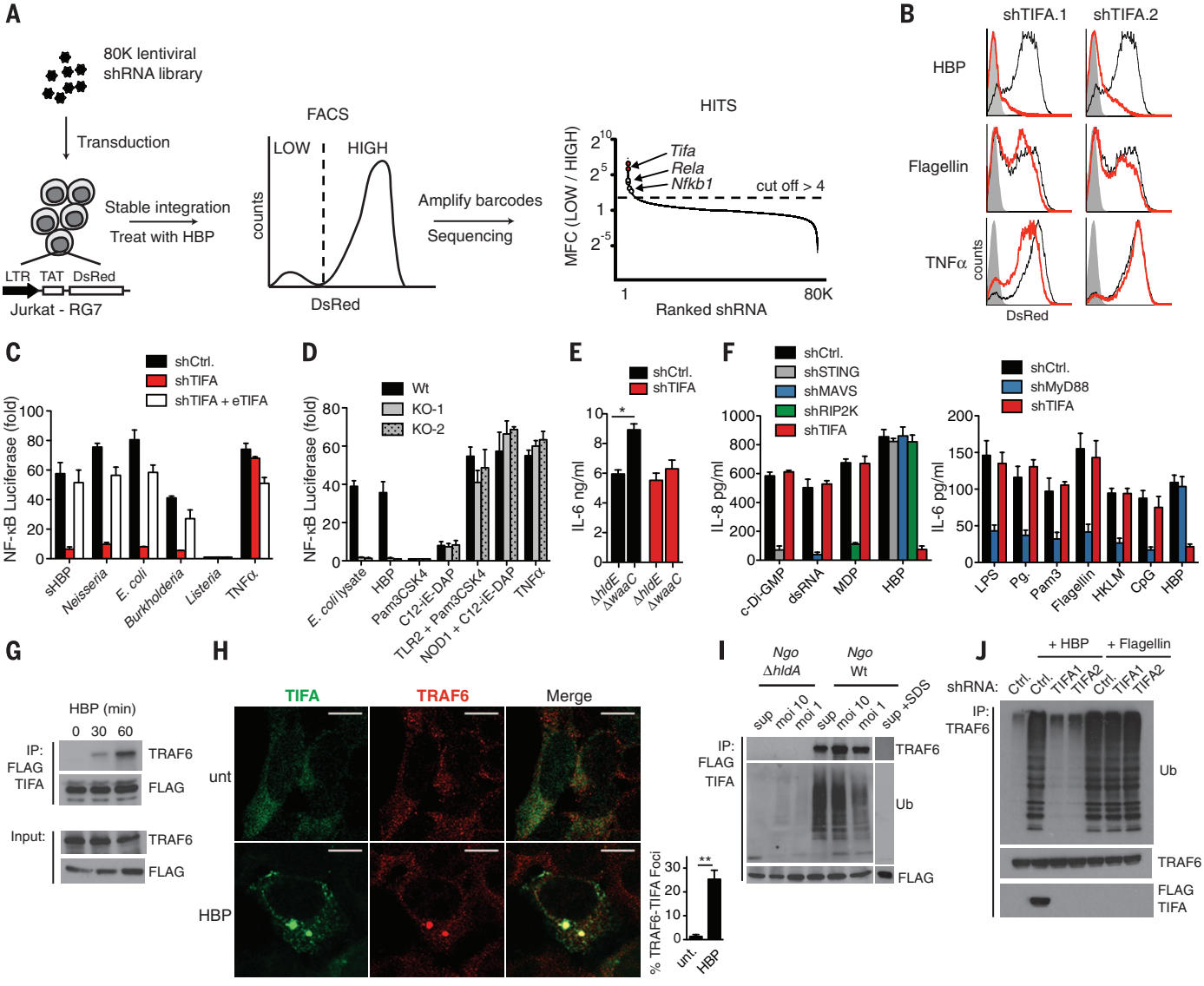


Fig. 2. TIFA mediates HBP signaling through TRAF6 activation. (**A**) Schematic of the RNAi screen. shRNAs are ranked by mean fold change (MFC) in hairpin frequency in low versus high HBP responders. Red or white circles are the resulting scores/positions of the *Tifa* and NF-κB hairpins, respectively. (**B**) Knockdown of TIFA (red) or scrambled shRNA (black) and flow cytometry analysis of DsRed expression in Jurkat-RG7 cells untreated (gray filled) or treated with HBP, flagellin, or TNFα (48 hours). (**C**) TIFA knockdown and NF-κB activity in 293T cells after ectopic TIFA expression (eTIFA) and treatment with enzymatically synthesized HBP (sHBP), or transfected with bacterial lysates (6 hours). (**D**) NF-κB activity in 293T *Tifa* knockout cells (KO-1/2 are two independent clones). Where indicated, cells were transfected with TLR2, or NOD1 expression plasmids, 72 hours before treatment. (**E**) TIFA knockdown and IL-6 production in THP-1 macrophages infected with serum-opsonized *E. coli* of the indicated genotype. (**F**) IL-8 at 24 hours or IL-6 at 6 hours in THP-1 macrophages expressing the indicated shRNA and treated with innate immune agonists. muramyl di-peptide (MDP), heat-killed *Listeria monocytogenes* (HKLM), peptidoglycan (Pg.) (**G**) Immunoprecipitation (IP) of FLAG-TIFA and immunoblot for TRAF6 in Jurkat cells stably complemented with TIFA-1XFLAG and treated with HBP. (**H**) Immunofluorescence microscopy and quantification of FLAG-TIFA and TRAF6 colocalization in 293T cells with or without HBP; scale bars, 10 μm. (**I** and **J**) IP analysis of the TIFA-TRAF6-ubiquitin complex in Jurkat cells infected with *N. gonorrhoeae* (Ngo) (I) or expressing the indicated shRNA and treated with flagellin or HBP (J). Data are representative of ≥2 independent experiments. Error bars are ±SEM. **P* < 0.05, ***P* < 0.01 by ANOVA (E) or Student's *t* test (H).

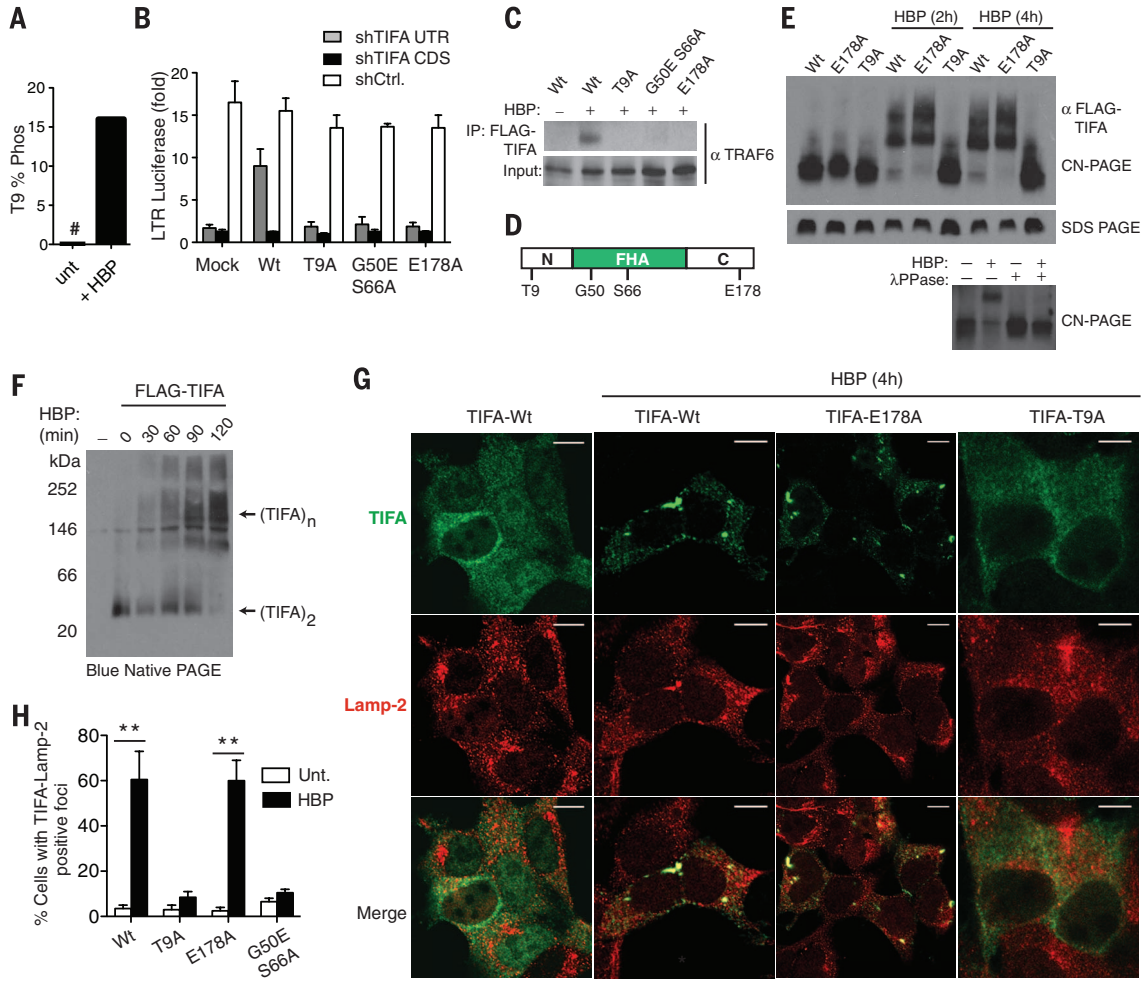


Fig. 3. HBP induces TIFA phosphorylation and oligomerization at lysosomal compartments. (**A**) Mass spectrometry quantification of TIFA-1XFLAG Thr[9] (T9) phosphorylation in Jurkat cells with or without HBP treatment. (**B** to **D**) HBP induced LTR-luciferase activity (B) or TIFA-TRAF6 binding (C) in Jurkat 1G5 cells expressing a scrambled (shCtrl), TIFA-3′ UTR, or coding sequence (CDS) targeting shRNA and complemented with FLAG-TIFA of the indicated genotype as shown in (D). (**E** and **F**) TIFA oligomerization in 293T cells, complemented with FLAG-TIFA of the indicated genotype, analyzed by clear native (CN) polyacrylamide gel electrophoresis (PAGE) (E), with or without lysate treatment with lambda protein phosphatase (λPPase) or by blue native PAGE (F). The band at ~45 to 50 kD corresponds to an intrinsic TIFA dimer (*21*). (**G**) FLAG-TIFA and Lamp-2 colocalization in 293T cells complemented with the FLAG-TIFA of the indicated genotype; scale bars, 10 μm. (**H**) Quantification of TIFA-Lamp-2–positive aggregates in (G). Data from (B) to (H) are representative of two or three independent experiments. Error bars are ±SEM. $^{**}P < 0.01$ by ANOVA. (#) none detected.

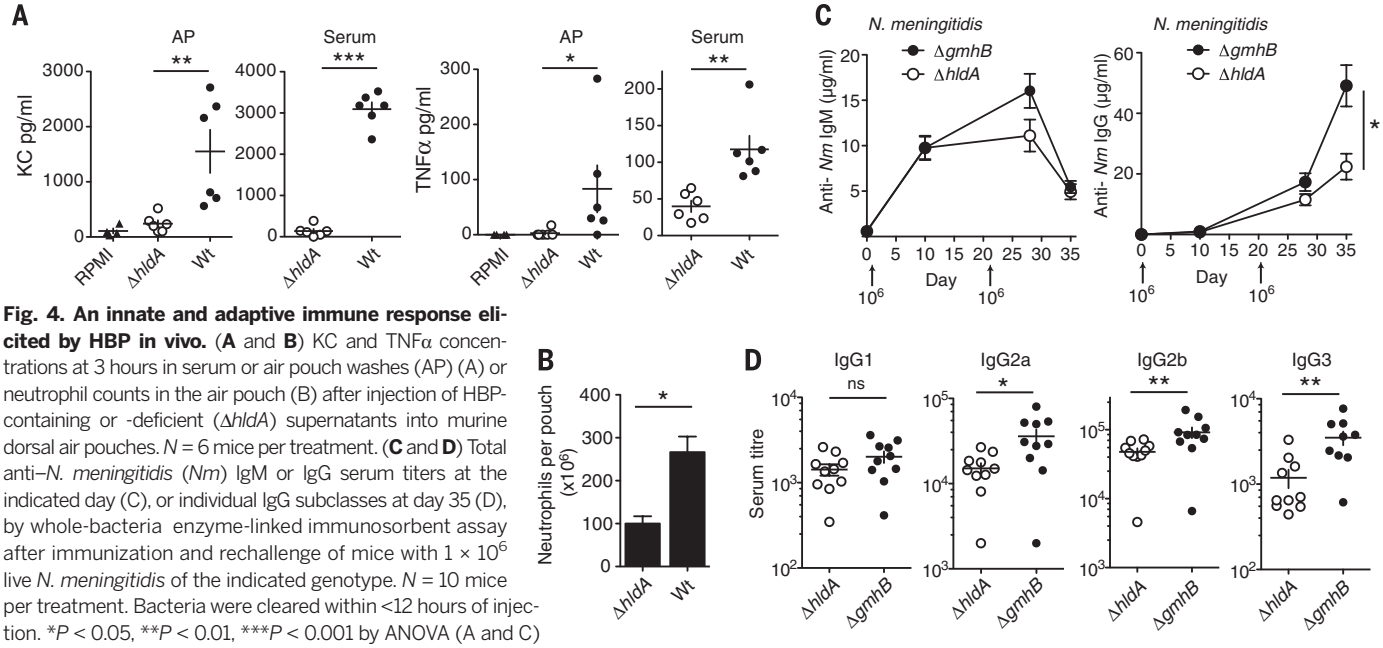


Fig. 4. An innate and adaptive immune response elicited by HBP in vivo. (**A** and **B**) KC and TNFα concentrations at 3 hours in serum or air pouch washes (AP) (A) or neutrophil counts in the air pouch (B) after injection of HBP-containing or -deficient (Δ*hldA*) supernatants into murine dorsal air pouches. $N = 6$ mice per treatment. (**C** and **D**) Total anti–*N. meningitidis* (*Nm*) IgM or IgG serum titers at the indicated day (C), or individual IgG subclasses at day 35 (D), by whole-bacteria enzyme-linked immunosorbent assay after immunization and rechallenge of mice with 1×10^6 live *N. meningitidis* of the indicated genotype. $N = 10$ mice per treatment. Bacteria were cleared within <12 hours of injection. $^{*}P < 0.05$, $^{**}P < 0.01$, $^{***}P < 0.001$ by ANOVA (A and C) or by Student's *t* test (B and D). ns, not statistically significant.

proteins, and TIFA has been reported to bind IRAK-1 (*14*). However, RNAi indicated that HBP signals independently of IRAK-1, -2, and -4 (fig. S13A). In contrast, knockdown of TAK1, IκKβ, or IκKγ (NEMO), but not IκKα, reduced HBP-mediated signaling (fig. S13B). Therefore, TIFA is the entry point into TRAF6-mediated canonical NF-κB activation induced by HBP.

In considering the upstream events in HBP detection, we asked whether TIFA itself was modified in response to HBP. Mass spectrometry of affinity-purified TIFA-1XFLAG from Jurkat cells identified an evolutionarily conserved amino acid (Thr^9) as being inducibly phosphorylated (pT9) by HBP (Fig. 3A). TIFA mutated to prevent phosphorylation (T9A) was unable to interact with TRAF6 or mediate NF-κB activation after treatment with HBP (Fig. 3, B to D). Moreover, substitutions at conserved residues in the phospho-threonine–binding FHA domain (G50E/S66A) or in the TRAF6 binding site (E178A) also prevented complementation. A previous report found that pT9 occurs upon TIFA overexpression, leading to oligomerization via intermolecular pT9 binding with the FHA domain (*21*). We observed that HBP triggered TIFA oligomerization, a process independent of TRAF6 binding but dependent on pT9 (Fig. 3, E and F). Given that soluble HBP can enter the cytosol via endocytosis and that bacterial phagocytosis liberates HBP, we asked whether lysosomes play a role in TIFA signaling. Treatment of 293T cells with HBP induced the formation of TIFA aggregates that colocalized with the lysosomal marker Lamp-2 (Fig. 3, G and H). TIFA aggregation was independent of TRAF6 binding but was dependent on pT9 and the FHA domain (Fig. 3, G and H, and fig. S14). Thus, phosphorylation-dependent oligomerization of TIFA triggers the HBP signaling cascade. Whether TIFA itself is the receptor for HBP, or a proximal adaptor in the signaling axis, needs to be determined.

To investigate the effect of HBP detection in vivo, we first used a mouse dorsal air pouch model to study acute inflammation (*22*). Injection of HBP-containing supernatant, absent other PAMP contamination (fig. S15A), into the air pouch induced local cytokine production in 1 hour (fig. S15B), systemic keratinocyte-derived chemokine (KC) (CXCL1) and TNFα production in 3 hours, and culminated in neutrophil recruitment (Fig. 4, A and B). Innate recognition of PAMPs provides critical instruction to the onset of adaptive immunity (*23*). Therefore, we analyzed the antibody titers produced after nonlethal challenge of mice with *N. meningitidis* Δ*gmhB* or Δ*hldA*, strains that differ only in the presence of HBP. The HBP-producing strain (Δ*gmhB*) induced a transient increase in meningococcal-specific immunoglobulin M (IgM) and significantly more class-switched antimeningococcal IgG, in particular T helper cell 1–associated subclasses IgG2a, b, and IgG3, upon rechallenge (Fig. 4, C and D).

Our findings identify HBP as a previously unrecognized component of the immunological signature of Gram-negative bacteria. That HBP can access the cytosol and engage the TIFA signaling axis in the absence of bacterial virulence factors distinguishes this pathway from other cytosolic PAMPS, like LPS or flagellin, that require bacterial-mediated cytoplasmic delivery (*24*–*26*). Accordingly, detection of HBP promotes inflammation and immune priming rather than inflammatory cell death. Therefore, HBP recognition may represent an important contextual cue in the immune response to Gram-negative bacteria.

REFERENCES AND NOTES

1. R. Medzhitov, *Immunity* **30**, 766–775 (2009).
2. R. Medzhitov, *Nature* **449**, 819–826 (2007).
3. R. J. Malott *et al.*, *Proc. Natl. Acad. Sci. U.S.A.* **110**, 10234–10239 (2013).
4. C. A. Schnaitman, J. D. Klena, *Microbiol. Rev.* **57**, 655–682 (1993).
5. S. E. Girardin *et al.*, *Science* **300**, 1584–1587 (2003).
6. E. Aguilar-Cordova, J. Chinen, L. Donehower, D. E. Lewis, J. W. Belmont, *AIDS Res. Hum. Retroviruses* **10**, 295–301 (1994).
7. E. Macia *et al.*, *Dev. Cell* **10**, 839–850 (2006).
8. B. Kneidinger *et al.*, *J. Bacteriol.* **184**, 363–369 (2002).
9. N. Desroy *et al.*, *J. Med. Chem.* **56**, 1418–1430 (2013).
10. L. Plant *et al.*, *Infect. Immun.* **74**, 1360–1367 (2006).
11. S. A. Loutet, R. S. Flannagan, C. Kooi, P. A. Sokol, M. A. Valvano, *J. Bacteriol.* **188**, 2073–2080 (2006).
12. M. Caroff, D. Karibian, *Carbohydr. Res.* **338**, 2431–2447 (2003).
13. M. Kanamori, H. Suzuki, R. Saito, M. Muramatsu, Y. Hayashizaki, *Biochem. Biophys. Res. Commun.* **290**, 1108–1113 (2002).
14. H. Takatsuna *et al.*, *J. Biol. Chem.* **278**, 12144–12150 (2003).
15. R. Medzhitov *et al.*., *Mol. Cell* **2**, 253–258 (1998).
16. K. Kobayashi *et al.*, *Nature* **416**, 194–199 (2002).
17. D. L. Burdette *et al.*, *Nature* **478**, 515–518 (2011).
18. E. Meylan *et al.*, *Nature* **437**, 1167–1172 (2005).
19. C.-K. Ea, L. Sun, J. Inoue, Z. J. Chen, *Proc. Natl. Acad. Sci. U.S.A.* **101**, 15318–15323 (2004).
20. R. Ferrao, J. Li, E. Bergamin, H. Wu, *Sci. Signal.* **5**, re3 (2012).
21. C.-C. F. Huang *et al.*, *Mol. Cell. Biol.* **32**, 2664–2673 (2012).
22. J. C. Edwards, A. D. Sedgwick, D. A. Willoughby, *J. Pathol.* **134**, 147–156 (1981).
23. A. Iwasaki, R. Medzhitov, *Science* **327**, 291–295 (2010).
24. J. Shi *et al.*, *Nature* **514**, 187–192 (2014).
25. L. Franchi *et al.*, *Nat. Immunol.* **7**, 576–582 (2006).
26. L. E. Sander *et al.*, *Nature* **474**, 385–389 (2011).

ACKNOWLEDGMENTS

We thank G. McSheffrey, E. Islam, S. McCaw, D. White, L. Zhang, J. Krieger, F. St. Michael, R. Molinaro, and C. Lai for technical help and T. Moraes, R. Malott, A. Aman, S. E. Girardin, and T. Ketela for helpful discussions and support. R.G.G. was supported by a Canadian Institutes of Health Research (CIHR)–Canada Graduate Scholarship Doctoral Award. The data reported in this paper are tabulated in the main text and supplementary materials. This work was supported by CIHR grants MOP-15499 and HOP-13769. Illumina microarray data have been deposited with the NCBI Gene Expression Omnibus (www.ncbi.nlm.nih.gov/geo/) under accession number GSE67840. R.G.G. and S.D.G.-O. have filed a provisional patent (U.S. patent application 62/062413) pertaining to biological applications relating to the use of heptose-1,7-bisphosphate in modulating immune system responses.

SUPPLEMENTARY MATERIALS

www.sciencemag.org/content/348/6240/1251/suppl/DC1
Materials and Methods
Supplementary Text
Author Contributions
Figs. S1 to S15
References (*27*–*41*)

14 December 2014; accepted 24 April 2015
10.1126/science.aaa4921

PHYSIOLOGY

Regulation of breathing by CO_2 requires the proton-activated receptor GPR4 in retrotrapezoid nucleus neurons

Natasha N. Kumar,[1] Ana Velic,[2] Jorge Soliz,[3,4] Yingtang Shi,[1] Keyong Li,[1] Sheng Wang,[1,5] Janelle L. Weaver,[1] Josh Sen,[1] Stephen B. G. Abbott,[1,6,7] Roman M. Lazarenko,[1] Marie-Gabrielle Ludwig,[8] Edward Perez-Reyes,[1] Nilufar Mohebbi,[2] Carla Bettoni,[2] Max Gassmann,[3] Thomas Suply,[8] Klaus Seuwen,[8] Patrice G. Guyenet,[1] Carsten A. Wagner,[2]* Douglas A. Bayliss[1]*

Blood gas and tissue pH regulation depend on the ability of the brain to sense CO_2 and/or H^+ and alter breathing appropriately, a homeostatic process called central respiratory chemosensitivity. We show that selective expression of the proton-activated receptor GPR4 in chemosensory neurons of the mouse retrotrapezoid nucleus (RTN) is required for CO_2-stimulated breathing. Genetic deletion of GPR4 disrupted acidosis-dependent activation of RTN neurons, increased apnea frequency, and blunted ventilatory responses to CO_2. Reintroduction of GPR4 into RTN neurons restored CO_2-dependent RTN neuronal activation and rescued the ventilatory phenotype. Additional elimination of TASK-2 ($K_{2P}5$), a pH-sensitive K^+ channel expressed in RTN neurons, essentially abolished the ventilatory response to CO_2. The data identify GPR4 and TASK-2 as distinct, parallel, and essential central mediators of respiratory chemosensitivity.

Central respiratory chemosensitivity refers to the homeostatic reflex by which brainstem circuits regulate breathing in response to changes in CO_2 or its proxy, H^+ (*1*, *2*). This requires sensory cells that detect CO_2 and/or H^+, and promote adjustments in ventilation that regulate CO_2 excretion and acid/base balance. A cluster of Phox2b (Paired-like homeobox 2b)–expressing excitatory neurons in the retrotrapezoid nucleus (RTN) subserve this

Downloaded from www.sciencemag.org on June 14, 2015

chemosensory role (*3*–*7*). RTN neurons do not develop in Phox2b$^{27Ala/+}$ mouse models carrying a human Phox2b mutation that causes congenital central hypoventilation syndrome (CCHS) (*6*, *7*); like CCHS patients, these mice display disrupted central respiratory chemosensitivity, increased apneas, and impaired survival. Alkaline-activated TASK-2 ($K_{2P}5$) background K^+ channels mediate pH sensitivity in a subset of RTN neurons, but other molecular pH sensors appear to be required (*8*, *9*).

In insects, receptors that couple via heterotrimeric guanine nucleotide–binding proteins (GPCRs) are sufficient for CO_2 chemosensation (*10*). We examined ventilatory responses to CO_2 in conscious, unrestrained mice deleted for each of the mammalian proton-activated GPCRs: GPR4, GPR65, and GPR68 (*11*, *12*). In mice lacking GPR65 and GPR68, the ventilatory effect of 5% CO_2 was identical to that in wild-type mice (fig. S1). In contrast, in mice lacking GPR4 (in two genetic backgrounds), ventilation was decreased over a range of CO_2 concentrations (by ~65% at 6 and 8% CO_2; Fig. 1A and figs. S1 and S2). GPR4 is expressed in the carotid body (fig. S1), but the blunted ventilatory response to raised CO_2 persisted in mice after bilateral transection of the carotid sinus nerve (fig. S1) and was observed under high O_2 conditions that minimize activation of carotid body chemoreceptors (Fig. 1A). Mice lacking GPR4 retained a normal ventilatory response to hypoxia (Fig. 1B and fig. S1). There were no effects of GPR4 deletion on spontaneous activity or exploratory behavior (fig. S3), and mice lacking GPR4 had only a mild renal acidotic phenotype (table S1) (*13*), without any of the vascular abnormalities previously associated with inactivation of this receptor (*12*, *14*). Finally, the incidence of spontaneous apneic events was about six times higher in GPR4$^{-/-}$ mice (Fig. 1C and fig. S2). Thus, GPR4 deletion in mice approximates breathing deficits caused by selective genetic loss of RTN neurons (*6*, *7*) and recapitulates two cardinal neurological features of CCHS: blunted central respiratory CO_2 chemosensitivity and increased apneic episodes (*6*, *7*, *15*).

[1]Department of Pharmacology, University of Virginia, Charlottesville, VA 22908, USA. [2]Institute of Physiology, University of Zurich, Zurich, CH-8057, Switzerland. [3]Institute of Veterinary Physiology, University of Zurich, Zurich, CH-8057, Switzerland. [4]Centre de Recherche du CHU de Québec, Département de Pédiatrie, Faculté de Médecine, Université Laval, Québec, QC, Canada. [5]Department of Physiology, Hebei Medical University, Shijiazhuang, Hebei, 050017, China. [6]School of Medical Sciences, University of New South Wales, New South Wales 2052, Australia. [7]Department of Neurology, Harvard Medical School and Beth Israel Deaconess Medical Center, Boston, MA, USA. [8]Novartis Institutes for Biomedical Research, Basel, CH-4002, Switzerland.
***Corresponding author. E-mail: Wagnerca@access.uzh.ch (C.A.W.); bayliss@virginia.edu (D.A.B.)**

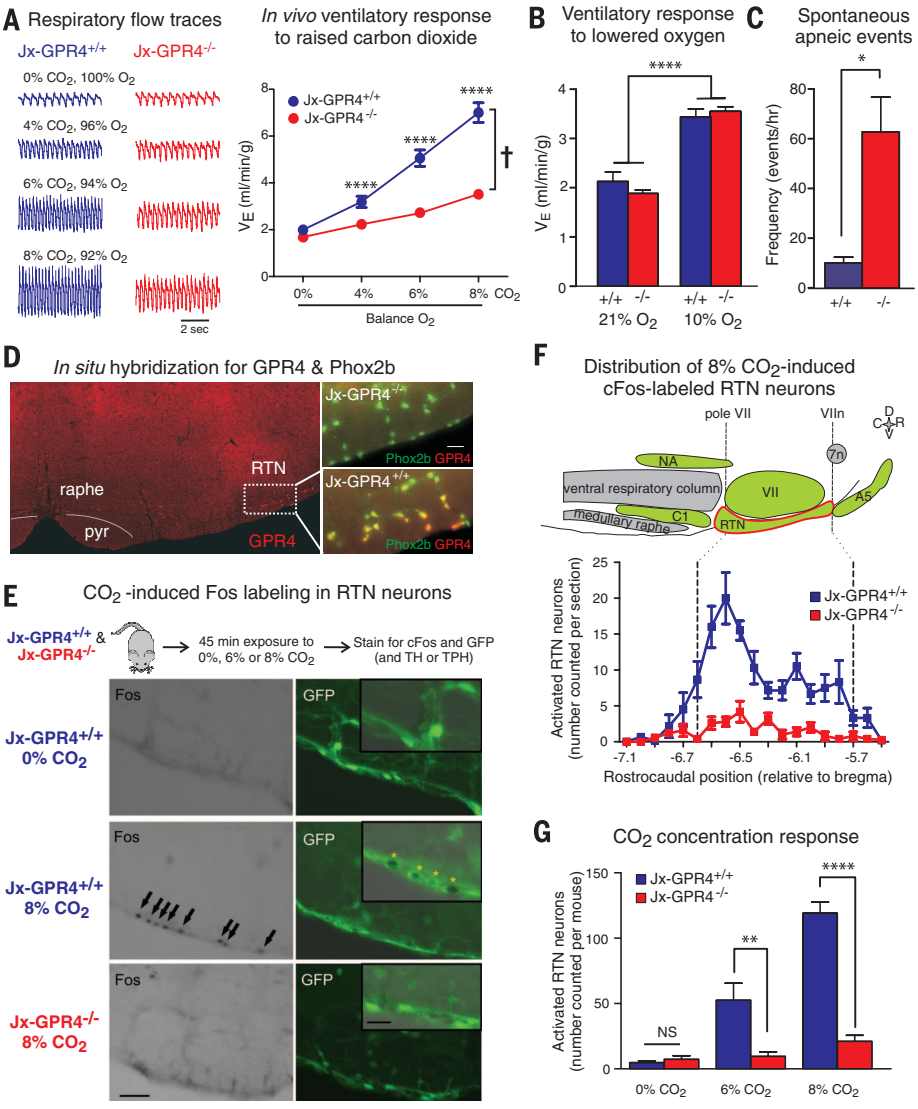


Fig. 1. GPR4 deletion disrupts CO_2-evoked ventilatory stimulation and RTN neuronal activation in vivo, and increases incidence of spontaneous apneas. (**A**) (Left) Respiratory flow recording from Jx-GPR4$^{+/+}$ and Jx-GPR4$^{-/-}$ mice (cross between Jx-Phox2b-eGFP and GPR4 lines) with increased CO_2 concentrations in the inspired air (balance O_2). (Right) Minute ventilation (V_E; product of milliliters per breath and breaths per minute, normalized to body weight) during incremental CO_2 challenge in Jx-GPR4$^{+/+}$ and Jx-GPR4$^{-/-}$ mice [n = 16 and 52; †P < 0.0001 between genotypes by two-way repeated measures analysis of variance (RM-ANOVA); ****P < 0.0001 for pairwise comparisons]. (**B**) Jx-GPR4$^{+/+}$ and Jx-GPR4$^{-/-}$ mice exhibited similar increases in peak V_E during exposure to 10% O_2 (n = 16 and 52; ****P < 0.0001 hypoxia versus normoxia, by two-way RM-ANOVA). (**C**) The frequency of spontaneous apneic events during quiet hyperoxic (100% O_2) breathing was greater in Jx-GPR4$^{-/-}$ than in Jx-GPR4$^{+/+}$ mice (n = 23 and 8; *P < 0.05 by unpaired t test). (**D**) GPR4 expression by in situ hybridization in coronal brainstem section from an adult Jx-GPR4$^{+/+}$ mouse. The inset is enlarged in a merged image; GPR4 mRNA is observed in 68.1 ± 5.1% of Phox2b+ neurons, n = 6; counts do not exclude C1 neurons); no labeling was detected in sections from Jx-GPR4$^{-/-}$ mice. pyr, pyramid. Scale bar = 25 μm. (**E**) Jx-GPR4$^{+/+}$ and Jx-GPR4$^{-/-}$ mice were exposed to CO_2 in vivo, and activated RTN (GFP+:TH-) neurons (asterisks) were identified by immunoreactivity for cFos (left, black reaction product in cell nuclei denoted by arrows) and GFP (right). Scale bars = 50 and 25 μm. (**F**) (Top) Parasagittal schematic of mouse brainstem depicting the RTN and surrounding neuronal populations, with areas containing Phox2b-expressing cells denoted in green. (Bottom) The number of RTN neurons activated by 8% CO_2 challenge (cFos+:GFP+:TH-) was strongly reduced throughout the RTN in Jx-GPR4$^{-/-}$ mice, as compared to Jx-GPR4$^{+/+}$ mice (n = 5 and 6). (**G**) The total number of RTN neurons counted (every third section) from Jx-GPR4$^{+/+}$ and Jx-GPR4$^{-/-}$ mice activated in response to 0% (n = 4 and 4), 6% (n = 5 and 5) or 8% CO_2 (n = 6 and 5). (P < 0.0001, between genotypes by two-way RM-ANOVA; **P < 0.01 and ****P < 0.0001 for pairwise comparisons; NS, not significant).

We examined expression of GPR4 in the RTN neurons that are implicated in CCHS and central respiratory CO_2 chemosensitivity (*6*, *7*, *9*). Multiplex in situ hybridization revealed strong GPR4 expression in a large fraction of Phox2b-expressing neurons throughout the rostrocaudal extent of the RTN (~68%, Fig. 1D); GPR4 expression was evident, but low, in some raphe neurons and undetectable elsewhere in the brainstem (Fig. 1D). We used a more sensitive multiplex single-cell polymerase chain reaction assay in dissociated green fluorescent protein (GFP)–expressing RTN neurons (from Jx-Phox2b-eGFP transgenic mice) and found that nearly all RTN neurons expressed GPR4 (91%) and very few expressed other members of the receptor family (fig. S4). Expression of GPR4 was eliminated in GFP-positive RTN neurons from Jx-GPR4$^{-/-}$ mice (crossed with a Jx-Phox2b-eGFP line), with no apparent compensatory up-regulation of other proton-activated GPCRs (fig. S4). Acute exposure of Jx-GPR4$^{+/+}$ mice to CO_2 (in hyperoxia) caused a concentration-dependent increase in cFos-immunoreactivity in RTN neurons (Fig. 1, E to G), which is indicative of neuronal activation in vivo (*16*, *17*). In contrast, very few CO_2-activated RTN neurons were found in Jx-GPR4$^{-/-}$ mice (Fig. 1, E to G). GPR4 expression was detected in C1 adrenergic and serotonergic raphe neurons (fig. S4), but there were no genotype-dependent differences in the small fraction of those neurons activated after CO_2 exposure (fig. S5).

Activation of RTN neurons by CO_2 and/or H^+ can also be observed in brainstem slice preparations in vitro (*18*). Most GFP-expressing RTN neurons from wild-type mice (~90%) increased firing rate during extracellular acidification and decreased firing rate with bath alkalization (Fig. 2, A, C, and D). In contrast to the nearly universal pH sensitivity of wild-type neurons (defined as >30% decrease in firing from pH 7.0 to pH 7.8; fig. S6), we found that ~40% of RTN neurons from Jx-GPR4$^{-/-}$ mice were pH-insensitive; the remaining ~60% of GPR4-deleted neurons were pH-sensitive, but they displayed lower firing rates across the pH range (Fig. 2, B to D). Under voltage clamp, a pH-dependent background K^+ current was observed in pH-sensitive RTN neurons from both wild-type and Jx-GPR4$^{-/-}$ mice (*3*, *4*), but this current was absent in the pH-insensitive population from Jx-GPR4$^{-/-}$ mice (Fig. 2, E and F). The residual pH-sensitive background K^+ current is probably mediated by TASK-2, an intrinsically pH-sensitive K_{2P} channel that is expressed in ~60 to 70% of RTN neurons from wild-type and GPR4-deleted mice (fig. S7) (*8*). However, it is unlikely that TASK-2 is the downstream effector for GPR4, because pH-dependent modulation of TASK-2 was unaffected by GPR4 signaling (fig. S7).

Incubation of brainstem slices from wild-type mice with a small-molecule GPR4 receptor antagonist (*19*) yielded results similar to those from GPR4 deletion. A prominent group of blocker-treated RTN neurons was insensitive to changes in pH (~40%), whereas a second group retained their pH sensitivity (~60%; Fig. 3, A to C); the basal firing rate was also reduced in cells treated with the GPR4 receptor blocker (Fig. 3C). To test whether G-protein activation modulates the activity of wild-type RTN neurons, we performed whole-cell recordings with pipettes containing either guanosine triphosphate (GTP) or GTP-γ-S (a poorly hydrolyzable GTP analog that can mimic and irreversibly sustain G-protein signaling). In the presence of GTP, repeated bouts of alkalization and acidification yielded reversible and reproducible changes in membrane potential and firing rate of RTN neurons (Fig. 3, D and F). However, RTN cells dialyzed with GTP-γ-S showed diminished membrane potential responses with repeated pH changes, accompanied by progressive membrane depolarization and increased baseline firing (Fig. 3, E and F). Likewise, the acid-induced inward shift in holding current showed little recovery or repeatability in neurons recorded with GTP-γ-S (Fig. 3, G to I). Strong membrane depolarization (or inward current) often occurred immediately upon whole-cell access in neurons recorded with GTP-γ-S

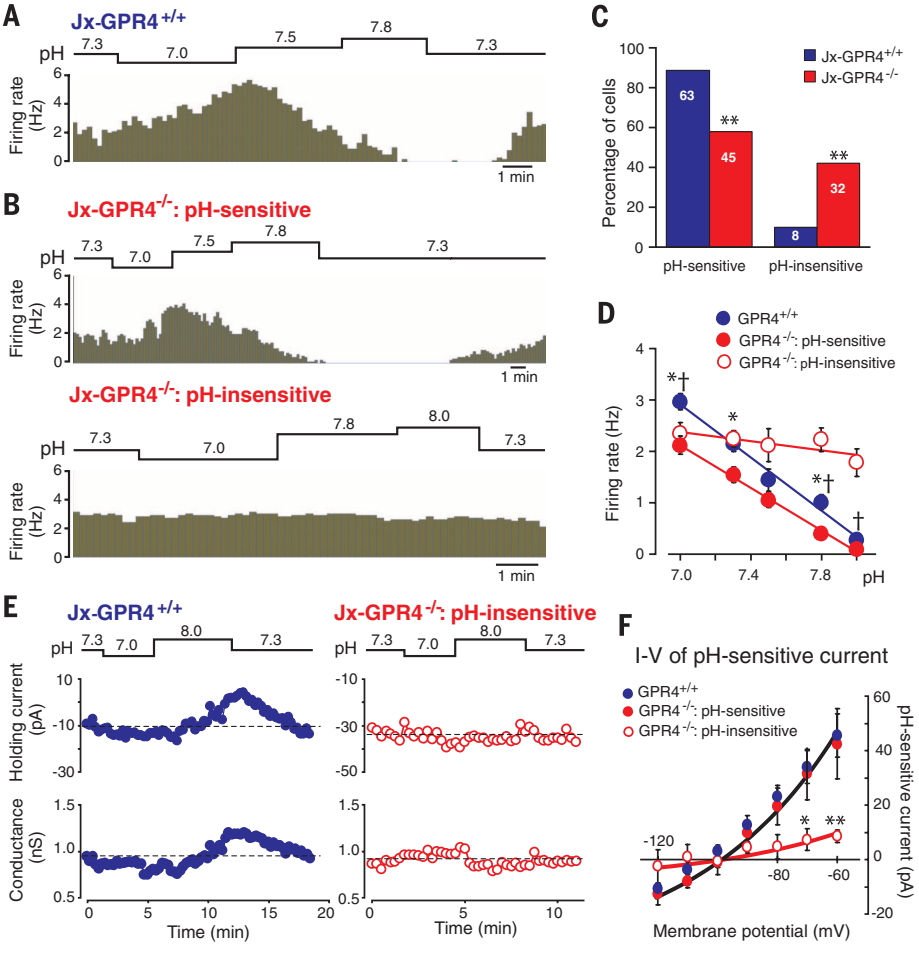


Fig. 2. GPR4 deletion ablates pH sensitivity and a pH-sensitive background K^+ current in a subset of RTN neurons in vitro. (**A** and **B**) Effects of bath pH on firing activity (cell-attached mode) in representative GFP-expressing RTN neurons. A typical pH-sensitive neuron from a GPR4$^{+/+}$ mouse is depicted (A); in GPR4$^{-/-}$ mice (B), RTN neurons that were either pH-sensitive (upper) or pH-insensitive (lower) are shown. (**C**) The percentage of pH-sensitive and pH-insensitive RTN neurons was significantly different between GPR4$^{+/+}$ and GPR4$^{-/-}$ mice (**P < 0.0001 by χ^2; numbers are provided for each group). (**D**) Averaged firing rates at different bath pH for RTN neurons from GPR4$^{+/+}$ mice (n = 71) and for RTN neurons from GPR4$^{-/-}$ mice that were identified as pH-sensitive (n = 45) or pH-insensitive (n = 32). *P < 0.05 for GPR4$^{+/+}$ versus GPR4$^{-/-}$: pH-sensitive; and †P < 0.05 for GPR4$^{+/+}$ versus GPR4$^{-/-}$: pH-insensitive, by two-way RM-ANOVA with Dunnett's test. (**E**) Effects of bath acidification and alkalization on holding current (at −60 mV) and conductance during whole-cell voltage clamp recordings in a pH-sensitive neuron from a Jx-GPR4$^{+/+}$ mouse (left) and a pH-insensitive neuron from a Jx-GPR4$^{-/-}$ mouse (right). (**F**) Current-voltage (I-V) relationship of pH-sensitive difference current (pH 8 minus pH 7) for RTN neurons from GPR4$^{+/+}$ mice (n = 16) and from GPR4$^{-/-}$ mice that were identified in cell-attached recordings as pH-sensitive (n = 11) or pH-insensitive (n = 5). Data are overlaid with fits using the Goldman-Hodgkin-Katz (GHK) equation for a "leak" K^+ current. **P < 0.05 versus GPR4$^{-/-}$: pH-insensitive, by two-way RM-ANOVA with Tukey's test.

(n = 8); after returning membrane potential and firing rate to normal levels with hyperpolarizing current injection (n = 3), those GTP-γ-S–containing cells were insensitive to changes in pH. In addition, bath acidification and alkalization failed to evoke membrane depolarization and hyperpolarization in a subset of RTN neurons recorded with GDP-β-S (n = 4 out of 7), a GDP analog that interferes with receptor-stimulated GDP:GTP exchange.

We tested whether targeted re-expression of GPR4 in Phox2b-expressing RTN neurons would rescue the defective respiratory phenotype of mice lacking GPR4. A lentiviral vector was prepared that used a Phox2b-responsive promoter (PRSx8) to drive GPR4 expression in RTN neurons (*5*, *20*); a control virus expressed GPR4(R117A), a mutated receptor that cannot engage downstream G-protein signaling (fig. S8) (*21*). Four weeks after virus injection into the RTN region of adult Jx-GPR4$^{-/-}$ mice (Fig. 4A), many RTN neurons and some nearby C1 neurons were transduced (Fig. 4, B to D, and fig. S9). Nearly all virally transduced cells expressed Phox2b (i.e., ~85% of mCherry+ cells were also GFP+). This RTN neuron–selective re-expression of GPR4 yielded a full rescue of the ventilatory response to CO_2 (Fig. 4E). In contrast, the signaling-deficient mutant of GPR4 failed to rescue the breathing deficits (Fig. 4F). Neither virus modified the hypoxic ventilatory response (fig. S9). An identical rescue was observed using a lentivirus in which GPR4 expression was controlled by a nonselective EF1α promoter (fig. S10). Re-expression of GPR4, but not GPR4(R117A), in RTN neurons reduced the number of apneic events in Jx-GPR4$^{-/-}$ mice (Fig. 4G) and restored CO_2-induced cFos expression in RTN neurons (Fig. 4, H and I). Virtually all the activated and transduced cells were Phox2b-expressing (~91%), and the majority of the activated RTN neurons were transduced (~64%) (Fig. 4I); in a mouse that received a unilateral virus injection,

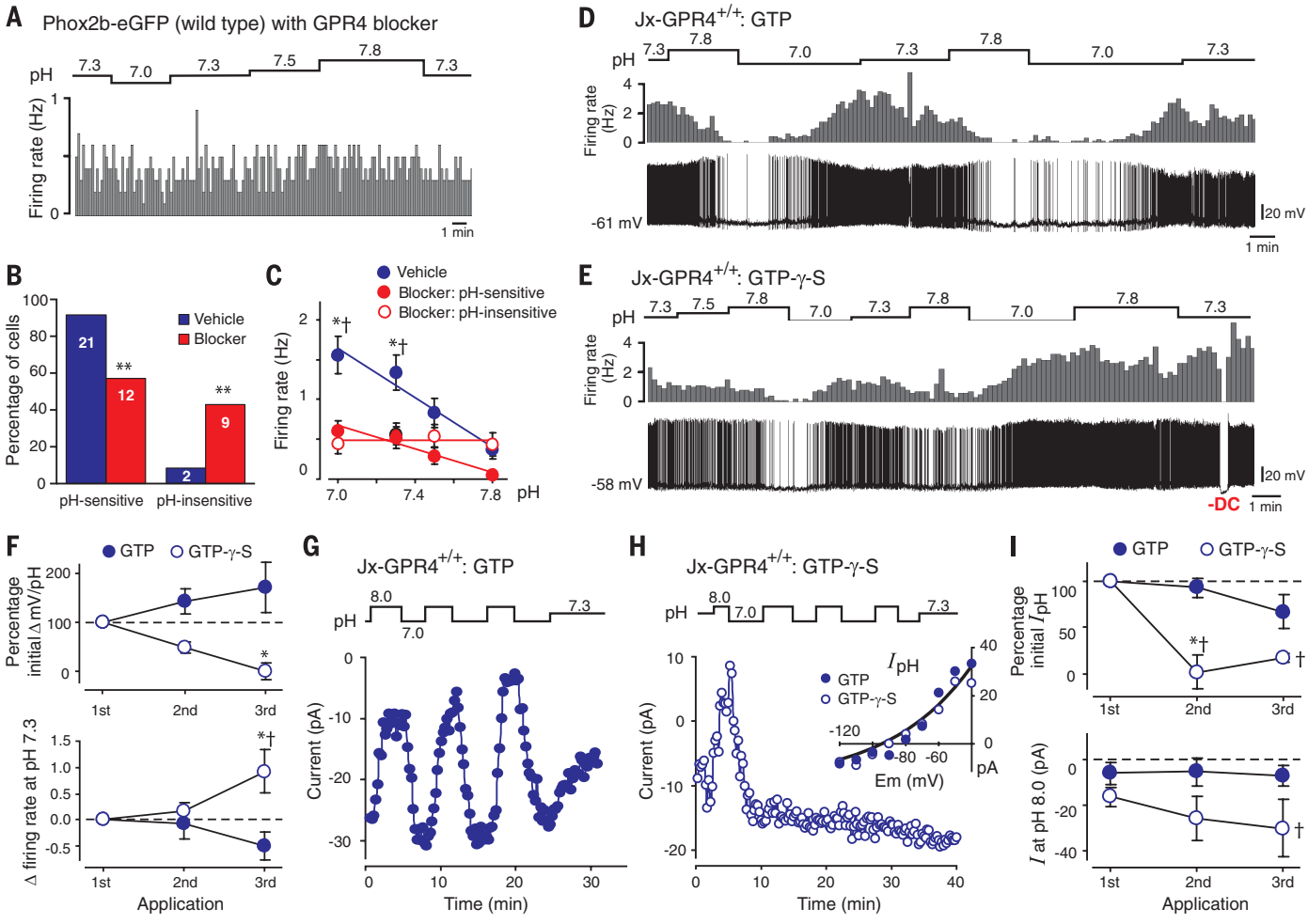


Fig. 3. GPR4 and G protein activation contribute to effects of pH on firing and background K^+ currents in RTN neurons from wild-type mice. (**A**) Firing activity in a wild-type RTN neuron incubated with a GPR4 antagonist (Dalton M46, 20 μM); the cell was insensitive to changes in bath pH. (**B**) The percentage of pH-sensitive and pH-insensitive wild-type RTN neurons was significantly different after treatment with the GPR4 blocker (**P < 0.0001 by χ^2; numbers are provided for each group). (**C**) Averaged firing rate at different bath pH from vehicle-treated RTN neurons (n = 21) or GPR4 blocker-treated cells that were identified as pH-sensitive (n = 12) or pH-insensitive (n = 9). *P < 0.05 for vehicle versus blocker:pH-sensitive; and †P < 0.05 for vehicle versus blocker:pH-insensitive, by two-way RM-ANOVA with Dunnett's test. (**D** and **E**) Effects of repeated changes in bath pH on firing rate (top) and membrane potential (bottom) recorded from wild-type RTN neurons in the whole-cell current clamp configuration with pipettes containing either GTP (D) or GTP-γ-S (E). (**F**)(Top) Membrane hyperpolarization (% initial) during multiple bouts of bath alkalization in RTN neurons recorded with GTP and GTP-γ-S. (Bottom) Change in baseline firing (at pH 7.3) after repeated bath alkalization in RTN neurons recorded with GTP and GTP-γ-S. (two-way RM-ANOVA; *P < 0.05 for GTP versus GTP-γ-S by Bonferroni test; and †P < 0.05 versus first application by Dunnett's test; n = 8 and 4). (**G** and **H**) Effects of repeated changes of bath pH on holding current in wild-type RTN neurons during whole-cell voltage clamp recording with pipettes that contained GTP (G) or GTP-γ-S (H). The inset shows the pH-sensitive I-V obtained during the first sojourn from pH 8 to pH 7 for both cells, overlaid with a fit using the GHK equation. (**I**) Normalized pH-sensitive current (pH 8 minus pH 7 at −60 mV, top) and holding current at pH 8 (bottom) during repeated bouts of bath acidification and alkalization (two-way RM-ANOVA; *P < 0.05 for GTP versus GTP-γ-S by Bonferroni test; and †P < 0.05 versus first application by Dunnett's test; n = 7 and 3).

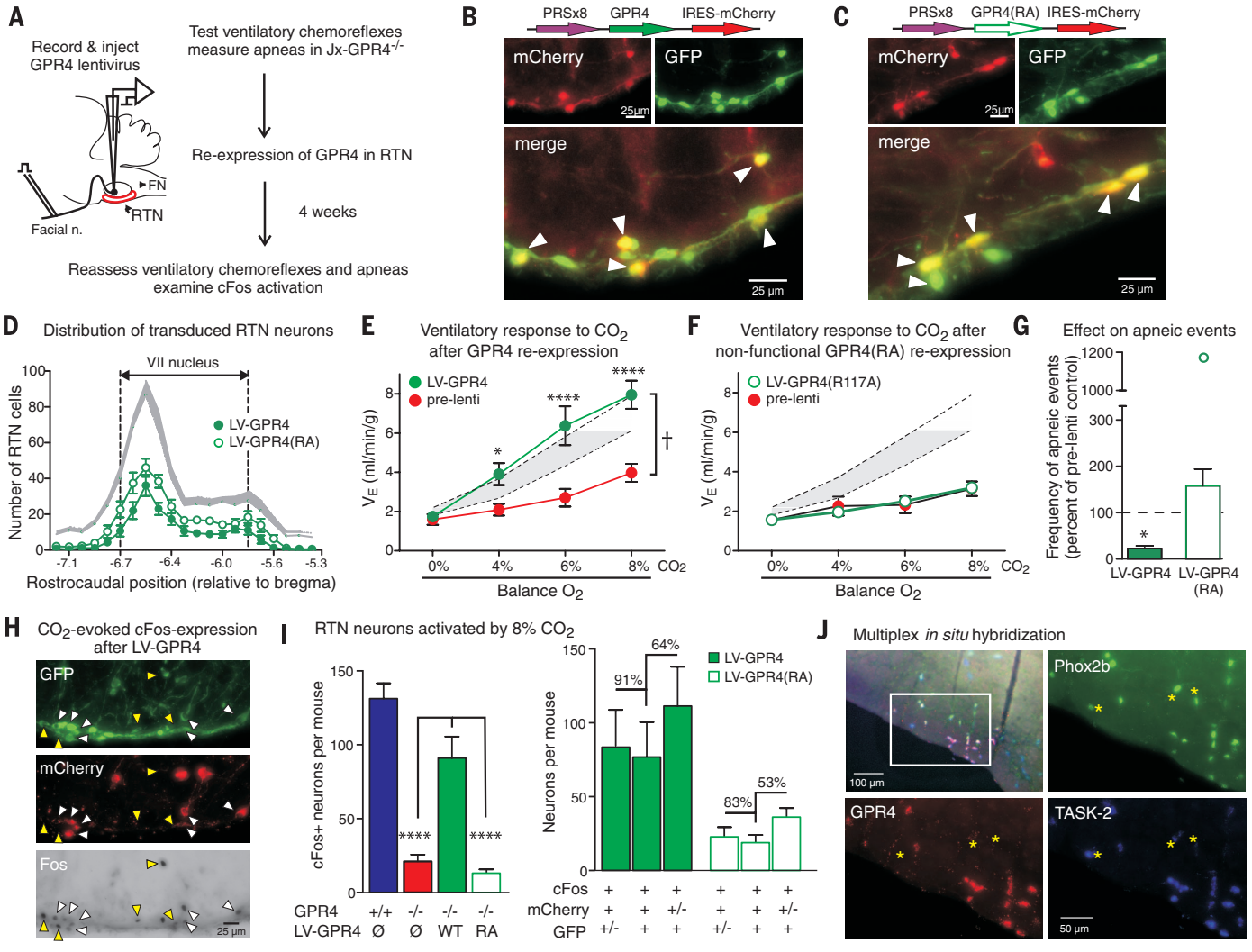


Fig. 4. Re-expression of GPR4 selectively in Phox2b-expressing neurons of the RTN restores CO_2-dependent neuronal activation and breathing in Jx-GPR4$^{-/-}$ mice. (**A**) Schematic of experimental design. (**B** and **C**) White arrows denote virally transduced (mCherry+) and Phox2b-expressing (GFP+) RTN neurons after injection of PRSx8-lentivirus driving expression of GPR4-mCherry (B) or GPR4(R117A)-mCherry (C). (**D**) Similar number and distribution of RTN neurons transduced with GPR4-mCherry ($n = 8$) and GPR4(R117A)-mCherry ($n = 7$) lentivirus. The shaded area represents a 95% confidence interval (CI) for the distribution of RTN (GFP+/TH−) neurons across all virus-injected animals ($n = 15$). (**E** and **F**) Effect of CO_2 on minute ventilation (V_E) in Jx-GPR4$^{-/-}$ mice before (pre-lenti) and 4 weeks after lentiviral injection into the RTN [(E): GPR4-mCherry, $n = 8$; or (F): GPR4(R117A)-mCherry, $n = 7$]. Shaded areas are 95% CIs for data from Jx-GPR4$^{+/+}$ mice (from Fig. 1A). (†$P < 0.0001$ by two-way RM-ANOVA, comparing mice before and after lentiviral delivery; *$P < 0.05$, ****$P < 0.0001$, pairwise comparisons at each CO_2 level by Bonferroni test). (**G**) The frequency of spontaneous apneic events was reduced after the injection of GPR4-mCherry lentiviral vector into the RTN ($n = 8$; *$P < 0.05$ by t test, ~22% of pre-injection control) but not GPR4(R117A)-mCherry ($n = 10$, $P > 0.18$ by t test). Note the outlying data point from one mouse that received GPR4(R117A)-mCherry. (**H**) Many virally transduced (mCherry+) RTN neurons (GFP+) were activated (cFos+) by 8% CO_2 exposure (white arrows) after injection of PRSx8-lentivirus expressing GPR4 into RTN of Jx-GPR4$^{-/-}$ mice; CO_2-activated GFP+ neurons that were not detectably transduced were also observed (yellow arrows). (**I**) (Left) CO_2-activated cFos expression in RTN neurons was rescued after the injection of PRSx8-GPR4 but not PRSx8-GPR4(R117A) lentivirus ($n = 4$ and 7, $P <$ 0.0001 by one-way ANOVA, ****$P < 0.0001$ by pairwise comparison); data from Jx-GPR4$^{+/+}$ and Jx-GPR4$^{-/-}$ mice are re-plotted from Fig. 1G. (Right) CO_2-activated transduced RTN neurons (cFos+/mCherry+/GFP+) in comparison to all CO_2-activated transduced neurons (cFos+/mCherry+) and all CO_2-activated RTN neurons (cFos+/GFP+). (**J**) Coexpression of Phox2b, GPR4, and TASK-2 in RTN neurons by in situ hybridization; the boxed region is enlarged in the merged image. A few TASK-2-expressing Phox2b+ neurons without GPR4 are indicated (asterisks). Among Phox2b+ neurons that expressed GPR4 and/or TASK-2, 72.9 ± 0.8% expressed both genes, 18.1 ± 1.0% were labeled only for TASK-2, and 9.0 ± 0.2% were labeled only for GPR4 ($n = 3$). (**K**) Minute ventilation (V_E) during incremental CO_2 challenge for the indicated genotypes. †, all controls greater than all single or double knockouts, $P < 0.0001$; *, both single knockouts greater than double knockouts (n values provided), by two-way RM-ANOVA with Bonferroni pairwise comparisons.

cFos-labeled neurons were found exclusively on the injected side (fig. S11). Despite transduction of some C1 neurons, GPR4 re-expression did not induce CO_2-driven cFos expression in those cells (fig. S9). Thus, RTN-selective re-expression of GPR4 in Jx-GPR4$^{-/-}$ mice reinstated CO_2-dependent neuronal activation and increased ventilation, and reduced the incidence of apneas.

The preferential brainstem localization of GPR4 to RTN neurons is similar to that of the pH-sensitive TASK-2 channel (*8*, *9*). Indeed, we found extensive coexpression of both GPR4 and TASK-2 in Phox2b-expressing RTN neurons (Fig. 4J). We therefore examined the effects of simultaneous genetic ablation of both GPR4 and TASK-2. Of >350 pups obtained by breeding mice heterozygous at both loci, 4 males survived past weaning (from 13 total double knockouts). For those surviving animals, the effect of CO_2 on ventilation was nearly completely suppressed (by ~85%, Fig. 4K), suggesting independent contributions of GPR4 and TASK-2.

Our data demonstrate that GPR4 is required for the normal ventilatory response to CO_2 and that this reflects its selective expression in Phox2b-expressing RTN chemosensory neurons, where it contributes to neuronal excitability and pH sensitivity. GPR4 thus provides proton-sensing capability in chemoreceptor neurons that acutely maintain physiological acid/base balance via the regulation of breathing (*1*, *2*). The signaling pathway and channel downstream of GPR4 remain to be determined, but it appears that GPR4 and TASK-2 provide independent molecular pH sensors in overlapping populations of RTN chemosensitive neurons (*8*), and thus redundancy for this vital function. Astrocytic purinergic signaling appears to be yet another distinct mechanism for modulating CO_2-activated RTN activity (*22*, *23*), because effects of gliotransmitters such as adenosine triphosphate or glutamate are not likely to involve GPR4 (fig. S8).

Mice lacking GPR4 recapitulate two cardinal features of CCHS patients—depressed respiratory chemosensitivity and increased apneas (*15*)—and both defects were rescued after selective GPR4 re-expression in a subset of Phox2b-expressing RTN neurons. Thus, reduced excitability and chemoresponsiveness in RTN neurons, effects more subtle than the outright genetic ablation of those cells observed in CCHS models (*6*, *7*, *9*), might predispose individuals to respiratory problems associated with reduced chemosensitivity (such as central sleep apnea, apnea of prematurity, or sudden infant death syndrome) (*24*, *25*), and activation of GPR4 in RTN neurons might provide a therapeutic option for treating these common respiratory ailments.

REFERENCES AND NOTES

1. P. G. Guyenet, R. L. Stornetta, D. A. Bayliss, *J. Comp. Neurol.* **518**, 3883–3906 (2010).
2. J. L. Feldman, G. S. Mitchell, E. E. Nattie, *Annu. Rev. Neurosci.* **26**, 239–266 (2003).
3. D. K. Mulkey *et al.*, *Nat. Neurosci.* **7**, 1360–1369 (2004).
4. S. Wang, Y. Shi, S. Shu, P. G. Guyenet, D. A. Bayliss, *J. Neurosci.* **33**, 7756–7761 (2013).
5. S. B. G. Abbott *et al.*, *J. Neurosci.* **29**, 5806–5819 (2009).
6. V. Dubreuil *et al.*, *Proc. Natl. Acad. Sci. U.S.A.* **105**, 1067–1072 (2008).
7. N. Ramanantsoa *et al.*, *J. Neurosci.* **31**, 12880–12888 (2011).
8. S. Wang *et al.*, *J. Neurosci.* **33**, 16033–16044 (2013).
9. C. Gestreau *et al.*, *Proc. Natl. Acad. Sci. U.S.A.* **107**, 2325–2330 (2010).
10. W. D. Jones, P. Cayirlioglu, I. G. Kadow, L. B. Vosshall, *Nature* **445**, 86–90 (2007).
11. M.-G. Ludwig *et al.*, *Nature* **425**, 93–98 (2003).
12. L. Wyder *et al.*, *Angiogenesis* **14**, 533–544 (2011).
13. X. Sun *et al.*, *J. Am. Soc. Nephrol.* **21**, 1745–1755 (2010).
14. L. V. Yang *et al.*, *Mol. Cell. Biol.* **27**, 1334–1347 (2007).
15. D. E. Weese-Mayer *et al.*, *Am. J. Respir. Crit. Care Med.* **181**, 626–644 (2010).
16. L. J. Teppema *et al.*, *J. Comp. Neurol.* **388**, 169–190 (1997).
17. M. G. Fortuna, R. L. Stornetta, G. H. West, P. G. Guyenet, *J. Physiol.* **587**, 5121–5138 (2009).
18. R. M. Lazarenko *et al.*, *J. Comp. Neurol.* **517**, 69–86 (2009).
19. L. Dong *et al.*, *PLOS ONE* **8**, e61991 (2013).
20. D.-Y. Hwang, W. A. Carlezon Jr., O. Isacson, K.-S. Kim, *Hum. Gene Ther.* **12**, 1731–1740 (2001).
21. A. Chen *et al.*, *PLOS ONE* **6**, e27586 (2011).
22. A. V. Gourine *et al.*, *Science* **329**, 571–575 (2010).
23. I. C. Wenker, O. Kréneisz, A. Nishiyama, D. K. Mulkey, *J. Neurophysiol.* **104**, 3042–3052 (2010).
24. A. J. Garcia 3rd, J. E. Koschnitzky, J.-M. Ramirez, *Respir. Physiol. Neurobiol.* **189**, 288–300 (2013).
25. N. A. Antic *et al.*, *Am. J. Respir. Crit. Care Med.* **174**, 923–927 (2006).

ACKNOWLEDGMENTS

The authors are grateful to members of the Bayliss and Guyenet laboratories and to Q. Al-Awqati (Columbia Univ., NYC) for useful suggestions on the studies. They thank S. Shu for technical assistance, R. L. Stornetta for advice on in situ hybridization, M. P. Beenhakker for the MATLAB routine used for Poincaré analysis, and K. S. Ravichandran and P. Q. Barrett for comments on the manuscript. S.B.G.A. was supported by a National Health and Medical Research Council of Australia Early Career Fellowship (GNT1052674). The use of the ZIRP Core Facility for Rodent Phenotyping is acknowledged. The work was supported by the Swiss National Science Foundation (31003A_155959/1, C.A.W.) and the National Institutes of Health (HL074011, P.G.G.; HL108609, D.A.B.). GPR65 and GPR4 KO mice are available from M.-G.L. under a Material Transfer Agreement with Novartis. M.-G.L., T.S., and K.S. are inventors on patents WO 2004/1183A1 and WO 2008/071771A2 that pertain to the use of GPR4, GPR65, and GPR68 as pH sensors.

SUPPLEMENTARY MATERIALS

www.sciencemag.org/content/348/6240/1255/suppl/DC1
Materials and Methods
Figs. S1 to S11
Tables S1 to S3
References (*26*–*42*)

16 October 2014; accepted 6 May 2015
10.1126/science.aaa0922

CELL DIVISION CYCLE

Kinetochore attachment sensed by competitive Mps1 and microtubule binding to Ndc80C

Zhejian Ji, Haishan Gao, Hongtao Yu*

The spindle checkpoint of the cell division cycle senses kinetochores that are not attached to microtubules and prevents precocious onset of anaphase, which can lead to aneuploidy. The nuclear division cycle 80 complex (Ndc80C) is a major microtubule receptor at the kinetochore. Ndc80C also mediates the kinetochore recruitment of checkpoint proteins. We found that the checkpoint protein kinase monopolar spindle 1 (Mps1) directly bound to Ndc80C through two independent interactions. Both interactions involved the microtubule-binding surfaces of Ndc80C and were directly inhibited in the presence of microtubules. Elimination of one such interaction in human cells caused checkpoint defects expected from a failure to detect unattached kinetochores. Competition between Mps1 and microtubules for Ndc80C binding thus constitutes a direct mechanism for the detection of unattached kinetochores.

Unattached kinetochores (KTs) recruit and activate spindle checkpoint proteins to produce wait-anaphase signals, ensuring the fidelity of chromosome segregation. Microtubule (MT) attachment releases checkpoint proteins from KTs and attenuates checkpoint signaling. Whether KT signaling of any checkpoint proteins is directly inhibited by MT attachment remains to be established, however. The KMN network of KT proteins acts both as a critical MT receptor and a signaling platform for the spindle checkpoint (*1*–*4*). In humans, KMN contains the kinetochore null 1 protein (Knl1), the minichromosome instability 12 complex (Mis12C), and the nuclear division cycle 80 complex (Ndc80C). Ndc80C directly engages MTs through the N-terminal tail of highly expressed in cancer 1 (Hec1) and Calponin Homology (CH) domains of Hec1 and nuclear filament–containing protein 2 (Nuf2) (*5*). Ndc80C also mediates the KT localization of key checkpoint proteins, including monopolar spindle 1 (Mps1) and the mitosis arrest deficiency 1–2 complex (Mad1–Mad2) (*6*, *7*). MT attachment releases both Mps1 and Mad1–Mad2 from KTs.

Howard Hughes Medical Institute, Department of Pharmacology, University of Texas Southwestern Medical Center, 6001 Forest Park Road, Dallas, TX 74390, USA.
*Corresponding author. E-mail: hongtao.yu@utsouthwestern.edu

Downloaded from www.sciencemag.org on June 14, 2015

In metazoans, removal of Mad1–Mad2 from KTs is, however, indirectly mediated through dynein-dependent poleward transport along MTs (*8*).

Mps1 phosphorylates Knl1 at multiple methionine-glutamate-leucine-threonine (MELT) motifs and creates docking sites for the budding uninhibited by benomyl 1–3 complex (Bub1–Bub3) (*9*–*12*). Mps1 further phosphorylates Bub1 and promotes its binding to Mad1–Mad2 (*13*–*15*). Mps1 is thus an initiator of checkpoint signaling and a candidate for being a direct sensor of KT-MT attachment.

We first tested whether human Mps1 directly interacted with Ndc80C. Mps1 contains an N-terminal extension (NTE) critical for KT targeting (*16*), a tetratricopeptide repeat (TPR) domain, and a C-terminal kinase domain (Fig. 1A). Purified recombinant Mps1 and Ndc80C interacted with each other (fig. S1A). Furthermore, Mps1 NTE and a conserved middle region (MR) each independently bound to Ndc80C or Ndc80C^{bonsai} [miniaturized Ndc80C comprising mostly the head domains of its subunits (*17*)] (Fig. 1A and fig. S1, B to E).

S281 of Mps1 MR is phosphorylated in mitotic human cells (*18*). The Mps1 MR24 and phospho-S281 pMR24 peptides bound to Ndc80C^{bonsai} with its Hec1 tail deleted (Δtail) with dissociation constants (K_d) of 8.4 and 2.0 μM, respectively, as measured with isothermal titration calorimetry (fig. S1F). Thus, S281 phosphorylation moderately enhanced binding of Mps1 MR to Ndc80C. Deletion of the Hec1 tail enhanced pMR24 binding to Ndc80C^{bonsai} (Fig. 1B), suggesting an autoinhibitory effect of this tail on binding of Mps1. The centromeric protein kinase Aurora B phosphorylates multiple residues in the Hec1 tail (*17*, *19*, *20*). Ndc80C^{bonsai} phosphorylated by Aurora B or with phosphomimicking mutations in Hec1 (9D) bound to pMR24 more strongly, indicating that Aurora B phosphorylation relieved the autoinhibition (Fig. 1, B and C, and fig. S1G). Thus, the Ndc80C–MR interaction appears to be regulated by mitotic phosphorylation of both partners.

Aurora B phosphorylation or deletion of the Hec1 tail had little effect on Mps1 NTE binding to Ndc80C (fig. S1H). The K_d of the NTE–Ndc80C interaction was 9.6 μM as determined by means of microscale thermophoresis (fig. S1J). Mps1$_{1\text{-}300}$ containing both motifs bound to Ndc80C^{bonsai} Δtail with a stoichiometry of 1:1 and a K_d of 8.7 μM, which was comparable with the affinity of either motif alone. Thus, Mps1 NTE and MR bind non-cooperatively to Ndc80C.

We mapped the sites within Ndc80C bound by the two Mps1 motifs. Mps1$_{1\text{-}200}$ bound to the CH domain of Hec1 (Fig. 1D) (*21*). K89E and K166E mutations of Hec1 CH compromise binding of Ndc80C to MTs (*17*). (Single-letter abbreviations for the amino acid residues are as follows: A, Ala; C, Cys; D, Asp; E, Glu; F, Phe; G, Gly; H, His; I, Ile; K, Lys; L, Leu; M, Met; N, Asn; P, Pro; Q, Gln; R, Arg; S, Ser; T, Thr; V, Val; W, Trp; and Y, Tyr. In the mutants, other amino acids were substituted at certain locations; for example, K89E indicates that lysine at position 89 was replaced by

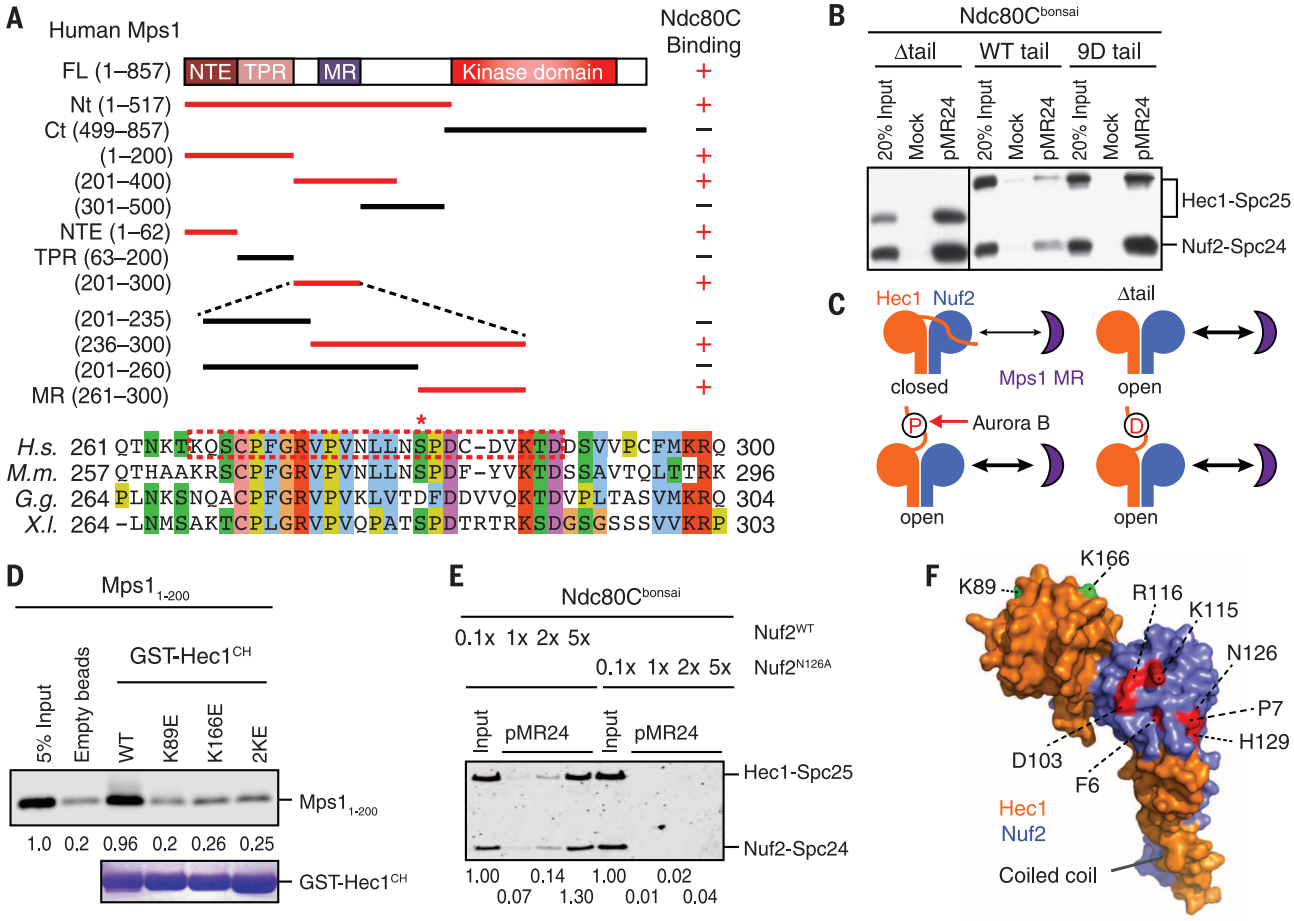


Fig. 1. Direct interactions of Mps1 with Ndc80C through two distinct motifs. (**A**) Domains and motifs of Mps1 and sequence alignment of the MR. Mps1 fragments that can or cannot bind to Ndc80C are depicted in red or black, respectively. *H.s.*, *Homo sapiens*; *M.m.*, *Mus musculus*; *G.g.*, *Gallus gallus*; *X.l.*, *Xenopus laevis*. The sequence of MR24 is boxed. Asterisk marks S281 phosphorylated in human Mps1. (**B**) Binding of Ndc80C^{bonsai} containing Hec1 WT, Δtail, or 9D (Spc24 and Spc25 blot) to pMR24-coupled beads. (**C**) Model explaining how Aurora B phosphorylation of the Hec1 tail stimulates MR binding to Ndc80C. (**D**) Binding of Mps1$_{1\text{-}200}$ (blotted with antibody to Mps1; top) to beads bound to GST-Hec1^{CH} WT or the indicated mutants (Coomassie staining; bottom). The relative band intensities (as ratios to that of WT) were indicated below. (**E**) Binding of Ndc80C^{bonsai} containing Nuf2 WT or N126A (Spc24 and Spc25 blot) to pMR24 beads. Relative band intensities were indicated below. (**F**) Surface drawing of the CH domains of Hec1 and Nuf2. Hec1 and Nuf2 residues critical for Mps1 NTE and MR binding were labeled.

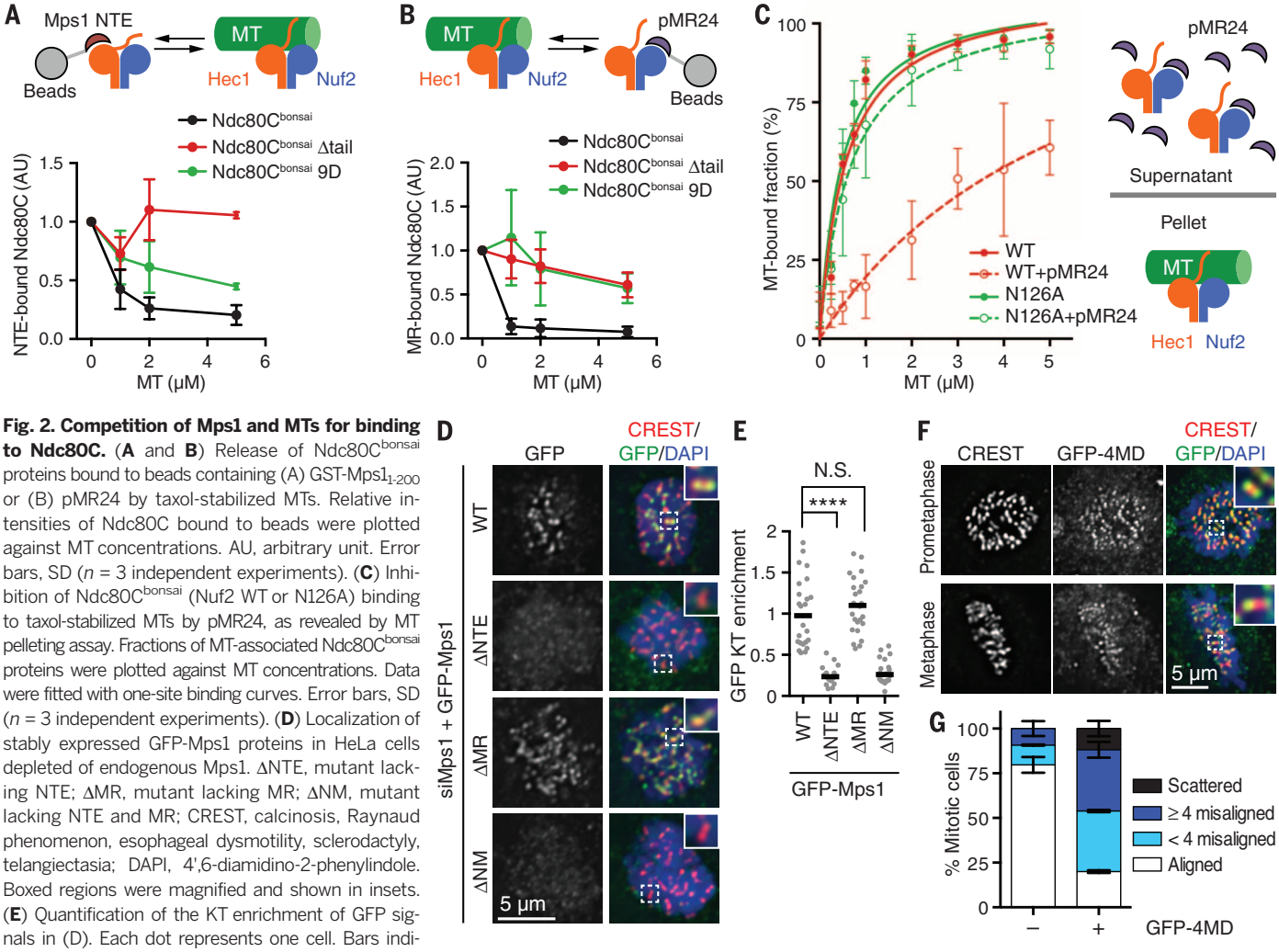


Fig. 2. Competition of Mps1 and MTs for binding to Ndc80C. (**A** and **B**) Release of Ndc80C^{bonsai} proteins bound to beads containing (A) GST-Mps1$_{1-200}$ or (B) pMR24 by taxol-stabilized MTs. Relative intensities of Ndc80C bound to beads were plotted against MT concentrations. AU, arbitrary unit. Error bars, SD (n = 3 independent experiments). (**C**) Inhibition of Ndc80C^{bonsai} (Nuf2 WT or N126A) binding to taxol-stabilized MTs by pMR24, as revealed by MT pelleting assay. Fractions of MT-associated Ndc80C^{bonsai} proteins were plotted against MT concentrations. Data were fitted with one-site binding curves. Error bars, SD (n = 3 independent experiments). (**D**) Localization of stably expressed GFP-Mps1 proteins in HeLa cells depleted of endogenous Mps1. ΔNTE, mutant lacking NTE; ΔMR, mutant lacking MR; ΔNM, mutant lacking NTE and MR; CREST, calcinosis, Raynaud phenomenon, esophageal dysmotility, sclerodactyly, telangiectasia; DAPI, 4′,6-diamidino-2-phenylindole. Boxed regions were magnified and shown in insets. (**E**) Quantification of the KT enrichment of GFP signals in (D). Each dot represents one cell. Bars indicate the median. ****P < 0.0001; N.S., not significant; Student's t test. (**F**) Immunofluorescence images of GFP-4MD–expressing HeLa cells. (**G**) Quantification of the percentages of mitotic cells with or without GFP-4MD expression that exhibited the indicated chromosome alignment phenotypes. Mean and range of two independent experiments (n > 100 cells each) are shown.

glutamic acid.) These mutations also diminished binding of Mps1$_{1-200}$ to Ndc80C (Fig. 1D), indicating that Mps1 NTE bound to the MT-binding surface on Hec1. Deletion of Nuf2 CH, but not Hec1 CH, abolished binding of pMR24 to Ndc80C (fig. S2A). Several Nuf2 CH single mutants exhibited reduced binding to pMR24, with N126A being the most deficient (Fig. 1E and fig. S2, B and C). These mutated residues cluster around the MT-binding site of Nuf2 (Fig. 1F) (*17*). Thus, Mps1 MR binds to the MT-binding site of Nuf2.

We tested whether Mps1 NTE and MR competed with MTs for Ndc80C^{bonsai} binding. Taxol-stabilized MTs reduced binding of Ndc80C to both Mps1$_{1-200}$ (containing NTE) and pMR24 in a dose-dependent manner (Fig. 2, A and B, and fig. S3, A and B). Binding of Mps1 to Ndc80C 9D or Δtail (which are deficient in binding to MT) was less affected by MTs. Unpolymerized tubulin did not block the two Mps1–Ndc80C interactions (fig. S3C). Conversely, pMR24 at high concentrations reduced the MT-binding affinity of Ndc80C from 0.56 to 5.87 μM (Fig. 3C and fig. S3D). It did not affect binding between MT and the MR-binding–deficient Ndc80C N126A. Thus, both Mps1 NTE and MR compete with MTs for binding to Ndc80C.

Dynein-dependent poleward transport (*8*, *22*) releases Mad1–Mad2 from attached KTs. This mechanism is blocked by the F258A mutation in Spindly, a KT receptor of dynein (*23*). Expression of Spindly F258A in HeLa cells depleted of endogenous Spindly blocked Mad1 release from attached KTs but did not block Mps1 release (fig. S4). Release of Mps1 from attached KTs is thus independent of dynein, likely through direct MT competition.

Mps1 ΔNTE failed to localize to unattached KTs, whereas Mps1 ΔMR localized normally to KTs (Fig. 2, D and E, and fig. S5A). Aurora B inhibition expectedly abolished the KT localization of both Mps1 wild type (WT) and ΔMR (fig. S5, B and C). Thus, the KT localization of Mps1 in vivo appears to depend mainly on the NTE–Ndc80C interaction. Competition of this interaction with MTs likely releases Mps1 from attached KTs. Four repeats of MR containing the phosphomimicking S281D mutation (4MD) fused to green fluorescent protein (GFP) localized to KTs (fig. S6). This localization was abolished by the Nuf2 N126A mutation, indicating that the MR–Nuf2 interaction could target Mps1 to KTs to some extent. GFP-4MD still localized to attached metaphase KTs and interfered with chromosome alignment (Fig. 2, F and G). The artificial GFP-4MD might outcompete MTs for binding to Ndc80C or displace the endogenous Mps1 bound to Nuf2.

HeLa cells depleted of endogenous Mps1 and expressing Mps1 ΔNTE failed to undergo mitotic arrest in nocodazole, demonstrating a requirement for NTE in checkpoint signaling (*16*) (Fig. 3A). Although Mps1 ΔMR was slightly deficient in supporting nocodazole-induced mitotic arrest, it was largely inactive when Aurora B was inhibited by ZM447439 (ZM). Bub1 KT localization was compromised in Mps1 ΔMR cells, even without Aurora B inhibition (fig. S7). Furthermore, the MR-binding–deficient Nuf2 N126A failed to restore mitotic

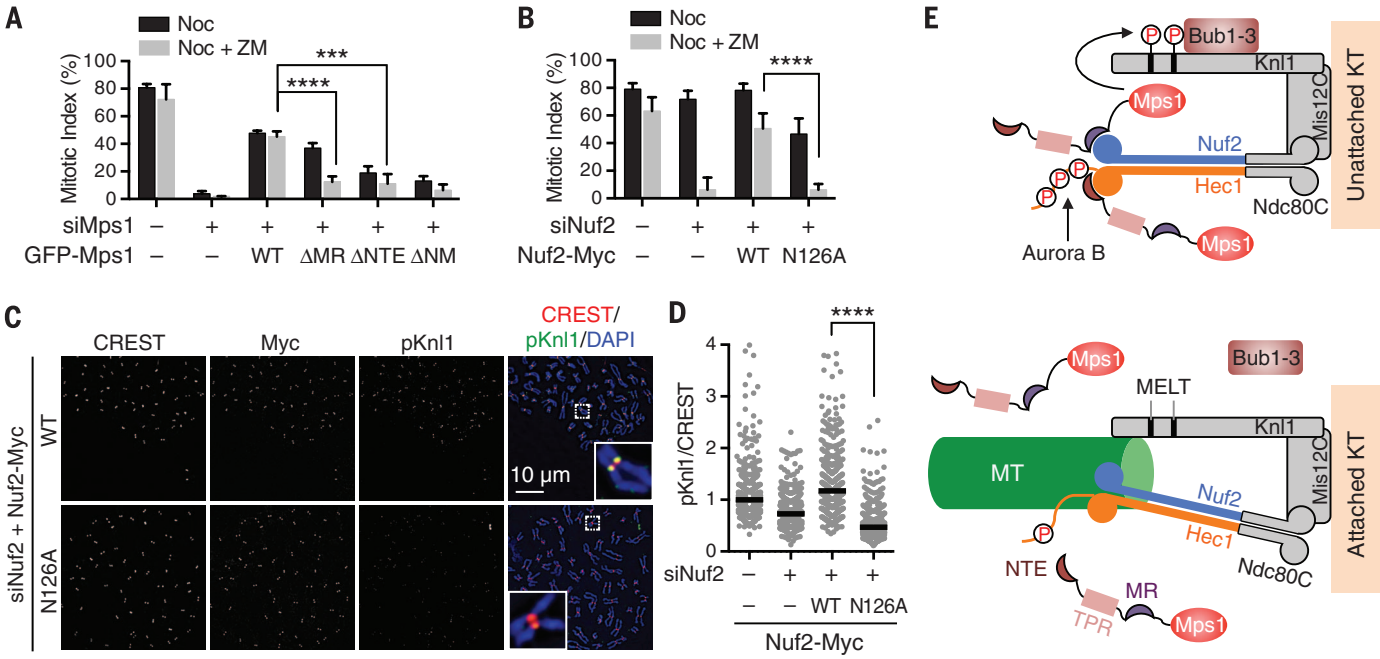


Fig. 3. Requirement of Mps1–Ndc80C interactions during checkpoint signaling. (**A** and **B**) Mitotic indices of HeLa cells stably expressing the indicated (A) GFP-Mps1 or (B) Nuf2-Myc proteins transfected with the indicated small interfering RNAs (siRNAs) and treated with nocodazole (Noc) with or without ZM447439 (ZM). WT, wild type. Error bars, SD (n = 4 independent experiments). ***P < 0.001; ****P < 0.0001; Student's t test. (**C**) Chromosome spreads of cells in (B) treated with nocodazole and MG132 were stained with DAPI and indicated antibodies. Boxed regions were magnified and shown in insets. (**D**) Quantification of the relative KT intensity of phospho-T875 Knl1 staining in (C). Each dot represents one KT pair. Bar indicates the median (n = 460 pairs of KTs). ****P < 0.0001; Student's t test. (**E**) Model of MT-mediated inhibition of Mps1 signaling at KTs. Molecules and structures are not drawn to scale. Knl1 and Ndc80C are drawn as straight rods for simplicity.

arrest of cells depleted of endogenous Nuf2 and treated with ZM (Fig. 3B and fig. S8A). Nuf2 N126A cells had moderate checkpoint defects, even in the absence of ZM. Mps1-dependent events, including Knl1 phosphorylation and Bub1-related protein 1 (BubR1) KT localization, were defective in Nuf2 N126A cells (Fig. 3, C and D, and fig. S8, B to E). Thus, the Mps1 MR–Nuf2 interaction also contributes to checkpoint signaling. Disruption of this interaction in nocodazole-treated cells (with KTs unattached) renders the checkpoint dependent on Aurora B, similar to the checkpoint in taxol-treated cells (with most KTs attached) (*24*). These findings suggest that the Mps1 MR–Nuf2 interaction senses the status of KT attachment in human cells.

Our results establish a straightforward cellular mechanism for sensing KT–MT attachment (Fig. 3E). Because NTE and MR bind independently to Hec1 and Nuf2 heads, there might be two types of Mps1–Ndc80C interactions at KTs: a major one involving the NTE–Hec1 interface and a minor one involving the MR–Nuf2 interface. Binding of MT to Ndc80C releases both and inhibits Mps1 signaling. The weak, multisite Mps1–Ndc80C interactions explain the transient nature of Mps1 at KTs and the inability to detect these interactions in human cell lysates. These interactions might have evolved to balance Mps1 recruitment to unattached KTs and its release from attached ones.

The MR–Nuf2 interaction is required for Mps1-dependent phosphorylation of Knl1 and events downstream of this phosphorylation. Because Knl1 and Ndc80C are components of the same constitutive protein network, the weak MR–Nuf2 interaction is reminiscent of docking interactions between kinases and substrates. In the case of Mps1, MR does not dock on Knl1 itself but on Ndc80C, which indirectly associates with Knl1 through Mis12C. The two degrees of separation ensure that Mps1 preferably phosphorylates Knl1 in the intact KMN.

Our study further points to an intricate cross-talk among the mitotic kinases Mps1, Bub1, and Aurora B in sensing KT–MT attachment. Increasing phosphorylation of the Hec1 tail by Aurora B progressively weakens MT binding by Ndc80C (*25*). In contrast, Aurora B–dependent phosphorylation of the same Hec1 tail enhances binding of Mps1 MR to Nuf2, which promotes phosphorylation of Knl1 and KT targeting of Bub1. In a feed-forward mechanism, Bub1 can then phosphorylate histone H2A and further enrich Aurora B at centromeres (*26*, *27*). Thus, Aurora B regulates the competing MT- and Mps1-binding activities of Ndc80C in opposite directions.

MT- and dynein-dependent release of Mad1–Mad2 from attached KTs indirectly contributes to KT–MT attachment sensing in metazoans but not in yeast (*28*). Our study establishes competition between Mps1 and MTs for binding to Ndc80C as a direct mechanism for monitoring KT attachment. Although the NTE and MR motifs of vertebrate Mps1 are not conserved in yeast, Mps1 interacts with Ndc80C in yeast (*29*). Thus, Mps1 may be a primordial sensor of KT–MT attachment.

REFERENCES AND NOTES

1. E. A. Foley, T. M. Kapoor, *Nat. Rev. Mol. Cell Biol.* **14**, 25–37 (2013).
2. L. Jia, S. Kim, H. Yu, *Trends Biochem. Sci.* **38**, 302–311 (2013).
3. C. Sacristan, G. J. Kops, *Trends Cell Biol.* **25**, 21–28 (2015).
4. S. Kim, H. Yu, *J. Cell Biol.* **208**, 181–196 (2015).
5. G. M. Alushin *et al.*, *Nat. Struct. Mol. Biol.* **19**, 1161–1167 (2012).
6. V. M. Stucke, C. Baumann, E. A. Nigg, *Chromosoma* **113**, 1–15 (2004).
7. S. Martin-Lluesma, V. M. Stucke, E. A. Nigg, *Science* **297**, 2267–2270 (2002).
8. B. J. Howell *et al.*, *J. Cell Biol.* **155**, 1159–1172 (2001).
9. Y. Yamagishi, C. H. Yang, Y. Tanno, Y. Watanabe, *Nat. Cell Biol.* **14**, 746–752 (2012).
10. L. A. Shepperd *et al.*, *Curr. Biol.* **22**, 891–899 (2012).
11. N. London, S. Ceto, J. A. Ranish, S. Biggins, *Curr. Biol.* **22**, 900–906 (2012).
12. I. Primorac *et al.*, *eLife* **2**, e01030 (2013).
13. P. E. Rischitor, K. M. May, K. G. Hardwick, *PLOS ONE* **2**, e1342 (2007).
14. S. Kim, H. Sun, D. R. Tomchick, H. Yu, X. Luo, *Proc. Natl. Acad. Sci. U.S.A.* **109**, 6549–6554 (2012).
15. N. London, S. Biggins, *Genes Dev.* **28**, 140–152 (2014).
16. W. Nijenhuis *et al.*, *J. Cell Biol.* **201**, 217–231 (2013).
17. C. Ciferri *et al.*, *Cell* **133**, 427–439 (2008).
18. J. Kang, Y. Chen, Y. Zhao, H. Yu, *Proc. Natl. Acad. Sci. U.S.A.* **104**, 20232–20237 (2007).
19. I. M. Cheeseman, J. S. Chappie, E. M. Wilson-Kubalek, A. Desai, *Cell* **127**, 983–997 (2006).
20. J. G. DeLuca *et al.*, *Cell* **127**, 969–982 (2006).
21. T. Zhu *et al.*, *J. Biol. Chem.* **288**, 36149–36159 (2013).
22. E. R. Griffis, N. Stuurman, R. D. Vale, *J. Cell Biol.* **177**, 1005–1015 (2007).
23. R. Gassmann *et al.*, *Genes Dev.* **24**, 957–971 (2010).
24. S. Hauf *et al.*, *J. Cell Biol.* **161**, 281–294 (2003).

25. A. V. Zaytsev, L. J. Sundin, K. F. DeLuca, E. L. Grishchuk, J. G. DeLuca, *J. Cell Biol.* **206**, 45–59 (2014).
26. S. A. Kawashima, Y. Yamagishi, T. Honda, K. Ishiguro, Y. Watanabe, *Science* **327**, 172–177 (2010).
27. Y. Yamagishi, T. Honda, Y. Tanno, Y. Watanabe, *Science* **330**, 239–243 (2010).
28. R. Karess, *Trends Cell Biol.* **15**, 386–392 (2005).
29. S. Kemmler *et al.*, *EMBO J.* **28**, 1099–1110 (2009).

ACKNOWLEDGMENTS

We thank C. Brautigam for assistance with isothermal titration calorimetry and microscale thermophoresis, H. Ball for peptide synthesis, and the Animal Resource Center on campus for antibody production. H.Y. is an investigator with the Howard Hughes Medical Institute. This work is supported by the Cancer Prevention and Research Institute of Texas (RP110465-P3 and RP120717-P2) and the Welch Foundation (I-1441).

SUPPLEMENTARY MATERIALS

www.sciencemag.org/content/348/6240/1260/suppl/DC1
Materials and Methods
Figs. S1 to S8
References (*30*–*35*)

1 December 2014; accepted 7 May 2015
10.1126/science.aaa4029

CELL DIVISION CYCLE

Competition between MPS1 and microtubules at kinetochores regulates spindle checkpoint signaling

Yoshitaka Hiruma,[1,2,3]* Carlos Sacristan,[2,3]* Spyridon T. Pachis,[2,3] Athanassios Adamopoulos,[1] Timo Kuijt,[2,3] Marcellus Ubbink,[4] Eleonore von Castelmur,[1] Anastassis Perrakis,[1]† Geert J. P. L. Kops[2,3]†

Cell division progresses to anaphase only after all chromosomes are connected to spindle microtubules through kinetochores and the spindle assembly checkpoint (SAC) is satisfied. We show that the amino-terminal localization module of the SAC protein kinase MPS1 (monopolar spindle 1) directly interacts with the HEC1 (highly expressed in cancer 1) calponin homology domain in the NDC80 (nuclear division cycle 80) kinetochore complex in vitro, in a phosphorylation-dependent manner. Microtubule polymers disrupted this interaction. In cells, MPS1 binding to kinetochores or to ectopic NDC80 complexes was prevented by end-on microtubule attachment, independent of known kinetochore protein-removal mechanisms. Competition for kinetochore binding between SAC proteins and microtubules provides a direct and perhaps evolutionarily conserved way to detect a properly organized spindle ready for cell division.

Attachment of microtubules to kinetochores of meiotic and mitotic chromosomes is essential for segregating a single copy of the genetic material to each of the daughter cells during cell division. This process is surveyed by the spindle assembly checkpoint (SAC), which orchestrates the assembly of an anaphase inhibitor (*1*, *2*) that delays mitotic progression until all kinetochores are attached to microtubules (*3*, *4*). Stable interaction of microtubules to all kinetochores silences the SAC, allowing anaphase to proceed. A key unresolved question is how the SAC machinery distinguishes attached from unattached kinetochores. In metazoa, poleward transport of SAC proteins by the dynein motor complex may contribute to extinguishing kinetochore-SAC signaling when microtubules have attached (*5*). However, kinetochore dynein is not widely conserved (*1*, *6*), and SAC protein removal and silencing can occur without kinetochore dynein in human cells (*7*, *8*). Kinetochore phosphatases are required to silence the SAC in fungi and metazoa (*9*–*11*), but there is no evidence that they are regulated by microtubule attachment.

The SAC relies on the kinetochore-localized protein kinase MPS1 (monopolar spindle 1). Failure to remove it from kinetochores prevents SAC silencing and timely anaphase onset (*12*, *13*). The microtubule-binding NDC80 (nuclear division cycle 80) complex [NDC80-C, which consists of HEC1 (highly expressed in cancer 1), NUF2 (nuclear filament–related 2), and SPC24 and SPC25 (spindle pole body component 24 and 25)] is needed for MPS1 localization to the kinetochores (*14*–*18*). The N-terminal calponin homology (CH) domain of human HEC1 is essential for that interaction (*14*), as also in *Saccharomyces cerevisiae* (*19*, *20*). The MPS1 tetratricopeptide repeat (TPR) domain and a 62–amino acid N-terminal extension (NTE) are required for localizing MPS1 to kinetochores (*14*).

To test whether the NTE-TPR localization module of MPS1 binds directly to the NDC80-C, we expressed ^{15}N-labeled MPS1 N-terminal domain variants—namely MPS1^{TPR}, MPS1$^{NTE\text{-}TPR}$, and MPS1$^{TPR\text{-}CTE}$ (CTE, C-terminal extension) (Fig. 1A and fig. S1A) (for details on all constructs, see the supplementary materials and methods). The corresponding ^{1}H-^{15}N heteronuclear single quantum coherence spectra showed dispersed peaks, as expected for the TPR structure (Fig. 1, B and C). The ^{1}H-^{15}N spectra recorded in the presence of the "Broccoli" variant of the NDC80-C [NDC80-C^{Broccoli} (*21*)] showed peak broadening, leading to the disappearance of many peaks (Fig. 1, D and E, and fig. S1B), which is indicative of the formation of a complex with higher molecular mass. Peak changes were also observed for binding to the "Bonsai" complex [NDC80^{Bonsai} (*22*)] (fig. S1, C to E).

We determined the strength of the interaction of the localization module of MPS1 and NDC80-C by microscale thermophoresis (MST) (all affinities determined in this study are summarized in table S1). The same variants as those used for the nuclear magnetic resonance (NMR) experiments (Fig. 1F and fig. S2, A and B) and MPS1$^{NTE\text{-}TPR\text{-}CTE}$ (Fig. 1G) showed weak binding affinities (3 to 11 μM) when titrated to fluorescently labeled NDC80^{Broccoli}. Relatively higher affinity was observed for NTE-containing constructs, consistent with our previous demonstration of NTE importance for MPS1 function (*14*) and with NMR spectra that show more changes in the presence of the NTE (Fig. 1E). Titrating NDC80^{Broccoli} to fluorescently labeled full-length MPS1 showed similar affinity to that of the TPR-containing constructs (~10 μM) (fig. S2C). However, when NDC80^{Broccoli} was titrated to fluorescently labeled MPS1$^{NTE\text{-}TPR\text{-}CTE}$, we did not observe clear binding (Fig. 2A).

The N-terminal localization module of MPS1 is heavily phosphorylated, and cyclin-dependent kinase 1, Aurora B, Polo-like kinase 1 (PLK1), and MPS1 itself have been implicated in regulating localization of MPS1 to kinetochores (*14*, *15*, *20*, *22*, *23*). Because most potential phosphorylation sites within NTE conform to an MPS1 or PLK1 consensus sequence, we used recombinant MPS1 to phosphorylate the N-terminal MPS1 localization module. Whereas titrating NDC80-C^{Broccoli} to labeled unphosphorylated MPS1$^{NTE\text{-}TPR\text{-}CTE}$ had resulted in no binding (Fig. 2A), exposing NDC80-C^{Broccoli} to phosphorylated, labeled MPS1$^{NTE\text{-}TPR\text{-}CTE}$ (pMPS1$^{NTE\text{-}TPR\text{-}CTE}$) resulted in clear interaction with an affinity of ~150 nM (Fig. 2A). The affinity of NDC80-C^{Broccoli} to pMPS1$^{TPR\text{-}CTE}$ remained undetectable, indicating that the phosphorylation events leading to increased affinity are in the NTE. Phosphorylated full-length MPS1 had similar affinity (~210 nM) as pMPS1$^{NTE\text{-}TPR\text{-}CTE}$ for NDC80-C^{Broccoli} (fig. S2D). In addition, the interaction of pMPS1$^{NTE\text{-}TPR\text{-}CTE}$ with NDC80-C^{Broccoli} was outcompeted by excess amounts of unlabeled MPS1$^{NTE\text{-}TPR\text{-}CTE}$ (fig. S3A), indicating that the unphosphorylated and phosphorylated forms at least partially share the interaction site. Finally, pMPS1$^{NTE\text{-}TPR\text{-}CTE}$ also interacted with NDC80-C^{Bonsai} (fig. S3B), as well as with only the CH domain of HEC1 (Fig. 2B). Collectively, these results

[1]Division of Biochemistry, Netherlands Cancer Institute, 1066 CX Amsterdam, Netherlands. [2]Molecular Cancer Research, University Medical Center Utrecht, 3584 CG Utrecht, Netherlands. [3]Cancer Genomics Netherlands, University Medical Center Utrecht, 3584 CG Utrecht, Netherlands. [4]Leiden Institute of Chemistry, Leiden University, Post Office Box 9502, 2300 RA Leiden, Netherlands.
*These authors contributed equally to this work. †Corresponding author. E-mail: g.j.p.l.kops@umcutrecht.nl (G.J.P.L.K.); a.perrakis@nki.nl (A.P.)

show that phosphorylation of the NTE of MPS1 increases affinity toward NDC80-C by at least a factor of 20 and that a main MPS1 interaction site in the outer kinetochore exists in the HEC1 CH domain.

We next tested whether microtubules could directly prevent the interaction of MPS1 to HEC1, which is known to contact microtubules (*22*). Binding of either MPS1$^{NTE\text{-}TPR\text{-}CTE}$ or pMPS1$^{NTE\text{-}TPR\text{-}CTE}$ to NDC80^{Broccoli} was compromised by the presence of taxol-stabilized microtubules, in a manner dependent on microtubule concentration and polymerization time (Fig. 2C and fig. S3, C and D).

To test whether competition between MPS1 and microtubules for NDC80-C binding also occurs in cells, we examined whether MPS1 and microtubules could bind kinetochores simultaneously. MPS1 amounts at kinetochores in prometaphase cells were high on unattached and laterally attached kinetochores but were almost undetectable on kinetochores that displayed clear end-on attachments (Fig. 3, A and B). Expression of the Phe^{258}→Ala^{258} mutant of Spindly, which specifically prevents activity of the kinetochore-localized pool of dynein (*7*), did not prevent microtubule

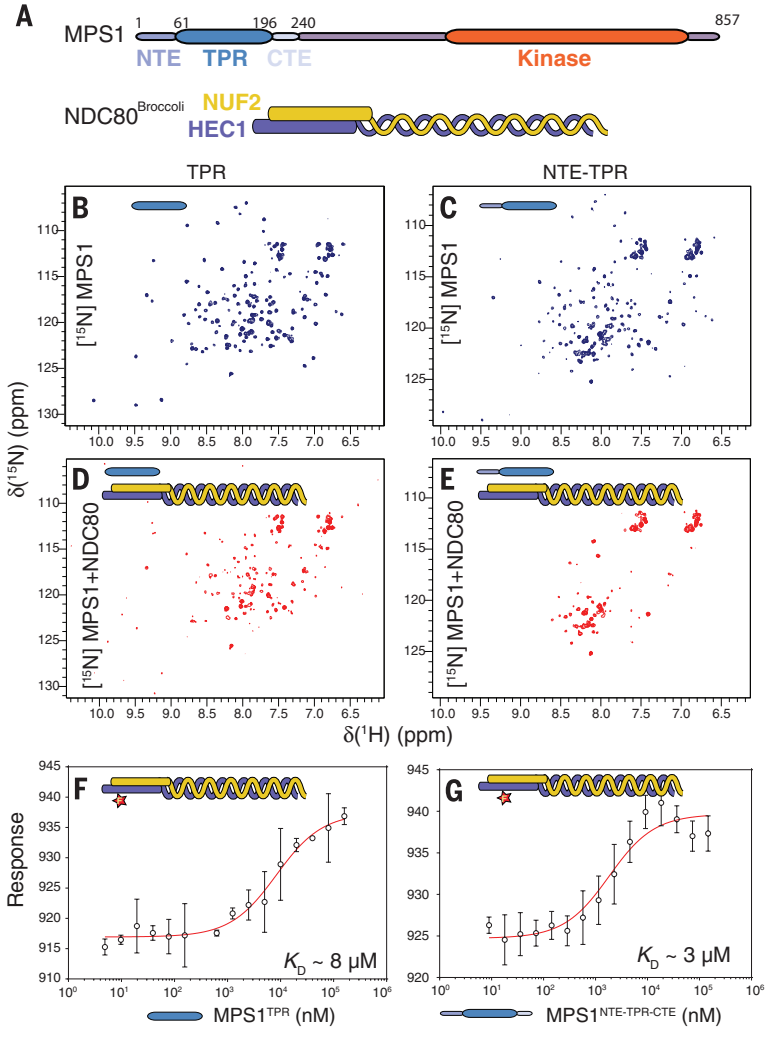


Fig. 1. Interaction of the N-terminal localization module of MPS1 with the NDC80 complex. (**A**) Diagrams of MPS1 and NDC80-C^{Broccoli}. (**B** to **E**) NMR spectra of [^{15}N] MPS1 variants, alone or mixed with NDC80-C^{Broccoli}. A ~10% molar excess of NDC80-C was used for the complex measurements. δ, chemical shift; ppm, parts per million. (**F** and **G**) MST binding curves of MPS1 variants titrated against fluorescent NDC80-C^{Broccoli} . Error bars show SDs from a triplicate experiment. K_D, dissociation constant.

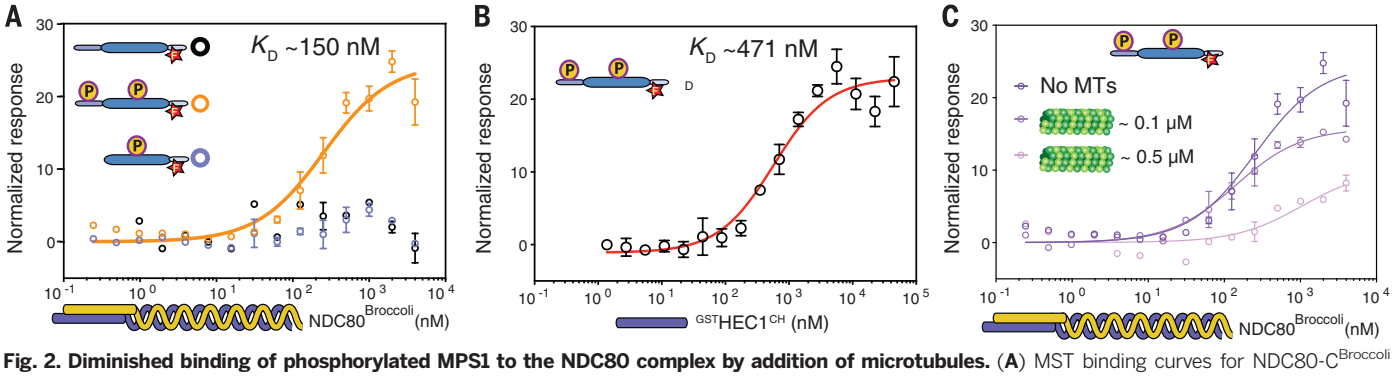


Fig. 2. Diminished binding of phosphorylated MPS1 to the NDC80 complex by addition of microtubules. (**A**) MST binding curves for NDC80-C^{Broccoli} titrated against the indicated fluorescent MPS1 variants. (**B**) MST binding curves for the glutathione *S*-transferase (GST)–HEC1 CH domain titrated against fluorescent pMPS1$^{NTE\text{-}TPR\text{-}CTE}$. (**C**) MST binding curves for NDC80-C^{Broccoli} titrated against fluorescent pMPS1$^{NTE\text{-}TPR\text{-}CTE}$, alone or with the addition of microtubules. Error bars show SDs from a triplicate experiment, except in (C) (duplicate experiment). MTs, microtubules; P, phosphate.

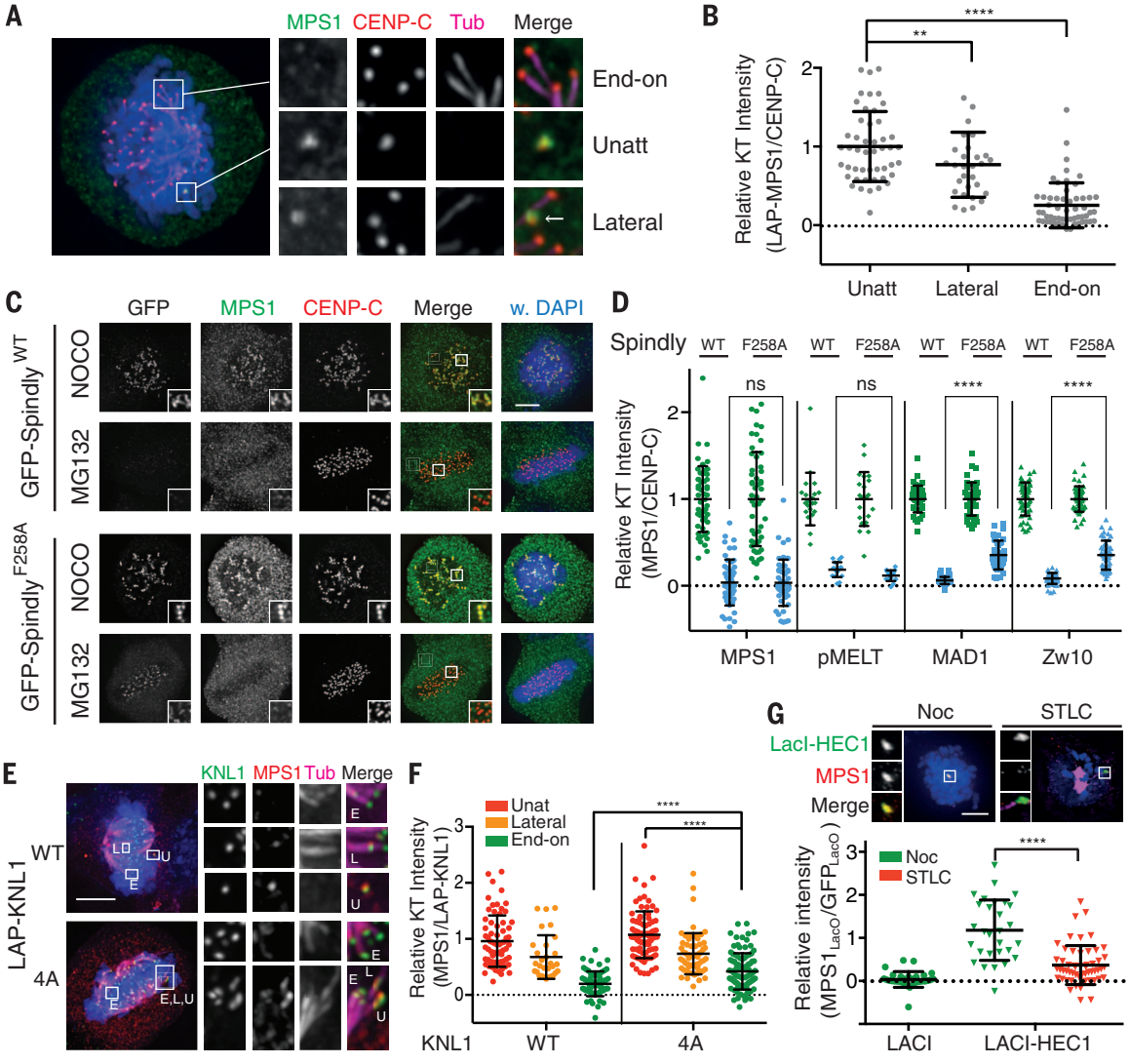


Fig. 3. Microtubule attachment–dependent delocalization of MPS1 from kinetochores, independent of dynein and phosphatase activity. (**A** to **F**) Representative images [(A), (C), and (E)] and quantification (±SD) [(B), (D), and (F)] of protein immunolocalization in HeLa cells subjected to cold treatment [(A) and (B)], HeLa FLP-In cells expressing Spindly variants and treated with nocodazole [NOCO; green in (D)] or MG132 [blue in (D)] for 1 hour [(C) and (D)], or HeLa FLP-In cells expressing KNL1 variants [(E) and (F)]. The arrow in (A) indicates a laterally attached kinetochore. Tub, tubulin; GFP, green fluorescent protein; WT, wild type; DAPI, 4′,6-diamidino-2-phenylindole; F258A, Phe^{258}→Ala^{258}; 4A, KNL1-4A; L; lateral, U; unattached, E; end-on attached. (**G**) Representative images and quantification (±SD) of protein localization in U2OS-LacO cells expressing LacI-LAP-HEC1 and treated with nocodazole or STLC. Cells expressing comparable levels of the LacI proteins were selected for analysis. Asterisks indicate significance (analysis of variance with Tukey's multiple comparison test). $^{**}P < 0.01$; $^{****}P < 0.0001$; ns, not significant. Scale bars in (C), (E), and (G), 5 μm.

attachment from removing MPS1 from kinetochores (Fig. 3, C and D), whereas it reduced the release of MAD1 (mitotic arrest deficient 1) and ZW10 (zeste white 10) (Fig. 3D and fig. S4A). Similar results were obtained by depletion of the dynactin subunits Arp1 or p150^{Glued} (*8*, *14*) or by treatment of cells with the small-molecule dynein inhibitor ciliobrevin D (*24*) (fig. S4, B to E). Ciliobrevin D caused high frequency of kinetochores bound to the microtubule lattice, and these kinetochores had substantial amounts of MPS1 (fig. S4D). This verified that initial lateral attachments, which in animal cells do not involve the NDC80-C, did not dislodge MPS1 from kinetochores.

Displacement of MPS1 from attached kinetochores coincided with dephosphorylation of one of its key SAC substrates, KNL1 (kinetochore null 1) (Fig. 3D and fig. S4A). Precluding localization of the main SAC-silencing phosphatase PP1 (protein phosphatase 1) to kinetochores by expressing KNL1-4A (*10*), however, did not prevent microtubules from inhibiting MPS1 kinetochore binding (Fig. 3, E and F).

Decorating ectopic LacO arrays on the arm of chromosome 1 with LacI-tethered HEC1 was sufficient to localize endogenous MPS1 to those arrays in the absence of microtubules (Fig. 3G and fig. S4F) (*14*). Allowing microtubules from a monopolar spindle to engage in interactions with the LacI-HEC1 molecules on the LacO arrays resulted in delocalization of MPS1 (Fig. 3G). Notably, the LacO arrays were devoid of dynein (fig. S4F). These data support the hypothesis that MPS1 and microtubules compete for binding to NDC80-C in cells.

To identify which residues in HEC1 bind MPS1, we reasoned that because of the preferential binding of phosphorylated MPS1, hydrogen donors within HEC1 were likely candidates. Based on the structure of NDC80-C bound to microtubules (*19*), we designed four NDC80^{Broccoli} mutants carrying clustered substitutions in the HEC1 CH domain, either directly in the interface with tubulin (M1) or peripheral to the interface (M2 to M4) (Fig. 4, A and B). Whereas M1 and M3 displayed a similar affinity for pMPS1$^{NTE\text{-}TPR\text{-}CTE}$ as wild-type NDC80^{Broccoli}, M2 and, in particular, M4 had reduced affinities (Fig. 4C and fig. S5A). M4 was compromised in recruiting endogenous

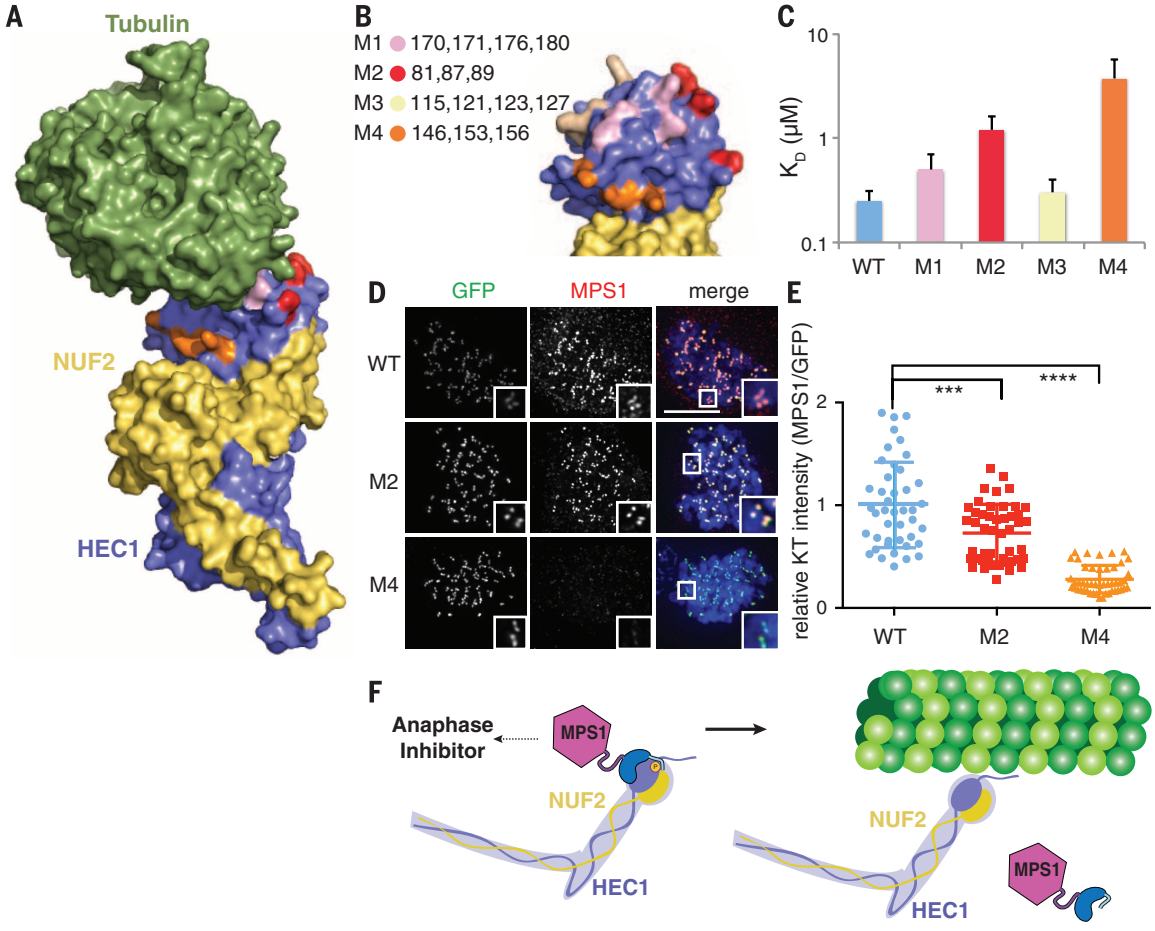


Fig. 4. Mutations in the CH domain of HEC1 preclude MPS1 binding. (**A** and **B**) Surface view of the NDC80 complex bound to tubulin (Protein Data Bank identification number: 3IZO) (A) or the HEC1 region close to tubulin (B), with the four HEC1 cluster mutants (M1 to M4) annotated in color. (**C**) Relative affinity of the NDC80-$C^{Broccoli}$ mutants binding to $pMPS1^{NTE\text{-}TPR\text{-}CTE}$. Error bars denote SD. (**D** and **E**) Representative images (D) and quantification (±SD) (E) of protein localization in HeLa Flp-IN cells expressing the indicated HEC1 variants and treated with nocodazole. ***$P < 0.001$; ****$P < 0.0001$. (**F**) Model for how microtubules inhibit signaling by the SAC kinase MPS1.

MPS1 to LacO arrays (fig. S5, B and C) and endogenous kinetochores (Fig. 4D) and was unable to support a robust SAC response (fig. S5D). However, M4 remained capable of binding microtubules in vitro (fig. S5E) and supporting stable kinetochore-microtubule interactions in cells (fig. S5F). These findings show that the HEC1-MPS1 interface is in close proximity to but is not identical to the HEC1-microtubule interface (fig. S5G) and suggest that inhibition of MPS1-HEC1 interaction by microtubules is at least partly noncompetitive in nature.

Our data reveal a mechanism for how kinetochore-microtubule interactions inhibit production of the anaphase inhibitor. MPS1 directly binds the outer kinetochore NDC80-C in a phosphorylation-dependent manner, orchestrating SAC signaling by ensuring localization of SAC proteins and by promoting assembly and stability of the anaphase inhibitor (*25*). As MPS1 cycles dynamically on and off the kinetochore (*12*), end-on attachments of microtubules to the NDC80-C can directly prevent rebinding of MPS1 (Fig. 4F). To extinguish the SAC, delocalization of MPS1 likely needs to coincide with removal of key downstream SAC effectors from kinetochores and with dephosphorylation of its substrates and perhaps of MPS1 (*10*, *26*).

REFERENCES AND NOTES

1. M. Vleugel, E. Hoogendoorn, B. Snel, G. J. P. L. Kops, *Dev. Cell* **23**, 239–250 (2012).
2. N. London, S. Biggins, *Nat. Rev. Mol. Cell Biol.* **15**, 736–747 (2014).
3. E. A. Foley, T. M. Kapoor, *Nat. Rev. Mol. Cell Biol.* **14**, 25–37 (2013).
4. C. Sacristan, G. J. P. L. Kops, *Trends Cell Biol.* **25**, 21–28 (2015).
5. B. J. Howell *et al.*, *J. Cell Biol.* **155**, 1159–1172 (2001).
6. J. A. Raaijmakers, R. H. Medema, *Chromosoma* **123**, 407–422 (2014).
7. R. Gassmann *et al.*, *Genes Dev.* **24**, 957–971 (2010).
8. J. A. Raaijmakers, M. E. Tanenbaum, R. H. Medema, *J. Cell Biol.* **201**, 201–215 (2013).
9. J. S. Rosenberg, F. R. Cross, H. Funabiki, *Curr. Biol.* **21**, 942–947 (2011).
10. W. Nijenhuis, G. Vallardi, A. Teixeira, G. J. P. L. Kops, A. T. Saurin, *Nat. Cell Biol.* **16**, 1257–1264 (2014).
11. A. Espert *et al.*, *J. Cell Biol.* **206**, 833–842 (2014).
12. N. Jelluma, T. B. Dansen, T. Sliedrecht, N. P. Kwiatkowski, G. J. P. L. Kops, *J. Cell Biol.* **191**, 281–290 (2010).
13. D. Ito, Y. Saito, T. Matsumoto, *Proc. Natl. Acad. Sci. U.S.A.* **109**, 209–214 (2012).
14. W. Nijenhuis *et al.*, *J. Cell Biol.* **201**, 217–231 (2013).
15. A. T. Saurin, M. S. van der Waal, R. H. Medema, S. M. A. Lens, G. J. P. L. Kops, *Nat. Commun.* **2**, 316–319 (2011).
16. S. Martin-Lluesma, V. M. Stucke, E. A. Nigg, *Science* **297**, 2267–2270 (2002).
17. S. Santaguida, C. Vernieri, F. Villa, A. Ciliberto, A. Musacchio, *EMBO J.* **30**, 1508–1519 (2011).
18. T. Zhu *et al.*, *J. Biol. Chem.* **288**, 36149–36159 (2013).
19. G. M. Alushin *et al.*, *Nature* **467**, 805–810 (2010).
20. S. Kemmler *et al.*, *EMBO J.* **28**, 1099–1110 (2009).
21. J. C. Schmidt *et al.*, *Dev. Cell* **23**, 968–980 (2012).
22. C. Ciferri *et al.*, *Cell* **133**, 427–439 (2008).
23. Q. Xu *et al.*, *Mol. Biol. Cell* **20**, 10–20 (2009).
24. A. J. Firestone *et al.*, *Nature* **484**, 125–129 (2012).
25. W. Lan, D. W. Cleveland, *J. Cell Biol.* **190**, 21–24 (2010).
26. M. Maldonado, T. M. Kapoor, *Nat. Cell Biol.* **13**, 475–482 (2011).

ACKNOWLEDGMENTS

We thank I. Cheeseman, R. Gassmann, S. Lens, R. Medema, and A. Musacchio for reagents; the Kops, Perrakis, Lens, and Biggins labs for discussions; S. Biggins for support; and H. Yu for sharing unpublished data. The work was supported by grants ERC-StG KINSIGN, NWO-Vici 865.12.004, KWF 2012-5427, SNF PBBSP3-133408, and NWO-Vici 700.58.441.

SUPPLEMENTARY MATERIALS

www.sciencemag.org/content/348/6240/1264/suppl/DC1
Materials and Methods
Figs. S1 to S5
Table S1
Reference (*27*)

2 December 2014; accepted 7 May 2015
10.1126/science.aaa4055

SEX DETERMINATION

A male-determining factor in the mosquito *Aedes aegypti*

Andrew Brantley Hall,[1,2,3]* Sanjay Basu,[3,4]* Xiaofang Jiang,[1,2,3] Yumin Qi,[2,3] Vladimir A. Timoshevskiy,[3,4] James K. Biedler,[2,3] Maria V. Sharakhova,[3,4] Rubayet Elahi,[2] Michelle A. E. Anderson,[3,4] Xiao-Guang Chen,[5] Igor V. Sharakhov,[1,3,4] Zach N. Adelman,[1,3,4]† Zhijian Tu[1,2,3]†

Sex determination in the mosquito *Aedes aegypti* is governed by a dominant male-determining factor (M factor) located within a Y chromosome–like region called the M locus. Here, we show that an M-locus gene, *Nix*, functions as an M factor in *A. aegypti*. *Nix* exhibits persistent M linkage and early embryonic expression, two characteristics required of an M factor. *Nix* knockout with clustered regularly interspaced short palindromic repeats (CRISPR)–Cas9 resulted in largely feminized genetic males and the production of female isoforms of two key regulators of sexual differentiation: *doublesex* and *fruitless*. Ectopic expression of *Nix* resulted in genetic females with nearly complete male genitalia. Thus, *Nix* is both required and sufficient to initiate male development. This study provides a foundation for mosquito control strategies that convert female mosquitoes into harmless males.

Insects employ diverse molecular mechanisms to determine sex (*1*–*3*). Sex is determined by X chromosome dosage in fruit flies (*4*), heterozygosity of the complementary sex determiner locus in honeybees (*5*), and a female-specific Piwi-interacting RNA in the silkworm *Bombyx mori* (*6*). Similar to mammals, sex determination in many insects is governed by an M factor located on a Y chromosome or homomorphic sex-determining chromosome (*1*). Despite the availability of genomic resources, no M factor has yet been characterized in any insect due to the difficulties of identifying genes in repeat-rich regions (*1*–*3*). Sex determination in mosquitoes is of particular interest because only adult females transmit pathogens responsible for dengue and yellow fever (*7*, *8*). Consequently, a mosquito M factor would be useful in implementing vector control strategies where female mosquitoes are converted into harmless males (*7*).

Male development in *Aedes aegypti* is initiated by an M factor located on the homomorphic sex-determining chromosome within a Y chromosome–like region called the M locus (*9*–*11*). The highly repetitive nature of the *Aedes aegypti* M locus has impeded the discovery of an M factor (*3*, *12*, *13*). To overcome this bottleneck, we developed the chromosome quotient method to find male-specific (M-linked) genomic sequences by comparing the ratio of female to male alignments to reference sequences (*12*, *13*). First, we separately sequenced the genomes of males and females from two strains of *A. aegypti*: Liverpool and kh^w. Then, we generated a rudimentary assembly using the male kh^w strain data because repeat-rich regions like the M locus are often underrepresented in Sanger-based genome assemblies (*14*). Next, we aligned the male and female Illumina data to this assembly and identified 164 contigs that were potentially M linked (defined as more than 5 times as many alignments from male data as from female data in both strains) (table S1). Of the 164 sequences, 140 were either absent from RNA sequencing (RNA-seq) data altogether, absent from early embryo RNA-seq samples, or present in female-derived RNA-seq samples. Within the 24 remaining sequences, we identified only one new gene that is a distant homolog of *transformer-2* (table S2), which is involved in the splicing of *doublesex* (*dsx*) and *fruitless* (*fru*), two key regulators of sexual differentiation in *Drosophila melanogaster* (*4*). We named this gene *Nix*. Because of the tantalizing link to sex determination, we hypothesized that *Nix* may function as an M factor in *A. aegypti*.

The *Nix* cDNA spans 985 base pairs and encodes a 288–amino acid polypeptide containing two RNA recognition motifs (GenBank KF732822) (fig. S1 and tables S2 and S3). Primers for *Nix* amplified a polymerase chain reaction (PCR) product exclusively in male genomic DNA (Fig. 1A). We previously described two transgenes (J2 and sensor) that closely flank the M locus (*13*). Fluorescence in situ hybridization (FISH) to mitotic chromosomes using $M^{J2sensor}$/m males confirmed that the *Nix* signal localizes to only one homologous copy of chromosome 1 at position 1q21, the location of the M locus (Fig. 1D and fig. S2) (*11*). Digital droplet PCR indicated that one haploid copy of *Nix* is present in males and zero copies of *Nix* are present in females (Fig. 1E). Next, we analyzed whether recombination could separate *Nix* from the M locus. By screening 5000 individuals, we identified 19 recombinants where the J2 transgene was separated from the M locus (*13*, *15*). In females from a colony established from these individuals, we could not identify *Nix* by PCR, supporting the conclusion that *Nix* is located within the M locus (Fig. 1B). Transcription of *Nix* was first detected 3 to 4 hours after oviposition (Fig. 1C and fig. S3), corresponding to the beginning of the syncytial blastoderm stage before sex is established (*16*). Thus, *Nix* exhibits two necessary characteristics of an M factor: persistent M linkage and early embryonic expression.

[1]Interdisciplinary PhD Program in Genetics, Bioinformatics, and Computational Biology, *Virginia* Polytechnic Institute and State University (Virginia Tech), Blacksburg, VA, USA. [2]Department of Biochemistry, Virginia Tech, Blacksburg, VA, USA. [3]Fralin Life Science Institute, Virginia Tech, Blacksburg, VA, USA. [4]Department of Entomology, Virginia Tech, Blacksburg, VA, USA. [5]School of Public Health and Tropical Medicine, Southern Medical University, Guangdong, People's Republic of China.
*These authors contributed equally to this work. †Corresponding author. E-mail: jaketu@vt.edu (Z.T.); zachadel@vt.edu (Z.N.A.)

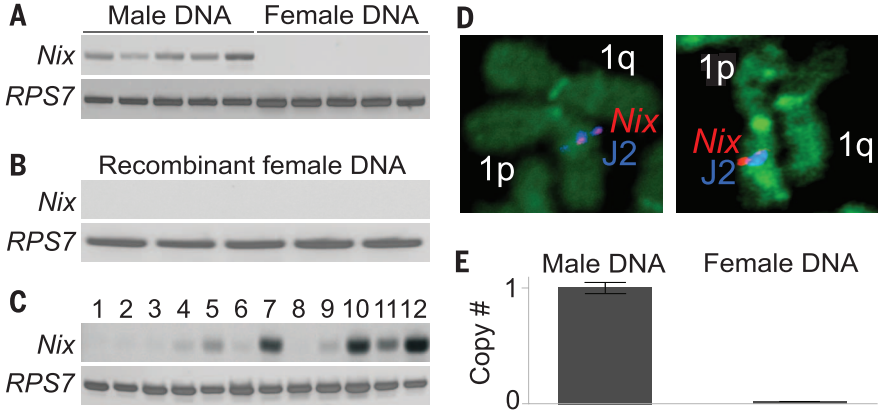


Fig. 1. *Nix* is located within the M locus. (**A**) PCR for *Nix* in male and female genomic DNA. For all PCR experiments, a ribosomal protein gene, *RPS7*, was used as a positive control. (**B**) PCR for *Nix* in genomic DNA from recombinant female $m^{J2sensor}$/m *A. aegypti*. (**C**) Reverse transcription PCR expression profile of *Nix* from 0- to 12-hour embryo cDNA starting at 0 to 1 hour in 1-hour increments. (**D**) FISH with a probe for *Nix* and the J2 transgene in mitotic chromosomes of J2 transgenic males. (**E**) *Nix* copy number as determined by digital droplet PCR (ddPCR) on male and female genomic DNA. Error bars, mean ± SEM.

Downloaded from www.sciencemag.org on June 14, 2015

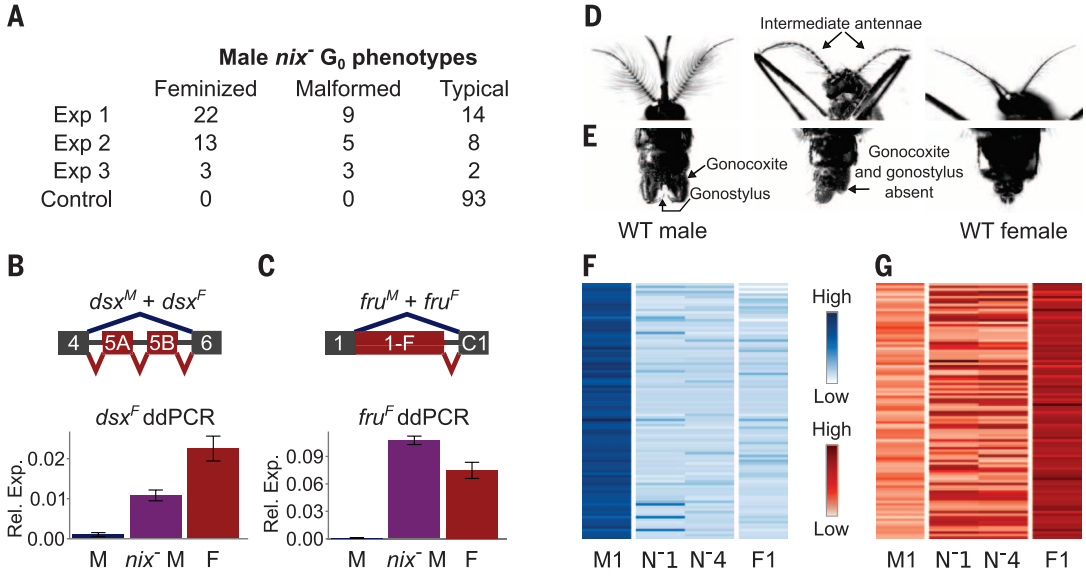


Fig. 2. Knockout with CRISPR-Cas9 demonstrates that *Nix* is required for male development. (**A**) Phenotypes of injected individuals. (**B**) The female isoform of *dsx* (dsx^F) is present in nix^- *A. aegypti* detected by ddPCR. Rel. Exp., relative expression. Error bars, mean ± SEM. (**C**) The female isoform of *fru* (fru^F) is present in the nix^- *A. aegypti* detected by ddPCR. Error bars, mean ± SEM. (**D**) Feminization of the antennae in a nix^- male individual. (**E**) Feminization in the genitals of a nix^- male individual. (**F** and **G**) The log2 reads per kilobase per million mapped reads expression level heat map of the top 100 male-biased (F) and female-biased (G) genes in wild-type males, nix^- males, and wild-type females. Two heat maps from nix^- males are shown here. All other heat maps are shown in fig. S10.

To investigate the role of *Nix* in mosquito development, we generated somatic loss-of-function mutants by injecting clustered regularly interspaced short palindromic repeats–Cas9 (CRISPR-Cas9) (*17*, *18*) and synthetic guide RNAs (sgRNAs) targeting *Nix* into embryos oviposited by females that had mated with double-marked $M^{J2sensor}$/m transgenic males (fig. S4). In the absence of any phenotypic changes, virtually all males resulting from this cross would be double-marked, whereas all females would be unmarked. Genetic lesions in *Nix* were confirmed by RNA-seq and DNA sequencing and were associated specifically with *Nix* guide RNA target sites (fig. S5 and table S4).

Somatic knockout of *Nix* resulted in feminization or deformities in sexually dimorphic organs in more than two-thirds (55 of 79) of double-marked males (designated hereafter as nix^- males), whereas unmarked females (control) were morphologically typical (Fig. 2A and figs. S6 to S8). As somatic mosaics, levels of feminization were variable among nix^- individuals. The phenotype of each nix^- male was scored for the extent of feminization (table S5 and figs. S6 to S8). A common morphological feminization that appeared in 53% (42 of 79) of nix^- males was the absence of one or both gonocoxites and gonostyli, features specific to male genitals used to grasp the female during mating (Fig. 2E and figs. S6 and S7) (*19*). We also observed feminized antennae with fewer and shorter setae than normal males in 44% (35 of 79) of nix^- males (Fig. 2D and figs. S6 and S8).

We further investigated the molecular mechanism of the feminization of nix^- males. *Dsx* and *fru* are essential genes in the sex-determination pathway of many insects, and differential splicing of each results in a downstream cascade that programs the development of sexually dimorphic traits (*20*–*23*). We confirmed that nix^- males produced female splice variants of both *dsx* and *fru* at 0.47 and 1.44 times the amounts in wild-type females, respectively (Fig. 2, B and C; table S6; and fig. S9). Using RNA-seq to examine the expression of sex-biased genes in nix^- males, we found a global feminization of sex-biased gene expression consistent with the observed morphological feminization and the key regulatory functions of *dsx* and *fru* (Fig. 2, F and G, and fig. S10). Thus, *Nix* is required to initiate male development and functions upstream of the two master regulators of sexual differentiation.

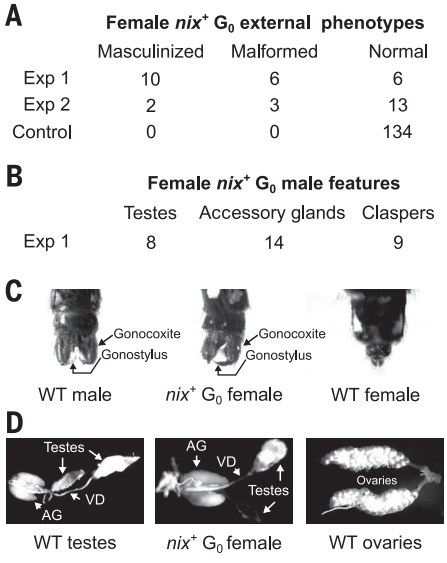


Fig. 3. Ectopic expression demonstrates that *Nix* is sufficient to initiate male development. (**A**) The phenotypes of nix^+ females. Thirty individuals were sacrificed at the larval stage to examine gene expression and therefore have an undetermined phenotype. (**B**) The number of nix^+ females with male-specific features from experiment 1. (**C**) Wild-type genitals compared with the genitals of a nix^+ female, which have gonocoxites and gonostyli. (**D**) Wild-type testes and ovaries compared with gonads of a nix^+ female, which had testes and accessory glands. Wild-type images and nix^+ images are viewed under 55x and 80x magnification, respectively. AG, accessory glands; VD, vas deferens.

To determine whether *Nix* was sufficient for male determination, we investigated the effect of ectopic expression of *Nix* in genetic females. Embryos oviposited by females that had mated with double-marked $M/m^{J2sensor}$ transgenic males were injected with a plasmid expressing *Nix* under the control of the *A. aegypti polyubiquitin* promoter (fig. S4) (*24*). In this case, virtually all genetic females would be double-marked, whereas genetic males would be unmarked. In our first experiment, more than two-thirds (16 of 23) of the double-marked females (designated hereafter as nix^+ females) exhibited extensive masculinization or deformities of the genitalia (Fig. 3A, table S7, and fig. S11). Two male-specific structures of the external genitalia, the gonocoxites and gonostyli (*19*), were clearly visible in 43% (10 of 23) of nix^+ females, whereas a further 26% (6 of 23) had deformed genitalia (Fig. 3, A and C, and table S7). Testes were identified in 34% (8 of 23) of nix^+ females and accessory glands; vasa deferentia were identified in 60% (14 of 23) of nix^+ females (Fig. 3, B to D; table S7; and fig. S11). In a second experiment, 27% (5 of 18) of nix^+ females exhibited masculinized or deformed genitalia (Fig. 3A and table S7). Thus, *Nix* is sufficient to initiate male development.

Using Illumina sequences from male genomic DNA and male RNA-seq, we identified a homolog of *Nix* in the Asian tiger mosquito, *A. albopictus*, with 52% identity at the amino acid level (e-value = 10^{-71}) (GenBank KP765684 and figs. S12 and S13). This gene is only found in male genomic DNA and is expressed in adult males and early embryos of *A. albopictus*, suggesting that *Nix* may be a conserved M factor in these *Aedes* mosquitoes. We also searched for *Nix* in other mosquito genera, including *Culex* and *Anopheles*, but found only autosomal or X-linked genes with RNA recognition motifs.

Here, we demonstrate that an M-locus gene, *Nix*, is an M factor in *A. aegypti* because it is both required and sufficient to initiate male development, although complete sex conversion has not been achieved in our transient assays. *Nix* encodes a potential splicing factor, and the absence of *Nix* shifts the alternative splicing of *dsx* and *fru* toward their female isoforms. The discovery of *Nix* provides an opportunity to characterize the remaining genes and interactions in the *A. aegypti* sex-determination pathway, which may be informative in unraveling the sex determination cascades of mosquitoes in general.

Aedes aegypti is a major vector for dengue, yellow fever, and chikungunya viruses, and only female mosquitoes feed on blood and transmit these pathogens. Thus, genetic control methods that introduce a male bias to reduce mosquito populations are attractive and potentially effective measures to reduce the incidence of mosquito-borne disease (*7*, *8*). When dosage compensation and sex determination are linked, as in the silkworm, manipulation of the sex-determination pathway results in sex-specific embryonic lethality due to misregulation of dosage compensation (*6*). In contrast, we have obtained partial sex-change phenotypes from both *Nix* knockout and ectopic expression, presumably because *A. aegypti* does not require dosage compensation. Thus, this study provides the foundation for developing mosquito control strategies by converting females into harmless males or selectively eliminating deadly females.

REFERENCES AND NOTES

1. D. Bachtrog *et al.*, *PLOS Biol.* **12**, e1001899 (2014).
2. Tree of Sex, *Sci. Data* **1**, 140015 (2014).
3. D. Charlesworth, J. E. Mank, *Genetics* **186**, 9–31 (2010).
4. H. K. Salz, J. W. Erickson, *Fly* **4**, 60–70 (2010).
5. M. Hasselmann *et al.*, *Nature* **454**, 519–522 (2008).
6. T. Kiuchi *et al.*, *Nature* **509**, 633–636 (2014).
7. P. A. Papathanos *et al.*, *Malar. J.* **8** (suppl. 2), S5 (2009).
8. M. R. Wise de Valdez *et al.*, *Proc. Natl. Acad. Sci. U.S.A.* **108**, 4772–4775 (2011).
9. B. M. Gilchrist, J. B. S. Haldane, *Hereditas* **33**, 175–190 (1947).
10. G. A. H. McClelland, *Trans. R. Soc. Trop. Med. Hyg.* **56**, 4 (1962).
11. M. E. Newton, R. J. Wood, D. I. Southern, *Genetica* **48**, 137–143 (1978).
12. A. B. Hall *et al.*, *BMC Genomics* **14**, 273 (2013).
13. A. B. Hall *et al.*, *Genome Biol. Evol.* **6**, 179–191 (2014).
14. R. A. Hoskins *et al.*, *Genome Biol.* **3**, research0085.1–research0085.16 (2002).
15. Z. N. Adelman, M. A. Anderson, E. M. Morazzani, K. M. Myles, *Insect Biochem. Mol. Biol.* **38**, 705–713 (2008).
16. J. K. Biedler, W. Hu, H. Tae, Z. Tu, *PLOS ONE* **7**, e33933 (2012).
17. M. Jinek *et al.*, *Science* **337**, 816–821 (2012).
18. L. Cong *et al.*, *Science* **339**, 819–823 (2013).
19. N. Becker, *Mosquitoes and Their Control* (Kluwer Academic/Plenum Publishers, New York, 2003).
20. K. C. Burtis, B. S. Baker, *Cell* **56**, 997–1010 (1989).
21. M. Salvemini *et al.*, *BMC Evol. Biol.* **11**, 41 (2011).
22. M. Salvemini *et al.*, *PLOS ONE* **8**, e48554 (2013).
23. S. Whyard *et al.*, *Parasit. Vectors* **8**, 96 (2015).
24. M. A. E. Anderson, T. L. Gross, K. M. Myles, Z. N. Adelman, *Insect Mol. Biol.* **19**, 441–449 (2010).

ACKNOWLEDGMENTS

We thank A. James and C. Barillas-Mury for critical review of the manuscript. We thank R. Saunders for mosquito care. Sequencing data used in this study have been submitted to the National Center for Biotechnology Information under accession numbers KF732822, KP765684, KP842989-KP843003, SRP044709, SRP046160, SRP047470, SRP047401, SRP034669, SRP055126, and SRP055127. The authors declare no competing financial interests. This research was supported by the National Institutes of Health grant AI113643, the National Science Foundation Graduate Research Fellowship grant DGE-1519168, the National Natural Science Foundation grant 81420108024, the Fralin Life Science Institute, and the Virginia Agriculture Experimental Station. This study was considered by the Virginia Tech Institutional Biosafety Committee and was determined not to fall under dual-use research of concern (DURC).

SUPPLEMENTARY MATERIALS

www.sciencemag.org/content/348/6240/1268/suppl/DC1
Materials and Methods
Figs. S1 to S14
Tables S1 to S9
References (*25*–*38*)

12 November 2014; accepted 7 May 2015
Published online 21 May 2015;
10.1126/science.aaa2850

jbc
the journal of biological chemistry

Binding together the world of biology

- ***Peer review by two leading scientists*** *selected from our panel of over 700 experts in their fields*
- *Average time to first decision is* ***21 days***
- ***Articles are published on the day of acceptance*** *as open-access Papers in Press*

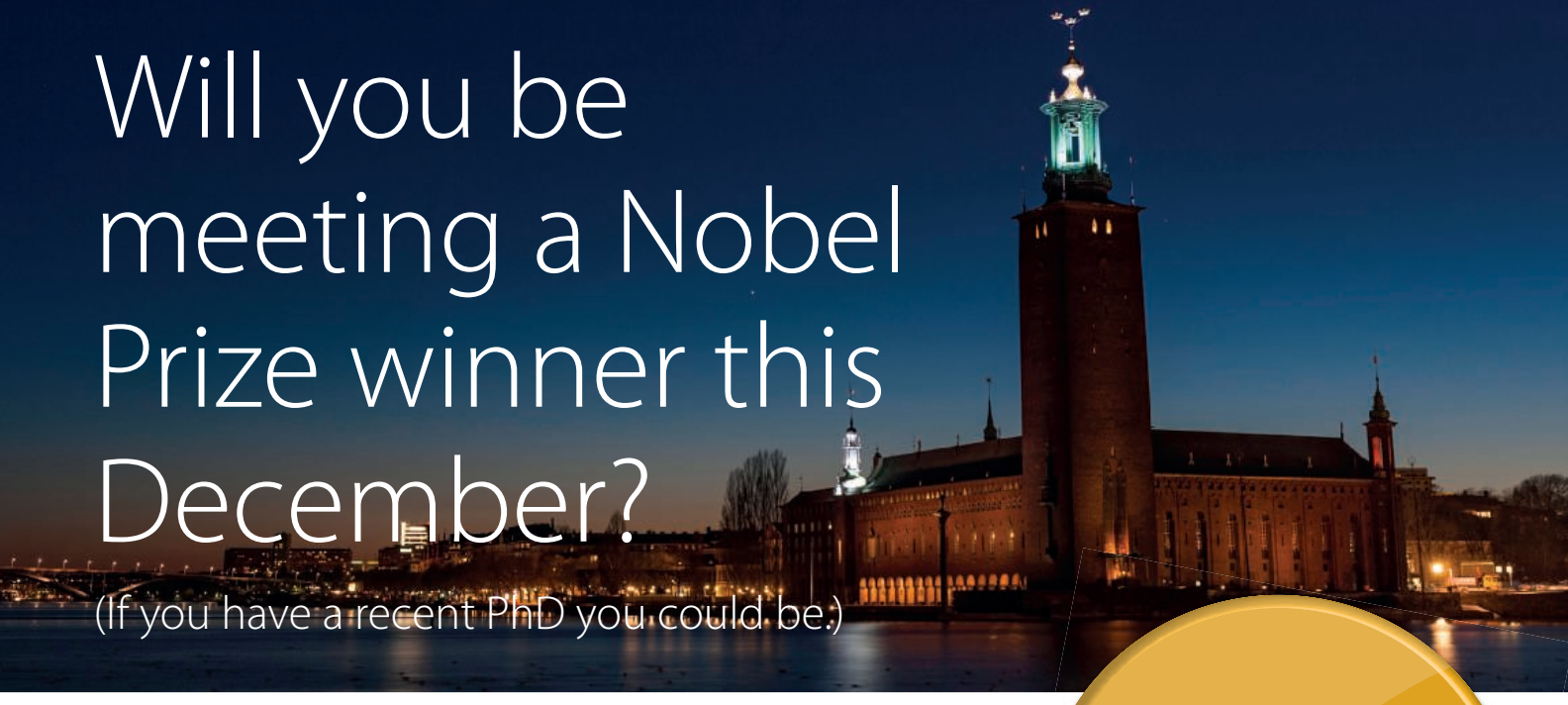
SUBMIT YOUR NEXT ARTICLE TO JBC

www.jbc.org

ASBMB
American Society for Biochemistry and Molecular Biology

WWW.ASBMB.ORG

Will you be meeting a Nobel Prize winner this December?



(If you have a recent PhD you could be.)

Stockholm in the second week of December is a special place. The city is alive with excitement as it welcomes and celebrates the new Nobel Laureates at the annual Nobel Prize ceremony.

If you are a PhD student, you could be here too – meeting a Nobel Laureate and receiving a rather special prize yourself.

The journal *Science* & SciLifeLab have established The *Science* & SciLifeLab Prize for Young Scientists, to recognize and reward excellence in PhD research and support young scientists at the start of their careers. It's about bright minds, bright ideas and bright futures.

Four winners will be selected for this international award. They will have their essays published in the journal *Science* and share a new total of 60,000 USD in prize money. The winners will be awarded in Stockholm, in December, and take part in a unique week of events including meeting leading scientists in their fields.

"The last couple of days have been exhilarating. It has been an experience of a lifetime. Stockholm is a wonderful city and the Award winning ceremony exceeds my wildest dreams."
–Dr. Dan Dominissini, 2014 Prize Winner

Who knows, The *Science* & SciLifeLab Prize for Young Scientists could be a major stepping stone in your career and hopefully one day, during Nobel week, you could be visiting Stockholm in December once again.

Science & SciLifeLab PRIZE FOR YOUNG SCIENTISTS

This prize is made possible with the kind support of the Knut and Alice Wallenberg Foundation. This Foundation grants funding in two main areas; research projects of high scientific potential and individual support of excellent scientists.

The 2015 Prize is now open. The deadline for submissions is August 1, 2015.
Enter today: www.sciencemag.org/scilifelabprize

The 2015 Prize categories are:

- Cell and Molecular Biology
- Ecology and Environment
- Genomics and Proteomics
- Translational Medicine

Knut och Alice Wallenbergs Stiftelse

Science AAAS

SciLifeLab



Small animal imaging: Data that's more than skin deep

To minimize complexity, researchers often study cellular proteins or nucleic acids in isolation. But sometimes—when testing a drug's efficacy and safety, for instance, or monitoring tumor progression—ex vivo just won't do. The only way to know how a compound or cells will behave in the body is to put them into an animal and watch what happens live. The results are easily recognizable in the pages of your favorite journal: the ghostly outline of a mouse, with a telltale multicolored heat bloom indicating where the action is. **By Jeffrey M. Perkel**

Molecular Imaging, a contract research organization (CRO) with locations in Ann Arbor, Michigan and San Diego, California, has a largely pharmaceutical clientele. Sometimes, says Chief Scientific Officer Patrick McConville, those clients are looking for drug screening services. More frequently, they have preliminary data but need help selecting the right candidate for clinical trials.

"It's about trying to obtain information that cannot be obtained other ways," he says.

How do Molecular Imaging's scientists obtain such information? By getting under the skin of the problem. Literally.

Small-animal imaging allows researchers to test-drive the therapies and compounds they hope eventually to apply in the clinic. It provides a way to monitor disease progression and mechanisms for tracking various disease phenomena over time, often using methods that are available for human patients as well.

Suppose, for example, a researcher wants a comprehensive view of the disease progression and therapeutic response in an animal model of Parkinson's disease, McConville says. One approach would be to obtain a set of genetically identical Parkinson's disease animals, dose them all with either the candidate therapeutic or a placebo, sacrifice a few at each time point, and dissect out and analyze the appropriate brain regions. That requires a lot of mice, of course, but also poses the difficulty of trying to average the responses of different animals over time. And it can't easily be applied to human patients.

The alternative is to exploit preclinical imaging to produce a multidimensional dataset in live animals. For instance, using [^{18}F]-fluorodeoxyglucose (FDG) positron emission tomography (PET), researchers can assess brain metabolic activity based on the rate at which different regions take up the radioactive probe. They can pinpoint functional dopaminergic neurons—the cells that are affected in Parkinson's disease—using a commercially available dopamine transporter-binding radiotracer called DaTscan (from GE), via single-photon emission coupled tomography (SPECT) imaging. And they can align those data with anatomical features using computed tomography (CT) data. Other than anesthesia to keep the animal calm and unmoving, the mouse is unaffected by the experiment, meaning it can be imaged repeatedly for days, weeks, or months. Bottom line: fewer animals, richer data, and better decisions.

"The beauty of in vivo imaging is that you don't need to sacrifice the animal," says Hong Yuan, director of the **Biomedical Research Imaging Center** (BRIC) Small Animal Imaging Facility at the University of North Carolina, Chapel Hill, School of Medicine. "You can look at changes due to treatment or any other manipulation over time, and that is a very powerful method compared to traditional immunochemistry."

The BRIC makes available to its users a broad suite of imaging modalities. These include a 9.4T Bruker magnetic resonance imager (MRI)—smaller in stature but more powerful than its clinical equivalent; a GE eXplore Vista PET/CT dual-modality imager; a GE eXplore speCZT SPECT/CT system; a Vevo 2100 ultrasound system from VisualSonics; and three standalone CTs—small animal analogs of equipment that would be at home in any (albeit extremely well-funded) medical facility. Also available are four optical imagers, including three In Vivo Imaging Systems (IVIS) and one fluorescence tomography system, all from **PerkinElmer**.

Generally speaking, imaging modalities fall into two categories, says Mario Bourdon, chief scientific officer at small animal imaging services provider **BioLaurus**: anatomic and molecular. Anatomic imagers includes X-ray, CT (which is essentially a 3-D X-ray), MRI (for soft tissue analysis), and ultrasound (for imaging blood flow, cardiac activity, and fetal development, for instance). Molecular imaging methods include nuclear medicine (PET and SPECT) and optical approaches, all of which allow researchers to track the abundance, location, and activity of specific molecular species in vivo.

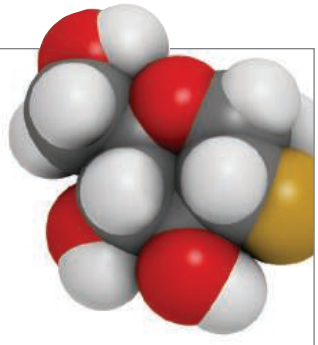
The Small Animal Imaging Facility at **The University of Texas MD Anderson Cancer Center** sports three MRI scanners in its instrument stable, and they are "by far the most widely used" of the lab's hardware, says John Hazle, professor of imaging physics and the facility director. Among other reasons, he says, MRI provides "excellent soft-tissue imaging and the ability to image some physiology and continued>

ILLUSTRATION: © MARQUES/SHUTTERSTOCK.COM

Upcoming Features

Transcriptomics—July 31 ■ *Proteomics—September 11* ■ *Genomics—September 25*

Using [18F]-fluorodeoxyglucose (FDG) positron emission tomography (PET), researchers can assess brain metabolic activity based on the rate at which different regions take up the radioactive probe.



Fluorodeoxyglucose

metabolic processes," allowing researchers to determine, for instance, how tumors respond to therapy.

But, by most accounts, optical imaging is the most widely used preclinical modality overall. Capable of recording both fluorescent and bioluminescent signals, "Optical imaging has a couple advantages," Yuan says. Among its virtues, optical imaging is relatively inexpensive and high throughput—researchers can image multiple animals simultaneously and rapidly, meaning it's relatively easy to image statistically significant population sizes. By comparison, MRI scans, which provide soft tissue anatomy, are done one or a few at a time. "Our MRI scanner runs around the clock, but the throughput is much lower [than optical]," says Christopher Contag, director of the **Stanford Center for Innovation in In Vivo Imaging**, where optical imaging also is the most widely used modality. "On the optical system we process probably hundreds of mice [per day], versus a handful on the MRI or PET."

Optical imaging also is technically easy to use. "We train users and they can handle the image acquisition and data interpretation pretty quickly," Yuan says. Other modalities typically are handled by trained staff.

Better optics

Optical imaging comes in two flavors: fluorescent and bioluminescent. In fluorescence imaging, a fluorescent marker (such as a labeled antibody or genetically encoded fluorescent protein) is introduced or expressed in the animal and excited with an external light source. Bioluminescence involves genetically modifying the animal to produce a light-generating protein, such as luciferase, and produces light only in response to a supplied substrate. In either case, the abundance and distribution of a specific molecular target is measured by recording the resulting photoemission through the skin.

But therein lies the problem. As anyone who has put a flashlight behind their hands knows, light does not travel in a straight line through biological tissue; it scatters and is absorbed. Thus, some fraction of the excitation (in the case of fluorescence) and emission light (fluorescence and bioluminescence) is inevitably lost in optical imaging—though this is less true of near-infrared light. Also, the signal's exact position is often difficult to work out. By contrast, PET and SPECT tracers can be localized precisely, as both emit high-energy particles that traverse the body unimpeded. As a result, optical imaging is rarely used on any animals other than mice, and even then, mostly for surface features such as subcutaneous tumors.

Researchers are working to change that, however.

One approach generating considerable excitement, for instance, is photoacoustic tomography (PAT). Lihong Wang, the Gene K. Beare Distinguished Professor of Biomedical Engineering at **Washington University in St. Louis**, Missouri who pioneered the technique, says that while optical imaging loses resolution beyond about a millimeter, ultrasound maintains resolution at greater depths. PAT effectively combines the two, using light to excite a molecular target but reading out the ultrasonic pressure wave caused by the target's heating and expansion. "It's similar to lightning and thunder," explains Andrew Needles, senior manager for product innovation at **FUJIFILM VisualSonics** in Toronto, Ontario, which has commercialized the technology. "The lightning causes the surrounding atmosphere to create a sound wave."

In theory, says Wang, PAT can detect any molecule, provided the laser is tuned to the correct wavelength for molecular absorption. His lab has imaged everything from nucleic acids and carbohydrates to organic dyes and water. One common application, says Needles, is measuring blood oxygenation, functional data that can be overlaid over a traditional ultrasound image for anatomic detail. Now, Wang's lab has been awarded BRAIN Initiative funding to image "the whole brain of a small animal in vivo and image action potentials."

TriFoil Imaging, in Chatsworth, California, has developed another optical technology. Launched in September 2014, called fluorescence-emission computed tomography (FLECT) is to traditional planar imagers what CT is to X-ray.

Laser energy strikes the animal through a thin slit while rotating around the whole animal in a helical scan. The resulting fluorescence emission is captured by a ring of 48 detectors positioned around the animal, which rotates through 360 degrees to produce a tomographic dataset, similar to PET.

Indeed, according to Staf Van Cauter, executive vice president for marketing and business development at TriFoil, FLECT "is a nonisotopic alternative to nuclear imaging techniques," and using it, he says, researchers can detect tumors and other features smaller than a millimeter in size, and identify exactly where in the body they are located.

A more accessible pet

Still, since optical modalities are for the most part not approved for human use, researchers interested in clinical medicine must look elsewhere for molecular imaging. One popular option is PET.

PET, explains John Gore, director of the **Vanderbilt University Institute of Imaging Science**, provides molecular information with exceptional sensitivity. The tradeoff is resolution: Where MRI can image down to 100 μm, PET voxels are millimeter-sized.

"The value of PET is it's a translational imaging modality," says Patrick Phelps, president and chief executive officer of **Sofie Biosciences** in Culver City, California, a company that develops PET imaging systems and probes. A PET probe that works in mice can thus also, in theory, be applied in humans.

But PET probes aren't easy to work with. The most widely

ILLUSTRATION: © MOLEKUUL.BE/SHUTTERSTOCK.COM

used probe, FDG, uses fluorine-18 (^{18}F), with a half-life of 110 minutes, meaning the material must be synthesized, delivered to the researcher, and used within hours. Another isotope, oxygen-15 has a 2-minute half-life, making it impractical for most applications.

"The access to PET probes has been a huge barrier to access," Phelps says.

Other isotopes, such as zirconium-89 (half-life 78.4 hours) and copper-64 (12.7 hours), open PET to researchers located at greater distances from synthesis laboratories. Or labs can generate their own probes, provided they have a cyclotron. But that isn't a trivial undertaking.

The BRIC, for instance, installed a cyclotron in late 2014. According to Yuan, the hardware itself cost a couple million dollars. But infrastructure upgrades also were required. "The cyclotron we purchased is not self-shielding," she explains, so the university had to install 6 feet of concrete underneath and lead-shielded walls surrounding the cyclotron. The room's lead-shielded door weighs 11 tons. Adding in the cost for a radiochemistry-capable "hot cell" lab and quality-control equipment, she says, and the hardware cost spirals to "probably in the range of $20 million."

Still, it takes more than access to isotopes to make PET practical. Given their short half-life, researchers also need a way to attach them to the desired molecule before they decay. Hidde Ploegh of the **Whitehead Institute for Biomedical Research** in Cambridge, Massachusetts, has developed a method that could simplify that process, at least for labeling antibody fragments.

Using an ^{18}F-labeled substrate and the sortase enzyme, Ploegh's team has labeled camelid-derived antibody fragments containing a sortase recognition sequence to create an immuno-PET probe. They then used that to observe myeloid cell infiltration of implanted tumors in vivo. The method provides a way to spy on tumors without knowing a priori where they are, Ploegh explains—just follow the macrophages. "It's like, if you are on safari and you want to know where the lions are sleeping, just follow the other Land Rovers."

Featured Participants

BioLaurus
www.biolaurus.com

BRIC Small Animal Imaging Facility
www.med.unc.edu/bric/small-animal-imaging

Bruker
www.bruker.com

FUJIFILM VisualSonics
www.visualsonics.com

Magnetic Insight
www.magneticinsight.com

Molecular Imaging
www.molecularimaging.com

Optical Imaging Laboratory, Washington University in St. Louis
oilab.seas.wustl.edu

PerkinElmer
www.perkinelmer.com

Sofie Biosciences
www.sofiebio.com

Stanford Center for Innovation in In Vivo Imaging
mips.stanford.edu/aboutus/facilities/clark/sci3/

TriFoil Imaging
www.trifoilimaging.com

UT MD Anderson Cancer Center Small Animal Imaging Facility
www.mdanderson.org/education-and-research/resources-for-professionals/scientific-resources/core-facilities-and-services/small-animal-imaging-facility/index.html

Vanderbilt University Institute of Imaging Science
www.vuiis.vanderbilt.edu

Whitehead Institute for Biomedical Research
wi.mit.edu

New modalities

Despite the rich set of imaging tools now available, development continues on multiple fronts.

Magnetic Insight, for instance, is advancing a method called "magnetic particle imaging" (MPI; also commercialized by **Bruker**). According to Patrick Goodwill, Magnetic Insight's chief technical officer, MPI provides molecular contrast, like PET and optical imaging, but with magnets. "It's nuclear medicine, but using an iron oxide nanoparticle."

Researchers can, for instance, load mesenchymal stem cells with antibody-coated nanoparticles and track them in vivo, Goodwill says, detecting as few as 200 cells at any depth. "We're using low-frequency magnetic fields, 20-kHz, that will pass through just about anything. If we had a whale-sized MPI scanner, we could see through a whale."

Contag, with Stanford colleague Sam Gambhir, is studying ways to capture Raman spectral fingerprints in vivo. In one recent paper, his team described a molecular endoscope that could theoretically assess the molecular status of colon polyps in real time, rather than sending biopsies to a histopathologist. The technique relies on surfaced-enhanced Raman spectroscopy (SERS) nanoparticles, which dramatically boost the Raman signal molecules normally produce. "You can spray these SERS nanoparticles on the [colon's] surface and as you withdraw the endoscope, it scans and searches for places where the particles stick," he explains.

And Hazle's lab has begun experimenting with new MRI contrast agents to better image metabolic activity—effectively blending MRI and molecular imaging—using "hyperpolarized" carbon 13 (^{13}C)-MRI. Molecular imaging, Hazle explains, tells researchers where the probe is located, but not its chemical structure. But ^{13}C-labeled pyruvate produces a different signal when converted into lactate, a transition that occurs at a different rate in cancerous tissues. "So not only do you know [the] tumor took up that sugar, but [also whether] it metabolized it in aerobic metabolism or anaerobic metabolism," he says.

Whatever the fate of these technologies in preclinical core facilities or the clinic, most researchers agree existing modalities aren't going anywhere. Different imaging methods, Wang says, exploit different contrast mechanisms and thus complement one another. "This is why you don't want to say one technology will replace the rest," Wang says. "I've found that never really happens, not in the medical-imaging world."

Jeffrey M. Perkel is a freelance science writer based in Pocatello, Idaho.

DOI: 10.1126/science.opms.p1500094

FT-IR/NIR Imaging Systems

Spotlight Systems are a complete family of high-performance FT-IR microscopy and FT-IR/NIR chemical imaging systems. The new Spotlight 150i and Spotlight 200i can be configured with either a PerkinElmer Frontier FT-IR optical bench, or a Spectrum Two optical bench. Both system configurations are powered by the acclaimed DynaScan Interferometer, which provides performance without the compromise of competitive designs. Frontier Spotlight Microscopy and Imaging System options include both transmission and reflection microsampling, and its Micro ATR Imaging option provides information down to areas as small as 3 µm. A number of sample automation and detector options are available to suit many applications. Each system is engineered to the highest quality specifications, providing high-energy throughput, reproducibility, and confidence in the quality of your result. Spotlight imaging systems reveal the identity of a vast array of chemical components within materials as well as displaying areas of homogeneity and variation.

PerkinElmer
For info: 800-762-4000
www.perkinelmer.com

EMCCD Spectroscopy Camera

The new Synapse EM is a deep-cooled EMCCD Scientific camera for low-light and ultrafast spectroscopy experiments. The Synapse EM is available in front and back illuminated for optimal quantum efficiency. With a sensor format of 1600 x 200 or 1600 x 400 and a pixel size of 16 µm, the Synapse EM is the ideal candidate for high spectral resolution measurements. The camera comes with a standard dual readout mode that allows the users to switch automatically between EMCCD mode for low-light measurements and conventional CCD mode for standard spectroscopy. QExtra technology is available standard in the Synapse EM-BIQX and is an antireflective multilayer coating designed to greatly improve quantum efficiency of back illuminated sensors over a broad spectral range, while suppressing undesirable etaloning effects. With a maximum frame rate above 1,600 spectra per second and outstanding linearity, the Synapse EM is the ideal EMCCD scientific camera for Raman, SERS/TERS, multitrack, transient, and single molecule spectroscopic applications.

Horiba
For info: 732-494-8660
www.synapseem.com



Compact Microscope

Enabling maximum comfort and ease-of-use for routine observations, the high-performing, ergonomically designed, compact, and robust CX23 microscope is packed full of features to enhance every step of the workflow. Delivering Olympus' renowned high-quality optics and featuring updates to increase portability, usability, sturdiness, and security, the new microscope is ideal both for educational and routine lab environments as well as for use in the field. High-performing, quality optics include a quadruple nosepiece equipped with Olympus' plan achromat objectives ensuring a wide field of view with a field number of 20. The objectives maintain superb image flatness throughout the field of view and long working distances supported by a focus lock to prevent objectives and specimens from damage. An LED light source provides both a long service time of 20,000 hours and lower power consumption while the reduced blue light preserves vivid color observation on HE staining.

Olympus
For info: +49-402-3773-5913
www.olympus-lifescience.com

Light Sheet Microscope Module

The Leica TCS SP8 DLS is a digital light sheet microscope, which is fully integrated into the Leica TCS SP8 confocal microscope for the observation of developmental processes in real time and 3-D. The synergy of light sheet and confocal microscopy opens novel fields of application. Light sheet microscopy is a gentle method of imaging light-sensitive samples or fast biological processes in whole organisms, since the specimen is illuminated in a single plane. The novelty of Leica Microsystems' approach lies in the integration of a light sheet module into an inverted Leica TCS SP8 confocal system. The TwinFlect mirror, which deflects the illuminating light sheet at a 90° angle, makes it possible to combine digital light sheet and confocal imaging in one system without compromising confocal functionality. This is a clear distinction from other solutions that require a dedicated optical setup on an independent system with perpendicular illuminating and detecting objectives.

Leica Microsystems
For info: 800-248-0123
www.leica-microsystems.com

Ultra Load Stage

The new Ultra Load Stage is designed for ZEISS Xradia Ultra 3-D X-ray microscopes and enables in situ nanomechanical testing—compression, tension, and indentation—with nondestructive 3-D tomographic imaging. For the first time, researchers will be able to image the evolution of structure in 3-D under load down to 50 nm resolution. Xradia Ultra Load Stage explores a new critical length scale for in situ materials characterization, enabling researchers to observe internal features such as nanoscale cracks and voids that ultimately lead to deformation and failure at the macroscale. Ultra Load Stage satisfies a void in the current availability of mechanical testing and imaging approaches, offering new capabilities to observe internal processes at nanoscale resolution. Until now, electron microscopy techniques provided resolution down to the nanometer range but are limited to surface imaging or required extremely thin samples whose mechanical behavior will be strongly affected by surface effects.

ZEISS
For info: +49-36-4164-3949
www.zeiss.com/xrm

Electronically submit your new product description or product literature information! Go to www.sciencemag.org/products/newproducts.dtl for more information.

Newly offered instrumentation, apparatus, and laboratory materials of interest to researchers in all disciplines in academic, industrial, and governmental organizations are featured in this space. Emphasis is given to purpose, chief characteristics, and availability of products and materials. Endorsement by *Science* or AAAS of any products or materials mentioned is not implied. Additional information may be obtained from the manufacturer or supplier.

63 north

KNOWLEDGE FOR A BETTER WORLD





Photo: Carl-Erik Eriksson

Trondheim is the ancient Viking capital of Norway. The Nidelva River flows through the city, and you can even fish for salmon during your lunch break. You'll find hiking, alpine and cross-country skiing, cycling and more within a 10-minute drive of the city centre.

Research adventure at 63 degrees north

Remote yet modern. Beautiful and peaceful. Quality and equality. All that combined with long-term government research funding and the UN's ranking as one of the best countries to live in. Welcome to Trondheim and NTNU. The best minds, world-class research, and just the right size city for a great life.

We welcome top scientists from all cultures and nations who want to contribute to our goal: Knowledge for a better world.

TOP RESEARCH DEMANDS BRILLIANT MINDS
– WE'RE ALWAYS LOOKING FOR THE BEST



Photo: Geir Mogen/Kavli Institute for Systems Neuroscience

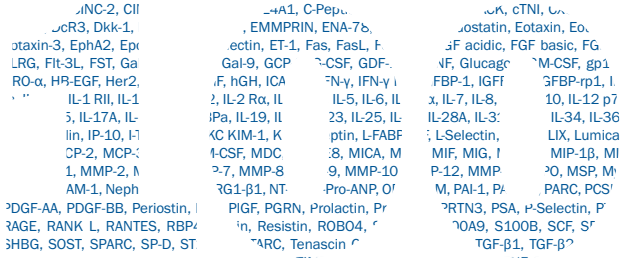
NTNU neuroscientists May-Britt and Edvard Moser were awarded the Nobel Prize in Medicine or Physiology in December 2014.

NTNU – Trondheim
Norwegian University of
Science and Technology

www.ntnu.edu

R&D SYSTEMS™
a bio-techne brand

Do You Suffer from **Panel Envy?**



analytes in 1 Luminex® assay.

EXPLORE NOW
rndsystems.com/**100Plex**

#PanelEnvy #100Plex



Science Careers Advertising

For full advertising details, go to ScienceCareers.org and click For Employers, or call one of our representatives.

Tracy Holmes
Worldwide Associate Director
Science Careers
Phone: +44 (0) 1223 326525

THE AMERICAS

E-mail: advertise@sciencecareers.org
Fax: 202 289 6742

Tina Burks
Phone: 202 326 6577

Nancy Toema
Phone: 202 326 6578

Marci Gallun
Sales Administrator
Phone: 202 326 6582

Online Job Posting Questions
Phone: 202 312 6375

EUROPE / INDIA / AUSTRALIA / NEW ZEALAND / REST OF WORLD

E-mail: ads@science-int.co.uk
Fax: +44 (0) 1223 326532

Axel Gesatzki
Phone: +44 (0) 1223 326529

Sarah Lelarge
Phone: +44 (0) 1223 326527

Kelly Grace
Phone: +44 (0) 1223 326528

JAPAN

Katsuyoshi Fukamizu (Tokyo)
E-mail: kfukamizu@aaas.org
Phone: +81 3 3219 5777

Hiroyuki Mashiki (Kyoto)
E-mail: hmashiki@aaas.org
Phone: +81 75 823 1109

CHINA / KOREA / SINGAPORE / TAIWAN / THAILAND

Ruolei Wu
Phone: +86 186 0082 9345
E-mail: rwu@aaas.org

All ads submitted for publication must comply with applicable U.S. and non-U.S. laws. *Science* reserves the right to refuse any advertisement at its sole discretion for any reason, including without limitation for offensive language or inappropriate content, and all advertising is subject to publisher approval. *Science* encourages our readers to alert us to any ads that they feel may be discriminatory or offensive.

ScienceCareers
FROM THE JOURNAL SCIENCE AAAS

ScienceCareers.org

Federal Ministry of Education and Research

ZENTREN FÜR INNOVATIONSKOMPETENZ
UNTERNEHMEN REGION
Die BMBF-Innovationsinitiative Neue Länder

IN SEARCH OF EXCELLENCE!

ZIK B CUBE / Technische Universität Dresden

The Centre for Innovation Competence (ZIK) B CUBE – Center for Molecular Bioengineering of the Technische Universität Dresden (www.tu-dresden.de/bcube) is an interdisciplinary research center focusing on research and teaching in the areas of Bioprospecting, BioNano Tools and Biomimetic Materials.

B CUBE and the German Federal Ministry of Education and Research (BMBF) invite applications to fill the following two positions by latest beginning of 2016:

Junior Research Group Leader for Multi-Scale Analysis

Equivalent to Junior (DE) or Assistant (USA) Professorship

The successful candidate will establish an international team of young, talented scientists to develop multi-scale analysis technologies for the investigation of the molecular and structural features of natural and synthetic materials for understanding their functions. The resulting technology will not only yield unique insights into the structure-function relationship of biological and biomimetic materials but also open new opportunities for medical diagnostics. This requires the development of an integral measurement system combining various analytical methods, e. g. spectroscopy, microscopy, rheology, image processing. Applicants should possess a university degree and PhD in biophysics, bioengineering or related fields and demonstrate postdoctoral experience in instrumentation development.

Junior Research Group Leader for Bottom-up Synthetic Biology

Equivalent to Junior (DE) or Assistant (USA) Professorship

The successful candidate will establish an international team of young, talented scientists to work on the self-assembly of responsive biofunctional systems. This preferably includes studies of biological sensor and actuator elements in reconstituted, lipid-based membrane systems. Towards possible applications in the fields of synthetic biology and/or nanotechnology the group will seek to optimize the reconstituted systems with regard to robustness, resilience and autonomy. Applicants should possess a university degree and PhD in biophysics, biochemistry or related fields and demonstrate postdoctoral experience in the in vitro investigation of sub-cellular functional units.

The group leader positions are funded initially for a period of five years with the option for an extension of at least two years. Subject to personal qualification the group leaders are remunerated according to salary group E 15 TV-L. The period of employment is governed by § 2 Fixed Term Research Contracts Act (Wissenschaftszeitvertragsgesetz - WissZeitVG). Both groups will receive funding from the BMBF for five years including start-up equipment, research staff (four full time positions) and consumables. Implementation of the expanded strategy concept of B CUBE is a requirement for both group leaders. Candidates are required to demonstrate a commitment to excellence in both research and teaching. Strong writing skills with a proven track record of successful research and publication is expected. Excellent communication skills in English are essential as this is the working language at the research center.

TU Dresden seeks to employ more women in leadership positions. Hence we should particularly like to encourage qualified women to apply. Applications from disabled candidates or those with additional support needs are welcome.

Applications including a CV, a publication list and a short description of current and future research ideas (maximum 10 pages) as well as three letters of reference should be sent to both ZIK B CUBE and the Project Management Jülich (representing the BMBF) until **19.07.2015** by email or regular mail (stamped arrival date applies) to:

TU Dresden
B CUBE
Prof. Nils Kröger
Arnoldstrasse 18
01307 Dresden, Germany
E-Mail: zikbcube@tu-dresden.de
(in a single pdf-file)

and

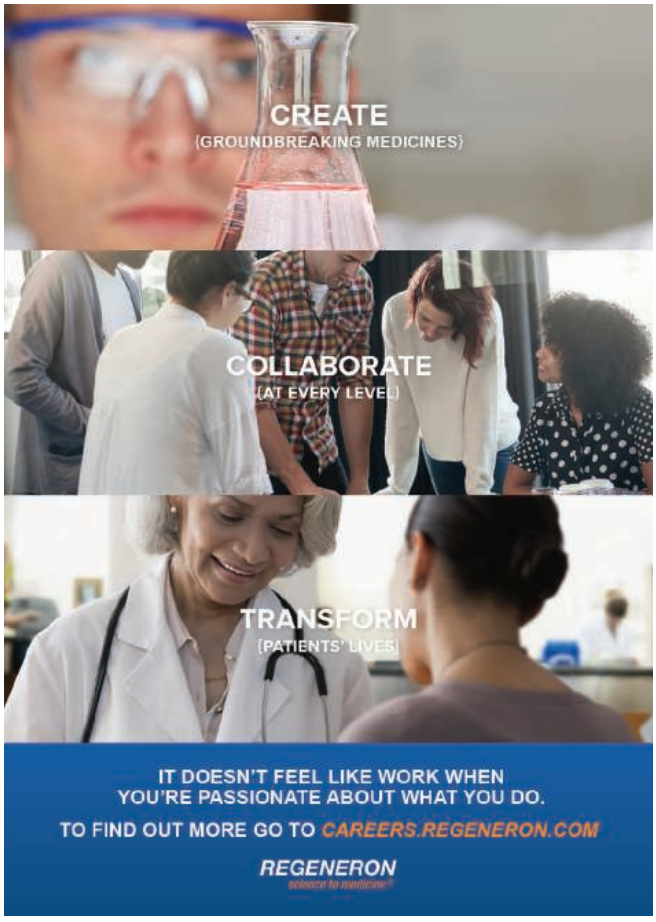
Project Management Jülich
Forschungszentrum Jülich GmbH
Dr. Christoph Wannek
Postfach 61 02 47
10923 Berlin, Germany
E-Mail: c.wannek@fz-juelich.de

TECHNISCHE UNIVERSITÄT DRESDEN

Please submit copies only, as your application will not be returned to you.

For further information please contact: Prof. Nils Kröger or Ms. Ines Kästner via phone (+49-351-463 43000) or E-Mail (zikbcube@tu-dresden.de)

For further details on the application requirements please see:
http://www.unternehmen-region.de/de/374.php



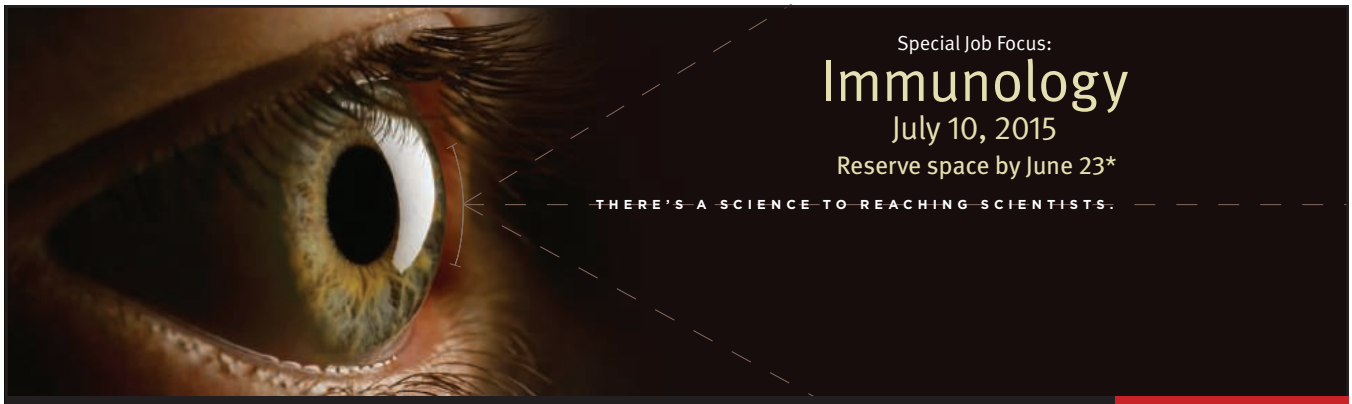
Faculty Position
MassBiologics and Department of Molecular, Cell and Cancer Biology
University of Massachusetts Medical School

MassBiologics and the Department of Molecular, Cell and Cancer Biology of the University of Massachusetts Medical School invite applications for a faculty investigator in synthetic biology. Applications from established investigators are encouraged. Rank will be commensurate with ability and experience. The successful candidate will develop a strong, extramurally funded and collaborative research program that establishes new research areas in synthetic biology focused on the engineering of biomolecular systems for the control of cellular processes in mammalian systems. Applicants must have a Ph.D. and/or M.D. degree and should have a strong background in disciplines such bioengineering, molecular engineering, molecular cell biology, genetics, chemistry, and be interested in engineering synthetic and/or cellular systems. Furthermore, candidates should have a strong publication record in disciplines related to the position, potential to initiate and sustain a strong externally funded research program in synthetic biology with a focus on mammalian systems, and a track record of interacting creatively, collaboratively, and productively with other scientists. The candidates will be selected, in part, on the basis of how well their research program interfaces and complements current faculty research at MassBiologics and the Molecular, Cell and Cancer Biology Department. Laboratory operations will be located at MassBiologics of UMMS in Boston, MA and the departmental appointment in MCCB on the Worcester campus.

Applicants should submit a cover letter, curriculum vitae, a brief summary of past accomplishments, a description of future research plans and contact information for three references to **https://academicjobsonline.org/ajo/jobs/5570**. Inquiries, but not application materials, may be directed to Professors Mark S. Klempner (mark.klempner@umassmed.edu) or Michael R. Green (michael.green@umassmed.edu). Review of applications will begin immediately and continue until the position is filled.

As an Equal Opportunity and Affirmative Action Employer, the University of Massachusetts recognizes the power of a diverse community and encourages applications from individuals with varied experiences, perspective and backgrounds.

UMASS MEDICAL SCHOOL
MassBiologics
Medicine for Better Lives



Why choose this immunology section for your advertisement?

- Relevant ads lead off the career section with special Immunology banner
- Bonus distribution to:

 8th International AIDS Society (IAS) Conference
 19–22 July, Vancouver, British Columbia, Canada

 Malaria
 25–26 July, Girona, Spain.

* Ads accepted until July 6 on a first-come, first-served basis.

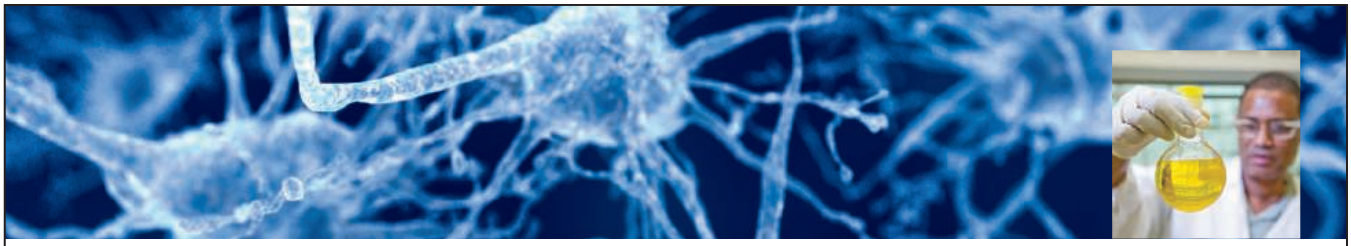
SCIENCECAREERS.ORG



To book your ad: **advertise@sciencecareers.org**

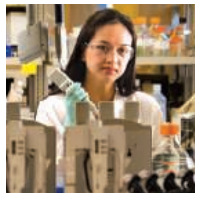
The Americas: 202-326-6582 **Europe/RoW:** +44-0-1223-326500
Japan: +81-3-3219-5777 **China/Korea/Singapore/Taiwan:** +86-186-0082-9345

ScienceCareers
FROM THE JOURNAL SCIENCE AAAS



Explore the Amgen Difference

In Thousand Oaks, CA and at Our Expanded Facilities in Cambridge, MA and South San Francisco, CA





The Amgen postdoctoral program is committed to providing future scientists with an enriching environment to inspire innovation that will contribute to the development of human therapeutics.

At Amgen, we are proud to have driven the discovery of innovative human therapeutics that have changed the practice of medicine. To us, nothing's more important than helping patients worldwide in the fight against cancer, cardiovascular disease, inflammatory and neurological disorders, and other serious illnesses.

Throughout our organization, you'll find an exciting group of departments that are looking forward to employing the skills and talents offered by postdoctoral fellows.

Amgen Postdoctoral Fellowships

- Oncology/Immuno-oncology
- Metabolic Disorders
- Protein Science
- Molecular Structure
- Toxicology
- Pharmacokinetics & Drug Metabolism
- Inflammation
- Neuroscience
- Medicinal Chemistry
- Medical Sciences
- Process Development

If you're ready for your next step, join us.
Visit amgen.com/careers,
Career Category "Postdoctoral".

AMGEN® 35 YEARS

Amgen is an Equal Opportunity employer and will consider all qualified applicants for employment without regard to race, color, religion, sex, sexual orientation, gender identity, national origin, protected veteran status, or disability status

Department of Health and Human Services (DHHS)
National Institutes of Health (NIH)
National Cancer Institute (NCI)
Center for Cancer Research (CCR)

NATIONAL® CANCER INSTITUTE

Tenure-Track Investigator Position in the HIV Dynamics and Replication Program

The HIV Dynamics and Replication Program (HIV DRP, formerly the HIV Drug Resistance Program), CCR, NCI, NIH, DHHS is seeking an outstanding tenure-track investigator to carry out original, independent, and innovative research in an area of virology including, but not limited to, HIV/retrovirus biology. This intramural position is similar to that of an Assistant Professor in a university setting.

The successful candidate will have expertise in HIV/retrovirus biology or cancer virology. Areas of emphasis include molecular aspects of viral replication, virus-host cell interactions, and drug resistance. Applicants must have a Ph.D. or equivalent doctoral degree, relevant postdoctoral experience, and a record of high achievement.

This position is located at the NCI campus in Frederick, Maryland, which offers state-of-the-art facilities, collaborative opportunities, and core facilities for advanced technologies. The investigator will have access to a wide array of intellectual and technological assets, including high-quality technology cores dedicated to protein chemistry, natural products chemistry, biophysics, mass spectrometry, imaging, microscopy, proteomics and genomics, bioinformatics/biostatistics, and flow cytometry, in addition to support for patient-based studies through the NIH Clinical Center. For an overview of CCR, please visit http://ccr.cancer.gov/.

Review of applications will begin on or about **August 3, 2015,** but applications will be accepted until the position is filled. Salary is competitive and will be commensurate with the candidate's experience. A full benefits package is available, including retirement, health insurance, life insurance, long-term care insurance, annual and sick leave, and a Thrift Savings Plan (401K equivalent). This position is not restricted to U.S. citizens.

To apply, please submit a cover letter, curriculum vitae, description of research plans (~5 pages), and 3 letters of recommendation to: **Ms. Valerie Turnquist, Administrative Laboratory Manager, NCI at Frederick, P.O. Box B, Bldg. 535, Frederick, MD 21702-1201**, Email: **turnquiv@mail.nih.gov**. PDF files are encouraged.

This position is subject to a background investigation. The NIH is dedicated to building a diverse community in its training and employment programs.

DHHS, NIH and NCI are Equal Opportunity Employers.

ScienceCareers online @sciencecareers.org

Department of Health and Human Services
National Institutes of Health
National Institute of General Medical Sciences
Division of Genetics and Developmental Biology

DIVISION DIRECTOR

The National Institute of General Medical Sciences (NIGMS), a major research component of the National Institutes of Health (NIH) and the Department of Health and Human Services (DHHS), is seeking exceptional candidates for the position of Director, Division of Genetics and Developmental Biology (GDB). Information about GDB is available at **http://www.nigms.nih.gov/About/Overview/pages/gdb.aspx.**

GDB has supported many of the exciting fundamental discoveries that have led to deeper knowledge of how cells and organisms function as well as to new technologies and approaches. In FY 2015, the Division of Genetics and Developmental Biology had an annual budget of about $439 million and is one of five scientific divisions within the NIGMS. GDB is organized into two branches, one focused on genetic mechanisms and one on developmental and cellular processes, and has 11 scientific staff members who serve as program officers. The division director reports to the NIGMS director and is a member of the NIGMS senior leadership team, which helps set policies and priorities for the Institute. There are also opportunities to participate in and advise on NIH-wide activities and collaborations with other federal agencies.

While concentrating on general principles of genetics, gene expression and developmental biology, often using model organisms, research supported by GDB underpins studies on human health and disease. The Director, GDB plans and directs a program of research grants and contracts, analyzes national research efforts on the problem of human genetic disease, makes recommendations to assist the National Advisory General Medical Sciences Council or other advisory committees or groups, identifies the need for research in the area of genetics and developmental biology, and advises universities, other centers of medical research, and professional and lay organizations about research needs and requirements. The Division supports research on genetic and molecular regulation, protein synthesis, gene expression, DNA and RNA, intracellular signaling pathway dynamics and network organization in genetics, among other areas. This position offers important opportunities to set scientific priorities, lead change and improve the research enterprise.

Qualifications: Candidates must possess an M.D., Ph.D., or equivalent degree in a field relevant to the position. The ideal candidate will have considerable research experience and will possess a broad spectrum of scientific knowledge related to the NIGMS mission. In addition, candidates should possess recognized research management and leadership abilities. A strong understanding of the fundamental mechanisms of inheritance, development, and cell function is desired. The position will be filled under a Title 42(f) excepted service appointment.

Salary/Benefits: Salary is competitive and will be commensurate with the experience of the candidate. A recruitment or relocation bonus may be available, and relocation expenses may be paid. A full package of Federal Civil Service benefits is available, including: retirement, health and life insurance, long term care insurance, leave, and a Thrift Savings Plan (401K equivalent). The successful candidate is subject to a background investigation and financial disclosure requirements.

How to Apply: Applicants must submit a current curriculum vitae, bibliography, copy of degree, and full contact details for three references. In addition, applicants are asked to prepare two statements: a vision statement and a statement that addresses the specific qualification requirements (please limit both statements to two pages each). NIGMS will be accepting applications and plans to have the position open for the next 45 days, but will not close the application process until a candidate has been selected. Please send your application package to **GDBDirectorApplicants@nigms.nih.gov**. You may contact Shea Keys with questions about this vacancy at **skeys@mail.nih.gov** or 301-594-0945.

HHS and NIH are Equal Opportunity Employers

Sequencing Core Director

The Center for Genetic Medicine of Northwestern University Feinberg School of Medicine in downtown Chicago invites applications for a full time position as Director of the Northwestern University Sequencing (NUSEQ) Core. The Core Director is expected to oversee NUSEQ Core personnel and lead efforts for the establishment of this new core facility. This includes planning and implementation of workflows and related processes and establishing the scope of services offered. Application deadline is **July 15, 2015**.

Applicants should have a Ph.D. or equivalent in relevant biological or chemical science field, with a minimum of 5 years experience in molecular biology/genomics and minimum 3 years of hands-on technical experience in next generation sequencing. The candidate should have experience in next generation sequencing methods development, experience with preparation of grant funding for next generation sequencing technology projects is helpful. We are seeking an individual with prior experience working within or directing a similar Core facility. A demonstrated ability to manage projects and lead interdisciplinary teams is required, and the candidate should possess excellent interpersonal as well as verbal and written skills.

Applicants should send (as a single PDF) a cover letter referencing the Core Director for Sequencing position, a curriculum vitae, and the name and contact information for four to six references to **CGMCoreSearch@northwestern.edu**.

NORTHWESTERN UNIVERSITY FEINBERG SCHOOL OF MEDICINE

Northwestern University is an Affirmative Action, Equal Opportunity Employer. Women and minorities are encouraged to apply. Hiring is contingent upon eligibility to work in the United States.

Cleveland Clinic

Pediatric Institute and Lerner Research Institute

New faculty positions at the Assistant or Associate Professor/Staff level. Exceptional candidates at the Professor/Staff level will also be considered. Based in the Lerner Research Institute of the Cleveland Clinic with a primary focus on basic or translational research. M.D., Ph.D., D.V.M. or equivalent degree with postdoctoral training and exceptional promise for an independent career in academic science. We are seeking individuals with a special interest in basic cellular and molecular processes, and/or translational studies. Areas of special interest include, but are not limited to:

- **Lung**
- **Kidney**
- **Pediatric Care**
- **Gastrointestinal**
- **Obesity and Diabetes**
- **Microbiology**
- **Epigenetics**
- **Autism**
- **Environmental Sciences**
- **Nanotechnology**
- **Immunology**

Candidates are expected to establish an innovative, extramurally funded research program and join a collaborative, interdisciplinary group of investigators. Interactions with excellent clinical programs are readily available and provide the potential to develop multi-disciplinary and translational research programs. We offer a strong tradition of collaborative research and established programs for pre- and post-doctoral M.D. and Ph.D. trainees. Outstanding facilities and generous start-up funds are available. Salary will be commensurate with academic credentials and experience.

Interested candidates should contact Ms. Monique Smith at SMITHM30@ccf.org/ The file should include a curriculum vitae, contact information for the references, a statement of research interests, and cover letter addressed to Monique Smith, Search Committee Coordinator, Pediatric Institute, Cleveland Clinic, 9500 Euclid Ave/NC22, Cleveland OH 44195.

Apply directly online at www.clevelandclinic.org/physicianrecruitment

We are proud to be an equal opportunity employer.
Smoke-free/ drug-free environment.

NANYANG TECHNOLOGICAL UNIVERSITY

RISE TO THE OPPORTUNITY

with the world's fastest-rising young university. **NTU.**









Young and research-intensive, Nanyang Technological University (NTU Singapore) is the fastest-rising university in the world's top 50 and ranked 39th globally. NTU is also placed 1st among the world's best young universities and is the No. 1 Asian university in terms of normalised research citation impact (Thomson Reuters InCites 2014).

NTU offers engineering, science, business, humanities, arts and social sciences, and medicine in its joint school with Imperial College London.

The 2016 Elite Nanyang Assistant Professorship
NTU invites outstanding young researchers and exceptional scholars to apply for appointment as a Nanyang Assistant Professor. Up to 10 appointments will be made.

Successful candidates will receive start-up research grant of up to SGD 1million (EUR 690K/ USD 740K/ JPY 88M) and an attractive remuneration package. They will hold tenure track appointments and play lead roles in NTU's multi-disciplinary, integrative research.

Candidates should be below 40 years of age, within 10 years of obtaining their PhD or equivalent degree in their respective field, possess a few years of post-doctoral research experience, and ready to independently lead their own research groups.

For enquiries, email: nanyangprofessorship@ntu.edu.sg

Applications now open
* Apply online at www.ntu.edu.sg/nap
by Friday, 2 Oct 2015, 11:59 P.M. (UTC / GMT +8:00)

* Only online applications will be accepted and only shortlisted applicants will be notified.

www.ntu.edu.sg

TENURE TRACK FACULTY POSITION
DEPARTMENT OF PHYSIOLOGY AT UCLA
(Neuroscience)

Assistant or Associate Professor

The **Department of Physiology** at the **David Geffen School of Medicine at UCLA** invites applications for a tenure track faculty position, preferably at the level of Assistant or Associate Professor.

Candidates interested in any aspect of molecular, cellular, computational or systems neuroscience, including the use of nanotechnology, are encouraged to apply. The Department of Physiology at UCLA has a strong tradition of excellence in molecular biophysics, neuroscience, cardiovascular research, and structural biology in a highly collaborative environment. Candidates must have a Ph.D., M.D. or equivalent and are expected to have a strong track record of research achievements and a demonstrated interest in tackling outstanding biological problems using state-of-the-art approaches. The position comes with generous support, excellent start-up funds and outstanding shared resources at UCLA.

The successful candidate will be expected to develop an independently funded and collaborative research program, and actively participate in the teaching mission of the Department for medical, dental, and graduate students.

Interested candidates should apply on line at UC Recruit:
https://recruit.apo.ucla.edu/apply/JPF01245
Diane Papazian, Ph.D., Search Committee Chair
physio_neuro@mednet.ucla.edu

The University of California is an Equal Opportunity/Affirmative Action Employer. All qualified applicants will receive consideration for employment without regard to race, color, religion, sex, sexual orientation, gender identity, national origin, disability, age or protected veteran status. For the complete University of California nondiscrimination and affirmative action policy see: UC Nondiscrimination and Affirmative Action Policy.

TENURE TRACK FACULTY POSITION
DEPARTMENT OF PHYSIOLOGY AT UCLA
(CARDIOVASCULAR SCIENCE)

Assistant or Associate Professor

The **Department of Physiology** in the **David Geffen School of Medicine at UCLA** invites applications for a tenure track faculty position, preferably at the level of Assistant or Associate Professor.

We are especially interested in candidates with a research focus combining hypothesis-driven and discovery-driven approaches to address cardiovascular physiology and/or pathophysiology. Candidates must have a Ph.D., M.D. or equivalent and are expected to have a strong background in molecular, cellular and/or systems biology including computational approaches and a demonstrated interest in addressing fundamental physiological questions.

The successful candidate will be expected to develop an independent, NIH-funded research program and to participate in the highly collaborative research programs in Physiology and the cardiovascular community at UCLA. S/he will also be a member of the UCLA Cardiovascular Research Laboratory and actively participate in the teaching mission of the Department of Physiology.

Interested candidates should apply on line at UC Recruit:
https://recruit.apo.ucla.edu/apply/JPF01244
Search Committee Chair - physio_cv@mednet.ucla.edu

The University of California is an Equal Opportunity/Affirmative Action Employer. All qualified applicants will receive consideration for employment without regard to race, color, religion, sex, sexual orientation, gender identity, national origin, disability, age or protected veteran status. For the complete University of California nondiscrimination and affirmative action policy see: UC Nondiscrimination and Affirmative Action Policy.

ScienceCareers online @sciencecareers.org



Call for candidates to head a Research Unit in cryo-electron microscopy/tomography at Institut Pasteur in Paris, France

Institut Pasteur is seeking to recruit a mid-career/senior scientist to head a new research unit specialized in cryo-electron microscopy and molecular/cellular cryo-tomography. The successful candidate will establish an independent research unit within the Structural Biology and Chemistry department, focused on the development and application of cutting-edge electron microscopy methods such as high-resolution single particle approaches and/or *in situ* structural biology research (Cryo-electron tomography, correlative light and electron microscopy, novel methods development in cellular cryo-EM, 3D EM methods for quantitative image processing and analysis). Applicants must have a Ph.D. (or equivalent) with significant experience in many aspects of electron microscopy and a record of independent scientific productivity as evidenced by citable publications and external funding.

The successful candidate will conduct research in the field of structural biology in relation to human health, in close interaction with other groups on campus. Research projects bridging the gap between structural and cell biology are strongly encouraged. Active cooperation with existing research units on campus and willingness to contribute to the scientific dynamism of the institute are expected. The group will contribute to maintaining a cryo-EM facility composed of 200kV and 300kV high-end cryo-electron microscopes equipped with direct detection cameras.

Applications will be evaluated on the basis of scientific excellence. A highly attractive package to match the experience of the successful applicant will be provided. Further information on the Institute and on-campus facilities can be found at **http://www.pasteur.fr**

The Application should comprise the following (in order) in a single pdf file:
A brief introductory letter;
A Curriculum Vitae, a list of 10 selected publications and a full publication list;
A description of past and present research activities (up to 3 pages with 1.5 spacing);
The proposed research project (with a title; 4 pages with 1.5 spacing);
The names of 3 scientists from whom letters of recommendation can be sought, together with the names of scientists with a potential conflict of interest from whom evaluations should not be requested.

Applications and requests for information should be addressed to **cryo-em@pasteur.fr** by **September 15, 2015 (5 pm CEST)**. Short-listed candidates will be called for interview which will take place at the end of October, and decisions will be announced by mid-December 2015.

Join the Conversation!

Twitter is a great way to connect with AAAS members and staff about the issues that matter to you most. Be a part of the discussion while staying up-to-date on the latest news and information about your personal member benefits.

Follow us @AAASmember and join the conversation with #AAAS

AAAS MemberCentral
MemberCentral.aaas.org

中国科学院北京基因组研究所
BEIJING INSTITUTE OF GENOMICS CHINESE ACADEMY OF SCIENCES

Faculty Positions: Beijing Institute of Genomics, Chinese Academy of Sciences

Beijing Institute of Genomics (BIG) is one of the leading institutes in genomics research in China. BIG has excellent infrastructures for genomic and bioinformatics research. BIG opens faculty positions of both junior and senior levels.

We seek dynamic individuals with innovative research programs in genomics, bioinformatics, genomic medicine, computational biology, systems biology, evolutionary biology and database construction. The successful candidates for the research group leader positions will be expected to develop novel computational or bioinformatics algorithms and methodologies, and/or to use bioinformatics, and genomics approaches to address fundamental questions in biology and precision medicine. Candidates are expected to develop independent research programs that can complement or integrate with existing research activities at BIG.

Candidates are expected to hold a Ph.D. degree, to have at least three-year postdoctoral research experiences and an outstanding publication record. Senior faculty positions are always open and will be negotiable on an individual basis. The appointment will be at Principal Investigator level. BIG offers a competitive start-up package that includes research funding, supporting staff, and personal benefits. Salary and benefits are competitive and commensurate with experience. More information about BIG can be found at **http://www.big.cas.cn/.**

Interested candidates shall prepare an application package that includes Curriculum Vitae, description of past achievement and proposed future research, copies of three representative publications, and a list of three referees with detailed contact information. All documents should be directed to **fanhy@big.ac.cn**.

Assistant/Associate Professor Faculty Position in Melanoma Research

University of Pittsburgh Cancer Institute

Applications are invited for an Assistant/Associate Professor-level faculty position at the University of Pittsburgh Cancer Institute (UPCI), specifically a scientist with PhD and/or MD working in the area of Melanoma Research. We seek applications from basic scientists developing exciting research programs focusing on the molecular mechanisms of melanoma progression including resistance to targeted therapies and tumor-host interactions using relevant model systems in vitro and in vivo. Recruited investigators will have the opportunity to interact closely with clinicians and scientists within the Melanoma Program. The incumbent will have primary appointment in an appropriate Department in the School of Medicine, University of Pittsburgh.

The University of Pittsburgh, School of Medicine ranks among the top 10 NIH-funded academic medical centers. At UPCI, research faculty and lab personnel have access to state-of-the-art shared facilities with animal care, microscopy, mass spectrometry, high throughput drug discovery, translational research and clinical pharmacology analytical capabilities. The UPCI laboratories and shared resources are located in the Hillman Cancer Center and Magee-Womens Research Institute.

Successful candidates should have a strong publication record and excellent communications skills. Candidates for Associate Professor level position should have a track record of extramurally-supported research grant funding. Salary and benefits will be commensurate with experience.

Applicants should provide a one-page statement of research objectives, curriculum vitae, and contact information for three professional references to:

Dr. Maryann Donovan, PhD, MPH
Associate Director for Research Administration, UPCI
C/O Lola Thompson
5150 Centre Avenue, Suite 532
Pittsburgh, PA 15232
Email: thompsonla3@upmc.edu

The University of Pittsburgh is an Affirmative Action/Equal Opportunity Employer.

leidos
Leidos Biomedical Research, Inc.

Frederick National Laboratory for Cancer Research
RAS Initiative
Postdoctoral Fellowship Opportunities

The Frederick National Laboratory for Cancer Research (FNLCR), operated by Leidos Biomedical Research, Inc., is an integral part of an aggressive national initiative to further scientific understanding of cancers driven by mutations of the RAS family of genes. Established by the National Cancer Institute (NCI), the RAS Initiative seeks to facilitate connections between and among researchers, bringing new ideas and technologies to bear on RAS. We are seeking Postdoctoral Fellows to join Dr. Frank McCormick and the FNLCR RAS Initiative team to work on these projects.

Areas of Interest:

- Analysis of signaling complexes associated with different K-Ras mutants
- Solving structures of oncogenic K-Ras complexed with effectors, regulators and small molecules
- The role of CaM kinase and non-canonical wnt signaling in K-Ras cancers
- Ras dependency in breast cancer and prostate cancer
- The mechanism by which loss of p53 activates Raf kinase

Required:

- Doctoral degree related to pharmaceutical science, medicinal chemistry, or chemistry
- Knowledge of cell biology, signal transduction pathways, or cancer biology

To apply, visit **www.leidosbiomed.com**, and search for ***Postdoctoral Fellow RAS Initiative-FNLCR***.

To learn more about the RAS Initiative, visit **http://www.cancer.gov/research/key-initiatives/ras**.

EGL
Charitable Foundation

The EGL Charitable Foundation
invites you to apply to the

Gruss Lipper Post-Doctoral Fellowship Program

Eligibility

- Israeli citizenship
- Candidates must have completed PhD and/or MD/PhD degrees in the Biomedical Sciences at an accredited Israeli University/Medical School or be in their final year of study
- Candidates must have been awarded a postdoctoral position in the U.S. host research institution.

Details regarding the fellowship are available at www.eglcf.org

NW210508R

GRANTS

2015 Yamada Research Grant

The Yamada Research Grant seeks applications to subsidize creative research in the fields of preventive medicine, environmental protection/apiculture, and specified themes for resolving critical issues through the use of honeybee products such as royal jelly, propolis, honey, bee larvae, bee pollen, or natural supplements such as bilberry and chlorella.

Grant Categories

1) **Preventive Medicine**
Research into preventive medicine to further longevity and improve health and QOL of the elderly.
 i. Grant-in-Aid for Young Scientists (under 45 years)
 Grant amount: 500,000 JPY/grant
 ii. General Research Grant
 Grant amount: (A) 1 million JPY/grant (*in vitro* or *in vivo*)
 (B) 2 million JPY/grant (clinical trial)
 iii. Continuing Research Grant (for previous recipients of the Yamada Research Grant)
 Grant amount: (A) 2 million JPY/grant (*in vitro* or *in vivo*)
 (B) 5 million JPY/grant (clinical trial)
2) **Environmental Protection/Apiculture**
Support for research in the advancement of apiculture.
Grant amount: 1 million JPY/grant
3) **Specified Themes**
Support for research into solutions for urgent and critical issues, with emphasis on supplement usage and/or tailor-made nutrition. This grant is not limited to research into honeybee products.
Grant Amount: (A) 3 million JPY/year, (B) 5 million JPY/year, (C) 10 million JPY/year

Language: English or Japanese
Application period: May 27 — June 30, 2015
Deadline is 17:00 Japan time.

For more information on how to apply, visit
http://www.bee-lab.jp/grant

For inquiries, email the secretariat at research-grant@yamada-bee.com

By **Michelle E. Portman**

You'll be OK

When I entered the workforce, at age 27, my goal was to shape environmental quality and protection in a relatively new country, Israel. My background—a bachelor's degree in political economy of natural resources from the University of California, Berkeley, and a master's degree in urban and regional planning from the Technion-Israel Institute of Technology—led to positions first in government and then at an environmental nongovernmental organization. My work was meaningful and influential, and it supported my husband's studies: He had just finished military service and had no family financial backing. I hoped I would get a chance to go back to school when he finished.

After he finished his degree, my husband left me and our 3-year-old son. I returned to higher paid government work. Soon I moved back to the United States, to what I hoped would be a better job and to be near my family. I wanted to go for a Ph.D., but without financial support or sufficient savings—and worried about raising my son while concentrating on a Ph.D.—I continued for years in a predictable 9-to-5 job. But the work was political and unchallenging, and I watched as many of my co-workers sat at their desks, counting the years, months, or weeks until retirement. I was unhappy. I longed for a job I would love.

One day, I saw an announcement on the bulletin board: "Seeking Ph.D. Students." The state university had opened a part-time public policy program and was recruiting state employees. It was what I was looking for: I could draw on my years of experience in government, and I could join a Ph.D. program and keep working part time. My recent remarriage meant I could afford to reduce my workload. My new partner was supportive.

I applied to the program and got in. I was 39 years old, pregnant with my second child—the first with my new husband—and looking forward to starting my studies in the fall. The pregnancy had no discoverable abnormalities, but when my daughter was 2 weeks old, she started having uncontrollable seizures. By the time I started the program, we were deep into dealing with severe birth defects. They led to a full right hemispherectomy when our baby was 10 months old.

I was on leave from work for most of this time, but I was always studying. I recall sitting at her hospital bed, reading literature and writing papers. Our daughter's prognosis was not good, but I found in my studies not an escape but a vivid alternative that drew me in effortlessly and gave me deep satisfaction.



"I have learned to value all of life's experiences, the ups and the downs."

In time, having arranged myriad therapies for our daughter, I returned to my paid job. I continued my studies. We adopted a second daughter, from Russia. I finished my Ph.D., with distinction. I left government service and started a 2-year fellowship at Woods Hole Oceanographic Institution's (WHOI's) Marine Policy Center. My love of research, writing, and mentoring grew. I published well.

As my WHOI tenure came to a close, I had five on-campus interviews—but it was the economically disastrous year of 2009, and none of those opportunities panned out. So I took another postdoc, at Hebrew University of Jerusalem, which led to my return to my alma mater—Technion—where today I am an assistant professor teaching and researching marine and coastal planning. My job is challenging and rewarding.

I have learned to value all of life's experiences, the ups and the downs. Our daughter will always be significantly handicapped—her rehab from many surgeries was long, and life with half a brain is no cakewalk—but all my children and my husband have brought joy and perspective. At the same time, work—good work that I am excited to wake up to every morning—has been a source of strength on all fronts, personal and professional. Loving what you do and believing it is important won't ensure that everything else is perfect, but if you persist you'll make it through. This is a message I hope to pass on to my students. ■

Michelle E. Portman is an assistant professor at Technion-Israel Institute of Technology in Haifa. For more on life and careers, visit ScienceCareers.org. Send your story to SciCareerEditor@aaas.org.

ILLUSTRATION: ROBERT NEUBECKER

Downloaded from www.sciencemag.org on June 14, 2015

Published by AAAS